Field Measurements and Analysis of Reactive Tropospheric Species Using the FAGE Technique

Hannah Marie Walker

Submitted in accordance with the requirements for the degree of Doctor of Philosophy

The University of Leeds
School of Chemistry

August 2013

The candidate confirms that the work submitted is her own, except where work which has formed part of jointly authored publications has been included. The contribution of the candidate and the other authors to this work has been explicitly indicated below. The candidate confirms that appropriate credit has been given within the thesis where reference has been made to the work of others.

The results of the modelling study presented in Chapter 4 of the thesis have appeared in publication as follows:

Stone, D., Evans, M. J., Walker, H. M., Ingham, T., Vaughan, S., Ouyang, B., Kennedy, O. J., McLeod, M. W., Jones, R. L., Hopkins, J., Punjabi, S., Lidster, R., Hamilton, J. F., Lee, J. D., Lewis, A. C., Carpenter, L. J., Forster, G., Oram, D., Reeves, C. E., Baugitte, S., Morgan, W., Coe, H., Aruffo, E., Dari-Salisburgo, C., Giammaria, F., Di Carlo, P. and Heard, D. E.: *Radical Chemistry at night: comparisons between observed and modelled HO_x, NO_3 and N_2O_5 during the RONOCO project,* Atmospheric Chemistry and Physics Discussions, 13 (4), 9519-9566, 2013

I was responsible for the measurements of OH and HO_2 made during the RONOCO project, along with T. Ingham and D. E. Heard, and for the processing and analysis of the observational data. D. Stone and M. J. Evans were responsible for developing and running the model, interpretation of the modelling results, and comparison of the model results to the measurements. The remaining authors were responsible for measurements of ambient concentrations of various chemical species during the RONOCO project, with which the model was constrained, or to which the model results were compared.

Acknowledgements

I would like to thank my supervisor, Dwayne Heard, for his advice, encouragement, and patience throughout my PhD, and for providing me with the opportunity to be involved in exciting science in wonderful places.

Thanks are due to Trevor Ingham for his friendship and good humour in the laboratory and in the field, and for maintaining perspective when things seemed bleak. I am extremely grateful for the technical help Trev has provided throughout my PhD. Thanks also go to Stewart Vaughan for his patient help at the beginning of my project.

I would like to thank my office mates, past and present, for their friendship, advice, and for providing welcome distractions. Special thanks are due to Daniel Stone for his seemingly limitless patience when teaching me how to use IDL, and for pointing me in the right direction on many occasions.

The field campaigns I took part in were made memorable and enjoyable (not to mention possible) by the scientists, engineers, and crew of the aircraft and the ship. I look forward to meeting them again in the future.

I am very grateful to my family for their constant encouragement and understanding. I am indebted to Ian for his tireless support and his confidence in me.

Statement of Contribution

This research was been carried out by a team that included Dr Trevor Ingham, Dr Stewart Vaughan, Dr Daniel Stone, and myself. The RONOCO and SHIVA field campaigns involved teams of scientists from numerous institutions in the UK, Germany, Malaysia, and Philippines. Where appropriate, the use of data recorded and analysed by members of other institutions has been acknowledged.

My own contributions, fully and explicitly indicated in the thesis, have been as follows: contribution to the installation of the FAGE and LIF instruments onboard the BAe-146 aircraft and the RV *Sonne* at the start of the RONOCO and SHIVA field campaigns, respectively; the calibration of the FAGE and LIF instruments used during the fieldwork; the maintenance and running of the instruments during the two field campaigns; the collection of OH and HO_2 data during the RONOCO flights; analysis and interpretation of the OH and HO_2 data; the collection of IO data during the SHIVA campaign; the installation of the I_2 and HOI + ICl sampling equipment, the timing of the samples, and the sample collection and storage during the SHIVA campaign; processing of the raw IO data into concentration data; analysis and interpretation of the IO, I_2, HOI + ICl data; development of the glyoxal laser-induced phosphorescence instrument; processing and analysis of the glyoxal data.

Dr Trevor Ingham was responsible for: the development of the FAGE and LIF instruments; the preparation of the instruments for fieldwork; the installation of the instruments onboard the BAe-146 research aircraft and the RV *Sonne*; the running and maintenance of both instruments during the field campaigns; development and calibration of the glyoxal laser-induced phosphorescence instrument. Dr Stuart Vaughan was responsible for the processing of the raw OH and HO_2 data collected in the RONOCO and SeptEx flights into concentration data. Dr Vaughan was also responsible for calibration of the FAGE instrument, though the calibration data shown in this thesis are my own work. Dr Daniel Stone was responsible for the collection of OH and HO_2 data during the SeptEx field campaign and contributed to the installation of the FAGE instrument onboard the aircraft at the beginning of the summer and winter RONOCO

campaigns. Dr Stone, along with Prof Matthew Evans (now at the University of York, UK), was also responsible for conducting the box modelling study for analysis of the processes controlling radical chemistry at night during the RONOCO project. Appropriate credit has been given wherever the results of the modelling study have been discussed. The I_2 and HOI + ICl measurements were made possible by the loan of diffusion-denuder tubes from Prof Thorsten Hoffmann (University of Mainz, Germany) and Dr Ru-Jin Huang (now at Paul Scherrer Institute, Switzerland). The samples were analysed by Dr Ru-Jin Huang, who provided concentration data for I_2 and HOI + ICl.

Abstract

Measurements of OH and HO_2 using the Fluorescence Assay by Gas Expansion (FAGE) technique were made during a series of nighttime and daytime flights over the UK in summer 2010 and winter 2011. OH was not detected above the instrument's limit of detection during any of the nighttime flights or during the winter daytime flights, placing upper limits on [OH] of 1.8×10^6 molecule cm^{-3} and 6.4×10^5 molecule cm^{-3} for the summer and winter flights, respectively. HO_2 reached a maximum concentration of 3.17×10^8 molecule cm^{-3} (13.6 pptv) during a nighttime flight on 20th July 2010. Analysis of the rates of reaction of O_3 and NO_3 with the alkenes measured indicates that the summer nighttime troposphere can be as important for the processing of VOCs as the winter daytime troposphere. Analysis of the instantaneous rate of production of HO_2 from the reactions of O_3 and NO_3 with alkenes has shown that, on average, reactions of NO_3 dominated nighttime production of HO_2 during summer, and reactions of O_3 dominated nighttime HO_2 production during winter.

Measurements of IO were made by laser-induced fluorescence (LIF) during a cruise between Singapore and Manila in November 2011. The mean IO mixing ratio was 0.8 pptv. No correlation was found between IO and sea surface temperature, salinity, air temperature, wind speed or concentrations of chlorophyll-*a*. Measurements of I_2 and the sum of HOI + ICl during the cruise contributed to a steady-state analysis of the IO measurements. Production of IO was dominated by photolysis of I_2, with a smaller but significant contribution from photolysis of HOI. Reasonable agreement was found between measurements of IO made by LIF, MAX-DOAS, and satellite-based DOAS.

A laser-induced phosphorescence instrument for detection of glyoxal is in development. The results of initial testing are reported here. The instrument, which will be deployed for field measurements in Cape Verde in 2014, has high sensitivity and a low 1 minute limit of detection (2.5×10^7 molecule cm^{-3} or 6.8 pptv), enabling detection of low ambient mixing ratios of glyoxal.

Table of Contents

List of Abbreviations

1,3,5-TMB	1,3,5-Trimethoxybenzene
2D-GC	2-Dimensional Gas Chromatography
α-CD	α-Cyclodextrin
ACE 2	Aerosol Characterisation Experiment 2
AIC	Activated Iodine Compounds
AMF	Air Mass Factor
AMMA	African Monsoon Multidisciplinary Analysis
APCI/MS/MS	Atmospheric Pressure Chemical Ionisation with 2-Dimensional Mass Spectrometry
ARCTAS	Arctic Research of the Composition of the Troposphere from Aircraft and Satellites
ARL	Air Resources Laboratory, USA
ATHOS	Airborne Tropospheric Hydrogen Oxides Sensor
BBO	Beta Barium Borate
BEARPEX	Biosphere Effects on Aerosols and Photochemistry Experiment
BERLIOZ	Berliner Ozone Experiment
BNC	Berkeley Nucleonics Corporation
BTCA	The British Technical Council for the petroleum and motor industries (calibration gases)
BVOC	Biogenic Volatile Organic Compound
CA	Chemical Amplification
CAM-Chem	Implementation of atmospheric chemistry in the Community Atmosphere Model
CCD	Charge Coupled Detector
CCN	Cloud Condensation Nuclei
CDOM	Chromophoric Dissolved Organic Matter
CE-DOAS	Cavity-Enhanced Differential Optical Absorption Spectroscopy
CFC	Chlorofluorocarbon
CHARLEX	Climate and Halogen Reactivity Tropical Experiment
Chl-*a*	Chlrorophyll-*a*
CI	Criegee Intermediate

CIMS	Chemical Ionisation Mass Spectrometry
CLBO	Cerium Lithium Borate
COBRA	Impact of Combined Iodine and Bromine release on the Arctic Atmosphere
CPM	Channel Photomultiplier
CRDS	Cavity Ring-Down Spectroscopy
CTD	Conductivity, Temperature, Depth
CVAO	Cape Verde Atmospheric Observatory
DLR	Deutsches Zentrum für Luft- und Raumfahrt e.V. (German Aerospace Centre)
DMS	Dimethyl Sulphide
DOAS	Differential Optical Absorption Spectroscopy
DSMACC	Dynamically Simple Model of Atmospheric Chemical Complexity
EASE97	Eastern Atlantic Spring Experiment 1997
ECMWF	European Centre for Medium-Range Weather Forecasts
EU	European Union
FAAM	Facility for Airborne Atmospheric Measurements, UK
FAGE	Fluorescence Assay by Gas Expansion
FLEXPART	Lagrangian particle dispersion model at the Norwegian Institute for Air Research
FSR	Free Spectral Range
FT	Free Troposphere
FWHM	Full Width at Half Maximum
GC	Gas Chromatography
GC/MS	Gas Chromatography coupled with Mass Spectrometry
GFD	Gesellschaft für Flugzieldarstellung mbH, Germany
GLOMAP	Global Model of Aerosol Processes
GTHOS	Ground-based Tropospheric Hydrogen Oxides Sensor
HaloCAST-P	Halocarbon Air Sea Transect - Pacific
HCFC	Hydrochlorofluorocarbon
HIAPER	High-performance Instrumented Airborne Platform for Environmental Research
HIRAC	Highly Instrumented Reactor for Atmospheric Chemistry

HORUS	Hydroxyl Radical Measurement Unit based on Fluorescence Spectroscopy
HO_x	$OH + HO_2$
HPLC	High-Performance Liquid Chromatography
HYSPLIT	Hybrid Single Particle Lagrangian Integrated Trajectory
ICARTT	International Consortium for Atmospheric Research on Transport and Transformation
IDL	Interactive Data Language data visualisation software
IFM-GEOMAR	Leibniz-Institut für Meereswissenschaften, Helmholtz Centre for Ocean Research Kiel, Germany
IN	Ice Nuclei
INTEX-B	Intercontinenal Chemical Transport Experiment, Spring 2006
IO_x	$IO + I$
IPCC	Intergovernmental Panel on Climate Change
IR	Infrared
IUPAC	International Union of Pure and Applied Chemistry
I_x	$I + IO + HI + HOI + 2I_2O_2 + INO_x$
I_xO_y	I_2O_2 and higher iodine oxides
LBO	Lithium Borate
LIF	Laser-Induced Fluorescence
LIFBASE	Spectral Simulation Software
LIP	Laser-Induced Phosphorescence
LIPGLOS	Laser-Induced Phosphorescence of (methyl)GLyOxal Spectrometry
LOD	Limit Of Detection
LOSU	Level Of Scientific Understanding
LP-DOAS	Long-Path Differential Optical Absorption Spectroscopy
MAD-LIP	Madison Laser-Induced Phosphorescence Instrument
MAX-DOAS	Multi-Axis Differential Optical Absorption Spectroscopy
MBL	Marine Boundary Layer
MCM	Master Chemical Mechanism
MCMA 2003	Mexico City Metropolitan Area study 2003
MERIS	Medium Resolution Imaging Spectrometer onboard Envisat Earth Observation Satellite
MIESR	Matrix Isolation Electron Spin Resonance

MIT	Massachusetts Institute of Technology
ML-CEAS	Mode-Locked Cavity-Enhanced Absorption Spectroscopy
MMD	Malaysian Meteorological Department
MODIS	Moderate Resolution Imaging Spectroradiometer
MPI Heidelberg	Max Planck Institute, Heidelberg
MVK	Methyl Vinyl Ketone
NAMBLEX	North Atlantic Marine Boundary Layer Experiment
NAME	Numerical Atmospheric-dispersion Modelling Environment
NASA	National Aeronautics and Space Administration, USA
NBL	Nocturnal Boundary Layer
NCAR	National Center for Atmospheric Research, USA
NCAS	National Centre for Atmospheric Science, UK
NCEP	National Centers for Environmental Prediction, USA
NERC	Natural Environment Research Council, UK
NMVOC	Non-Methane Volatile Organic Compound
NO_{3x}	$NO_3 + N_2O_5$
NOAA	National Oceanic and Atmospheric Administration, USA
NO_x	$NO + NO_2$
NSF	National Science Foundation, USA
OD	Optical Density
ODP	Ozone Depletion Potential
ODS	Ozone-Depleting Substance
ORC^3	Oceanic Reactive Carbon: Climate Impacts
OVOC	Oxidised Volatile Organic Vompound
PARFORCE	New Particle Formation and Fate in the Coastal Environment
PERCA	Peroxy Radical Chemical Amplification
PerCIMS	Peroxy radical Chemical Ionisation Mass Spectrometry
PFBHA	o-(2,3,4,5,6-Pentafluorobenzyl)-hydroxylamine
PM	Particulate Matter
PMT	Photomultiplier Tube
PMTACS-NY	PM2.5 Technology Assessment and Characterisation Study - New York
POA	Primary Organic Aerosol

ppbv	Parts per billion by volume (10^{-9})
ppmv	Parts per million by volume (10^{-6})
pptv	Parts per trillion by volume (10^{-12})
PRF	Pulse Repetition Frequency
PSU	Practical Salinity Units
PTFE	Polytetrafluoroethylene
PTRMS	Proton Transfer Reaction Mass Spectrometry
PUMA	Pollution of the Urban Midlands Atmosphere
RACM	Regional Arctic Climate Model
RAQMS	Realtime Air Quality Modeling System
RF	Radiative Forcing
RH	Relative Humidity
RHaMBLe	Reactive Halogens in the Marine Boundary Layer
RONOCO	Role of Nighttime Chemistry in Controlling the Oxidising Capacity of the Atmosphere
ROXMAS	RO_x Chemical Conversion/Chemical Ionisation Mass Spectrometry
RRS	Royal Research Ship
RSMAS	Rosenstiel School for Marine and Atmospheric Science, USA
RV	Research Vessel
SAPHIR	Simulation of Atmospheric Photochemistry in a Large Reaction Chamber
sccm	Standard cubic centimetres per minute
SCD	Slant Column Density
SCI	Stabilised Criegee Intermediate
SCIAMACHY	Scanning Imaging Absorption Spectrometer for Atmospheric Chartography
SeptEx	September Extension to the RONOCO project
SHIVA	Stratospheric Ozone: Halogen Impacts in a Varying Atmosphere
SLIMCAT	Single Layer Isentropic Model of Chemistry And Transport
slm	Standard litres per minute
SML	Sea Surface Microlayer
SNR	Signal-to-Noise Ratio
SOA	Secondary Organic Aerosol
SOS	Seasonal Oxidant Study

SST	Sea Surface Temperature
SZA	Solar Zenith Angle
TAO	Tropical Atmosphere Ocean program
TexAQS	Texas Air Quality Study
TF-CIMS	Turbulent-Flow Chemical Ionisation Mass Spectrometry
Tg	Teragram, 10^{12} grams
THAMO	Tropospheric Halogen Chemistry Model
TM4-ECPL	Global 3-dimensional chemistry/transport model at the Royal Netherlands Meteorological Institute
TME	2,3-Dimethyl-2-butene
TOMCAT	Toulouse Off-line Model of Chemistry And Transport
TORCH	Tropospheric Organic Chemistry Experiment
TORERO	Tropical Ocean Troposphere Exchange experiment
TROPOS	Leipzig Institute for Tropospheric Research, Germany
TTL	Time-Transistor Logic
TTL	Tropical Tropopause Layer
TUV	Tropospheric Ultraviolet and Visible radiation model
UM	University of Malaya (Kuala Lumpur)
UMS	University of Malaya Sabah
UN-HABITAT	United Nations Human Settlements Programme
UNIMAS	University of Malaya Sarawak
UTC	Coordinated Universal Time
UV	Ultraviolet
VCD	Vertical Column Density
VOC	Volatile Organic Compound
VOCALS-Rex	Variability of the American Monsoon Sytems (VAMOS) Ocean-Cloud-Atmosphere-Land Study Regional Experiment
VSLS	Very Short-Lived Substances
WHO	World Health Organisation

List of Figures

List of Tables

Chapter 1. Introduction

1.1 Motivation for the study of atmospheric chemistry

This chapter gives an introduction to atmospheric chemistry, highlighting the importance of field measurements and modelling studies for improving our understanding of the atmosphere, with particular focus on the chemical species that have been studied in this work. The study of atmospheric chemistry becomes increasingly important as the extent of the irreversible anthropogenic impact on Earth's climate is revealed. World leaders are under increasing pressure to take action to limit the impacts of climate change, for example by reducing emissions of greenhouse gases, and their decisions are informed by mathematical models of future climate scenarios. These global models make use of measurements of physical and chemical properties of the atmosphere. More than half of the global population now lives in urban regions (WHO and UN-HABITAT, 2010), and the quality of air in these regions has severe impacts on human health. Urban air contains gaseous and particulate emissions from vehicle exhausts and industrial processes, exposure to which causes disease. Chemical processing of these atmospheric constituents leads to production of many other gas- and aerosol-phase species with impacts on human health and the climate. The rapid increase of the number of people living in cities is expected to be the one of the most important global health issues of the 21st century (WHO and UN-HABITAT, 2010). As with projections of future climate change, future air pollution events and effective measures to improve air quality are investigated using mathematical models of the atmosphere, constrained by observations of atmospheric constituents and laboratory studies of rate constants. Air pollution is exacerbated by climate change (Campbell-Lendrum and Corvalán, 2007) so that the two issues are closely linked. For both of these issues, the combination of modelling, observations, and laboratory studies is the key to understanding the complex chemical system and to making accurate predictions about the future. These are the motivations for making observations of key chemical species in the atmosphere.

This thesis presents field measurements and analysis of the gas-phase radical species OH, HO_2, and IO, and describes the development of an instrument for measurement of glyoxal (CHOCHO). The importance of each of these species in atmospheric chemistry is discussed in this chapter. Chapter 2 describes techniques for the measurement of OH and HO_2, and describes in detail the instrument used in this work. Similarly, Chapter 3 discusses techniques for the measurement of IO, again focussing on the instrument used in this work. The study of processes controlling the nighttime concentrations of OH and HO_2, and important oxidative mechanisms in the nighttime troposphere, are the subject of Chapter 4. Chapter 5 describes results and analyses from a scientific cruise in the South China Sea, including measurements of IO and its precursors I_2, HOI and ICl. Chapter 6 describes the development of a new instrument for measurements of glyoxal, which will be deployed during a field campaign in 2014.

1.1.1 Climate change

Earth's global mean temperature at the surface is controlled by the balance of incoming and outgoing radiation through reflection, absorption, and emission processes within the atmosphere and at the surface. Changes in greenhouse gases, aerosols, solar radiation, and land surface properties affect these processes and therefore the radiation balance. Measurements of the global mean temperature taken over the last 150 years have shown an increase of approximately 0.8º C since 1850, with the most rapid temperature rise occurring in the last 50 years. This trend, referred to as global warming, has been largely attributed to the increased emission of the anthropogenic greenhouse gas carbon dioxide (CO_2), which has resulted from the increased use of fossil fuels. Smaller contributions are made by methane (CH_4), nitrous oxide (N_2O), halocarbons, and ozone (O_3), and there is a contribution from natural factors such as solar irradiance (Solomon *et al.*, 2007). Figure 1.1 shows the global impact of these factors and others in terms of radiative forcing, where negative values indicate cooling and positive values indicate warming. Large uncertainties are associated with the radiative forcing caused by individual factors, in particular the direct and indirect effects of aerosols, and with the overall effect.

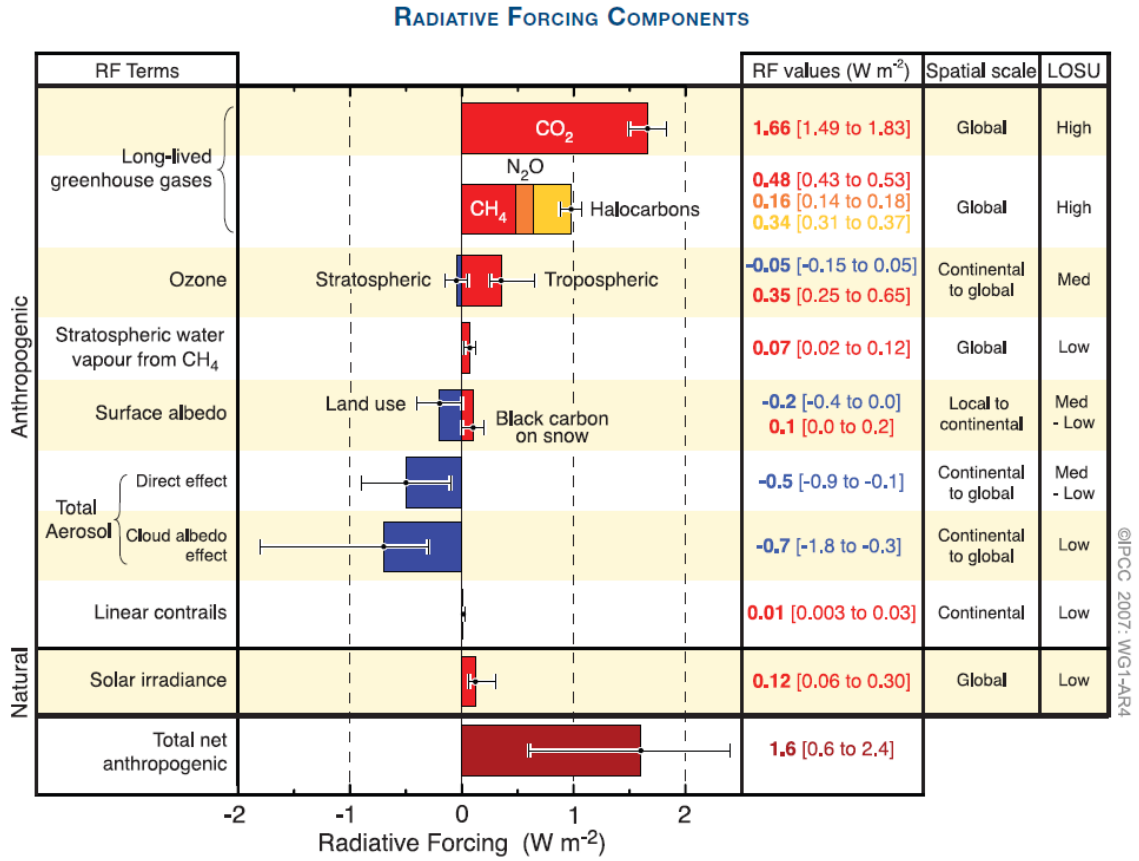

Figure 1.1. Global average radiative forcing (RF) estimates and ranges in 2005 for important atmospheric constituents, with the spatial scale of the forcing and the level of scientific understanding (LOSU) indicated at the right hand side of the figure. Total net anthropogenic forcing is shown at the bottom of the figure. Figure from 2007 IPCC report (Solomon *et al.*, 2007).

Observations of atmospheric constituents, laboratory studies, and modelling studies are the key to reducing these uncertainties. There is now very high confidence that the net effect of human activity since 1750 has been warming at the surface (Solomon *et al.*, 2007). The net anthropogenic radiative forcing is equal to 1.6 W m^{-2}, with the range of predicted values being 0.6–2.4 W m^{-2}. The impacts of a warming climate on life on Earth are serious and wide-ranging (*e.g.* sea level rise, drought, floods, changing seasonality, loss of habitat, species extinction, food shortage, decreased availability of drinking water, increased occurrence of infectious disease) (Bernstein *et al.*, 2007, Diffenbaugh and Field, 2013, Wheeler and von Braun, 2013). It is vital that measures are taken to reduce emissions of greenhouse gases in order to minimise future climate change, but the economic impacts associated with reducing emissions act as a deterrent to measures being introduced. Accurate knowledge of the future course of climate

change and its effects are required in the decision-making process. Model projections of future climate change are based on a number of different emission scenarios, in which emissions or concentrations of greenhouse gases are maintained at the current level, are reduced, or are increased according to a range of economic and demographic forecasts. For several of these scenarios, the global mean temperature is predicted to rise by 0.2º C over the next 20 years, and warming is likely to continue for centuries even if greenhouse gas concentrations are stabilised at the current level (Solomon *et al.*, 2007). The prediction of the overall response of the global climate to radiative forcing is complicated by numerous feedback systems, the largest of which is the increase in the atmospheric concentration of water vapour (the strongest greenhouse gas) with increasing temperature. Another example is the reduced uptake of CO_2 by land and oceans with increasing temperature (Solomon *et al.*, 2007).

Accurate prediction of the strength and impact of these feedbacks requires knowledge of a complex system of chemical and physical processes. Key uncertainties in the climate system are the roles played by clouds, the cryosphere, oceans, land use, and the coupling between climate and biogeochemical cycles. Our understanding of climate change and our ability to predict the properties of the future climate are improved by the number of model simulations available, model complexity and realism, and by increasing the number, quality, and spatial extent of field measurements of the drivers and effects of climate change (Solomon *et al.*, 2007).

1.1.2 Air quality

Atmospheric constituents such as SO_2, NO_x ($NO + NO_2$), CO, O_3, volatile organic compounds (VOCs), and airborne particles have adverse effects on human health. Air pollution is generally worst in areas with emissions from motorised vehicles and from industry, since the above constituents are primarily produced in combustion of fossil fuels. Measures are taken to reduce the levels of these compounds to safe limits in areas of human habitation, but the limits are often exceeded in large, densely populated urban regions (*e.g.* Baldasano *et al.*, 2003, Molina *et al.*, 2007, Streets *et al.*, 2007). Air pollutants can be emitted directly from sources (primary pollutants, *e.g.* SO_2 and particulate elemental carbon), or can be formed by reaction of precursor compounds

(secondary pollutants, *e.g.* ozone). SO_2, NO_x, and CO are released in the combustion of fossil fuels in power stations and vehicle engines. The majority of NO_x is emitted as NO, with the main source of NO_2 being oxidation chemistry (see section 1.2). The main urban source of VOCs is evaporation from fuel tanks, such as benzene from motor vehicles, or methane from natural gas storage and transport. Ground-level ozone has three sources: stratospheric air, background chemistry (hemispheric scale), and local and regional ozone formation (see section 1.2.3). Local and regional ozone formation depends on the presence of NO_x and VOCs, which are typically highest in urban regions. The geographical scale of ozone production can range from a city (*e.g.* Los Angeles) to a continent (*e.g.* western Europe) (WHO, 2006).

Airborne particulate matter (PM) consists of sulphate (SO_4^{2-}), nitrate (NO_3^-), organic carbon (low-volatility oxidised organic compounds), elemental carbon, mineral dust, and sea salt. Sulphate, nitrate, and organic carbon are produced by oxidation of SO_2, NO_x, and non-methane volatile organic compounds (NMVOCs). Elemental carbon particles (soot) are emitted directly by combustion. In addition, oxidation of biogenic volatile organic compounds (BVOCs, such as isoprene and terpenes) produces low-volatility oxidised organic compounds that contribute to the formation of secondary organic aerosols. Mineral dust is injected into the atmosphere by weathering of land surfaces by wind, and airborne sea-salt is formed in bubble bursting at the sea surface (Lewis and Schwartz, 2004).

Air quality is dependent on local and regional weather, and is therefore sensitive to climate change. Surface ozone concentrations in polluted regions are predicted to increase with increasing temperature, while the background ozone concentration is predicted to decrease as atmospheric water vapour concentrations increase. The effects of climate change on particulate matter are less clear, but the main sink for PM is uptake in rain droplets, so changes in weather patterns will certainly affect PM concentrations (Jacob and Winner, 2009).

Emission inventories of primary pollutants, combined with knowledge of local, regional, and global meteorology, feed into model predictions of air quality. For secondary pollutants, the emission of their precursors and the processes leading to their

formation must be considered in order to make model predictions of their concentrations in specific regions (WHO, 2006). Ozone, sulphate particles, $PM_{2.5}$, and black carbon particles have atmospheric lifetimes of days or weeks, so that long-range transport processes can distribute them on continental scales (WHO, 2006). Long-lived components of air pollution, such as CO, have atmospheric lifetimes of years, so that they can be transported around the globe. The impacts of air pollution are therefore wide-ranging and are not confined to the emission region. It is vital to know how the components of air pollution are processed, in order that accurate predictions can be made about future air pollution events, and so that measures can be taken to effectively reduce air pollution. Oxidation is the most important removal mechanism for many pollutants (VOCs) but can lead to the production of ozone in polluted (high NO_x and high VOC) environments. The production of ozone is discussed further in section 1.2.3. The following section features a discussion of key aspects of tropospheric oxidation chemistry.

1.2 Tropospheric chemistry of the OH radical

The troposphere is the lowermost layer of Earth's atmosphere, extending from the surface to a height of between 7 and 20 km depending on latitude and season. Within the troposphere is the boundary layer, a shallow layer immediately above Earth's surface characterised by turbulent mixing of atmospheric constituents. Many of the gas-phase species emitted at the surface (including greenhouse gases, air pollutants, and biogenic compounds) undergo chemical and physical processing in the troposphere that leads to their conversion to inert species, such as CO_2, and their physical removal through, for example, deposition to solid surfaces. Oxidation is crucial in this chemical processing scheme, with the hydroxyl radical (OH) being the most important tropospheric oxidant (Forster *et al.*, 2007). The concentration of OH determines the oxidation capacity of the atmosphere, i.e. the rate at which trace gases are oxidised and removed. The atmospheric lifetime of methane (12 years, Solomon *et al.*, 2007), the most abundant hydrocarbon in the atmosphere and the second most important anthropogenic greenhouse gas, is determined predominantly by its reaction with OH ($k = 6.3 \times 10^{-15}$ cm^3 molecule^{-1} s^{-1} at 298 K) (Sander *et al.*, 2011). 80 % of methane removal occurs *via* reaction with OH in the tropical troposphere, where high

concentrations of water vapour and high solar irradiance lead to high daytime concentrations of OH (Bloss *et al.*, 2005). OH reacts with numerous atmospheric trace gases, including volatile organic compounds (VOCs), CO, SO_2, and with long-lived anthropogenic halogenated compounds (see section 1.4), and is therefore responsible for the removal of greenhouse gases and air pollutants from the troposphere.

1.2.1 Daytime production of OH

During the day, primary production of OH (i.e. initialisation of the radical chain) occurs predominantly *via* photolysis of ozone at $\lambda \leq 340$ nm, yielding an excited oxygen atom, $O(^1D)$. The majority of $O(^1D)$ produced is quenched by collision with O_2 and N_2 to form ground-state $O(^3P)$, which reacts with O_2 to reform O_3 (Levy, 1971) as follows:

$$O_2 + h\nu \xrightarrow{\lambda \leq 340\ \text{nm}} O(^1D) + O_2 \quad \text{(R1.1)}$$

$$O(^1D) + N_2 \rightarrow O(^3P) + N_2 \quad \text{(R1.2)}$$

$$O(^1D) + O_2 \rightarrow O(^3P) + O_2 \quad \text{(R1.3)}$$

$$O(^3P) + O_2 + M \rightarrow O_3 + M \quad \text{(R1.4)}$$

Approximately 10 % of the $O(^1D)$ formed in reaction (R1.1) (Levy, 1971) reacts with water vapour to form two OH radicals:

$$O(^1D) + H_2O \xrightarrow{k_{O^1D+H_2O}} OH + OH \quad \text{(R1.5)}$$

where $k_{O^1D+H_2O}$ = 2.0×10^{-10} cm^3 molecule^{-1} s^{-1} at 298 K (Sander *et al.*, 2011).

1.2.2 OH-initiated oxidation and radical recycling

Some important features of OH reactivity can be illustrated with the reaction scheme for CO and CH_4:

$$OH + CO \rightarrow H + CO_2 \quad \text{(R1.6)}$$

$$H + O_2 + M \rightarrow HO_2 + M \quad \text{(R1.7)}$$

$$OH + CH_4 \rightarrow H_2O + CH_3 \quad \text{(R1.8)}$$

$$CH_3 + O_2 + M \rightarrow CH_3O_2 + M \quad \text{(R1.9)}$$

The hydroperoxy radical, HO_2, is closely linked to OH through rapid interconversion reactions. Together OH and HO_2 form the HO_x family. CH_3O_2 is the methyl peroxy radical, and is the simplest and often the most abundant organic peroxy radical (RO_2) in the troposphere. In the presence of NO_x (NO_2 + NO), HO_2 and RO_2 react as follows:

$$HO_2 + NO \rightarrow OH + NO_2 \quad \text{(R1.10)}$$
$$RO_2 + NO \rightarrow RO + NO_2 \quad \text{(R1.11)}$$
$$RO_2 + NO_2 + M \rightarrow RO_2NO_2 + M \quad \text{(R1.12)}$$
$$RO + O_2 \rightarrow R'O + HO_2 \quad \text{(R1.13)}$$

where RO is an organic alkoxy radical, RO_2NO_2 is a peroxy nitrate, and R′O is a carbonyl species (CH_3O, $CH_3O_2NO_2$, and HCHO, respectively, in the case of CH_4 oxidation). At very low concentrations of NO_x, for example in pristine marine air, the loss of HO_2 and RO_2 is dominated by their self-reaction:

$$RO_2 + HO_2 \rightarrow ROOH + O_2 \quad \text{(R1.14)}$$
$$HO_2 + HO_2 \rightarrow H_2O_2 + O_2 \quad \text{(R1.15)}$$
$$RO_2 + RO_2 \rightarrow RO + RO + O_2 \quad \text{(R1.16)}$$
$$\rightarrow ROOR + O_2 \quad \text{(R1.17)}$$
$$\rightarrow ROH + R'O + O_2 \quad \text{(R1.18)}$$

where ROOH is a hydroperoxide, ROOR is an organic peroxide, and ROH is an alcohol species. In clean air, reactions (R1.14), (R1.15), and (R1.16), along with the reaction of OH with HO_2, are the dominant radical termination reactions.

$$OH + HO_2 \rightarrow H_2O + O_2 \quad \text{(R1.19)}$$

Under high NO_x conditions, radical termination occurs primarily through the reaction of OH with NO_2, with smaller contributions from the reactions of OH and HO_2 with NO:

$$OH + NO + M \rightarrow HONO + M \quad \text{(R1.20)}$$
$$OH + NO_2 + M \rightarrow HNO_3 + M \quad \text{(R1.21)}$$
$$HO_2 + NO + M \rightarrow HNO_3 + M \quad \text{(R1.22)}$$

Formation of HNO_3 is an important loss mechanism for both HO_x and NO_x since HNO_3 is removed from the atmosphere by dry or wet deposition (Wurzler *et al.*, 1995,

Bytnerowicz and Fenn, 1996). HO_2 is also lost by heterogeneous uptake to aerosol, and this mechanism is known to be an important HO_x sink in some environments, especially the clean marine boundary layer and polar regions (*e.g.* Sommariva *et al.*, 2004, Haggerstone *et al.*, 2005, Mao *et al.*, 2010, Whalley *et al.*, 2010, Edwards *et al.*, 2011). Heterogeneous uptake of HO_2 is predicted to have significant regional impacts on concentrations of HO_x and O_3 (Martin *et al.*, 2003, Thornton *et al.*, 2008, Macintyre and Evans, 2011, Mao *et al.*, 2013). However, the HO_2 uptake coefficient (the probability that a molecule impacting an aerosol surface undergoes irreversible reaction) is not well quantified, and is the subject of numerous laboratory studies (*e.g.* Thornton and Abbatt, 2005, Taketani *et al.*, 2008, Bedjanian *et al.*, 2013, George *et al.*, 2013). Uptake of OH to organic aerosols is known to occur but loss of OH through this channel is negligible compared to the much faster gas-phase reactions (Abbatt *et al.*, 2012).

Photolysis of formaldehyde (HCHO), peroxides (H_2O_2, CH_3OOH), and nitrous acid (HONO) are known to be important sources of OH and HO_2 under certain conditions, particularly in polluted and low photolysis environments (*e.g.* Emmerson *et al.*, 2005, Dusanter *et al.*, 2009, Volkamer *et al.*, 2010) (wavelength thresholds from Sander *et al.*, 2011):

$$HCHO + h\nu \xrightarrow{\lambda \leq 330\ nm} HCO + H \quad \text{(R1.23)}$$

$$HCHO + h\nu \xrightarrow{\lambda \leq 361\ nm} H_2 + CO \quad \text{(R1.24)}$$

$$HCO + O_2 + M \rightarrow HO_2 + CO + M \quad \text{(R1.25)}$$

$$H + O_2 + M \rightarrow HO_2 + M \quad \text{(R1.7)}$$

$$HONO + h\nu \xrightarrow{\lambda \leq 579\ nm} OH + NO \quad \text{(R1.26)}$$

$$H_2O_2 + h\nu \xrightarrow{\lambda \leq 557\ nm} OH + OH \quad \text{(R1.27)}$$

$$CH_3OOH + h\nu \xrightarrow{\lambda \leq 645\ nm} CH_3O + OH \quad \text{(R1.28)}$$

The reactions of NO_3 and O_3 with alkenes are also sources of OH and HO_2 in low photolysis or dark environments. These reactions are discussed in detail in section 1.2.5. The OH-initiated oxidation mechanism can proceed as far as production of CO_2 and H_2O, but stable oxidised intermediates (oxidised volatile organic compounds, OVOCs) may be removed from the atmosphere by dry deposition onto surfaces such as soil, plant

leaves, or water, or by wet deposition onto aerosols, clouds and rain droplets. Figure 1.2 shows a simplified reaction scheme of the HO_x radical and VOC oxidation cycle.

1.2.3 Production of tropospheric ozone

The recycling of OH and production of NO_2 in reactions (R1.10) and (R1.11) are key features of the oxidation process. Photolysis of NO_2 at $\lambda < 398$ nm (Sander *et al.*, 2011) yields $O(^3P)$:

$$NO_2 + h\nu \xrightarrow{\lambda < 398\ \text{nm}} NO + O\left(^3P\right) \qquad \text{(R1.29)}$$

Reaction (R1.29), followed by reaction (R1.4), is the only known chemical mechanism for production of ozone in the troposphere (Chameides and Walker, 1973, Crutzen, 1973, Ehhalt, 1999). Production of O_3 is vital to the propagation of the radical chain since it is the primary daytime source of OH, but tropospheric ozone is also a pollutant, being harmful to human health, and is a greenhouse gas. In low NO_x environments the reactions of OH and HO_2 with O_3 form a HO_x interconversion mechanism, and the dominant non-photolytic mechanism for loss of tropospheric O_3 (Jacob, 2000):

$$OH + O_3 \rightarrow HO_2 + O_2 \qquad \text{(R1.30)}$$

$$HO_2 + O_3 \rightarrow OH + 2O_2 \qquad \text{(R1.31)}$$

$$\text{Net: } 2O_3 \rightarrow 3O_2 \qquad \text{(R1.32)}$$

In polluted environments, with high concentrations of NO_x and VOCs, OH-initiated oxidation leads to production of RO_2, conversion of NO to NO_2, and production of ozone (reactions (R1.10), (R1.11), and (R1.29)). This regime can be limited by the concentration of NO or by the concentration of VOCs (Sillman, 1993). In a low NO_x environment the reactions of OH and HO_2 with O_3 (reactions (R1.30) and (R1.31)) dominate over the reactions of HO_2 and RO_2 with NO, so ozone is destroyed. The balance of O_3 production versus O_3 destruction is determined by the concentrations of NO_x and VOCs. Reducing concentrations of tropospheric ozone therefore requires a detailed understanding of the HO_x radical budget, the oxidation chain, and the interplay between NO_x and VOC-limited regimes.

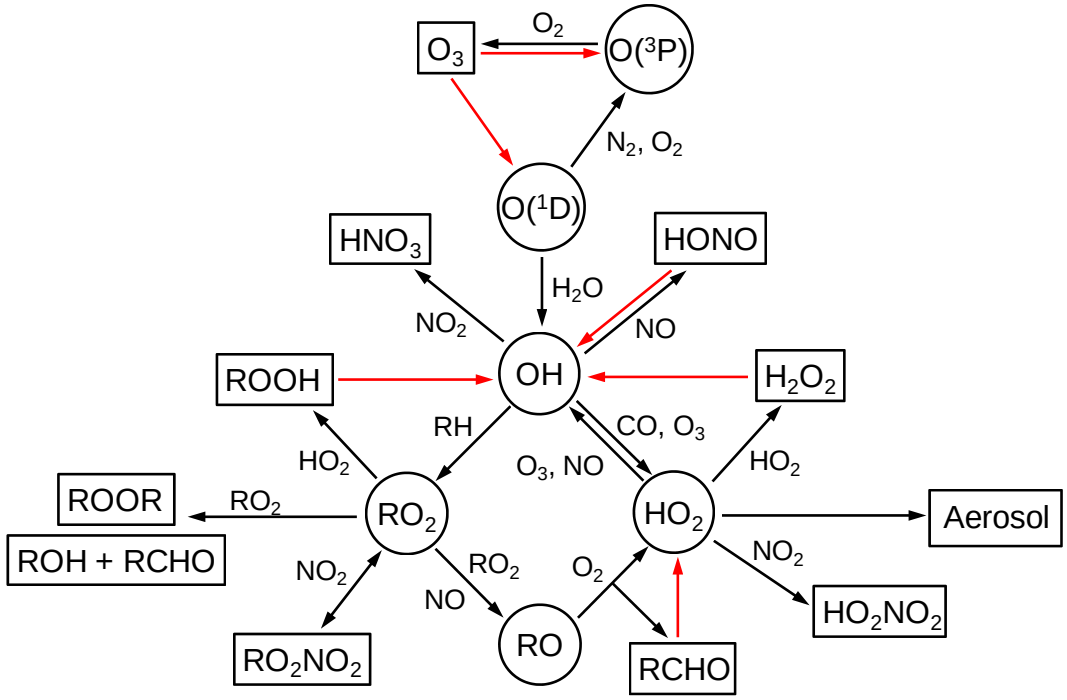

Figure 1.2. Simplified schematic representation of the HO_x reaction cycle. Red arrows indicate photolysis. Adapted from Stevens *et al.* (1997) and Smith (2007).

1.2.4 Production and importance of secondary organic aerosol

Aerosols affect Earth's radiation balance directly, by reflecting incoming radiation, and indirectly, by acting as cloud condensation nuclei (CCN) and ice nuclei (IN). The radiative forcing associated with aerosols is currently a source of large uncertainty in climate modelling (see section 1.1.1). Organic aerosol constitutes a significant fraction of fine particulate matter ($PM_{2.5}$) that has adverse effects on human health (see section 1.1.2). Organic aerosol may be emitted directly, or may form from the oxidation products of anthropogenic and biogenic VOCs. These two components are referred to as primary organic aerosol (POA) and secondary organic aerosol (SOA), respectively. SOA may form by uptake of OVOCs onto existing inorganic particles, or by new particle formation from clusters of very low volatility oxidation products followed by growth by further uptake of OVOCs (Zhang *et al.*, 2004, Laaksonen *et al.*, 2008). SOA can constitute a substantial fraction of total organic particulate matter in both forested and polluted regions, depending on season and location (de Gouw *et al.*, 2005, Yu *et al.*,

2007). In polluted regions SOA forms mainly from the oxidation products of anthropogenic VOCs and OVOCs, emitted from fuel processing, transport, and storage facilities, from motor vehicles, and from industrial processes (Dechapanya *et al.*, 2004, de Gouw *et al.*, 2005). The OH- and ozone-initiated oxidation of BVOCs emitted in forested regions, such as isoprene (C_5H_8), monoterpenes ($C_{10}H_{16}$, *e.g.* α-pinene), and sesquiterpenes ($C_{15}H_{24}$) leads to formation of oxidised products with sufficiently low vapour pressure that they will partition between the gas and aerosol phase (Kanakidou *et al.*, 2005, Carlton *et al.*, 2009). In some regions there is a contribution from both anthropogenic and biogenic VOCs (*e.g.* Shilling *et al.*, 2013).

Marine aerosol has the potential for large-scale direct radiative forcing effects, and strongly affects the properties and lifetime of stratiform clouds (O'Dowd and De Leeuw, 2007, Gantt *et al.*, 2009). Clouds over oceans are believed to be more susceptible to changing concentrations of CCN or IN than clouds over land, so the indirect aerosol effect is possibly stronger over oceans than over land (Lohmann and Feichter, 2005). While marine aerosol is largely composed of primary components such as sea salt particles and organic compounds from the sea surface (Facchini *et al.*, 2008), there is a contribution from secondary organic aerosol (*e.g.* Charlson *et al.*, 1987, Vaattovaara *et al.*, 2006, O'Dowd and De Leeuw, 2007, Rinaldi *et al.*, 2010). BVOCs emitted from the sea surface, and their oxidation products, can form new particles and can condense onto pre-existing particles. The well-documented role of iodine oxides in new particle formation is discussed in section 1.4.1.4. Dimethyl sulphide (DMS), produced by phytoplankton, is emitted from the ocean surface and oxidised by OH to form SO_2 and methane sulphonate, which constitute a large part of oxidised marine aerosol (Charlson *et al.*, 1987). It has been proposed that oxidation of atmospheric isoprene, produced by phytoplankton and emitted from the sea surface, leads to enhanced production of aerosol and CCN (Meskhidze and Nenes, 2006), but the global contribution from marine isoprene is predicted to be negligible (Arnold *et al.*, 2009, Gantt *et al.*, 2009). However, model calculations imply a missing source of marine SOA, which may be attributable to isoprene oxidation products (Anttila *et al.*, 2010). The significance of the SOA fraction of total marine aerosol therefore remains uncertain, making measurements and modelling of oxidation processes of marine organic compounds an important area

of study. Section 1.6 of this chapter discusses the role of oceanic reactive carbon in the context of the present work.

The rate of formation and concentrations of SOA in the terrestrial and marine boundary layer and free troposphere are generally underestimated by models (*e.g.* de Gouw *et al.*, 2005, Heald *et al.*, 2005, Volkamer *et al.*, 2006). Estimates of SOA formation can be based on emission rates of SOA precursors and predicted aerosol yields, requiring knowledge of the gas-phase photochemical oxidation of the precursors (Dechapanya *et al.*, 2004). Given the uncertainty associated with the radiative forcing effects of aerosols, their impact on air quality, and the underestimation of the rate of production and concentration of SOA in various regions of the troposphere, field measurements and modelling of the oxidation of anthropogenic and biogenic VOCs remain important.

1.2.5 Nocturnal tropospheric HO_x chemistry

The production of OH through photolysis of ozone (and other species at longer wavelengths) is limited to daylight hours, and oxidation of trace gases at night must proceed through alternative mechanisms. Two mechanisms are known to initiate HO_x radical chemistry at night: ozonolysis of alkenes, and reactions of the nitrate radical, NO_3, with alkenes. Ozonolysis of alkenes is known to occur throughout the troposphere, and has been shown to be an important source of OH and HO_2 during the day and at night (Paulson and Orlando, 1996, Donahue *et al.*, 1998, Kanaya *et al.*, 1999, Salisbury *et al.*, 2001, Geyer *et al.*, 2003, Ren *et al.*, 2003b, Ren *et al.*, 2006, Sommariva *et al.*, 2007). NO_3 reacts with a range of species in the troposphere, and its reaction with alkenes is known to be an important nighttime oxidation mechanism (Salisbury *et al.*, 2001, Geyer *et al.*, 2003, Sommariva *et al.*, 2007, Emmerson and Carslaw, 2009, Brown *et al.*, 2011).

1.2.5.1 Alkene ozonolysis

Figure 1.3 shows a schematic of the reaction of ozone with a generic alkene. Reactions of ozone with alkenes occur *via* addition of ozone to the double bond to form a five-membered ring called a primary ozonide. The primary ozonide decomposes to form two pairs of products, each pair consisting of a carbonyl compound and a vibrationally- and

rotationally-excited carbonyl oxide biradical called a Criegee intermediate (CI) (R_2COO):

$$O_3 + R_2C{=}CR_2 \rightarrow R_2C[OOO]CR_2 \quad \text{(R1.33)}$$

$$R_2C[OOO]CR_2 \rightarrow R_2COO + R_2CO \quad \text{(R1.34)}$$

The Criegee intermediate is known to be an important source of HO_x in low photolysis environments with substantial concentrations of unsaturated VOCs, as evidenced by elevated concentrations of OH in winter urban atmospheres (*e.g.* Heard *et al.*, 2004, Harrison *et al.*, 2006). The simplest gas-phase CI, CH_2OO, has been observed directly by photoionisation mass spectrometry (Taatjes *et al.*, 2008, Welz *et al.*, 2012). A small fraction of the excited CI produced in reaction (R1.34) is stabilised by collision with surrounding molecules, while the majority undergoes unimolecular reaction (isomerisation, decomposition) (Johnson and Marston, 2008). Stabilised Criegee intermediates (SCIs) are also known to react with H_2O, NO_2, and SO_2 and various organic compounds (Calvert *et al.*, 1978, Su *et al.*, 1980, Becker *et al.*, 1993, Neeb *et al.*, 1997, Welz *et al.*, 2012). Alkyl-substituted excited CIs can isomerise to form an excited hydroperoxide, which quickly dissociates to produce OH or H, and subsequently HO_2 (reaction (R1.35)) (Paulson and Orlando, 1996, Kroll *et al.*, 2001, Johnson and Marston, 2008).

$$R_2COO \rightarrow R'RCOOH \rightarrow R'RCO + OH \quad \text{(R1.35)}$$

OH formation from ethene ozonolysis has been ascribed to decomposition of a hot carboxylic acid product formed in the rearrangement of the CI (Kroll *et al.*, 2002). The yield of OH from ozonolysis of alkenes that form methyl-substituted CIs, (*e.g.* 0.64 for *trans*-2-butene) is significantly greater than from unsubstituted CIs (*e.g.* 0.13 for ethene) (Johnson and Marston, 2008).

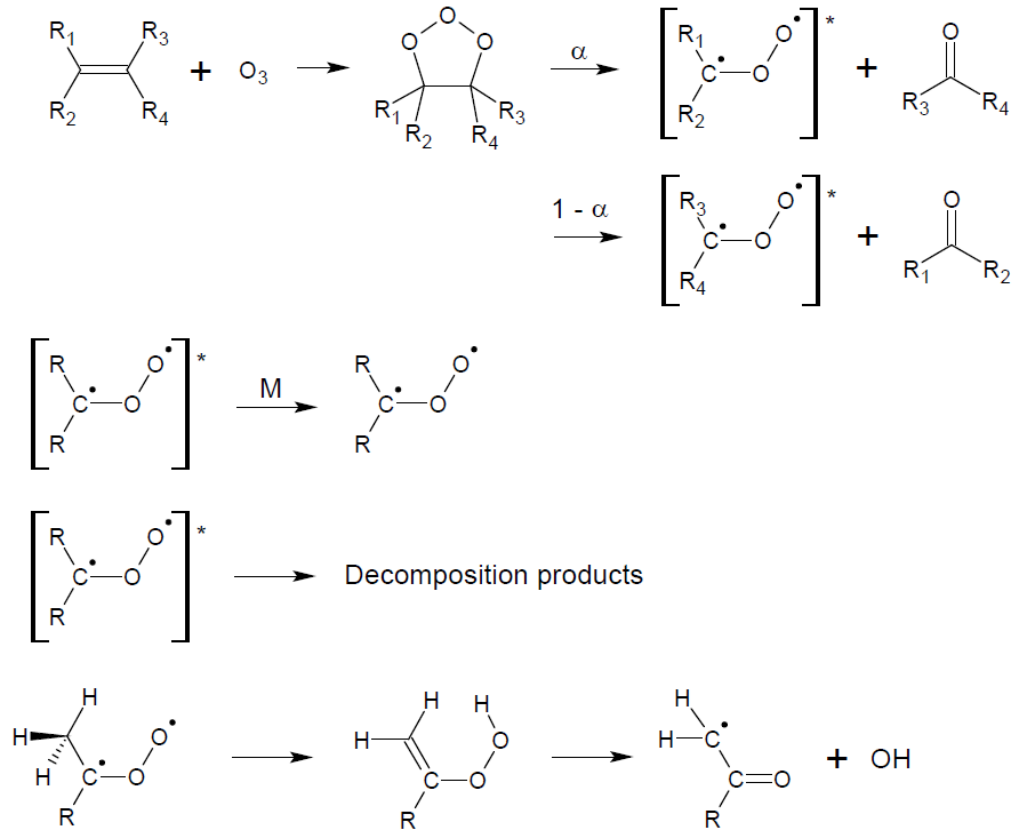

Figure 1.3. Schematic representation of the reaction of O_3 with a generic alkene, leading to formation of OH. Redrawn from Salisbury *et al*. (2001).

It should also be noted that there is experimental evidence for the formation of OH from SCIs, though the decomposition of SCIs occurs on a much longer timescale than the decomposition of excited CIs (Kroll *et al.*, 2001). The decomposition of SCIs is postulated to occur in the inlet and detection cells of some FAGE instruments, causing an interference in measurements of OH and HO_2 (Mao *et al.*, 2012) (see Chapter 2). This interference has been used to detect what is postulated to be SCI in forested environments (Novelli, 2012). The OH produced through each of these mechanisms will go on to oxidise other VOC species.

1.2.5.2 Reaction of NO_3 with alkenes

NO_3 is formed primarily by reaction of NO_2 with ozone, and exists in thermal equilibrium with N_2O_5. Fast interconversion between N_2O_5 and NO_3 means that these radicals are collectively referred to as NO_{3x}:

$$NO_2 + O_3 \rightarrow NO_3 + O_2 \quad \text{(R1.36)}$$

$$NO_2 + NO_3 + M \leftrightarrow N_2O_5 + M \quad \text{(R1.37)}$$

Heterogeneous reaction of N_2O_5 with water vapour, and the subsequent dissolution of HNO_3 in cloud droplets is an important removal mechanism for NO_3:

$$N_2O_5 + H_2O \rightarrow 2HNO_3 \quad \text{(R1.38)}$$

NO_3 is also lost by fast reaction with NO ($k = 1.5 \times 10^{-11}$ cm^3 molecule^{-1} s^{-1}) (Sander *et al.*, 2011), which means that NO_3 and NO are not simultaneously present in the atmosphere at significant concentrations (Atkinson and Arey, 2003):

$$NO_3 + NO \rightarrow 2NO_2 \quad \text{(R1.39)}$$

NO_3 is present in significant concentrations only at the night because it is quickly photolysed during the day (j_1 = 0.156 s^{-1}, j_2 = 0.0201 s^{-1}) (Johnston *et al.*, 1996) yielding NO or NO_2:

$$NO_3 + h\nu \xrightarrow{j_1} NO_2 + O(^3P) \quad \text{(R1.40)}$$

$$NO_3 + h\nu \xrightarrow{j_2} NO + O_2 \quad \text{(R1.41)}$$

Figure 1.4 shows a schematic of the reaction between NO_3 and a generic alkene. The mechanism proceeds primarily *via* addition to a double bond, to form a nitrooxyalkyl radical:

$$NO_3 + R1\text{–}C{=}C\text{–}R2 \rightarrow R1\text{–}C\text{–}C(ONO_2)\text{–}R2 \quad \text{(R1.42)}$$

At atmospheric pressure, the main fate of the nitrooxyalkyl radical produced in reaction (R1.42) is reaction with O_2 (Berndt and Böge, 1994) to produce a nitrooxyalkyl peroxy radical, R–ONO_2–O_2. The nitrooxyalkyl peroxy radical can react with NO_2, HO_2, RO_2, NO and NO_3, of which the latter two reactions lead to formation of the nitrooxyalkoxy radical, R–ONO_2–O:

$$R\text{–}ONO_2\text{–}O_2 + NO_3 \rightarrow R\text{–}ONO_2\text{–}O + NO_2 + O_2 \quad \text{(R1.43)}$$

$$R\text{–}ONO_2\text{–}O_2 + NO \rightarrow R\text{–}ONO_2\text{–}O + NO_2 \quad \text{(R1.44)}$$

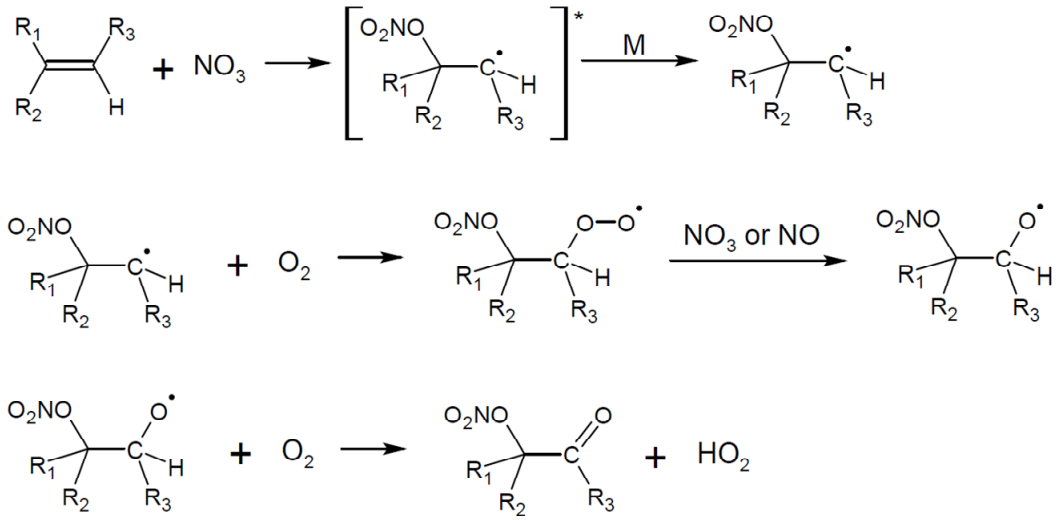

Figure 1.4. Schematic representation of the reaction of NO_3 with a generic alkene, leading to formation of HO_2. Adapted from Salisbury *et al*. (2001).

The nitrooxyalkoxy radical can undergo isomerisation, decomposition, or reaction with O_2. Reaction with O_2, analogous to the reaction of organic alkoxy radicals, yields HO_2:

$$R–ONO_2–O + O_2 \rightarrow R'–ONO_2–R''CO + HO_2 \qquad \text{(R1.45)}$$

Thus, nighttime oxidation of hydrocarbons by NO_3 leads to production of HO_2. Reaction of HO_2 with NO, O_3 and NO_3 can generate OH:

$$HO_2 + NO \rightarrow OH + NO_2 \qquad \text{(R1.10)}$$

$$HO_2 + O_3 \rightarrow OH + 2O_2 \qquad \text{(R1.31)}$$

$$HO_2 + NO_3 \rightarrow OH + NO_2 + O_2 \qquad \text{(R1.46)}$$

Atkinson and Arey (2003) published a detailed review of tropospheric degradation of VOCs, including reaction with O_3 and NO_3. A comprehensive review of nighttime radical chemistry is given by Brown and Stutz (2012).

1.3 Measurements and modelling of OH and HO_2

Recycling of OH maintains a mean daytime concentration of ~ 1×10^6 molecule cm^{-3}. OH is highly reactive, having a lifetime of ~ 1 second in clean air. HO_2 has a lifetime of

~ 100 seconds, and typical daytime HO_2 concentrations are on the order of 1×10^8 molecule cm^{-3}. The atmospheric lifetime of a species, given by the reciprocal of its total rate of removal, determines whether the species can be transported away from its source, and therefore have an impact on regional and global chemistry, or whether the species is confined to a local region. The high reactivities of OH and HO_2 mean that they fall into the latter category, their concentrations at a particular place and time being determined by the chemical composition of the local atmosphere, pressure, temperature and intensity of solar radiation, but not by long-range transport processes (Heard and Pilling, 2003). They are therefore ideal candidates for testing our understanding of tropospheric chemistry by the use of zero-dimensional models, also known as box models. Good agreement between ambient measurements of [OH] and [HO_2] under a variety of atmospheric conditions and the results of box models constrained to the concentrations of long-lived species such as VOCs, NO_x, and O_3 indicates that our knowledge and understanding of the oxidation chemistry in these regions of the troposphere is robust, though it should be noted that agreement can also be achieved if sinks and sources of similar magnitude are missing from the model. Poor agreement indicates that chemical or physical processes are missing from the model, and usually prompts further atmospheric measurements to elucidate the missing part of the mechanism. This combination of field measurements and modelling studies is the key to the study of atmospheric chemistry. Details of techniques used for measurement of OH and HO_2 are discussed in Chapter 2.

Comprehensive reviews of measurements and modelling of OH and HO_2 in the troposphere can be found in Heard and Pilling (2003) and Stone *et al.* (2012). Measurements and models have been used to investigate HO_x chemistry in a wide range of environments throughout the troposphere and lower stratosphere, with the majority of measurements being made in the terrestrial boundary layer. Some key uncertainties remaining in our understanding of HO_x chemistry are summarised here. The regional impacts of heterogeneous uptake of HO_2 to aerosols are thought to be significant (*e.g.* Macintyre and Evans, 2011), and HO_2 uptake coefficients are not well determined. HO_x photochemistry is known to be active in polar regions (*e.g.* Edwards *et al.*, 2011), but the contribution of photolabile compounds emitted from the snow pack to the radical budget (*e.g.* Chen *et al.*, 2004, Bloss *et al.*, 2007, Chen *et al.*, 2007), and the role of

halogens on the HO_x budget and therefore O_3 production and loss (*e.g.* Bloss *et al.*, 2010), remain uncertain. Both sources and sinks of OH have been found to be missing from models of forested regions, where concentrations of biogenic VOCs are high and concentrations of NO_x are low (*e.g.* Whalley *et al.*, 2011, Edwards *et al.*, 2013). OH concentrations in tropical forested regions have been significantly underestimated by models, with a simultaneous overestimation of HO_2. Reconciliation of the measurements and model results requires a currently unidentified mechanism that recycles HO_2 into OH, leading to an 88 % increase in noon OH concentrations, with significant impacts for the rate removal of CH_4 in the tropics (Stone *et al.*, 2011, Whalley *et al.*, 2011). OH reactivity has also been underestimated by models in urban regions with high concentrations of anthropogenic VOCs, with the missing reactivity being attributed to unmeasured VOCs and OVOCs (*e.g.* Sadanaga *et al.*, 2005, Shirley *et al.*, 2006).

Nocturnal oxidation is a little-studied area of atmospheric chemistry. The oxidising capacity of the nocturnal troposphere is thought to be controlled by the reactions described in section 1.2.5, with a limited role for OH and HO_2. Oxidation of VOCs at night can have significant effects on daytime air quality and tropospheric ozone production (*e.g.* Brown *et al.*, 2004, Wong and Stutz, 2010, Brown *et al.*, 2011). Several field measurement campaigns have involved nighttime measurements of OH, HO_2, RO_2, and NO_3 (see Table 1.1), but there has been no dedicated nighttime study of HO_x and oxidation chemistry. Chapter 4 of this thesis describes airborne measurements of OH and HO_2 made during the RONOCO (ROle of Nighttime chemistry in controlling the Oxidising Capacity of the atmOsphere) field campaign in 2010 and 2011, and investigates the production of HO_2 at night and the contribution of reactions of O_3 and NO_3 (see section 1.2.5) to nighttime oxidation of VOCs. There have been no previous aircraft-based studies of nighttime chemistry involving measurements of both NO_3 and HO_2, which would enable vertical profiling of the lower atmosphere and full evaluation of the nocturnal radical budget.

1.3.1 Previous nighttime radical studies

Table 1.1 gives details of previous measurements and modelling of nighttime HO_x concentrations in polluted or semi-polluted environments. Highlights from these studies

are discussed here, with particular attention paid to those studies involving HO_x and NO_3 measurements in polluted and semi-polluted locations, and in which the contribution made by O_3 and NO_3 to nighttime radical chemistry have been considered.

Geyer *et al*. (2003) report radical measurements and modelling from the 1998 Berliner Ozone Experiment (BERLIOZ). Measurements of NO_3, RO_2, HO_2 and OH were made by matrix isolation electron spin resonance (MIESR), laser-induced fluorescence (LIF) spectroscopy, and chemical amplification (CA) at a site approximately 50 km from Berlin. HO_2 was detected at night with concentrations frequently as high as 5×10^7 molecule cm^{-3} (approximately 2 pptv), and an average concentration of 1×10^8 molecule cm^{-3} over one hour (02:00 to 03:00) of nocturnal measurements during an intensive period of the study (Holland *et al.*, 2003). OH was usually below the limit of detection of the LIF instrument (3.5×10^5 molecule cm^{-3}). Modelling revealed that nitrate radical reactions with terpenes were responsible for producing 53 % of HO_2, and 36 % of OH radicals in the night, with ozonolysis accounting for production of the remaining 47 % of HO_2, and 64 % of OH radicals. A positive linear correlation between RO_2 and NO_3 was observed and was reproduced by the model.

Modelling results from the MCMA-2003 (Mexico City) field campaign (Volkamer *et al.*, 2010) indicate that nighttime radical production at roof-top level (approximately 16 m above the ground) were dominated by ozonolysis of alkenes, and that reactions of NO_3 with alkenes played only a minor role. The measurements site was located in a polluted urban environment, with high levels of NO, NO_2 and O_3. NO_3 was observed at a maximum concentration of 50 pptv during the night at a mean height above the ground of 70 m, but roof-top level concentrations were predicted to be much lower, accounting for the relative unimportance of NO_3 reactions in radical initiation at that height. Propagation of RO_2 radicals to HO_2 and OH, by reaction with NO_3, was found to be negligible.

Table 1.1. Examples of modelling studies and observations of HO_x radicals and VOC oxidation at night.

Location, Campaign, Date	Methods	Results	Reference
Mace Head, Ireland, EASE97, 1997	Measurements ($[HO_2+RO_2]$ measured by chemical amplification (PERCA); HO_x measured by FAGE; NO_3 measured by DOAS); modelling: Campaign-tailored box model constrained to measurements, based on MCM	2 nights of HO_x measurements: HO_2 = 1–2 and 0.5–0.7 pptv; OH not detected above limit of detection (~ 2.5×10^5 cm^{-3}). NO_3 dominated radical production in westerly (clean) air masses; O_3 dominated in south westerly (semi-polluted) air masses and dominated radical production overall during the campaign.	Salisbury *et al.* (2001), Creasey *et al.* (2002)
Pabstthum, Germany, BERLIOZ 1998,	Measurements (HO_x measured by LIF; NO_3 measured by DOAS and MIESR); modelling: Zero-dimensional model using inorganic chemistry from MCM, and lumped VOC reactivity, constrained to measured species	Nighttime OH = 1.85×10^5 cm^{-3}, compared to modelled value of 4.1×10^5 cm^{-3}. Nighttime $HO_2 = 3 \times 10^7$ cm^{-3}, model results in agreement. NO_3 chemistry responsible for 53 % of HO_2 and 36 % of OH during the night. O_3 + alkene responsible for 47 % of HO_2 and 64 % of OH during the night.	Geyer *et al.* (2003), Holland *et al.* (2003)
Birmingham, PUMA, 1999 and 2000	Measurements (HO_x measured by FAGE); modelling: Photochemical box model constrained to measurements, based on MCM	Daytime OH initiation dominated by O_3 + alkenes, HONO photolysis, and $O(^1D) + H_2O$ during summer. O_3 + alkenes dominated in winter. O_3 + alkenes main radical source at night.	Emmerson *et al.* (2005), Harrison *et al.* (2006)
New York, PMTACS-NY, 2001	Measurements (GTHOS: Ground-based Tropospheric Hydrogen Oxides Sensor, Penn State, LIF at λ = 308 nm)	Nighttime OH ~ 7×10^5 cm^{-3} and nighttime HO_2 ~ 8×10^6 cm^{-3}. Increase in HO_x after midnight attributed to increase in O_3 due to transport. O_3 + alkenes main source of nighttime HO_x.	Ren *et al.* (2003a), Ren *et al.* (2003b)
Mace Head, NAMBLEX, 2002	Measurements (HO_x measured by FAGE; NO_3 measured by DOAS); modelling: Zero-dimensional box models constrained to measured species, based on MCM	Nighttime $HO_2 = 2–3 \times 10^7$ cm^{-3}; OH below detection limit (6×10^4 cm^{-3}). Model overestimated HO_2. On average, O_3 + alkene reactions contributed 59 % and NO_3 + alkene reactions contributed 41 % to RO_2 production at night, but NO_3 and RO_2 concentrations were always higher in semi-polluted air masses than in clean marine air masses and NO_3 reactions dominated in these conditions.	Fleming *et al.* (2006), Smith *et al.* (2006), Sommariva *et al.* (2007)

Table 1.1 (continued).

Location, Campaign, Date	Methods	Results	Reference
Writtle, London, TORCH, 2003	Measurements (HO_x measured by FAGE, RO_2 measured by PERCA) during a heatwave/pollution episode; modelling: zero-dimensional box model constrained to measured species	OH and HO_2 were observed above the limit of detection on several nights. OH peaked at 8.5×10^5 molecule cm^{-3}; HO_2 peaked at 1×10^8 molecule cm^{-3}. Model over-predicted nighttime OH and HO_2 on average by 24 % and 7 %; under-predicted [HO_2+ΣRO_2] by 22 %.	Lee *et al.* (2006), Emmerson *et al.* (2007), Emmerson and Carslaw (2009)
Mexico City, MCMA 2003	Measurements (HO_x measured by GTHOS, NO_3 measured by DOAS); modelling: Zero-dimensional model based on MCM v3.1, constrained to measured species	Polluted city location characterized by high levels of NO, NO_2 and O_3. Maximum nighttime OH ~ 1×10^6 cm^{-3}; maximum nighttime HO_2 ~ 6 pptv. Nighttime production of radicals (ΣOH_{new}) dominated by O_3 + alkene reactions (76–92%); NO_3 + alkene plays a minor role. Daytime radical production ~ 25 times higher than night.	Shirley *et al.* (2006), Sheehy *et al.* (2010), Volkamer *et al.* (2010)
New York City, PMTACS-NY winter 2004	Measurements (HO_x measured by GTHOS); modelling: Zero-dimensional model based on RACM and constrained by measurements	Mean maximum OH = 0.05 pptv; mean maximum HO_2 = 0.7 pptv. Model underprediction of HO_2 was pronounced when NO was high. O_3 + alkene reactions were dominant nighttime source.	Ren *et al.* (2006)
Houston, Texas, TexAQS, 2006	Measurements (NO_3 and N_2O_5 measured by cavity ring down spectroscopy, VOCs measured by CIMS, GC, PTRMS). No direct measurements of OH, HO_2, or RO2.	Loss rates and budgets of NO_3 and highly reactive VOCs calculated. NO_3 primarily lost through reaction with VOCs. VOC oxidation dominated by NO_3, which was 3–5 times more important than O_3.	Brown *et al.* (2011)

The 2006 Texas Air Quality Study (TexAQS) involved a series of nighttime flights onboard the NOAA P-3 aircraft over Houston, Texas and along the Gulf Coast (Brown *et al.*, 2011). Loss rates and budgets of NO_3 and highly reactive VOCs were calculated, but there were no measurements of OH, HO_2 and RO_2 during the flights. Budgets for NO_3 show that it was lost primarily through reactions with VOCs, but the contribution to NO_3 loss through reaction with peroxy radicals was uncertain because of the lack of direct measurements of RO_2 during the flights. NO_3 dominated VOC oxidation, being 3–5 times more important than O_3.

Reactions of O_3 with alkenes were found to be responsible for the majority of formation of OH during the winter PUMA campaign (a low photolysis urban environment) (Heard *et al.*, 2004, Emmerson *et al.*, 2005, Harrison *et al.*, 2006). Measurements of OH, HO_2 and RO_2 were unavailable at night, but model-predicted values of these radicals were used to calculate that 90 % of nighttime initiation *via* HO_2 was from O_3 reactions. Without measurements of NO_3 during the campaign, there was no estimate of the contribution to radical initiation from reactions of NO_3 with alkenes.

In summary, NO_3 and O_3 have both been found to dominate radical initiation in the nighttime troposphere, and in some situations the two mechanisms were found to be equally important. The relative importance of O_3- and NO_3-initiated oxidation depends on the availability of NO_3, which is determined by the amount of NO_x present in the atmosphere and the ratio of NO to NO_2 (see reactions (R1.36), (R1.37), and (R1.39)), and the concentration and species distribution of VOCs (Bey *et al.*, 2001, Geyer *et al.*, 2003). A modelling study by Bey *et al.* (2001) suggested that nocturnal radical initiation is driven by alkene ozonolysis in urban environments and in environments with low NO_x concentrations, and that both O_3 and NO_3 contribute to radical initiation in rural environments with moderate NO_x levels. It is expected that NO_3 dominates nocturnal radical initiation in air masses containing sufficient NO_2 and O_3 for NO_3 production, but removed from NO sources (*e.g.* air masses downwind of urban areas). Geyer and Stutz (2004) have found that the effects of suppressed mixing in the nocturnal boundary layer can also control whether NO_3 or O_3 dominates nighttime radical chemistry.

1.4 Halogen chemistry in the marine boundary layer

Stratospheric ozone absorbs nearly all incoming solar radiation between λ = 240 nm and λ = 290 nm (Wayne, 2000). Without this protective barrier, Earth's biosphere would be subject to damage and disease caused by exposure to this UV light (Caldwell *et al.*, 1998, Kane, 1998, Madronich *et al.*, 1998). Stratospheric ozone also has a negative radiative forcing effect (see Figure 1.1). Depletion of the stratospheric ozone layer, which was first reported by Farman *et al.* (1985), therefore has severe implications for life on Earth. It is well-established that halogen atoms produced by photolysis of anthropogenic, chemically inert halocarbons (such as chlorofluorocarbons, CFCs) are responsible for stratospheric ozone depletion in the middle latitudes and the formation of the Antarctic ozone hole (Molina and Rowland, 1974, Solomon *et al.*, 1986). In addition, bromine, chlorine and iodine released from sea-salt, ice, and snow *via* photochemical and heterogeneous reactions, are known to be responsible for regular, complete ozone depletion events in the Artic (Oltmans, 1981, Bottenheim and Gallant, 1986, Oltmans and Komhyr, 1986, Barrie *et al.*, 1988, Barrie *et al.*, 1989) and Antarctic (Kreher *et al.*, 1997, Wessel *et al.*, 1998) springtime boundary layers.

Numerous long-lived halogenated anthropogenic compounds, with atmospheric lifetimes ranging from 1 to 1000 years, are now known to be efficient ozone depleting substances (ODS). CFCs were phased out of use under the 1987 Montreal Protocol, and the atmospheric concentrations of the majority of CFCs are now declining. The phasing out of hydrochlorofluorocarbons (HCFCs) began in 1996 following an amendment to the Montreal Protocol, but their atmospheric concentrations are currently increasing (Montzka and Reimann, 2010). The atmospheric concentrations of methyl chloroform (CH_3CCl_3), carbon tetrachloride (CCl_4), and methyl bromide (CH_3Br) are all in decline, while the total concentration of halons (long-lived compounds containing carbon, bromine and fluorine) has stopped increasing. The overall effect is that stratospheric chlorine concentrations are decreasing, and bromine concentrations have stopped increasing. The globally-averaged total ozone column has ceased to decline, and is expected to recover as a result of decreasing anthropogenic ODS (Bekki and Bodeker, 2010, Douglass and Fioletov, 2010).

As the role of anthropogenic ODS declines, natural ozone depleting substances are predicted to have an increasingly important role in stratospheric ozone depletion as the global climate warms (Montzka and Reimann, 2010). This is the motivation for the EU-funded SHIVA (Stratospheric ozone: Halogen Impacts in a Varying Atmosphere) project (see Chapter 5). Halogenated very short-lived substances (VSLS), with atmospheric lifetimes ranging from 0.003 to 149 days, are emitted from the ocean surface and transported to the stratosphere, where they are known to contribute to ozone depletion. The rate of emission and rate of loss (by reaction with OH or by photolysis) of these species, and the fraction transported from the surface to the stratosphere, is predicted to change with the changing climate. Prediction of future ozone abundances based on the complex coupling between emission, transport, and loss of VSLS in future climates is a major scientific challenge (WMO, 2010). Within the scope of the SHIVA project, measurements of the iodine monoxide radical (IO), I_2, and the sum of HCl and HOI were made in the Western Pacific marine boundary layer. These measurements are discussed and analysed in Chapter 5 of this thesis. Given in the following sections are a description of important aspects of marine boundary layer iodine chemistry, a discussion of sources of iodine, and examples of measurements of IO over the open ocean.

1.4.1 Importance of iodine in the atmosphere

Although the current understanding is that iodine contributes relatively little to stratospheric ozone depletion (Montzka and Reimann, 2010), with the right emission location and transport conditions, iodinated VSLS could make a contribution to stratospheric ozone depletion. Iodine chemistry certainly contributes to tropospheric ozone loss (Vogt *et al.*, 1999), has an impact on the HO_x and NO_x cycles (Davis *et al.*, 1996) and therefore the oxidising capacity of the marine boundary layer, and has an important role in the formation of new particles (*e.g.* Saiz-Lopez *et al.*, 2006). Since the measurements analysed in this work were made in the marine boundary layer, the remainder of this discussion will focus on iodine in the troposphere. Figure 1.5 shows a simplified iodine reaction scheme.

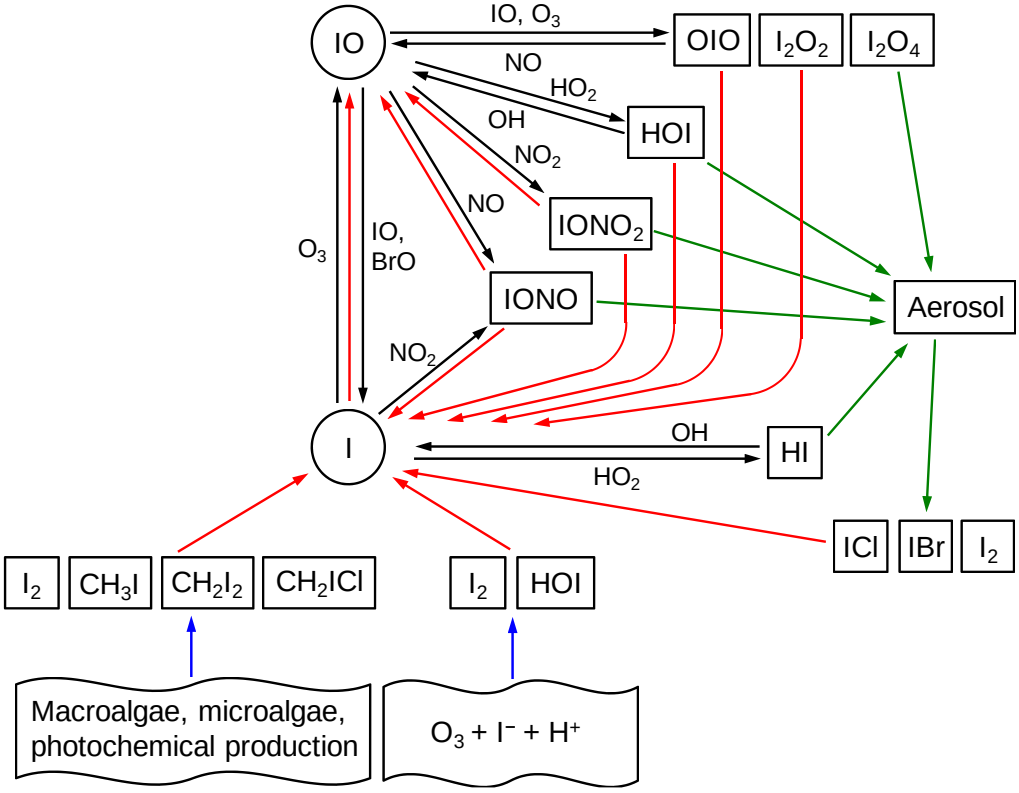

Figure 1.5. Simplified schematic representation of I and IO reaction cycles in the marine boundary layer. Blue arrows indicate emission from the ocean surface, red arrows indicate photolysis, and green arrows indicate uptake or emission from aerosol. Adapted from Furneaux (2009).

1.4.1.1 Role of iodine in tropospheric ozone depletion

Tropospheric ozone has a positive radiative forcing effect, contributing approximately +0.35 W m^{-2} (best estimate) to a net human effect of 1.6 W m^{-2} (see Figure 1.1) (Forster *et al.*, 2007). Tropospheric ozone is produced following the OH-initiated oxidation of trace gases such as CO and CH_4, in the presence of NO_x (reactions (R1.6) to (R1.13) and reaction (R1.20)).There is also a contribution from down-mixing of stratospheric air into the troposphere. Ozone destruction in the troposphere occurs through photolysis and by reaction with OH and HO_2 (reactions (R1.30) to (R1.32)) (Levy, 1972, Crutzen, 1974). Tropospheric ozone has increased in concentration since pre-industrial times, and has therefore contributed to positive radiative forcing, though the strength and sign (+ or −) of the ozone trend changes between different geographical regions, and considerable uncertainty is associated with estimates of the radiative forcing effect of tropospheric ozone (Forster *et al.*, 2007, Stevenson *et al.*, 2013). As well as the direct radiative forcing effect (absorption of IR radiation), ozone affects

climate change and air quality in its role as the main source of the oxidising hydroxyl radical, OH, in the troposphere. Approximately 75 % of global tropospheric ozone production and loss occurs in the tropics, driven by high photolysis rates and high concentrations of water vapour (Horowitz *et al.*, 2003). Very low ozone events in the remote marine boundary layer have been observed on numerous occasions (*e.g.* Singh *et al.*, 1996, and references therein).

Iodine atoms are released by photolysis of iodine-containing compounds such as CH_2I_2 and I_2 (see section 1.4.2), and react with O_3 to form IO. IO is rapidly photolysed, and a steady state is formed between IO and I atoms, with no net effect on O_3 (Vogt *et al.*, 1999):

$$I + O_3 \rightarrow IO + O_2 \quad \text{(R1.47)}$$

$$IO + h\nu \rightarrow I + O \quad \text{(R1.48)}$$

$$O + O_2 + M \rightarrow O_3 + M \quad \text{(R1.49)}$$

Iodine-mediated ozone destruction occurs through reactions of IO with other species, in three cycles. At low concentrations of IO, the following reactions are important (Chameides and Davis, 1980, Vogt *et al.*, 1999):

$$I + O_3 \rightarrow IO + O_2 \quad \text{(R1.47)}$$

$$I + HO_2 \rightarrow HI + O_2 \quad \text{(R1.50)}$$

$$IO + HO_2 \rightarrow HOI + O_2 \quad \text{(R1.51)}$$

$$HOI + h\nu \rightarrow OH + I \quad \text{(R1.52)}$$

$$\text{Net: } O_3 + HO_2 \rightarrow OH + 2\,O_2 \quad \text{(R1.53)}$$

At higher concentrations of IO, the self-reaction becomes more significant (Chameides and Davis, 1980, Jenkin *et al.*, 1985, Chatfield and Crutzen, 1990, Harwood *et al.*, 1997, Vogt *et al.*, 1999):

$$2\,(I + O_3) \rightarrow 2\,(IO + O_2) \quad \text{(R1.54)}$$

$$IO + IO \rightarrow I + OIO \textit{ or } I_2O_2 \quad \text{(R1.55)}$$

$$OIO + h\nu \rightarrow I + O_2 \quad \text{(R1.56)}$$

$$I_2O_2 + h\nu \rightarrow 2\,I + O_2 \quad \text{(R1.57)}$$

$$\text{Net: } 2\,O_3 \rightarrow 3\,O_2 \quad \text{(R1.58)}$$

Reactions of iodine involving Br and, to a lesser extent, Cl, also lead to ozone destruction (Solomon *et al.*, 1994):

$$I + O_3 \rightarrow IO + O_2 \quad \text{(R1.47)}$$

$$Br + O_3 \rightarrow BrO + O_2 \quad \text{(R1.59)}$$

$$IO + BrO \rightarrow I + Br + O_2 \quad \text{(R1.60)}$$

$$\text{Net: } 2\ O_3 \rightarrow 3\ O_2 \quad \text{(R1.61)}$$

The reaction between IO and NO_2 can also contribute to ozone depletion (see reaction (R1.63)). Numerous modelling and measurement studies have confirmed that the above reactions lead to significant tropospheric ozone destruction (Davis *et al.*, 1996, Read *et al.*, 2008, Commane *et al.*, 2011, Saiz-Lopez *et al.*, 2012). In many cases the iodine-mediated ozone destruction is comparable to ozone removal by HO_x reactions (Vogt *et al.*, 1999, McFiggans *et al.*, 2000, Read *et al.*, 2008). Modelling studies have also predicted that iodine chemistry accelerates the release of bromine and chlorine from sea salt, thereby enhancing tropospheric ozone destruction (von Glasow *et al.*, 2002).

1.4.1.2 Role of iodine in controlling HO_x

Reactions (R1.50) and (R1.51) participate in the HO_x radical cycling mechanism by converting HO_2 to OH, thereby having an impact on the oxidising capacity of the marine boundary layer. The HOI produced in reaction (R1.51) can be photolysed to release I atoms and OH, or be uptaken by aerosols, leading to loss of HO_x from the gas phase (Bloss *et al.*, 2005). Reaction of HOI with Cl^-, Br^-, or I^- in the aerosol phase leads to production of ICl, IBr and I_2, which are released into the gas phase, thereby recycling iodine. HI, produced in reaction (R1.50), is also readily taken up by aerosol (McFiggans *et al.*, 2000). The reaction of IO with HO_2 has been shown to dominate HO_2 loss under clean marine conditions, accounting for 40 % of the total HO_2 loss rate (Bloss *et al.*, 2005). With sufficiently high IO concentrations, reactions (R1.51) and (R1.52) can be the most important HO_x recycling mechanism in low NO_x marine environments, pushing the HO_2/OH ratio towards OH (Sommariva *et al.*, 2006, Commane *et al.*, 2011). Uptake of HOI to aerosols can also be a significant HO_x loss process (Mahajan *et al.*, 2010). In the presence of NO_x the effect of IO on HO_x recycling is reduced, due to competition between reactions (R1.10) and (R1.51), and the

reactions of IO with NO and NO_2 (see reactions (R1.62) to (R1.66)) (Furneaux *et al.*, 2010).

Although considered separately here, the impacts of iodine chemistry on ozone and on HO_x are not easily isolated from one another, since photolysis of O_3 is the primary source of OH in the troposphere, and the modulation of the HO_2/OH ratio itself has an impact on the production and loss of O_3 *via* reactions (R1.10) and (R1.29) to (R1.32). Similarly, iodine chemistry has an indirect effect on NO and NO_2 *via* the HO_2/OH ratio, as well as a more direct effect, which is discussed below.

1.4.1.3 Role of iodine in controlling NO_x

IO and the higher oxide, OIO, react with NO and NO_2 in the marine boundary layer, as follows (Chameides and Davis, 1980, McFiggans *et al.*, 2000, Saiz-Lopez *et al.*, 2012):

$$I + NO_2 + M \rightarrow INO_2 + M \quad \text{(R1.62)}$$

$$IO + NO_2 + M \rightarrow IONO_2 + M \quad \text{(R1.63)}$$

$$I + NO + M \rightarrow INO + M \quad \text{(R1.64)}$$

$$IO + NO \rightarrow INO_2 \quad \text{(R1.65)}$$

$$OIO + NO \rightarrow IO + NO_2 \quad \text{(R1.66)}$$

It is worth noting that reaction (R1.63), followed by photolysis of $IONO_2$ to release an I atom, can contribute to ozone depletion under moderately polluted conditions (Davis *et al.*, 1996, Saiz-Lopez *et al.*, 2012). In polluted environments, reaction with NO_2 becomes an important loss pathway for IO (Saiz-Lopez *et al.*, 2012). INO_2 and $IONO_2$ can be taken up into the aerosol phase, and hydrolysed to produce HOI, which then recycles iodine back into the gas phase by reaction with halide ions. INO_2 and $IONO_2$ can also decompose thermally or be photolysed. Photolysis of $IONO_2$ can yield I + NO_3 or IO + NO_2. If the former is the dominant path, this reaction cycle can contribute to O_3 destruction by releasing an I atom (Allan and Plane, 2002).

1.4.1.4 Role of iodine in new particle formation

Quantification of reflection and absorption of radiation by marine aerosols (direct radiative forcing), and their behaviour as cloud condensation nuclei (indirect radiative forcing), is a large source of uncertainty in climate modelling (see Figure 1.1). The formation of new particles proceeds *via* homogeneous nucleation of gas-phase compounds into a thermodynamically stable cluster of approximately 1 nm diameter. These small particles then grow by coagulation with other particles or condensation of gas-phase compounds (O'Dowd *et al.*, 2002). Iodine oxides (I_xO_y) are formed following the UV photolysis of iodocarbons and molecular iodine in the presence of ozone, and are responsible for new particle formation (*e.g.* O'Dowd *et al.*, 2002). New particle formation events have been observed during numerous field measurements at coastal sites where exposure of macroalgae at low tide leads to high mixing ratios of I_2 and subsequently IO (*e.g.* Mäkelä *et al.*, 2002, Saiz-Lopez *et al.*, 2006, Furneaux *et al.*, 2010, McFiggans *et al.*, 2010, Mahajan *et al.*, 2011). Despite numerous laboratory and field studies, the chemistry leading to the production of I_xO_y remains uncertain. Proposed mechanisms include addition of O_3 to I_2O_y and polymerisation of OIO (Sommariva and von Glasow, 2012). Both mechanisms begin with the self-reaction of IO or reaction of IO with O_3 (Burkholder *et al.*, 2004):

$$IO + IO \rightarrow OIO + I \textit{ or } I_2O_2 \quad \text{(R1.55)}$$

$$IO + O_3 \rightarrow OIO + O_2 \quad \text{(R1.67)}$$

$$OIO + h\nu \rightarrow I + O_2 \quad \text{(R1.56)}$$

$$I_2O_2 + h\nu \rightarrow IO + IO \textit{ or } I + OIO \quad \text{(R1.57)}$$

Self-reaction and polymerisation of OIO could proceed as follows, with reaction (R1.69) representing multiple addition steps to lead to the formation of an iodine oxide nucleus (Hoffmann *et al.*, 2001, Burkholder *et al.*, 2004):

$$OIO + OIO \rightarrow I_2O_4 \quad \text{(R1.68)}$$

$$I_2O_4 + OIO \rightarrow \rightarrow \text{particle} \quad \text{(R1.69)}$$

Gómez Martín *et al*. (2007) propose that the reaction between OIO and IO also leads to cluster formation:

$$OIO + IO \rightarrow I_2O_3 \quad \text{(R1.70)}$$

The authors conclude that I_2O_4 is the most important species in the formation of iodine oxide particles, with nucleation most likely occurring through dimerisation of I_2O_4 (Gálvez *et al.*, 2013, Gómez Martín *et al.*, 2013). As well as the uncertainty surrounding the mechanism by which the particles are formed, and their chemical composition, the impact of coastal particle formation on a regional or global scale is also unclear (Saiz-Lopez *et al.*, 2012).

1.4.2 Sources of iodine in the marine boundary layer

In the present atmosphere the largest source of iodine to the atmosphere is biogenic in origin, though biomass burning in Africa releases small amounts of CH_3I (Mead *et al.*, 2008), and both CH_3I and CF_3I are being considered as potential replacements for CH_3Br as a fire retardant (Montzka and Reimann, 2010). Emissions to the atmosphere occur mainly over the oceans. The primary sources of iodine to the marine boundary layer can be classified as biological or abiotic, though this division is not straightforward since because many of the abiotic mechanisms involve reactions of dissolved organic matter in sea water, which is biological in origin. Here, these release mechanisms are separated into direct emission from macroalgae and phytoplankton (section 1.4.2.1), and those which involve photochemistry, aqueous, or heterogeneous chemistry in the sea surface layer (section 1.4.2.2).

1.4.2.1 Biological sources of iodine in the marine boundary layer

A significant source of atmospheric iodine is production of iodine-containing compounds (such as CH_2I_2 and molecular iodine) by marine macroalgae and phytoplankton. Halogenated compounds protect macroalgae from grazing, control infection, and act as antioxidants by removing, for example, hydrogen peroxide produced in defence reactions (Leedham *et al.*, 2013, and references therein). Thus when species are exposed to air and high temperatures at low tide in coastal regions (*e.g.* Carpenter *et al.*, 1999), macroalgae emit halogenated compounds to the atmosphere. Iodocarbons such as diiodomethane (CH_2I_2) and chloroiodomethane (CH_2ICl), and molecular iodine (I_2), are also produced by macroalgae and phytoplankton in ocean water (Moore *et al.*, 1996, Küpper *et al.*, 2008, Bronwell *et al.*,

2010), and are volatilised to the atmosphere, where they are rapidly photolysed to release I atoms:

$$CH_2ICl + h\nu \rightarrow \rightarrow CH_2 + I + Cl \quad \text{(R1.71)}$$

$$I_2 + h\nu \rightarrow I + I \quad \text{(R1.72)}$$

Early studies of iodine-containing species in the coastal midlatitude boundary layer suggested that iodocarbons were the primary source of iodine to the atmosphere in these regions (*e.g.* Carpenter *et al.*, 1999, Carpenter, 2003). However, it is now thought that the primary source of iodine in the midlatitude marine boundary layer is I_2 emitted by macroalgae when exposed at low tide (Saiz-Lopez and Plane, 2004, Commane *et al.*, 2011).

Mixing ratios of iodocarbons in coastal regions tend to be higher and more variable than over the open ocean (Carpenter *et al.*, 2000, Yokouchi *et al.*, 2008, Jones *et al.*, 2009), because macroalgae, which grow in abundance only in coastal regions, are strong producers of iodocarbons, and emission directly to the atmosphere occurs when the macroalgae are exposed at low tide. For example, typical open ocean mixing ratios of CH_3I are in the range of around 0.1–2.0 pptv, while coastal mixing ratios range between 0.1 and 12.0 pptv (Saiz-Lopez *et al.*, 2012). In addition, different macroalgae species emit different amounts of iodocarbons (Carpenter *et al.*, 2000, Leedham *et al.*, 2013). In regions with large macroalgae populations, emission from macroalgae are likely to be the dominant source of atmospheric iodine, but open ocean sources can make a contribution (Carpenter *et al.*, 2001). Emission from macroalgae is not currently thought to be a globally important source of iodine to the atmosphere (Saiz-Lopez *et al.*, 2012). Lifetimes and atmospheric mixing ratios of several iodocarbons are given in Table 1.2.

Production of iodocarbons by phytoplankton is assumed to dominate biological iodine emission in open-ocean regions. Phytoplankton exist over the entire ocean surface, in contrast to the relatively restricted coastal habitat of macroalgae. Phytoplankton are known to produce CH_3I (Itoh *et al.*, 1997, Manley and de la Cuesta, 1997, Scarratt and Moore, 1999) and there is evidence to suggest that they also produce CH_2I_2 and CH_2ICl (Klick and Abrahamsson, 1992, Moore and Tokarczyk, 1993, Schall *et al.*, 1997, Yamamoto *et al.*, 2001, Archer *et al.*, 2007).

Table 1.2. Lifetimes and abundances of iodocarbons in the marine boundary layer (results from polar regions are not included).

Species	Lifetime	Range of measured mixing ratios / pptv	References
CH_3I	5–6 days	0.1–12.0	Bell *et al.* (2002), Carpenter (2003), Ko and Poulet (2003), Yokouchi *et al.* (2008)
C_2H_5I	4 days	0.06–0.46	Carpenter *et al.* (1999), Jones *et al.* (2009)
C_3H_7I		<0.02–0.74	Jones *et al.* (2009)
CH_2ICl	0.1 days	0.01–3.4	Varner *et al.* (2008)
CH_2IBr	1 hour	0.01–0.32	Carpenter *et al.* (1999), Jones *et al.* (2009)
CH_2I_2	2–10 minutes	<0.01–1.02	Carpenter (2003), Jones *et al.* (2010)

Not all species produce the same species or amounts of halocarbons, and environmental factors are known to effect production (Smythe-Wright *et al.*, 2010). It is clear that there is a biological source of volatile iodocarbons in the open ocean and shelf regions, but the exact nature of the production and the significance of the contribution to atmospheric iodine is less certain. The picture is confused by the rapid photolysis of iodocarbons in surface waters and in the atmosphere, so that the concentration in sea water, sea-to-air flux and atmospheric mixing ratios do not show clear relationships (*e.g.* Butler *et al.*, 2007, Yokouchi *et al.*, 2008, Jones *et al.*, 2010).

1.4.2.2 Abiotic sources of iodine in the marine boundary layer

The sea surface microlayer (SML) is the uppermost tens to hundreds of μm of the surface of the ocean, and is the interface between the ocean and the atmosphere. The SML is enriched in organic material (*e.g.* chlorophyll-*a*), and has measurably different physical, chemical and biological properties to the water beneath. The SML is present over the entire ocean surface, even in areas with high turbulence, and is the site of ocean-atmosphere exchange (Cunliffe *et al.*, 2013). It therefore plays a role in emission of iodine species from the ocean to the atmosphere. Three classes of release mechanism

have been studied. These are: 1. Reactions of gaseous ozone with aqueous iodide at the air-water interface; 2. Photolysis of organic compounds in the sea surface, and reactions of the radicals produced; 3. Reactions of photosensitised organic compounds with halide ions in the sea surface layer. In addition, O'Neill and Hinrichs (2011) have demonstrated the production of gaseous I_2 in the dark, heterogeneous reaction between gaseous NO_2 and solid potassium iodide, which is a component of dehydrated sea salt aerosol, pointing towards a heterogeneous mechanism for the release of iodine from aerosols.

The ocean surface is a sink and a source of gas-phase species, including ozone. Deposition of ozone to the ocean surface is an important loss mechanism, and leads to heterogeneous chemistry with impacts on halogen release from the aqueous phase. In sea water, iodine exists mainly as iodate (IO_3^-), iodide (I^-), and non-volatile dissolved organic iodine (R-I^- and R-IO_3^-) (Wong and Cheng, 2001), with iodide being the most abundant form at the ocean surface (Campos *et al.*, 1996). Modelling and measurement studies have shown that dissolved iodide makes a significant enhancement to the rate of deposition of ozone to sea water surface (Garland *et al.*, 1980, Chang *et al.*, 2004), and that deposition of ozone results in release of molecular iodine from the sea surface (Garland and Curtis, 1981). The reaction mechanism is as follows (Sakamoto *et al.*, 2009, Hayase *et al.*, 2010):

$$H^+ + I^- + O_3 \rightarrow \rightarrow HOI + O_2 \qquad \text{(R1.73)}$$

$$H^+ + HOI + I^- \rightleftharpoons I_2 + H_2O \qquad \text{(R1.74)}$$

Sakamoto *et al*. (2009) have observed the release of I_2 and IO into the gas phase by dark reactions of gaseous O_3 with aqueous iodide. The reaction was assumed to occur at the air–water interface, where I^- is enhanced compared to the bulk water. Very recent work has shown that both I_2 and HOI are released into the gas phase following the ozone–iodide reactions (Carpenter *et al.*, 2013). Importantly, HOI (not previously considered as a carrier of iodine to the atmosphere) is emitted into the gas phase at a rate ten times higher than molecular iodine, and the total iodine flux could account for 75 % of IO observed over the tropical Atlantic Ocean.

Several studies have focussed on the effects of the enrichment of organic matter in the sea surface microlayer on the release of halogens into the gas phase. For example, a study by Reeser *et al*. (2009) has shown that reactive halogen atoms are produced by oxidation of halide ions by photoexcited chlorophyll-*a* at the sea surface, potentially releasing halogen species to the gas phase. It has also been shown that the release of I_2 into the gas phase, following the reaction of O_3 with dissolved I^- at the aqueous surface, is enhanced by the presence of octanol at the sea surface (Reeser and Donaldson, 2011). Other studies have highlighted the importance of photosensitive carbonyl species at the sea surface microlayer to the release of iodine from sea water (Jammoul *et al.*, 2009, Hayase *et al.*, 2010, Hayase *et al.*, 2012).

Moore and Zafiriou (1994) first observed production of CH_3I from seawater irradiated with natural or artificial sunlight, and proposed that the mechanism of production is reaction of photochemically produced methyl radical and iodine atoms. The observed CH_3I production rates were higher than algal production rates, and could be globally significant. The photolysis of dihalomethanes in surface sea water has been studied, and it has been shown that CH_2ICl is produced following the direct photolysis of CH_2I_2 (Martino *et al.*, 2005). CH_2ICl was also found to be produced partly by photolysis of CH_2I_2 in sea water measurements of dihalomethanes in the English Channel (Archer *et al.*, 2007). Measurements of CH_3I in the tropical Atlantic Ocean, in an area characterised by low biological activity, suggest that photochemical production could be the dominant source in the open ocean (Happell and Wallace, 1996). Numerous studies have highlighted the correlation between atmospheric concentrations of iodocarbons and sea surface temperature, pointing towards a photochemical production mechanism (*e.g.* Chuck *et al.*, 2005, Yokouchi *et al.*, 2008, Jones *et al.*, 2010). Miyake and Tsunogai (1963) observed evaporation of I_2 from sea water, containing iodide and iodate, when the water was irradiated with UV and visible light.

1.5 Measurements of IO over the open ocean

The SHIVA cruise followed the northern coast of Borneo through the South China Sea, but experienced airflow predominantly from the north-east with little coastal influence, and growth of macroalgae along that coast is limited. The conditions encountered were

therefore more characteristic of the open ocean than of midlatitude coastal sites with significant growth of macroalgae. IO measurements at these coastal sites are characterised by high variability, and high mixing ratios associated with exposure of macroalgae at low tide. For example, IO reached a maximum daytime mixing ratio of 30.0 pptv at the semi-polluted coastal site of Roscoff, and was found to be strongly dependent on tidal height (Furneaux *et al.*, 2010). At Mace Head, a clean coastal site, IO mixing ratios varied from 0 pptv at high tide to a maximum of 49.8 pptv at low tide (Commane *et al.*, 2011). In contrast, IO measurements over the open ocean (summarised in Table 1.3) are characterised by relatively low mixing ratios and little variability. Some aspects of the processes controlling IO mixing ratios over the open ocean are discussed here.

Satellite measurements in the Eastern Pacific suggest a link between chlorophyll-*a* concentrations (a marker for oceanic biological activity) and IO mixing ratios (Schönhardt *et al.*, 2012). Measurements of up to 3.5 pptv of IO over biologically active open ocean upwelling regions support this link (Volkamer *et al.*, 2010). Other studies have shown IO to be negatively correlated to concentrations of Chl-*a* and chromophoric dissolved organic matter (Mahajan *et al.*, 2012, Gómez Martín *et al.*, 2013, Großmann *et al.*, 2013), indicating that biological activity could inhibit production of reactive iodine, or at least that it has no significant contribution. Several studies have found IO to be positively correlated with sea surface temperature and air temperature, indicating enhanced production or enhanced sea-to-air emission of iodine precursors at higher temperatures. The same studies also found that IO was correlated with salinity, suggesting an abiotic production mechanism with the rate of production limited by the amount of aqueous iodide (Mahajan *et al.*, 2012, Gómez Martín *et al.*, 2013, Großmann *et al.*, 2013).

Table 1.3. Measurements and modelling of IO over the open ocean.

Location, Campaign, Date	Methods	Results	Reference
Tenerife, tropical Atlantic Ocean, ACE 2, 1997	Long-path differential optical absorption spectroscopy (LP-DOAS). Total light path = 9.3km, 162 m above sea level, across a coastal bay. LOD = 0.24 pptv.	Island surrounded by oligotrophic (low biological activity) ocean water. Meteorological conditions brought air from open ocean. Up to 3.5 pptv IO detected in air from open ocean.	Allan *et al.* (2000)
Cape Verde, Eastern tropical Atlantic Ocean, 2006–2007	Measurements by LP-DOAS. Total light path = 12 km, 10 m above sea level, across a coastal bay. LOD = 0.3−0.5 pptv. One-dimensional chemistry and transport model used to study iodine species.	Maximum IO mixing ratio = 3.1 pptv. Daytime average IO = 1−2 pptv. Highest mixing ratios measured between 09:00–17:00. IO below detection limit at night. Measured iodocarbons insufficient to account for measured IO; additional I atom source required, possibly by release of I_2 from ocean surface by O_3.	Mahajan *et al.* (2010)
Eastern tropical Pacific Ocean, VOCALS-Rex and TAO, 2008	Multi Axis Differential Optical Absorption Spectroscopy (MAX-DOAS); measurements made onboard NOAA Research Vessel *Ron Brown*.	Up to 3.5 pptv of IO over biologically active upwelling regions of Pacific Ocean. IO located mainly in marine boundary layer. Tropical Pacific Ocean is a source of reactive iodine compounds.	Volkamer *et al.* (2010)
Western Pacific, TransBrom, 2009	MAX-DOAS measurements onboard RV *Sonne* between Japan and Australia. Telescope positioned on port side of upper deck, 15 m above sea level. Viewing direction perpendicular to the direction of the ship.	IO mixing ratios between 1 and 2.2 pptv. Higher mixing ratios measured in the tropics (between 20º N and 5º S). IO present in a shallow layer next to the surface. Photochemical modelling showed that organic iodine precursors insufficient to explain the observed IO, and weak correlation with halocarbon fluxes suggested halocarbons were not a dominant IO source. Additional sea-air flux of I_2 required in the model to reproduce observed IO. IO correlated with relative humidity and sea surface temperature, and anticorrelated with Chl-*a*.	Großmann *et al.* (2013)

Table 1.3 (continued).

Location, Campaign, Date	Methods	Results	Reference
Southeastern Pacific Ocean, HaloCAST-P, 2010	MAX-DOAS measurements made onboard RV *Thomas Thompson*.	IO mixing ratios 0.25–1 pptv. IO correlated with sea surface temperature and salinity. IO negatively correlated with Chl-*a* and chromophoric dissolved organic matter. Iodine release dependent on multiple factors.	Mahajan *et al.* (2012)
Galápagos Islands, tropical eastern Pacific, CHARLEX, 2010	LP-DOAS: Total light path of 9.08 km, 1–5 m above sea level, over a bay. LOD = 0.9 pptv. MAX-DOAS: 1. Telescope ~ 3 m above sea level and ~ 15 m away from tide level, pointing almost parallel to the LP-DOAS light path. 2. Telescope ~ 5 m above sea level, ~ 160 m from the coastline.	No beds of known iodine-emitting macroalgae present at the measurement sites. Meteorological conditions brought air from open ocean, influenced by biologically productive upwelling regions. IO mixing ratios up to 0.9 pptv observed by MAX-DOAS. IO below LP-DOAS detection limit. IO correlated with sea surface temperature and salinity, and negatively correlated with Chl-*a*, indicating an abiotic iodine source.	Gómez Martín *et al.* (2013)

Measured halocarbon fluxes have been found to be insufficient to support the observed IO mixing ratios on several occasions. For example, Mahajan *et al*. (2010) report IO mixing ratios of up to 3.1 pmol mol^{-1} (pptv) over the open ocean at São Vicente, Cape Verde Islands. A one-dimensional model of tropospheric halogen chemistry, using measurements of sea-to-air fluxes of several iodocarbons (CH_2I_2, CH_2IBr, CH_2ICl, CH_3I, C_2H_5I, C_3H_7I) predicted daytime IO levels equal to ~ 30 % of the observed values. An additional flux of I_2 from the sea was required to reconcile the model with the measurements, and the best fit of the modelled data to the observed data was achieved if the O_3-mediated release of I_2 was only active during daylight hours. Similarly, IO mixing ratios of approximately 1 pptv were observed by ship-based MAX-DOAS during a cruise in the Southeastern Pacific ocean (Mahajan *et al.*, 2012). CH_3I was found to contribute just 20 % of the observed IO_x (IO + I) concentrations, the remainder of the observed IO_x being attributed to photolysis of I_2 emitted from the ocean. Measurements of IO have been made by long path DOAS and MAX-DOAS in the Galápagos Islands, where the prevailing winds bring air from the Eastern Pacific open ocean (Gómez Martín *et al.*, 2013). IO was detected within the ~ 1000 m height layer of the MAX-DOAS instrument up to a maximum mixing ratio of ~ 0.9 pptv. IO was not detected above the 0.9 pptv detection limit of the LP-DOAS instrument, which measured between 1 and 5 m above the ocean surface. No correlation was observed between CH_3I and IO_x during the measurement period, indicating that CH_3I was not the main source of IO_x during that time, and CH_3I was calculated to contribute approximately 30 % of the observed IO_x concentration. IO has been measured in the Western Pacific marine boundary layer by MAX-DOAS onboard the RV *Sonne* during the TransBrom project (Großmann *et al.*, 2013). Mixing ratios between 1 and 2.2 pptv were observed in the open ocean environment during the cruise from Japan to Australia. A photochemical box model, constrained by sea-air fluxes of iodine-containing halocarbons, was able to reproduce the observed IO levels only when an additional flux of I_2 from the ocean was included.

Overall, the measurements indicate that iodine monoxide is ubiquitously present at low mixing ratios over the open ocean. What remains unclear is whether abiotic or biological sources, if either, dominate iodine emission from the ocean. Mahajan *et al*. (2012) propose that the source mechanism varies between different oceanic regions. For

example the phytoplankton species distribution in the Eastern Pacific is different to that in the Atlantic, and some species produce iodine more than others. In addition, several source mechanisms may operate at one time to produce the observed IO concentrations, with small contributions from various sources (*e.g.* 20−30 % IO_x from CH_3I in the Eastern Pacific ocean, combined with photolysis of I_2 and evidence to suggest other mechanisms at work (Mahajan *et al.*, 2012, Gómez Martín *et al.*, 2013).

1.5.1 Sources and measurements of nocturnal IO

IO is primarily formed in the reaction between ozone and iodine atoms, which are released on photolysis of iodine-containing compounds such as CH_2I_2. Without this photolytic route to iodine atoms, it is unclear how IO is formed in the nocturnal marine boundary layer. Despite this, several groups have reported observations of IO at night, suggesting that the lifetime of IO is extended under certain conditions, or that there is another production mechanism that does not rely upon photolysis. These observations are summarised in Table 1.4. It is worth noting that there are no reported nighttime measurements of IO in open ocean locations, though IO has been detected at night over the biologically-poor Dead Sea. A summary of possible nighttime sources of IO is given here.

Chambers *et al.* (1992) measured the rate constants of the gas-phase reactions between I_2 and NO_3 ($k = 1.5 \times 10^{-12}$ cm^3 molecule^{-1} s^{-1}), and I and NO_3 ($k = 4.5 \times 10^{-10}$ cm^3 molecule^{-1} s^{-1}). The reactions proceed as follows:

$$I_2 + NO_3 \rightarrow I + IONO_2 \quad \text{(R1.75)}$$

$$I + NO_3 \rightarrow IO + NO_2 \quad \text{(R1.76)}$$

A recent study of reaction (R1.76) suggests a smaller rate constant ($k = 1.0 \times 10^{-10}$ cm^3 molecule^{-1} s^{-1}) but concludes that the reaction is fast at all pressures and that IO is produced with near-unity yield (Dillon *et al.*, 2008). Calculations by Kaltsoyannis and Plane (2008) concluded that reaction (R1.75) is the most likely source of iodine oxides at night.

Table 1.4. Measurements of IO at night in the coastal marine boundary layer.

Location, Campaign, Date	Methods	Results	Reference
Mace Head, Ireland, PARFORCE, 1998	Long-path Differential Optical Absorption Spectroscopy (LP-DOAS); total light path = 15 km, over tidal regions	Coastal location with large macroalgae beds. Nighttime IO remained below 0.25 pptv and was independent of tidal height.	Carpenter *et al.* (2001)
Dead Sea, Israel, 2003	LP-DOAS; total light path = 8.5 km, < 10 m above sea surface	No macroalgae present in Dead Sea because of very high salinity, but phytoplankton are present. 3−4 pptv of IO (above LOD) observed at night on several occasions, though always close to the detection limit. Mixing ratios were higher before midnight than after midnight. Nighttime IO attributed to: $IO + NO \rightarrow I + NO_2$, $I + NO_3 \rightarrow IO + NO_2$, and thermal decomposition of INO_2 and INO_3.	Zingler and Platt (2005)
Mace Head, Ireland, 2002	LP-DOAS; total light path = 8.4 km, 20 m above sea level.	IO measured during two nights, reaching a maximum of 3 pptv. Main source of IO thought to be I_2. I_2 reached a night-time maximum of 93 pptv. NO_3 ~ 7 pptv in the oceanic air sector. Nighttime production of IO thought to be *via* $NO_3 + I_2$. Main loss of IO at night probably $IO + NO_2 \rightarrow IONO_2$. Steady state IO = 2 pptv.	Saiz-Lopez and Plane (2004)
Mace Head, Ireland, NAMBLEX, 2002	LP-DOAS; total light path = 8.4 km, 5–20 m above sea level. Iodine chemistry model used to assess results.	IO measured during two nights, up to 2.5 pptv. Nighttime production of IO *via* $I_2 + NO_3 \rightarrow INO_3 + I$, and thermal decomposition of I_2O_4 and I_2O_2 that form from OIO and IO, respectively. In the model, peak low tide nighttime I_2 was ~ 40 pptv, and NO_3 was fixed at 10 pptv. Modelled IO peaks at 2 pptv coincident with low tide.	Saiz-Lopez *et al.* (2006)

Table 1.4 (continued).

Location, Campaign, Date	Methods	Results	Reference
Lilia, Brittany, France, 2003	LP-DOAS; total light path = 18.94 km, a few metres from the high tide line, 10–14 m above average sea level. LOD = 0.23–0.96 pptv.	High biological activity along the coast. Nighttime IO mixing ratios up to 0.5 pptv reported, but unclear whether above LOD. Daytime IO was anti-correlated with tidal height, but no dependence was found during night.	Peters *et al.* (2005)
Roscoff, France, RHaMBLe, 2006	Laser-induced fluorescence (LIF) with excitation at λ = 445 nm, and off-resonance fluorescence at λ = 521 nm. LOD = 0.3 pptv. Instrument located a few metres from water at high tide.	IO detected above the LOD on 2 nights during of 1 month of measurements. Up to 1.8 pptv observed at night just after low tide.	Whalley *et al.* (2007)
Roscoff, France, RHaMBLe, 2006	LP-DOAS; Total light path = 6.7 km, 7–12 m above sea level. Modelling using one-dimensional photochemistry and transport model 'THAMO'	Maximum nighttime IO = 3.0 pptv. Maximum nighttime I_2 = 52 pptv. Nighttime NO_3 ranged from < 2 – 72.1 pptv. The three species were not measured simultaneously, but in north-westerly air flows. I_2 and IO correlated with low tide at night. Nighttime IO explained by I_2 + NO_3.	Mahajan *et al.* (2009)
Roscoff, France, RHaMBLe, 2006	LIF; LOD 0.4–4.0 pptv. Instrument inlet located on roof of shipping container, 3.5 m above the ground. At high tide the inlet was 3.5 m horizontally from the water. Photochemical box model used to assess measurements.	IO detected during 2 nights out of 20, ranging from 1.1–2.0 pptv (60 minute average), around low tide. Daytime IO anti-correlated with tidal height. The model required 320 pptv of I_2 to account for the observed nighttime IO.	Furneaux *et al.* (2010)
Roscoff, France, 2011	Mode-locked cavity enhanced spectroscopy *via* a frequency comb based spectrometer: Femtosecond laser pulses at 338 and 436 nm are injected alternately into two parallel high-finesse cavities, for measuring BrO and HCHO and IO and NO_2. Broadband light transmitted through the cavity dispersed and detected by a spectrograph.	Coastal location with large intertidal macroalgae beds. Nighttime IO varied between 0 and 2 pptv. IO was anti-correlated with NO_2 due to loss through IO + NO_2 → $IONO_2$.	Grilli *et al.* (2012)

Nakano *et al*. (2003) measured the rate constant of the reaction between NO_3 and CH_3I ($k = 4.1 \times 10^{-13}$ cm^3 molecule^{-1} s^{-1}) and proposed that IO is produced in the following reactions:

$$NO_3 + CH_3I \rightarrow HNO_3 + CH_2I \quad \text{(R1.77)}$$

$$CH_2I + O_2 \rightarrow IO + HCHO \quad \text{(R1.78)}$$

Dillon *et al*. (2008) calculated an IO yield of less than 0.1 for reaction (R1.78), suggesting that it is not an important source of IO in the atmosphere. Sakamoto *et al*. (2009) have reported the release of gaseous I_2 and IO from the dark, heterogeneous reaction of ozone with aqueous potassium iodide solution. The authors propose that O_3 reacts with I^- at the sea surface to produce I_2. IO could be produced at the interface in a number of reactions, and then emitted to the gas phase:

$$IOOO^- \rightarrow IO + O_2 \quad \text{(R1.79)}$$

$$IOOO^- + I^- \rightarrow \rightarrow IO + \text{products} \quad \text{(R1.80)}$$

$$IOOO^- + IOOO^- \rightarrow \rightarrow IO + \text{products} \quad \text{(R1.81)}$$

$$IOOO^- + HOI \rightarrow \rightarrow IO + \text{products} \quad \text{(R1.82)}$$

$$IO\ (aq) \rightarrow IO\ (g) \quad \text{(R1.83)}$$

Since this mechanism does not involve photolysis, it could contribute to nighttime IO formation, though the amount of IO produced is 100 times smaller than the amount of I_2 produced. The authors note that these reaction mechanisms can be applied to the air/aerosol interface, and that I^- is enhanced in sea salt aerosol by 2–4 orders of magnitude compared to sea water (*e.g.* Baker, 2004), so that reactions at the aerosol interface could be a more important source of nighttime IO than reactions at the sea water interface.

1.6 Oceanic reactive carbon: Glyoxal

Glyoxal, CHOCHO, is the smallest α-dicarbonyl, and is of interest in atmospheric chemistry because of its role as a tracer for oxidation of organic compounds (Fu *et al.*, 2008), its role in the formation of secondary organic aerosols and therefore in climate change (*e.g.* Liggio *et al.*, 2005), and in its role in photochemical smog formation (*e.g.* Grosjean *et al.*, 2002, Derwent *et al.*, 2005). The final experimental chapter of this

thesis focuses on the development of a laser-induced phosphorescence instrument for the measurement of ambient concentrations of glyoxal. The instrument is being developed specifically for deployment in the ORC^3 project (Oceanic Reactive Carbon: Climate Impacts) (see section 1.6.5). A summary of tropospheric glyoxal chemistry, its sources, sinks, and climate impacts, is given here, along with an introduction to the ORC^3 project.

1.6.1 Sources

The strongest source of glyoxal is the oxidation of the biogenic VOC isoprene, which accounts for nearly half of global production (Fu *et al.*, 2008). Oxidation of isoprene by OH produces glyoxal and methyl glyoxal (CH_3COCHO) as second-generation products. Oxidation by NO_3 also produces glyoxal and methyl glyoxal, but represents a small fraction of isoprene reactivity. Acetylene (C_2H_2), which is produced in combustion, is the second largest source of glyoxal and is the most important anthropogenic precursor (Fu *et al.*, 2008). Glyoxal is also formed as a ring-fragmentation product in the OH-initiated degradation of several anthropogenic aromatic species, including benzene, toluene, xylene and 1,2,4-trimethylbenzene (*e.g.* Bandow and Washida, 1985, Smith *et al.*, 1999, Volkamer *et al.*, 2001). Aromatic hydrocarbons represent a significant fraction (30-40 %) of hydrocarbons emitted in urban regions and contribute to the formation of ozone and secondary organic aerosol (Smith *et al.*, 1999). Glyoxal is formed as a minor product following the OH- and ozone-initiated oxidation of some anthropogenic alkenes (*e.g.* Martinez and Herron, 1988, Grosjean, 1990, Liu *et al.*, 1999), and in the ozonolysis of other unsaturated VOCs (*e.g.* Grosjean and Grosjean, 1999, Magneron *et al.*, 2002) including the biogenic primary emitted species α-pinene, carene, geraniol and citral (Yu *et al.*, 1998, Fick *et al.*, 2003, Nunes *et al.*, 2005). In urban environments, primary biogenic and anthropogenic emissions of glyoxal are negligibly small compared to production through VOC oxidation (Volkamer *et al.*, 2005). On a global scale, evaporation from biofuels and biomass burning contribute 17 % of annual production (Fu *et al.*, 2008).

There is evidence to suggest that glyoxal and methyl glyoxal are produced photochemically in the sea surface microlayer (SML) (Zhou and Mopper, 1997, van Pinxteren and Herrmann, 2013). Van Pinxteren and Herrmann (2013) observed no

uniform correlation or anti-correlation between glyoxal in sea water and surface chlorophyll-*a* concentrations from satellite data, which are used as a marker for biological activity, though the authors note that chlorophyll-*a* is a broad indicator for biological activity, and does not reflect production of different compounds by different phytoplankton species. Work by Arnold *et al*. (2010) supports this point. Some authors have suggested that carbonyl compounds may be taken up by microorganisms (Kieber and Mopper, 1987, Vranckx *et al.*, 2008). Overall, direct production of oceanic glyoxal is thought to be controlled by photochemistry rather than biological activity (van Pinxteren and Herrmann, 2013). In contrast, satellite-based measurements of gas-phase glyoxal show that its spatial distribution is similar to that of chlorophyll-*a*, (Fu *et al.*, 2008). Chlorophyll-*a* appears as a blue colouration of the ocean, which may affect the retrieval of glyoxal in the blue spectral range. The correlation may otherwise be caused by the co-location of glyoxal with chromophoric dissolved organic matter (CDOM), or it may indicate that there is an oceanic source of glyoxal which is linked to biological activity (Volkamer *et al.*, 2010).

Isoprene is produced by phytoplankton and emitted from the oceans (Shaw *et al.*, 2010), and is known to be an important source of glyoxal. However, measurements of high concentrations of glyoxal in the remote marine boundary layer cannot not be explained by isoprene measurements from similar oceanic regions, suggesting that there is a missing source of marine glyoxal (Sinreich *et al.*, 2010). The oxidation products of isoprene are thought to have a small contribution to the formation of marine secondary organic aerosol but the strength of this contribution remains uncertain. These aspects of glyoxal chemistry are discussed further in sections 1.6.4 and 1.6.5.

1.6.2 Sinks

Glyoxal is removed through photolysis, dry deposition, oxidation, and irreversible uptake by aerosols and cloud droplets (Fu *et al.*, 2008), with photolysis being the most important loss mechanism (Moortgat, 2001, Salter *et al.*, 2013a, Salter *et al.*, 2013b). Glyoxal reacts rapidly with OH ($k = 9.7 \times 10^{-12}$ cm^3 molecule^{-1} s^{-1}) (Feierabend *et al.*, 2007) and is readily photolysed ($J_{CHOCHO} = 1.4 \times 10^{-4}$ s^{-1}) (Klotz *et al.*, 2001), with HCO + HCO, HCO + H + CO, and HCHO + CO being the major product channels at $\lambda \leq 350$ nm, and HCO + HCO being the dominant product channel at $\lambda > 350$ nm (Salter

et al., 2013a). Each of the radical products leads to formation of HO_2, so that photolysis of glyoxal is a source of HO_x. The tropospheric lifetime of glyoxal is of the order of one to three hours (*e.g.* Moortgat, 2001, Volkamer *et al.*, 2005, Fu *et al.*, 2008). Glyoxal is also oxidised by NO_3 ($k = 4.0 \times 10^{-16}$ cm^3 molecule^{-1} s^{-1}) (Talukdar *et al.*, 2011), but OH accounts for 99 % of gas phase oxidation.

Secondary organic aerosols (SOA), formed by condensation of gas-phase oxidation products of atmospheric hydrocarbons, have impacts on atmospheric chemistry, climate change, and air quality (see Chapter 1). High water solubility (Betterton and Hoffman, 1988) means that glyoxal is scavenged by aqueous aerosol ($\gamma = 2.9 \times 10^{-3}$) (Kroll *et al.*, 2005, Liggio *et al.*, 2005), by water on the surface of solid-phase aerosol (Hastings *et al.*, 2005, Corrigan *et al.*, 2008), and by cloud droplets (Lim *et al.*, 2010), and therefore contributes to SOA loading. A global modelling study has predicted that the majority of SOA formation through the uptake of glyoxal and methyl glyoxal occurs in clouds, and that glyoxal and methyl glyoxal increase the global SOA concentration by 40 % (Fu *et al.*, 2008). Uptake onto aqueous aerosols has been shown to compete with loss *via* oxidation in some regions (Liggio *et al.*, 2005, Volkamer *et al.*, 2007).

1.6.3 Measurements and modelling

A global modelling study by Fu *et al*. (2008) predicted daytime glyoxal mixing ratios at the surface in the range 20–100 pptv over continental regions, and 0−5 pptv over the oceans, reflecting high production in biomass burning and isoprene-rich regions. Terrestrial anthropogenic sources were found to be more important in winter, the contribution from forested regions being diminished outside of the growing season, with significant production over polluted regions of the northern hemisphere. There was reasonable agreement with measurements made in rural and semi-rural environments. There is some agreement between the model results and the global glyoxal distribution retrieved from the SCIAMACHY satellite instrument (Wittrock *et al.*, 2006), particularly over biomass burning regions, but the model does not predict the elevated columns observed over the tropical oceans, or over densely populated regions of China. There appears to be a marine source of glyoxal missing from the model, as evidenced by disagreement between the model results and *in situ* measurements in various oceanic

locations around the coast of North America, the Caribbean Sea and the Sargasso Sea (Fu *et al.*, 2008).

The total continental emission of glyoxal to the atmosphere is estimated to be between 94 and 108 Tg yr^{-1}, based on satellite measurements (Harris, 2003). Known sources are insufficient to account for the satellite observations, with global models missing a glyoxal source on the order of 20 Tg yr^{-1} (Skoog *et al.*, 1996). An additional source of glyoxal from oxidation of an unknown VOC, amounting to 56 Tg yr^{-1}, improves the agreement of modelled results with satellite and *in situ* measurements (Harris, 2003).

Measurements of glyoxal have been made using a variety of techniques in urban and rural regions. Prior to the first direct measurement of glyoxal by long-path DOAS, the majority of measurements were conducted by sampling ambient air in sorbent cartridges, followed by HPLC or GC analysis. The first direct measurements were made in Mexico City, by long-path differential optical absorption spectroscopy (see Chapter 3 for a description of the DOAS technique) (Volkamer *et al.*, 2005). Mixing ratios ranged from < 0.15 ppbv to 1.82 ppbv, and had a distinct diurnal profile dependent on the rate of VOC oxidation and photolysis, with only limited influence from vehicle exhausts. Atmospheric mixing ratios are significantly lower in rural and remote regions (Müller *et al.*, 2005) than in urban regions, and are typically controlled by photochemical production with a small contribution from direct emission from vehicle exhausts (*e.g.* Possanzini *et al.*, 2007). Measurements in forested regions have highlighted the importance of isoprene, among other biogenic precursors, for production of glyoxal (*e.g.* Huisman *et al.*, 2011, MacDonald *et al.*, 2012).

1.6.4 Glyoxal in the marine boundary layer

Table 1.5 summarises measurements of glyoxal in the coastal marine boundary layer and in the open ocean marine boundary layer. Reported coastal mixing ratios range between 0.08 ppbv in the Caribbean and Sargasso Sea, and 0.3 ppbv in the Gulf of Maine. Measurements of glyoxal in the marine boundary layer currently present a confused picture. Mixing ratios range from less than 20 pptv off the coast of Florida (Bevington and Robinson, 2003), to 340 ± 110 pptv in the Gulf of Maine (Sinreich *et al.*, 2007). Measurements of glyoxal over the remote open ocean were first reported by

Sinreich *et al*. (2010), who detected up to 140 pptv of glyoxal at sea level by MAX-DOAS onboard RV *Ronald Brown*, 3000 km distant from the South American coast, and above a biologically active upwelling region. The measurements could not be explained by the levels of isoprene and acetylene observed in other upwelling regions, and suggest that the Pacific Ocean is a source of glyoxal (Volkamer *et al.*, 2010). However, glyoxal's high solubility makes emission from the sea to the atmosphere unlikely, and extremely high oceanic glyoxal concentrations would be required to support a sea-to-air flux large enough to explain the observations. The atmosphere may even be a source of glyoxal in the ocean (Baker *et al.*, 2001).

Glyoxal was recently detected in the marine boundary layer and the free troposphere above the eastern Pacific Ocean (Dix *et al.*, 2012). The measurements were made by MAX-DOAS onboard the NSF/NCAR Gulfstream V research aircraft 'HIAPER'. Glyoxal was present throughout the free troposphere, with maximum mixing ratios of ~ 15 pptv being measured near the surface. A modelling study using RAQMS, a global chemical and aerosol model, and CAM-Chem, a coupled climate-chemistry model, predicted very low continental influence for the majority of the research flights (Apel *et al.*, 2012).

The implication of the measurements is that the Pacific Ocean is a source of oxygenated VOCs, in agreement with previous field measurements (Singh *et al.*, 2003). However, the magnitude and direction of the sea-air flux of OVOCs differs between chemical species and is the cause of much debate (*e.g.* Heikes *et al.*, 2002, Sinha *et al.*, 2007, Beale *et al.*, 2010). For example, recently reported long-term measurements of acetone, methanol and acetaldehyde over the tropical North Atlantic Ocean were significantly underestimated by the global chemical transport model CAM-Chem. The model predicted that the tropical Atlantic Ocean is a net sink for acetone but a net source for methanol and acetaldehyde (Read *et al.*, 2012).

Table 1.5. Measurements of glyoxal in the coastal marine boundary layer and in the remote marine boundary layer.

Location, Campaign, Date	Methods	Results	Reference
Coastal marine boundary layer			
Caribbean Sea and Sargasso Sea, October 1988 to March 1989	Air sampling by sorbent cartridge, followed by analysis by HPLC. Seawater analysis by HPLC. Sample collection onboard RV *Columbus Iselin* during three cruises.	Typical marine air concentration of glyoxal = 0.08 ppbv. Predicted oceanic concentration = 30000 nM; measured oceanic concentration = 0.5–5 nM. High solubility causes atmosphere-ocean exchange to be towards the ocean, and equilibrium is never reached.	Zhou and Mopper (1990)
Giesta, Portugal, July & August 1997	Air sampling by sorbent cartridge, followed by analysis by HPLC. Sampling duration 6 hours during day, 12 hours at night.	Rural location near coast, south of Oporto, influenced by Atlantic air masses. Nearby forest of pine and eucalyptus. Mean mixing ratio of glyoxal = 1.54 ppbv; range = 0.52−2.42 ppbv.	Borrego *et al.* (2000)
Gulf of Maine, USA, ICARTT, 2004	MAX-DOAS onboard RV *Ron Brown* during cruise in Gulf of Maine. Glyoxal detected in wavelength range 420−460 nm.	Measurements were influenced by air mass origin, showing higher mixing ratios with lower aerosol loading, and lacking a clear diurnal profile. Mixing ratios measured in Gulf of Maine were much higher than at MIT, up to 340 pptv, and were assumed to be the result of transport of the photochemical plume from the east coast rather than emissions from the ocean.	Sinreich *et al.* (2007)
Salt Point, California, USA, 2005	Collection of carbonyls by formation of carbonyl-bisulphite adducts in mist chamber, followed by derivitisation and analysis by GC/MS. Detection limit range 0.050–0.216 μg m^{-3}.	Coastal location with clean marine boundary air and no terrestrial sources of carbonyls. Glyoxal remained below the detection limit (0.050 μg m^{-3}).	Bevington and Robinson (2003)

Table 1.5 (continued).

Location, Campaign, Date	Methods	Results	Reference
Remote marine boundary layer			
Global remote satellite-based observations, 2004–2005	SCIAMACHY instrument onboard Envisat satellite. Glyoxal retrieved by DOAS technique in the wavelength range 436−457 nm	Measurements over water are treated with caution, but enhanced columns are evident over biologically active areas, especially tropical oceans. Global model TM4-ECPL generally reproduces spatial distributions, but no enhancement over tropical oceans.	Skoog *et al.* (1996), Wittrock *et al.* (2006)
Remote tropical Eastern Pacific, VOCALS-REx & TAO, 2008−2009	University of Colorado Ship MAX-DOAS onboard RV *Ronald H. Brown*. Glyoxal retrieved in wavelength range 433–458 nm. LOD a few 10 pptv.	Cruise from Panama to Chile and return journey. Mixing ratios up to 140 pptv, 3000 km from the continental coast, over biologically active upwelling region. Authors conclude that open ocean must be a source of glyoxal, but known chemistry of dissolved organic matter, isoprene and acetylene over other phytoplankton bloom areas not sufficient to explain observed values.	Sinreich *et al.* (2010)
Eastern Pacific Ocean, 40ºN−45ºS, HEFT-10, 2010, and TORERO, 2012	University of Colorado MAX-DOAS onboard NSF/NCAR Gulfstream V aircraft ‘HIAPER’. Glyoxal retrieved in wavelength range 433–458 nm.	Airborne measurements throughout the marine boundary layer and free troposphere above Pacific Ocean. Numerous OVOC species, including glyoxal, detected in the remote marine boundary layer and free troposphere. Mixing ratios from 40 pptv at the surface to ~ 2.2 pptv at 5.5 km. Short atmospheric lifetime (1–2 hours) precludes significant transport from MBL to FT. Source of glyoxal in free troposphere is unclear, but glyoxal enhanced in regions of convective outflow, so rapid vertical transport could play a role. ~ 50 % of glyoxal column located above MBL, so satellite retrievals assuming all in MBL will overestimate mixing ratios.	Dix *et al.* (2012), Dix *et al.* (2013), Volkamer and Apel (2013)

Glyoxal is a prominent oxidation product of acetylene and ethene, which are present in the marine troposphere. Acetylene is transported from the continents, while ethene is emitted from the oceans. A modelling study of multiphase marine tropospheric oxidation chemistry revealed that glyoxal is produced mainly in the gas phase with a small contribution from oxidation in aerosols and clouds (Warneck, 2005). OH-initiated oxidation of ethene proceeds *via* numerous oxidised intermediates, of which hydroperoxy ethanal ($OCHCH_2OOH$) and glycol aldehyde ($HOCH_2CHO$) produce glyoxal; oxidation of acetylene yields glyoxal directly. The rates of production and loss of glyoxal were found to increase significantly in the aqueous phase (cloud water droplets), with the gas-phase concentration of glyoxal being significantly reduced in the presence of cloud water droplets, and excess glyoxal being emitted to the gas phase when the cloud dissipated. Oxidation of water-soluble VOCs in cloud droplets is therefore an important route to the formation of SOA and a minor route to production of gas-phase OVOCs. With initial mixing ratios of acetylene and ethene set to values characteristic of the northern hemisphere (0.3 and 0.08 ppbv, respectively) the model predicted a maximum gas-phase glyoxal mixing ratios of 7 pptv at 900 m above sea level.

1.6.5 Climate impacts of oceanic reactive carbon

Oceanic carbon emitted into the gas phase can partition into the aerosol phase, causing direct and indirect effects on radiative forcing (scattering of light by aerosols and modification of cloud formation and properties) (Gantt *et al.*, 2009), and can modify the oxidising capacity of the atmosphere through reaction with OH and HO_2 (*e.g.* Lewis *et al.*, 1997, Liakakou *et al.*, 2007, Mahajan *et al.*, 2010). Two mechanisms have been proposed for the contribution of oceanic carbon to the aerosol phase: bubble-bursting at the ocean surface (primary formation) (O'Dowd *et al.*, 2004), and production of secondary organic aerosol through oxidation of ocean-emitted gas phase compounds (secondary formation) (O'Dowd and De Leeuw, 2007). Large numbers of organic carbon aerosols have been observed above regions of enhanced oceanic biological activity (O'Dowd *et al.*, 2004), suggesting that emissions of organic compounds from phytoplankton are involved in aerosol formation. However, the mechanism and magnitude of the contribution of oceanic carbon to marine organic aerosol is uncertain.

Top-down estimates of global oceanic carbon fluxes into the aerosol phase vary from 2.3 Tg C yr^{-1} (Langmann *et al.*, 2008) to 75 Tg C yr^{-1} (Roelofs, 2008).

Among the gas-phase compounds emitted from the ocean is isoprene, which is produced by seaweed (Broadgate *et al.*, 2004) and phytoplankton (Shaw *et al.*, 2003, Bonsang *et al.*, 2010). The oxidation products of isoprene are thought to have a small contribution to marine aerosol and cloud condensation nuclei formation, but estimates of global oceanic isoprene emissions vary between 0.1 and 11.6 Tg C yr^{-1} (Palmer and Shaw, 2005, Arnold *et al.*, 2009, Gantt *et al.*, 2009, Luo and Yu, 2010). In addition, isoprene emission rates vary with temperature, light, and phytoplankton species, which further complicates the picture (Shaw *et al.*, 2010). The impact of isoprene on marine aerosol and cloud formation is therefore not well quantified (*e.g.* Roelofs, 2008, Spracklen *et al.*, 2008, Arnold *et al.*, 2009).

Global models currently underestimate the concentration of organic carbon aerosol in the marine troposphere compared to observations (*e.g.* Spracklen *et al.*, 2008, Lapina *et al.*, 2011), and estimated isoprene emissions are not enough to account for the missing source (Lapina *et al.*, 2011). However, emissions of other organic compounds such as monoterpenes (Yassaa *et al.*, 2008) and glyoxal (Sinreich *et al.*, 2010) are not well quantified. Glyoxal and methylglyoxal and their oxidation products are thought to be important contributors to secondary organic aerosol (Hastings *et al.*, 2005, Ervens and Volkamer, 2010, Connelly *et al.*, 2012, van Pinxteren and Herrmann, 2013), with glyoxal uptake enhanced on marine particles (Liggio *et al.*, 2005).

Several studies have highlighted the contribution of oceanic organic species to OH reactivity. For example, Lewis *et al.* (1997) reported that isoprene was responsible for removing up to 20 % of OH at a midlatitude coastal site, and Liakakou *et al.* (2007) reported that marine emissions of isoprene in the Mediterranean decrease daytime OH concentrations by up to 26 %. The tropics are thought to be an important source region for oceanic terpenes (Gantt *et al.*, 2009), yet global climate models do not currently include the impact of oceanic emissions of such compounds (Arnold *et al.*, 2013). Glyoxal is a tracer of oxidation of reactive oceanic carbon (Fu *et al.*, 2008), and is

therefore an important species to consider when investigating the effects of oceanic carbon on the HO_x budget.

The ORC^3 (Oceanic Reactive Carbon: Climate Impacts) project aims to address uncertainties in the emission, processing and climate impacts of oceanic carbon (especially isoprene, monoterpenes and glyoxal) through combined fieldwork and modelling studies. Fieldwork will take place at the NCAS Cape Verde Atmospheric Observatory, which is located on north-eastern coast of the island of São Vicente (16.9° N, 24.9° W). The island shelves steeply into the ocean, with no coastal shallows and no large beds of macroalgae, and is therefore representative of the open ocean (*e.g.* Mahajan *et al.*, 2010). Long-term measurements of O_3, CO, NO, NO_2, VOCs, and aerosol composition have been conducted at the site since 2006, with halocarbon measurements beginning in 2007 and aerosol physical properties and greenhouse gases in 2008. Numerous short-term field measurement campaigns have been conducted at CVAO, including measurements of OH and HO_2 (Whalley *et al.*, 2010, Vaughan *et al.*, 2012), reactive halogen species (Read *et al.*, 2008, Mahajan *et al.*, 2010), and OVOCs (Mahajan *et al.*, 2010). Read *et al*. (2012) recently reported results from a measurement and modelling study at CVAO that indicate that the tropical Atlantic Ocean is a source of the OVOCs methanol and acetaldehyde. The seasonal meteorology of the site is well characterised. Prevailing north-easterly trade winds blow directly from the ocean to the measurement site. CVAO is downwind of the Mauritanian upwelling, a region of high biological activity, and is an ideal site to investigate links between marine biology, atmosphere, and climate. Throughout the year the site is influenced by marine air masses, with Atlantic marine and coastal African air being the predominant features in spring and summer, and continental African air with sporadic but significant Saharan dust events influencing the site in autumn and winter (Carpenter *et al.*, 2010).

Partners from the University of Leeds, the University of York, and Leipzig Institute for Tropospheric Research (TROPOS) will conduct measurements in spring and summer 2014. Measurements will include speciated monoterpenes, glyoxal, water-soluble and water-insoluble organic carbon aerosol, satellite measurements of chlorophyll-*a*, coloured dissolved organic matter (CDOM), and phytoplankton community structure, and the long-term measurements currently in place at CVAO. A global atmospheric

chemistry-climate model, TOMCAT/GLOMAP (Spracklen *et al.*, 2005), will be used to assess the impacts of oceanic VOC emissions on atmospheric composition, cloud condensation nuclei, and climate. The University of Leeds glyoxal laser-induced phosphorescence instrument is being developed specifically for deployment during the ORC^3 fieldwork (Chapter 6). The *in situ* measurements of glyoxal will contribute to the currently sparse observational database of glyoxal in remote marine environments and will be a vital input to the global modelling study of aerosol and CCN formation and climate impacts.

1.7 Summary

This chapter has highlighted the importance of field measurements and modelling to the study of atmospheric chemistry. The OH radical is the most important oxidising species in the troposphere, being responsible for the removal of many greenhouse gases, air pollutants, and ozone depleting substances. Comprehensive knowledge of its distribution and its sources and sinks throughout the atmosphere is vital if accurate model predictions of future properties of the atmosphere are to be made. The oxidation of VOCs in the nocturnal troposphere is known to have significant impacts on daytime air quality in urban regions, but the roles of O_3, NO_3, OH and HO_2 above the boundary layer are little studied, and there have been few dedicated studies of nighttime chemistry. The RONOCO project (see Chapter 4) aims to address these issues with a suite of airborne measurements combined with modelling studies.

The role of halogen chemistry in stratospheric and tropospheric ozone depletion is well-documented, and the impact of halogens on OH and HO_2, and therefore the oxidising capacity of the atmosphere, has been highlighted by recent studies. The contribution of biogenic halogen-containing compounds to stratospheric ozone depletion becomes more important as the impact of anthropogenic compounds declines. Emissions and transport of biogenic halogenated VSLS are expected to change as the climate warms, but large uncertainty is associated with predicting the coupled behaviour of the changing climate and biogeochemical cycles. The SHIVA project (see Chapter 5) aims to reduce some of these uncertainties.

Finally, the influence of oceanic reactive carbon on SOA formation and on the oxidising capacity of the marine boundary layer is not well understood. Emission strengths and source mechanisms for oceanic biogenic VOCs, such as isoprene, and their oxidation products, are not well known. Measurements of high concentrations of glyoxal in the remote marine boundary layer cannot be explained by concentrations of known precursors. Glyoxal's high solubility means that the ocean could be a sink rather than a source, and that uptake onto aqueous aerosol and cloud droplets is rapid, so that glyoxal has the potential to contribute significantly to the formation of SOA. The ORC^3 project will involve measurements and modelling of gas-phase oceanic carbon compounds, including glyoxal (see Chapter 6), and will therefore improve our understanding of the global impacts of oceanic carbon.

1.8 Project aims

The aims of this PhD project are to:

- Make nighttime airborne measurements of OH and HO_2 over the UK using the FAGE technique.
- Analyse nighttime routes to HO_x radical production using measurements of O_3, NO_3, RO_2, VOCs, and other species and parameters measured onboard the aircraft.
- Make ship-based measurements of IO using LIF in an observationally sparse oceanic region, requiring preparation of the LIF instrument for measurements onboard a research vessel and improvements to the instrument's sensitivity and limit of detection.
- Investigate the major sources and sinks of IO during the cruise, facilitated by measurements of I_2, the sum of HOI + ICl, and various species and parameters measured during the cruise.
- Build, test, and calibrate a laser-induced phosphorescence instrument for detection of atmospheric glyoxal at low pptv levels, in preparation for further development of the instrument for use during the field campaign in Cape Verde in 2014.

Chapter 2. HO_x instrumentation

Measurements of ambient concentrations of OH and HO_2 are vital to our understanding of tropospheric oxidation chemistry. Both radical species have short lifetimes and low atmospheric concentrations, meaning that measurement techniques must be sensitive and have good temporal resolution. Since OH and HO_2 are readily lost to surfaces, measurements must be made *in situ*. Two techniques are currently in use for the measurement of OH and HO_2 in the troposphere: Fluorescence Assay by Gas Expansion (FAGE), and Chemical Ionisation Mass Spectrometry (CIMS). Both of these techniques are used for ground-based and aircraft-based measurements. Differential Optical Absorption Spectroscopy (DOAS) is used for measurements of OH at the Simulation of Atmospheric Photochemistry in a Large Reaction Chamber (SAPHIR) facility. HO_2 is also detected by RO_x chemical conversion/CIMS (ROXMAS or PerCIMS) (Hanke *et al.*, 2002, Edwards *et al.*, 2003), turbulent-flow chemical ionisation mass spectrometry (TF-CIMS) (Raventós-Duran *et al.*, 2007), and is measured as part of the total sum of peroxy radicals, $\sum RO_2 + HO_2$, using the Peroxy Radical Chemical Amplification (PERCA) technique (Cantrell *et al.*, 1984, Green *et al.*, 2003, Green *et al.*, 2006). The higher heterogeneous loss rate of HO_2 compared to RO_2 can be used to selectively remove HO_2 from sampled air by fitting a pre-inlet filled with small beads to a PERCA instrument, enabling discrimination between RO_2 and HO_2 (Miyazaki *et al.*, 2010). HO_2 has been measured by matrix isolation electron spin resonance (MIESR) (Mihelcic *et al.*, 1985, Mihelcic *et al.*, 1990, Mihelcic *et al.*, 2003) but this instrument is no longer in use. Details of the HO_x measurement methods currently in use in the field and in chamber studies are summarised in Table 2.1, with descriptions given in section 2.1 to 2.3. Reviews of field measurements of OH and HO_2 can be found in Heard and Pilling (2003) and Stone *et al.* (2012). A summary of nighttime field measurements of OH and HO_2 can be found in Table 1.1 in Chapter 1. The remainder of this chapter describes a compact, portable FAGE instrument for the measurement of OH and HO_2 in the troposphere, developed at the University of Leeds and employed during the RONOCO and SeptEx campaigns (see Chapter 4).

Table 2.1. Summary of techniques currently employed for tropospheric field and chamber measurements of OH and HO_2.

Method	Details	Typical 1σ accuracy	Typical limit of detection / molecule cm^{-3}	References
Long-path Differential Optical Absorption Spectroscopy (LP-DOAS)	Optical absorption spectroscopy using active light source (UV laser) at λ = 308 nm. Multiple species can be detected and quantified in a single spectrum (OH, HCHO, SO_2, naphthalene). White-type multiple reflection cell gives path lengths of up to 3 km. Absolute technique requiring no calibration. Not currently used in the field, but used in SAPHIR chamber.	OH: 6.5 %	OH:1–4 × 10^6 (3–6 minutes)	Hausmann *et al.* (1997), Brandenburger *et al.* (1998), Brauers *et al.* (2001), Schlosser *et al.* (2007), Schlosser *et al.* (2009)
Chemical Ionisation Mass Spectrometry (CIMS), Peroxy Radical CIMS (PerCIMS and ROXMAS)	Ambient air sampled into flow tube. Chemical conversion of OH to H_2SO_4 by titration with SO_2, followed by conversion to HSO_4^- and detection by quadrupole mass spectrometry. HO_2 detected by conversion to OH with NO (PerCIMS and ROXMAS). Conditions tuned to minimize RO_2 detection. Ground-based and aircraft-based instruments.	OH: 19 % HO_2: 17 %	OH: 1–4 × 10^5 (5–10 minutes) HO_2: 1–4 × 10^7 (15 seconds)	Berresheim *et al.* (2000), Hanke *et al.* (2002), Edwards *et al.* (2003), Rohrer and Berresheim (2006), Sjostedt *et al.* (2007), Kukui *et al.* (2008), Schlosser *et al.* (2009), Hornbrook *et al.* (2011)
Laser-induced fluorescence spectroscopy (LIF), or Fluorescence Assay by Gas Expansion (FAGE)	Excitation of OH using laser light at λ ~ 308 nm followed by detection of resulting on-resonance fluorescence at λ ~ 308 nm. Measurements of HO_2 achieved by conversion to OH with excess NO. Instruments require calibration with known concentrations of OH and HO_2. Ground-based, aircraft-based and zeppelin-based instruments.	OH: 16 % HO_2: 16 %	OH: 2–4 × 10^5 (1–5 minutes) HO_2: 1–4 × 10^6 (30 seconds–5 minutes)	Holland *et al.* (2003), Faloona *et al.* (2004), Ren *et al.* (2006), Kanaya *et al.* (2007), Dusanter *et al.* (2009), Furneaux (2009), Commane *et al.* (2010), Martinez *et al.* (2010)

2.1 Long-path Differential Optical Absorption Spectroscopy

The principles of differential optical absorption spectroscopy (DOAS) are described in detail in Chapter 3. Briefly, the intensity of light transmitted through a sample of an absorbing gas species is given by the Beer-Lambert law (Plane and Saiz-Lopez, 2006):

$$I(\lambda) = I_0(\lambda)\exp\left(-l\left(\sum_{i=1}^{n}\sigma_i(\lambda)\overline{c_i}\right)\right) \tag{2.1}$$

where $\overline{c_i}$ is the average concentration of species i over the light path of length l, $I_0(\lambda)$ and $I(\lambda)$ are the intensities of light at wavelength λ transmitted by an air mass without and with the absorbing species, respectively, and $\sigma_i(\lambda)$ is the absorption cross section of the absorbing species. The concentration of an absorbing species can therefore be found by absorption spectroscopy, in which the wavelength-dependent intensity of light transmitted through a sample is measured. In the DOAS technique, narrow spectral absorption features are used to identify absorbing species, and their concentrations are determined by least-squares fitting of reference absorption spectra to the measured atmospheric spectrum.

LP-DOAS has been used to make OH measurements in the field (Dorn *et al.*, 1996, Brauers *et al.*, 2001), but is now solely used in the atmospheric simulation chamber SAPHIR at Jülich. The following details pertain to the Jülich instrument (Brauers *et al.*, 2001, Schlosser *et al.*, 2009). The LP-DOAS instrument uses broadband laser light at $\lambda \sim 308$ nm to record atmospheric absorption spectra over a long light path. The laser bandwidth (0.41 nm) spans 6 rotational lines in the $A^2\Sigma^+ (v'=0) \leftarrow X^2\Pi (v''=0)$ transition. OH is detected by absorption of laser light in these rovibronic transitions. The instrument consists of the laser light source, an open White-type multiple-reflection cell, a high-resolution spectrograph, and a photodiode array detector. The multiple-reflection cell has a base length of 20 m and provides a total light path length of 1−3 km, so that high sensitivity is achieved without loss of spatial resolution. The 2σ limit of detection for a 3 minute data point (~ 1.5×10^6 molecule cm^{-3}) is determined by

the signal-to-noise ratio of the measured spectrum, which is in turn determined by the path length. The accuracy of the measurements (~ 6.5 %, 1σ) depends primarily on the accuracy of the OH reference spectrum (wavelength-dependent absorption cross section) (Hausmann *et al.*, 1997, Schlosser *et al.*, 2007). Despite low temporal resolution and high limit of detection compared to LIF (see Table 2.2), LP-DOAS provides a calibration standard for comparison with other instruments (LIF and CIMS) because of the high accuracy of the measurements. During a comparison study, simultaneous LIF and DOAS measurements in the SAPHIR chamber were generally in good agreement, with higher values measured by the LIF instrument when the conditions in the chamber were characterised by high NO_x (Schlosser *et al.*, 2007).

2.2 Chemical Ionisation Mass Spectrometry

The CIMS technique relies upon chemical conversion of a reactive trace gas to an ion product that can be detected by mass spectrometry. A detailed description of an OH CIMS instrument is given by Berresheim *et al.* (2000). Ambient air is drawn through a 100 mm wide sample tube under laminar flow conditions. The central portion of the flow is sampled by a 10 mm nozzle shortly after the main inlet. $^{34}SO_2$, distinguishable from the naturally abundant $^{32}SO_2$, is introduced before the nozzle in a flow of nitrogen. OH is titrated with SO_2 to form H_2SO_4 as follows (Eisele and Tanner, 1991):

$$OH + SO_2 + M \rightarrow HSO_3 + M \quad \text{(R2.1)}$$

$$HSO_3 + O_2 \rightarrow SO_3 + HO_2 \quad \text{(R2.2)}$$

$$SO_3 + H_2O + M \rightarrow H_2SO_4 + M \quad \text{(R2.3)}$$

The mixing ratio of SO_2 in the flow (~ 10 ppmv) ensures that the majority of the sampled OH reacts with SO_2, rather than ambient trace gases such as CO and CH_4, within approximately 20 ms. Losses of H_2SO_4 to aerosol particles and the walls of the flow tube are considered to be negligible within the 1–2 seconds required for the measurement. Recycling of OH from reaction of the HO_2 produced in reaction (R2.2) with ambient NO or O_3 occurs on a timescale of less than 1 second. Propane is therefore added downstream of the nozzle to scavenge 98 % of the recycled OH, with the remaining 2 %, along with ambient H_2SO_4, being accounted for in background

measurements. Following the conversion of ambient OH to H_2SO_4, the flow is allowed to become laminar and enters the ion source region, where NO_3^- is added to the flow, forming HSO_4^- as follows:

$$H_2SO_4 + NO_3^- \rightarrow HSO_4^- + HNO_3 \qquad \text{(R2.4)}$$

The HSO_4^- and NO_3^- ions, and other ions produced by the ion source, are forced through a 200 μm pinhole into a vacuum region by an electric field. Most of the ions are present as clusters with neutral ligands such as HNO_3. These ligand molecules are removed by collision with N_2 molecules in a collision-dissociation chamber, through which they are accelerated by a positive electric field. Finally the ions are focussed by electronic lenses and detected by a quadrupole mass spectrometer. For background measurements, the concentration of ambient H_2SO_4 is given by the rate constant, k, of reaction (R2.4), the reaction time, t, and the ratio of signal counts from HSO_4^- and NO_3^- as follows (Berresheim *et al.*, 2000):

$$\left[H_2SO_4\right] \approx \frac{1}{kt}\frac{\left\{HSO_4^-\right\}}{\left\{NO_3^-\right\}} \qquad (2.2)$$

where square and curly brackets denote concentrations and signal counts, respectively. Background measurements are enabled by titration of ambient OH with an excess (~ 400 ppmv) of propane. The concentration of OH is determined from the difference in HSO_4^- signal counts between background and OH measurements, $\Delta\left\{HSO_4^-\right\}$, as follows:

$$\left[OH\right] = F\frac{\Delta\left\{HSO_4^-\right\}}{\left\{NO_3^-\right\}} \qquad (2.3)$$

where F is a calibration factor. The instrument is calibrated for H_2SO_4 and OH by generating known concentrations of OH in the inlet *via* photolysis of ambient water vapour with light from a pen-ray mercury lamp centred at λ = 184.9 nm. The water vapour concentration in the inlet is determined by a hygrometer. An OH measurement cycle takes 30 s, with the OH and background signals being integrated for 8 s. The uncertainty in the measurements depends on the uncertainty in the calibration factor, F, uncertainty in the signal count rate, wind-induced turbulence, and chemical

interferences. The 1σ accuracy of CIMS OH measurements is 19 % (Schlosser *et al.*, 2009) and the 2σ detection limit is 2×10^5 molecule cm^{-3} (Berresheim *et al.*, 2000).

The CIMS technique has also been used to detect HO_2 by addition of NO to convert HO_2 and RO_2 to OH. This adapted technique is known as ROXMAS (RO_x chemical conversion/chemical ionisation mass spectrometry) (Hanke *et al.*, 2002) or PerCIMS (peroxy radical chemical ionisation mass spectrometry) (Edwards *et al.*, 2003, Hornbrook *et al.*, 2011). The concentrations of NO, SO_2, and a dilution gas (O_2 or N_2) in the inlet are adjusted to favour conversion of either HO_2 or HO_2 + RO_2 to H_2SO_4. PerCIMS has been used to measure RO_2 and HO_2 during numerous aircraft-based field measurement campaigns.

During the international HO_x comparison study HOxComp in 2005, comparisons of measurements of OH by LIF and CIMS instruments were conducted in ambient air, and comparisons of LIF and DOAS were conducted in the SAPHIR chamber. Generally good agreement was found between ambient measurements by the CIMS instrument and the three LIF instruments tested, though the CIMS instrument generally measured lower values than the LIF instruments. Excellent agreement was found between the DOAS and LIF instruments measuring in the chamber, with slopes between 1.01 and 1.13 in the linear regression between data sets (Schlosser *et al.*, 2009). An aircraft-based HO_x comparison study was conducted during the ARCTAS (Arctic Research of the Composition of the Troposphere from Aircraft and Satellites) project in 2008. Measurements of OH were made by LIF and CIMS, and measurements of HO_2 were made by LIF and PerCIMS. The LIF instrument reported higher values than the CIMS instruments, with linear regression of the data sets yielding $r^2 = 0.72$ for both OH and HO_2. Differences in the data could generally be attributed to the uncertainties associated with each instrument (Ren *et al.*, 2012). Other intercomparison studies are reviewed by Heard and Pilling (2003).

2.3 Measurements of OH and HO_2 by Laser-Induced Fluorescence spectroscopy: the FAGE technique

Following the discovery of the importance of OH in atmospheric oxidation (Weinstock, 1969, Levy, 1971, Weinstock and Niki, 1972), laser-induced fluorescence (LIF) spectroscopy was used to make the first measurements of OH in the atmosphere (Wang and Davis Jr, 1974). LIF involves the excitation of a molecule in a rovibronic transition from its ground state to a bound electronically excited state using laser light. The subsequent relaxation of the molecule from the excited state is accompanied by spontaneous emission of light (fluorescence), the intensity of which is directly proportional to the concentration of the molecule. The molecule can also relax *via* non-radiative processes such as collisional quenching, in which the excess energy is transferred to another molecule (*e.g.* O_2 or N_2).

In early OH instruments, laser light at λ = 282 nm was used to excite OH radicals in the $A^2\Sigma^+(v'=1) \leftarrow X^2\Pi_i(v''=0)$ transition. Fluorescence in the (1,1) and (0,0) bands, between λ = 308 nm and λ = 315 nm, is sufficiently separated from the excitation wavelength (282 nm) to enable discrimination of the weak fluorescence signal from the strong signal due to scattered laser light (Baardsen and Terhune, 1972). Although initial measurements appeared to be promising (Wang and Davis Jr, 1974, Wang *et al.*, 1975), it was later discovered that photolysis of ozone at λ = 282 nm caused production of OH in the path of the laser beam (reactions (R2.5) and (R1.5)), with the resulting signal, following absorption of a second photon, being far larger than the signal from ambient OH (Wang *et al.*, 1975, Hanabusa *et al.*, 1977, Davis *et al.*, 1981, Smith and Crosley, 1990).

$$O_3 + h\nu\ (\lambda = 282\ \text{nm}) \rightarrow O(^1D) + O_2 \qquad \text{(R2.5)}$$

$$O(^1D) + H_2O \rightarrow OH + OH \qquad \text{(R1.5)}$$

All tropospheric LIF instruments now use laser light at λ = 308 nm to excite OH in the $(v'=0) \leftarrow (v''=0)$ transition, and detect on-resonance fluorescence at the same wavelength (see Figure 2.1). The absorption cross-section of O_3 is 23 times smaller at

λ = 308 nm than at λ = 282 nm (Sander *et al.*, 2011), so the interference from laser-generated OH is much reduced. The absorption cross section of OH is approximately 4 times larger at λ = 308 nm than at λ = 282 nm, so the ratio of ambient to laser-generated OH is two orders of magnitude larger at the longer wavelength (Crosley, 1995). Finally, laser photolysis of O_3 and subsequent production of OH is further reduced by the use of high pulse repetition rate lasers with low pulse energies, necessitating a high gas flow rate through the detection cell. It should be noted that successful measurements of OH using an excitation wavelength of λ = 282 nm have been made in the stratosphere, where low water vapour concentrations (< 10 ppmv) and low pressure (< 100 mb) minimise the interference from reaction (R1.5) (*e.g.* Stimpfle and Anderson, 1988).

Since the fluorescence at λ = 308 nm is not spectrally separated from the excitation wavelength, the fluorescence signal is discriminated from laser scattered light by temporal gating. At 760 Torr, collisional quenching results in an OH fluorescence lifetime on the order of 1 ns (Heard and Pilling, 2003). The fluorescence lifetime of an excited state, τ_F, is given by:

$$\tau_F = \frac{1}{k_r + k_{nr}} \tag{2.4}$$

where k_r and k_{nr} are rate constants for radiative and non-radiative decay processes, respectively. Reducing the rate of non-radiative decay therefore extends the fluorescence lifetime and increases fluorescence quantum yield, Φ_F:

$$\Phi_F = \frac{\text{number of photons emitted}}{\text{number of photons absorbed}} = \frac{k_r}{k_r + k_{nr}} \tag{2.5}$$

In the FAGE (Fluorescence Assay by Gas Expansion) technique, ambient air is sampled through a small hole or pinhole (< 2 mm diameter) into a low-pressure detection chamber (0.7−4 Torr). The sampled air forms a supersonic gas expansion beam, in which the rate of collision between OH radicals and ambient air molecules is reduced.

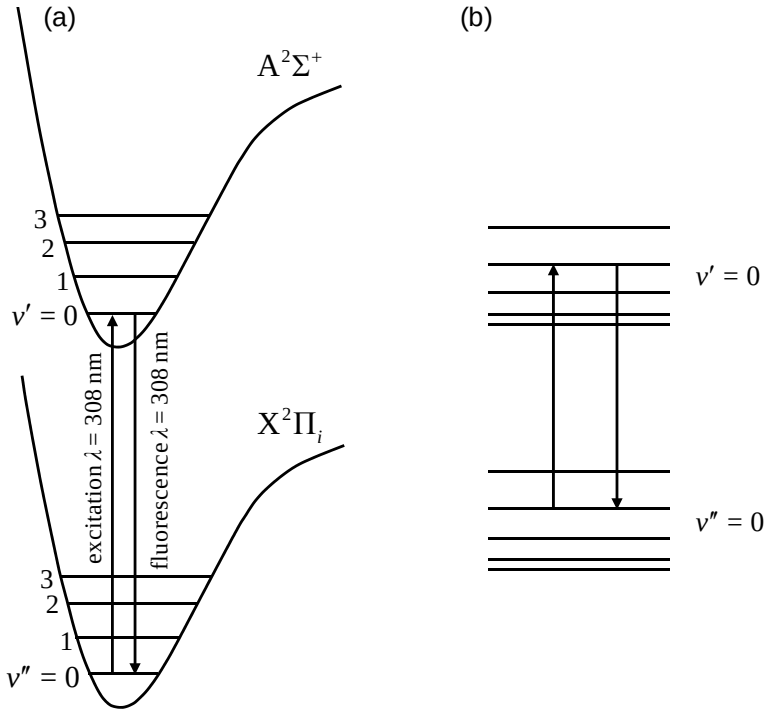

Figure 2.1. Excitation and fluorescence scheme of the $A^2\Sigma^+(v'=0) \leftarrow X^2\Pi_i(v''=0)$ OH transition at λ = 308 nm, showing (a) the $v'=0 \leftarrow v''=0$ transition, and (b) excitation to, and fluorescence from, a single rotational level. Vibrational levels higher than $v=3$ have been excluded for clarity. Redrawn from Heard (2006).

The fluorescence lifetime is therefore extended to several hundred nanoseconds, significantly longer than the laser pulse, so that the measured signal can be temporally discriminated from laser scattered light. The decrease in total number density, and therefore in the number of OH radicals excited, is compensated by the increase in fluorescence quantum yield (Hard *et al.*, 1984).

Detection of HO_2 using the FAGE technique is achieved by titrating HO_2 with an excess of NO in the detection cell to yield OH:

$$HO_2 + NO \rightarrow OH + NO_2 \qquad \text{(R1.10)}$$

Detection of OH and HO_2 can be achieved by using two detection cells with separate inlets, or by positioning the HO_2 cell in-line and downstream of the OH cell, or by using a single cell and alternating between OH and HO_2 measurements. Unlike DOAS, FAGE is not an absolute technique, and FAGE instruments require calibration with known concentrations of OH and HO_2 in order to interpret measured fluorescence signals as

concentrations. Details of the FAGE calibration technique employed for the Leeds Aircraft FAGE instrument are given in section 2.5. The 1σ accuracy of the measurements, determined by the instrument calibration, is on the order of 16 %. Typical one minute limits of detection are 1.0×10^6 molecule cm^{-3} for OH and 6.0×10^5 molecule cm^{-3} for HO_2.

FAGE instruments are suited to ground-based, ship-based, and aircraft-based field measurements. The instrument described in this chapter was designed specifically for use onboard the Facility for Airborne Atmospheric Measurements (FAAM) BAe-146 G-LUXE research aircraft, which is discussed in section 1.1. Table 2.2 gives details of the three aircraft-based FAGE instruments currently in use worldwide for field measurements. In addition the Jülich FAGE instrument has been installed onboard a Zeppelin NT during several successful field campaigns. The portable nature of aircraft-based instruments also makes them suitable for use on ground-based and ship-based platforms. All of the aircraft-based FAGE instruments currently in use probe the $A^+\Sigma^2\left(v'=0\right) \leftarrow X^2\Pi_i\left(v''=0\right)$ transition at λ = 308 nm, and detect on-resonance fluorescence. Detection of OH and HO_2 occurs in two fluorescence cells in series with ATHOS and HORUS using White-type multi-pass cells and the Leeds Aircraft FAGE using single-pass cells. The calibration of all three instruments is based on production of known concentrations of OH and HO_2 *via* photolysis of water vapour by a UV lamp, with HORUS alone being calibrated both in flight and on the ground. Each of the instruments has been calibrated for different internal cell pressures by using inlet pinholes of different diameters, under the assumption that the diameter of the pinhole does not affect radical loss. This assumption has been validated by an alternative calibration method (see section 2.8.3).

Table 2.2. Details of aircraft-based FAGE instruments currently in use for atmospheric measurements of OH and HO_2.

Instrument	Aircraft	Details	Typical 1σ uncertainty	Typical limit of detection / molecule cm^{-3}	References
Pennsylvania State University, Airborne Tropospheric Hydrogen Oxides Sensor: ATHOS	NASA DC-8	Front-facing inlet housed in nacelle (cover housing) on the underside of the aircraft, with two concentric airfoils to reduce speed of air past inlet. 1.5 mm diameter inlet nozzle. Measurement cycle is 15 seconds online, 5 seconds offline. Solar scatter assumed to be constant between online and offline cycle. Cell pressure range: 2.3 Torr at 12 km to 9 Torr at sea level.	OH: 16 % HO_2: 16 %	OH: 0.5–2.5 × 10^5 HO_2: 0.5–2.5 × 10^6 (1 minute)	Faloona *et al.* (2004), Ren *et al.* (2012)
Max Planck Institute for Chemistry, Hydroxyl Radical Measurement Unit based on Fluorescence Spectroscopy: HORUS	GFD Learjet 35A	Design based on ATHOS. Front-facing inlet, detection cells, pumps, and gas cylinders are mounted in a wing pod. 1.25 mm pinhole. In-flight calibrations to complement ground-based calibrations. Measurement cycle is 5 seconds online, 5 seconds offline. Cell pressure range: 1.5 Torr at 13 km to 3.75 Torr at sea level.	OH: 16 % HO_2: 17 %	OH: 1.0 × 10^6 HO_2: 2.0 × 10^6 (1 minute)	Martinez *et al.* (2010)
University of Leeds Aircraft-based Fluorescence Assay by Gas Expansion instrument: Aircraft FAGE	FAAM BAe-146	Inlet mounted perpendicular to direction of aircraft through window blank on side of aircraft, with front-facing shrouded inlet to slow air flow. 5 cm diameter sampling tube. Solar scatter recorded for each pulse. Cell pressure range: 1.3 Torr at 10 km to 2.1 Torr at sea level.	OH: 16 % HO_2: 16 %	OH: 1.0 × 10^6 HO_2: 6.0 × 10^5 (1 minute)	Commane (2009), Commane *et al.* (2010)

2.4 The Leeds Aircraft FAGE Instrument

The aircraft FAGE instrument used during this work was designed specifically for use onboard the FAAM (Facility for Airborne Atmospheric Measurements) BAe-146 G-LUXE research aircraft, shown in Figure 2.2. Airborne measurements enable *in situ* measurements of short-lived species such as OH and HO_2 from close to the surface to the stratosphere, and over a wide horizontal range. Specific air masses, such as an urban or industrial plume, can be characterised according to their chemical signature and can be intercepted multiple times, or tracked through the atmosphere. Flight plans can be altered mid-flight according to the chemical and physical conditions encountered. An overview of the chemical composition of the atmosphere above a large area of land or ocean can be gained very quickly. The BAe-146 has an altitude ceiling of ~12 km (~ 40,000 feet) and, when operating for atmospheric chemistry measurements with a full payload of instruments, 3 flight crew, and 18 scientists, the aircraft has a maximum flight duration of ~ 5 hours. Typical air speeds during science flights are ~ 120 m s^{-1}.

The design requirements for aircraft-based instruments are more stringent than for ground-based instruments, with weight, power consumption, mechanical strength of components, instrument housing, and changing ambient pressure being some of the necessary considerations. The design of the Leeds aircraft FAGE instrument and requirements for operation onboard the BAe-146 are discussed in detail by Floquet (2006). The Leeds aircraft FAGE instrument is housed in two double-width 19 inch aircraft racks, with the inlet and detection cells, and pump set, being separate to the two racks. Being portable and compact, the instrument is suitable for deployment for ground-based and ship-based measurements as well as on the BAe-146 aircraft. The instrument has been used in numerous measurement campaigns, including the African Monsoon Multidisciplinary Analysis (AMMA) in 2006 (Commane *et al.*, 2010), the Impact of Combined Iodine and Bromine release on the Arctic Atmosphere (COBRA) in 2008 (Edwards *et al.*, 2011), and the Seasonal Oxidant Study (SOS) in 2009 (Vaughan *et al.*, 2012). The instrument has also been adapted to measure ambient concentrations of IO (Commane *et al.*, 2011) (see Chapter 3 and Chapter 5).

Figure 2.2. The BAe-146 G-LUXE research aircraft in flight, showing the FAGE Eisele inlet (circled) on the starboard side of the aircraft (see section 2.4.3). Photograph by David McIntosh of BAE Systems.

2.4.1 Laser system

A diagram of the laser system is shown in Figure 2.3. An all solid-state Nd:YAG pumped tunable Ti:Sapphire laser generates pulsed light at λ = 308 nm. The Nd:YAG (Neodymium-ion doped Yttrium Aluminium Garnet, $Y_3Al_5O_{12}$) laser (Photonics Industries DS-532-10) is diode pumped, Q-switched, and intracavity frequency-doubled using a lithium triborate crystal (LBO) to give ~10 W of light at λ = 532 nm, at a pulse repetition frequency (PRF) of 5 kHz. This green light is polarised, focussed and used to pump a tunable Ti:Sapphire (Ti:Al_2O_3) laser (Photonics Industries TU-UV-308nm) to produce 1.5 W of infrared light at λ ~ 924 nm, with a temporal delay of 220 ns from the Nd:YAG pulse when perfectly aligned. The wavelength of the IR light is tuned by changing the angle of incidence of a diffraction grating positioned in the Ti:Sapphire cavity, using a software-controlled stepper motor. The IR light is passed through two temperature-controlled non-linear crystals (lithium triborate, LBO, followed by beta barium borate, BBO). The first generates the second harmonic at λ = 462 nm. The polarisation of the blue light is rotated before passing through the second crystal, where sum-frequency mixing of the first and second harmonics generates the third harmonic at λ = 308 nm. The pulse width (full width at half maximum) of the UV light is approximately 35 ns, the linewidth is approximately 0.06 cm^{-1}, and the beam width is approximately 2 mm.

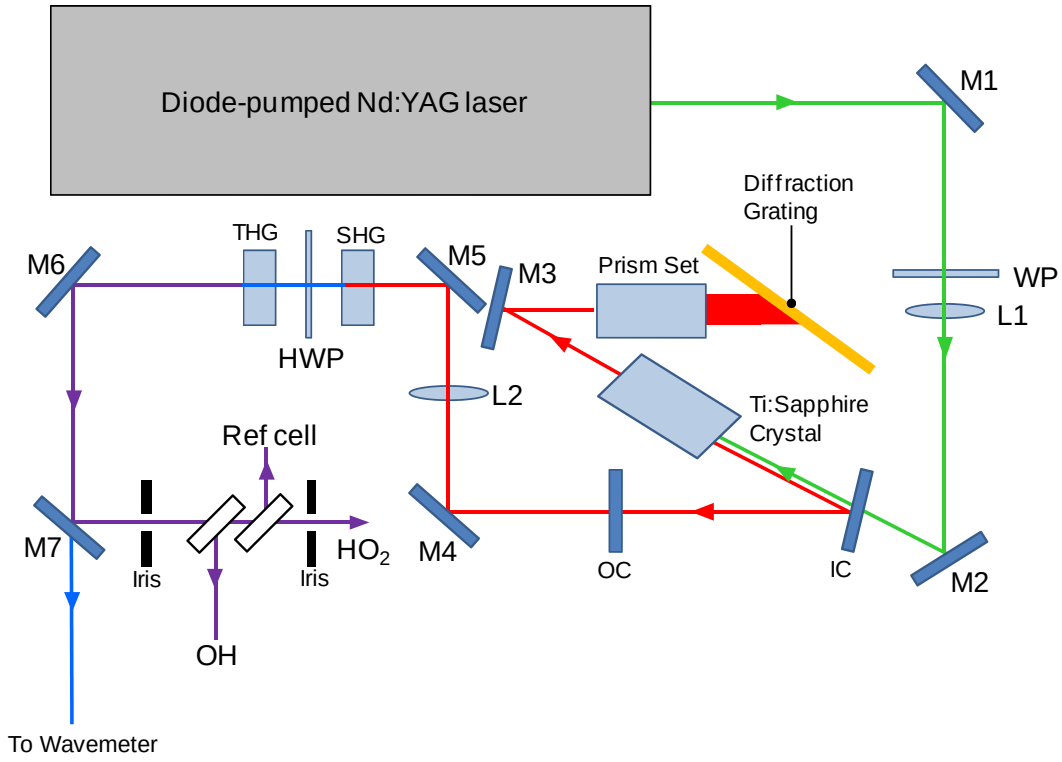

Figure 2.3. Diagram of laser system for HO_x aircraft FAGE instrument. M = mirror; WP = wave plate; L = lens; IC = input coupler; OC = output coupler; SHG = second harmonic generation; HWP = half wave plate; THG = third harmonic generation. 'OH', 'HO_2' and 'Ref cell' indicate fibre launchers for detection and reference cells, respectively. Green lines represent light at λ = 532 nm, red lines represent light at λ = 924 nm, blue lines represent light at λ = 462 nm, and purple lines represent light at λ = 308 nm.

The UV laser power is typically 50–100 mW, giving pulse energies between 10 and 20 μJ. Two turning mirrors direct the UV light onto two dielectric-coated beamsplitters, which divide the light between three optical fibre launchers, from where fibre optic cables (Oz Optics QMNJ-55-UVVis-200/240-3-4) deliver the light to the OH, HO_2, and reference cells, as shown in Figure 2.3. Typically 50 % of the light is delivered to the OH detection cell, with 45 % going to the HO_2 cell, and 5 % going to the reference cell, though this ratio can be altered according to the total laser power available and measurement priorities. The detection cell fibres are 5 m long and have a transmission efficiency of 50−75 %. The Nd:YAG and Ti:Sapphire lasers are mounted on an aluminium base plate and housed in a metal casing. The laser assembly is mounted on anti-vibration mounts on the top of one of the double-width 19 inch aircraft racks. To enable measurement of the laser wavelength, a small amount of λ = 462 nm light leaks through a mirror onto the probe of a wavemeter (Coherent WaveMaster; resolution:

± 0.001 nm; accuracy: ± 0.005 nm) which is positioned outside the laser casing. A fast photodiode (Thorlabs DET10A/M) is positioned to receive laser light reflected from the window of the wavemeter probe. The fast photodiode is connected to an oscilloscope (LeCroy, WaveRunner LT372), providing a means of monitoring the temporal positions of the laser trigger, the laser pulse, and the switch-on of the channel photomultipler tube.

2.4.2 Reference cell

A reference cell aids the tuning of the laser wavelength to the OH $Q_1(2)$ rotational line of the $A^+\Sigma^2(v'=0) \leftarrow X^2\Pi_i(v''=0)$ transition (λ = 307.995 nm) (see Figure 2.4). The reference cell is a black anodised aluminium cylinder, through which a slow flow of humidified air from a water bubbler is passed. The pressure inside the cell is maintained at ~ 2 Torr by a small vacuum pump (Edwards E2M1.5 rotary pump). A heated coiled filament (0.2 mm diameter 80:20 Ni:Chrome wire, supplied with 1.5 A at 2.5 V) inside the cell causes thermolysis of water vapour, which produces high concentrations of OH. Laser light at λ = 308 nm is delivered to the cell *via* a 3 m long optical fibre and a fibre collimator, on an axis perpendicular to the air flow. The signal from OH fluorescence is detected on the third axis by a channel photomultiplier tube (CPM) (Perkin Elmer C943P). A single biconvex lens and an interference filter centred at λ = 308 nm focus the fluorescence and minimise transmission of laser scattered light to the CPM. The concentration of OH in the reference cell is sufficiently high that the fluorescence signal can be observed above the signal due to scattered laser light, so no temporal gating of the CPM is required. The signal from the CPM is detected by a photon counting card (Becker & Hickl PMS 400) in the data acquisition computer. The photon counting card is switched on after scatter from the laser pulse has diminished. The fluorescence signal is monitored by the acquisition software in the computer.

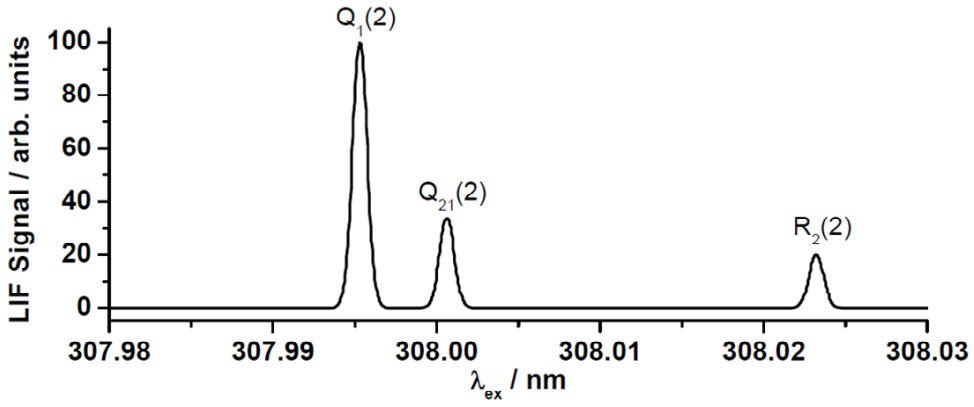

Figure 2.4. LIFBASE simulation of the OH fluorescence spectrum around λ = 308 nm (298 K), showing three rotational lines: $Q_1(2)$ (λ = 307.9952 nm), $Q_{21}(2)$ (λ = 308.0007 nm), and $R_2(2)$ (λ = 308.0232 nm). Resolution = 0.25 pm. Simulation and figure by Commane (2009). The Leeds aircraft FAGE instrument probes the $Q_1(2)$ line.

Prior to the start of each OH and HO_2 measurement cycle, the laser wavelength is scanned from 307.933 nm to 308.000 nm, which encompasses the $Q_1(2)$ rotational line (see Figure 2.4). The scan is then repeated until the signal from the reference cell is equal to at least 95 % of the peak signal from the initial scan. At this wavelength (the 'online' wavelength), the stepper motor is halted and the OH and HO_2 measurements proceed. Following the online measurement period, the laser wavelength is changed to an 'offline' position, ~0.005 nm to the short wavelength side of the $Q_1(2)$ peak.

2.4.3 Inlet and pre-detection assembly

OH and HO_2 are readily lost to surfaces, so sampling ambient air *via* long sampling tubes is not suitable for FAGE measurements. Rather the instrument must sample ambient air directly, and the distance between the inlet and the detection axes must be as short as possible to minimise loss of radicals on the inside of the inlet. For airborne measurements, this requires the inlet to be located outside the skin of the aircraft. In the case of the Pennsylvania State instrument, ATHOS, the inlet is housed in a nacelle beneath the aircraft, and in the case of MPI Heidelberg instrument, HORUS, the inlet, detection cells, pump, and gas cylinders are housed in a wing pod (see Table 2.2). The Leeds aircraft FAGE instrument is positioned on the starboard side of the aircraft cabin, with all components of the instrument except the inlet positioned inside the aircraft, as shown in Figure 2.5. The inlet is mounted through a window blank perpendicular to the direction of travel, so that sampled air travels along a straight tube to the detection axes.

This arrangement helps to minimise loss of radicals to the walls of the inlet, but means that ambient air must be sampled at 90º to the airflow outside the aircraft, which is moving in excess of 100 m s^{-1} relative to the inlet. To achieve this, the air flow is slowed down by an 'Eisele' inlet (Eisele *et al.*, 1997, designed for the BAe-146 by Jack Fox, NCAR, Boulder, USA), consisting of two concentric cylinders with restrictions at the downstream ends, fitted to the outside of the aircraft (see Figure 2.2, Figure 2.5, and Figure 2.6). Air is slowed by a factor of ~ 16 between the entrance of the Eisele inlet and the FAGE inlet.

The FAGE inlet is a 0.7 mm pinhole in the centre of a conical nozzle, sealed to a 5 cm internal diameter aluminium flow tube. The section of tube between the pinhole and the OH detection axis is called the pre-detection assembly, and can be changed in length according to the measurement requirements. For aircraft measurements, the total distance between the inlet and the OH detection axis is 50 cm, with the HO_2 detection axis located a further 24 cm downstream. When the aircraft instrument is deployed for ground-based measurements, a much shorter pre-detection assembly can be used to further reduce loss of OH and HO_2 to the walls. The expansion of sampled air through the pinhole results in significant cooling in the gas stream. The temperature profile of the gas expansion beam between the pinhole and the detection axis has been experimentally determined for the Leeds ground-based FAGE instrument by Creasey *et al*. (1997). For a pinhole of 0.6 mm diameter, rapid cooling to ~ 25 K occurs immediately downstream of the pinhole. 50 cm downstream of the pinhole, i.e. at the OH detection axis, the gas beam is no longer expanding, and warms to the ambient temperature. Thus the mean temperature between the inlet and the detection axis is lower than the ambient temperature. Becker *et al.* (1993) estimated the mean temperature between the inlet and the HO_2 detection axis to be 255 K, and though this value may not be applicable to the instrument used in this work, it is a useful approximation. The mean inlet temperature has been taken into account wherever temperature-dependent rate constants have been used in calculations concerning the FAGE cell (see section 2.8.1 and section 2.9.1).

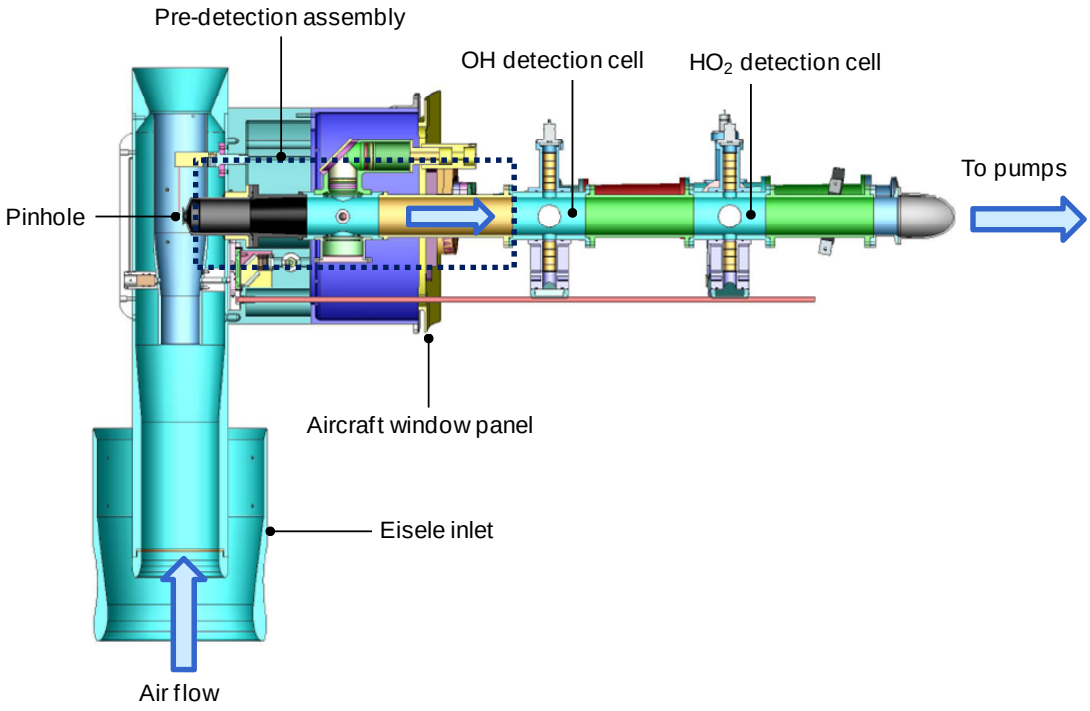

Figure 2.5. SolidWorks drawing of the Eisele inlet, FAGE inlet, and detection cells as they are installed on the BAe-146 aircraft. Diagram adapted from Floquet (2006).

Figure 2.6. Photograph of the FAGE Eisele inlet from inside the aircraft, showing concentric cylinders. Photograph by Dr Jim McQuaid.

2.4.4 Detection cells

The OH and HO_2 detection cells are positioned in series, with the HO_2 detection cell downstream of the OH cell, as shown in Figure 2.7. The cells are black anodised aluminium cylinders, sealed to the pre- and post-detection assemblies by rubber o-rings. Laser light is delivered to the cells *via* optical fibres, and collimated and focussed by a fibre collimator (Oz Optics, HPUCO-25-308-M-25PQ). The light is transmitted along a baffled side arm, through the fluorescence region, and along a second side arm, where a 45º mirror reflects the laser light to a UV photodiode (Laser Components UK UDT-555UV) which measures the laser power. Laser light scattered from the input arm, the fluorescence region, and the output arm contribute to the background signal, so the input and output arms are baffled with small aluminium rings to trim the laser beam and to prevent reflection of laser light from the 45º mirror back into the cell. OH fluorescence is detected on an axis perpendicular to the laser beam and the air flow. Light from the fluorescence region passes through an interference filter (Barr Associates, 50 % transmission at λ = 308 nm, FWHM ~ 5 nm) and is focussed by two plano-convex lenses (UQG Optics, f = 75 mm at λ = 250 nm, d = 50 mm) onto the photocathode of a UV-sensitive channel photomultiplier (Perkin Elmer C943P, 15 % quantum efficiency at λ = 308 nm). A retroreflector (CVI Optics fused silica plano-concave spherical mirror, broadband coated, radius of curvature = 50.8 mm) positioned opposite the detector maximises the collection of light from the fluorescence region. The signal from the CPM is sent to a photon counting card (Becker & Hickl PMS 400) in the measurement computer. HO_2 is detected by conversion to OH with an excess (10 sccm) of NO (Air Products, 99.9 %). NO is stored in a 2 litre cylinder in a sealed container, and is delivered to the HO_2 cell through ⅛ inch stainless steel tubing 9.5 cm upstream of the HO_2 fluorescence region.

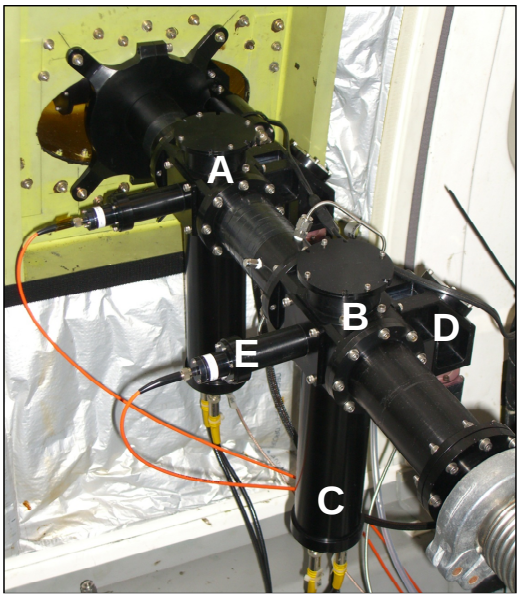

Figure 2.7. FAGE detection assembly mounted in the aircraft window blank (yellow), showing OH and HO_2 detection cells (A, B), channel photomultiplier (C), laser power photodiode (D), and optical fibre delivering laser light (E).

The low pressure inside the fluorescence cells is maintained by an Eaton M90 supercharger (roots blower) backed by a Leybold Trivac D25B rotary oil pump, both of which have been adapted to use the 400 Hz / 115 V aircraft power (Floquet, 2006). A separate, unmodified pump set is therefore used for ground-based measurements. Both pump sets are capable of maintaining fluorescence cell pressures between ~ 1 Torr at 10 km and ~ 2 Torr at sea level, giving a flow rate through the detection cells of 4 slm (standard litres per minute). The pumps are connected to the fluorescence cell by KF-50 flexible steel bellows. When installed on the aircraft, the inlet and pumps are positioned between the two instrument racks, to minimise the length of the pumping line.

2.4.5 Data acquisition and analysis

The key to the FAGE technique is the expansion of ambient air into a low-pressure chamber, to extend the OH fluorescence lifetime beyond the laser pulse, enabling temporal gating of fluorescence signal acquisition. The temporal gating of the OH and HO_2 CPMs is facilitated by two custom-made high voltage gating boxes (Floquet, 2006), which switch the CPMs between high and low gain states as required. A delay generator (BNC 555) is used as a master clock and triggers each laser pulse, the gating

boxes, and the photon counting cards. Figure 2.8 shows a schematic of the signal acquisition cycle. At the beginning of the cycle, the photon counting cards and CPM gain are switched off (low gain state), to prevent saturation of the CPM photocathode and generation of after-pulses. The photon counting cards are switched on 100 ns prior to the UV laser pulse, to allow for their 50 ns clock cycle. The Nd:YAG laser pulse occurs 5 μs after the trigger from the delay generator, but the delay between the trigger and the Ti:Sapphire pulse changes with laser power, alignment of the Ti:Sapphire cavity, ambient temperature, and time since the laser was switched on (Floquet, 2006, Commane, 2009). To account for this instability the laser trigger, the second harmonic of the Ti:Sapphire pulse (λ = 462 nm), and the switch on of the CPM gain are monitored on an oscilloscope (see section 2.4.1). The delay between the laser trigger and the Ti:Sapphire pulse is monitored by software in the data acquisition computer, and the software maintains a constant delay of 70 ns between the Ti:Sapphire pulse and the CPM switch on. This ensures that the start of fluorescence collection always occurs at the same time relative to the start of the fluorescence. Once the CPM is switched to its high-gain state, the fluorescence signal is collected for 1 μs (gate A), during which time the fluorescence decays completely. Following a wait of 5 μs, the sum of the solar background signal (typically 0 counts) and dark count background signal (typically 0–1 counts) is collected for 20 μs (gate B). The CPMs and photon counting cards are switched off at 200 μs, ready for the next laser pulse.

The signal measured in this cycle is integrated over 1 second, or 5000 laser pulses. The OH fluorescence signal, OHSignal, is calculated as follows:

$$\mathrm{OHSignal} = OHSigA - \frac{OHSigB}{x} \tag{2.6}$$

where $OHSigA$ is the number of counts per second in collection gate A, $OHSigB$ is the number of counts in collection gate B, and x is the ratio of the width of gate B to the width of gate A $(x = 20)$.

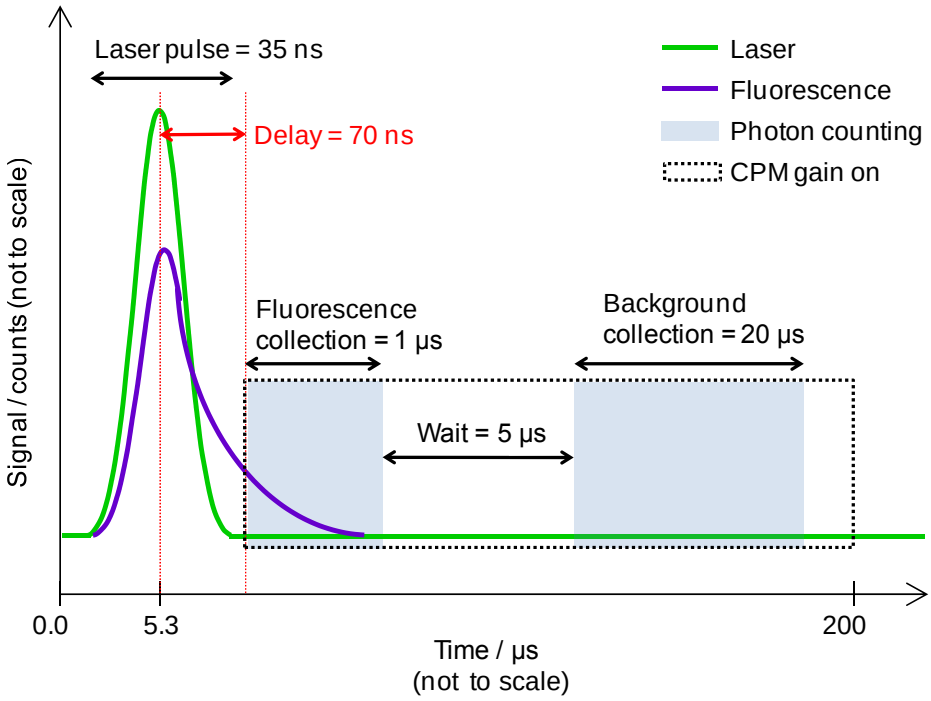

Figure 2.8. Timing scheme for signal acquisition in aircraft FAGE measurements. The green line represents UV Ti:Sapphire laser pulse at λ = 308 nm, the purple line represents OH fluorescence, shaded blue areas represent photon counting, and the dotted black box represents the time for which the CPM is in the high gain state. The photon counting card is switched on prior to the laser pulse. The delay between the laser pulse and the start of the fluorescence photon counting bin, shown in red, is maintained at 70 ns by accounting for changes in the timing of the laser pulse, as described above.

Due to the long pre-detection assembly effectively eliminating solar scattered light (see 2.4.3) and low CPM dark counts (typically 0–1 per second) the value of B is typically between 0 and 1 count s^{-1}. Similarly, the signal due to OH fluorescence in the HO_2 cell is given by:

$$\mathrm{HO_2Signal} = HO_2SigA - \frac{HO_2SigB}{x} \qquad (2.7)$$

Under normal operation (such as during the RONOCO fieldwork, described in Chapter 4) the laser is tuned to the online wavelength (λ ~ 307.995 nm) for up to 12 minutes, and then to the offline wavelength (λ ~ 307.990 nm) for 60 seconds. The first 60 seconds of online data are dedicated to measuring OH in both the OH and the HO_2 cells, so 12 minutes of online data gives 12 minutes of 1 Hz online OH data ($OHSignal_{on}$) and 11 minutes of 1 Hz online HO_2 data ($HO_2Signal_{on}$). To account for any backlash in the gearing system of the stepper motor used to change the angle of incidence on the

diffraction grating, the online and offline wavelengths are always approached from a shorter wavelength.

The length of the online measurement period can be controlled by the operator and can be changed during a flight, according to the stability of the laser wavelength (monitored by the reference cell signal) and the measurement requirements. In addition, the measurements can easily be stopped and restarted. During the RONOCO project flights (see Chapter 4) the measurements were stopped and started to ensure that features of interest, such as missed approaches and shipping plumes, were not intercepted during the offline measurement period. During ascent and descent the change in pressure and therefore in the refractive index of the air in the aircraft cabin can be sufficient to cause the laser wavelength to move away from the online position, resulting in a sharp decrease in the reference cell signal. This does not occur during every ascent or descent, so measurements are possible during some profiles and missed approaches. The laser system has recently been rebuilt in a sealed aluminium casing to eliminate this effect.

The 1 Hz OH signal is normalised for the laser power measured in the OH cell, OHP. The mean normalised offline OH signal is subtracted from the normalised online OH signal, to calculate the signal due to OH fluorescence alone, $\mathrm{Sig_{OH}}$:

$$\mathrm{Sig_{OH}} = \frac{\mathrm{OHSignal_{on}}}{\mathrm{OHP_{on}}} - \left(\frac{\mathrm{OHSignal_{off}}}{\mathrm{OHP_{off}}} \right)_{\mathrm{mean}} \tag{2.8}$$

where $\mathrm{OHSignal_{on}}$ and $\mathrm{OHSignal_{off}}$ are the 1 Hz online and offline OH signals, and $\mathrm{OHP_{on}}$ and $\mathrm{OHP_{off}}$ are the 1 Hz online and offline laser powers recorded in the OH cell, respectively. $\mathrm{Sig_{OH}}$ is then divided by the sensitivity of the instrument to OH, C_{OH} (count $\mathrm{s^{-1}}$ $\mathrm{mW^{-1}}$ $\mathrm{molecule^{-1}}$ $\mathrm{cm^3}$), to give [OH] in molecule $\mathrm{cm^{-3}}$:

$$[\mathrm{OH}] \,/\, \mathrm{molecule\ cm^{-3}} = \frac{\mathrm{Sig_{OH}}}{C_{\mathrm{OH}}} \tag{2.9}$$

The 1Hz HO_2 signal is normalised for the laser power measured in the HO_2 cell, HO_2P. The HO_2 "offline" period is the first 60 seconds of the online OH measurement, when no NO is injected into the cell. During this time, the signal recorded in the HO_2 cell,

$HO_2Signal_{off}$, is the sum of the signals due to laser scattered light and OH fluorescence. The normalised signal due to HO_2 alone is calculated as:

$$Sig_{HO_2} = \frac{HO_2Signal_{on}}{HO_2P_{on}} - \left(\frac{HO_2Signal_{off}}{HO_2P_{off}} \right)_{mean} \quad (2.10)$$

where $HO_2Signal_{on}$ and $HO_2Signal_{off}$ are the 1 Hz online and offline (no NO) HO_2 signals, and HO_2P_{on} and HO_2P_{off} are the 1 Hz online and offline laser powers recorded in the HO_2 cell, respectively. The concentration of HO_2 is calculated as:

$$[HO_2] \text{ / molecule cm}^{-3} = \frac{Sig_{HO_2} - Int_{HO_2}}{C_{HO_2}} \quad (2.11)$$

where Int_{HO2} is the intercept of the HO_2 calibration plot, caused by interference from added NO (discussed further in section 2.5.2). C_{OH}, C_{HO2}, and Int_{HO2} are determined by calibration of the instrument with known concentrations of OH and HO_2, as described in section 2.5. Following a field measurement campaign the data files are analysed and accepted or rejected according to fluctuations in the reference cell signal, laser power, laser wavelength, detection cell pressure, and background signal. The precision of the measurements is sufficient that changes in [OH] and [HO_2] can be seen on a 1 second timescale. For RONOCO and SeptEx the data were averaged to 60 seconds.

2.5 Calibration

Laser-induced fluorescence spectroscopy is not an absolute technique, and measurements of OH and HO_2 in ambient air require knowledge of the instrument's sensitivity. Measured concentrations of OH and HO_2 are calculated using equations (2.9) and (2.11), respectively, where C_{OH} and C_{HO2} are determined in a calibration. The aircraft FAGE instrument is calibrated by generating known concentrations of OH and HO_2 in a flow tube known as the calibration wand. The technique is described below. Examples of OH and HO_2 calibration results are given in section 2.5.2.

2.5.1 Calibration method

2.5.1.1 Water vapour photolysis

A flow of synthetic air (BOC, BTCA 178), controlled by a mass flow controller (Brooks Smart Flow 5850S), is humidified by diverting a variable portion of the flow through an ambient temperature distilled water bubbler. The humidified flow is passed down a 30 cm long, square-section aluminium flow tube (internal dimension 1.27 cm) at a flow rate of ~ 50 slm. Extensive characterisation of the flow tube, which is known as the calibration wand, has shown that flow rates greater than 45 slm produce turbulent flow, so that the flow velocity across the width of the tube is uniform (Floquet, 2006, Commane, 2009). A mercury pen-ray lamp (Oriel Instruments Hg(Ar) Spectral Calibration Lamp, model number 6035) is fixed side-on to the outside of the wand in an aluminium casing, and a 3.81 cm quartz (Suprasil) window transmits the λ = 184.9 nm light produced by the lamp to the inside of the calibration wand. The lamp is purged with a 5 slm flow of nitrogen to prevent formation of O_3 and absorption of radiation by ambient water vapour and oxygen, and is heated to > 36º C to ensure that the spectral output remains stable throughout a calibration and between calibrations. Light from the lamp is collimated by thin-walled tubes (3 mm diameter, 8 mm length) arranged in a close-packed array between the lamp and the quartz window. The water vapour in the calibration flow is photolysed to produce known concentrations of OH and HO_2:

$$H_2O \xrightarrow{h\nu} OH + H \qquad \text{(R2.6)}$$

$$H + O_2 + M \longrightarrow HO_2 + M \qquad \text{(R1.7)}$$

where M is either N_2 or O_2. The concentrations of OH and HO_2 can be calculated as follows:

$$[OH] = [HO_2] = [H_2O]\ \sigma_{H_2O}\ \phi_{OH}\ Ft \qquad (2.12)$$

where σ_{H_2O} is the absorption cross-section of water vapour at λ = 184.9 nm ($7.14 \pm 0.2 \times 10^{-20}$ molecule^{-1} cm^{-2}) (Cantrell *et al.*, 1997), ϕ_{OH} is the photolysis quantum yield of OH (= 1), F is the actinic flux of the mercury lamp at λ = 184.9 nm, and t is the residence time in the photolysis region. The concentration of water vapour

is measured by diverting a small portion of the calibration flow, prior to entering the wand, to a dew point hygrometer (Buck Research Instruments CR-4 chilled mirror hygrometer). The product of the lamp flux and the photolysis time is determined *via* the turbulent-flow NO actinometry method (Edwards *et al.*, 2003, Faloona *et al.*, 2004, Floquet, 2006), as described in section 2.5.1.2. The flow exiting the calibration wand is directed over the FAGE inlet so that the flow over-fills the pinhole.

During a calibration, the flow rate of air and the water vapour concentration are kept constant (within the variability of the mass flow controllers), and the concentrations of OH and HO_2 produced are varied by changing the lamp flux. For each setting of the lamp flux, two minutes of online OH data, one minute of online HO_2 data, and one minute of offline data are recorded. The data are analysed as described in section 2.4.5. Flow rates, water vapour concentration, gas temperature, ambient pressure, and lamp temperature and current are recorded automatically every 5 seconds during the calibration. Mean values of the OH and HO_2 signals and $[HO_x]$ are calculated for each lamp flux setting. A straight line, weighted by the standard deviations of the concentration of HO_x and the OH and HO_2 signals, is fitted to the averaged data. The sensitivity of the instrument, C_{OH} or C_{HO2}, is equal to the gradient of the line:

$$C_{OH} = \frac{Sig_{OH}}{[OH]} = \frac{1}{[OH]}\left(\frac{OHSignal_{on}}{OHP_{on}} - \left(\frac{OHSignal_{off}}{OHP_{off}}\right)_{mean}\right) \qquad (2.13)$$

2.5.1.2 Determination of lamp flux by turbulent-flow NO actinometry

The most reliable way of determining the actinic flux of the mercury lamp in the calibration wand is to use an actinometric method, in which a gas-phase species, with a well-known absorption cross-section at the wavelength of interest and a detectable photolysis product, is introduced into the wand under calibration flow conditions. For determination of the FAGE wand lamp flux, N_2O is introduced into the wand in a turbulent flow of synthetic air, yielding NO, the concentration of which can be measured with a commercial NO_x analyser. N_2O is photolysed to produce $O(^1D)$, as follows:

$$N_2O \xrightarrow{h\nu} N_2 + O(^1D) \quad \text{(R2.7)}$$

$$N_2O \xrightarrow{h\nu} N_2 + O(^3P) \quad \text{(R2.8)}$$

$$N_2O \xrightarrow{h\nu} N(^4S) + NO(^2\Pi) \quad \text{(R2.9)}$$

Reaction (R2.7) dominates N_2O photolysis, with the yield of (R2.8) being less than 0.05 % (Nishida *et al.*, 2004), and the yield of (R2.9) being less than 1 % (Greenblatt and Ravishankara, 1990). The quantum yield for photodissociation of N_2O is unity (Sander *et al.*, 2011). The rate of production of $O(^1D)$ is given by:

$$\frac{d[O(^1D)]}{dt} = [N_2O]\sigma_{N_2O}\phi_{O(^1D)}F \quad (2.14)$$

where σ_{N_2O} is the absorption cross-section of N_2O at λ = 184.9 nm (1.43×10^{-19} cm^2 molecule^{-1}) (Sander *et al.*, 2011), $\phi_{O(^1D)}$ is the photodissociation quantum yield of $O(^1D)$ (~ 1) (Sander *et al.*, 2011), and F is the lamp flux. $O(^1D)$ will be quenched by N_2O, N_2, and O_2, and will react with N_2O to produce NO, as follows:

$$O(^1D) + O_2 \xrightarrow{k_1} O(^3P) + O_2 \quad \text{(R1.3)}$$

$$O(^1D) + N_2 \xrightarrow{k_2} O(^3P) + N_2 \quad \text{(R1.2)}$$

$$O(^1D) + N_2O \xrightarrow{k_3} O(^3P) + N_2O \quad \text{(R2.10)}$$

$$O(^1D) + N_2O \xrightarrow{k_4} N_2 + O_2 \quad \text{(R2.11)}$$

$$O(^1D) + N_2O \xrightarrow{k_5} 2\,NO \quad \text{(R2.12)}$$

The rate constants k_1 to k_5 are given in Table 2.3. Reaction (R2.10) has a yield of less than 1 % at 298 K, and can therefore be completely neglected in calculating the rate of production of NO (Vranckx *et al.*, 2008). The quenching of $O(^1D)$ to $O(^3P)$ in reactions (R1.3) and (R1.2), and the reaction with N_2O in reaction (R2.11), are fast enough to compete with formation of NO. The rate of loss of $O(^1D)$ is therefore given by:

$$-\frac{d[O(^1D)]}{dt} = \left(k_1[O_2] + k_2[N_2] + (k_4 + k_5)[N_2O]\right)[O(^1D)] \quad (2.15)$$

The rate of production of NO is given by:

$$\frac{d[\mathrm{NO}]}{dt} = 2\,k_5[\mathrm{N_2O}]\left[\mathrm{O}\left(^1\mathrm{D}\right)\right] \tag{2.16}$$

Combining equations (2.14), (2.15), and (2.16) yields the following rate expression for [NO]:

$$\frac{d[\mathrm{NO}]}{dt} = \frac{2\,k_5[\mathrm{N_2O}]\left([\mathrm{N_2O}]\sigma_{\mathrm{N_2O}}\phi_{\mathrm{O}\left(^1\mathrm{D}\right)}F\right)}{k_1[\mathrm{O_2}] + k_2[\mathrm{N_2}] + \left(k_4 + k_5\right)[\mathrm{N_2O}]^2} \tag{2.17}$$

The photolysis time is determined by the known dimensions of the photolysis region in the calibration wand and the volumetric flow rate of the humidified air. While the total flow rate is set to 50 slm during the calibration and actinometry experiments, slight variations in the flow rate (± 0.1 %) caused by the mass flow controllers mean that the exact photolysis time cannot be kept constant. The photolysis time during the actinometry and calibration experiments is therefore calculated from the internal dimensions of the wand and the total flow rate. This method eliminates the uncertainty associated with assuming the same total flow rate for both experiments, and does not introduce any extra uncertainty since the internal dimensions of the wand do not change. For a given photolysis time, *t*, the lamp flux can be calculated as follows:

$$F = \frac{[\mathrm{NO}]\left(k_1[\mathrm{O_2}] + k_2[\mathrm{N_2}] + \left(k_4 + k_5\right)[\mathrm{N_2O}]\right)}{2\,k_5[\mathrm{N_2O}]^2\,\sigma_{\mathrm{N_2O}}\,\phi_{\mathrm{O}\left(^1\mathrm{D}\right)}\,t} \tag{2.18}$$

The experimental details of NO actinometry are now described. A 5 slm flow of N_2O (BOC, 98 % N_2O in N_2, medical grade) is mixed into a 45 slm flow of synthetic air (BOC, BTCA 178) or nitrogen (BOC, oxygen-free nitrogen) to give a total flow rate of ~ 50 slm. The air and N_2O gas flows are controlled by mass flow controllers (Brooks Smart Flow 5850S), and the exact flows are recorded every 5 seconds by the calibration software.

Table 2.3. Rate constants for quenching and reaction of $O(^1D)$ in NO actinometry experiments.

Rate constant	Value / cm^3 $molecule^{-1}$ s^{-1}	Value at 298 K / cm^3 $molecule^{-1}$ s^{-1}	Reference
k_1	$3.3 \times 10^{-11} e^{(55/T)}$	3.95×10^{-11}	Sander *et al.* (2011)
k_2	$2.15 \times 10^{-11} e^{(110/T)}$	3.1×10^{-11}	Sander *et al.* (2011)
k_3	not available	2.0×10^{-11}	Vranckx *et al.* (2008)
k_4	$4.63 \times 10^{-11} e^{(20/T)}$	4.95×10^{-11}	Sander *et al.* (2011)
k_5	$7.25 \times 10^{-11} e^{(20/T)}$	7.75×10^{-11}	Sander *et al.* (2011)

The combined flow is passed through the calibration wand, where light at λ = 184.9 nm from the mercury lamp photolyses N_2O. NO is produced through reactions (R2.7) to (R2.12). $[O_2]$, $[N_2]$ and $[N_2O]$ are known from their relative flow rates. The photolysis time, *t*, is calculated from the total flow rate recorded by the software, the cross-sectional area (1.61 cm^2) of the photolysis region, and the length (3.81 cm) of the photolysis region. The flow exiting the wand is directed to a commercial NO_x analyser (Thermo Environmental 42C) where the concentration of NO is measured and recorded every 5 seconds. The ambient pressure and the temperature of the gas are recorded.

During an actinometry experiment, the lamp current is varied to give a range of lamp fluxes and the calculated lamp flux is plotted against lamp current, as shown in Figure 2.9. Data are typically recorded for 10 minutes at each lamp current. The *x* error bars in Figure 2.9 are the standard deviations of the lamp current during each ten minute measurement period. The *y* error bars are calculated by propagating the uncertainties in each of the terms on the right hand side of equation (2.22), details of which are given in Table 2.4.

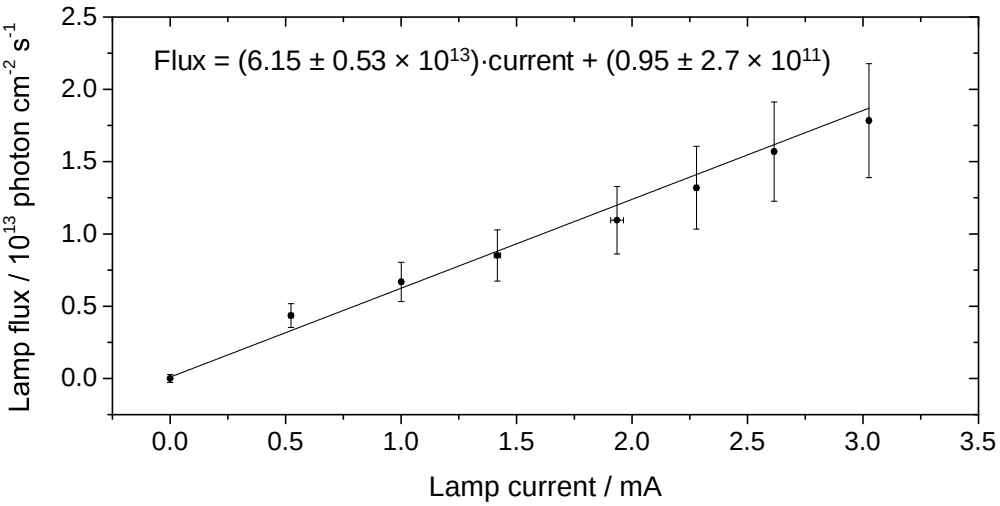

Figure 2.9. Lamp flux versus lamp current. Data points represent values averaged over 10 minutes.

The uncertainties in [NO], [O_2], [N_2], and [N_2O] are calculated from the uncertainties in flow rate, temperature, and pressure. The uncertainties in the rate constants k_1 to k_5 are given by Sander *et al*. (2011). The uncertainties in σ_{N_2O} and $\phi_{O(^1D)}$ are considered to be negligible. The uncertainty in t is calculated from the uncertainty in the total flow rate and the uncertainty in the gas temperature. The total uncertainty in the calculated flux is typically 25 %.

Absorption of light at λ = 184.9 nm by N_2O and O_2 in the wand leads to an exponential decay of light intensity across the width of the photolysis region. The lamp flux calculated in equation (2.18), which is used in the calculation of [OH] and [HO_2] in equation (2.12), must be corrected to account for this absorption because N_2O is not present during the HO_x calibration. Photolysis of N_2O leads to production of O_3, which also absorbs light at λ = 184.9 nm:

$$N_2O \xrightarrow{h\nu} O(^3P) + N_2 \qquad \text{(R2.13)}$$

$$O_2 \xrightarrow{h\nu} O(^3P) + O(^3P) \qquad \text{(R2.14)}$$

$$O(^3P) + O_2 + M \longrightarrow O_3 + M \qquad \text{(R1.4)}$$

Table 2.4. Summary of parameters contributing to total uncertainty in the calculated lamp flux.

Parameter	Uncertainty calculation	Typical uncertainty	References
Flow rate	(0.007 × flow rate) + (0.002 × full range)	1 %	Brooks Smart 5850S Manual
Temperature		1 %	
Pressure		1 %	
k_1	$1.1\times\exp\left\lvert 10\left(\frac{1}{T}-\frac{1}{298}\right)\right\rvert$	10 %	Sander *et al.* (2011)
k_2	$1.1\times\exp\left\lvert 20\left(\frac{1}{T}-\frac{1}{298}\right)\right\rvert$	10 %	Sander *et al.* (2011)
k_4	$1.1\times\exp\left\lvert 25\left(\frac{1}{T}-\frac{1}{298}\right)\right\rvert$	10 %	Sander *et al.* (2011)
k_5	$1.1\times\exp\left\lvert 25\left(\frac{1}{T}-\frac{1}{298}\right)\right\rvert$	10 %	Sander *et al.* (2011)
F		25 %	

The absorption of light by O_2 and by the O_3 produced in reaction (R1.4) has been shown to be negligible at the N_2O concentrations used in the calibration (~ 10 % of the total flow) (Floquet, 2006). The transmittance of radiation across the tube, *T*, is therefore calculated using the Beer-Lambert law as follows:

$$T = \frac{I}{I_0} = e^{\left(-\sigma_{N_2O}\left[N_2O\right]l\right)} \tag{2.19}$$

where l is the distance across the calibration wand. It is worth noting that turbulent mixing in the calibration wand ensures that [NO] has a flat profile across the width of the wand, so that the position of the sampling line does not affect the measured value of [NO]. The total transmittance, $T_{total,}$ across the width of the calibration wand, w (= 1.27 cm) is found by integrating T with respect to w, and the mean transmittance, $\overline{T}$, is found by dividing the result by w as follows:

$$T_{\text{total}} = \int_0^w e^{\left(-\sigma_{N_2O}\left[N_2O\right]w\right)}\, dw \tag{2.20}$$

$$\overline{T} = \frac{T_{\text{total}}}{w} = \frac{1}{w}\left(\frac{1}{\sigma_{N_2O}\left[N_2O\right]} - \frac{e^{\left(-\sigma_{N_2O}\left[N_2O\right]\right)}}{\sigma_{N_2O}\left[N_2O\right]}\right) \tag{2.21}$$

The calculated flux is divided by the mean transmittance, $\overline{T}$, to give the final flux corrected for absorption by N_2O:

$$F = \frac{1}{\overline{T}}\left(\frac{\left[NO\right]\left(k_1\left[O_2\right] + k_2\left[N_2\right] + \left(k_4 + k_5\right)\left[N_2O\right]\right)}{2\,k_5\left[N_2O\right]^2\,\sigma_{N_2O}\,\phi_{O(^1D)}\,t}\right) \tag{2.22}$$

With an N_2O flow equal to 10 % of the total flow, $\overline{T}$ is calculated to be 0.61. The uncertainty in $\overline{T}$, which contributes to the total uncertainty in *F*, is calculated from the uncertainty in $[N_2O]$ (see Table 2.4).

2.5.1.3 NO_x analyser calibration

The NO_x analyser uses the chemiluminescence produced in the reaction between NO and O_3 to measure concentrations of NO:

$$NO + O_3 \rightarrow NO_2^* + O_2 \tag{R2.15}$$

$$NO_2^* \rightarrow NO_2 + h\nu \tag{R2.16}$$

NO_2 is formed in an electronically excited state (NO_2^*), and emits visible and IR light upon relaxation to a lower state. The intensity of the emitted light is directly proportional to the concentration of NO. Collisional quenching of NO_2^* by N_2O in the calibration flow will reduce the intensity of emitted light for a given NO concentration. The analyser must therefore be calibrated for the effect of N_2O. Variable flows of NO (NPL certified, 474 ± 14 ppbv NO in N_2) and N_2O are mixed with a flow of synthetic air or nitrogen, using mass flow controllers. The total flow is passed through the calibration wand, without the lamp switched on, and is sampled by the NO_x analyser. The fraction of N_2O in the total flow, f_{N2O}, typically ranges between 0.0 and 0.20, and

the fraction of NO typically ranges between 0.0 and 0.02, giving ratio ranges of 0−20 ppmv and 0–10 ppbv, respectively. For each experiment, the N_2O fraction is held constant while the NO fraction is varied. The slope of a plot of measured NO against calculated NO gives the NO_x analyser correction factor, C_{NO}. Several experiments are conducted at different N_2O fractions, to determine the effect of N_2O on C_{NO}. Figure 2.10 shows the results from 4 calibration experiments, with f_{N2O} = 0.0, 0.6, 0.14 and 0.20. The values of C_{NO} for each N_2O fraction are given in the legend. The intercept of each individual calibration plot is the result of the non-zero offset on the NO_x analyser, which is known to change over time. The intercepts are therefore not taken into account. Rather, each time the NO_x analyser is used, a note is made of the zero offset and the data are adjusted accordingly.

Figure 2.11 shows C_{NO} plotted against f_{N2O}, showing decreasing NO_x analyser sensitivity with increasing N_2O concentration. The *y* error bars are the standard errors on C_{NO}, calculated by the plotting software OriginPro 9. The *x* error bars are calculated from the uncertainties in the air, N_2O, and NO flows. A linear fit to the data yields an expression for C_{NO} as a function of f_{N2O}: $C_{NO} = (-7.0 \pm 0.4 \times 10^{-3}) \cdot f_{N2O} + (0.99 \pm 0.005)$. The NO_x analyser is calibrated in this way prior to each set of actinometry experiments. C_{NO} is calculated for each value of f_{N2O} in the actinometry experiment, and the measured values of [NO] are divided by C_{NO} to give the corrected [NO].

2.5.2 HO_x calibration results

Examples of OH and HO_2 calibration plots from February 2011, following the RONOCO winter campaign, are shown in Figure 2.12a, and Figure 2.12b, respectively. The water vapour concentration was 9×10^{16} molecule cm^{-3}, which is equal to 0.4 % of the total flow. The sensitivity of the instrument to OH, C_{OH}, given by the gradient of a linear fit to the data, is equal to $(3.84 \pm 0.17) \times 10^{-8}$ count s^{-1} mW^{-1} $molecule^{-1}$ cm^3. The linear fit to the OH data has a non-zero intercept of -0.03 ± 0.13 count s^{-1} mW^{-1}, which is caused by random noise in the measurements, and is considered to be negligible since the signal recorded at [OH] = 0 is zero within error.

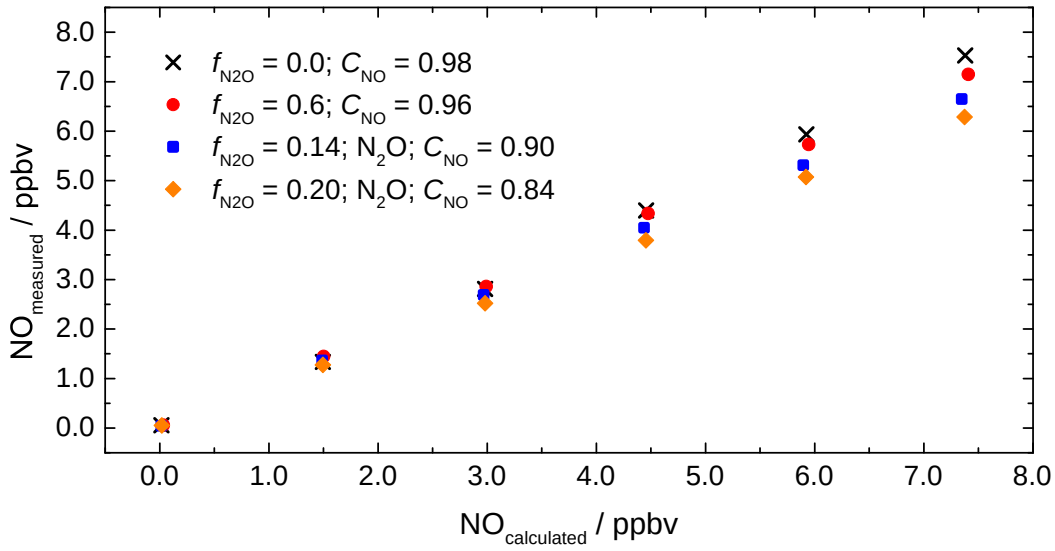

Figure 2.10. NO_x analyser calibration plots (measured NO vs calculated NO) with f_{N2O} = 0.0, 0.6, 0.14, and 0.20. Data points represent values averaged over 3 minutes. For clarity, neither error bars nor linear fits to the data have been shown. Values of C_{NO} are given by the slope of each plot.

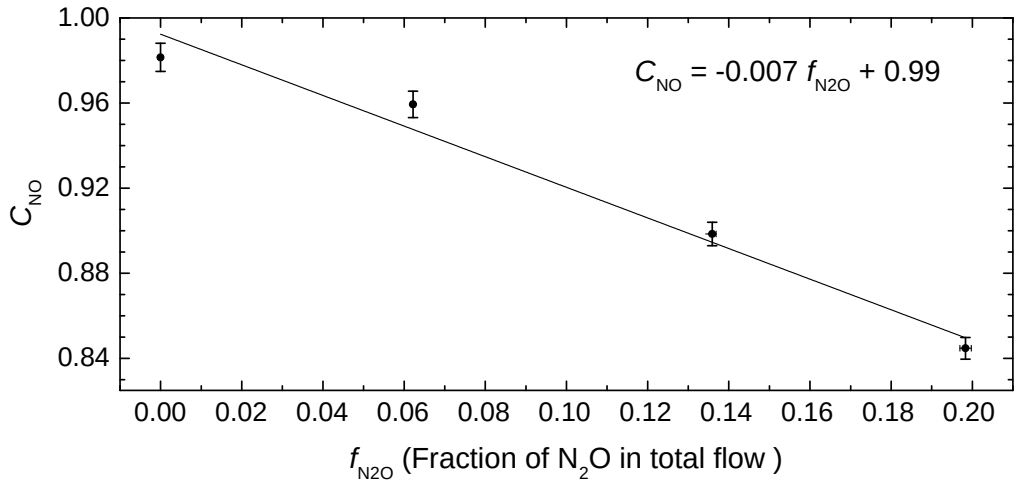

Figure 2.11. Effect of N_2O on C_{NO}, showing decreasing sensitivity with increasing N_2O concentration.

Only the gradient is used in data analysis. The sensitivity of the instrument to HO_2, C_{HO2}, given by the gradient of a linear fit to the data, is equal to $(1.18 \pm 0.05) \times 10^{-7}$ count s^{-1} mW^{-1} $molecule^{-1}$ cm^3. The linear fit has a non-zero intercept of 2.1 ± 0.13 count s^{-1} mW^{-1}, which is not negligible. This intercept is seen in all aircraft FAGE HO_2 calibrations, and is caused by an interference from the addition of NO to the HO_2 cell (Edwards, 2011).

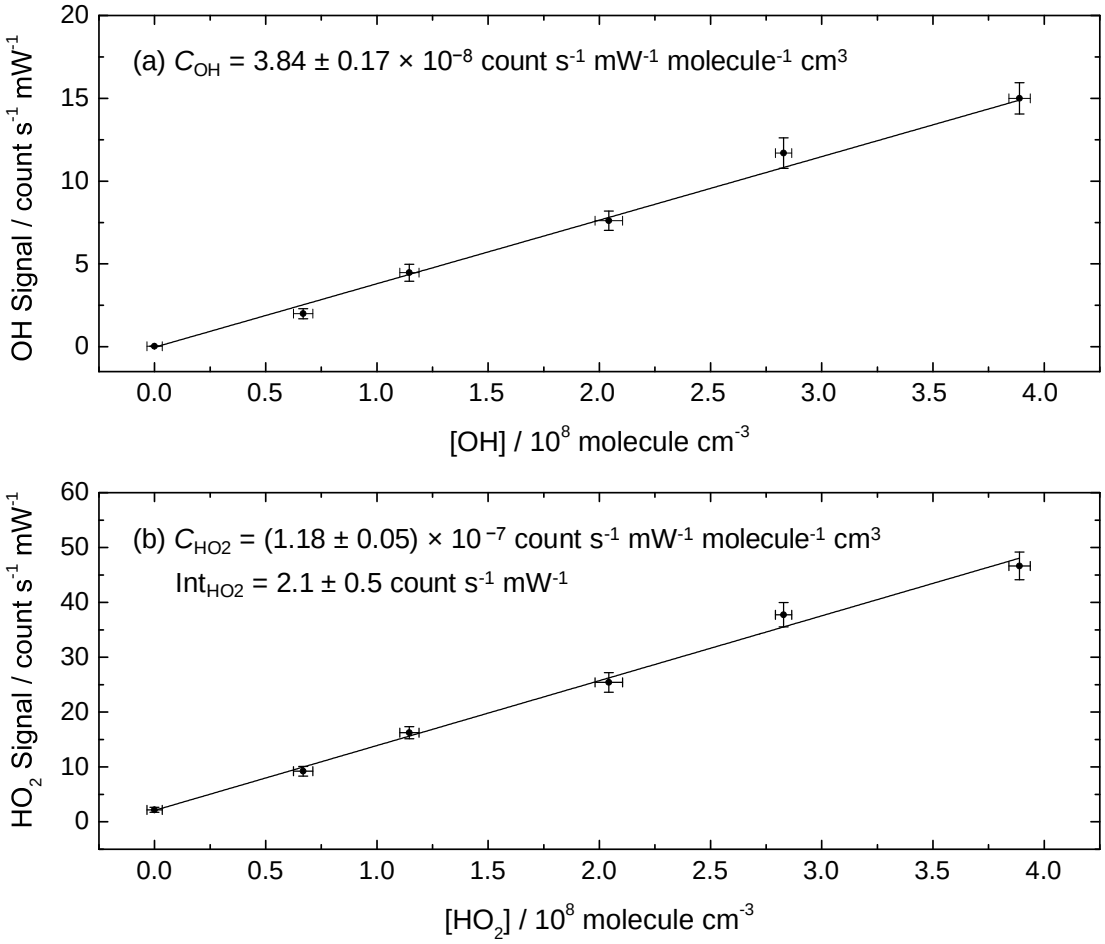

Figure 2.12. Results from a calibration of the aircraft FAGE instrument in February 2011, following the winter RONOCO fieldwork, at $[H_2O] = 9 \times 10^{16}$ molecule cm^{-3} (0.4 %). Data points represent average values for one minute of online data. *x* and *y* error bars represent the standard deviations of [OH] and $[HO_2]$, and the normalised FAGE signals, respectively. The instrument sensitivity to OH, C_{OH}, is equal to $(3.84 \pm 0.17) \times 10^{-8}$ count s^{-1} mW^{-1} $molecule^{-1}$ cm^{-3}. The instrument sensitivity to HO_2, C_{HO2}, is equal to $(1.18 \pm 0.05) \times 10^{-7}$ count s^{-1} mW^{-1} $molecule^{-1}$ cm^3. The intercept of the HO_2 calibration plot, caused by an interference from the addition of NO, is equal to 2.1 ± 0.5 count s^{-1} mW^{-1}.

The *x*-error bars are equal to the standard deviation (1σ) of [OH] and $[HO_2]$ over the period of each FAGE file (approximately 3 minutes). The *y*-error bars are equal to the standard deviation (1σ) of Sig_{OH} and Sig_{HO2} from each FAGE file (see equations (2.8) and (2.10)). The precision of the values of C_{OH} (4.4 %), C_{HO2} (4.2 %), and Int_{HO2} (23.8 %) are given by the standard errors on the slopes and intercept of the linear fit to the data, calculated by the plotting software OriginPro 9.

The instrument was also calibrated in October 2010, following the summer RONOCO and SeptEx measurement campaigns. The results from the calibration were

C_{OH} = (3.0 ± 0.5) × 10^{-8} count s^{-1} mW^{-1} $molecule^{-1}$ cm^3, and C_{HO2} = (9.3 ± 1.5) × 10^{-8} count s^{-1} mW^{-1} $molecule^{-1}$ cm^3. The increase in sensitivity between the summer and winter calibrations is attributed to the cleaning of the windows between the OH and HO_2 detection cells and their respective CPM arms (see Figure 2.7). C_{HO2} is generally higher than C_{OH} due to the rate loss of HO_2 on the walls of the inlet being lower than the rate of loss of OH (see section 2.8).

2.5.3 Alternative calibration methods

2.5.3.1 Laminar flow O_3 actinometry

The aircraft FAGE instrument has also been calibrated using the laminar flow O_3 actinometry method used by several FAGE groups (*e.g.* Hofzumahaus *et al.*, 1996, Creasey *et al.*, 1997, Kanaya *et al.*, 2001). A humidified flow of air is introduced into a quartz flow tube, where OH and HO_2 are produced in equal concentrations following the photolysis of water vapour by light at λ = 184.9 nm from a mercury lamp (see equations (R2.6) and (R1.7) in section 2.5.1.1). At the same time, ozone is formed by photolysis of O_2:

$$O_2 \xrightarrow{h\nu} 2\,O(^3P) \qquad \text{(R2.14)}$$

$$O(^3P) + O_2 + M \longrightarrow O_3 + M \qquad \text{(R1.4)}$$

The concentration of O_3 produced is given by:

$$[O_3] = [O_2]\ \sigma_{O_2}\ \phi_{O_3}\ Ft \qquad (2.23)$$

where σ_{O_2} is the O_2 absorption cross-section at λ = 184.9 nm and ϕ_{O_3} is the yield of O_3 from the photodissociation of O_2 (= 2, Sander *et al.*, 2011). The advantage of this technique over the turbulent-flow NO actinometry method described in section 2.5.1.2 is that F and t do not need to be calculated. [H_2O] is measured by a dew point hygrometer, [O_3] is measured by a commercial O_3 analyser (Thermo Environmental Instruments 49C), and the concentrations of OH and HO_2 are given by:

$$[OH] = [HO_2] = \frac{[O_3][H_2O]\sigma_{H_2O}\phi_{OH}}{[O_2]\sigma_{O_2}\phi_{O_3}} \quad (2.24)$$

Both the O_2 absorption spectrum in the region of 185 nm (Schumann-Runge bands) and the mercury lamp emission spectrum are very structured, so slight changes in the spectral output of the mercury lamp will change the effective O_2 absorption cross-section. Different lamps are known to have different spectral outputs, and the emission spectrum is known to change with the operating current, temperature, and age of the lamp. In addition, light is absorbed by O_2 in the photolysis region, so that the lamp emission spectrum and intensity change as light is propagated across the width of the calibration wand. These two effects must be taken into account by determining the effective O_2 absorption cross-section for each different lamp (Lanzendorf *et al.*, 1997, Heard and Pilling, 2003). [OH] and [HO_2] are varied by attenuating the lamp output with a flow of N_2O in N_2 through the lamp housing. For generation of atmospherically-relevant concentrations of OH and HO_2, the lamp flux must be further attenuated, to the extent that [O_3] is below the limit of detection of the analyser. To overcome this problem, the lamp flux is measured by a phototube positioned across the flow tube from the lamp. At high fluxes, where [O_3] is easily measured, a linear relationship is established between [O_3] and measured relative lamp flux. At low fluxes, the measured relative flux is used to calculate [O_3], which is then used to calculate [OH] and [HO_2].

To ensure that the concentration of O_3 produced is above the 1 ppbv detection limit of the O_3 analyser, the flow rate down the quartz tube is limited to ~ 12 slm. This forms a laminar flow so that the gas flow velocity has a parabolic profile across the flow tube, with the maximum velocity at the centre of the flow. The FAGE inlet pinhole samples gas from the centre of the flow, while O_3 is sampled in the excess flow from around the pinhole, so that the gas sampled by FAGE has a shorter photolysis time than the gas sampled by the O_3 analyser. To account for this, O_3 is measured at the centre of the flow as well as in the excess around the FAGE inlet, and a profile factor, *P*, is calculated:

$$P = \frac{[O_3]_{excess}}{[O_3]_{centre}} \quad (2.25)$$

For a perfectly laminar flow, P is equal to 2. For the ground-based FAGE calibration flow tube, P is equal to 1.57 ± 0.09 for 0.7 mm and 0.8 mm diameter pinholes (Furneaux, 2009). [OH] and [HO_2] are then given by:

$$[\mathrm{OH}] = [\mathrm{HO_2}] = \frac{[\mathrm{O_3}][\mathrm{H_2O}]\sigma_{\mathrm{H_2O}}\phi_{\mathrm{OH}}}{[\mathrm{O_2}]\sigma_{\mathrm{O_2}}\phi_{\mathrm{O_3}}P} \quad (2.26)$$

The disadvantage of this laminar-flow O_3 actinometry technique is the need for the gas profile factor. A comparison of the O_3 actinometry and NO actinometry calibration techniques was conducted by Furneaux *et al.* (2009) using the Leeds ground-based FAGE instrument. The O_3 actinometry flow tube and the NO actinometry wand were used to generate HO_x in the concentration ranges 7.6–21.1 × 10^8 molecule cm^{-3} and 1.3−17.1 × 10^8 molecule cm^{-3}, respectively. The ground-based FAGE instrument was first calibrated using the O_3 actinometry method, then the wand was used to supply a range of [HO_x], measured by the calibrated instrument. Excellent agreement was found between the wand-supplied [OH] and LIF-measured [OH], with $[OH]_{measured}$ = (1.00 ± 0.03)$[OH]_{wand}$ + (0.39 ± 0.17) × 10^8 molecule cm^{-3} (r^2 = 0.99). Good agreement was found between the measured and supplied [HO_2], with $[HO_2]_{measured}$ = (0.95 ± 0.10)$[HO_2]_{wand}$ + (0.71 ± 0.45) × 10^8 molecule cm^{-3}. This discrepancy was within the 1σ uncertainties of the O_3 actinometry (15 %) and NO actinometry (13 %) methods. These results validate both calibration methods.

2.5.3.2 HCHO photolysis

The Highly Instrumented Reactor for Atmospheric Chemistry (HIRAC) is an atmospheric simulation chamber at the University of Leeds (Glowacki *et al.*, 2007). The chamber is a 2.25 m^3 stainless steel cylinder, fitted with gas chromatography, Fourier transform infra-red spectroscopy, cavity ring-down spectroscopy, and FAGE. Pressure, temperature, and photolysis rates inside the chamber can be controlled to enable the study of gas-phase reactions under a range of conditions not accessible in other atmospheric chambers. Installed in HIRAC is a FAGE instrument similar in design to the aircraft FAGE instrument, enabling measurements of OH and HO_2 with high temporal resolution. During the Transnational Access Campaign in 2011, technical

issues with the HIRAC FAGE instrument meant that the aircraft FAGE instrument was temporarily installed in its place. This provided an opportunity to calibrate the aircraft instrument with an alternative calibration method. The experiments and analysis were conducted by Dr Shona Smith and Mr Fred Winiberg. The instrument was calibrated for HO_2 only. Formaldehyde, HCHO, was photolysed by the UV lamps inside HIRAC, producing HO_2 as follows:

$$HCHO \xrightarrow{h\nu} H + HCO \quad \text{(R1.23)}$$

$$\xrightarrow{h\nu} CO + H_2 \quad \text{(R1.24)}$$

$$HCO + O_2 + M \longrightarrow HO_2 + CO + M \quad \text{(R1.25)}$$

$$H + O_2 + M \longrightarrow HO_2 + M \quad \text{(R1.7)}$$

HO_2 was allowed to reach a steady state, at which point the photolysis lamps were switched off, and the decay of HO_2 was recorded with the FAGE instrument. The rate of loss of HO_2 was determined by its self-reaction and loss to the walls of the chamber:

$$HO_2 + HO_2 \xrightarrow{k_{HO_2+HO_2}} H_2O_2 + O_2 \quad \text{(R1.15)}$$

$$HO_2 + HO_2 + M \xrightarrow{k_{HO_2+HO_2+M}} H_2O_2 + O_2 + M \quad \text{(R2.17)}$$

$$HO_2 \xrightarrow{k_{loss}} \text{loss} \quad \text{(R2.18)}$$

The overall rate coefficient for the self-reaction of HO_2, k, is the sum of the pressure-independent rate constant, $k_{HO_2+HO_2}$, and the pressure-dependent rate constant, $k_{HO_2+HO_2+M}$, both of which are also dependent on the concentration of water vapour (Sander *et al.*, 2011). The values of the rate constants are given in Table 2.5. The rate of loss of HO_2 is given by:

$$-\frac{d[HO_2]}{dt} = k_{loss}[HO_2] + 2k[HO_2]^2 \quad (2.27)$$

The sensitivity of the FAGE instrument to HO_2 was determined by equating $[HO_2]$ to $S_{HO2} \times C_{HO2}$ (see equation (2.11)). Integration and rearrangement of equation (2.27) gives:

$$S_t = \frac{S_0 C_{HO_2} k_{loss}}{C_{HO_2} \exp(k_{loss} t) + 2S_0 k \exp(k_{loss} t) - 2S_0 k} \quad (2.28)$$

where S_t is the normalised HO_2 signal at time *t*, S_0 is the normalised HO_2 signal at time $t = 0$, and C_{HO_2} is the instrument sensitivity to HO_2.

A plot of S_t versus time, followed by non-linear least squares regression, yields C_{HO2} and k_{loss}. Reasonable agreement was found between C_{HO2} calculated using water vapour photolysis (wand calibration) and HCHO photolysis (chamber calibration), though the wand calibration gave consistently higher values. At a chamber pressure of 760 Torr, C_{HO2} was calculated to be (1.2 ± 0.2) × 10^{-7} count s^{-1} mW^{-1} $molecule^{-1}$ cm^3 from the HCHO photolysis calibration. The wand calibration gave a value of C_{HO2} = (1.4 ± 0.3) × 10^{-7} count s^{-1} mW^{-1} $molecule^{-1}$ cm^3, so the two values are the same within their combined uncertainties. The HCHO photolysis calibration method was used to investigate the pressure-dependence of C_{HO2}. These experiments are described in section 2.8.3.

2.6 Calibration and measurement uncertainty

The total uncertainty in the values of C_{OH} and C_{HO2} is calculated as a combination (sum in quadrature) of the accuracy and precision of each value. The precision is given by the standard error on the slope of the linear fit to the calibration data, as shown in Figure 2.12, which accounts for statistical or random errors occurring during the calibration. The accuracy is given by sum in quadrature of the fractional uncertainties in each of the terms on the right hand side of equation (2.12), along with the measured laser power and the position of the online wavelength, details of which are given in Table 2.6.

$$[OH] = [HO_2] = [H_2O]\ \sigma_{H_2O}\ \phi_{OH}\ Ft \quad (2.12)$$

It is worth noting that the uncertainty in *t* stems from the uncertainties in total flow rate and gas temperature (see Table 2.4), and not from the internal dimensions of the calibration wand.

Table 2.5. Values of rate constants and the water vapour enhancement factor for the self-reaction of HO_2.

Rate constant	Value / cm^3 $molecule^{-1}$ s^{-1} or no units	Value at 298 K / cm^3 $molecule^{-1}$ s^{-1} or no units	Reference
$k_{HO_2+HO_2}$	$3.3 \times 10^{-13} e^{(460/T)}$	1.5×10^{-12}	Sander *et al.* (2011)
$k_{HO_2+HO_2+M}$	$2.1 \times 10^{-33}[M] e^{(920/T)}$	$4.6 \times 10^{-32}[M]$	Sander *et al.* (2011)
H_2O_{vap} enhancement factor	$1 + 1.4 \times 10^{-21}[H_2O] e^{(2200/T)}$	$1 + 2.3 \times 10^{-18}[H_2O]$	Atkinson *et al.* (2004)

Table 2.6. Summary of uncertainties contributing to the accuracy of C_{OH} and C_{HO2}.

Term	Value or range of values	Uncertainty
$[H_2O]$	$0.29–2.5 \times 10^{17}$ molecule cm^{-3}	1 %
σ_{H_2O}	7.14×10^{-20} cm^2 $molecule^{-1}$	2.8 %
ϕ_{OH}	1	negligible
F	$0.0–1.5 \times 10^{13}$ photon cm^{-2} s^{-1}	~ 13 %
t	7.5×10^{-3} seconds	~ 1.3 %
Online wavelength position	~ 308 nm	5 %
OHP	20–30 mW	8 %
HO_2P	10–20 mW	10 %
Accuracy	16 %	
Precision	4 %	
Final uncertainty	17 %	

The largest uncertainty comes from the determination of the lamp flux. Note that, while the uncertainty in the flux values calculated in an NO actinometry experiment is ~ 25 %, the uncertainty in the flux values calculated in a FAGE HO_x calibration are considerably smaller (~ 10 %) since they are calculated from the standard error in the slope and

intercept of the NO actinometry plot, as shown in Figure 2.9. The uncertainty in the measured laser power is determined from calibration of the OH and HO_2 photodiodes at a range of laser powers. The uncertainty in the position of the online wavelength stems from procedure for finding the online wavelength, which scans the laser wavelength until the reference cell signal reaches 95 % of the maximum signal obtained when scanning over the OH $Q_1(2)$ rotational line (see section 2.4.2).

The uncertainty in measurements of ambient [OH] is given by the sum in quadrature of the fractional uncertainty in C_{OH}, the fractional precision of the online and offline OH signals, and the fractional precision (standard deviation, SD) of the laser power measurement in the OH cell:

$$\sigma_{OH} = \sqrt{\left(\frac{\sqrt{SD^2_{OHSignal_{on}} + SD^2_{OHSignal_{off}}}}{OHSignal_{on} - OHSignal_{off}}\right)^2 + \left(\frac{SD_{OHP}}{OHP}\right)^2 + \left(\frac{\sigma_{C_{OH}}}{C_{OH}}\right)^2} \quad (2.29)$$

The uncertainty in measurements of ambient [HO_2] is calculated in a similar way to equation (2.29), with the addition of the uncertainty in the HO_2 intercept:

$$\sigma_{HO_2} = \sqrt{\left(\frac{\sqrt{SD^2_{HO_2Signal_{on}} + SD^2_{HO_2Signal_{off}}}}{HO_2Signal_{on} - HO_2Signal_{off}}\right)^2 + \left(\frac{SD_{HO_2P}}{HO_2P}\right)^2 + \left(\frac{\sigma_{C_{HO_2}}}{C_{HO_2}}\right)^2 + \left(\frac{\sigma_{Int_{HO_2}}}{Int_{HO_2}}\right)^2} \quad (2.30)$$

Typical uncertainties in HO_2 measurements during the SeptEx and RONOCO field campaigns were on the order of 30 %. The uncertainties in OH measurements were much larger, ranging from 50 % to several hundred per cent, owing to low concentrations and high variability in the online and offline signals.

2.7 Instrumental limit of detection

The aircraft FAGE instrument's limit of detection (LOD) for OH and HO_2 is determined by the instrument's sensitivity and the standard deviation of the background signal as follows:

$$[\mathrm{OH}]_{\mathrm{min}} = \frac{\mathrm{SNR}}{C_{\mathrm{OH}} \times \mathrm{OHP}_{\mathrm{on}}} \sigma_{\mathrm{off}} \sqrt{\frac{1}{m} + \frac{1}{n}} \tag{2.31}$$

where $[\mathrm{OH}]_{\mathrm{min}}$ is the minimum detectable OH concentration (the limit of detection), SNR is the signal-to-noise ratio above which OH can be detected (= 2 for a 95 % confidence interval), σ_{off} is the standard deviation of the background (offline) signal, and m and n are the number of 1-second online and offline points, respectively (60 and 60 for a 1 minute average). Since the photon counting signal can be described by a Poisson distribution (Stevens *et al.*, 1994, Holland *et al.*, 1995, Faloona *et al.*, 2004), σ_{Off} is defined as:

$$\sigma_{\mathrm{off}} = \sqrt{\left(S_{\mathrm{lb}} + S_{\mathrm{sb}} + S_{\mathrm{dc}}\right)_{\mathrm{mean}}} \tag{2.32}$$

where S_{lb} is the signal due to laser scatter (typically 0.5–1.5 count s^{-1} mW^{-1}), S_{sb} is the signal due to solar counts (typically zero), S_{dc} is the signal due to dark counts (typically zero), and $\left(S_{\mathrm{lb}} + S_{\mathrm{sb}} + S_{\mathrm{dc}}\right)_{\mathrm{mean}}$ is the mean of the sum of these values. During the RONOCO and SeptEx fieldwork in 2010 and 2011, the LOD for a one minute averaging period ranged between 0.64 and 1.80×10^6 molecule cm^{-3} for OH, and between 5.9 and 6.9×10^5 molecule cm^{-3} for HO_2.

2.8 Factors affecting instrument sensitivity

The sensitivity of the FAGE instrument to OH is determined by the number of fluorescence photons detected per ambient OH molecule. The sensitivity is therefore dependent on the transmission of OH through the inlet, the rate of excitation of OH, the

OH fluorescence quantum yield, and the efficiency of fluorescence collection. The theoretical sensitivity, as a function of the detection cell pressure, is given by:

$$C\left(P_{\text{int}}\right) = D \cdot T_{\text{OH}} \cdot \phi_{\text{f}} \cdot f_{\text{gate}} \cdot \left[\text{OH}\right]_{\text{int}} \tag{2.33}$$

where P_{int} is the pressure inside the detection cell, D is a collective term for pressure-independent variables (laser power, OH absorption cross-section, laser linewidth, physical overlap of laser and gas beams, solid angle of fluorescence collection, transmission of collection optics, quantum yield of the channel photomultiplier tube), T_{OH} is the transmission of OH through the inlet and pre-detection assembly, ϕ_{f} is the OH fluorescence quantum yield, f_{gate} is the fraction of the total OH fluorescence detected within the photon counter gate, and $\left[\text{OH}\right]_{\text{int}}$ is the number density of OH in the detection cell (Creasey *et al.*, 1997, Faloona *et al.*, 2004, Heard, 2006, Dusanter *et al.*, 2009).

Apart from the laser power, the terms contributing to *D* remain constant throughout a measurement period, and are accounted for by regular calibrations. Laser power is measured by photodiodes positioned in the OH and HO_2 detection cells, and the recorded OH and HO_2 signals are normalised to the measured laser power as described in 2.4.5. Over the range of laser powers typically used during field measurements, the rate of excitation of OH, and therefore the instrument sensitivity to OH and HO_2, has been found to vary linearly with laser power (Floquet, 2006, Edwards, 2011). The transmission of OH to the detection region is dependent on the rate of loss of OH to the walls of the inlet and the pre-detection assembly. At detection cell pressures below 2 Torr, the rate of loss of OH to the walls, k_{w}, has been determined to be 87 s^{-1} (Commane, 2009). For the aircraft instrument, with a total inlet-to-detection distance of 50 cm and a transmission time of less than 0.03 seconds, approximately 90 % of the sampled OH is lost to the walls. The sensitivity of the instrument could therefore be improved significantly by mounting the entire detection cell outside the skin of the aircraft, requiring a much shorter pre-detection assembly. The instrument sensitivity to HO_2 is usually greater than the sensitivity to OH, since the rate of loss of HO_2 to the walls is less than the rate of loss of OH. The effect of detection cell pressure on OH transmission is discussed in section 2.8.3.

The fluorescence quantum yield, ϕ_f, is given by the ratio of the rate of radiative decay to the total rate of decay:

$$\phi_f = \frac{\tau^{-1}}{\Gamma} = \frac{k_{rad}}{k_{rad} + \sum_i k_{qi}[q_i]} \quad (2.34)$$

where τ is the fluorescence lifetime of the OH in the absence of quenchers (= 688 ns) (German, 1975), Γ is the total rate of decay of excited OH, $k_{rad} = \frac{1}{\tau_{rad}}$ is the rate constant for radiative decay, k_{qi} is the rate constant for quenching of the OH fluorescence by ambient molecules, and $[q_i]$ is the number density of the quenching species. N_2, O_2, and H_2O are the most important atmospheric quenchers of OH fluorescence. The ambient concentrations of N_2 and O_2 are essentially constant. The ambient concentration of water vapour, however, varies sufficiently (1–3 %) that its effect on instrument sensitivity must be taken into account following field measurements (Stevens *et al.*, 1994). The fraction of OH fluorescence collected within the photon counting gate, f_{gate} (Gate A, see section 2.4.5), is dependent on the OH fluorescence lifetime, and therefore on the rate of quenching by H_2O. Finally, the number density of OH inside the detection cell, $[OH]_{int}$, is dependent on the cell pressure, which changes with ambient pressure. The effects of pressure and water vapour concentration on sensitivity are discussed further in section 2.8.1 and section 2.8.3, respectively.

2.8.1 Effects of water vapour concentration on sensitivity

The dependence of the aircraft FAGE instrument sensitivity on water vapour has been thoroughly investigated by Commane (2009), in which C_{OH} and C_{HO2} were measured with ambient water vapour concentrations ranging from 7.2×10^{15} molecule cm^{-3} (0.03 %) to 2.4×10^{17} molecule cm^{-3} (1 %), and a detection cell pressure of 4 Torr. These calibrations were performed following the COBRA field measurements, and will hereafter be referred to as the 2008 calibrations. There was a linear dependence of C_{OH} and C_{HO2} on $[H_2O]$, with both sensitivities decreasing with increasing water vapour concentration (see Figure 2.14). Given a measured sensitivity at a known water vapour

concentration, the theoretical reduction or increase in sensitivity at other water vapour concentrations can be calculated. The fraction of OH fluorescence collected in the photon counting gate, f_{gate}, and the fluorescence quantum yield, ϕ_{f}, are given by:

$$f_{\text{gate}} = e^{-\Gamma t_1} - e^{-\Gamma t_2} \tag{2.35}$$

$$\phi_{\text{f}} = \frac{\tau^{-1}}{\Gamma} \tag{2.34}$$

$$\Gamma = k_{\text{rad}} + k_{q,\text{N}_2}\left[\text{N}_2\right]_{\text{cell}} + k_{q,\text{O}_2}\left[\text{O}_2\right]_{\text{cell}} + k_{q,\text{H}_2\text{O}}\left[\text{H}_2\text{O}\right]_{\text{cell}} \tag{2.36}$$

where t_1 = 110 ns and t_2 = 1110 ns are the start and end times of the photon-counting gate, respectively, and $\left[\text{N}_2\right]_{\text{cell}}$, $\left[\text{O}_2\right]_{\text{cell}}$, and $\left[\text{H}_2\text{O}\right]_{\text{cell}}$ are the concentrations inside the detection cell. The values of the rate constants in equation (2.36) are given in Table 2.7. Using values of the rate constants for an estimated mean inlet temperature of 255 K rather than 298 K (see section 2.4.3) reduced the values of f_{gate} and ϕ_{f} by 2 % and 1 %, respectively.

Knowledge of the ambient pressure and the detection cell pressure enables calculation of $\left[\text{N}_2\right]_{\text{cell}}$, $\left[\text{O}_2\right]_{\text{cell}}$, and $\left[\text{H}_2\text{O}\right]_{\text{cell}}$, and therefore f_{gate} and ϕ_{f}, to be calculated for any ambient water vapour concentration. Since C_{OH} is directly proportional to the product of f_{gate} and ϕ_{f}, a correction factor A can be calculated for C_{OH} as follows:

$$\text{A} = \frac{f_{\text{gate}} \cdot \phi_{\text{f}}}{f'_{gate} \cdot \phi'_{\text{f}}} \tag{2.37}$$

$$C_{\text{OH}}\left(\text{H}_2\text{O}\right) = C_{\text{OH,meas}} \cdot \text{A} \tag{2.38}$$

where f_{gate} and ϕ_{f} are the values calculated for a calibration at a known water vapour concentration, and f'_{gate} and ϕ'_{f} are the values calculated for other water vapour concentrations.

Table 2.7. Rate constants for radiative and non-radiative decay of excited OH.

Rate constant	Value at 255 K / s^{-1} or cm^3 $molecule^{-1}$ s^{-1}	Reference
k_{rad}	$1.45 \pm 0.04 \times 10^{6}$	German (1975)
k_{q,N_2}	$3.50 \pm 0.1 \times 10^{-9}$	Bailey *et al.* (1997)
k_{q,O_2}	$1.45 \pm 0.04 \times 10^{-10}$	Bailey *et al.* (1997)
k_{q,H_2O}	$6.94 \pm 0.7 \times 10^{-10}$	Bailey *et al.* (1999)

The measured dependence of C_{OH} and C_{HO2} on water vapour concentration was compared to the theoretical dependence predicted by equations (2.35) to (2.38). The measured C_{HO2} agreed well with the theoretical calculations. However, the decrease in measured C_{OH} with increasing water vapour concentration was stronger than predicted by the calculations. This effect has been seen in another FAGE instrument (Martinez *et al.*, 2010) but is as yet unexplained.

The aircraft FAGE instrument was calibrated at different water vapour concentrations following the summer and winter RONOCO fieldwork in October 2010 and February 2011. The results from October 2010 are shown in Figure 2.13, plotted as the relative sensitivity against water vapour concentration. The relative sensitivity is calculated as the ratio of the sensitivity at any water vapour concentration, $C(H_2O)$, to the sensitivity at a reference water vapour concentration, C (usually the lowest value). Calibrations were performed over water vapour concentrations from 1.1 to 2.4×10^{17} molecule cm^{-3}, corresponding to detection cell concentrations of 2.8 to 5.9×10^{14} molecule cm^{-3}. The detection cell pressure, which determines the concentration of water vapour inside the cell, varied from 1.86 to 1.88 Torr.

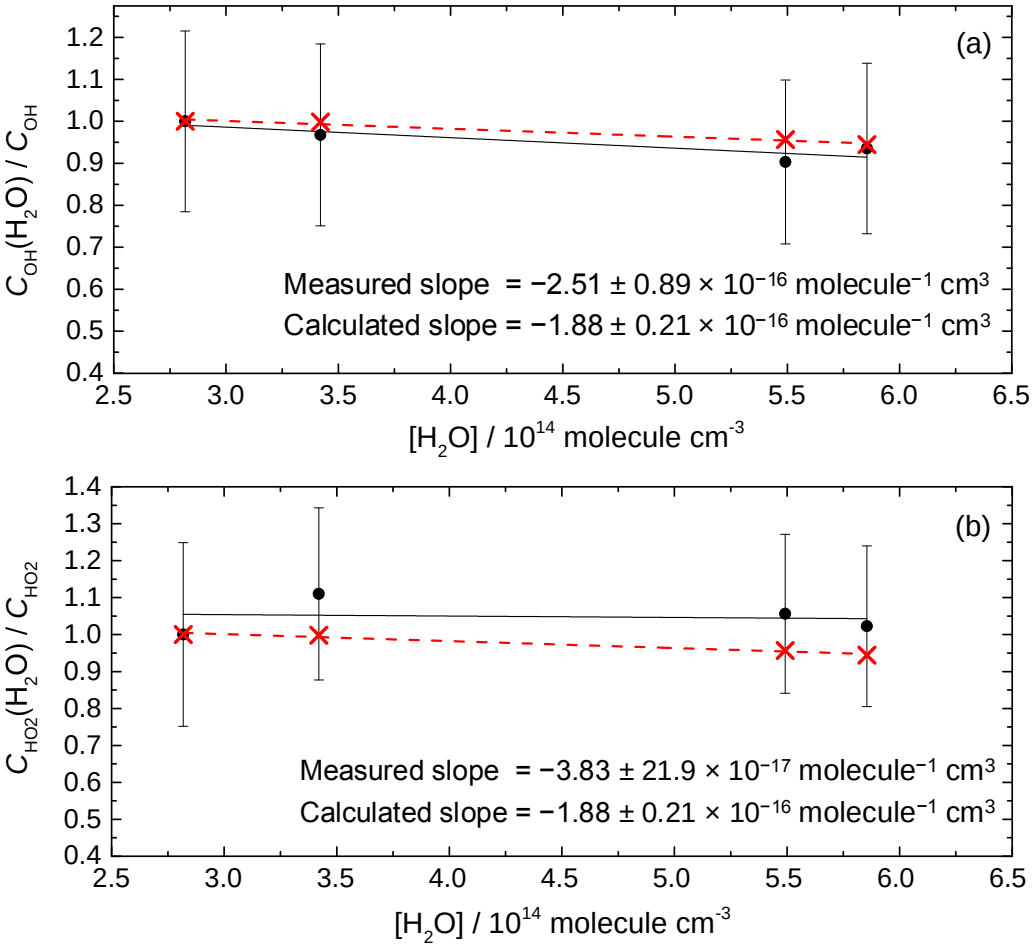

Figure 2.13. Relative sensitivities to (a) OH and (b) HO_2 as a function of the concentration of water vapour in the detection cell, at ~ 255 K, with a cell pressure of 1.86–1.88 Torr. C_{OH} and C_{HO2} are the sensitivities measured or calculated at the lowest water vapour concentration (= 2.8×10^{14} molecule cm^{-3}); $C_{OH}(H_2O)$ and $C_{HO2}(H_2O)$ are sensitivities measured or calculated at higher water vapour concentrations. Black data points are results from calibrations at single water vapour concentrations in October 2010, and error bars represent 1σ uncertainty in the measured relative sensitivities (~ 21 %). Solid black line is the line of best fit to the measured sensitivities. Red crosses represent calculated relative sensitivities, and the dashed red line is the line of best fit to the calculated sensitivities.

The slopes of the lines of best fit, which give the dependence of sensitivity on water vapour concentration, and their uncertainties, are given in each plot. For OH, the experimentally-determined water vapour dependence is stronger than the calculated dependence, as reported by Commane (2009), but the slopes are the same within their combined uncertainties. For HO_2, the experimentally-determined water vapour dependence is weaker than the calculated dependence, and has a large relative uncertainty due to the small value of the slope relative to the scatter of the measured sensitivities around the line of best fit. The experimental and calculated slopes are

therefore the same within error, but the experimental slope should be treated with caution. The current results are in contrast with the 2008 results, when the calculated water vapour dependence was weaker than the measured value for both OH and HO_2, and the agreement between measured and calculated values was better for HO_2 than for OH.

A comparison of the water vapour dependent relative sensitivities from the 2008 calibrations and from this work is given in Figure 2.14. The slopes of the lines of best fit to the data are given in Table 2.8. There is excellent agreement between the relative OH sensitivities measured by Commane and those measured in this work, with the slopes of the lines of best fit to the data being the same within their combined uncertainties. While the HO_2 slope from the current work is clearly different to the 2008 slope, the data points from the current work lie well within the combined uncertainties of the two data sets. The discrepancy between the 2008 work and the current work is therefore attributed to the relatively small range of water vapour concentrations investigated in this work. It is worth noting that during the 2008 calibrations, the detection cell pressure was set to 4 Torr to mimic the sampling conditions during the COBRA field measurements, when the extension of the pumping line resulted in higher-than-normal cell pressures (Edwards, 2011). Higher detection cell water vapour concentrations were therefore achieved compared to the current work.

2.8.2 Analysis of field data

The range of water vapour concentrations achievable during a calibration is determined by the temperature of the calibration gas flow, the temperature of the water bubbler, and the calibration flow rate. Turbulent flow cannot be maintained at flow rates less than 45 slm (Commane, 2009), so the use of slower flow rates to achieve higher water vapour concentrations is not an option. The temperatures of the gas and the water bubbler are determined by the ambient temperature, which, during laboratory calibrations, is controlled by the laboratory air conditioning. Heating the water bubbler to achieve higher saturation increases the uncertainty in HO_x calibrations, due to increased variability in $[H_2O]$ measured by the hygrometer, and therefore in [OH] and $[HO_2]$ produced by the system (F. Winiberg, personal communication).

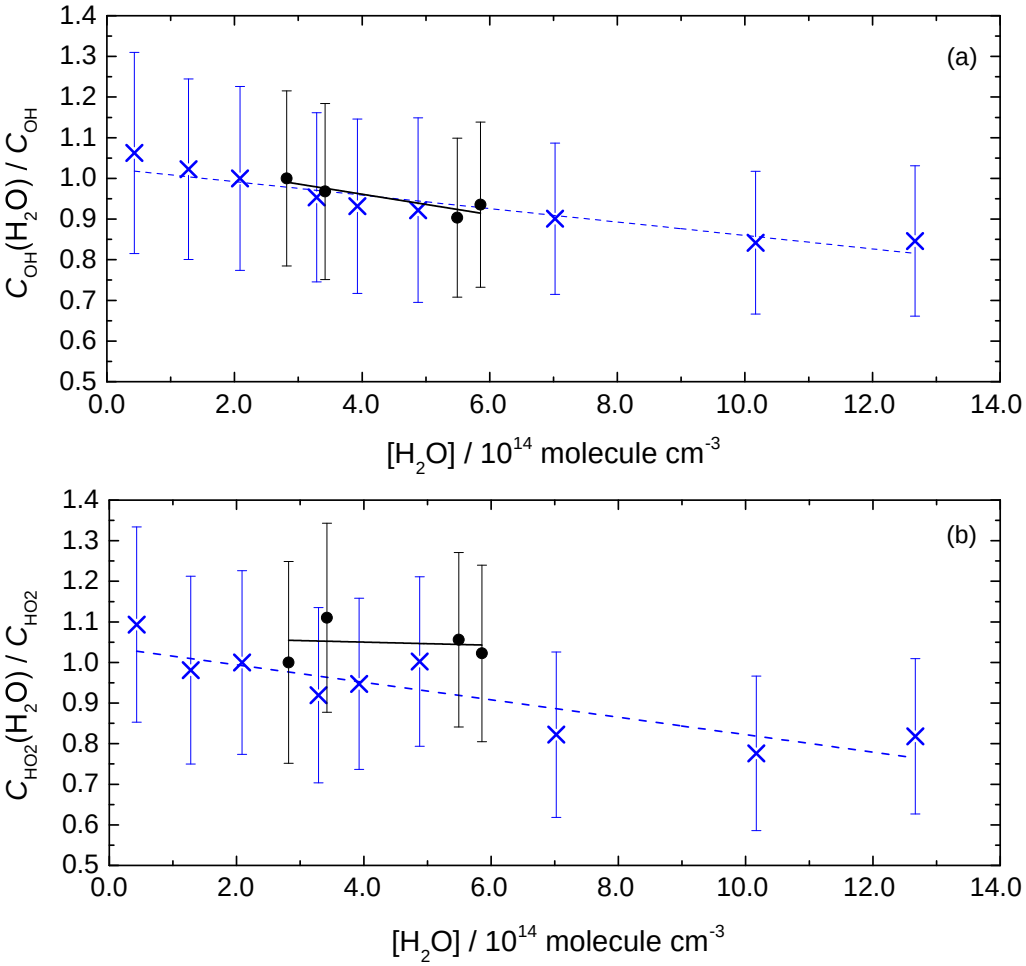

Figure 2.14. Comparison of water-dependence of instrument sensitivity to (a) OH and (b) HO_2 determined by calibration from Commane (2009) (blue crosses, dashed blue line) with current work (black dots, solid black line).

Table 2.8. Slopes of lines of best fit to relative sensitivity data, indicating the water vapour dependence of the instrument's sensitivity to OH and HO_2, from Commane (2009) and from the current work.

Relative sensitivity	Slope from Commane / molecule^{-1} cm^3	Slope from current work / molecule^{-1} cm^3
$C_{OH}(H_2O) / C_{OH}$	$(-1.68 \pm 0.22) \times 10^{-16}$	$(-2.51 \pm 0.89) \times 10^{-16}$
$C_{HO2}(H_2O) / C_{HO2}$	$(-2.28 \pm 0.42) \times 10^{-16}$	$(-3.83 \pm 21.9) \times 10^{-17}$

The range of water vapour concentrations in the current work was achieved by diverting between 0 and 100 % of the calibration flow through the water bubbler, and therefore represents the greatest range that can be achieved with the current calibration apparatus.

A summary of ambient and detection cell water vapour concentrations and the instrument sensitivity to OH and HO_2 during the RONOCO and SeptEx field measurement campaigns is given in Table 2.9. The range of ambient water vapour concentrations exceeds the range that can be reliably achieved during a calibration. For this reason, theoretical water-dependent sensitivities were calculated for the RONOCO and SeptEx data, using the ambient water vapour concentration, the ambient pressure, and the detection cell pressure measured during the flights, to adjust the sensitivities measured during the calibrations that followed each measurement campaign.

2.8.3 Effects of pressure on sensitivity

The pressure inside the detection cell, P_{int}, changes with external pressure during aircraft FAGE measurements. The internal pressure affects the number density of OH inside the detection cell, $[\text{OH}]_{\text{int}}$, OH transmission, T_{OH}, OH fluorescence quantum yield, ϕ_{f}, and the fraction of OH fluorescence detected in the photon counting gate, f_{gate}. Neglecting loss on the inside of the pinhole, the rate of loss of OH is directly proportional to the gas diffusion coefficient, D_{g}, which is inversely proportional to pressure (Faloona *et al.*, 2004):

$$k_{\text{w}} \propto D_{\text{g}} \propto \frac{1}{P_{\text{int}}} \tag{2.39}$$

OH transmission, $\frac{[\text{OH}]_t}{[\text{OH}]_0}$, can be approximated as:

$$\frac{[\text{OH}]_t}{[\text{OH}]_0} = \exp(-k_{\text{w}} t) \tag{2.40}$$

$$= \exp\left(-\frac{A}{P_{\text{int}}}\right) \tag{2.41}$$

$$\approx \left(1 - \frac{A}{P_{\text{int}}}\right) \tag{2.42}$$

where $[\text{OH}]_0$ is the concentration of OH before the inlet, t is the transmission time of OH (< 0.03 seconds), $[\text{OH}]_t$ is the concentration of OH at time t, and A is a constant that includes t and other pressure-independent factors.

Table 2.9. Ambient and detection cell water vapour concentrations, C_{OH}, and C_{HO2} during RONOCO and SeptEx. Mean values are given in parentheses.

	RONOCO summer, 2010	SeptEx, 2010	RONOCO winter, 2011
Ambient $[H_2O]$ / 10^{17} molecule cm^{-3}	1.03–3.55 (2.64)	0.318–3.63 (2.34)	0.016–4.37 (1.49)
Detection cell $[H_2O]$ / 10^{14} molecule cm^{-3}	2.64–9.18 (6.67)	0.648–8.86 (5.60)	0.004–10.6 (3.43)
C_{OH} / count s^{-1} mW^{-1} molecule^{-1} cm^3	3.0×10^{-8}	3.0×10^{-8}	3.8×10^{-8}
C_{OH} corrected for mean $[H_2O]$ / count s^{-1} mW^{-1} molecule^{-1} cm^3	2.9×10^{-8}	3.1×10^{-8}	4.25×10^{-8}
C_{HO2} / count s^{-1} mW^{-1} molecule^{-1} cm^3	9.3×10^{-8}	9.3×10^{-8}	1.1×10^{-7}
C_{HO2} corrected for mean $[H_2O]$ / count s^{-1} mW^{-1} molecule^{-1} cm^3	9.5×10^{-8}	9.6×10^{-8}	1.2×10^{-7}

The flow rate through the cell is assumed to change very little over the range of pressures encountered during aircraft measurements, since the pumping system provides a constant volumetric flow, so the transmission time remains nearly constant (Faloona *et al.*, 2004, Martinez *et al.*, 2010). Figure 2.15 shows the theoretical pressure dependence of C_{OH}, OH transmission, OH fluorescence quantum yield, the number density of OH inside the cell, and f_{gate}, calculated using equations (2.33) to (2.42). C_{OH} shows a maximum at a cell pressure of 1.7 Torr, but is nearly constant between 1.2 and 2.2 Torr. The OH fluorescence quantum yield, ϕ_f, is given by the ratio of radiative and non-radiative rate constants for the decay of the OH excited state, so that the fluorescence quantum yield is inversely proportional to cell pressure. f_{gate} is an exponential function of Γ, t_1, and t_2 (see equation (2.36)), and has a maximum value at P_{int} ~ 0.4 Torr, decreasing with higher pressures. Equations (2.40) to (2.42) predict a sharp increase in OH transmission between 0 and 0.4 Torr, with a gradual increase at higher pressures.

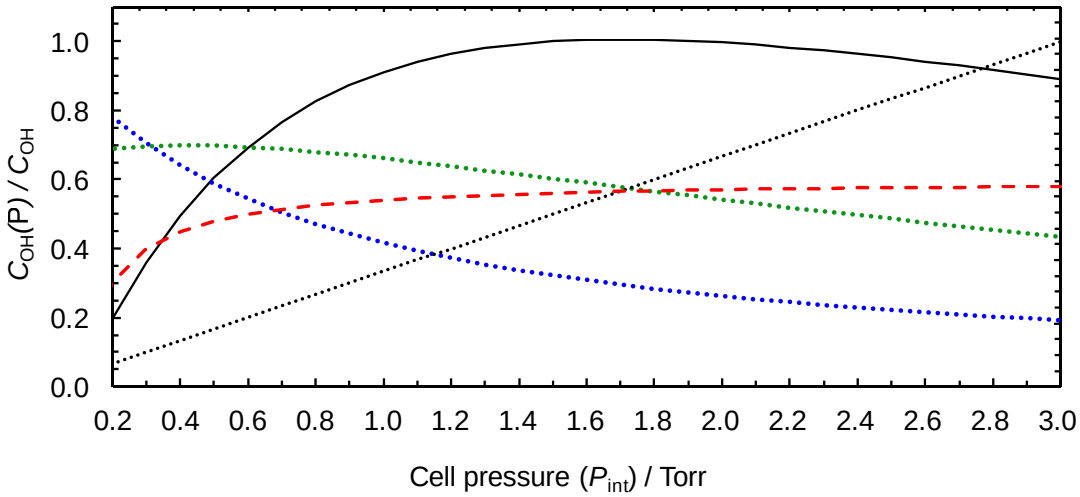

Figure 2.15. Theoretical pressure-dependent sensitivity to OH calculated at a constant water vapour mixing ratio (10,000 ppmv, 1 %), showing overall sensitivity (solid black line), $[OH]_{int}$ (dotted black line), OH transmission (dashed red line), f_{gate} (dotted green line), and OH fluorescence quantum yield (dotted blue line). $C_{OH}(P)$ is the pressure-dependent sensitivity to OH and C_{OH} is a reference value calculated at P_{int} = 1.5 Torr.

However, the experimentally determined OH transmission was found to be nearly constant (~ 7 %) at P_{int} = 1.5−2 Torr, increasing to ~ 25 % at P_{int} = 2.7 Torr (Commane, 2009). This suggests that k_w and T are not dependent on P_{int} alone, but that loss on the inlet pinhole, and perhaps a change in the gas flow regime, are affected by the change in pinhole size.

The experimental pressure dependence of C_{OH} and C_{HO2} has been investigated by Commane (2009, see also Commane *et al.*, 2010) following the method of Faloona *et al*. (2004) and Martinez *et al*. (2010). The pressure inside the detection cell, P_{int}, can be varied between 1.6 and 2.7 Torr by varying the size of the inlet pinhole between 0.50 and 0.85 mm, to mimic a change in external pressure. Calibrations can therefore be conducted over a range of cell pressures applicable to aircraft-based measurements. During the RONOCO aircraft campaign, P_{int} ranged between a maximum of 2.0 Torr at ground level, to 1.3 Torr at 3.3 km. Figure 2.16 shows the results from the pressure-dependent calibrations. Despite the discrepancy between the theoretical and experimental pressure dependence of OH transmission, C_{OH} and C_{HO2} were found to be independent of pressure over the range of pressures experienced during typical aircraft-based measurements, and within the reproducibility of calibration results, in agreement with the theoretical results shown in Figure 2.15.

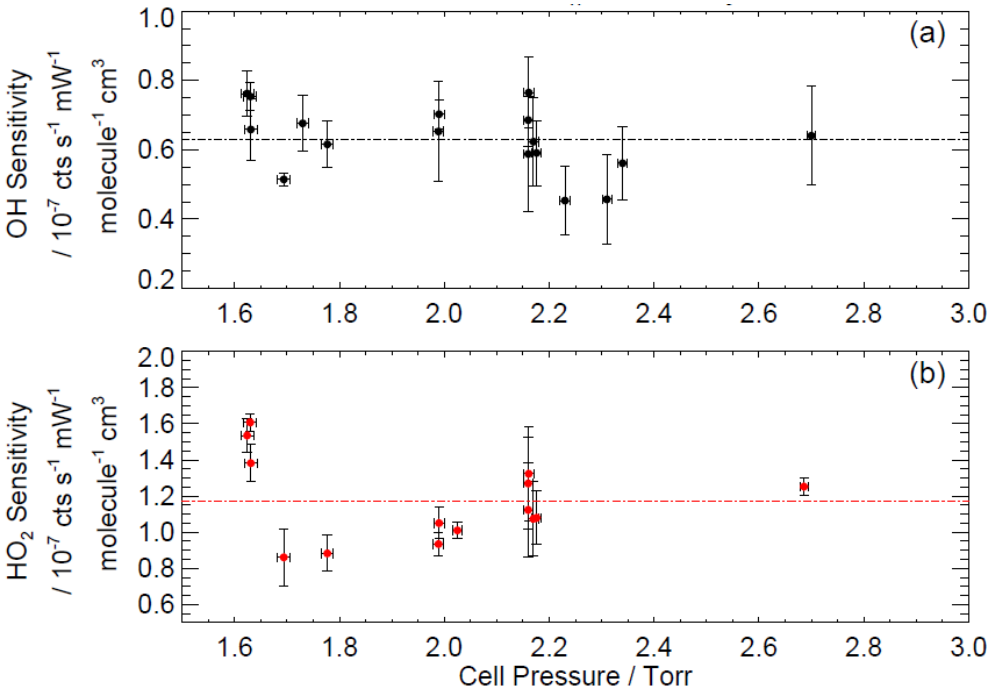

Figure 2.16. Experimentally-determined aircraft FAGE instrument sensitivity to (a) OH, and (b) HO_2 as a function of cell pressure (P_{int}), measured before and after the AMMA field measurement campaign in 2006. The water vapour mixing ratio was between 380 and 420 ppmv (0.038−0.042 %). *y* error bars are the 1σ standard errors in the slope of each calibration plot. *x* error bars are standard deviations in the cell pressure during each calibration. The instrument sensitivity shows no dependence on cell pressure over the range of pressures investigated, within the reproducibility of the calibrations performed at each pressure. Figure from Commane (2009).

The pressure-dependent calibration method using different sized pinholes relies on the assumptions that loss of OH and HO_2 to the inside of the pinhole does not change significantly with pinhole size, and that the flow regime remains similar for pinholes of different sizes. The method has been validated by calibration of both the aircraft and HIRAC FAGE instruments at different external pressures inside the atmospheric simulation chamber HIRAC at the University of Leeds. The experiments were conducted by Dr Shona Smith and Fred Winiberg (Winiberg *et al.*, 2013). The FAGE inlet was positioned inside the chamber, with the detection cells located outside the chamber. The pressure inside the detection cells ranged between 1.1 and 1.9 Torr. The HIRAC instrument was calibrated for both OH using a hydrocarbon decay method, and for HO_2 using the HCHO photolysis method described in section 2.5.3.2; the aircraft instrument was calibrated for HO_2 only. Good agreement was found between the results of the two OH calibration techniques, and between the two HO_2 calibration techniques.

For the aircraft instrument, the wand calibration always gave slightly higher values of C_{HO2} than the chamber calibration (6.3–17.4 %). This effect was not seen for the HIRAC FAGE instrument. The HCHO photolysis experiments validate the pressure-dependent calibrations conducted by changing the size of the inlet pinhole. Little variation in C_{HO2} was found over the range of pressures studied, in agreement with the results of Commane (2009). At 1.1 Torr, C_{HO2} was 8.0 ± 1.6 × 10^{-8} count s^{-1} mW^{-1} $molecule^{-1}$ cm^3, and at 1.9 Torr C_{HO2} was 1.2 ± 0.24 × 10^{-7} count s^{-1} mW^{-1} $molecule^{-1}$ cm^3, the two values being the same within their combined uncertainties.

2.9 Chemical and spectral interferences

Chemical interferences result from the production of OH or HO_2 in the pre-detection assembly or inside the detection cell, either by photolysis of parent compounds in the laser beam or by chemical reaction. Ren *et al.* (2004) conducted a study of potential chemical interferences in the Penn State FAGE instrument and found that neither O_3, H_2O_2, HONO, HCHO, HNO_3, acetone, nor a variety of VOCs produced significant concentrations of OH. Theoretical (Zeng *et al.*, 1998) and experimental (Schlosser *et al.*, 2009) studies of the potential interference from ozone photolysis at λ = 308 nm have also concluded that the OH production *via* this route is negligible. However, Holland *et al.* (2003) and Kanaya *et al.* (2007) have reported interferences in measurements of OH and HO_2 that scale linearly with [O_3] and laser power, suggesting that the ozone interference is instrument-specific.

Spectral interferences result from the fluorescence of molecules other than OH at the online or offline wavelengths, contributing to the online or offline signals, respectively. Ren *et al.* (2004) analysed spectral interference from naphthalene, SO_2, and HCHO, and found no significant interference from SO_2 or HCHO. Naphthalene, however, has narrow absorption features around 308 nm, and has the potential to cause a positive interference in offline OH measurements at wavelengths longer than the $Q_1(2)$ rotational line. The naphthalene absorption cross-section at λ ~ 308 nm is 200 times smaller than that of OH (Neuroth *et al.*, 1991), so the interference is small, and can be avoided altogether by taking offline measurements at a wavelength shorter than the $Q_1(2)$ line (Martinez *et al.*, 2004, Ren *et al.*, 2004).

2.9.1 RO_2-based interference in HO_2 measurements

It has recently been shown that reaction of alkene-derived peroxy radicals, RO_2, with NO inside the HO_2 detection cell, can lead to interference in all FAGE HO_2 measurements (Fuchs *et al.*, 2011, Whalley *et al.*, 2013). Organic peroxy radicals are primarily produced in the reactions of OH, O_3, and NO_3 with volatile organic compounds (VOCs), and are present in the atmosphere at similar concentrations to HO_2. RO_2 radicals react with NO as follows:

$$RO_2 + NO \xrightarrow{k_{1,RO_2+NO}} RO + NO_2 \quad \text{(R1.11)}$$

$$RO_2 + NO \xrightarrow{k_{2,RO_2+NO}} RONO_2 \quad \text{(R2.19)}$$

$$RO + O_2 \xrightarrow{k_{RO+O_2}} R'O + HO_2 \quad \text{(R1.13)}$$

$$RO + NO \xrightarrow{k_{RO+NO}} RONO \quad \text{(R2.20)}$$

$$RO_2 + HO_2 \xrightarrow{k_{RO_2+HO_2}} ROOH \quad \text{(R1.14)}$$

Prior to the work of Fuchs *et al*. it was believed that the contribution to the HO_2 signal from RO_2 radicals was negligible, as theoretical sensitivity to RO_2, laboratory experiments investigating C_1 to C_4 alkyl peroxy radicals, and field measurements did not suggest a significant interference (*e.g.* Hard *et al.*, 1984, Mather *et al.*, 1997, Kanaya *et al.*, 2001). Reaction (R1.13) is slow at the reduced pressure of the detection cell compared to the atmosphere, because of the reduced number density of O_2. In addition, formation of $RONO_2$ competes with reaction (R1.11), limiting the production of HO_2. Alkanes react with OH *via* OH-abstraction, forming alkyl radicals, $R^{\bullet}$, and, following reaction with O_2, alkyl peroxy radicals, $RO_2^{\bullet}$. Alkenes, on the other hand, react *via* OH-addition, forming *β*-hydroxyalkyl peroxy radicals, $HO–RO^{\bullet}_2$ (Atkinson and Arey, 2003). Following reaction of RO_2 or HO-RO_2 with NO, the resulting alkoxy ($RO^{\bullet}$) and *β*-hydroxy alkoxy ($HO–RO^{\bullet}$) radicals can react with O_2, decompose, or isomerise. For *β*-hydroxy alkoxy radicals (excluding the ethane-derived 2-hydroxy-1-ethoxy radical) (Atkinson, 1997), decomposition and isomerisation are the dominant room temperature pathways (Atkinson and Arey, 2003). Decomposition occurs quickly (k_{dec} = 10^4–10^6 s^{-1}) (Berndt and Böge, 1994, Johnston *et al.*, 1996, Atkinson, 1997, Atkinson, 1997) and yields a hydroxyalkyl radical, $HO–R^{\bullet}$, which reacts quickly with O_2 to

produce a carbonyl compound and HO_2 (Atkinson, 1997, Orlando *et al.*, 2003). This reaction is the source of potential interference in FAGE measurements of HO_2 (Fuchs *et al.*, 2011).

The rate of reaction between RO_2 and NO at 298 K (k_{1,RO_2+NO} = 9.0 × 10^{-12} cm^3 $molecule^{-1}$ s^{-1}) (Atkinson and Arey, 2003) is similar to that between HO_2 and NO (k_{HO_2+NO} = 8.0 × 10^{-12} cm^3 $molecule^{-1}$ s^{-1}) (Sander *et al.*, 2011). Under the right conditions, the reaction of RO_2 sampled by the FAGE inlet with the NO in the HO_2 detection cell can lead to production of HO_2 on a timescale which is fast enough for the extra HO_2 to be converted to OH and detected as part of the HO_2 signal. The overall rate at which RO_2 is converted to OH, and therefore the magnitude of the interference, depends on the residence time and mean temperature inside the cell, and the amount of NO injected. The interference therefore differs between different FAGE instruments. In view of this, the ground-based and aircraft FAGE instruments at the University of Leeds have been tested for RO_2 interference. The testing of three FAGE cells that have been used with the ground-based instrument was performed by Dr Lisa Whalley, and the testing of the aircraft instrument was performed by Dr Trevor Ingham. A thorough description of the ground-based experimental method, results, and the results of a modelling study are given in Whalley *et al.* (2013). A summary of the method and results pertaining to the aircraft instrument are given here.

Following the method of Fuchs *et al.* (2011), RO_2 radicals were generated in the calibration wand (see 2.5.1.1) by reaction of OH with an excess of the parent hydrocarbon, to ensure complete titration of OH. Equal concentrations of HO_2 and RO_2 were therefore generated in the flow. Photolysis of the parent hydrocarbon was avoided by introducing the hydrocarbon after the mercury lamp. The RO_2 interference, i.e. the relative OH yield from each RO_2, was determined by comparing the HO_2 signal with and without RO_2 as follows:

$$\text{Relative OH yield} = \frac{S_{HO_2+RO_2} - S_{HO_2}}{S_{HO_2}} \qquad (2.43)$$

where $S_{HO_2+RO_2}$ and S_{HO_2} are the HO_2 detection cell signals with and without the addition of RO_2, respectively. Whalley *et al*. tested interference caused by RO_2 radicals derived from methane, propane, ethene, isoprene, toluene, cyclohexane, and methanol. No significant interference was observed from methane and propane-derived RO_2 radicals, as expected. For the ground-based FAGE cell that most resembles the aircraft instrument cell, the relative OH yield from ethene-derived RO_2 radicals was determined to be 0.463 ± 0.030, with a cell pressure of 1 Torr, a flow rate of 3 slm, and an NO flow of 10 sccm. In the other ground-based FAGE cells, significant interference was observed from ethene, methanol, isoprene, cyclohexane, and toluene-based RO_2 radicals. A model based on the Master Chemical Mechanism (v3.2 Jenkin *et al.*, 1997, Jenkin *et al.*, 2003, Saunders *et al.*, 2003, Bloss *et al.*, 2005, *via* http://mcm.leeds.ac.uk/MCM), constrained to the temperature, pressure, and [NO] inside the FAGE cell, and initialised with the concentrations of RO_2 used in the experiments, was used to predict interferences from each of the RO_2 radicals tested (Whalley *et al.*, 2013). Good agreement was found between the model results and the experimental results. The same experimental method was used to test the aircraft FAGE instrument, yielding very similar results. The strongest interference was observed for ethene-derived RO_2, amounting to an increase of 39.7 ± 4.8 % in the observed HO_2 signal, with a cell pressure of 1.8 Torr, an estimated detection cell temperature of 255 K, and $[NO]_{cell} = 10^{14}$ molecule cm^{-3}. Similar results were also obtained for the HIRAC FAGE instrument, which is similar in design to the aircraft instrument, with a measured interference from ethene-derived RO_2 of ~ 50 % at $[NO]_{cell} = 10^{14}$ molecule cm^{-3} (F. Winiberg, personal communication).

The results of the ethene-derived RO_2 interference testing were applied to a modelling study conducted by Dr Daniel Stone to assess the effect of the interference on the HO_2 measurements made during the RONOCO and SeptEx campaigns (Stone *et al.*, 2013). A box model using the MCM chemistry scheme was used to calculate a total potential interference in the RONOCO HO_2 measurements. The model was constrained to the conditions in the detection cell (1.8 Torr, 255 K, [NO] ~ 10^{14} molecule cm^{-3}). Equal concentrations of HO_2 and $\sum RO_2$ (sum of all peroxy radicals in the MCM) were used to initialise the model. The model was run until the modelled interference (i.e.

concentration of OH produced) from ethene-derived RO_2 radicals matched the interference measured in the aircraft instrument experiments described above (~ 40 %). An interference factor, f, was calculated for each RO_2 in the MCM as follows:

$$f = \frac{[OH]_{HO_2+RO_2} - [OH]_{HO_2}}{[OH]_{HO_2}} \quad (2.44)$$

where $[OH]_{HO_2+RO_2}$ and $[OH]_{HO_2}$ are the modelled concentrations of OH produced from the reactions of RO_2 and HO_2, and the concentration from HO_2 alone, respectively. Table 2.10 gives interference factors for RO_2 radicals from selected parent hydrocarbons included in the MCM model. The greatest interference comes from isoprene-derived peroxy radicals, followed by aromatic compounds and C_2 to C_5 alkenes. The smallest interference is from the C_1 to C_3 alkanes. A modelled value of HO_2 including the total potential interference, $[HO_2]^*$, was calculated using:

$$[HO_2]^* = [HO_2]_{mod} + f[RO_2]_{mod} \quad (2.45)$$

Direct comparison between modelled values of $[HO_2]^*$ and the FAGE-measured values of $[HO_2]$ was therefore made possible. The average model-predicted interference during the RONOCO campaign was small, with $[HO_2]^* = 1.15[HO_2]_{mod} + 2\times10^5$ molecule cm^{-3}. Given that the expected interference is small, the HO_2 measurements discussed in Chapter 4 have not been adjusted. The magnitude of the RO_2 interference can be reduced by reducing the concentration of NO in the detection cell. This also reduces the instrument sensitivity to HO_2. Since conversion of RO_2 to OH requires at least two NO molecules, while conversion of HO_2 requires only one molecule, the ratio of HO_2 signal to RO_2 signal can be made favourable by reducing [NO] (Whalley *et al.*, 2013). This effect has been investigated for the ground-based instrument, and will be investigated for the aircraft instrument prior to future HO_x measurement campaigns.

Table 2.10. Interference factors, *f*, of RO_2 radicals derived from selected hydrocarbons in the MCM model, calculated by Dr Daniel Stone.

Parent Hydrocarbon	*f*
Isoprene	0.573
Pentene	0.572
Toluene	0.405
Propene	0.402
Trans-2-butene	0.398
Ethene	0.394
Octane	0.335
Butane	0.160
Propane	0.069
Ethane	0.073
Methane	0.011

2.9.2 Interference in OH measurements in forested environments

Though not directly applicable to the current work, a brief summary of potential chemical interferences in OH measurements made in forest regions is given here. Mao *et al*. (2012) recently reported a new chemical removal method for OH background measurements. The Penn State Ground-based Tropospheric Hydrogen Oxides Sensor (GTHOS) instrument was deployed for measurements of OH and HO_2 during the 2009 BEARPEX study in a Ponderosa pine plantation. Two methods for determining the background signal were used during the measurement campaign. The first, labelled OHwave, was the traditional method of modulating the laser wavelength to an 'online' and 'offline' position. The second, labelled OHchem, was by the addition of high-purity gaseous hexafluoropropene (C_3F_6) prior to the detection cell, to scavenge ambient OH and provide a background measurement. Significantly different background OH measurements were recorded using the two techniques, with the OHchem background being significantly higher than the OHwave background. The resulting $[OH]_{wave}$ was up to 4 times higher than the $[OH]_{chem}$, and the agreement between modelled OH and

$[OH]_{chem}$ was much better than between modelled OH and $[OH]_{wave}$. The difference in background measurements was attributed to the formation of OH in the FAGE cell, but not by photolysis in the laser beam. Rather, the interference was postulated to be caused by decomposition of stabilised Criegee intermediates produced in the ozonolysis of biogenic VOCs. The authors also propose that other biogenic oxidation intermediates also contribute to the interference signal.

A similar interference has also been reported in the Mainz LIF instrument (Novelli, 2012). Ozone and TME (2,3-dimethyl-2-butene) were injected into the detection cell, forming a stabilised Criegee intermediate that subsequently decomposed to yield OH. This experiment was repeated with the Leeds ground-based FAGE instrument. In contrast to the results of Novelli *et al*., no OH interference was observed following the reaction of O_3 and TME (L. Whalley, personal communication), suggesting that the interference differs between FAGE instruments. A non-photolytic interference was observed when ozone and isoprene were added to the FAGE cell, but at ambient concentrations of ozone (15 ppbv) and isoprene (300 pptv) the expected interference is equal to an OH concentration of 7×10^4 molecule cm^{-3}, and is therefore unlikely to cause a problem for FAGE measurements under ambient conditions.

A recent comparison of LIF and DOAS measurements in the SAPHIR chamber found no evidence for interference in LIF measurements of OH in the presence of isoprene, methacrolein, or a variety of aromatic compounds (Fuchs *et al.*, 2012). LIF measurements were 30–40 % higher than DOAS measurements when MVK and toluene had been added to the chamber, though the exact value of the discrepancy is uncertain, and the authors note that further studies are required to fully characterise the interference. The source of the interference therefore remains unclear, the magnitude of the interference is likely to differ between FAGE instruments, and the current understanding suggests that the interference will only be present in OH measurements in forested regions. During future field measurements, particularly in forest regions, periodic scavenger experiments following the method of Mao *et al*. will help to highlight any interference in OH and HO_2 measurements.

2.10 Conclusions

The aircraft FAGE instrument has been calibrated using the water vapour photolysis technique at a range of water vapour concentrations. The experimentally-determined and theoretical dependence of C_{OH} and C_{HO2} on water vapour concentration were found to be the same within their combined errors, though large uncertainty is associated with the HO_2 slope. These experimental results compare favourably with those of Commane (2009). The range of ambient water vapour concentrations encountered during RONOCO and SeptEx exceeded the range that can reliably be generated during a calibration, so a theoretical water quenching correction factor was applied to the RONOCO and SeptEx sensitivities, giving C_{OH} = 2.9–4.3 × 10^{-8} count s^{-1} mW^{-1} $molecule^{-1}$ cm^3, and C_{HO2} = 9.5–12.0 × 10^{-8} count s^{-1} mW^{-1} $molecule^{-1}$ cm^3. The effect of detection cell pressure on sensitivity has been determined by Commane using different-sized pinholes to mimic a change in external pressure. Neither C_{OH} nor C_{HO2} were found to change significantly between cell pressures of 1.6 Torr and 2.7 Torr, in agreement with theory. These results are supported by the work of Winiberg *et al.* (2013) in which the sensitivity of the aircraft instrument to HO_2 was determined at a range of pressures inside the atmospheric simulation chamber HIRAC.

Measurements of ambient [OH] and [HO_2] remain important to advancing our understanding of tropospheric oxidation chemistry on local, regional, and global scales. FAGE is the most widely-used technique for detection of OH and HO_2, having good sensitivity, good spatial and temporal resolution, and sufficiently low detection limits to enable detection of HO_x radicals at low atmospheric concentrations, and being suitable for use on a variety of measurement platforms. Several recent studies have investigated chemical interferences in both OH and HO_2 measurements by FAGE (Fuchs *et al.*, 2011, Fuchs *et al.*, 2012, Mao *et al.*, 2012, Whalley *et al.*, 2013). Progress has been made in quantifying the effect of RO_2-based interference in HO_2 measurements, with three of the Leeds FAGE instruments having been characterised in this respect. Ethene-derived peroxy radicals were found to cause an interference of ~ 40 % in measurements of HO_2 using the aircraft FAGE instrument. A model using the MCM chemistry scheme was used to predict interference factors from a wide range of peroxy radicals, and the results were used to assess the magnitude of the interference in the measurements of OH

and HO_2 during the RONOCO and SeptEx projects. The interference was found to be small, with $[HO_2]^* = 1.15[HO_2]_{mod} + 2\times10^5$.

Chapter 3. IO instrumentation

IO was first detected in the atmosphere at Mace Head by Alicke *et al*. (1999) using Long-Path Differential Optical Absorption Spectroscopy (LP-DOAS), which gives the average concentration of a trace gas along a light path of several kilometres. Long-path DOAS and multi-axis DOAS are the most widely used techniques for measurements of IO in the field. Measurements of IO from satellites using the DOAS technique provide a picture of the global distribution, but require validation by *in situ* measurements from ground-based, ship-based and airborne measurement platforms. The spatial averaging inherent to the LP-DOAS and MAX-DOAS (Multi-Axis DOAS) techniques means that features with narrow temporal and spatial scales, which are common in radical distributions, are often disguised in the measurements. Four 'point' or *in situ* techniques are currently in use for the measurement of IO. These are cavity ring down spectroscopy (CRDS, not commonly used in field measurements), cavity-enhanced DOAS spectroscopy (CE-DOAS), laser-induced fluorescence (LIF), and frequency comb based or mode-locked cavity enhanced absorption spectroscopy (ML-CEAS). Details of these methods are summarised in Table 3.1. Summaries of field measurements of IO in open ocean environments can be found in Table 1.3.

This chapter describes a compact, portable LIF instrument for the measurement of IO, developed at the University of Leeds and employed during the SHIVA campaign. A brief review of IO measurement techniques is given prior to the description of the Leeds instrument as it was deployed during the SHIVA project. Details of the calibration procedure and results, instrument bias, and potential interferences are given.

Table 3.1. Summary of techniques for field measurements of IO.

Method	Details	Typical limit of detection	Selected References
Differential Optical Absorption Spectroscopy (DOAS), including LP-DOAS, MAX-DOAS, CE-DOAS, satellite DOAS	Optical absorption spectroscopy using active (lamps, lasers) and passive (scattered sunlight) light sources. Multiple species detected and quantified in a single spectrum. Spatially averaged data. Remote sensing.	LP-DOAS: 0.2–2.0 pptv MAX-DOAS: 0.1–0.5 pptv CE-DOAS: 0.7–0.9 pptv Satellite DOAS: 1.4–3.3 pptv assuming 1 km mixing height	Allan *et al.* (2000), Plane and Saiz-Lopez (2006), Schönhardt *et al.* (2008), Mahajan *et al.* (2010), Thalman and Volkamer (2010), Dix *et al.* (2013), Gómez Martín *et al.* (2013), Großmann *et al.* (2013)
Cavity Ring-Down Spectroscopy (CRDS)	Absorption spectroscopy enhanced by multiple reflections of light in a highly-reflecting optical cavity. Closed-path and open-path configurations. Multiple species detectable in a single spectrum. *In situ*, point measurements.	10 pptv for a 30 second average	Wada *et al.* (2007)
Mode-locked or frequency comb based spectroscopy (ML-CEAS)	Cavity-based absorption spectroscopy enhanced by matching mode-locked laser modes to cavity modes. Simultaneous measurement of BrO + HCHO or IO + NO_2. Species deconvoluted by linear fitting of reference spectra to measured spectra.	0.04 pptv for a 5 minute average	Gherman and Romanini (2002), Grilli *et al.* (2012), Grilli *et al.* (2013)
Laser-induced fluorescence spectroscopy (LIF)	Excitation of IO using laser light at $\lambda \sim 445$ nm followed by detection of resulting fluorescence at $\lambda \sim 521$ nm. *In situ*, point measurements of a single species.	0.4 pptv (for 150 second average) – 1.25 pptv (for 60 second average)	Whalley *et al.* (2007), Furneaux *et al.* (2010), Gravestock *et al.* (2010), Commane *et al.* (2011)

3.1 Differential Optical Absorption Spectroscopy

Light passing through an air mass containing optically absorbing gas-phase species will be transmitted with an intensity that is proportional to the concentration of the species as follows (Plane and Saiz-Lopez, 2006):

$$I(\lambda) = I_0(\lambda)\exp\left(-l\left(\sum_{i=1}^{n}\sigma_i(\lambda)\overline{c_i}\right)\right) \tag{3.1}$$

$$or \quad \overline{c_i} = \frac{\ln\left(I_0(\lambda)/I(\lambda)\right)}{\sigma_i(\lambda)l} \tag{3.2}$$

where $\overline{c_i}$ is the average concentration of species i over the light path of length l, $I_0(\lambda)$, and $I(\lambda)$ are the intensities of light transmitted by an air mass without and with the absorbing species, respectively, and $\sigma_i(\lambda)$ is the absorption cross section of the absorbing species. With the exception of the path length, each of the above parameters is wavelength-dependent. The term $\ln\left(I_0(\lambda)/I(\lambda)\right)$ is the optical density, $\mathrm{OD}(\lambda)$, which is the sum of the optical densities of all contributing absorbers, at wavelength λ (Plane and Saiz-Lopez, 2006). Equation (3.2) is the Beer-Lambert law, and is the basis for optical absorption spectroscopy.

Making a measurement of $I_0(\lambda)$ in the real atmosphere is often impossible, due to the ubiquitous presence of absorbing trace gases and scattering particles and molecules. Therefore, measurements are made by making use of 'differential' parts of the absorption spectrum, i.e. narrow absorption features (wavelength range < 10 nm) that provide a unique fingerprint for each species of interest (Plane and Saiz-Lopez, 2006). The absorption cross section of a molecule, $\sigma_i(\lambda)$, is considered to be the sum of the differential absorption cross-section, $\sigma_i'(\lambda)$, which varies rapidly with wavelength, and a component $\sigma_i^s(\lambda)$ which varies slowly with wavelength:

$$\sigma_i(\lambda) = \sigma_i'(\lambda) + \sigma_i^s(\lambda) \tag{3.3}$$

In addition to absorption by gas-phase species, light is also attenuated by Mie scattering (elastic scattering by aerosols) and Rayleigh scattering (elastic scattering by air molecules), which contribute to broadband fluctuations in the atmospheric absorption spectrum. Equation (3.3) is substituted into equation (2.1), and the effects of Rayleigh and Mie scattering, $\varepsilon_{\mathrm{R}}(\lambda)$ and $\varepsilon_{\mathrm{M}}(\lambda)$, and broadband instrumental effects, $F_{ins}(\lambda)$, are taken into account to give:

$$I(\lambda) = I_0(\lambda)\exp\left[-l\left(\sum_{i=1}^{n}\sigma_i'(\lambda)\overline{c_i}\right)\right]\times\exp\left[-l\left(\sum_{i=1}^{n}\sigma_i^s(\lambda)\overline{c_i}+\varepsilon_{\mathrm{R}}(\lambda)+\varepsilon_{\mathrm{M}}(\lambda)\right)\right]F_{ins}(\lambda) \tag{3.4}$$

The first exponential term describes the effect of differential absorption features, and the second exponential term describes the combined broadband effects of slowly varying absorption, Rayleigh and Mie scattering, and instrumental effects. The intensity in the absence of differential absorption, $I_0'(\lambda)$, can therefore be defined as (Platt, 1999):

$$I_0'(\lambda) = I_0(\lambda)\exp\left[-l\left(\sum_{i=1}^{n}\sigma_i^s(\lambda)\overline{c_i}+\varepsilon_{\mathrm{R}}(\lambda)+\varepsilon_{\mathrm{M}}(\lambda)\right)\right]F_{ins}(\lambda) \tag{3.5}$$

$I_0'(\lambda)$ and $\sigma_i'(\lambda)$ are substituted for $I_0(\lambda)$ and $\sigma_i(\lambda)$ in equation (2.1), and the differential optical density, $\mathrm{OD}'(\lambda)$, is then given by:

$$\mathrm{OD}'(\lambda) = \ln\left(\frac{I_0'(\lambda)}{I(\lambda)}\right) = l\sum_{i=1}^{n}\sigma_i'(\lambda)\overline{c_i} \tag{3.6}$$

Absorption cross-sections, $\sigma_i(\lambda)$, are either taken from the literature and degraded to match the resolution of the DOAS spectrometer, or are measured directly with the DOAS instrument so that instrumental effects are automatically accounted for.

The light source for DOAS measurements can be artificial, such as a laser or xenon lamp, or extra-terrestrial (primarily sunlight). Techniques using artificial light sources include long-path DOAS, cavity ring-down spectroscopy, and cavity-enhanced DOAS. These are known as active DOAS techniques. Methods using direct or scattered sunlight

include multi-axis DOAS and satellite-based DOAS. These are known as passive techniques. Uncertainties in DOAS measurements are determined by the size and structure of differential absorption cross-sections, the number of absorbers, the optical path length, and the intensity of light transmitted through the atmosphere (Plane and Saiz-Lopez, 2006).

3.1.1 Long-Path DOAS

An LP-DOAS instrument uses a collimated beam of light from a broadband light source (high pressure Xe lamp, incandescent lamp, or dye laser), a telescope coupled to a spectrometer, comprising a grating and a detector to record the dispersed spectrum. The light source and detector are co-located, and the light is folded using a reflector at some distance to the light source, so that the total light path length (usually between 8 and 14 km) is twice the distance between the spectrometer and the reflector. Optical components within the instrument enable measurement of the unattenuated lamp spectrum, and of scattered ambient light spectra. During ambient measurements, three different spectra are taken: an atmospheric plus scattered light spectrum (*A*), a scattered light spectrum (*S*), and a lamp plus atmospheric plus scattered light spectrum (*L*). A 'processed' spectrum, I_{pr}, is calculated as follows (Plane and Saiz-Lopez, 2006):

$$I_{\mathrm{pr}} = \frac{A - S}{L - A} \tag{3.7}$$

Dividing the atmospheric spectrum by the unattenuated lamp spectrum reduces the effect of strong features in the lamp output and instrumental effects that would otherwise dominate the measured spectrum (Allan *et al.*, 2000). I_{pr} is then converted into a differential optical density spectrum, $\mathrm{OD}'(\lambda)$. This is achieved either by using a polynomial function to describe the broadband elements of the recorded spectrum, or by Fourier transforms using a combination of low-pass and high-pass filters. Both methods have the effect of deconvoluting the broadband features, $I_0'(\lambda)$, from the differential features (Plane and Saiz-Lopez, 2006). The differential optical density is then calculated as $\ln\left(I_0'(\lambda)/I_{\mathrm{pr}}\right)$, according to equation (3.6) (Plane and Nien, 1992). The method used to extract the differential and broadband features from the measured spectrum is then

used to calculate the differential absorption cross-sections, $\sigma_i'(\lambda)$, from reference absorption spectra in the relevant wavelength region. Analysis software performs least-squares fitting of the differential reference absorption spectra to obtain the concentrations of each absorbing species along the light path (see equation (3.6)). The minimum detectable concentration of a species is calculated from the root mean square of the residual spectrum (Plane and Saiz-Lopez, 2006), and is dependent on the differential absorption cross sections of absorbing species, the path length, the intensity of the signal, scattered sunlight, and the degree of overlapping between absorption spectra.

The majority of ground-based measurements of IO have been made by LP-DOAS (*e.g.* Peters *et al.*, 2005, Saiz-Lopez *et al.*, 2006, Seitz *et al.*, 2010). IO is commonly detected in a wavelength range around 430 nm (*e.g.* Seitz *et al.*, 2010). In coastal locations the spectrometer and reflector are often positioned so that the light path runs across the intertidal zone, in order to capture the high mixing ratios of IO produced by seaweed exposed at low tide (Peters *et al.*, 2005). Although the technique is sensitive and low detection limits are achieved (*e.g.* 0.2 pptv, see Table 3.1), the spatial averaging inherent to the technique means that small scale events, such as the 'hot spots' of IO observed at Mace Head, are disguised in the data (Furneaux *et al.*, 2010, Commane *et al.*, 2011).

3.1.2 Cavity Ring-Down Spectroscopy

Cavity ring-down spectroscopy is a sensitive technique for measuring concentrations of absorbing species on a much smaller spatial scale than long-path DOAS. Pulsed or continuous-wave laser light is injected into an optical cavity (typically ~ 1 m long) formed by two highly reflecting mirrors (Ball and Jones, 2003). Upon each reflection a fixed fraction of the pulse of light leaks out of the mirrors. As the intensity of light inside the cavity decreases, so too does the intensity transmitted. The rate of decay of the transmitted light is monitored by a photodiode or photomultiplier tube positioned at the opposite end of the cavity to the laser. In an empty cavity the time taken for the light to decay to 1/*e* of its original intensity (the ring-down time, τ_0) is given by:

$$\tau_0 = \frac{L}{c|\ln R|} \tag{3.8}$$

where L is the length of the cavity, c is the speed of light, and R is the reflectivity of the mirrors (Ball and Jones, 2003). The presence of absorbing species inside the cavity causes further absorption so that the decay remains exponential but occurs on a faster timescale (Brown, 2003). Measurement of the decay time in the absence and presence of an absorber yields its concentration through:

$$\alpha_i = \frac{R_L}{c}\left(\frac{1}{\tau} - \frac{1}{\tau_0}\right) \tag{3.9}$$

where α_i is the absorption coefficient for species i (equal to its absorption cross-section multiplied by its concentration), R_L is the ratio of the cavity length to the length in the cell over which the absorbing species is present, c is the speed of light, and $1/\tau$ and $1/\tau_0$ are the decay rate constants with and without the absorbing species in the cavity. For atmospheric measurements, τ_0 must account for losses including the mirror transmission and other optical losses, Rayleigh scattering, Mie scattering and absorption by species other than the target molecule. This is achieved by measuring τ_0 in a cavity purged with filtered ambient air.

The long effective path length (10 km or more (Ball and Jones, 2003)) achieved in CRDS results in high sensitivity. Good temporal and spatial resolution make it a useful technique for studying radical chemistry. CRDS is commonly used in laboratory applications, and few measurements of IO by CRDS have been made in the field. The first reported CRDS measurements of IO were made at Roscoff (Wada *et al.*, 2007). CRDS detection limits (~ 10 pptv) (Wada *et al.*, 2007) are determined by the stability of the ring-down time. Changes in aerosol scattering or trace gas concentrations between measurements of τ_0 increase the variability in the measurement, and therefore the limit of detection.

3.1.3 Cavity-Enhanced DOAS

Cavity-enhanced DOAS combines the high spatial resolution and sensitivity of a cavity instrument with the ability to detect a number of species in a single spectrum. Incoherent broadband radiation from an LED is introduced into a cavity formed by two highly-reflecting mirrors. The cavity may be enclosed by a tube or may be open to the atmosphere. The spectrum transmitted from the cavity is recorded by a dispersing element and detector. CE-DOAS has the advantage over other cavity techniques that the transmitted light intensity in the absence of absorbers does not need to be known explicitly (Thalman and Volkamer, 2010). Instead, background measurements, $I_0(\lambda)$, are made in the absence of the species of interest only, and the differential optical density is calculated as $\mathrm{OD}_i(\lambda) = \ln\left(I_0(\lambda)/I(\lambda)\right)$. Broadband and differential features in the measured optical density are separated with a high-pass filter or a polynomial function. The concentrations of absorbing species in the cavity are determined by the DOAS fitting routine. Since only the differential parts of the spectrum are considered, the effects of changes in mirror reflectivity or Mie scattering throughout the course of a measurement, which adversely affect other cavity methods, are eliminated in CE-DOAS measurements (Meinen *et al.*, 2010).

Unlike LP-DOAS, in which the path lengths is simply twice the distance between the light source and the reflector, the path length in cavity measurements is many times the length of the cavity, determined by the number of times the light is reflected by the mirrors. In the absence of any scattering or absorbing molecules in the cavity, the path length is determined entirely by the wavelength-dependent reflectivity of the mirrors, $R(\lambda)$, where light is reflected $1/1-R(\lambda)$ times on average (Platt *et al.*, 2009). In atmospheric measurements, the 'empty' cavity usually contains zero air, so that extinction from Rayleigh scattering also contributes to the average path length. The Rayleigh extinction of pure air is therefore included in an effective mirror reflectivity, $R_0(\lambda)$. Since the presence of even a weakly absorbing trace gas inside the cavity reduces the effective path length (the basis of cavity ring-down spectroscopy), this must be corrected for in the data analysis (Platt *et al.*, 2009). $R_0(\lambda)$, and therefore the average path length, can be determined in a number of ways, including by monitoring

the change in the background spectrum upon the introduction of gases with different Rayleigh cross-sections, such as helium and zero air (Washenfelder *et al.*, 2008).

Measurements of IO and NO_2 were made during the SHIVA campaign using an open-path CE-DOAS instrument in the wavelength range 425–460 nm. The empty cavity light path length was determined by fixing a helium-filled tube in position in the cavity, following the method of Washenfelder *et al*. (2008). Background spectra were recorded at night, when it was assumed that no IO was present (J. Lampel, personal communication). Detection limits for NO_2 and IO were 80 pptv and 0.9 pptv, respectively.

3.1.4 Multi-Axis DOAS

In passive DOAS techniques, the Beer-Lambert law is modified to account for the fact that the light source is outside Earth's atmosphere:

$$I(\lambda) = I_0(\lambda)\exp\left(-\sigma(\lambda)\mathrm{SCD}\right) \tag{3.10}$$

$$or \quad \mathrm{SCD} = \frac{\ln\left(I_0(\lambda) \big/ I(\lambda)\right)}{\sigma(\lambda)} \tag{3.11}$$

where SCD is the slant column density (molecule cm^{-2}) of an atmospheric species integrated along the path taken by solar photons through the atmosphere before reaching the detector (Plane and Saiz-Lopez, 2006). The total optical density, with contributions from *n* absorbing species, is equal to:

$$\mathrm{OD}(\lambda) = \ln\left(\frac{I_0(\lambda)}{I(\lambda)}\right) = \sum_{i=1}^{n}\sigma_i(\lambda)\ \mathrm{SCD}_i \tag{3.12}$$

Extinction by Rayleigh and Mie scattering is also taken into account, as for LP-DOAS measurements (see equations (3.4) to (3.6)). Where in LP-DOAS the measured spectrum is divided by the unattenuated lamp spectrum to remove strong features, in MAX-DOAS $I_0(\lambda)$ is usually taken to be the solar spectrum measured when the solar zenith angle is at a minimum, when the light has traversed the smallest path through the

atmosphere. This has the effect of removing strong solar spectrum features known as Fraunhofer lines. A polynomial function describing broadband spectral features, reference absorption spectra for known absorbing species in the relevant wavelength range, and a reference spectrum accounting for the filling-in of Fraunhofer lines (known as the Ring effect), are fitted to the measured optical density spectrum using a least-squares method. This yields differential slant column densities (DSCDs) (Hönninger and Platt, 2002).

More useful than slant column densities are vertical column densities (VCD) which give information on the total column of an absorbing species in the atmosphere. VCDs are calculated from SCDs using an air mass factor (AMF):

$$\mathrm{AMF} = \frac{\mathrm{SCD}}{\mathrm{VCD}} \tag{3.13}$$

The AMF depends on the radiative transfer through the atmosphere, and therefore on the profiles of trace gases, pressure, temperature, strong absorbers (*e.g.* ozone), aerosols, clouds, the solar zenith angle, the viewing angle, and the surface albedo (Hönninger *et al.*, 2004). Air mass factors are calculated using radiative transfer models, assuming single or multiple scattering, and are constrained to measurements of temperature, pressure and estimated vertical profiles of absorbing species (Hönninger and Platt, 2002).

In multi-axis DOAS measurements, a telescope directs scattered sunlight onto a spectrometer and detector, to record an atmospheric absorption spectrum. The telescope is mounted to enable several viewing angles. Light collected by the telescope with a zenith viewing angle has a relatively long path through the stratosphere, compared to light collected at low viewing angles. In addition, low solar zenith angles also increase the path length through the lowest layers of the atmosphere, so that measurements made in early morning or late evening with a low viewing angle have high sensitivity to absorbing species in the boundary layer (Plane and Saiz-Lopez, 2006). Measurements at different elevation angles are therefore sensitive to absorbers in different vertical layers of the atmosphere, so a series of measurements at different elevation angles can give the vertical profile of a gas and the concentration as a function of altitude (Hönninger and

Platt, 2002, Hönninger *et al.*, 2004). In a technique known as optimal estimation, measured slant column densities of the target species and the oxygen dimer (O_4), at several elevation angles, are compared with slant column densities predicted by a radiative transfer model. A statistical model, using an initial guess of the vertical profiles as a constraint, is used to find the actual profile from the best fit of the model data to the measurements (Frieß *et al.*, 2011, Großmann *et al.*, 2013).

MAX-DOAS instruments are suitable for ground-based, aircraft-based and ship-based measurements (*e.g.* Hönninger and Platt, 2002, Volkamer *et al.*, 2010, Dix *et al.*, 2013, Gómez Martín *et al.*, 2013, Großmann *et al.*, 2013). The University of Bremen MAX-DOAS instrument was installed on the RV *Sonne* during SHIVA for the measurement of IO. The measurements have good temporal resolution (~15 minutes) and low limits of detection (0.5–0.7 pptv). A comparison of IO measurements by LIF and MAX-DOAS during SHIVA is given in Chapter 5.

3.1.5 Satellite-based DOAS

The Scanning Imaging Absorption Spectrometer for Atmospheric Chartography (SCIAMACHY), onboard the European Space Agency's Envisat satellite, measures the continuous spectrum from direct, scattered and reflected sunlight, in the range 240–1700 nm. The DOAS retrieval technique is used to determine the atmospheric abundances of absorbing species. For the retrieval of IO from nadir viewing geometries, the $I_0(\lambda)$ background spectrum is measured over the equator where the IO column is expected to be small. A polynomial function describes broadband absorption and scattering features in the wavelength range 416–430 nm, and reference absorption spectra of IO, NO_2, O_4, O_3, H_2O and the Ring effect are fitted to the resulting differential optical density spectrum to yield differential slant column densities (Saiz-Lopez *et al.*, 2007, Schönhardt *et al.*, 2012).

The slant columns are converted to vertical column abundances using air mass factors that take into account the expected vertical distribution of the chemical species within the atmosphere, as well as the effect of viewing geometry of the instrument, the solar zenith angle (SZA), and the surface albedo. The presence of clouds and aerosols in the

atmosphere can distort the resulting vertical column abundances because reflection from a layer of aerosols will increase the sensitivity of the spectrometer in the atmosphere above the aerosol layer, and decrease the sensitivity below the aerosol layer. The same is true for the presence of clouds. These factors contribute significantly to uncertainties in satellite measurements (Palmer *et al.*, 2001). Retrieval of mixing ratios from vertical column densities is difficult, and relies upon an estimated vertical profile of the trace gas (Saiz-Lopez *et al.*, 2007). Most retrievals assume that IO is restricted to a shallow layer near the surface, but recent measurements of 0.1 pptv of IO in the free troposphere (Dix *et al.*, 2013) indicate that this assumption may be invalid.

Saiz-Lopez *et al*. (2007) reported the first measurements of IO from space, using the SCIAMACHY instrument. IO was found to be enhanced over Antarctic sea ice and around the ice shelf. Assuming that IO was contained and well-mixed within the lowest 1 km of the atmosphere, the authors reported mixing ratios in excess of 12 pptv, in agreement with *in situ* ground-based measurements made during Antarctic springtime. The assumed boundary layer height of 1 km is a source of uncertainty in these measurements, along with no reliable separation of clouds and snow when viewed from the satellite (Schönhardt *et al.*, 2008). The detection limit of the satellite instrument is partly determined by the signal-to-noise ratio of the measured spectrum. The number of photons reflected into the detector, and therefore the signal strength, depends to an extent on the surface reflectivity, so that measurements over oceans, which have low surface reflectivity, have higher limits of detection than measurements over snow- and ice-covered regions. Retrieval of slant columns close to the limit of detection are sensitive to the fit settings used to determine species concentrations from the measured spectrum. Measurements over oceans should therefore be treated with caution (Schönhardt *et al.*, 2008). Discrepancies between satellite measurements of IO (limit of detection = 1.4–3.3 pptv assuming 1 km mixing height) and ground-based measurements of IO (limit of detection = 0.9 pptv) (*e.g.* Gómez Martín *et al.*, 2013) have highlighted the importance of evaluating remote and spatially-averaged measurements alongside *in situ* measurements.

3.2 Frequency comb based spectroscopy

Grilli *et al.* (2012) have recently described the development and deployment of a portable, compact IO cavity-based instrument based on mode-locked cavity enhanced absorption spectroscopy (ML-CEAS). Mode-locked lasers, in which the phase of each longitudinal mode of the laser cavity is fixed relative to the other modes, produce extremely short pulses of light on the order of picoseconds or femtoseconds. The time delay between the pulses is equal to the time taken for light to make one round trip of the cavity, T, and corresponds to the frequency spacing, $\Delta\nu$, between the different modes. $\Delta\nu$ is given by:

$$\Delta\nu = \frac{c}{2L} \tag{3.14}$$

where c is the speed of light and L is the length of the cavity. The term 'frequency comb' describes the appearance of the emission spectrum of the laser, being a series of equally-spaced pulses with a frequency separation (free spectral range, FSR) equal to $\Delta\nu$ (Gherman and Romanini, 2002).

The resonant frequencies of an optical cavity can also be described as a frequency comb, with equal spacing between the frequencies supported by the cavity. The presence of an absorbing species inside the cavity will cause resonating light to be absorbed at particular frequencies. The light will interact with the absorber, before being emitted from the cavity, on a timescale, t, on the order of

$$t = \frac{\ell}{c} \tag{3.15}$$

$$\text{where } \ell = \frac{L}{1-R} \tag{3.16}$$

where c is the speed of light and R is the reflectivity of the cavity mirrors. On each pass of the light through the cavity, the peak transmission of a cavity mode will decrease according to:

$$\alpha(\nu)\ell \times \frac{2F}{\pi} \tag{3.17}$$

where $\alpha(\nu)$ is the frequency-dependent absorption coefficient of the gas and F is the cavity finesse, given by the ratio of the cavity free spectral range (FSR) and the full-width half maximum (FWHM) bandwidth of its resonances (for $R > 0.5$):

$$F = \frac{\Delta\nu}{\delta\nu} \approx \frac{\pi\sqrt{R}}{1-R} \tag{3.18}$$

Since the light traverses the cavity many times, even weak absorptions can be used to sensitively detect and quantify trace gas species, and the higher the cavity finesse, the greater the sensitivity. This is the principle behind cavity-enhanced absorption spectroscopy. A broadband light source, having traversed the cavity, will produce a spectrum containing the absorption lines of the absorbing gas, with the intensity of the lines enhanced by $\frac{F}{\pi}$. The intensity of the broadband light, regardless of absorbing species, decreases with $\frac{1}{F}$ due to the finite reflectivity of the mirrors. Further to this, the poor spatial coherence and lack of mode structure of a broadband light source means that only a small fraction of the incident light is transmitted through the cavity, giving a weak signal. Broadband pulsed lasers overcome this problem to an extent through good spatial coherence, but structure in the laser spectrum introduces noise into the measurement. The smooth spectral envelope of a mode-locked laser provides a good background on which to observe absorption lines, and high transmission efficiency can be gained when the laser modes coincide with the cavity modes. This is achieved when the cavity FSR is an integer number, *N*, times the laser repetition rate. Under these conditions, one in *N* laser modes will be transmitted by the cavity (Gherman and Romanini, 2002).

The frequency comb based IO instrument relies upon alternate injection of femtosecond laser radiation at λ = 338 nm and λ = 436 nm into two 94 cm long, parallel, high-finesse cavities for the measurement of BrO + HCHO, and IO + NO_2, respectively. The length of the cavity is finely adjusted so that its free spectral range is equal to twice the laser repetition rate. A feedback system ensures that the cavity length is correctly adjusted to account for laser jitter and mechanical instabilities that would otherwise disrupt the matching of the laser and cavity modes. The cavity mirrors have reflectivities of

99.953 % and 99.993 % at 338 nm and 436 nm, respectively, giving a 10 km optical path length at λ = 436 nm. Light exiting the cavity is directed onto a spectrograph (~ 5 pm resolution), comprising a dispersion grating and a CCD (charge coupled detector) camera to record the transmitted spectrum. A diaphragm pump maintains a flow of 800 sccm through the cavity. The cavity samples ambient air or filtered air, free of IO, BrO, NO_2 and HCHO, enabling measurement of the background spectra and cavity ring-down parameters that are required for calibration.

The frequency-dependent absorption coefficient, $\alpha(\nu)$, is given by:

$$\alpha(\nu) = \left(\frac{I_0(\nu)}{I(\nu)} - 1 \right) \frac{1}{\tau_0 c} \tag{3.19}$$

where $I_0(\nu)$ and $I(\nu)$ are the intensities of transmitted laser light at frequency ν with and without absorbing species in the cavity, and τ_0 is the ring-down time of the empty cavity. Spectral data, $\alpha(\nu)$, are analysed by fitting reference spectra of BrO and HCHO, or IO and NO_2, to the measured spectrum:

$$\alpha(\nu) = \sum_i \alpha_i(\nu) \cdot c_i + p(\nu) \tag{3.20}$$

where $\alpha_i(\nu)$ and c_i are the reference spectra and concentrations of the measured species i (BrO and HCHO, or IO and NO_2), and $p(\nu)$ is a polynomial function accounting for broad absorption features and any changes in the laser spectrum between the measurement of $I_0(\nu)$ and $I(\nu)$. The reference spectra are measured using the ML-CEAS instrument so that instrumental effects, such as the wavelength sensitivity of the spectrometer, are taken into account. The instrumental limit of detection for IO, determined by the minimum detectable change in output intensity and the number of spectral elements in the wavelength region used in the fitting, is 20 ppqv (parts per quadrillion by volume) for a 5 minute integration time.

The instrument was deployed at Roscoff (Grilli *et al.*, 2012), where IO mixing ratios up to 2 pptv were observed. This is significantly lower than IO mixing ratios observed

previously at this site, by LIF (up to 30 pptv) and LP-DOAS (up to 10 pptv) (Mahajan *et al.*, 2009, Furneaux *et al.*, 2010). An anti-correlation between IO and NO_2 was observed, in agreement with the results of Furneaux *et al*. (2010) and Mahajan *et al.* (2009), though the NO_2 mixing ratios reported by Grilli *et al*. do not appear to be high enough to account for the relatively low levels of IO measured. Measurements in East Antarctica (Grilli *et al.*, 2013) revealed very low IO mixing ratios, from below the detection limit (0.04 pptv) to 0.15 pptv. These levels are an order of magnitude lower than those observed in West Antarctica, where high mixing ratios of halogen oxides are thought to originate from sea ice emissions. The instrument provides excellent sensitivity, low detection limit, and high temporal resolution, and has the potential to be extended to measurements of other atmospheric species such as OIO and OClO (Grilli *et al.*, 2012). A comparison study of simultaneous IO measurements made by the frequency comb instrument and the established LIF and DOAS instruments would be very useful.

3.3 Laser-Induced Fluorescence spectroscopy

Sensitive and selective laser-induced fluorescence spectroscopy requires a molecule to have strong absorption at accessible laser wavelengths, good fluorescence quantum yield, and extensive rotational structure. The transition from the ground state, $X^2\Pi_{3/2}\ (v''=0)$, to the lowest electronically excited state, $A^2\Pi_{3/2}\ (v'=2)$, of IO exhibits these properties, and is therefore ideal for the measurement of IO by LIF (Gravestock *et al.*, 2010). However the $A^2\Pi_{3/2}$ state is highly predissociative (Bekooy *et al.*, 1983, Newman *et al.*, 1998) and has a lifetime of less than 1 ns (Newman *et al.*, 1998), so that temporal gating cannot be used to separate the laser scattered light and the laser-induced fluorescence, as is the case for HO_x. Rather, an optical filter is used to separate the red-shifted fluorescence from the laser scattered light. Fluorescence from $A^2\Pi_{3/2}$ $(v'=0,\ 1,\ 2)$ occurs to many vibrational levels ($v''=0$ to $v''=12$) in the ground state (Gravestock *et al.*, 2010), with strong fluorescence at λ = 521 nm from the (2,5) band being sufficiently red-shifted from the laser wavelength to ensure effective discrimination (Whalley *et al.*, 2007). The fluorescence cell optics and photon collection system in the Leeds IO instrument are therefore optimised to select this wavelength.

The excitation and fluorescence scheme used in LIF measurements of IO is shown in Figure 3.1.

The IO LIF instrument used during this work was adapted from the aircraft HO_x instrument, and followed the design of the container-based instrument developed by Gravestock *et al*. (2010) and described in detail in Whalley *et al*. (2007). The instrument has previously been deployed for ground-based measurements at Mace Head (Commane *et al.*, 2011) and for ship-based measurements onboard the RRS *Discovery* during the RHaMBLe (Reactive Halogens in the Marine Boundary Layer) project (Lee *et al.*, 2010). Previously installed in two aircraft racks, the instrument was built into a single rack for use onboard the RV *Sonne* during the SHIVA project, where the instrument was installed in a 10 ft × 8 ft specially prepared shipping container on the front deck of the ship (see Figure 3.2), along with two German Aerospace Center (Deutsches Zentrum für Luft- und Raumfahrt e.V., DLR) CIMS instruments. No difficulties were caused by reducing the footprint of the instrument, and installation on the front deck ensured the best chance of sampling air that was not influenced by the ship's stack. The inlet and fluorescence cell assembly were positioned in the container roof as described in Chapter 5, and the pump was located in a deck store approximately 10 m from the instrument rack. The pressure in the cell was not affected by the long pumping line that resulted from this arrangement.

3.3.1 Laser system

The laser system described in Chapter 2 for FAGE measurements of HO_x is used in the IO LIF instrument. Light at λ = 532 nm from the frequency-doubled Nd:YAG laser pumps the Ti:Sapphire cavity, which is tuned to produce 1.5 W of light at λ = 890 nm. The IR light is passed through a lithium borate (LBO) doubling crystal to produce up to 100 mW of blue light at λ ~ 445 nm with a pulse width of ~ 30 ns and a linewidth of ~ 0.043 cm^{-1}. The laser wavelength is tuned by changing the angle of the grating in the Ti:Sapphire cavity with a computer-controlled stepper motor, as described in Chapter 2 for the HO_x instrument. A turning mirror directs the blue light towards a single dielectric coated beam splitting plate.

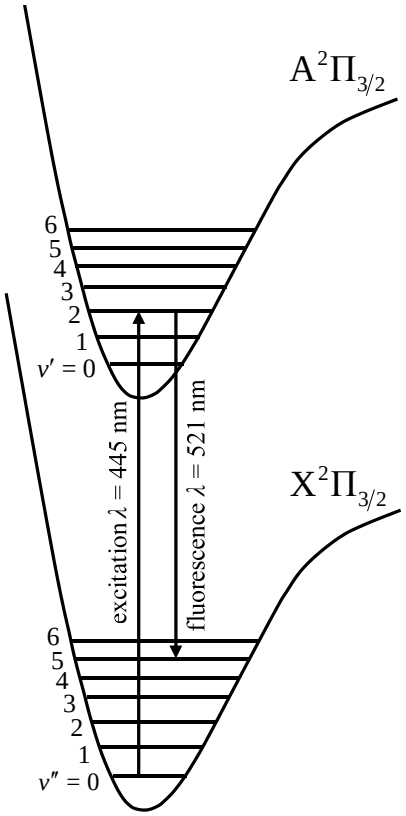

Figure 3.1. IO excitation and fluorescence scheme for the $A^2\Pi_{3/2} \leftarrow X^2\Pi_{3/2}$ transition. Vibrational levels higher than $v = 6$ have been excluded for clarity. Arrows indicate excitation from $v'' = 0$ to $v' = 2$ at λ = 445 nm, and fluorescence from $v' = 2$ to $v'' = 5$ at λ = 520 nm. Fluorescence is known to occur to many vibrational levels of the ground state (Gravestock *et al.*, 2010). Redrawn from Furneaux (2009).

To enable measurement of the laser wavelength, a small amount of light leaks through the mirror onto the wavemeter probe (Coherent WaveMaster Wavelength Meter; resolution: ± 0.001 nm; accuracy: ± 0.005 nm). A fast photodiode (Thorlabs DET10A/M high-speed photodetector) is positioned to receive laser light reflected from the window of the wavemeter probe. The fast photodiode is connected to an oscilloscope (LeCroy, WaveRunner LT372), providing a means of monitoring the temporal positions of the laser pulse and the trigger. Of the light reflected by the turning mirror onto the beam splitter, approximately 96 % is directed onto a fibre launcher contained within the laser casing, from where it is delivered *via* a 4 m optical fibre (Oz Optics QMNJ-55-UVVis-200/240-3-4) to the fluorescence cell, with a transmission efficiency of 50–75 %. During the SHIVA fieldwork, the remaining 4 % of the blue light was directed through a hole in the laser casing to a photodiode (UDT Instruments UDT-555UV) used to monitor the laser power.

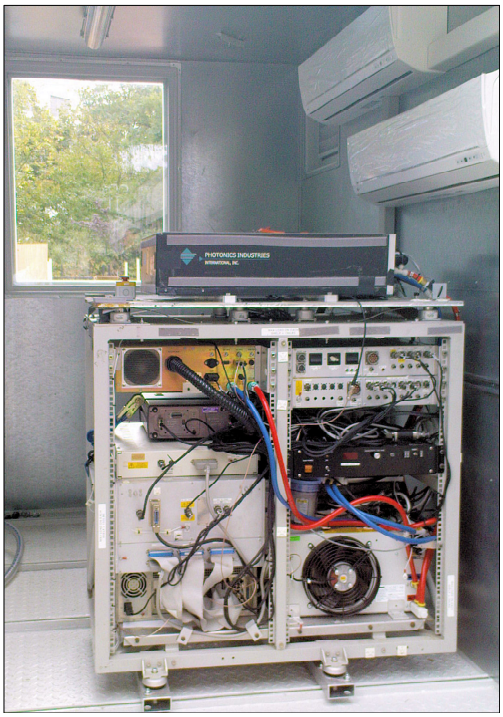

Figure 3.2. IO instrument rack installed in the 10 ft shipping container in preparation for SHIVA fieldwork. The laser is on top of the rack in the black casing.

3.3.2 Inlet

The inlet is similar to that for the HO_x instrument, consisting of a pinhole (0.8 mm diameter) in the centre of a conical nozzle, and a stainless steel inlet tube (45 mm internal diameter). For the SHIVA project, an extended stainless steel inlet was constructed to enable ambient air to be sampled from above the roof of the container, while the fluorescence cell remained inside the container (see Figure 3.3). The resulting distance between the pinhole and the centre of the fluorescence region was 600 mm, which is significantly longer than during previous fieldwork (Commane, 2009). To reduce loss of IO radicals on the inside of the extended inlet and to exclude solar scattered counts in the background signal, a black Nylon insert was fitted to the inside of the inlet, reducing the internal diameter to 35 mm. A rotary pump (Leybold TRIVAC-B rotary vane vacuum pump) maintains the pressure inside the cell at approximately 150 Torr, at which pressure the observed IO fluorescence signal shows a broad maximum, changing by less than 5 % between 100 and 200 Torr (Commane, 2009). Ambient air is drawn through the pinhole at a flow rate of 8.5 slm.

Figure 3.3. View of the 10 ft shipping container installed on the starboard side of the front deck of the RV *Sonne* during the SHIVA fieldwork, showing the DLR CIMS inlet and the LIF inlet.

3.3.3 Fluorescence cell

Laser light exiting from the optical fibre is collimated and focussed (fibre collimator, Oz Optics, HPUCO-25-308-M-25PQ) through a baffled input arm into the fluorescence region. Scattered laser light from the input arm, the fluorescence region, and the photodiode side arm, contribute to the background signal (solar scattered light is eliminated by the black Nylon insert in the inlet) and affect instrument sensitivity and limit of detection. Prior to the SHIVA fieldwork an extended baffled photodiode side arm was built to reduce reflection of laser light off the photodiode surface into the fluorescence region. The baffles inside the laser light input arm and the photodiode side arm were coated with a mixture of carbon black (Orion Engineered Carbons, Printex 35 amorphous carbon black, kindly provided by Muhammad Ali at the University of Leeds) and optically black paint (Alion Technology MH2200 Thermal Control Coating) following the method of Huisman *et al*. (2008) to reduce laser scattered light. The dye used in anodising the inside of the cell is known to fluoresce at λ = 525 nm following excitation at λ = 445 nm (Commane, 2009). The fluorescence produces a background signal that increases with laser power. To eliminate this problem and reduce the

instrumental limit of detection, an aluminium insert, coated with the optically black paint mixture, was fitted to the inside of the cell.

During the SHIVA fieldwork it was suspected that large variations in the laser power measurement were being caused in part by the location of the photodiode at the end of the baffled arm, while the laser power measured with an analogue power meter just outside the laser casing was stable. In addition, high background counts were recorded with the photodiode in this position. For these reasons, the photodiode was moved to measure laser power outside the laser casing. This reduced the magnitude of the variations in laser power sufficiently that the laser power measurement could be used to normalise the data (see section 2.4.5).

Photons are collected in a similar way to the HO_x instrument described in Chapter 2. Fluorescence is detected on an axis perpendicular to the laser beam and the air flow. Light from the fluorescence cell passes through a window with a broadband visible anti-reflection coating centred at $\lambda = 521$ nm, and through an interference filter centred at $\lambda = 521$ nm (Barr Associates, 2 nm fwhm, 52 % peak transmission). The light is focussed by two lenses (2 inch diameter, 52 mm focal length, broadband anti-reflection coating centred at $\lambda = 521$ nm) onto the photocathode of a yellow sensitive channel photomultiplier (CPM) (Perkin Elmer, C993 P). The photocathode of the CPM is not gated. The signal from the CPM is sent to a photon counting card (Becker & Hickl, MSA 300) in the data acquisition computer, which is triggered by a time-transistor logic (TTL) pulse from the delay generator. Photon counting begins 50 ns prior to the laser pulse.

3.3.4 Data acquisition and analysis

The short lifetime of IO fluorescence means that the LIF signal must be collected at the same time as the signal caused by scattered light from the laser pulse. Photons are collected in two time gates. The first (A) is 100 ns wide and is centred over the laser pulse, to collect the LIF signal, laser scattered light, and solar scattered light. The second gate (B) begins 50 μs after the laser pulse and the IO fluorescence have

subsided, and is 1000 ns long. Gate B collects solar scattered light and CPM dark counts. The IO fluorescence signal, $\text{Signal}_{\text{IO}}$, is calculated as follows:

$$\text{Signal}_{\text{IO}} = A - \frac{B}{x} \tag{3.21}$$

where x is the ratio of the width of gate B to the width of gate A (x = 1000/100). The elimination of solar scattered light from the fluorescence cell, and the low dark count rate of the photomultiplier tube mean that the value of B is typically zero.

Under normal operation (such as during the SHIVA fieldwork) the laser is tuned to the online wavelength (λ = 444.885 nm) for 60 seconds, and then to the offline wavelength (λ = 444.879 nm) for 60 seconds, giving 1 minute of 1 Hz online data ($\text{Signal}_{\text{on}}$) and 1 minute of 1 Hz offline data ($\text{Signal}_{\text{off}}$). The (2,0) band head of the IO spectrum is broad enough to enable the online and offline wavelengths to be selected by measurement with the wavemeter, rather than by measurement of signal from a reference cell. To account for any backlash in the gearing system of the stepper motor used to change the angle of incidence on the diffraction grating, the online and offline wavelengths are always approached from a shorter wavelength. Including the time taken for the tuning of the laser wavelength, the whole duty cycle lasts approximately 3 minutes. The laser power measured by the photodiode during the SHIVA project was very scattered, with large peaks and troughs that were not reproduced when the power was measured with an analogue power meter. The large variations in the measurements were therefore considered to be artefacts, and not to represent actual fluctuations in laser power. For this reason, the raw signal and the laser power were averaged over the 1 minute online and offline periods, and the mean online and offline signals, S_{on} and S_{off}, were normalised using the mean laser power P_{on} and P_{off}:

$$S_{\text{on}} = \frac{\overline{\text{Signal}_{\text{on}}}}{\overline{P_{\text{on}}}} \tag{3.22}$$

$$S_{\text{off}} = \frac{\overline{\text{Signal}_{\text{off}}}}{\overline{P_{\text{off}}}} \tag{3.23}$$

The difference between the normalised online and offline signals, Sig_{IO}, is then divided by the sensitivity of the instrument, C_{IO}, to give an IO mixing ratio in pptv:

$$Sig_{IO} = S_{on} - S_{off} \tag{3.24}$$

$$\text{IO / pptv} = \frac{Sig_{IO}}{C_{IO}} \tag{3.25}$$

The online and offline wavelengths were chosen by repeatedly scanning over the (2,0) band head of the IO spectrum. In previous work (Whalley *et al.*, 2007, Commane *et al.*, 2011), the online wavelength was at λ = 444.885 nm, and the offline wavelength was at λ = 444.882 nm. The IO absorption spectrum displays a sharp fall-off at wavelengths shorter than that of the band head as shown in Figure 3.4, so tuning the laser to slightly shorter wavelengths provides an ideal offline measurement. The exact choice for the online wavelength is more critical. The difference between the online wavelength chosen in previous work and in this work is attributed to the different wavemeters used to measure the laser wavelength, as noted by Commane (2009).

3.4 Calibration

Laser-induced fluorescence spectroscopy is not an absolute technique, and measurements of IO in ambient air require knowledge of the instrument's sensitivity. The IO instrument is calibrated in a similar way to the HO_x instrument, using the calibration wand to produce a known concentration of IO in a turbulent flow, which is sampled by the instrument. The technique is described below.

3.4.1 Calibration method

A flow of nitrous oxide (BOC, 98 % N_2O in N_2, medical grade) is mixed with an excess of trifluoromethane (CF_3I, Aldrich, 99 %) in a 45 slm flow of N_2 (BOC, oxygen-free nitrogen) and passed down the aluminium calibration tube (see section 2.5.1.1 in Chapter 2).

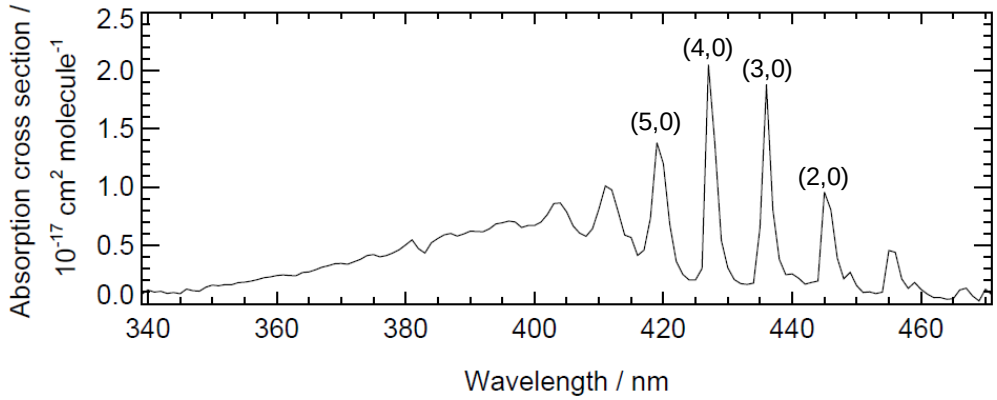

Figure 3.4. Absorption spectrum of IO between 340 nm and 471 nm at 298 K and 760 Torr, with vibrational bands from $v''=0$ to $v'=2$—5 labelled as (v',v'') (Coleman *et al.*, 1948, Cox and Coker, 1983, Sander *et al.*, 2011).

A mercury pen-ray lamp (Oriel Instruments Hg(Ar) Spectral Calibration Lamp, model number 6035) produces light at λ = 184.9 nm. The N_2O is photolysed to produce a known concentration of $O(^1D)$:

$$N_2O \xrightarrow{h\nu} N_2 + O(^1D) \qquad \text{(R2.7)}$$

Photolysis of CF_3I by light at λ = 184.9 nm is negligible, since the CF_3I absorption cross section at 185 nm is much smaller than that of N_2O (see Table 3.2). The lamp has a strong emission at λ = 253.7 nm (15 times stronger than the 184.9 nm line) (Reader and Corliss, 2013-2014), where CF_3I has a larger absorption cross section (see Table 3.2). CF_3I remains in excess of N_2O, so loss of CF_3I through photolysis does not perturb the concentration of IO generated. Loss of IO through reaction with the CF_3 produced in photolysis is considered to be negligible (Commane, 2009).

The photolysis product $O(^1D)$ can be quenched to $O(^3P)$ by N_2, and can react with N_2O:

$$O(^1D) + N_2 \xrightarrow{k_1} O(^3P) + N_2 \qquad \text{(R1.2)}$$

$$O(^1D) + N_2O \xrightarrow{k_2} N_2 + O_2 \qquad \text{(R2.11)}$$

$$O(^1D) + N_2O \xrightarrow{k_3} 2\,NO \qquad \text{(R2.12)}$$

Based on the value of the rate constant reported in the literature (Vranckx *et al.*, 2008) quenching of $O(^1D)$ by N_2O is negligible at atmospheric temperatures. The rate constants k_1 to k_3 are given in Table 3.2. The fraction of $O(^1D)$ quenched, Ω, is given by:

$$\Omega = \frac{k_1[N_2]}{k_1[N_2] + (k_2 + k_3)[N_2O]} \tag{3.26}$$

The $O(^3P)$ produced reacts with CF_3I to produce IO:

$$O(^3P) + CF_3I \xrightarrow{k_4} IO + CF_3 \tag{R3.1}$$

$$O(^3P) + CF_3I \xrightarrow{k_5} I + F + CF_2O \tag{R3.2}$$

The concentration of IO is then given by:

$$[IO] = [N_2O] \cdot \sigma_{N_2O} \cdot \phi_{IO} \cdot \Omega \cdot F \cdot t \tag{3.27}$$

where σ_{N_2O} is the absorption cross-section of N_2O at λ = 184.9 nm, ϕ_{IO} is the yield of IO from reaction (R3.1) (values given in Table 3.2), Ω is the fraction of $O(^1D)$ quenched to $O(^3P)$, F is the lamp flux determined by NO actinometry (see Chapter 2) and t is the irradiation time. IO concentrations in molecule cm^{-3} are converted to mixing ratios in pptv using the temperature and pressure recorded during the calibration.

During a calibration, the flows of N_2O, CF_3I and N_2 are kept constant, and the concentration of IO produced is varied by changing the lamp flux. For each setting of the lamp flux, one minute of online data and one minute of offline data are recorded. The data are analysed as described in section 2.4.5. Flow rates, temperature, pressure, and lamp current are recorded automatically every 5 seconds during the calibration. Mean values of signal and [IO] are calculated for each lamp flux setting. A straight line, weighted by the errors on the concentration of IO and the signal, is fitted to the averaged data. The sensitivity of the instrument is equal to the gradient of the line.

Table 3.2. Details of absorption cross sections, rate constants and yields relevant to calibration of the IO instrument.

Parameter	Value	References
σ_{CF_3I}, λ = 185 nm	7.5×10^{-21} cm^2 molecule^{-1}	Sander *et al.* (2011)
σ_{CF_3I}, λ = 254 nm	4.52×10^{-19} cm^2 molecule^{-1}	Sander *et al.* (2011)
σ_{N_2O}, λ = 185 nm	1.43×10^{-19} cm^2 molecule^{-1}	Sander *et al.* (2011)
k_1	$2.15 \times 10^{-11} e^{(110/T)}$	Sander *et al.* (2011)
k_2	$4.63 \times 10^{-11} e^{(20/T)}$	Sander *et al.* (2011)
k_3	$7.25 \times 10^{-11} e^{(20/T)}$	Sander *et al.* (2011)
ϕ_{IO}	0.83 ± 0.09	Gilles *et al.* (1996)

3.4.2 Calibration results

An example of a calibration plot, from September 2011, is shown in Figure 3.5. The sensitivity of the instrument, C_{IO}, given by the gradient of the line, is equal to $(4.46 \pm 0.27) \times 10^{-2}$ count s^{-1} mW^{-1} pptv^{-1}. The line has a non-zero intercept of -0.02 ± 0.17 count s^{-1} mW^{-1}, which is caused by random noise in the measurements, and is considered to be negligible since the signal recorded at 0 pptv is zero within error. Only the gradient is used in data analysis.

The instrument was also calibrated during the SHIVA fieldwork (November 2011), yielding a sensitivity of $(3.22 \pm 0.40) \times 10^{-2}$ count s^{-1} mW^{-1} pptv^{-1}. The reduction in sensitivity was due to increased radical losses on the extended inlet (see section 2.4.3). The sensitivity of the instrument during the SHIVA fieldwork was comparable to sensitivities reported by Commane *et al.* (2011) during ground-based measurements at Mace Head, when the distance between the pinhole and the fluorescence region was shorter (330 mm) than the distance imposed by the extended inlet used during SHIVA (600 mm).

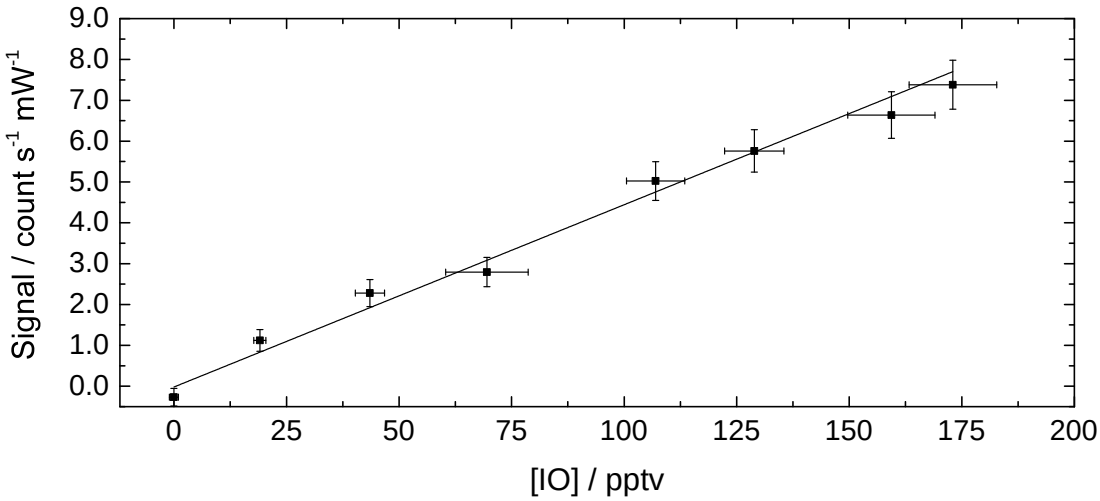

Figure 3.5. Results from calibration of the IO instrument in September 2011. Data points represent average values for one minute of online data. *x* and *y* error bars represent the total uncertainty (combined accuracy and precision) in the calculated IO mixing ratio and the normalised LIF signal, respectively. The instrument sensitivity or calibration factor, *C*, is given by the gradient, which for this calibration is equal to $(4.46 \pm 0.27) \times 10^{-2}$ count s^{-1} mW^{-1} $pptv^{-1}$. The intercept is equal to -0.02 ± 0.17 count s^{-1} mW^{-1}, and is considered to be negligible.

Calibrations in the laboratory (June 2012) following the SHIVA fieldwork yielded a sensitivity of $(1.89 \pm 0.15) \times 10^{-2}$ count s^{-1} mW^{-1} $pptv^{-1}$. The instrument was disassembled, the optics cleaned and the fluorescence cell checked for leaks prior to the laboratory calibration. The cause of the reduction in sensitivity between September 2011 and June 2012 is unknown, but may be due to deterioration of components (*e.g.* PMT sensitivity) in the intervening period. In previous work (Commane *et al.*, 2011) the sensitivity of the instrument was determined down to 2 pptv, and was found to be linear with IO mixing ratio at these low levels.

3.4.3 Calibration uncertainty

The final uncertainty in the instrument sensitivity is given by the standard error of regression on the gradient of the line, calculated by the fitting software (OriginPro 9). The fitting procedure is weighted by *x* and *y* errors. The *x* errors, σ_x, are the uncertainties in each average IO concentration produced by the wand, $\sigma_{[\mathrm{IO}]_{\mathrm{average}}}$, calculated as the sum in quadrature of the accuracy, a, and precision, p:

$$\sigma_x = \sigma_{[\mathrm{IO}]_{\mathrm{average}}} = \sqrt{a^2 + p^2} \tag{3.28}$$

The precision in IO is given by the standard deviation of the 5 second concentrations over each different lamp flux. The IO accuracy is calculated for each 5 second data point, determined from uncertainties in flow rates, temperature, pressure, rate constants, and lamp flux. The accuracies of the $[IO]_{average}$ values, *a*, are calculated as the standard error of the mean, *S.E.*, as follows:

$$a = S.E. = \frac{\sqrt{\sum \sigma_{IO}^2}}{N} \tag{3.29}$$

where σ_{IO}^2 are the squared uncertainties on each 5 second IO value contributing to the mean, and N is the number of 5 second data points. Table 3.3 gives details of the parameters contributing to the uncertainty in [IO].

The *y* errors, σ_y, are the uncertainties in the measured signal, $\sigma_{Sig_{IO}}$, calculated as the sum in quadrature of the uncertainties in the mean normalised online and offline signals:

$$\sigma_y = \sigma_{Sig_{IO}} = \sqrt{\sigma_{On}{}^2 + \sigma_{Off}{}^2} \tag{3.30}$$

The uncertainty in the mean normalised online signal, σ_{on}, is calculated as follows:

$$\sigma_{On} = S_{On}\sqrt{\left(\frac{\sigma_{Signal_{On}}}{\overline{Signal_{On}}}\right)^2 + \left(\frac{\sigma_{P_{On}}}{\overline{P_{On}}}\right)^2} \tag{3.31}$$

where $\sigma_{Signal_{on}}$ and $\sigma_{P_{on}}$ are the uncertainties in the mean online signal and mean online laser power, respectively, S_{On} is the mean normalised online signal, $\overline{Signal_{On}}$ is the mean unnormalised online signal, and $\overline{P_{On}}$ is the mean online laser power.

Table 3.3. Details of parameters contributing to the total uncertainty in the concentration of IO produced during a calibration. A range of values is given where the percentage uncertainty varies significantly over the range of values of the parameter. The values given are samples from a calibration, and can change slightly between calibrations. The final uncertainty on [IO] is for 5 second data, and is reduced to the when the data are averaged for each value of the lamp flux (see Figure 3.5).

Parameter	Uncertainty	Contributing factors
$[N_2O]$	1.9 %	Flow rates, temperature, pressure
σ_{N_2O}	< 1 %	
ϕ_{IO}	10.8 %	
Ω	14.1 %	Rate constants, flow rates, temperature, pressure
F	1.8–23.4 %	NO actinometry experiment
t	1.3 %	Flow rates, temperature
$[IO]$ (5 second data)	29.7 %	
$[IO]$ (average)	5.1–13.2 %	

$\sigma_{\text{Signal}_{On}}$ is calculated as the sum in quadrature of the standard deviation ($S.D.$) and the standard error ($S.E.$) of the mean online signal, as follows:

$$S.D. = \sqrt{\overline{\text{Signal}_{On}}} \tag{3.32}$$

$$\sigma_{\text{Signal}_{On}} = \sqrt{S.D.^2 + S.E.^2} \tag{3.33}$$

The uncertainty used to calculate the standard error on the raw signal is given by the reproducibility of finding the online wavelength using the wavemeter, as described in section 2.4.5. The uncertainty has been well characterised by Commane (2009), and is equal to ±18.5 % of the raw LIF signal. $\sigma_{P_{On}}$ is also calculated as the sum in quadrature of the standard deviation of the 1 second data and the standard error, where the uncertainty contributing to the standard error is defined by the photodiode calibration, and is approximately equal to 19 % of the 1 second laser power measurement. The

uncertainty in the mean normalised offline signal, σ_{on}, is calculated using the equations above for the offline data.

3.5 Instrument bias

The IO instrument is known to have a small negative bias, such that when measurements are made in air or nitrogen containing no IO, the derived concentrations are centred around a negative value rather than being centred around zero. This effect has been reported by Commane *et al.* (2009, 2011), with the bias having a value of −0.05 pptv when sampling nitrogen in the laboratory, and −0.49 pptv when sampling at night at Mace Head. Since the value of the bias appears to change depending on location and conditions, laboratory work following the SHIVA fieldwork aimed to determine the value under the current instrument conditions. The instrument sampled synthetic air (BOC, BTCA) or nitrogen (BOC, oxygen free nitrogen) during three days of experiments, totalling 939 minutes of data. No difference was observed whether the instrument was sampling air or nitrogen. The data were analysed as described in section 2.4.5, averaged to one minute and 15 minute time bases, and were plotted in frequency distribution histograms, shown in Figure 3.6 (one minute data) and Figure 3.7 (15 minute data). A Gaussian function was fitted to the histogram using an IDL fitting routine. The centre of the distribution gives the mean value, and the width gives the standard deviation, providing a measure of the negative bias and of the instrument precision, following the methods used by Schlosser *et al.* (2007).

The reason for the negative bias is unknown, but the effect is evident in both normalised and un-normalised data, and is manifested as the mean offline signal being larger than the mean online signal. Since the effect is present whether sampling nitrogen, synthetic air or ambient air, it is not caused by a trace gas absorber with a highly structured absorption cross section around the online and offline laser wavelengths. There is a change in laser power between the online and offline wavelengths, with the mean offline power being 0.45 mW higher on average than the mean online power. However, this does not explain the bias in the data, since the online and offline data are normalised with mean online and offline laser powers, respectively, to take this into account.

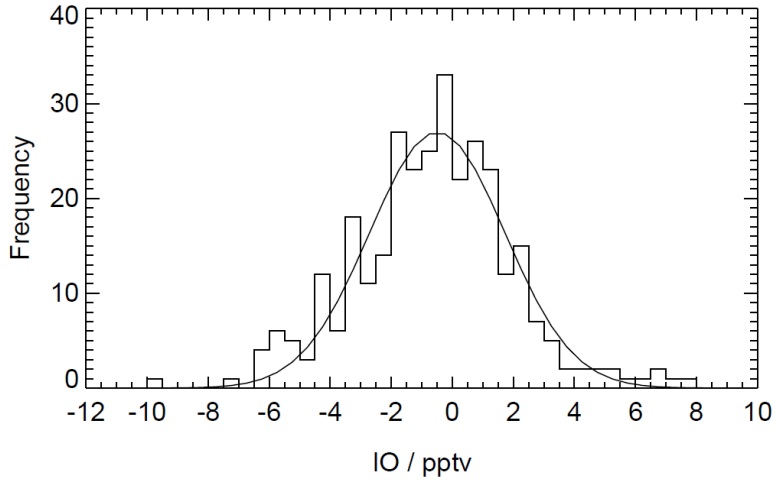

Figure 3.6. Frequency distribution of 1 minute averaged IO data from measurements of air and nitrogen in June 2012. The curve is a Gaussian fit to the histogram. Mean = −0.74 ± 0.11 pptv. 1σ (standard deviation) = 2.22 ± 0.11 pptv.

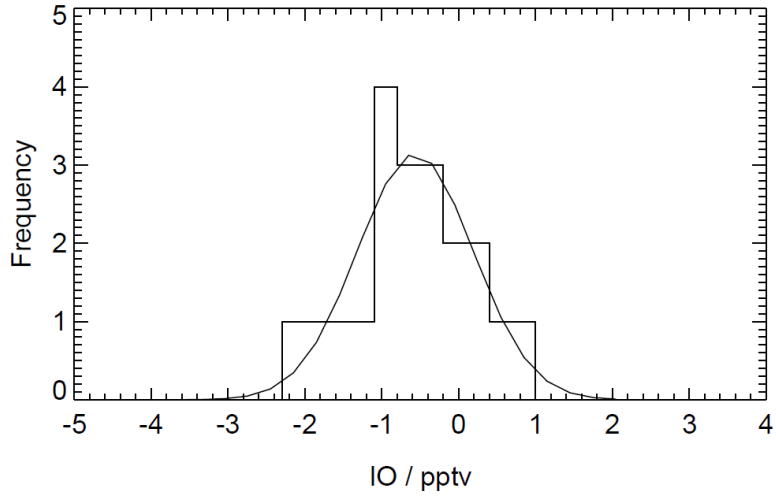

Figure 3.7. Frequency distribution of 15 minute averaged IO data from measurements of air and nitrogen in June 2012. The curve is a Gaussian fit to the histogram. Mean = −0.71 ± 0.07 pptv. 1σ (standard deviation) = 0.75 ± 0.07 pptv.

A smoother curve is achieved for the 1 minute data but the 15 minute data gives a better approximation of the precision of the SHIVA measurements, which were averaged to 15 minutes. The 1 minute and 15 minute distributions have similar mean values (−0.74 and −0.71 pptv, respectively), as expected, but the standard deviation is significantly reduced in the 15 minute distribution. Although the −0.71 pptv bias is within the precisional uncertainty of the measurements (0.75 pptv), it is significantly different

from zero ($p < 0.001$), and for this reason the 15 minute SHIVA data were adjusted to account for the negative bias by adding 0.7 pptv onto each 15 minute data point:

$$\text{IO / pptv} = \frac{Sig_{\text{IO}}}{C_{\text{IO}}} + 0.7 \tag{3.34}$$

Whilst this approach is justified, it adds uncertainty to reported field data where IO mixing ratios are close to the limit of detection. It was not possible to conduct zero measurements on the ship due to the large volumes of nitrogen or synthetic air required, but the value of the bias gained from the laboratory experiments is similar to the value of −0.59 pptv reported previously during fieldwork at Mace Head (Commane *et al.*, 2011) and is believed to be applicable to measurement conditions during the SHIVA fieldwork.

The final uncertainty on a measured IO mixing ratio is determined from the calibration uncertainty and the precision of the instrument. For data collected during the SHIVA project, the final uncertainty was given as the sum in quadrature of the calibration uncertainty (12.3 % of the measurement), and the precision (0.75 pptv). For an IO mixing ratio of 1.5 pptv the final uncertainty is ± 0.77 pptv or 51.5 %.

3.6 Instrumental limit of detection

The IO instrument limit of detection (LOD) is determined by the instrument's sensitivity and the standard deviation of the background signal as follows:

$$[\text{IO}]_{\text{min}} = \frac{\text{SNR}}{C_{\text{IO}} \times P_{\text{On}}} \sigma_{\text{Off}} \sqrt{\frac{1}{m} + \frac{1}{n}} \tag{3.35}$$

where $[\text{IO}]_{\text{min}}$ is the minimum detectable IO mixing ratio or concentration (the limit of detection), SNR is the signal-to-noise ratio above which IO can be detected (= 2 for a 95 % confidence interval), C_{IO} is the instrument sensitivity determined in a calibration, P_{On} is the mean online laser power over a given period, σ_{Off} is the standard deviation of the background (offline) signal, and m and n are the number of 1-second online and

offline points, respectively (60 and 60 for a 1 minute average). Since the photon counting signal can be described by a Poisson distribution, σ_{Off} is defined as:

$$\sigma_{\mathrm{Off}} = \sqrt{\left(\overline{S_{\mathrm{lb}}} + \overline{S_{\mathrm{sb}}} + \overline{S_{\mathrm{dc}}}\right)_{\mathrm{mean}}} \tag{2.32}$$

where $\overline{S_{\mathrm{lb}}}$ is the signal due to laser scatter (typically 0.5–1.5 count s^{-1} mW^{-1}), $\overline{S_{\mathrm{sb}}}$ is the signal due to solar counts (typically zero), and $\overline{S_{\mathrm{dc}}}$ is the signal due to dark counts (typically zero). During the SHIVA fieldwork in November 2011, the LOD for a 1 minute averaging period ranged between 1.7 and 2.1 pptv. The LOD for a 15 minute averaging period ranged between 0.34 and 0.68 pptv.

3.7 NO_2 interference in IO measurements

NO_2 is known to absorb light in the blue region of the spectrum used in IO LIF, and fluoresces over a wide wavelength range, including in the transmission region of the optical filter between the detection cell and the PMT (λ = 520 nm). The absorption spectrum of NO_2 at 151 Torr (approximately equal to the pressure inside the LIF cell) is shown in Figure 3.8. There is a small difference in the NO_2 absorption cross section at the online IO wavelength ($\sigma_{\mathrm{N_2O}} = 3.570\times10^{-19}$) and the offline IO wavelength ($\sigma_{\mathrm{N_2O}} = 3.817\times10^{-19}$), as shown in Figure 3.8b. Thus a small amount of interference from NO_2 fluorescence is possible in the IO measurements, dependent on [NO_2].

The effect of NO_2 on IO measurements using the container-based IO instrument has been thoroughly investigated by Whalley *et al*. (2007), who found that the interference from NO_2 amounted to 0.001 count s^{-1} mW^{-1} $ppbv^{-1}$ of NO_2 present. Commane (2009) tested the effect of NO_2 on IO measurements made using the instrument used in this work, and found no response in signal above the instrument's IO limit of detection for NO_2 mixing ratios up to 500 ppbv of NO_2. Upon addition of more than 500 ppbv of NO_2, an interference of −0.004 pptv per ppbv of NO_2 was recorded.

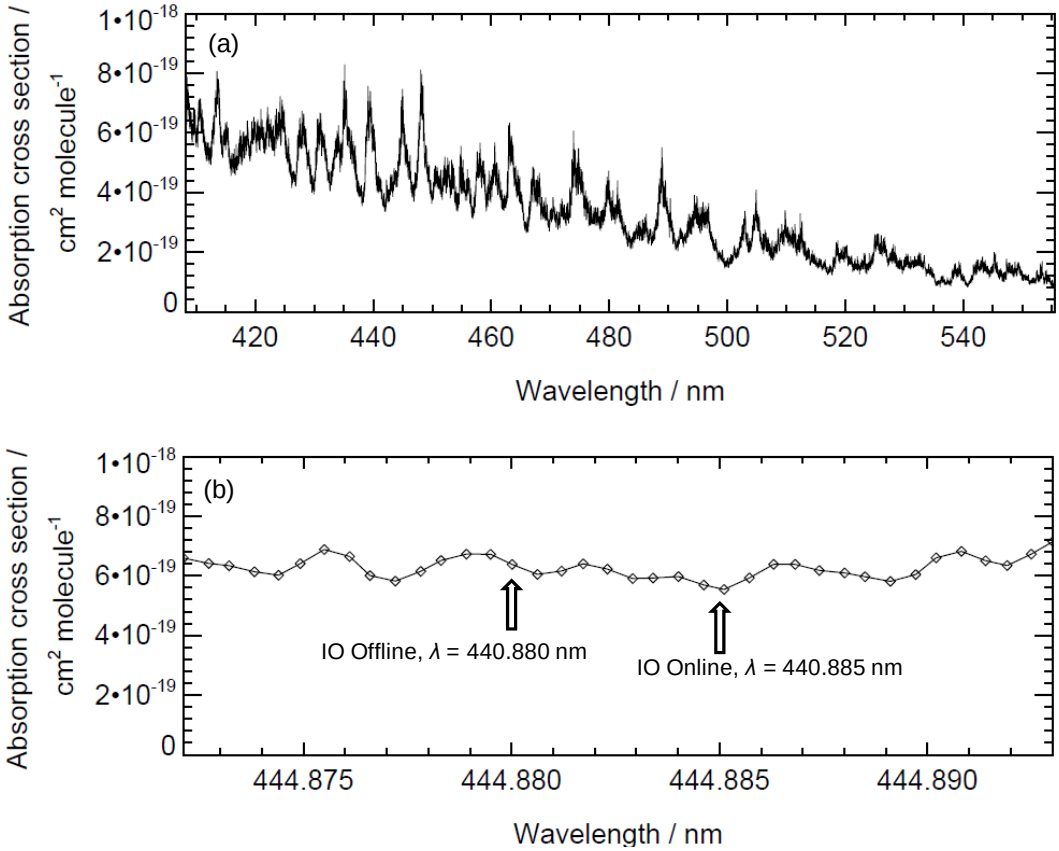

Figure 3.8. a) Absorption spectrum of NO_2 between 408 nm and 555 nm at 299 K and 151 Torr (Nizkorodov *et al.*, 2004); b) Absorption spectrum of NO_2 in the region of the laser wavelengths used for IO LIF measurements (Nizkorodov *et al.*, 2004), showing the online (λ = 440.885 nm) and offline (λ = 440.880 nm) wavelengths used during the SHIVA fieldwork.

The online and offline wavelengths used in previous work (Whalley *et al.*, 2007, Commane *et al.*, 2011) were 444.887 nm and 444.882 nm, respectively. The reason for the change in online and offline wavelengths is likely to do with the calibration of the wavemeter, as discussed in section 2.4.5, and so, despite the apparent change in online and offline wavelength, the magnitude of the NO_2 interference in the IO measurements is likely to be similar to that measured by Commane (2009). The maximum NO_2 mixing ratio measured during the SHIVA fieldwork was 21.5 ppbv, which would cause a maximum interference of −0.086 pptv in the IO measurements, which is within the 1σ precision. These high values were short-lived, and the NO_2 mixing ratio was typically less than 400 pptv during the cruise. Positive interference could be caused if very high mixing ratios of NO_2 were present and varied significantly between the online and offline IO measurement. The influence of NO_2 on IO measurements during SHIVA is discussed in more detail in section 1.12.1 in Chapter 5.

3.8 Conclusions

LP-DOAS and MAX-DOAS are currently the most widely used techniques for measurements of IO from ground-based and ship-based measurement platforms, but a complete picture of boundary layer IO is gained only when these measurements are used in conjunction with *in situ* measurements, such as cavity-enhanced DOAS, mode-locked cavity enhanced absorption spectroscopy, and LIF. A one-dimensional modelling study by Mahajan *et al*. (2010) revealed that IO has a strong vertical gradient near the ocean surface, with mixing ratios decreasing by a factor of 2 between the surface and 200 m. Point measurements close to the ocean surface, by LIF or other *in situ* techniques, are therefore very important. The recent detection of IO in the free troposphere (Dix *et al.*, 2013), and discrepancies with *in situ* measurements (Gómez Martín *et al.*, 2013), indicate that satellite-based DOAS measurements of IO are currently problematic. The satellite instrument's limit of detection is determined partly by the signal-to-noise ratio of the measured spectrum. Low surface reflectivity over the ocean results in fewer photons being reflected into the detector compared to over ice-covered polar regions with high surface reflectivity, resulting in relatively low signal-to-noise ratios and a high limits of detection (Schönhardt *et al.*, 2008). For example, a slant column detection limit of 7×10^{12} molecule cm^{-2} is achieved for measurements over regions with 90 % surface reflectivity. For 5 % surface reflectivity, the detection limit is increased to 2×10^{13} molecule cm^{-2} (Schönhardt *et al.*, 2008). The low sensitivity over oceans results in high sensitivity of the retrieved IO columns to fitting parameters, and the authors note that the data should be treated with caution (Schönhardt *et al.*, 2008). Finally, comparison between satellite-based measurements and *in situ* measurements requires conversion of the measured slant column into a volume mixing ratio. The conversion is partly dependent upon an initial guess of the vertical profile of IO, which can only be measured by *in situ* methods. However, assessing the role of IO on a global scale can only be achieved with knowledge of its global distribution. *In situ* measurements of IO are sparse, and satellite measurements offer a means of obtaining a global picture.

The Leeds IO LIF instrument has been modified for measurements onboard the RV *Sonne* during the SHIVA project. The instrument has been built into a single rack

for installation in a 10 ft × 8 ft shipping container on the front deck of the RV *Sonne* to maximise the chance of sampling clean air. An extended stainless steel inlet has been designed and constructed to enable sampling of ambient air through the roof of the container, thereby eliminating the need for a long sampling line. The resulting distance between the pinhole and the centre of the fluorescence region is 600 mm, which is significantly longer than during previous fieldwork (Commane, 2009), and has a significant effect on instrument sensitivity.

Several measures were taken to overcome the effect of the extended inlet on instrument sensitivity. To minimise loss of radicals between the inlet pinhole and the fluorescence region, and to exclude solar scattered light from the fluorescence cell, a black Nylon insert was fitted inside the stainless steel inlet. An extended baffled photodiode side arm was constructed to minimise reflection of laser light from the photodiode surface into the fluorescence region. To eliminate fluorescence of the anodising dye inside the fluorescence cell, a cylindrical aluminium insert was constructed and fitted to the inside of the cell. Both the side arm baffles and the insert were coated with a mixture of optically black paint and carbon black to reduce laser scattered light, thereby reducing the limit of detection. Calibration of the instrument in the laboratory and during the SHIVA fieldwork have revealed that the instrument sensitivity was significantly higher in the laboratory, but that the sensitivity in the field was comparable to previously reported values (Commane *et al.*, 2011) despite the extended inlet. The instrument's 45 minute limit of detection (15 minutes of online data) during the SHIVA fieldwork ranged between 0.4 and 0.7 pptv. A negative bias observed in the SHIVA field measurements, which has also been observed during previous measurement campaigns, has been investigated in a series of laboratory experiments, to give a value of −0.7 pptv. The measurements of IO made during the SHIVA fieldwork have been adjusted to take this negative bias into account.

Chapter 4. Measurements and analysis of nighttime HO_2 over the UK

4.1 The RONOCO project

The ROle of Nighttime chemistry in controlling the Oxidising Capacity of the atmOsphere (RONOCO) project is a NERC-funded consortium project aimed at improving our understanding of nighttime oxidation chemistry. The extent of oxidation at night, the contribution of oxidation reactions to the radical budget, and the chemistry of the radical pair NO_3 and N_2O_5, are key points of focus in the RONOCO project. Of particular interest to the Leeds Aircraft FAGE group are measurements of OH and HO_2 concentrations at night and the contribution of O_3- and NO_3-initiated oxidation reactions to the HO_x budget. The RONOCO project is unique in that it is the first airborne study of nighttime chemistry to include measurements of OH, HO_2, RO_2 and NO_3.

4.1.1 RONOCO aircraft campaigns

Aircraft measurements were conducted onboard the UK FAAM BAe-146 aircraft during July 2010 and January 2011, with flights over the UK and the North Sea, between altitudes of 50 metres and 6 kilometres. An additional measurement campaign, SeptEx, took place during September 2010. The summer, SeptEx, and winter aircraft campaigns were based at East Midlands Airport (52.8° N, 1.3° W) in the UK. Summaries of the flights are given in Table A1 to Table A3 in Appendix A. Flight tracks for the summer, SeptEx and winter flights for which FAGE was operational are given in the Supplementary Information. Measurements of NO_3, N_2O_5 and a suite of longer-lived species were made during the flights; Table A4 in Appendix A lists the instruments that were onboard and the species that were measured. Of the data that appear in this chapter, NO_3 and N_2O_5 were measured by O. Kennedy, B. Ouyang, and R. Jones of the University of Cambridge; NO, CO, and O_3 were measured by FAAM; VOCs were measured by the University of York.

The daytime boundary layer is the lowest section of the troposphere (up to ~ 3 km), influenced by the Earth's surface. The boundary layer responds to forcings such as evaporation and transpiration, heat transfer, gas phase emissions, and terrain. Vertical transport within the boundary layer is characterised by turbulence, which is caused by solar heating of the surface and the resultant convection, and by frictional drag and the resultant wind shear. Gases emitted at the surface tend to be well-mixed into the boundary layer by turbulent vertical transport and by advection (horizontal transport) by wind. Just before sunset, warm air masses called thermals, which are generated by heat transport from the surface to the overlying air, cease to form and the boundary layer begins to stabilise with respect to vertical transport. The resultant 'residual layer', left over from the daytime mixed layer, contains gases emitted into the daytime mixed layer and is characterised by weak mixing and layering. The lowest part of the residual layer is stabilised by the influence of the increasingly cool ground, separating the air above from surface emissions (Stull, 1988). The nocturnal boundary layer (NBL) is commonly thought to consist of this stable layer, which is on the order of 100–200 m deep. The exception to this isolation of the residual layer from surface emissions is warm plumes, for example from power stations and ships, which can rise through the stable layer and into the residual layer (Brown *et al.*, 2011).

Flights during the summer and winter periods were mostly at night, with occasional dawn and dusk flights; flights during SeptEx were entirely in daylight. The RONOCO flights aimed to sample plumes emitted from urban and industrial areas of the UK, such as Humberside, London, and Edinburgh, downwind of the emission zone. In the chemical environments observed, the reaction of NO_2 with O_3 resulted in significant concentrations of NO_3 so that the nighttime oxidation chemistry of this radical could be studied. The air masses were sampled away from sources of NO, limiting the reaction of NO_3 with NO. In addition the conversion of HO_2 to OH proceeded through reaction channels other than reaction with NO. Several missed approaches at airports enabled sampling of the nocturnal boundary layer for short periods of time.

4.1.2 Performance of the Leeds Aircraft FAGE instrument during RONOCO

The Leeds Aircraft FAGE instrument was installed in the BAe-146 aircraft and operated as described in Chapter 2. The concentrations of OH and HO_2 were calculated as described in Chapter 2 using instrumental sensitivities determined by calibrations before and after the summer and winter fieldwork (see Chapter 2 and Table 4.1 for calibration results). The 1 Hz OH and HO_2 data were averaged to a 60 second time base for analysis alongside the measurements of other species made from the aircraft, and comparison with the results of a box model. FAGE was operational for 16 of the 17 RONOCO flights, and 9 of the 10 SeptEx flights, with problems with the wavemeter during both campaigns causing one flight from each to be missed. There was insufficient laser power during flights B534 to B536 in the summer campaign to measure both OH and HO_2 by dividing the laser light between the two cells. OH was therefore not measured during these flights. Low laser power throughout the summer fieldwork caused relatively high fluctuation in laser power and therefore high background variability. This resulted in high limits of detection for OH (1.8×10^6 molecule cm^{-3}) and HO_2 (6.9×10^5 molecule cm^{-3}).

4.2 Overview of OH and HO_2 measurements

Table 4.2 summarises the OH and HO_2 measurements during RONOCO and SeptEx and gives the instrument's average limit of detection for one minute of data. OH was not detected above the limit of detection during the summer or winter RONOCO flights, resulting in an upper limit of 1.8×10^6 molecule cm^{-3} and 6.4×10^5 molecule cm^{-3} for mean summer and winter concentrations, respectively. These values are comparable to previous nighttime OH measurements (Geyer *et al.*, 2003, Holland *et al.*, 2003, Ren *et al.*, 2003b, Emmerson and Carslaw, 2009). The mean OH concentration during SeptEx was 1.8×10^6 molecule cm^{-3}, which was above the limit of detection. The HO_2 concentrations reported here have a small (~10 %) contribution from interference caused by RO_2 radicals (see Chapter 2 and section 4.7).

Table 4.1. Sensitivities to OH and HO_2 during RONOCO and SeptEx flights. C_{OH} = instrumental sensitivity to OH; C_{HO2} = instrumental sensitivity to HO_2; Int_{HO2} = intercept of HO_2 calibration plot. Calibration uncertainties were calculated as described in Chapter 2.

	Summer RONOCO & SeptEx	Winter RONOCO
C_{OH} / count s^{-1} mW^{-1} $molecule^{-1}$ cm^3	$(2.95 \pm 0.46) \times 10^{-8}$	$(3.94 \pm 0.67) \times 10^{-8}$
C_{HO2} / count s^{-1} mW^{-1} $molecule^{-1}$ cm^3	$(9.32 \pm 1.48) \times 10^{-8}$	$(1.14 \pm 0.20) \times 10^{-7}$
Int_{HO2} intercept / count s^{-1} mW^{-1}	3.63 ± 0.69	2.10 ± 0.40

Table 4.2. Mean mixing ratios (pptv) and concentrations (10^5 molecule cm^{-3}) of OH and HO_2, with the FAGE instrument's average limits of detection during the RONOCO and SeptEx fieldwork.

	Summer		SeptEx		Winter	
	OH	HO_2	OH	HO_2	OH	HO_2
Mean mixing ratio / pptv	0.04	1.6	0.07	2.9	0.005	0.7
Limit of detection / pptv	0.07	0.03	0.05	0.02	0.03	0.02
Mean concentration / 10^5 molecule cm^{-3}	8.9	370	18	660	1.2	170
Limit of detection / 10^5 molecule cm^{-3}	18.0	6.9	12.0	5.9	6.4	6.0

The mean HO_2 concentration was highest during SeptEx (2.9 pptv), and was higher during summer (1.6 pptv) than during winter (0.7 pptv). This feature could be the result of colder temperatures during the winter campaign since the rates of the O_3 + alkene and NO_3 + alkene reactions that are responsible for production of HO_2 at night are temperature dependent.

Table 4.3 gives the mean and maximum HO_2 mixing ratios at different times of day during summer, SeptEx and winter. Dawn, day, dusk and night are defined by the solar zenith angle as follows: dawn and dusk are between 90 and 102°; day is between 0º and 90°; night is between 102° and 180°. Dawn and dusk are distinguished by the time of day (i.e. a.m. or p.m).

Table 4.3. Mean and, in parentheses, maximum HO_2 mixing ratios measured during RONOCO and SeptEx.

	Mean (maximum) HO_2 mixing ratio / pptv		
	Summer	SeptEx	Winter
Dawn	0.74 (1.19)		0.54 (1.81)
Day		3.78(11.79)	0.49 (1.68)
Dusk	2.73 (9.97)		0.32 (0.97)
Night	1.86 (13.58)		0.98 (2.02)

The mean dusk HO_2 mixing ratio in summer is higher than the mean nighttime concentration, suggesting that photochemical production is still active at dusk in summer. The reverse is true for the winter data, with the highest mean HO_2 mixing ratio being at night. This suggests that when photochemical production is suppressed in the winter daytime due to low photolysis rates, production *via* reactions of NO_3 and O_3 with alkenes is the most important route to radical initiation. The highest 60 second averaged HO_2 concentration (3.17×10^8 molecule cm^{-3}; 13.6 pptv) was measured during nighttime flight B537 (see Table A1 in Appendix A). Table 1.1 gives an overview of recent campaigns involving winter and nighttime (i.e. low photolysis) measurements of OH and HO_2. The RONOCO HO_2 measurements are similar to other nighttime, urban measurements. For example, during the TORCH campaign, [HO_2] peaked at 1×10^8 molecule cm^{-3} at night (Emmerson *et al.*, 2007), and during the PMTACS-NY 2001 field campaign, nighttime [HO_2] concentrations of 8×10^6 molecule cm^{-3} were measured (Ren *et al.*, 2003a).

Figure 4.1 shows the mean daytime altitude profile of OH during SeptEx. OH concentrations decrease with increasing altitude, with the highest OH concentrations being observed below 500 m. In contrast to previous daytime aircraft-based measurements of OH, the maximum in the altitude profile during SeptEx is close to the surface, and concentration generally decreases with increasing altitude. Tan *et al.* (2001) report that OH increased with altitude between 0 and 4 km over the tropical Pacific. Ren *et al.* (2008) report that OH remained nearly constant between 0 and 4 km above the surface over North America and the western North Atlantic Ocean. Martinez *et al.*

(2008) report that measurements of OH over the tropical Atlantic Ocean and tropical rainforest in Suriname increased with altitude until around 3 km, and decreased with increasing altitude above ~ 3 km. However, Mao *et al*., (2009) report that measurements of OH over the Pacific Ocean during INTEX-B increased with increasing altitude between 0 and 2 km, then decreased with higher altitude. Finally, Commane *et al*. (2010) report that OH concentrations over West Africa during AMMA were almost constant with altitude between 0 and 4 km.

Figure 4.2 shows the dawn, day, dusk and night altitude profiles of HO_2 for the RONOCO and SeptEx data. The highest HO_2 mixing ratios were observed at altitudes below 1 km, where the majority of flying took place. The dawn profile shows little variation due to the small number of data points in this category. The daytime profile shows a gradual increase with increasing altitude between 0 and 2.25 km, followed by a decrease between 2.25 and 4 km. Similar daytime profiles were reported by Ren *et al*. (2008), Martinez *et al*. (2008), and Mao *et al*. (2009). The dusk profile is almost constant with increasing altitude. The nighttime profile shows a small increase with altitude between 0 and 1.25 km, then a decrease between 1.25 and 3.25 km.

Figure 4.3 shows the nighttime altitude profiles of a) HO_2; b) O_3; c) NO_3 during RONOCO. No similarity is found between the O_3 and HO_2 profiles. Both the HO_2 and NO_3 profiles display a maximum between 1.0 and 1.5 km altitude. However the highest NO_3 concentration was observed at ~ 1.1 km altitude, and the highest HO_2 concentration was observed at ~ 500 m altitude, suggesting that production of HO_2 at this point was not controlled solely by reactions of NO_3 with VOCs.

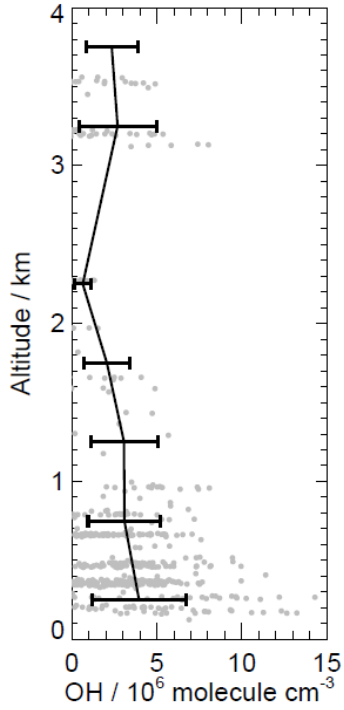

Figure 4.1. OH altitude profile during SeptEx, showing 60 second data (grey dots) and the mean OH value for 500 m altitude bins (solid black lines). Error bars represent one standard deviation of the data each side of the mean.

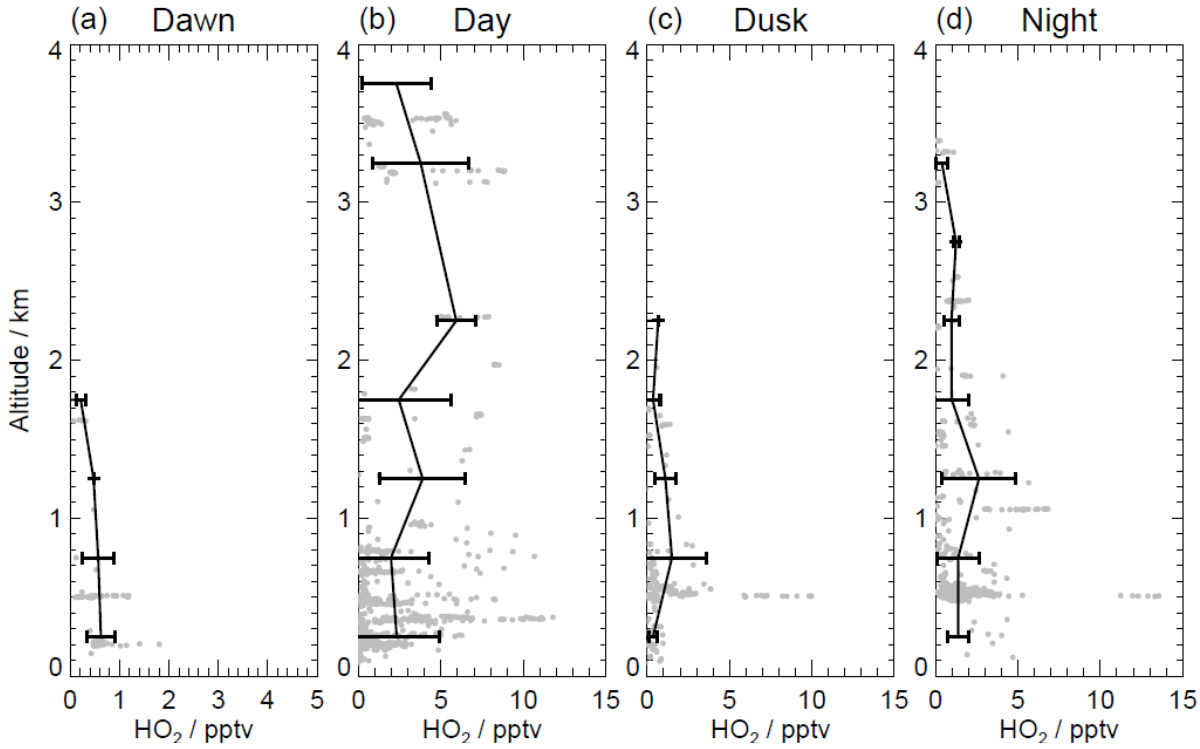

Figure 4.2. Altitude profiles of HO_2 in RONOCO and SeptEx during: a) dawn; b) day; c) dusk; d) night, showing 60 second data (grey dots) and mean values for 500 m altitude bins (solid black lines). Error bars represent one standard deviation each side of the mean.

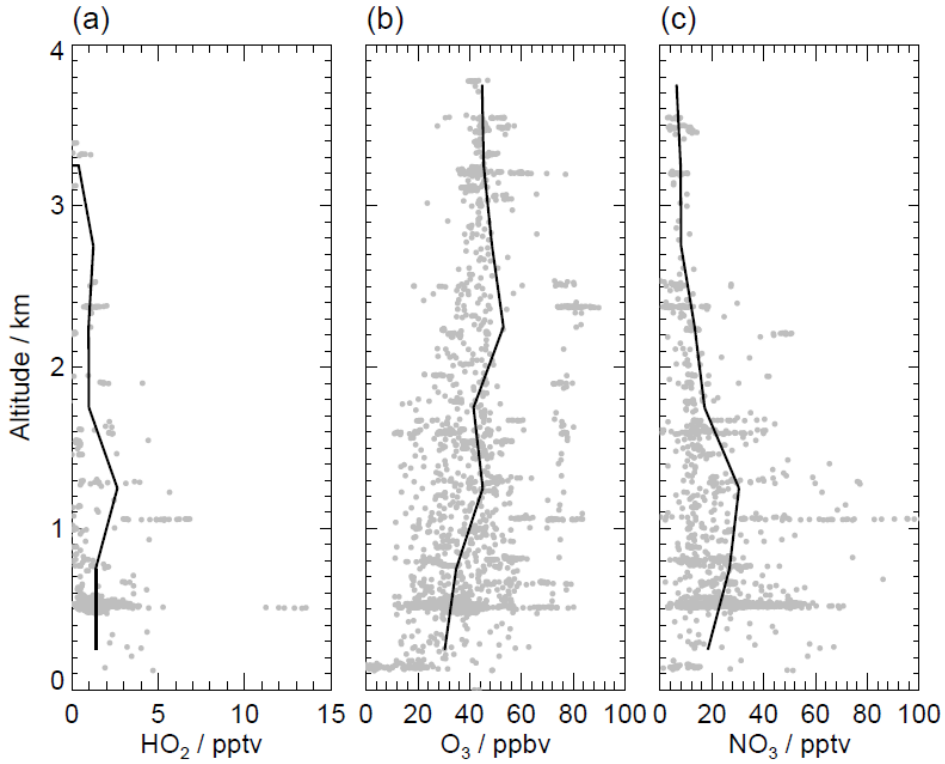

Figure 4.3. Altitude profiles of: a) HO_2; b) O_3; c) NO_3 during nighttime RONOCO flights, showing 60 second data (grey dots) and mean value for 500 m altitude bin (solid black line).

The highest HO_2 concentration (3.2×10^7 molecule cm^{-3}; 13.7 pptv) was measured during flight B537 on 20th July 2010. Take-off from East Midlands Airport was at 22:00 local time (21:00 UTC). The flight track is shown in Figure 4.4. The flight involved a profile descent from 11,000 ft to 1500 ft down the Norfolk coast and a missed approach at Southend Airport. The London plume was intersected by a series of runs at altitudes between 1500 ft and the upper boundary of the polluted layer. Figure 4.5 shows a time series of altitude, HO_2, O_3, and NO_3 mixing ratios during the flight, demonstrating very similar behaviour between the two radical species. During the missed approach at Southend Airport (51.6° N, 0.70° E) the mixing ratios of HO_2 and NO_3 increased with decreasing altitude, to reach maximum values of 4.5 pptv and 35 pptv, respectively, at 50 m above the ground. Figure 4.7 in section 4.3 shows scatter plots of HO_2 and NO_3, and HO_2 and O_3, during flight B537, showing a strong positive correlation between HO_2 and NO_3, with $r = 0.97$. No correlation is evident between HO_2 and O_3 during the flight. The correlation between HO_2 and NO_3 is discussed further in section 4.3.

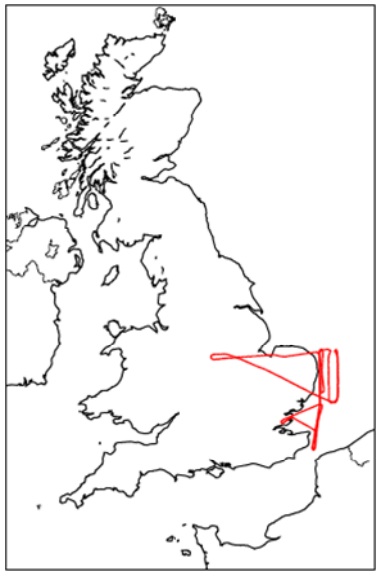

Figure 4.4. Flight track of flight B537 on 20th July 2010.

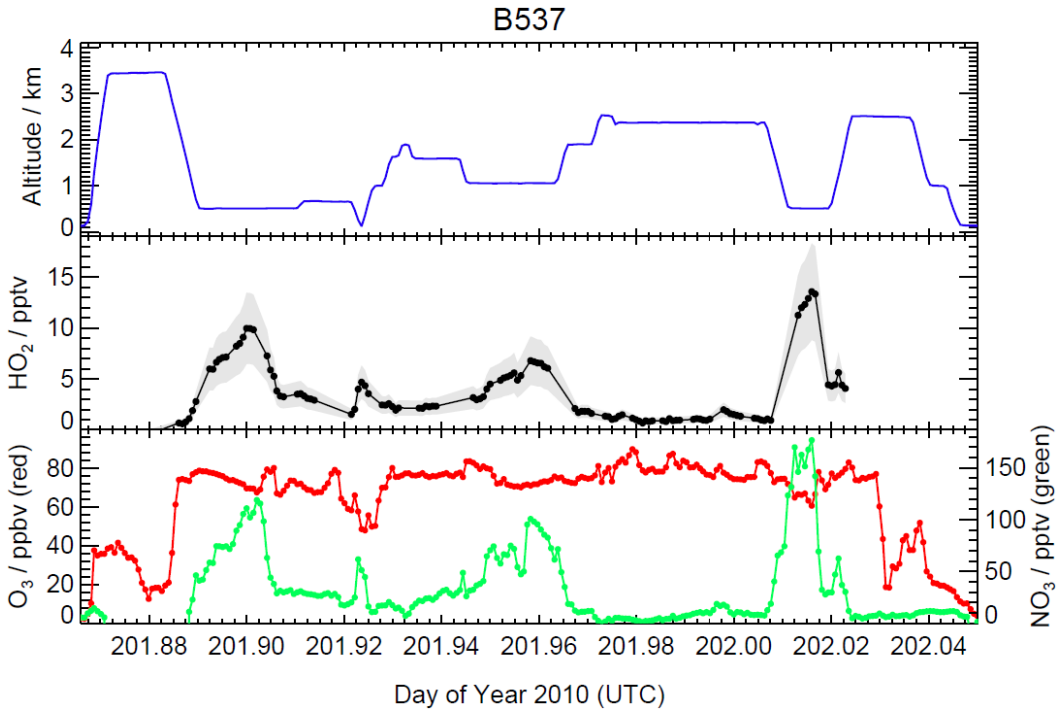

Figure 4.5. Time series of altitude (blue), HO_2 (black, with grey shading representing the uncertainty in the measurements), O_3 (red) and NO_3 (green) during flight B537. Missed approach at Southend Airport was at 201.9225 (UTC). Time series from all of the RONOCO and SeptEx flights are given in the Supplementary Information.

4.3 Correlation between HO_2 and NO_3

Reactions of NO_3 with alkenes are a source of RO_2 and HO_2 radicals, while reactions of NO_3 with RO_2 and HO_2 are a sink. It is therefore not a foregone conclusion that a correlation will exist between NO_3 and RO_2 or HO_2, yet positive correlation has been observed during previous nighttime measurement campaigns. For example, a positive correlation was found between RO_2 and NO_3 measured at Pabstthum, Germany, during the BERLIOZ campaign (Geyer *et al.*, 2003). It was found that in environments where NO_3 + VOC reactions were the only important loss path of NO_3, the correlation between the two radicals was attributable to negative correlations between NO_3 and NO, and RO_2 and NO, rather than production of RO_2 in NO_3 + VOC reactions. On nights with high NO and low VOC levels, reactions of NO_3 with VOCs were not a significant NO_3 sink. Rather, loss of both NO_3 and RO_2 was dominated by reaction with NO. In addition, NO_3 + VOC reactions were the primary source of RO_2, so a positive correlation between NO_3 and RO_2 was found. Emmerson and Carslaw (2009) report a weak positive correlation (r = 0.12) between modelled RO_2 and modelled NO_3 for the TORCH campaign, and conclude that O_3 was more important than NO_3 for radical production. No significant correlation (r = 0.002) was observed between measured HO_2+RO_2 and NO_3, or between HO_2 and NO_3, during measurements at Mace Head in 1997 (Salisbury *et al.*, 2001). Semi-polluted and clean air masses were sampled during the measurements, and no correlation was found for any of the conditions encountered. Moderate positive correlation (r = 0.54) was found between the total rate of NO_3 and O_3 reactions with alkenes and HO_2+RO_2.

Figure 4.6 shows HO_2 plotted against NO_3 for all the RONOCO flights. A strong, positive correlation exists between the two radicals, with r = 0.89. Strong positive correlation between HO_2 and NO_3 (r > 0.7) was found during 5 flights, all of which were nighttime flights sampling semi-polluted air masses. The most striking example of this correlation is flight B537 (Figure 4.7; r = 0.97), which has been identified as an interesting flight within the RONOCO data set. During this flight, no correlation was observed between HO_2 and O_3 (r = 0.003). Strong positive correlation between HO_2 and O_3 was observed during 5 daytime flights and during 1 nighttime flight (B536). The data for this flight are shown in Figure 4.8.

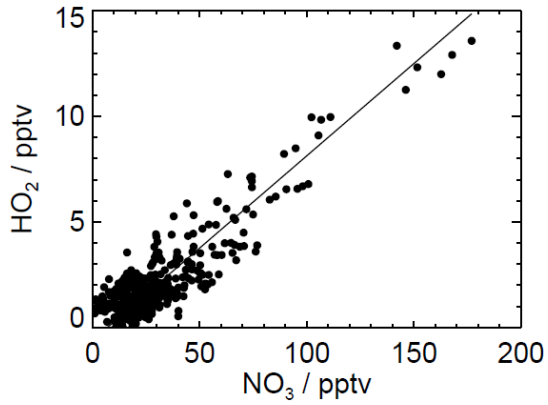

Figure 4.6. HO_2 *versus* NO_3 during all RONOCO flights; r = 0.89.

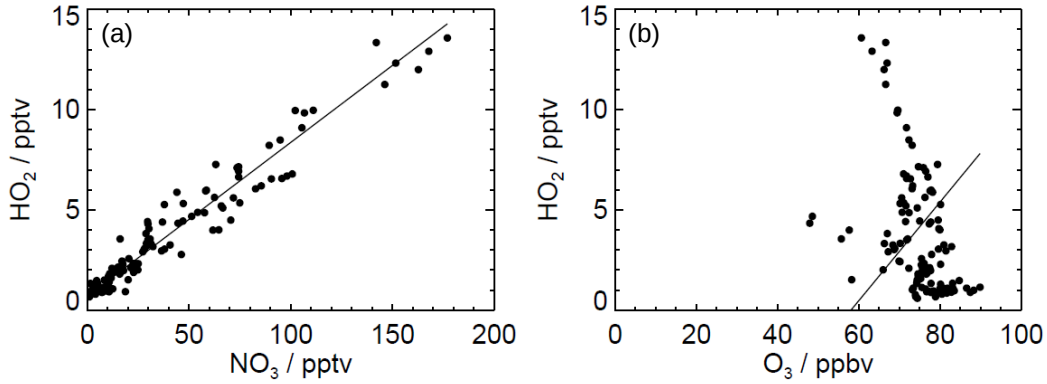

Figure 4.7. a) HO_2 *versus* NO_3 (r = 0.97); b) HO_2 vs O_3 (r = 0.003) during flight B537.

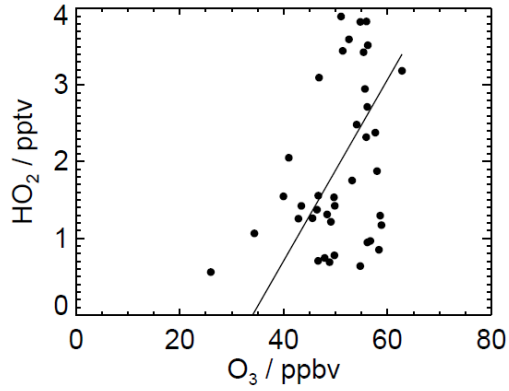

Figure 4.8. HO_2 *versus* O_3 during nighttime flight B536. r = 0.76.

In line with the reasoning put forward by Geyer *et* al. (2003) it is worth investigating the effect of NO on the correlation between HO_2 and NO_3. RONOCO flights sampled semi-polluted air masses removed from sources of NO, so it is expected that the dominant sink of NO_3 is reaction with alkenes rather than removal by NO. NO data are available for flights B534, B535, B536 and B537. A weak positive correlation was found between

HO_2 and NO_3 for the first two flights, and strong positive correlation was found for the second two flights. The mean NO concentrations during these flights were low (6.8−8.7 pptv) and there was little variation in the NO mixing ratio during the flights (maximum 23 pptv). No strong correlation was found between HO_2 and NO or NO_3 and NO during these flights. These results suggest that the correlation observed between HO_2 and NO_3 was not caused by their reactions with NO, but by production of HO_2 by reactions of NO_3 with alkenes. In addition, the data suggest that VOC levels were sufficiently low not to perturb NO_3 concentrations, and that reactions of NO_3 with alkenes were the dominant source of RO_2 and HO_2. Figure 4.9 compares the correlation between HO_2 and NO_3 during summer and winter flights. For summer, r = 0.89, and for winter r = 0.71. The concentrations of HO_2 and NO_3 were much lower in winter than in summer, and as a result appear more scattered though the majority of the data are clustered around low values, as they are in the summer plot. HO_2 was found to correlate with CO during the summer flights, with r = 0.72, as shown in Figure 4.10. This relationship was not observed for the winter flights (r = −0.03). The relationship suggests that the reaction OH + CO is an important source of HO_2 at night during RONOCO, despite low concentrations of OH.

4.4 Analysis of HO_2 production

This analysis focuses on nighttime HO_2 production but a brief comparison of daytime and nighttime chemistry is given, which includes OH measurements made during SeptEx.

4.4.1 Method of analysis

Salisbury *et al.* (2001) investigated nighttime peroxy radical production by calculating total rates, Φ, for reactions of O_3 and NO_3 with the alkenes measured:

$$\Phi_{O_3} = \sum_{i}^{\text{alkene}} k_{O_3+\text{alk}_i} [O_3][\text{alkene}_i] \quad (4.1)$$

$$\Phi_{NO_3} = \sum_{i}^{\text{alkene}} k_{NO_3+\text{alk}_i} [NO_3][\text{alkene}_i] \quad (4.2)$$

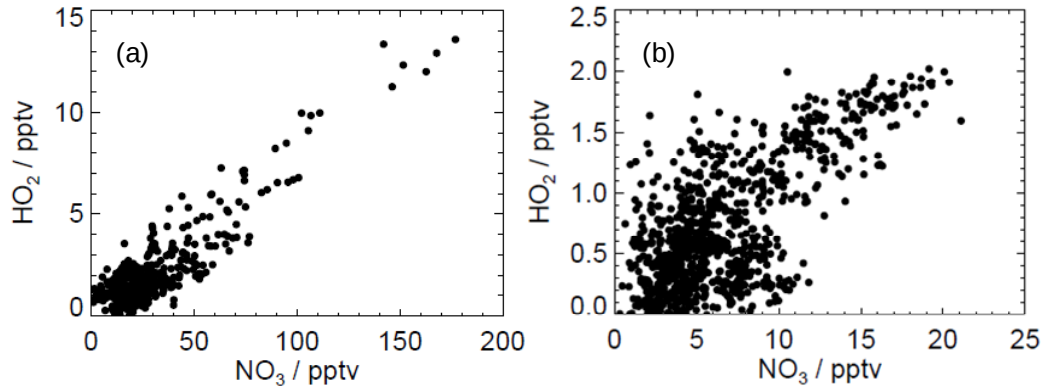

Figure 4.9. HO_2 *versus* NO_3 during: a) RONOCO summer nighttime flights (r = 0.89); b) RONOCO winter nighttime flights (r = 0.71).

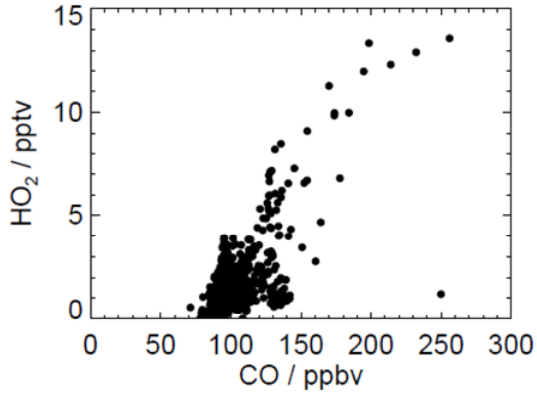

Figure 4.10. HO_2 *versus* CO during summer RONOCO flights. r = 0.72.

The reactions of O_3 and NO_3 with alkenes yield OH, HO_2, and RO_2 radicals (reaction schemes given in Figure 4.11 to Figure 4.14 in this Chapter and in the Supplementary Information) so consideration of the reaction mechanisms of NO_3 and O_3 enabled calculation of the rate of peroxy radical production by each oxidant. A similar approach was taken in the current work to calculate the rate of instantaneous production of HO_2 (P_{HO2}) from the reactions of NO_3 and O_3 with the alkenes measured during RONOCO, using the chemistry scheme, rate constants and branching ratios in the MCM. The mechanisms of radical production from reactions of NO_3 and O_3 are now discussed.

Figure 4.11 shows a simplified reaction scheme for NO_3 with a general alkene. The reaction proceeds *via* addition of NO_3 to the double bond to form a nitrooxyalkyl radical, followed by rapid reaction with oxygen to yield a nitrooxyalkyl peroxy radical, RO_2 (see reaction (R1.42)) . This is shown as a single step in Figure 4.11, with the rate

constant k_1. The RO_2 radical can react with a number of species, of which NO, NO_3 and RO_2 lead to production of an alkoxy radical (RO). Radical termination occurs *via* reaction of RO_2 with HO_2 to yield a peroxide (ROOH) or with RO_2 to yield carbonyl ($RC(O)CH_3$) and alcohol (RCH_2OH) products. Reaction of RO with oxygen proceeds *via* abstraction of a hydrogen atom to yield HO_2 or an aldehyde (RCHO).

This generalised scheme can be applied to the reactions of NO_3 with all the alkenes measured (see Table A5 to Table A7 for lists of the alkenes measured). Values of the rate constants k_1 to k_7 are given in Table A11 in Appendix A. The rate of production of HO_2 is found by calculating the fraction of RO_2 that reacts to produce RO (F_{RO}), and the fraction of RO that reacts to produce HO_2 (F_{HO2}):

$$F_{RO} = \frac{k_3[NO] + k_4[NO_3] + 0.6k_5[RO_2]}{k_2[HO_2] + k_3[NO] + k_4[NO_3] + k_5[RO_2]} \quad (4.3)$$

$$F_{HO_2} = \frac{k_6[RO][O_2]}{k_7[RO] + k_6[RO][O_2]} \quad (4.4)$$

where k_2 to k_7 are rate constants as shown in Figure 4.11, and RO_2 represents all peroxy radicals. F_{HO2} varies between 0 and 1 for the alkenes studied. Overall, the rate of production of HO_2 (P_{HO2}) from reactions of NO_3 with alkenes is:

$$P_{HO_2} = k_i[NO_3][\text{alkene}_i] \times F_{RO} \times F_{HO_2} \quad (4.5)$$

The reaction scheme for the reaction of O_3 with alkenes is more complicated because the number and type of radicals produced in the O_3 + alkene reaction depends on the structure of the alkene (Salisbury *et al.*, 2001). The simplest case is the reaction of ozone with ethene (see Figure 4.12). Ozone adds to the double bond of the alkene to form a five-membered ring called a primary ozonide. Decomposition of the ozonide yields an excited Criegee intermediate (CH_2OO^*) and a carbonyl compound (in this case formaldehyde, HCHO). The energy-rich Criegee intermediate can be stabilised by collision with a third body or undergo decomposition to yield products including OH, CO, and HO_2.

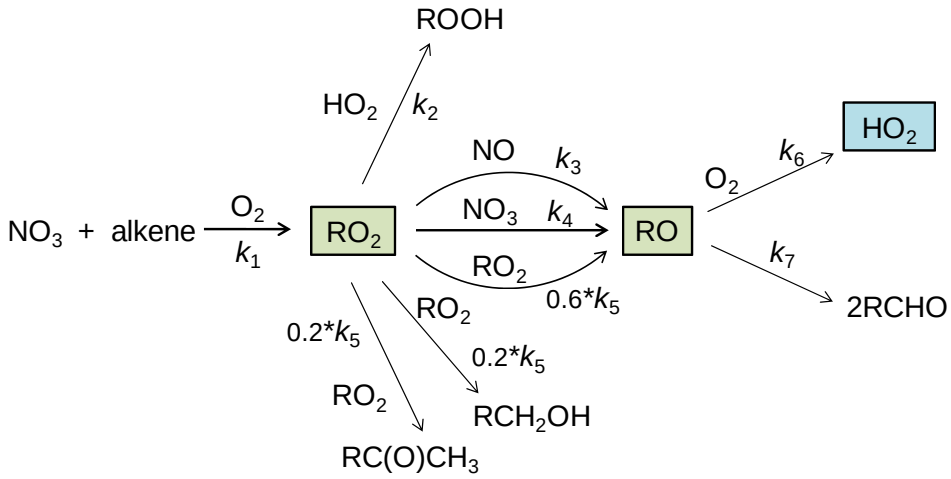

Figure 4.11. Reaction scheme for NO_3 with a general alkene, showing routes to production of RO_2 and HO_2. The values of the rate constants k_1 to k_7 are given in Table A11 in Appendix A.

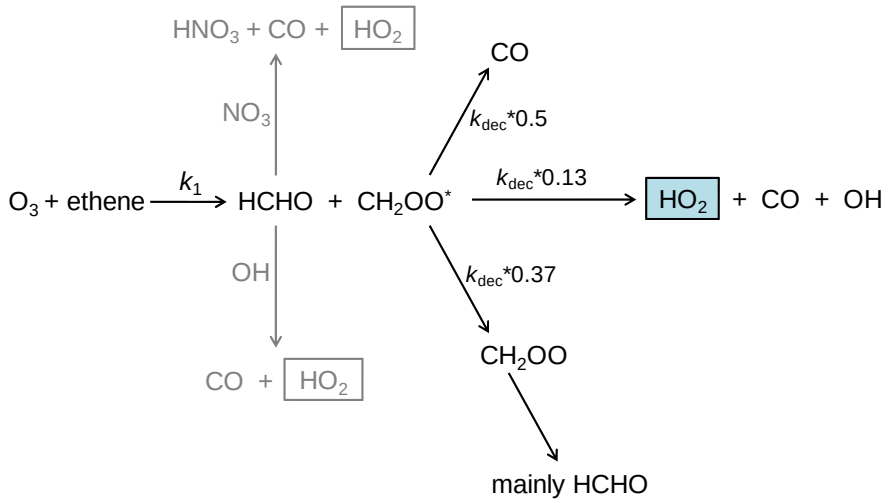

Figure 4.12. Reaction scheme for O_3 + ethene. CH_2OO^* is an excited Criegee intermediate. Rate constants, k_1, for the reactions of O_3 with all the alkenes, are given in Table A10 in Appendix A. k_{dec}, the rate constant for decomposition of the Criegee intermediate, is 1.0×10^6 molecule^{-1} cm^3 s^{-1} (MCM v3.2, Jenkin *et al.*, 1997, Saunders *et al.*, 2003). Reaction channels which are considered to be negligible are shown in grey, and have not been included in the calculation. Where appropriate species names are given as they appear in the MCM.

The primary ozonide produced in the O_3 + propene reaction (see Figure 4.13) can decompose *via* two channels, yielding carbonyls and Criegee intermediates with different structures and different products, including RO_2. Reaction of RO_2 with NO, NO_3 and RO_2 (all peroxy radicals) yields RO, which in turn yields HO_2, as shown in Figure 4.14. Reaction schemes for O_3 with the remaining measured alkenes, and for RO_2 radicals produced in these reactions, are given in the Supplementary Information.

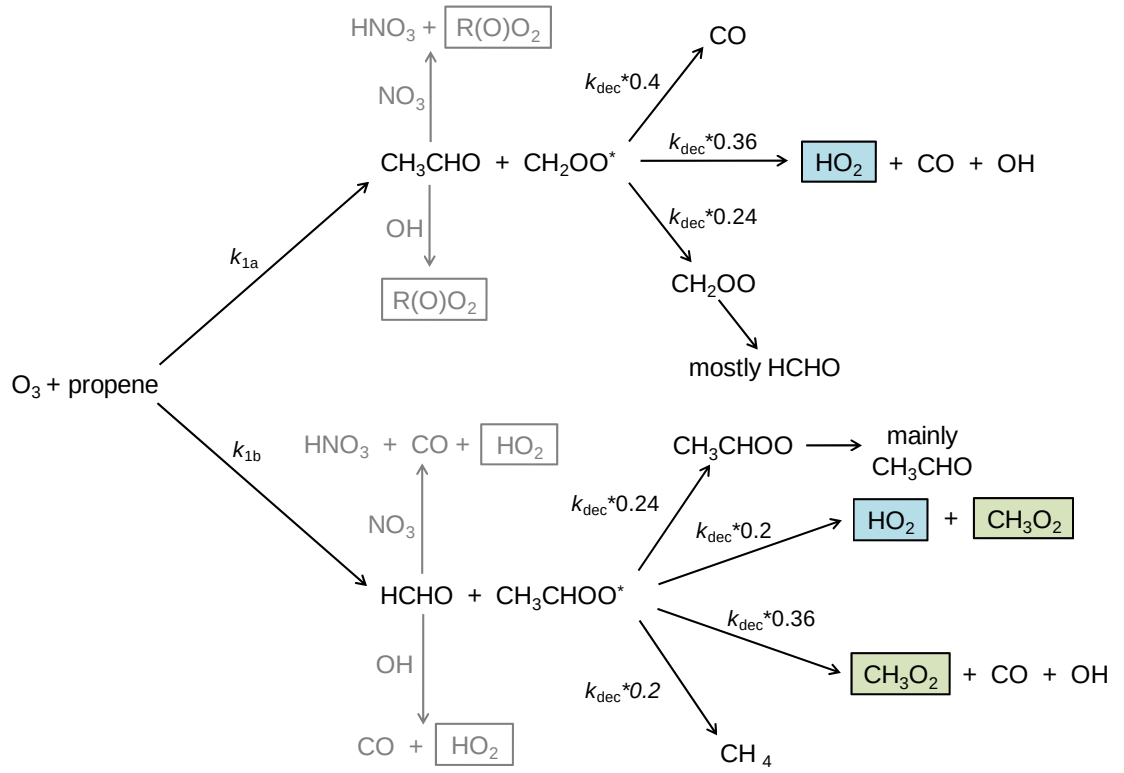

Figure 4.13. Reaction scheme for O_3 + propene. k_{1a} and k_{1b} are the rate constants for the reaction of O_3 with propene, multiplied by the branching ratio for the two channels shown (see Table A10 in Appendix A). CH_2OO^* and CH_3CHOO^* are excited Criegee intermediates. Reactions shown in grey are considered to be negligible, and have not been included in the calculation. RO_2 radicals are shown in a green box to indicate further reaction to produce HO_2. Where appropriate species names are given as they appear in the MCM v3.2 (Jenkin *et al.*, 1997, Saunders *et al.*, 2003).

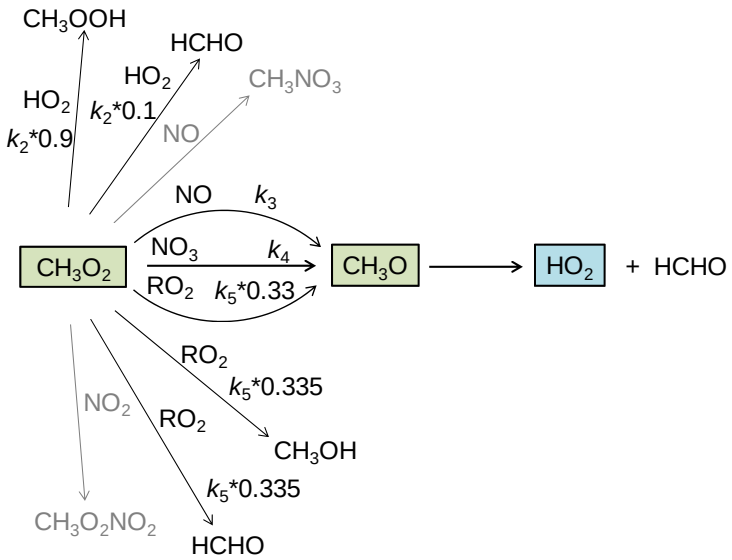

Figure 4.14. Reaction scheme of the methylperoxy radical, CH_3O_2, which is produced in the reaction of O_3 with various alkenes. Reaction channels which are considered to be negligible are shown in grey, and have not been included in the calculations. k_2, k_3, k_4, and k_5 are rate constants for the reactions shown, given in Table A9 in Appendix A. Branching ratios are from the MCM v3.2 (Jenkin *et al.*, 1997, Saunders *et al.*, 2003).

The rates of production of HO_2 from reactions of O_3 with alkenes (P_{HO2}) have been calculated as follows:

$$P_{HO_2,Direct} = k_i [O_3][alkene_i] \times BR_{HO_2} \quad (4.6)$$

$$P_{HO_2,RO_2} = k_i [O_3][alkene_i] \times BR_{RO_2} \times F_{RO} \times F_{HO_2} \quad (4.7)$$

$$P_{HO_2} = P_{HO_2,Direct} + P_{HO_2,RO_2} \quad (4.8)$$

where $P_{HO2,Direct}$ is the rate of direct HO_2 production from Criegee intermediate decomposition (*e.g.* channel 'a' in Figure 4.13), BR_{HO2} is the branching ratio to HO_2-producing channels from the Criegee intermediate (*e.g.* BR_{HO2} = 0.36 in channel 'a' of Figure 4.13), $P_{HO2,RO2}$ is the rate of HO_2 production from RO_2 radicals produced in the O_3 + alkene reaction, BR_{RO2} is the branching ratio to RO_2-producing channels from the Criegee intermediate (*e.g.* 0.2+0.36 in channel 'b' of Figure 4.13), F_{RO} is the fraction of RO_2 radicals that react to produce RO radicals, and F_{HO2} is the fraction of RO radicals that react to produce HO_2 radicals, which is equal to 1 for all the alkenes studied. These rate constants for these reactions are given in Table A9 and Table A10 in Appendix A.

The reactions of RO_2 with NO to form $RONO_2$ have been omitted from the calculations because the branching ratio is small (0.001 to 0.02) for the radicals studied. The reaction of CH_3O_2 with NO_2 to form $CH_3O_2NO_2$ has been omitted from the calculations, since the reverse reaction is fast, with a rate constant of 1.08 s^{-1} at the mean RONOCO temperature of 286.5 K.

The primary aims of the analysis presented here are threefold: (1) To calculate the total rate of initiation through reactions of NO_3 and O_3 with alkenes and to compare these results with results from previous nighttime studies; (2) to determine the relative importance of NO_3 and O_3 in nighttime HO_2 production; and (3) to determine whether there is a difference in radical production between different seasons and different times of day. The correlation between [HO_2] and [NO_3] observed during some flights, especially flight B537, will be investigated. The analysis will also seek to determine whether HO_2 production is a major reaction channel of RO_2 radicals.

P_{HO2} has been calculated for each alkene measured for every 60 s data point where all the requisite data were available and where HO_2 was above the limit of detection of the FAGE instrument (see Table 4.2). Mean concentrations of the alkenes measured during the summer, SeptEx and winter measurement campaigns are given in Table A5 to Table A7 in Appendix A. Measurements of RO_2 concentrations from the PERCA instrument were not used in this analysis because of the high uncertainty associated with the measurements and the sparse data coverage. Instead, RO_2 was calculated by scaling the observed HO_2 concentrations with the modelled RO_2/HO_2 ratio, i.e. $RO_{2,obs} = HO_{2,obs} \times RO_{2,mod}/HO_{2,mod}$. Measurements of NO were made by the FAAM fast NO_x instrument and were available for the first four summer flights only. The mean NO mixing ratios for the flights where measurements were available were between 6.8 and 8.7 pptv. Measurements of formaldehyde (HCHO) were made by the University of East Anglia HCHO GC instrument onboard the aircraft, and were available for summer flights only. With this in mind, NO and HCHO have been included in the analysis where data is available and these results have been compared to the results where these species are omitted from the analysis, using the same data points. The rest of the analysis sets the concentrations of these species to zero. This approach is valid in the case of NO since the measurements were made away from the source of NO, and it is assumed that NO_x is present mainly as NO_2.

4.5 Results

4.5.1 Rates of reaction of NO_3, O_3 and OH with alkenes

Table 4.4 gives total rates of reaction of NO_3 and O_3 with alkenes (Φ_{NO3} and Φ_{O3}), averaged over the summer and winter RONOCO flights. The sum of Φ_{NO3} and Φ_{O3} at dusk and at night in summer was more than twice that in winter. At night in summer, Φ_{NO3} was more than double Φ_{O3} (138 %), but in winter the trend was reversed with Φ_{O3} being 61 % higher than Φ_{NO3}. During summer Φ_{O3} was highest at dusk, though there are few data points at dusk in summer. During winter Φ_{O3} was highest during the day, and was higher at dusk than at dawn or during the night, though the difference in the total rates of reaction is small. As expected, the highest values of Φ_{NO3} were at night in both summer and winter.

Table 4.4. Total rates of reaction (Φ) of NO_3 and O_3 with alkenes measured during RONOCO, averaged over summer and winter flights.

	Total rate of reaction / 10^4 molecule cm^{-3} s^{-1}			
	Dawn	Day	Dusk	Night
Summer				
Φ_{NO3}	0.0		8.57	9.80
Φ_{O3}	2.62		5.11	4.12
Total	2.62		13.68	13.92
Winter				
Φ_{NO3}	1.85	1.80	1.88	2.42
Φ_{O3}	4.01	4.75	4.26	3.90
Total	5.86	6.55	6.14	6.32

Salisbury *et al.* (2001) report total rates of reaction between NO_3 and O_3 and alkenes measured at Mace Head. Average nighttime total reaction rates of NO_3 + alkenes ranged between 0.52–2.2 × 10^4 molecule cm^{-3}, and total O_3 + alkene rates ranged between 2.0−8.3 × 10^4 molecule cm^{-3}. Φ_{O3} was higher than Φ_{NO3} in all wind sectors. Φ_{O3} calculated for the summer and winter nighttime RONOCO data is within the range reported by Salisbury *et al.* Φ_{NO3} calculated for the summer and winter nighttime RONOCO data is higher than the numbers reported by Salisbury *et al.*, and was higher than Φ_{O3} in summer, in contrast to the results from Mace Head.

Brown *et al.* (2011) report that total VOC loss rate *via* reaction with NO_3 was 3–5 times faster than *via* reaction with O_3 during two flights of the 2006 Texas Air Quality Study. Total rates of reaction of NO_3 and O_3 with alkenes were calculated for measurements made during the NAMBLEX project at Mace Head, 2002 (Fleming *et al.*, 2006). Reactions of O_3 with alkenes dominated radical production on most nights, except when NO_3 concentrations were high, when semi-polluted air masses were sampled. The majority of the O_3 + alkene rates were below 5.0 × 10^4 molecule cm^{-3} s^{-1}, with a high outlying value of 2.5 × 10^5 molecule cm^{-3} s^{-1}. NO_3 + alkene rates were mainly below 1.5 × 10^5 molecule cm^{-3} s^{-1}, with a high value of 3.0 × 10^5 molecule cm^{-3} s^{-1}. The RONOCO O_3 + alkene rates are very similar to these results, while the RONOCO

NO_3 + alkene rates tended to be higher during summer and lower during winter. Emmerson and Carslaw (2009) report that the average nighttime rate of initiation of HO_2 from O_3 was 1.4×10^5 molecule cm^{-3} s^{-1} during the TORCH campaign. This value is higher than the O_3 + alkene rates calculated for RONOCO. No measurements of NO_3 were made during TORCH, and no model calculation of the rate of reaction of NO_3 with alkenes is given.

4.5.1.1 Nighttime alkene oxidation

The rates of reaction of NO_3, O_3 and OH with the alkenes measured during RONOCO have been examined in more detail. For these calculations, the limit of detection of the FAGE instrument was used as an upper limit on nighttime OH concentrations, which was 1.8×10^6 molecule cm^{-3} in summer, and 6.4×10^5 molecule cm^{-3} in winter. The calculations therefore represent upper limits of the rates of reaction between OH and alkenes, and the results are treated with caution. Figure 4.15 shows histograms of the rate of reaction between O_3, NO_3 and OH with individual alkenes during summer and winter, for the nighttime data only. The reactivity of alkenes ($\Phi_{O3} + \Phi_{NO3} + \Phi_{OH}$) was greater in summer than in winter. The reactions of NO_3 are largley responsible for this seasonal difference, since the contribution from O_3 + alkene reactions varies little between summer (4.1×10^4 molecule cm^{-3} s^{-1}) and winter (3.9×10^4 molecule cm^{-3} s^{-1}). The 75 % difference in the rate of NO_3 reactions between summer (9.8×10^4 molecule cm^{-3} s^{-1}) and winter (2.4×10^4 molecule cm^{-3} s^{-1}) can be attributed to the higher mean concentration of NO_3 in summer (5.8×10^8 molecule cm^{-3}) compared to winter (2.0×10^8 molecule cm^{-3}). The mean summer temperature was 286.7 K, and the mean winter nighttime temperature was 277.7 K. The colder temperatures in winter will have forced the NO_3–N_2O_5 equilibrium towards N_2O_5, as well as decreasing the rates of reaction between NO_3 and some of the alkenes in winter compared to summer. The difference of 71.9 % between Φ_{OH} in summer and winter is the result of the difference of 64.4 % between the summer and winter upper limit OH concentrations used in the analysis.

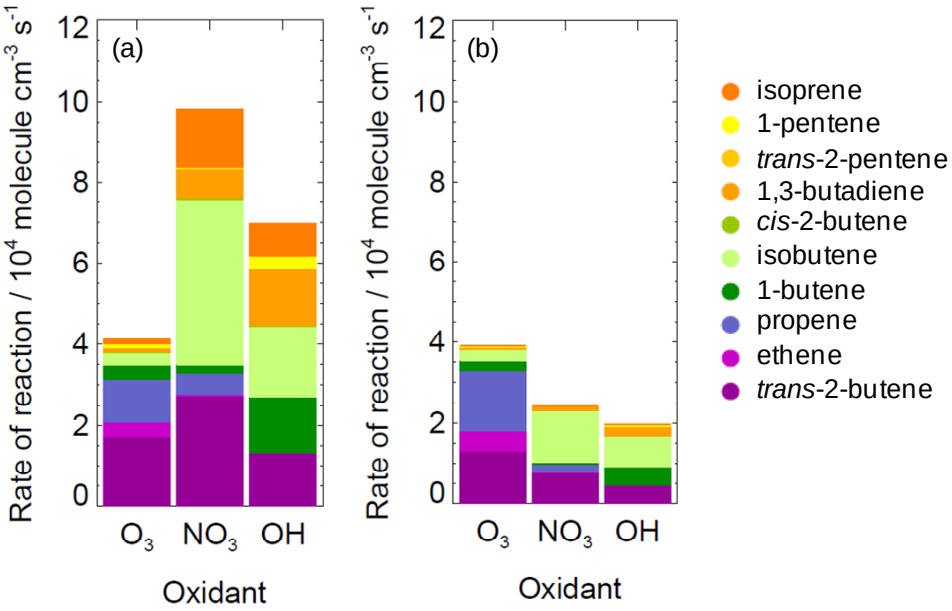

Figure 4.15. Nighttime rates of reaction between O_3, NO_3 and OH with alkenes during: a) summer; and b) winter RONOCO flights. The rates of reaction of OH with alkenes are upper limits.

Figure 4.15b shows that Φ_{O3} was greater than Φ_{OH} in winter. Although Φ_{OH} includes only reactions with alkenes, and therefore does not represent the total reactivity of OH, this result is in agreement with a number of previous studies that have found ozonolysis of alkenes to be the dominant radical source during the day and the night. Ren *et al*. (2003b, 2006) found that reactions of O_3 with alkenes were the dominant HO_x source at night in New York city, in both summer and winter. Emmerson *et al*. (2005) found that ozonolysis of alkenes was a dominant daytime HO_x source in the urban atmosphere near Birmingham, UK, particularly during winter. The authors also found that OH was more important for removing non-methane hydrocarbons (NMHCs) than ozone, both during the day and the night in summer and winter. However, when alkenes were considered separately, nighttime loss *via* reaction with ozone in winter was slightly faster than with OH, assuming a lower limit for OH concentrations, in agreement with the present study. Geyer *et al*. (2003) report that nighttime VOC oxidation by OH (including VOCs, CO and methane) was equal to 15 % of the oxidation capacity of NO_3 during the night.

Figure 4.15 illustrates the importance of the butane isomers in the reactions of O_3, NO_3 and OH, and therefore radical initiation and propagation. Reactions with *iso*-butene dominated NO_3 reactivity in summer and winter, with *trans*-2-butene also contributing

significantly. Reactions of O_3 were dominated by *trans*-2-butene and propene. Finally, reactivity of OH with alkenes had almost equal contributions from *trans*-2-butene, 1-butene, *iso*-butene and 1,3-butadiene in summer. In winter OH + *iso*-butene was dominant, with significant contributions from *trans*-2-butene and 1-butene.

4.5.1.2 Daytime alkene oxidation

Figure 4.16 shows histograms of rates of reaction of O_3, NO_3 and OH with alkenes during SeptEx and winter RONOCO flights, for daytime data only. OH was detected above the limit of detection (1.2×10^6 molecule cm^{-3}) during the SeptEx flights, so the FAGE OH data were used in the calculations. NO_3 was not detected during the day in SeptEx. During SeptEx, Φ_{OH} exceeded Φ_{O3} by a factor of 1.7. In winter, Φ_{O3} was greater than both Φ_{OH} and Φ_{NO3}. In contrast to the summer nighttime data illustrated in Figure 4.15, isoprene contributed significantly to OH reactivity with alkenes. This result highlights the increased sampling of biogenic airmasses during SeptEx compared to the summer flights. Reactions with isomers of butene account for the remaining OH reactivity. The total rate of reaction of O_3 and NO_3 with alkenes during nighttime summer flights ($\sim 1.39 \times 10^5$ molecule cm^{-3} s^{-1}) is comparable to the total rate of reaction of O_3 and OH with alkenes during daytime SeptEx flights ($\sim 1.57 \times 10^5$ molecule cm^{-3} s^{-1}), indicating that the nocturnal atmosphere can be as important for the oxidation of VOCs as the daytime atmosphere.

Figure 4.17 compares the daytime and nighttime reactivity of O_3, NO_3 and OH with alkenes, for the winter RONOCO data, using an OH upper limit of 6.4×10^5 molecule cm^{-3}. Reactions with O_3 dominated alkene reactivity during day and night. The concentrations of alkenes were generally higher at night (see Table A7 in Appendix A), with the total alkene concentration (sum of concentrations of alkenes measured) being 2.1×10^9 molecule cm^{-3} in the day, and 3.4×10^9 molecule cm^{-3} at night. The mean daytime temperature was 274.2 K, and the mean nighttime temperature was 277.7 K. The contribution to reactivity from individual alkenes is similar during day and night for all three oxidants. The total alkene reactivity ($\Phi_{O3} + \Phi_{NO3} + \Phi_{OH}$) was 9.0 % lower at night than during the day. This difference is attributable mainly to the change in Φ_{O3}.

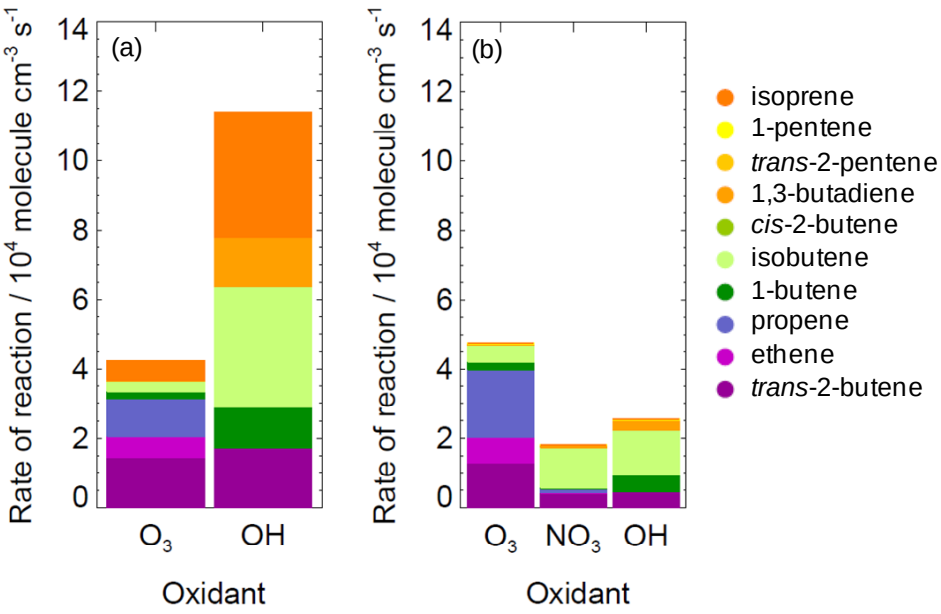

Figure 4.16. Daytime rates of reaction between O_3, OH and NO_3 with alkenes during: a) SeptEx; b) winter RONOCO flights. NO_3 was not detected during daytime SeptEx flights. Winter OH rates are upper limits.

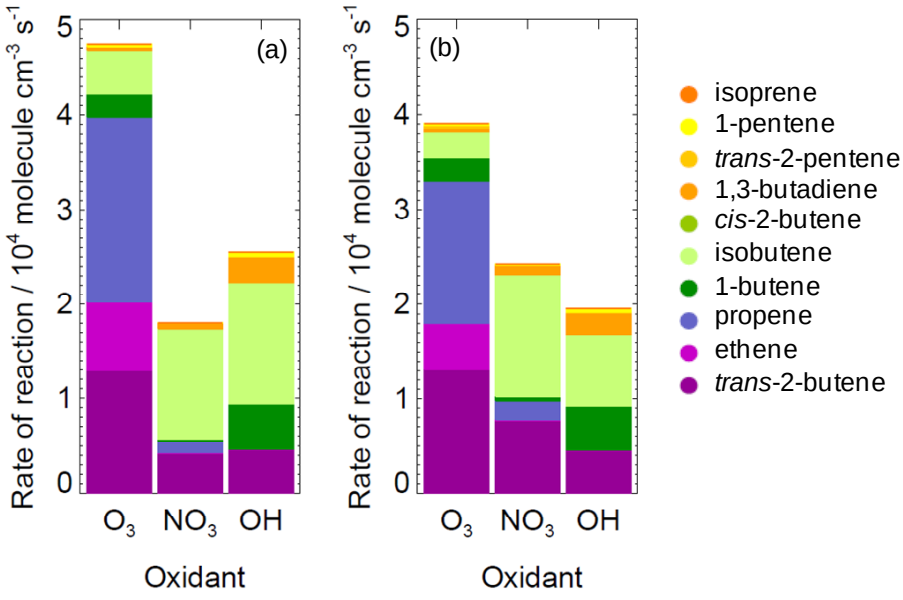

Figure 4.17. Rates of reaction between O_3, OH, and NO_3 with alkenes during: a) daytime; b) nighttime winter RONOCO flights. OH rates are upper limits.

4.5.2 Importance of HO_2-producing reaction channels

As described in section 4.4.1, the rates of production of HO_2 (P_{HO2}) from reactions of NO_3 and O_3 have been calculated for every time point where all of the requisite data are available. Figure 4.18a shows mean fractional reactivities (i.e. the rate of an individual reaction divided by the sum of the rates of all reactions) of one of the RO_2 radicals produced in the reaction of NO_3 with propene, excluding the RO_2 + NO channel. The pie chart shows that 46.1 % of total RO_2 reactivity was with NO_3, to produce RO and therefore HO_2. The total reactivity through all channels that produce RO (F_{RO}), and therefore HO_2, was 51.2 %. The data shown are from the summer flights, and are representative of all the RO_2 radicals produced in the reaction schemes included in this analysis.

The overall pattern is for reaction with NO_3 to dominate, followed closely by reaction with HO_2, with reactions with RO_2 being minor channels. Radical propagation *via* production of RO was therefore an important fate of all RO_2 radicals generated by reactions of O_3 and NO_3 with the alkenes measured. On average, the total proportion of reactivity through radical-propagating channels (F_{RO}) was approximately 10 % higher for O_3-generated RO_2 radicals than for NO_3-generated RO_2 radicals. Figure 4.18b shows the same calculations for the data points where measurements of NO were available, and includes the reaction of RO_2 with NO. The RO_2 + NO reaction dominates RO_2 reactivity (40.7 %), and the reaction with NO_3 contributes only 31.4 %. The impact of these results on production of HO_2 is examined later.

4.5.3 Nighttime production of HO_2

Table 4.5 gives the rates of production of HO_2, summed over the alkenes measured, for reactions of O_3 and NO_3 ($\Sigma P_{HO2,NO3}$ and $\Sigma P_{HO2,O3}$ respectively), as percentages of the total HO_2 production rate, which for the purposes of this analysis is assumed to be equal to the sum of the rate of production from NO_3 reactions and the rate of production from O_3 reactions (i.e. total = $\Sigma P_{HO2,NO3}$ + $\Sigma P_{HO2,O3}$). During summer, O_3 dominated HO_2 production at dawn because NO_3 was not detected at these times. There were no daytime flights during summer.

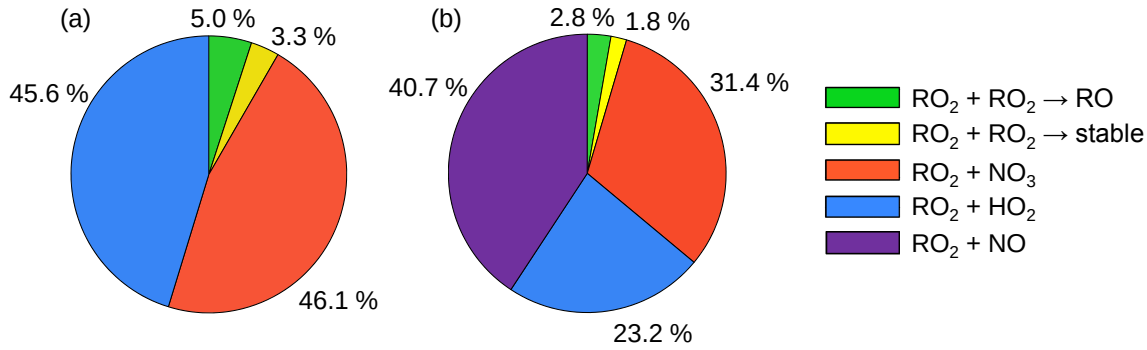

Figure 4.18. Pie charts showing average values of relative contributions to reactivity of the RO_2 radical PRONO3AO2, produced in the reaction of NO_3 with propene. Chart (a) does not include the RO_2 + NO channel; chart (b) does include the RO_2 + NO channel. Numbers are given as percentages of the total reactivity of the RO_2 radical, calculated from summer measurements. $RO_2 + RO_2 \rightarrow RO$ is the radical propagating channel; $RO_2 + RO_2 \rightarrow$ stable is the radical terminating channel (see Figure 4.11).

Table 4.5. HO_2 production rates (ΣP_{HO2}) from O_3 and NO_3 reactions with alkenes, as percentages of the total production rate (total = $\Sigma P_{HO2,NO3} + \Sigma P_{HO2,O3}$).

	HO_2 production rate (ΣP_{HO2}) as percentage of total			
	Dawn	Day	Dusk	Night
Summer				
NO_3	0.0		56.9	68.4
O_3	100.0		43.1	31.6
Winter				
NO_3	21.0	20.0	25.0	29.8
O_3	79.0	80.1	75.0	70.2

NO_3 dominated HO_2 production during dusk and night (68.4 %), in agreement with Geyer *et al*. (2003) who found that NO_3 was responsible for 53 % of HO_2 production at night in the BERLIOZ campaign. During winter, O_3 dominated HO_2 production at all times, with a nighttime contribution of 70.2 %. This is in agreement with the results from the winter PMTACS-NY 2004 field campaign (Ren *et al.*, 2006). NO_3 is not expected to be present at measurable concentrations during daylight hours due to photolysis, but a mean concentration of 8.3×10^7 molecule cm^{-3} (3.3 pptv) was measured during the day in the winter flights. These measurements of low mixing ratios

of NO_3 may be partly caused by interference from other daytime species (such as H_2O, O_3, and NO) as observed by Wagner *et al*. (2011), or by the variability of the instrument baseline, which can be on the order of 1–2 pptv during vertical profiles on the aircraft (B. Ouyang, personal communication). If these measurements are real, reactions of NO_3 with alkenes may have a small contribution to HO_2 production in daytime in winter.

Table 4.6 gives the absolute values of ΣP_{HO2} calculated from the measurements. The total rate of instantaneous production of HO_2 at night was 2.9 times greater in summer than in winter, with production from O_3 decreasing by 23 % and production from NO_3 decreasing by 85 % from summer to winter. The mean temperature difference between summer and winter of 9 K is thought to be responsible for the lower NO_3 concentrations in winter (2.0×10^8 molecule cm^{-3}, 8.2 pptv, compared to 5.8×10^8 molecule cm^{-3}, 24.5 pptv in summer), and for the reduced rate of temperature-dependent reactions between NO_3 and alkenes, and subsequent reactions. There was very little difference between summer and winter O_3 mixing concentrations (9.6×10^{11} molecule cm^{-3}, 39.6 ppbv, and 9.4×10^{11} molecule cm^{-3}, 38.6 ppbv, respectively), so the reduction in production of HO_2 from alkene ozonolysis is attributed to reduced rate of reaction in colder temperatures.

Production of HO_2 *via* reactions of NO_3 and O_3 with alkenes has been examined in more detail. The rate of production from individual alkenes was calculated, and plotted in a histogram, as shown in Figure 4.19 for the summer and winter nighttime data. During both summer and winter, reactions of O_3 and NO_3 with *trans*-2-butene were important sources of HO_2, contributing 66 % to O_3-initiated HO_2 production and 30 % to NO_3-initiated production. Reactions of NO_3 with isoprene were important during summer, contributing 26 % to NO_3-initiated production. The plot highlights the small change in total production from O_3 between summer and winter, and the dramatic change in total production from NO_3 between summer and winter.

Table 4.6. Rates of instantaneous HO_2 production from reactions of O_3 and NO_3 with alkenes.

Measurements	HO_2 production rate (ΣP_{HO2}) / 10^3 molecule cm^{-3} s^{-1}			
	Dawn	Day	Dusk	Night
Summer				
NO_3	0		24.7	32.4
O_3	4.9		18.7	14.9
Total	4.9		43.4	47.3
Winter				
NO_3	3.7	3.7	4.1	4.9
O_3	13.9	14.9	12.3	11.5
Total	17.6	18.6	16.3	16.3

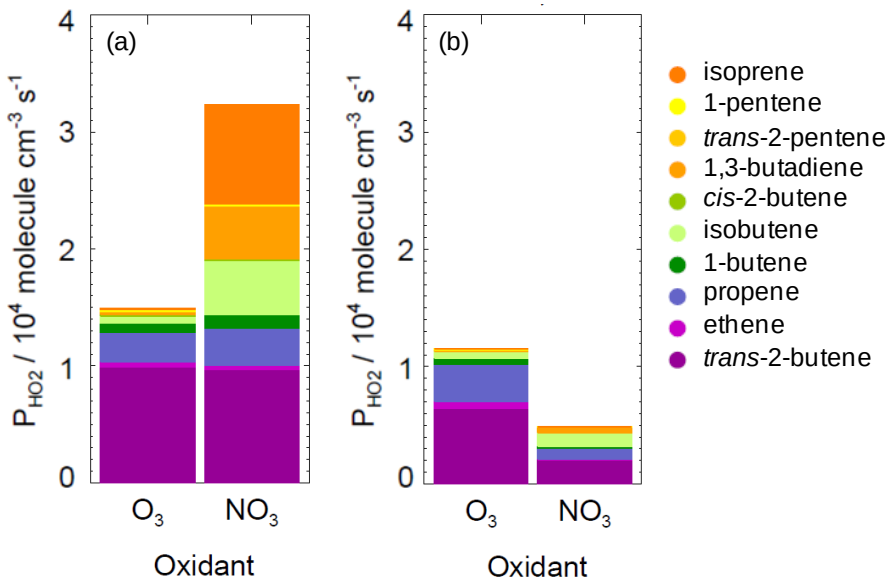

Figure 4.19. Rates of instantaneous production of HO_2 from reactions of O_3 and NO_3 with alkenes during: a) summer; and b) winter RONOCO flights.

Reactions of formaldehyde with NO_3 were included in the analysis where formaldehyde data were available. The results are shown in Figure 4.20. The NO_3 + HCHO reaction contributed a further 5.5×10^3 molecule cm^{-3} s^{-1} (17 %) to HO_2 production from NO_3 reactions, so that production from NO_3 contributed 80 % of the total production. This result is in contrast to that found by Salisbury *et al*. (2001) who report that reactions of NO_3 with HCHO were unimportant at night, with a maximum rate of 9.1×10^2 molecule cm^{-3} s^{-1}.

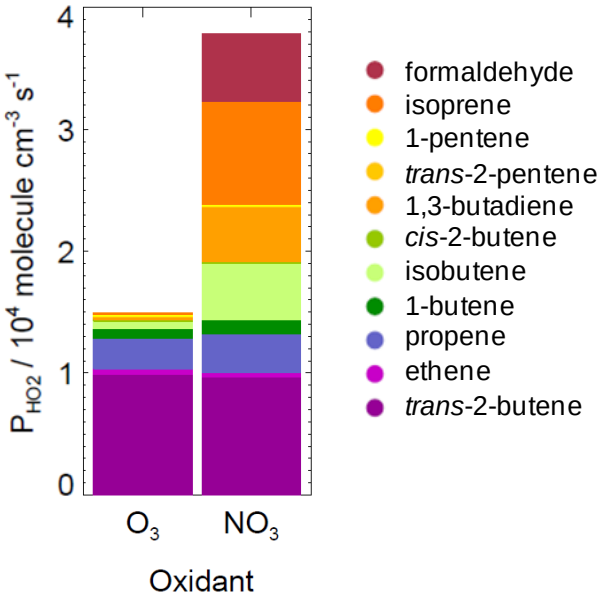

Figure 4.20. Rates of instantaneous production of HO_2 from reactions of O_3 and NO_3 with alkenes and formaldehyde. Data are from summer, nighttime RONOCO flights where measurements of HCHO are available.

The reaction of RO_2 with NO is one of three radical-propagating channels for the RO_2 radical. This reaction has been included in the analysis where NO data were available, and the results are shown in Figure 4.21. The additional flux from RO_2 to RO resulted in a small increase (16 %) in production of HO_2 from O_3 reactions, and a slightly larger increase (20 %) in production from NO_3 reactions.

Although a positive correlation was observed between HO_2 and O_3 during just one of the nighttime RONOCO flights (see Figure 4.8), it is expected that HO_2 will be correlated with the instantaneous rate of production of HO_2 from O_3 + alkene reactions, particularly at times when these reactions are more important than NO_3 + alkene reactions. Figure 4.22 shows scatter plots of HO_2 against P_{HO2} from reactions of O_3 with individual alkenes for summer nighttime measurements (equivalent plots for the winter data are given in the Supplementary Information). The correlation coefficient, *r*, is given in each plot. Strong to moderate correlation exists between HO_2 and P_{HO2} for *trans*-2-butene, ethene, propene, 1-butene and 1-pentene. From the histogram plots it is expected that $P_{HO2,trans\text{-}2\text{-}butene}$ would have the strongest correlation with HO_2 since it has the fastest rate of instantaneous production. However there seems to be no relationship between the rate of instantaneous production and the degree of correlation.

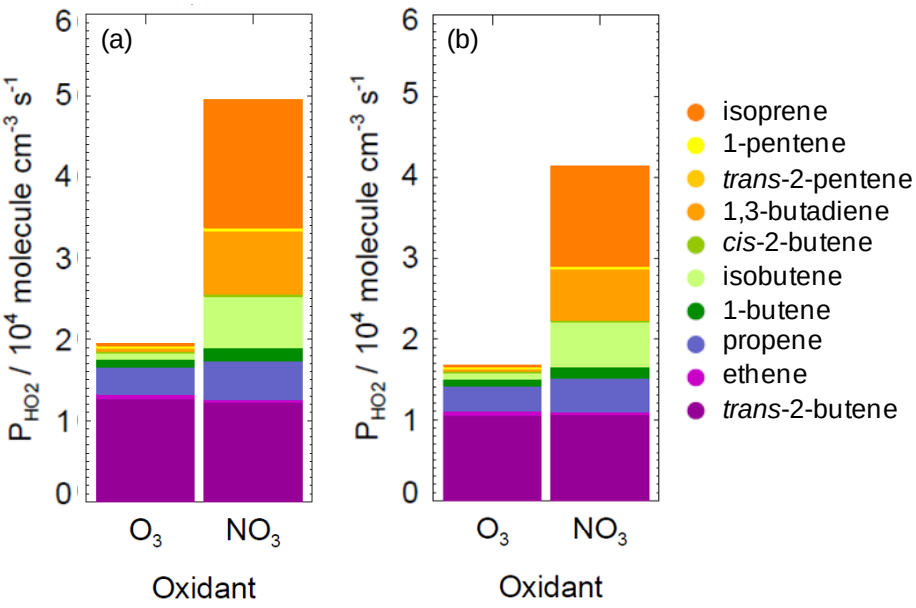

Figure 4.21. Rates of instantaneous production of HO_2 from reactions of O_3 and NO_3 with alkenes: a) with reactions of RO_2 with NO; b) without reactions of RO_2 with NO, during summer nighttime flights. The same data points are used in each plot.

Equivalent plots for the rate of instantaneous production of HO_2 from NO_3 + alkene reactions are shown in Figure 4.23. Strong positive correlation was observed between HO_2 and NO_3 during several RONOCO flights, and it is expected that if this correlation is the result of production of HO_2 from NO_3 reactions then positive correlation would also be observed between HO_2 and $P_{HO2,NO3}$. Strong positive correlation exists between HO_2 and the rate of instantaneous production from the reactions of NO_3 with *trans*-2-butene, ethene, propene, 1-butene and 1,3-butadiene, with moderate positive correlation for *iso*-butene and 1-pentene. As for the reactions of O_3 with alkenes there seems to be no relationship between the apparent importance of a reaction based on the histograms in Figure 4.19 and the degree of correlation in Figure 4.23. In all cases the correlations are weaker for the winter data, with some very weak negative correlations observed for the O_3 reactions. Figure 4.24 shows scatter plots of HO_2 against total rate of instantaneous HO_2 production (ΣP_{HO2}, summed over the measured alkenes) from reactions of O_3 and NO_3 with alkenes during the summer and winter flights. Strong correlation (r = 0.6) exists between $\Sigma P_{HO2,O3}$ and HO_2 for the summer flights, and moderate correlation (r = 0.5) exists between $\Sigma P_{HO2,NO3}$ and HO_2 for the summer flights. Moderate correlation (r = 0.4 for both O_3 and NO_3 reactions) exists for the winter flights.

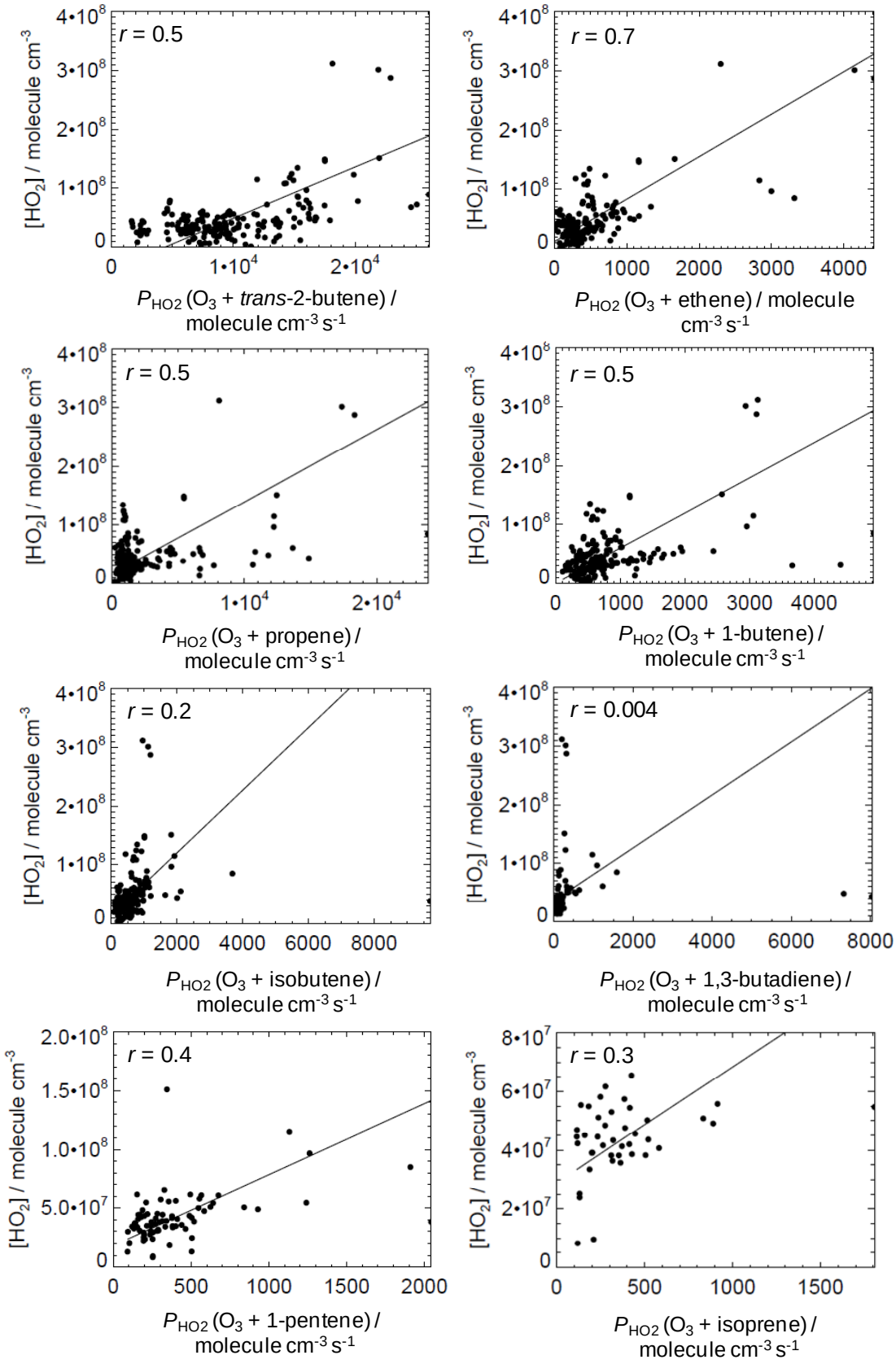

Figure 4.22. HO_2 *versus* rates of instantaneous production from reactions of ozone with alkenes, for nighttime summer RONOCO flights. Correlation coefficients, *r*, are given in each plot. Solid lines are lines of best fit to the data.

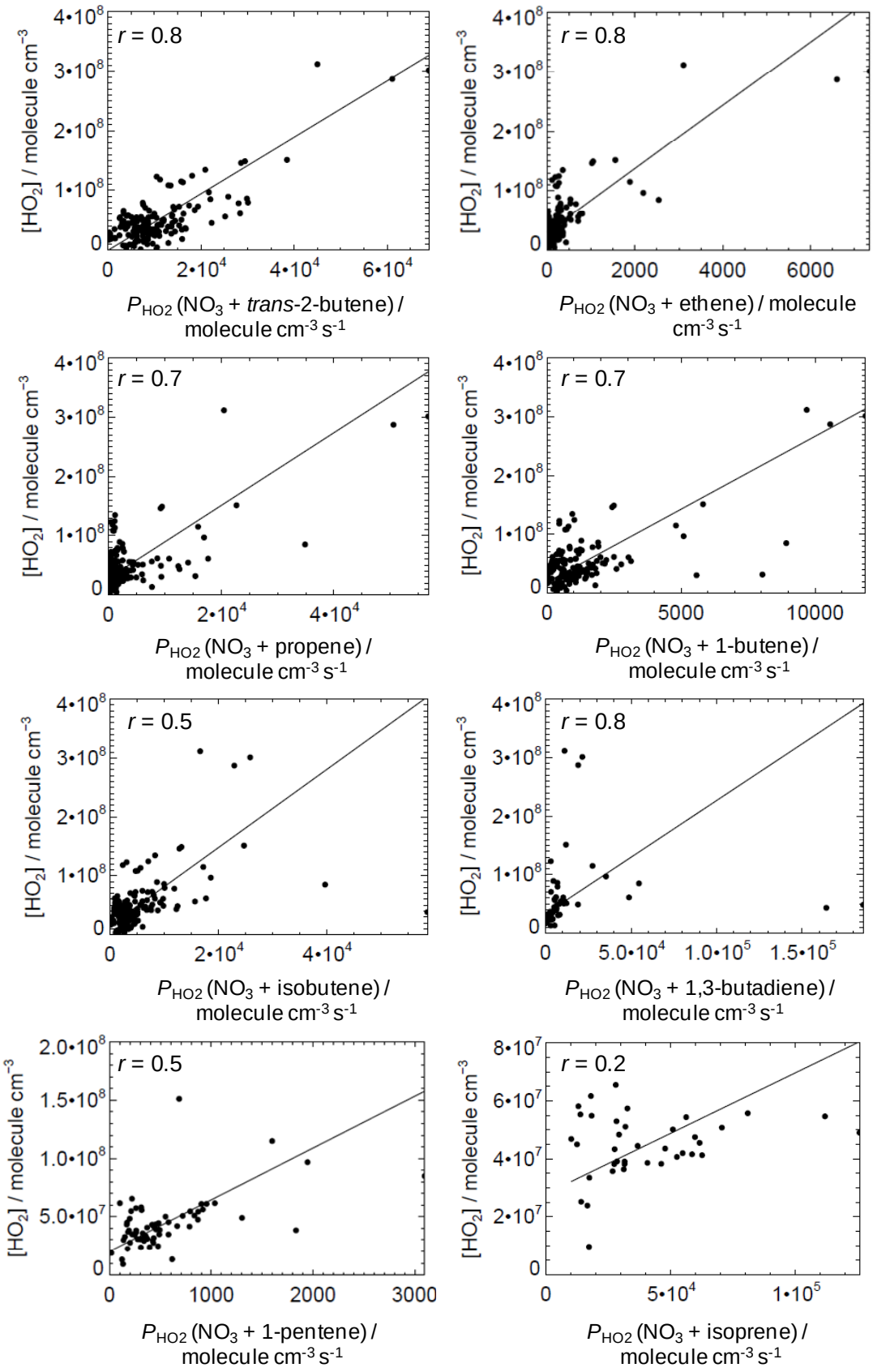

Figure 4.23. HO_2 *versus* rates of instantaneous production of HO_2 (P_{HO2}) from reactions of NO_3 with alkenes, during summer nighttime RONOCO flights. Correlation coefficients, *r*, are given in each plot. Solid lines are lines of best fit to the data.

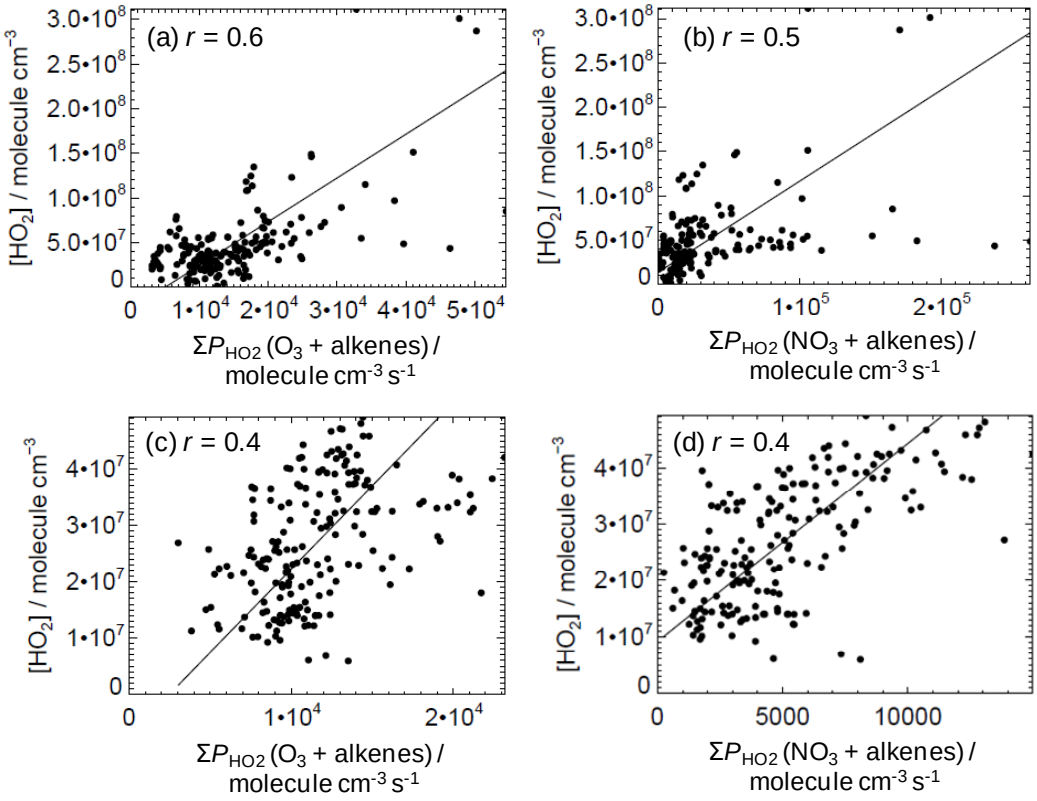

Figure 4.24. HO_2 *versus* total rate of instantaneous production of HO_2 from reactions of O_3 and NO_3 with alkenes during: a), b) summer; and c), d) winter nighttime RONOCO flights. Correlation coefficients (r) are given in each plot. Solid lines are lines of best fit to the data.

Flight B537, on 20th July 2010, has been identified as an interesting flight, with high concentrations of HO_2 (3.2×10^8 molecule cm^{-3}; 13.6 pptv), ozone (peaking at 1.8×10^{12} molecule cm^{-3}, 89.9 ppbv) and NO_3 (peaking at 4.1×10^9 molecule cm^{-3}; 176.9 pptv), and a strong positive correlation between HO_2 and NO_3 (r = 0.97). NO, NO_2, and aerosol surface area were also elevated during the flight during flight B537 compared to their mean summer values. The highest concentration of ethene (1.43×10^{10} molecule cm^{-3}; 0.61 ppbv) during the summer RONOCO flights was measured during B537. ΣP_{HO2} from O_3 + alkene reactions (2.2×10^4 molecule cm^{-3} s^{-1}) was higher in flight B537 than in all the other summer flights, contributing 40.5 % of HO_2 production, with NO_3 + alkene reactions contributing 3.2×10^4 molecule cm^{-3} (59.5 %).

The total rate of HO_2 production from both O_3 and NO_3 reactions was 5.4×10^4 molecule cm^{-3} s^{-1}, which is higher than the average total rate of production during the summer flights (4.4×10^4 molecule cm^{-3} s^{-1}) but not the highest. Figure 4.25 shows that the reactions of O_3 and NO_3 with *trans*-2-butene are once again important, contributing 70.2 % of $\Sigma P_{HO2,O3}$, and 44.1 % of $\Sigma P_{HO2,NO3}$. As mentioned in section 1.2.5.1 of Chapter 1, the yield of OH from ozonolysis of alkenes that form methyl-subsituted Criegee intermediates, (*e.g.* 0.64 for *trans*-2-butene) is significantly greater than from unsubstituted CIs (*e.g.* 0.13 for ethene) (Johnson and Marston, 2008). Of the NO_3 + alkene reactions studied, the NO_3 + isoprene reaction has the highest rate constant (6.9×10^{-13} cm^3 $molecule^{-1}$ s^{-1} at 298 K), followed by NO_3 + *trans*-2-butene (3.9×10^{-13} cm^3 $molecule^{-1}$ s^{-1} at 298 K). However, the average concentration of isoprene during the summer flights (1.35×10^7 molecule cm^{-3}, 0.6 pptv) was low compared to the concentration of *trans*-2-butene during the summer flights (4.06×10^7 molecule cm^{-3}, 1.7 pptv) so that the reaction of NO_3 with *trans*-2-butene was the more important route to production of HO_2. The results of the box modelling study by Stone *et al*. (2013) are in agreement with these calculations. Modelled NO_3 reactivity was dominated by *iso*-butene (36 %) and *trans*-2-butene (27 %), and modelled O_3 reactivity was dominated by *trans*-2-butene (51 %).

Neither HO_2 nor NO_3 exhibited correlation with NO (0.0–16.8 pptv) during the flight (r = 0.18 for HO_2 and r = 0.22 for NO_3). The total alkene concentration during flight B537 was 1.9×10^9 molecule cm^{-3} (88.1 pptv). This was not the highest total alkene concentration during the summer flights, which was seen during flight B353 (3.4×10^9 molecule cm^{-3}, 143.8 pptv) but is higher than the summer nighttime average (1.6×10^9 molecule cm^{-3}, 68.5 pptv). The correlation between HO_2 and NO_3 is therefore attributed to production of HO_2 by reactions of NO_3 with alkenes, especially *trans*-2-butene. Figure 4.26 shows HO_2 versus the total instantaneous rate of production from the reactions of O_3 and NO_3 with alkenes during flight B537. A strong positive correlation exists between HO_2 and both $\Sigma P_{HO2,O3}$ (r = 0.7) and $\Sigma P_{HO2,NO3}$ (r = 0.8), indicating the importance of these reactions for production of HO_2 during this flight.

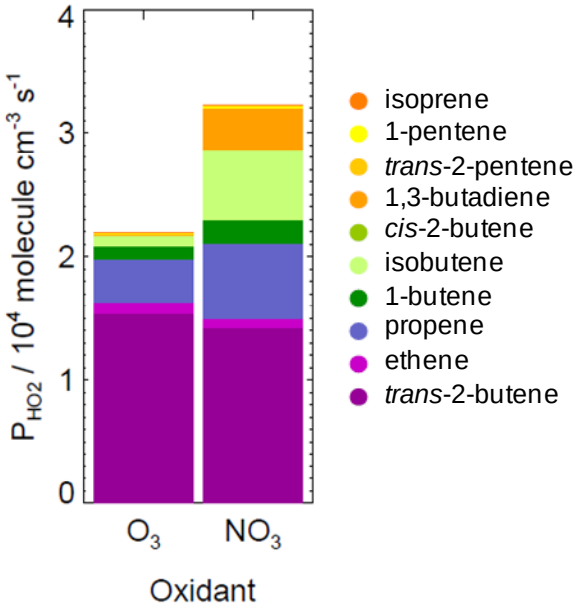

Figure 4.25. Rates of instantaneous production of HO_2 (P_{HO2}) from reactions of O_3 and NO_3 with alkenes during flight B537. Histograms of rates of production of HO_2 are given for all summer, SeptEx, and winter flights in the Supplementary Information.

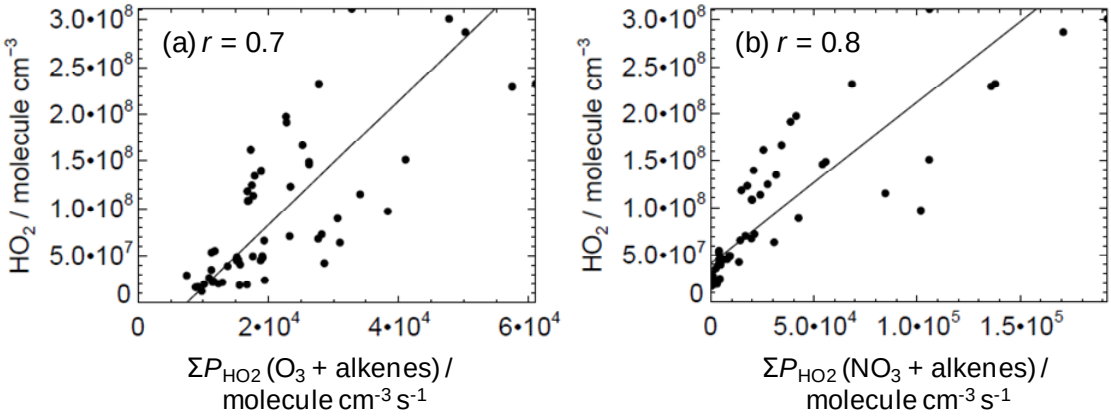

Figure 4.26. HO_2 versus total rate of instantaneous production of HO_2 from reactions of: a) O_3; and b) NO_3 during flight B537. Correlation coefficients (r) are given in each plot. Solid lines are lines of best fit to the data.

Scatter plots of HO_2 versus P_{HO2} from individual O_3 + alkene reactions during flight B537 are shown in Figure 4.27, and equivalent plots for NO_3 + alkene reactions are shown in Figure 4.28. Moderate or strong positive correlation (r = 0.5–0.7) exists between P_{HO2} and HO_2 for all the O_3 + alkene reactions. Stronger correlation (r = 0.6–0.9) exists between P_{HO2} and HO_2 for the NO_3 + alkene reactions, with the strongest correlation observed between HO_2 and P_{HO2} from the NO_3 + *trans*-2-butene reaction, confirming the importance of this reaction for production of HO_2.

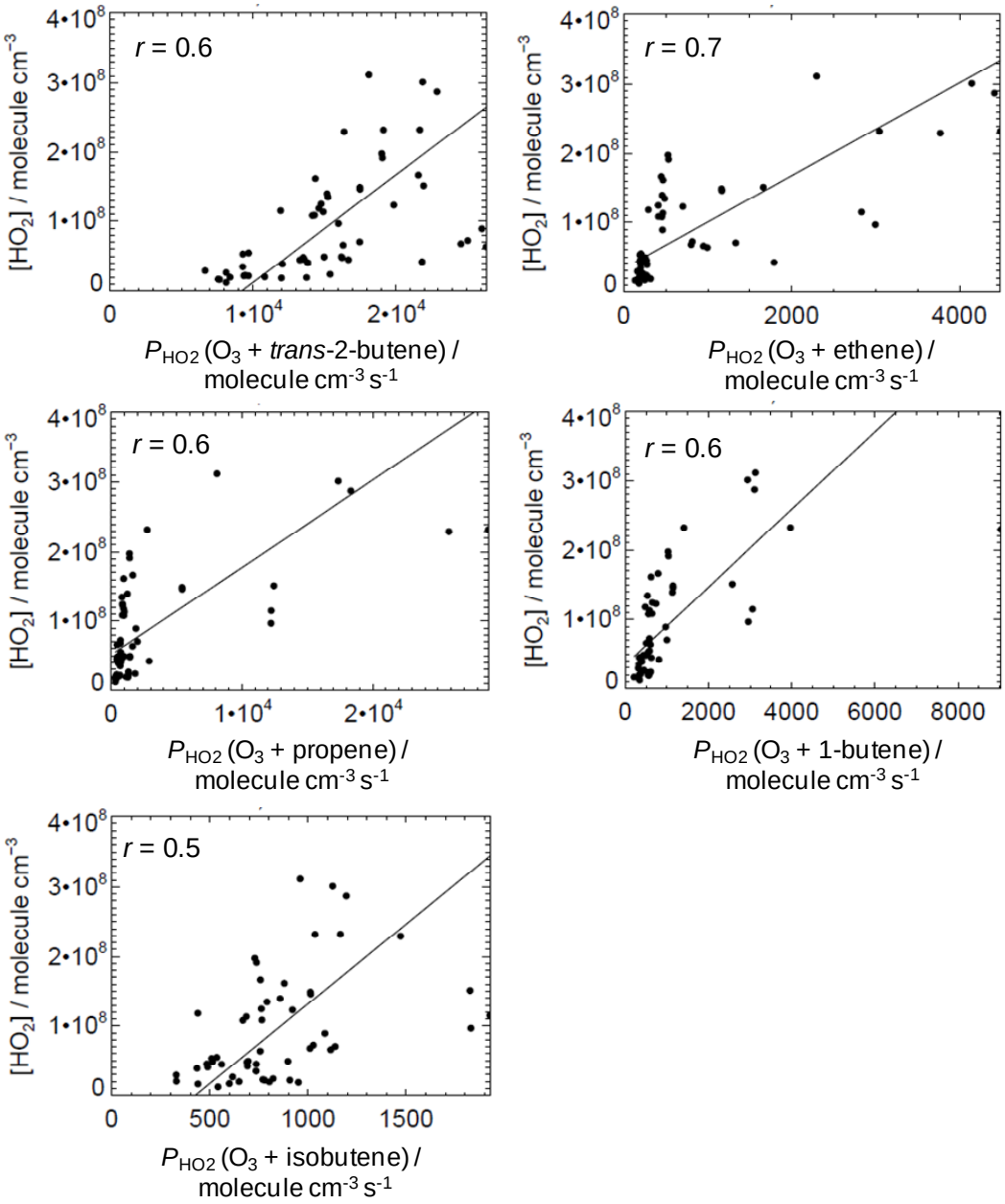

Figure 4.27. HO_2 versus rates of instantaneous production of HO_2 from reactions of O_3 with alkenes during flight B537. Correlation coefficients (r) are given in each plot. Solid lines are lines of best fit to the data. Only alkenes with which a moderate or strong correlation was observed have been plotted.

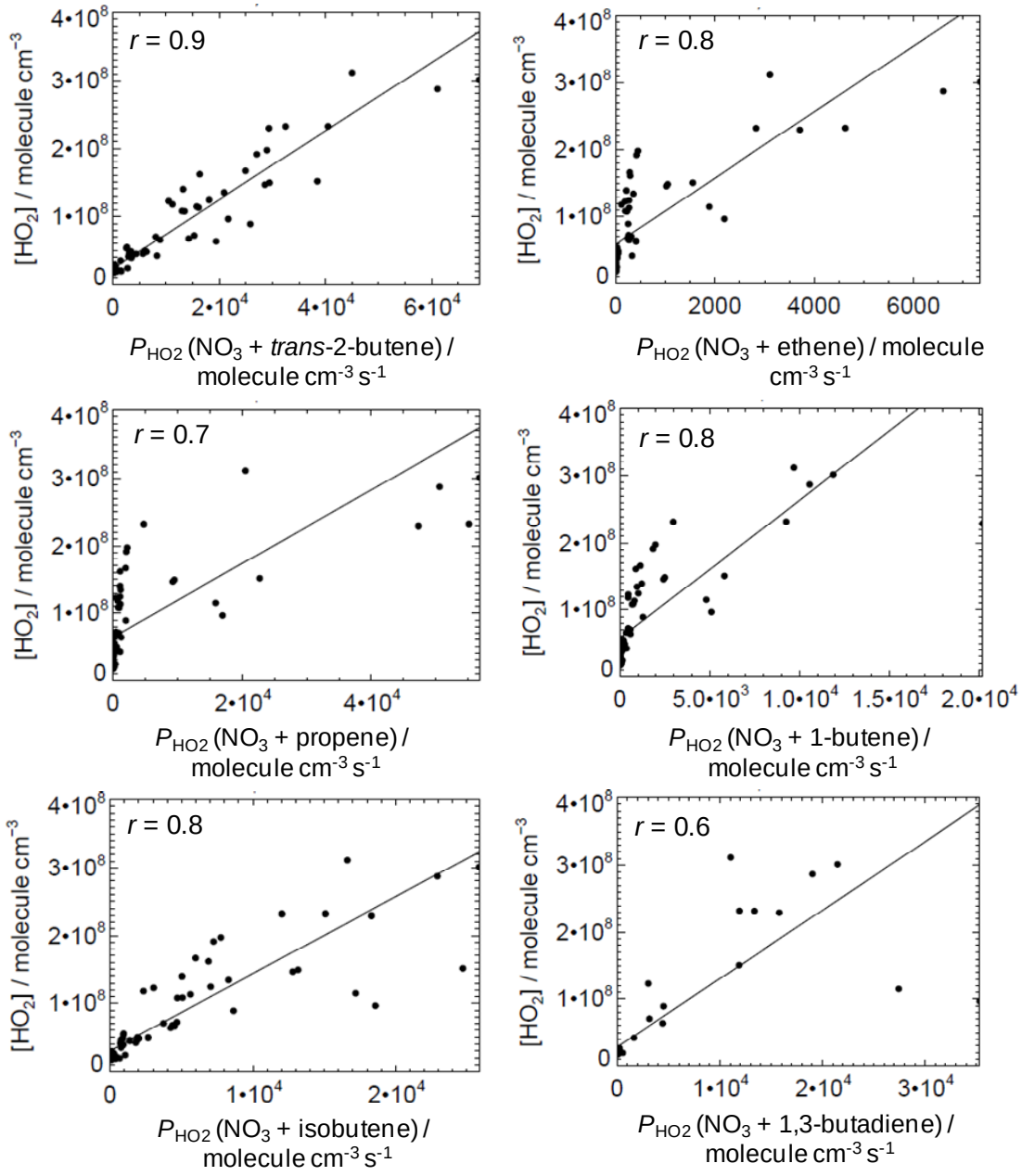

Figure 4.28. HO_2 versus rates of instantaneous production of HO_2 from reactions of NO_3 with alkenes during flight B537. Correlation coefficients (r) are given in each plot. Solid lines are lines of best fit to the data. Only alkenes with which a moderate or strong correlation was observed have been plotted.

4.6 Modelling approach

The observations of OH, HO_2, NO_3 and N_2O_5 have been interpreted in the context of nighttime oxidation chemistry using a box model. Model calculations have been run and interpreted by Dr Daniel Stone using the Dynamically Simple Model of Atmospheric Chemical Complexity (DSMACC) (Emmerson and Evans, 2009, Stone *et al.*, 2010, Stone *et al.*, 2013). The model is constrained to observations of VOCs, NO_x ($NO + NO_2$), O_3, CO and other species measured during the RONOCO flights, and is allowed to run to diurnal steady state. The model output includes concentrations of OH, HO_2, NO_3, RO_2, and other species. The chemistry scheme in the model is based on the Master Chemical Mechanism (MCM, version 3.2: Jenkin *et al.*, 1997, Saunders *et al.*, 2003, *via* http://mcm.leeds.ac.uk/MCM). The MCM is a near-explicit chemical mechanism which describes the tropospheric degradation of 143 VOCs. The DSMACC model used by Stone *et al.* (2013) is initiated with 657 chemical species. Data from daytime flights, or during dawn or dusk periods, were not included in the model analysis. Data from flight B537 were also excluded, owing to the atypical observations of HO_2, NO_3, O_3 and other chemical species made during this flight.

4.7 Model performance and results

Potential interferences from RO_2 radicals in FAGE measurements of HO_2 have been assessed in the modelling study. Modelled values of HO_2^* are reported, where $HO_2^* = HO_2 + fRO_2$. The factor f has been derived from the results of a laboratory study into RO_2 interferences in the Leeds Aircraft FAGE instrument (described in detail in Chapter 2), and use of MCM chemistry in the model to calculate the speciation of RO_2 radicals in the campaign data. For the RONOCO campaign, interferences in HO_2 measurements are calculated to be small, with $HO_2^* = [1.15 \times HO_2] + 2 \times 10^5$ cm^{-3}, on average. The model predicts a mean OH concentration of 2×10^4 molecule cm^{-3} for the summer flights, which is in agreement with the measured OH concentrations in that both numbers are below the instrument's limit of detection.

The model underpredicts HO_2^* and overpredicts NO_3 and N_2O_5, as shown in Figure 4.29. These discrepancies were investigated by determining the processes controlling radical production and loss in the model, and using those results to improve model performance. Figure 4.30 shows processes controlling instantaneous production (a) and loss (b) of HO_2 in the model. Production is dominated by reactions of RO + O_2 (42 %), with a significant contribution from OH + CO (31 %) despite low OH concentrations at night. Reactions with NO_3 (45 %) and O_3 (27 %) dominate HO_2 loss, with a further 17 % through reactions with RO_2 and HO_2. Production of OH at night is dominated by HO_2 + NO_3 (53 %) and HO_2 + O_3 (33 %). OH loss is dominated by reactions with CO (35 %), NO_2 (21 %), and CH_4 (12 %). Figure 4.31 shows the processes controlling production (a) and loss (b) of RO_x (= RO + RO_2 + OH + HO_2) radicals at night in the model, which gives a clearer picture of what dominates radical initiation than considering the production and loss of HO_2 only. Radical initiation is dominated by reactions of NO_3 with unsaturated VOCs (80 %), with a much smaller contribution (18 %) from alkene ozonolysis. Radical loss is dominated (21 %) by the reactions HO_2 + RO_2 and HO_2 + HO_2 to form peroxides. The decomposition of RO radicals to produce stable products, and the reaction of OH with NO_2, also make significant contributions to radical loss.

The model results indicate that HO_2 production is dominated by the reaction of RO radicals with O_2, and that the dominant source of RO radicals is the reaction of NO_3 with alkenes. These results are in general agreement with the results of the analysis presented in section 4.5.3, though the model predicts a more important role for NO_3 (80 % of RO_x radical production) than is predicted by the analysis based on the observations alone (68 % of HO_2 radical production during summer), and predicts a relatively small role for O_3 in radical initiation (18 % of modelled RO_x radical production compared to a minimum value of 32 % calculated using the observations). The model is constrained to measured values of O_3, but overpredicts NO_3. The mean measured NO_3 nighttime mixing ratio was 24.5 pptv in the summer and 8.2 pptv in the winter. The mean modelled summer and winter values are 37.4 pptv and 20.7 pptv, respectively. This discrepancy between modelled and measured NO_3 explains the model overprediction of the role of NO_3 in nighttime HO_x radical initiation. The model predicts that, despite low concentrations of OH, the reaction between OH and CO is an

important route to HO_2 production, in agreement with the the strong positive correlation observed between measured values of HO_2 and CO.

Improvement to the model predictions of NO_3, N_2O_5 and HO_2^* is made by increasing the concentration of unsaturated VOCs in the model. Increasing the total observed alkene concentration by 4 times resulted in a modelled to observed ratio of 1 for HO_2^* and of ~1.2 for NO_3 and N_2O_5. 2 dimensional gas chromatography (2D-GC) analysis of the whole air samples taken during RONOCO has revealed a large number of VOCs extra to those normally measured (Stone *et al.*, 2013). Calibration standards for these species are not yet available, and so quantification of their concentrations is not possible, but their detection confirms that the model overprediction of NO_3 and underprediction of HO_2^* are attributable to reactions of NO_3 with unquantified unsaturated hydrocarbons.

Overprediction of NO_3 and underprediction of HO_2 and RO_2 is a feature of previous nighttime radical studies in both forested and urban environments. For example, nighttime measurements of HO_2, RO_2 and NO_3 were made in the Black Forest, Germany, approximately 10 km distant from the city of Freiburg (Mihelcic *et al*., 1993). Measured anthropogenic VOCs were not sufficient to explain the measured RO_2 concentrations, and model underestimation of RO_2 by up to an order of magnitude coincided with overestimation of NO_3. The authors suggest that monoterpenes were responsible for the overestimation of NO_3 and the underestimation of RO_2 in the model. Ren *et al*. (2003b, 2006) report model underestimation of HO_2 during the PMTACS-NY summer 2001 and winter 2004 measurement campaigns in New York city. Emmerson and Carslaw (2009) report underprediction of OH, HO_2 and $[HO_2+\Sigma RO_2]$ for the TORCH field campaign near London. Finally, Brown *et al*. (2011) attribute missing NO_3 reactivity in sharp industrial plumes, measured during a flight downwind of the Houston Ship Channel in Texas, to unmeasured highly reactive VOCs.

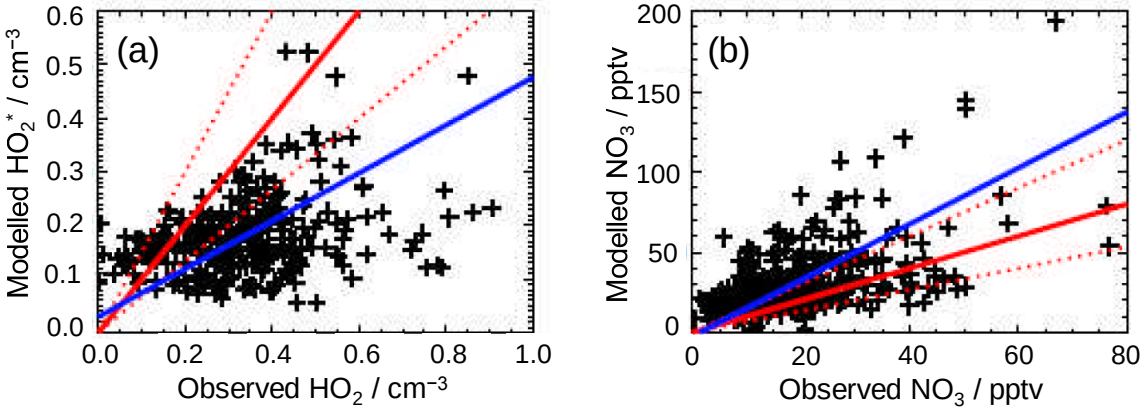

Figure 4.29. Comparison of modelled and observed concentrations of: a) HO_2; b) NO_3 for the base model run, with 1:1 line (solid red line), 50 % limits (broken red lines), and best fit line (blue). Figure supplied by Dr Daniel Stone, University of Leeds. Best fit lines are described by:

$[HO_2^*]_{mod} = [(0.45 \pm 0.07) \times [HO_2^*]_{obs}] + (2.95 \pm 2.23) \times 10^6$ cm^{-3} ($r = 0.10$);

$[NO_3]_{mod} = [(1.75 \pm 0.17) \times [NO_3]_{obs}] - (2.33 \pm 3.61)$ pptv ($r = 0.29$).

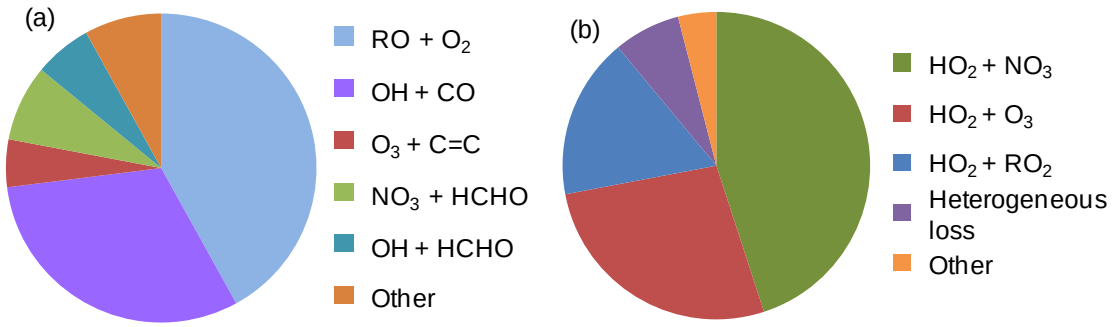

Figure 4.30. Processes controlling: a) instantaneous production; b) loss of HO_2 radicals at night in the model. Figure supplied by Dr Daniel Stone, University of Leeds.

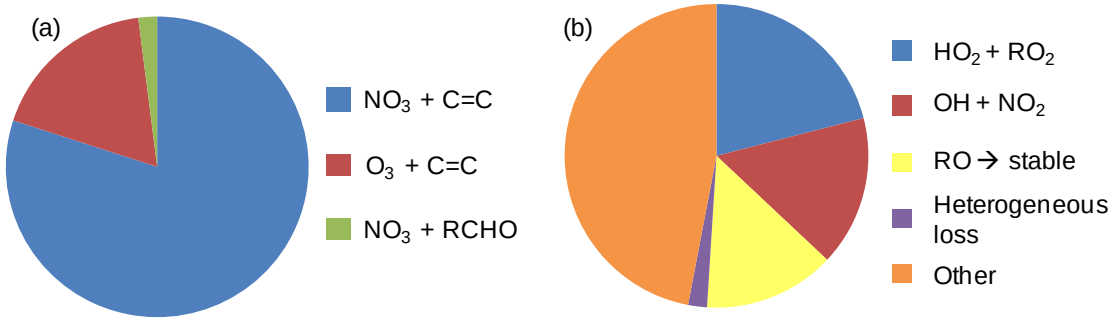

Figure 4.31. Processes controlling: a) Instantaneous production; b) loss of RO_x radicals (= RO + RO_2 + OH + HO_2) in the model. Figure supplied by Dr Daniel Stone, University of Leeds.

The presence of unmeasured unsaturated VOCs during the RONOCO campaign, suggested by the model and confirmed by the 2 dimensional GC analysis, has implications for the conclusions drawn from the analysis of observations. The relative contributions of NO_3 and O_3 to nighttime radical initiation will change with the composition of unsaturated VOCs in the sampled air, due to the different rates of reaction of NO_3 and O_3 with different VOC species, and the rates of production of HO_2 following these reactions. The model results indicate that reaction of NO_3 with the unmeasured VOCs leads to increased production of HO_2, suggesting that the role of NO_3 in nighttime radical production would be enhanced by the inclusion of the unmeasured VOCs in the observational analysis.

4.8 Conclusions

Nighttime radical chemistry has been studied as part of the RONOCO and SeptEx campaigns onboard the BAe-146 research aircraft during summer 2010 and winter 2011. NO_3, N_2O_5, OH and HO_2 were measured simultaneously for the first time from an aircraft, with OH and HO_2 being measured by the University of Leeds aircraft FAGE instrument. OH was detected above the limit of detection during the daytime SeptEx flights only, with a mean concentration of 1.8×10^6 molecule cm^{-3}. Upper limits of 1.8×10^6 molecule cm^{-3} and 6.4×10^5 molecule cm^{-3} are placed on mean OH concentrations for the summer and winter RONOCO measurement campaigns, respectively. During SeptEx, the highest OH concentrations were measured at altitudes less than 500 m, and concentrations decreased with decreasing altitude. HO_2 was detected above the limit of detection during the summer and winter RONOCO flights and during SeptEx, with a maximum mixing ratio of 13.6 pptv measured during nighttime flight B537 on 20th July 2010. Mean HO_2 mixing ratios were highest during daytime SeptEx flights. Mean nighttime HO_2 mixing ratios were significantly higher in summer than in winter. The highest HO_2 mixing ratios were observed at altitudes less than 1.0 km. The nighttime HO_2 altitude profile shows a slight increase with altitude between 0 and 1.25 km, and a decrease between 1.25 and 3.25 km. Significant concentrations (up to 176.9 pptv) of NO_3 were measured during nighttime flights, since the air masses sampled were sufficiently removed from the surface that the loss of NO_3 by reaction with NO was minimised. The RONOCO flights were therefore an excellent

opportunity to study the role of NO_3 in nocturnal oxidation and radical initiation, as set out in the aims of the project.

The rates of reaction of O_3, NO_3 and OH with the alkenes measured have been calculated. At night during summer, NO_3 dominated alkene reactivity. Several previous nighttime studies have also found NO_3 to be the dominant nocturnal oxidant (*e.g.* Geyer *et al.*, 2003, Brown *et al.*, 2011). During nighttime winter RONOCO flights the total rates of reaction of NO_3 with alkenes was much reduced, but the rate of reaction of O_3 with alkenes was similar to that in summer. During day and night in winter, O_3 + alkene reactions were significantly faster than both NO_3 + alkene and OH + alkene reactions. Overall, during RONOCO, the combined rate of alkene oxidation by O_3 and NO_3 was highest at night during summer.

Calculation of rates of instantaneous production of HO_2 from reactions of O_3 and NO_3 with alkenes, using measurements made during the flights, has revealed that nighttime production was dominated by NO_3 in summer and by O_3 in winter. The rate of instantaneous production of HO_2 from reactions of NO_3 with alkenes decreased significantly from summer to winter (85 %), whereas production from O_3 + alkene reactions was similar in summer and winter, decreasing by just 23 %. Strong positive correlation between HO_2 and NO_3, especially during flight B537, is attributed to the production of HO_2 from reactions of NO_3 with alkenes, particularly *trans*-2-butene and other isomers of butene.

Significant concentrations of HO_2 were detected at night, with the highest HO_2 concentration (13.6 pptv) being measured during a summer nighttime flight, indicating that HO_x radical chemistry remains active at night under the right conditions. The role of HO_x appears to be diminished in the low photolysis winter daytime atmosphere, with alkene ozonolysis being primarily responsible for oxidation and radical initiation, in agreement with previous studies (*e.g.* Heard *et al.*, 2004, Emmerson *et al.*, 2005). Both the analysis presented here and the results of the box modelling study by Stone *et al.* (2013) indicate that in air masses removed from sources of NO, NO_3 plays an important role in the oxidation of alkenes and radical initiation at night, in agreement with previous studies (*e.g.* Brown *et al.*, 2011). Alkene ozonolysis also plays a significant

role in nocturnal oxidation in agreement with Salisbury *et al.* (2001), Geyer *et al.* (2003), Ren *et al.* (2006), and others. The balance between the roles of NO_3 and O_3 was controlled in part by [NO_3], with colder winter temperatures forcing the NO_3–N_2O_5 equilibrium towards N_2O_5. The total rate of reaction of O_3 and NO_3 with alkenes during nighttime summer flights (~ 1.39×10^5 molecule cm^{-3} s^{-1}) was comparable to the total rate of reaction of O_3 and OH with alkenes during daytime SeptEx flights (~ 1.57×10^5 molecule cm^{-3} s^{-1}). Whilst it should be remembered that the measurements at different times of day and in different seasons were sampling entirely different air masses, this result supports the hypothesis that oxidation of VOCs in the nocturnal summer atmosphere can be as rapid as in the daytime atmosphere.

A box model of nighttime chemistry constrained to measurements of long lived species has been used to investigate the nighttime chemistry sampled during RONOCO (Stone *et al.*, 2013). Production of HO_2 in the model is dominated by reactions of RO + O_2 (from RO_2 radicals generated in NO_3 + alkene reactions), and OH + CO. HO_2 loss is dominated by HO_2 + NO_3 and HO_2 + O_3. RO_x loss is dominated by HO_2 + RO_2 and HO_2 + HO_2 reactions. At night, NO_3 is important in both radical initiation and propagation, and therefore fills the role of OH and NO during the day.

The base model underpredicts HO_2 and overpredicts NO_3. These discrepancies were minimised by increasing the concentration of alkenes in the model, thereby increasing reaction of NO_3 with alkenes, and production of HO_2. The presence of unmeasured unsaturated VOCs during the RONOCO campaign, suggested by the model and confirmed by 2 dimensional GC analysis, has implications for the conclusions drawn from the analysis based on the observations. The relative contributions of NO_3 and O_3 to nighttime radical initiation will change with the composition of unsaturated VOCs in the sampled air, due to the different rates of reaction of NO_3 and O_3 with different VOC species, and the rates of production of HO_2 following these reactions. The model results indicate that reaction of NO_3 with the unmeasured VOCs leads to increased production of HO_2, suggesting that the role of NO_3 in nighttime radical production would be enhanced by the inclusion of the unmeasured VOCs in the observational analysis.

Chapter 5. Measurements of reactive iodine in the Western Pacific marine boundary layer

5.1 Motivation for the SHIVA project

Halogenated very short-lived substances (VSLS) such as dibromomethane (CH_2Br_2), bromoform ($CHBr_3$), and methyl iodide (CH_3I) are emitted from the oceans by marine species such as macroalgae (seaweed) and phytoplankton (photosynthesising microscopic algae) and contribute to halogen loading and ozone depletion in the troposphere and lower stratosphere (see section 1.4 in Chapter 1). *In situ* measurements of VSLS in the marine boundary layer and aloft are sparse, and the measurements that exist may not be representative of global emissions and concentrations (*e.g.* Quack and Wallace, 2003, Quack *et al.*, 2007, Palmer and Reason, 2009). In order for models to accurately predict the effect of halogens on stratospheric ozone, there must be a robust understanding of their emission rates, distribution, transport and processing.

The SHIVA (Stratospheric Ozone: Halogen Impacts in a Varying Atmosphere) project (EU project reference SHIVA-226224-FP7-ENV-2008–1) aims to address these problems through comprehensive fieldwork and modelling studies. Key aims are to reduce uncertainties in the amount of halogenated VSLS reaching the stratosphere, the associated ozone depletion, and the effects of a changing climate on these processes. To enable this, the SHIVA fieldwork combined ship-borne, aircraft-based and ground-based measurements in and over the South China Sea and the Sulu Sea, and around the coast of Malaysian Borneo. The SHIVA project has focussed on quantifying 'missing' sources of stratospheric bromine. The 2006 report Scientific Assessment of Ozone Depletion prepared by the World Meteorological Organization concluded that there was substantially more Br_y (total inorganic bromine) in the stratosphere than could be accounted for by the contribution from halons (long-lived bromine-containing alkanes) and methyl bromide (CH_3Br) alone (Law and Sturges, 2007).

Brominated VSLS have been found to contribute a small but significant amount of bromine to the stratosphere (Dorf *et al.*, 2006). The latest figure for this contribution is 6 pptv, with a range of 3−8 pptv (Montzka and Reimann, 2010). These values are derived from photochemical modelling based on balloon-borne and ground-based measurements of BrO, with the contribution from halons and methyl bromide also taken into account. The maximum BrO measurements were made by ground-based UV-Visible spectroscopy at Harestua, Norway (Hendrick *et al.*, 2008) and indicate a possible 7 pptv contribution from brominated VSLS. One aspect of the SHIVA project is to further constrain the contribution to stratospheric bromine from brominated VSLS, to account for the concentrations of BrO that have been observed.

5.1.1 The importance of the Western Pacific

The efficiency of VSLS to deplete stratospheric ozone (the ozone depletion potential, ODP) depends in part on the fraction of the species emitted at the surface that reaches the stratosphere, which is determined by emission, chemical and physical processing, and transport (Brioude *et al.*, 2010). The local lifetimes of VSLS vary between different locations because of variation in solar actinic flux and, therefore, rates of photolysis and reaction with OH (Brioude *et al.*, 2010). Convective and large-scale transport of VSLS from the surface to the tropical tropopause layer (TTL) is not well represented in global models (*e.g.* Lin *et al.*, 2012), and is dependent on location and season. These factors are the motivation for measurements of VSLS and their products in regions of strong emissions and rapid vertical transport, such as the Western Pacific (*e.g.* Pisso *et al.*, 2010).

5.1.1.1 Emissions

Palmer and Reason (2009) calculated that the tropical oceans account for 73.6 ± 46 % of the global bromoform flux, highlighting the importance of production by phytoplankton in open-ocean regions, and the relative unimportance of coastal regions with emissions from macroalgae, since there are few areas of macroalgae growth in the tropics. The authors note that the high uncertainty surrounding this calculation stems from the sparsity of open-ocean measurements of sea surface bromoform concentrations. Results from scientific cruises over ten years reveal that the Pacific Ocean is a stronger source

of $CHBr_3$ to the marine boundary layer than the Atlantic Ocean (Butler *et al.*, 2007). These results are supported by a modelling study by Tegtmeier *et al.* (2012), who found that the Western Pacific was an important source region for $CHBr_3$. The model was based on measurements made during the TransBrom cruise in the tropical Western Pacific.

5.1.1.2 Transport

Transport of halogenated VSLS into the stratosphere occurs mainly in the tropics, where ascending warm air carries them aloft. The tropical marine environment is therefore an important region in which to study the effects of these short-lived halogen species on ozone depletion. Transport from the TTL to the stratosphere takes place primarily *via* large-scale horizontal and slow vertical motion, with a timescale of weeks, with a smaller contribution from infrequent overshooting convective airmasses reaching through the TTL into the stratosphere (Fueglistaler *et al.*, 2009, Montzka and Reimann, 2010). The rate of transport through the TTL varies throughout the year, and peaks in the Western Pacific during northern hemisphere winter (Fueglistaler *et al.*, 2005, Law and Sturges, 2007). Several modelling studies (Levine *et al.*, 2007, Aschmann *et al.*, 2009, Hosking *et al.*, 2010, Pisso *et al.*, 2010) have shown that transport of VSLS to the stratosphere is most likely in the Western Pacific and Southeast Asia.

Trajectory calculations by the UK Met Office dispersion model, NAME, were performed prior to the SHIVA fieldwork campaign to aid flight planning in order to maximise the chance of sampling VSLS in air transported from the surface (Ashfold *et al.*, 2012). Air masses arriving at the lower TTL (below 15 km) were likely to have originated in the Western Pacific boundary layer (below 1 km) in the previous 15 days. In contrast to the results discussed above, few air masses above 16 km were found to have travelled from below 1 km in the previous 15 days, indicating a limited influence of boundary layer VSLS on upper tropospheric/lower stratospheric composition in the model. However, the authors found year-to-year variability, with enhanced transport above 15 km during La Niña conditions (cold Eastern Pacific surface waters, associated with low surface air pressure in the Western Pacific), with 2011 being a La Niña year (NOAA, 2013).

5.1.2 Emission, chemistry and transport of VSLS in future climates

Future climate changes could influence the emission, transport and chemical processing of VSLS, and therefore their stratospheric ozone depletion potential (Montzka and Reimann, 2010). One of the aims of the SHIVA project is to reduce the uncertainty associated with the emission and transport of VSLS in future climates. One means of reducing these uncertainties is to make measurements in those areas that have seen relatively few observations, and which are thought to be important to the global halocarbon flux from the oceans. The Western Pacific is one such area.

Instantaneous sea-to-air flux of a gas is determined by sea surface temperature (SST), which determines solubility and diffusivity of the gas, and wind speed, which drives transfer from the ocean to the atmosphere (Butler *et al.*, 2007). Increasing SST in a warming climate, amongst other factors such as plankton biomass (Schmitter *et al.*, 2008), could therefore change the flux of VSLS from the oceans to the atmosphere (Kloster *et al.*, 2007, Montzka and Reimann, 2010). Dessens *et al*. (2009) modelled the impact of the change in delivery of brominated VSLS into the lower stratosphere on stratospheric ozone. Increased temperatures led to more intense convection, which resulted in increased transport of bromine from the surface to the upper troposphere. Stratospheric bromine increased by 1 to 2 pptv, an increase of ~ 10 % above current levels, which led to an ozone reduction of approximately 8 % at the tropopause. Though not a large change, this is considered to be significant. Pyle *et al*. (2007) also found that changes in atmospheric circulation, in particular increased intensity of convection, could lead to small increases in tropospheric stratospheric bromine. Hossaini *et al*. (2012) have modelled source gas injection of bromocarbons into the stratosphere, and predict an increase of approximately 1 pptv between the years 2000 and 2100. The increased input of VSLS into the stratosphere is attributed to increased convective uplift of $CHBr_3$ in a warmer troposphere.

5.2 Details of the SHIVA field campaign

The SHIVA project involved an intensive measurement campaign in the Western Pacific during September to December 2011. Ground-based measurements of atmospheric concentrations of halogenated VSLS, longer lived chlorofluorocarbons (CFCs) and transport tracers, IO, BrO, O_3, NO_2, HCHO and CHOCHO, along with meteorological parameters, were made at Tawau, Sabah (4.28° N, 117.91° E) and Semporna, Sabah (4.48° N, 118.62° E). Coastal studies of halocarbon emissions by macroalgae were made at Pangkor Island, Perak (4.22° N, 100.56° E), Port Dickson, Negeri Sembilan (2.52° N, 101.80° E), and the Morib mangroves, Selangor (2.75° N, 101.45° E). A 14 day scientific cruise 'SO218' was undertaken onboard the RV *Sonne* between Singapore (1.37° N, 103.75° E) and Manila, Philippines (14.58° N, 121.00° E), between the 15th and 29th November. The cruise is described in more detail below. Measurements of VSLS, IO, BrO, and various trace gases including O_3, NO_2, and CO, along with physical atmospheric parameters, were made onboard the DLR (Deutsches Zentrum für Luft- und Raumfahrt e.V., German Aerospace Center) Falcon D-CMET research aircraft. Sixteen flights were conducted around Borneo and the South China Sea, from an airfield in Miri, Sarawak, Malaysia (4.34° N, 113.99° E). During two flights the aircraft flew over the *Sonne* and close to the ocean surface (approximately 15 m above sea level) to provide a complete profile from the sea surface to the upper troposphere. Finally, measurements of atmospheric and oceanic concentrations of halocarbons, oceanic chlorophyll and nutrient concentrations, phytoplankton speciation and abundances, and physical oceanic parameters were made onboard local boats, departing from Port Dickson, Kuching, Sarawak (1.55° N, 110.34° E), Kota Kinabalu, Sabah (5.98° N, 116.12° E) and Semporna. Two of the local boat journeys, on 19th and 23rd November, were from the coast to the RV *Sonne* to enable profiling of atmospheric and oceanic constituents from the shore to the ocean.

The field measurements were supported by laboratory studies at the University of Malaya (UM) in Kuala Lumpur, the University of Malaya Sabah (UMS), the University of Malaya Sarawak (UNIMAS), and the University of East Anglia, UK, by space-borne observations of ocean colour, IO and BrO from the MERIS and SCIAMACHY instruments onboard the European Envisat satellite, and by chemistry and transport

modelling using the FLEXPART (Stohl *et al.*, 2005), HYSPLIT (Draxler and Hess, 1997, Draxler and Hess, 1998, Draxler, 1999) and TOMCAT/SLIMCAT (Chipperfield, 2006) models. Meteorological data was provided by regional weather forecasts from the European Centre for Medium-Range Weather Forecasts (ECMWF) and other publicly-available weather forecasts, by radio sondes launched at regular intervals during the measurement campaign, and by radar imagery from the Malaysian Meteorological Department (MMD).

5.2.1 Scientific cruise SO218 onboard RV *Sonne*

The aims of cruise SO218 were to investigate tropical trace gas emissions in the South China Sea and the Sulu Sea and to assess the contribution of trace gases to stratospheric halogen loading. To this end, a suite of oceanic and atmospheric measurements was made onboard the German Research Vessel (RV) *Sonne*, a converted fishing trawler, equipped mainly for geophysics and multidisciplinary oceanography. The ship has space for 25 crew members and 25 scientists. During cruise SO218 in the SHIVA project instruments were housed and operated in indoor laboratory space and on deck. A submersible water pump enabled underway water samples to be taken throughout the cruise. A winch enabled deployment of a 'CTD' (conductivity, temperature and depth) instrument, combined with a bottle rosette sampling system for collecting samples throughout the depth of the water column. Measurements of halocarbon concentrations were made in the atmosphere and in ocean water samples. Chlorophyll, phytoplankton, pigments, nutrients and zooplankton were measured in water samples. Atmospheric measurements of gas-phase species included the radicals IO, BrO, and Br, iodine atom sources I_2 and the sum of HOI + ICl, and the trace gases HCl, HBr, SO_2, NO_2, CH_4, O_3, H_2O, CO_2 and CO. Ozone sondes and radio sondes were released from the ship at regular intervals. Details of the instruments onboard during cruise SO218, the species or parameters measured, and their operators, are given in Table B1 and Table B2 in Appendix B.

The cruise began at 20:00 (local time, UTC + 8h) on 15th November in Singapore, and finished at 08:44 (local time) on 29th November in Manila, Philippines. The cruise track is shown in Figure 5.1.

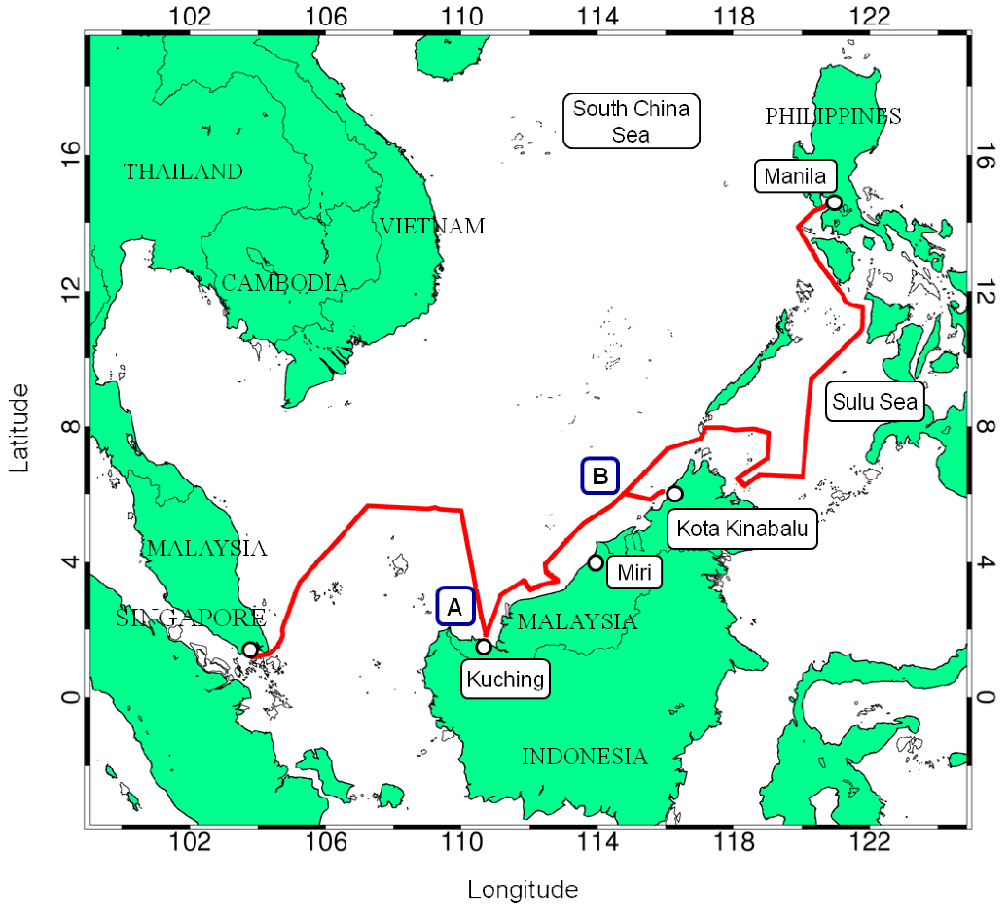

Figure 5.1. Map of SO218 cruise track (red line) between Singapore and Manila in November 2011. Points A and B mark position of 24 hour stationary 'diurnal stations' near Kuching and Kota Kinabalu, respectively.

The cruise track was designed to enable measurements of halocarbons in various biogeochemical regimes, such as coastal, coral reef, oceanic upwelling, river outflow, and open ocean regions. Modification of the ideal cruise track was necessary to avoid dangers presented by shallow water, coastal fishing activity, and oil and gas platforms, as well as the threat of piracy. Constraints were also placed on the cruise track by restrictions governing passage through disputed waters. The actual cruise track enabled sampling in and over coastal and open ocean waters (coast of Borneo and the South China Sea), near river outflows (Kuching), and in regions with high oceanic chlorophyll concentrations. Measurements of oceanic and atmospheric constituents made onboard local boats provided a profile from the shore to the coastal and open ocean environment.

The air temperature during the cruise varied between 24.2° C and 31.7° C. The minimum and maximum atmospheric pressures were 1002.6 mb and 1010.4 mb,

respectively. Wind speed varied from 0.01 m s^{-1} to 18.3 m s^{-1}. A time series of wind direction for the whole cruise is shown in Figure 5.2. The wind direction was generally northerly between 15th and 17th November, southwesterly to northwesterly between 17th and 19th November, and northeasterly for the remainder of the cruise. Measurements of air temperature, pressure, humidity, wind speed and wind direction were made continuously during the cruise, and are shown as a time series for each day in the Supplementary Information.

Air mass trajectories were calculated by S. Fuhlbrügge of IFM-GEOMAR (Leibniz-Institut für Meereswissenschaften, Germany) using the NOAA Air Resources Laboratory (ARL) Hybrid Single Particle Lagrangian Integrated Trajectory (HYSPLIT) model (Draxler and Hess, 1997, Draxler and Hess, 1998, Draxler, 1999, Draxler and Rolph, 2013, Rolph, 2013) based on NCEP/NCAR 1948–present reanalysis data (Kalnay *et al.*, 1996). 3-day backward trajectories for cruise SO218 are shown in Figure 5.3. The top panel (a) shows a map of the cruise with the ship's track in white. The coloured tracks represent the trajectories of air masses reaching the ship at 00:00 and 12:00 UTC on each day of the cruise (08:00 and 20:00 local time), with the colour representing the date on which the air mass reached the ship. The triangles indicate the position of the air mass at the start of the three days. Between the 15th and 17th of November (dark blue), the ship was cruising to the north of the Natuna Islands in the South China Sea, and the 3-day air mass origin was to the north east, in the South China Sea. Between the 17th and 19th November (mid blue), the ship was navigating along the northern coast of Borneo, and the air mass origin was to the south west, north and west of Borneo in the South China Sea. For the remainder of the cruise (light blue to dark red), during which time the ship continued along the northern coast of Borneo and through the Sulu Sea to Manila, air masses reaching the ship originated over the Western Pacific, to the north east. 5-day back trajectories show similar patterns, with air masses from the 20th to the 29th of November originating south of China, passing over the open Western Pacific Ocean and the Philippines, before reaching the ship. The bottom panel (b) shows the height above sea level of the air masses during the three days prior to reaching the ship, with air masses in the later part of the cruise having spent longest near the surface.

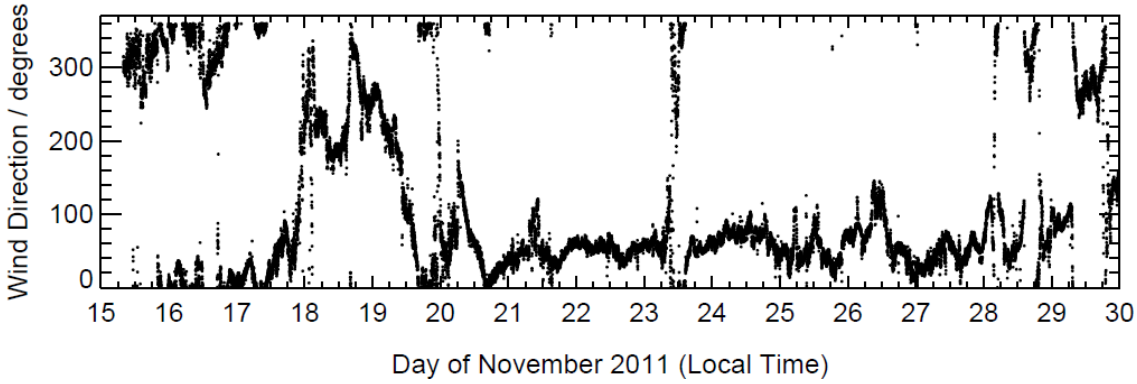

Figure 5.2. Time series of wind direction during cruise SO218.

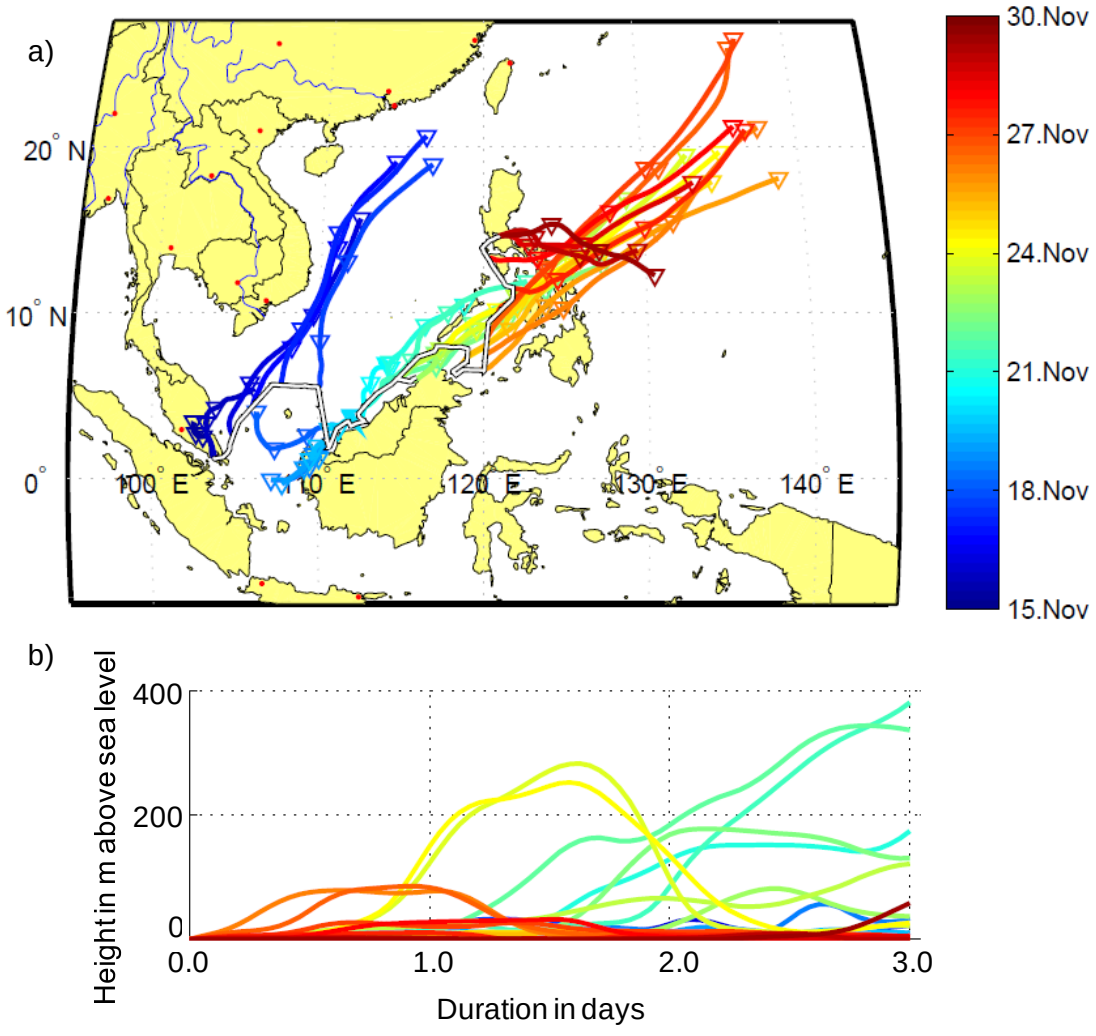

Figure 5.3. a) HySplit 3-day backward trajectories for cruise SO218 based on NCEP/NCAR reanalysis data. The cruise track is shown as a white line. The triangles represent the starting point for the air mass, and the coloured lines indicate the trajectory before meeting the ship. The calculations were started every day at 00:00 and 12:00 UTC (08:00 and 20:00 local time). The colours of the trajectories indicate the day on which the air mass reached the ship, as shown in the colour bar on the right hand side of the plot. b) HySplit 3-day backward trajectories shown as a function of height above sea level during the three days prior to reaching the ship. Plots prepared by Steffen Fuhlbrügge, IFM-GEOMAR, Germany.

Measurements of O_3 and NO_2 were made by a commercial UV O_3 analyser (Thermo Electron 49C) operated by DLR and University of Malaya Sabah (UMS), and the University of Heidelberg cavity-enhanced DOAS instrument (described in section 5.3.3), respectively. A time series of O_3 for the whole cruise is given in Figure 5.4. The mean and maximum O_3 mixing ratios were 25.4 ppbv and 76.1 ppbv, respectively. O_3 levels increased with increasing proximity to Manila, a large and heavily polluted city, on the 28th and 29th of November. This feature is matched in the NO_2 data (see Figure 5.5).

A time series of NO_2 for the whole cruise is given in Figure 5.5a. The mean and maximum NO_2 mixing ratios were 0.59 ppbv and 21.5 ppbv, respectively, with typical values, shown in Figure 5.5b, ranging between 100 and 400 pptv. For comparison, mean NO_2 mixing ratios measured during a seasonal study of tropical marine boundary layer air at Cape Verde ranged from 13.7 pptv in clean, Atlantic marine air to 43.0 pptv in continental African air, which had passed over large cities and shipping regions (Carpenter *et al.*, 2010). The air encountered during cruise SO218 was therefore not clean, marine air but was likely influenced by industry on land, by shipping in the South China Sea, and by oil and gas platforms along the northern coast of Borneo and around the Philippines. Measurements of NO_2 can indicate when emissions from the ship's stack are being sampled by instruments onboard, with sharp 'spikes' in the data indicating a very local source of NO_2, and broader features indicating a distant source. The NO_2 data suggest that the ship's stack occasionally influenced measurements on the monkey deck and on the bridge. However, measurements of NO_2 from the 2007 RHaMBLe cruise in the tropical Atlantic Ocean, were on the order of 350 ppbv when sampling fresh ship exhaust (Commane, 2009), indicating that the influence of the ship's exhaust during the SHIVA cruise SO218 was relatively small. Time series of O_3 and NO_2 for each day of the SHIVA cruise are given in the Supplementary Information.

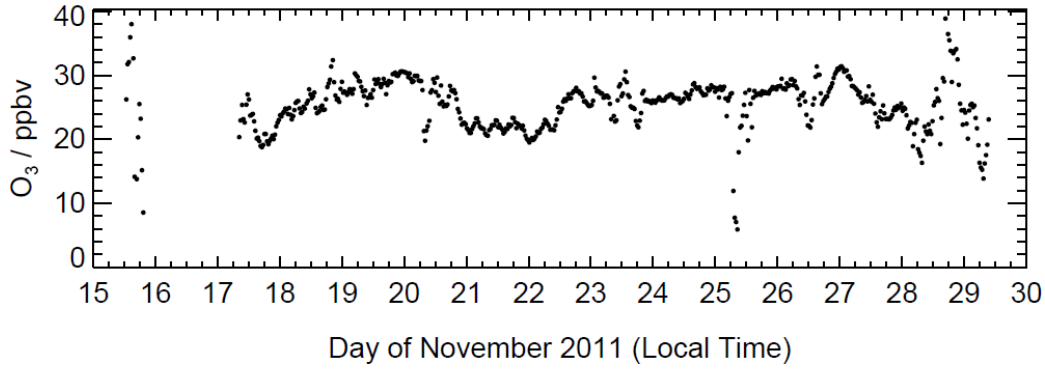

Figure 5.4. Time series of 30 minute averaged O_3 data during cruise SO218.

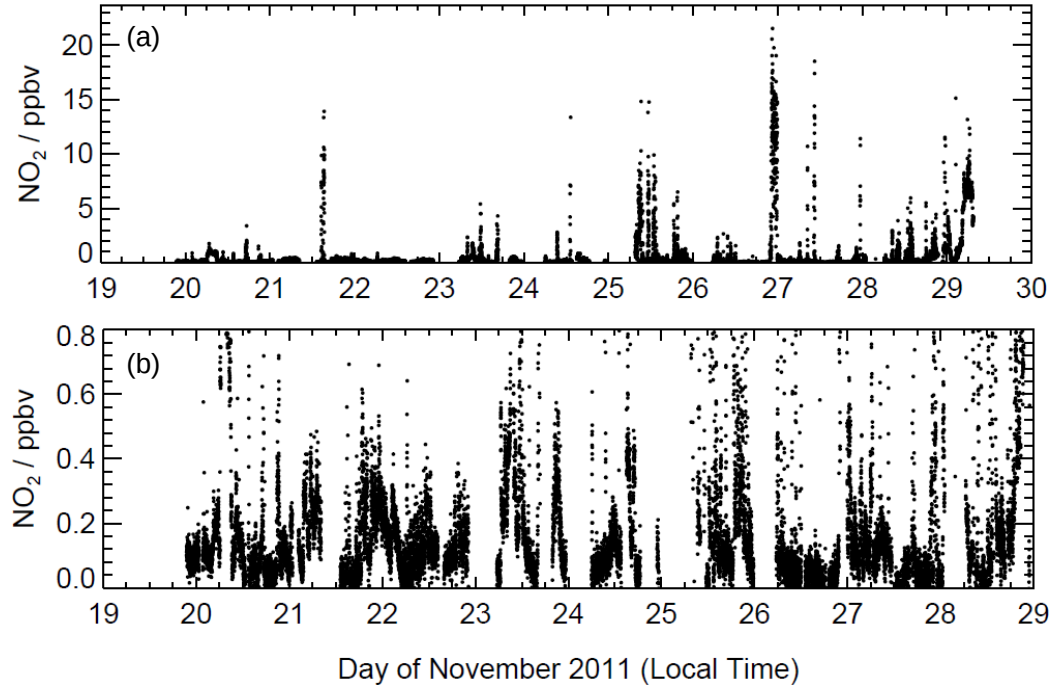

Figure 5.5. a) Time series of 30 second averaged NO_2 data during cruise SO218, showing full range of mixing ratios measured. b) Time series of NO_2 showing typical values without short-lived high NO_2 events. Time series for each day in the cruise are given in the Supplementary Information.

5.3 Measurements of iodine monoxide during cruise SO218

IO was measured by three instruments onboard the RV *Sonne* during the SHIVA cruise: the University of Leeds IO Laser-Induced Fluorescence instrument, the University of Bremen Multi-Axis DOAS instrument, and the University of Heidelberg Cavity-Enhanced DOAS instrument. These instruments are described briefly in this section. Figure 5.6 shows the positions of the three instruments onboard the RV *Sonne* during the cruise.

5.3.1 Leeds IO Laser-Induced Fluorescence instrument

The Leeds IO laser-induced fluorescence instrument (described in detail in Chapter 3) was housed in a 10 ft × 8 ft specially-modified shipping container on the front deck of the ship, along with two DLR CIMS instruments. A circular hole in the roof of the container enabled the inlet of the LIF instrument to sample air outside the container (approximately 15 m above sea level) without the need for sampling lines, thereby minimising loss of IO radicals before the fluorescence region. A stainless steel extended inlet was constructed to enable this arrangement, as shown in Figure 5.7. Only the inlet was located above the roof of the container. The fluorescence cell, laser fibre collimator, photodiode and photomultiplier tube were all located below the container roof, as shown in Figure 5.8. The instrument rack was installed on the floor of the container and fixed into position on rails. Laser light was delivered to the fluorescence cell *via* optical fibres. The vacuum oil pump was located in a deck store next to the container, so the pumping line extended from the connection at the end of the fluorescence cell, through a port in the container wall, a short distance across the deck, and through a vent in the wall of the deck store. The long pumping line did not significantly affect the pressure inside the cell.

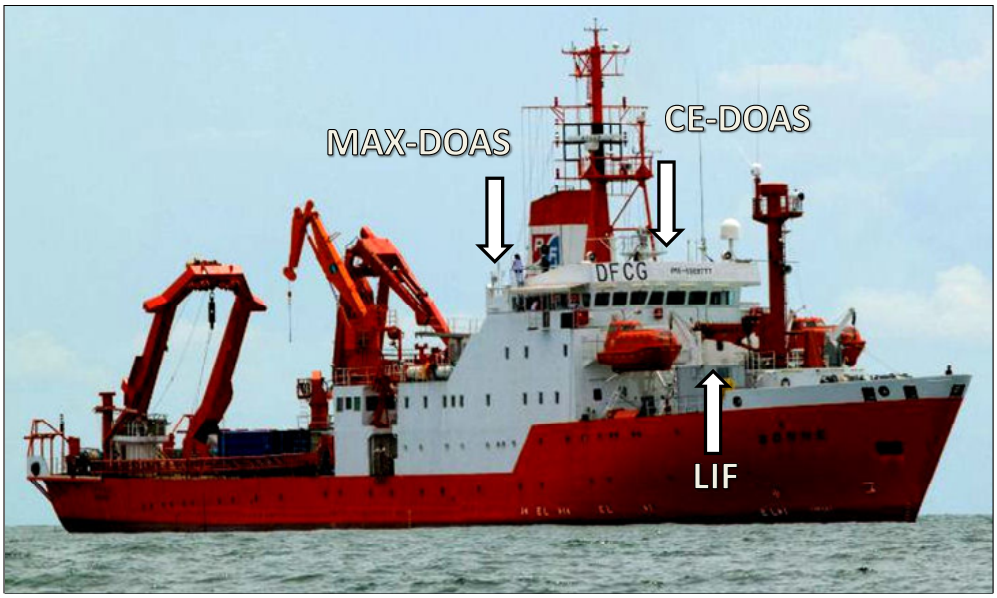

Figure 5.6. RV *Sonne* in the South China Sea during the SHIVA cruise SO218, November 2011. White arrow labelled 'LIF' indicates the location of the 10 ft shipping container on the front deck of the ship, housing the Leeds LIF instrument and two DLR CIMS instruments. The CE-DOAS instrument and the MAX-DOAS instrument were located on the 'monkey deck' above the bridge. I_2 and HOI + ICl samples were taken on the front deck, on the port side, approximately beneath the lifeboat. Photograph by Johannes Lampel, University of Heidelberg.

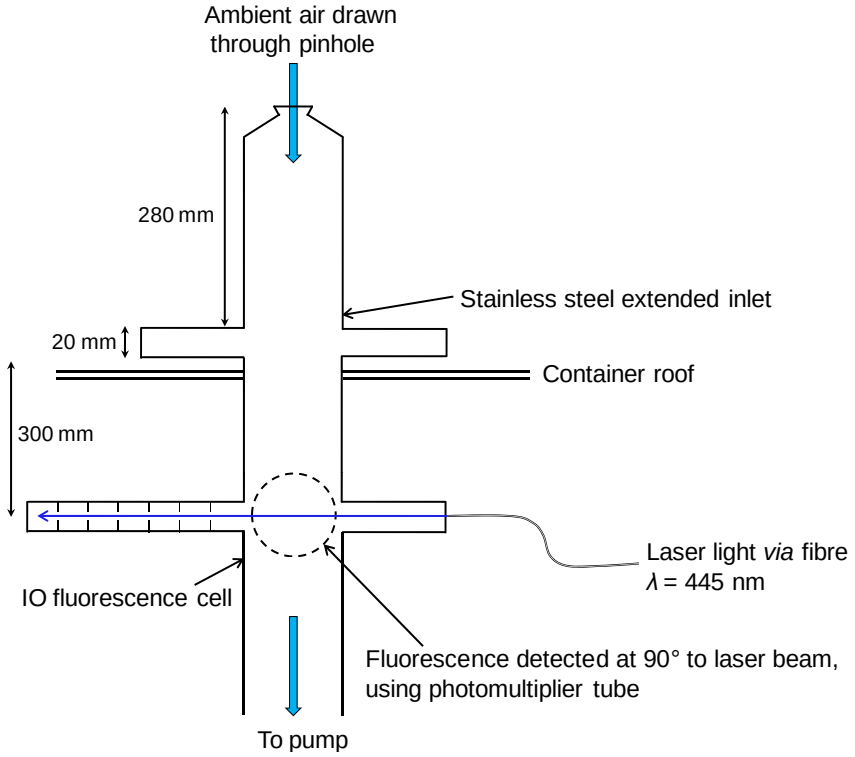

Figure 5.7. Schematic of the installation of the Leeds IO LIF instrument inlet and fluorescence cell in the roof of the container, showing the inlet extending above the roof, and the rest of the detection cell below the roof. Further details are given in Chapter 3.

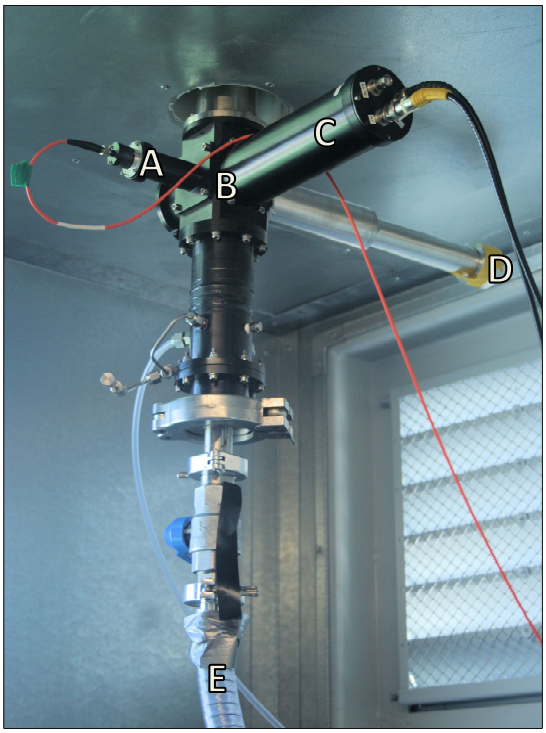

Figure 5.8. The Leeds IO LIF instrument fluorescence cell showing the fibre collimator (A), fluorescence region (B), photomultiplier tube (C), photodiode arm (D), and pumping line (E) installed beneath the roof of the container, with the stainless steel inlet extending above the roof visible towards the top of the picture.

5.3.2 University of Bremen Multi-Axis Differential Optical Absorption Spectroscopy (MAX-DOAS) instrument

The MAX-DOAS instrument consists of a small telescope, containing a quartz lens that collects scattered sunlight. The telescope is mounted on a stepper motor-controlled pan-and-tilt head that enables the telescope to point in any direction. The sunlight is focussed through the lens onto an array of quartz optical fibres, which transmits the light to a spectrograph, where the light is separated into a frequency-resolved spectrum. The spectrum is recorded by an array of detectors. For tropospheric measurements, the telescope points at low viewing angles, relative to the horizon. When deployed on a research vessel, the spectra and the pitch and roll of the ship are recorded with a high time resolution (10 s^{-1}) so that the actual viewing angle can be adjusted accordingly. During cruise SO218 the telescope was mounted on railings at the starboard side of the upper deck (position indicated in Figure 5.6), approximately 30 m above sea level. The

telescope and optical fibres are shown in Figure 5.9. The MAX-DOAS technique is described in more detail in Chapter 3. The instrument was operated from the 17th to 29th November. Since the measurement technique depends on scattered sunlight, the instrument does not operate at night. Measurements in the boundary layer were taken at the lowest elevation angle (2^{o}), corresponding to a layer immediately above the sea surface approximately 200 m deep. The measurements were averaged over 15 minutes, giving limits of detection between 0.3 and 0.7 pptv.

5.3.3 University of Heidelberg Cavity-Enhanced DOAS instrument

The DOAS technique utilises long absorption path lengths (several kilometres) to achieve the sensitivity required to measure trace gas species, which means *in situ* or 'point' measurements are not possible. The cavity-enhanced DOAS technique achieves long absorption light paths in a compact instrument (<2.0 m length) to give selective, sensitive, *in situ* measurements (Pöhler *et al.*, 2012). The instrument is relatively light-weight and portable, and during cruise SO218 during the SHIVA project was installed on the 'monkey deck' of the ship (position shown in Figure 5.6), approximately 30 m above sea level. The cavity mirrors were each housed in an aluminium case, supported by a tripod, to protect the surface of the mirrors from contamination. The broadband nature of the light source, and the DOAS retrieval technique, means that several trace gases can be detected and quantified in a single measurement (Fiedler *et al.*, 2003). During cruise SO218, IO and NO_2 were detected in the wavelength range 425–460 nm, with limits of detection of 0.9 pptv and 80 pptv, respectively, for a 5 minute averaging time. The instrument was operational between 19th and 29th November, with occasional gaps in the data set for maintenance such as cleaning the mirrors, aligning the cavity, and taking reference spectra. The 'empty' path length of the cavity was determined using a helium-filled tube and the reference spectra during the SHIVA campaign were measured using dry air, or at night. The instrument is shown in Figure 5.10. Further details about cavity-enhanced DOAS measurements are given in Chapter 3.

Figure 5.9. The University of Bremen MAX-DOAS telescope installed on the starboard side of the upper deck of the RV *Sonne*. The red Y-shaped optical fibre bundles leave the telescope and transmit light to the two spectrometers, housed in an indoor laboratory. Photograph by Dr Folkard Wittrock, University of Bremen.

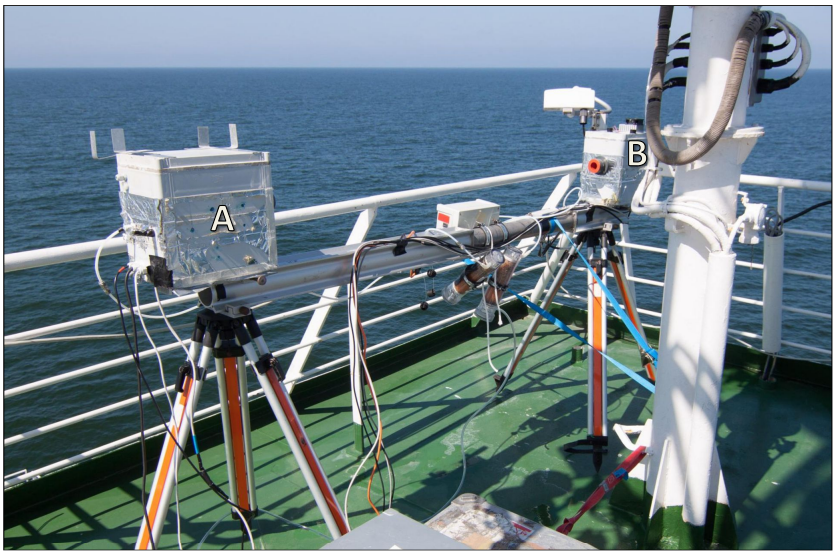

Figure 5.10. University of Heidelberg CE-DOAS instrument set up on the uppermost deck of the RV *Sonne* during SHIVA. The aluminium boxes housing the cavity mirrors are labelled 'A' and 'B'. The orange circle near B indicates the position of the cavity mirror. Photograph by Johannes Lampel, University of Heidelberg.

5.4 Measurements of sources of iodine during cruise SO218

Measurements of the sources and sinks of iodine are necessary to calculate expected steady-state concentrations of IO, and to calculate the role of iodine in tropospheric ozone depletion. To this end, measurements of I_2, and the sum of HOI and ICl, were made using the diffusion denuder technique developed at the University of Mainz. Measurements of iodinated VSLS (CH_3I) were made by canister sampling and gas chromatography, and μDirac (see section 5.4.2).

5.4.1 Measurements of I_2, ICl and HOI

I_2 and the sum of ICl and HOI were measured separately using the University of Mainz coupled diffusion denuder system (Huang and Hoffmann, 2009, Huang *et al.*, 2010a, Huang *et al.*, 2010b), and the samples were analysed by gas chromatography/ion trap mass spectrometry (GC/MS) by Dr. Ru-Jin Huang at the University of Mainz. The sampling system consists of three brown borosilicate glass tubes, 50 cm in length and 6 mm in internal diameter. The coated tubes, prepared by R.-J. Huang, were sealed with polypropylene end caps and stored under refrigeration. The tubes were transported from Mainz to Singapore in poster tubes, inside boxes packed with freezer ice packs, and were stored in a chest freezer onboard the ship until needed for sampling. During sampling, the tubes are arranged vertically, and are connected with short lengths of Teflon tube that fit tightly over the end of the glass tubes. The diffusion denuder system differentiates between particulate and gaseous iodine by sampling in a vertical orientation, to avoid settling out of particles onto the walls of the sample tube, so that there is no artefact in the gas phase measurement from particles containing iodine. Air is drawn upward through the tubes using a diaphragm pump (Charles Austen, DYMAX 30), and the flow rate is controlled using a variable flow meter (Key Instruments, FR2A13, 0.1−1.0 L min^{-1}) at 500 mL min^{-1}, for around 30 minutes per sample (the exact length of each sample was recorded). The first (lowermost) tube is uncoated on the inside and acts to ensure that the flow through the two sample tubes is laminar. The second (middle) tube is coated on the inside with 1,3,5-trimethoxybenzene (1,3,5-TMB) for collection of ICl and HOI (collectively termed activated iodine compounds, AIC),

and the third (uppermost) tube is coated on the inside with α-cyclodextrin/$^{129}I^-$ (α-CD/$^{129}I^-$) for collection of I_2. After sampling, the caps were replaced and sealed with Teflon tape, and the tubes were returned to the chest freezer. The tubes were transported from Manila, Singapore to Leeds, UK, packed on dry ice in polystyrene boxes, and from Leeds to Mainz, Germany, packed in boxes with freezer ice packs. The tubes were then refrigerated until they could be analysed.

α-cyclodextrin forms an inclusion complex with iodine, facilitated by the added $^{129}I^-$ ions, temporarily trapping I_2 on the inside wall of the denuder tube (Huang *et al.*, 2010a). I_2 can be released relatively easily in aqueous solution, but remains in a stable complex in the solid state. The organic processing then converts the iodine to an organic form which can be separated and detected by the GC/MS. The collection efficiencies of the two tubes have been determined at gas flow rates of 350 mL min^{-1} (Huang and Hoffmann, 2009). I_2 is collected with an efficiency of 1.2 % on 1,3,5-TMB, and 98.2 % on α-CD/$^{129}I^-$. ICl is collected with an efficiency of 99.4 % on 1,3,5-TMB, and 29.1 % on α-CD/$^{129}I^-$, hence the need for the 1,3,5-TMB tube to be upstream of the α-CD/$^{129}I^-$ tube, and the ability to separate I_2 and ICl from the same air sample using the two tubes. Increasing the sampling flow rate to 500 mL min^{-1}, which was the flow rate used during the SO218 cruise, does not appreciably decrease the collection efficiency, and increases the volume of gas sampled during a limited sampling time. Collection efficiencies over a range of relative humidities from 0−100 % varies by less than 8.6 % for ICl and less than 5.7 % for I_2. Significant interference from IO, OIO, IBr or iodocarbons is not expected but cannot be completely ruled out (Huang *et al.*, 2010a).

The sample analysis is described here as described by Huang and Hoffmann (2009). Samples collected with α-CD were eluted with five 2.0 mL aliquots of deionised water into 25 mL calibrated flasks. 500 μL of phosphate buffer (pH 6.4), 100 μL of 2,4,6-tribromoaniline (2.5 mg L^{-1}), 400 μL of 2-iodosobenzoate (4.0 g L^{-1}), and 300 μL of dimethylacetamide (0.2 g L^{-1}) were added to the flask, and the sample was diluted down to 23 mL with deionised water. The solution was shaken in a mechanical shaker for 120 minutes. 2.0 mL of sodium acetate solution (20 % by mass) was added and the solution was made up to 25 mL with deionised water. Finally, the solution was extracted with 100 μL of cyclohexane. Samples collected with 1,3,5-TMB were eluted

with five 2.0 mL aliquots of ethanol/ethyl acetate (1:1 by volume). 100 μL of 2,4,6-tribromoanisole (6.0 mg L^{-1} in ethyl acetate) was added. The mixture was concentrated almost to dryness with a gentle stream of purified nitrogen and dissolved in 100 μL of ethyl acetate. Two 1 μL aliquots of each sample were analysed. The aliquot was injected into a gas chromatograph through an injector line at 250 ºC and a transfer line at 300 ºC, with high-purity helium as the carrier gas through the fused-silica capillary column. Following separation of the products in the column, the gas phase species were subject to electron ionisation at 70 eV, and the resulting ions were detected by mass spectrometry in the mass/charge ratio (*m/z*) range of 45–450. Quantification of the derivatives was carried out in selected ion monitoring mode. The standard deviation of the two results was used as the uncertainty on the measurement, which ranged from 0.002 % to 17.9 % (relative standard deviation) for the I_2 measurements, and from 0.07 % to 21.5 % for the AIC measurements. The limit of detection for I_2 was 0.17 pptv, and for AIC was 0.05 pptv.

Diffusion denuder samples were taken several times each day, and were planned to coincide where possible with gas canister samples being taken on the ship, or with particular times of day. The frequency of sampling was increased during the diurnal stations in an attempt to track the changing iodine source throughout the day. The tubes were positioned as close to the front of the ship as possible, to minimise the effect of iodine release from sea salt on the ship surface, and to minimise interference from the ship's stack (see Figure 5.11). To this end, a steel bar was attached to the railings on the port side of the front deck. Bosses and clamps were attached to the steel bar and were arranged to clamp the three tubes. The pump was located in the 10 ft shipping container which housed the Leeds IO LIF instrument and DLR CIMS instruments. The tubes were connected to the pump with PTFE tubing. During daylight samples, the tubes were covered with aluminium foil to prevent the tubes being heated by direct sunlight, which would affect the collection efficiency of the tubes and the stability of the complexes formed between the target molecules and the coatings, and to prevent photolysis of the iodine species inside the tube. A cut-off plastic bottle was attached to the lowest and uppermost tubes to prevent splashing by sea-spray and rain.

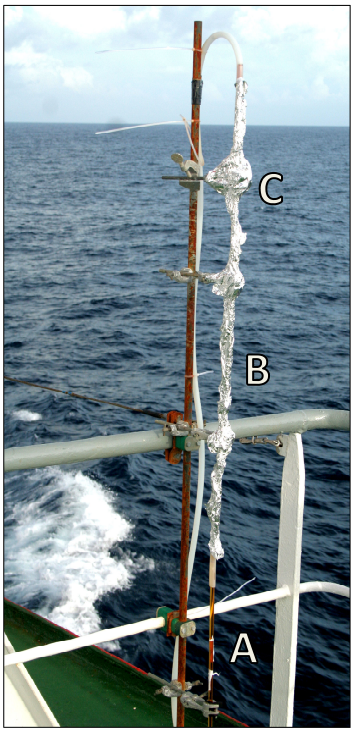

Figure 5.11. The diffusion denuder sampling system set up on the port side of the front deck of the RV *Sonne*. A, B and C mark the positions of the blank, 1,3,5-TMB and α-CD/$^{129}I^-$ tubes, respectively. The tubes are covered in aluminium foil to prevent heating by direct sunlight. The tubes are connected to the pump, which is located in the 10 foot shipping container on the front deck, by PTFE tubing, which is cable-tied to the steel bar.

5.4.2 Measurements of iodocarbons

Iodocarbons were measured by scientists from IFM-GEOMAR, and the Rosenstiel School for Marine and Atmospheric Science (RSMAS). 195 air samples were pressurised into stainless steel canisters, taken at the top of a 4 metre pole, positioned on the port side of the ship, approximately 15 metres above the sea surface. The samples were taken every three hours during normal conditions, with the sampling frequency increased to 1 per hour during diurnal stations and close to the northern coast of Borneo. 200 samples were taken in total. Halocarbon concentrations were analysed at RSMAS within 3 months of the end of the cruise, by pre-concentration of the samples at −185° C, separation by gas chromatography and detection by ion mass spectrometry (GC/MS) (Schauffler *et al.*, 1999). CH_3I was the only iodocarbon analysed in the air samples. CH_3I was also measured by the University of Cambridge by temperature-programmed gas chromatography coupled with electron capture ionization and

detection (μDirac). The μDirac instrument was located on the scientific bridge, where access to the outside was provided for a sampling tube, the end of which was positioned on the port side of the upper deck. Air samples were taken approximately every 45 minutes, giving a higher time resolution than the canister data. The μDirac and canister CH_3I data are very similar, with mean mixing ratios of 0.32 and 0.39 pptv, respectively, though fast peaks in CH_3I are captured by the higher time resolution of the μDirac (maximum CH_3I = 3.39 pptv) and not by the canister measurements (maximum CH_3I = 0.78 pptv).

Sea water samples were taken and analysed by scientists from IFM-GEOMAR. Surface samples were taken while the ship was underway, from a continuous water supply from a pump submersed below the ship. Deep water samples were taken during the CTD casts using a rosette bottle sampler, enabling sampling throughout the depth of the water column. Halocarbons in the water samples were analysed onboard using a purge and trap multidimensional GC/MS system. Volatile compounds in the sea water were pre-concentrated using a flow of helium, with the temperature of the sample being increased during the purging from ambient temperature to 70–80° C. The volatile compounds were collected on a porous polymer on the inner wall of fused silica capillary columns at −70°C, released from the columns by thermal desorption, separated by gas chromatography, and detected by ion selective mass spectrometry (Quack *et al.*, 2004). CH_3I and CH_2I_2 were analysed in the water samples.

Air-sea fluxes of halocarbons (including CH_3I) were calculated by Dr B. Quack of IFM-GEOMAR, using the measured sea surface concentrations, atmospheric mixing ratios, and wind speed. Atmospheric measurements were converted to equilibrium water concentrations at 1 atm and the temperature at the sea-water interface, using calculated Henry's law constants. Gas transfer coefficients were calculated from instantaneous wind speeds (1 hour means) according to Nightingale *et al*. (2000). Fluxes were calculated as the product of the gas transfer coefficient and the air-sea concentration difference (Quack and Wallace, 2003, Quack *et al.*, 2007).

5.5 Performance of the Leeds IO LIF instrument during SHIVA

The Leeds IO LIF instrument was calibrated before and during the cruise: the results of the calibrations are given in Table 5.1. For details of the calibration method and results see section 3.4 in Chapter 3. The SHIVA measurements were analysed with the field calibration, since it is a measure of the sensitivity of the instrument under the exact conditions in which the measurements were made. Several difficulties were encountered with the IO instrument during the cruise. The first of these was the measurement of laser power in the fluorescence cell using a photodiode. Measurements with the photodiode positioned at the end of a long, baffled arm at the beginning of the cruise showed large, rapid variations in laser power that were not reflected in measurements of laser power at the laser casing, using an analogue power meter. The photodiode was removed from the cell arm and was positioned on the instrument rack such that laser light reflected from the entrance window of the wavemeter probe was incident upon the surface of the photodiode. The 10ft shipping container in which the instrument was housed had a window facing the bow of the ship. Direct sunlight was able to enter the container, and a shield was necessary to prevent the photodiode being saturated by the bright sunlight in the container. This arrangement provided a more stable measurement of laser power than when the photodiode was positioned at the end of the cell arm, though some large variations in laser power were still observed, and were found to persist when the instrument was tested in the laboratory following the cruise. It was concluded that the rapid variations in laser power measurement by the photodiode were spurious, since they were not reproduced in the laser power measured by an analogue power meter or in the online or offline IO signal.

The IO data were analysed as described in Chapter 3. The IO measurement cycle consists of 1 minute of online measurements followed by 1 minute of offline measurements. When the time taken for the laser wavelength to be changed between the two measurement periods and at the end of the file is taken into account, each cycle lasts for approximately 3 minutes. The data were averaged to either 15 minutes of online measurements or 30 minutes of online measurements, which resulted in total averaging times of 45 minutes or 1.5 hours, respectively.

Table 5.1. Sensitivities to IO from calibrations prior to the SHIVA measurement campaign, and from field calibrations onboard the RV *Sonne* during cruise SO218. C_{IO} = instrumental sensitivity to IO; C_{IO} intercept = intercept of IO calibration plot (see Chapter 3). Intercepts are considered to be negligible and are not used in data evaluation.

	Laboratory calibration	Field calibration
C_{IO} / count s^{-1} mW^{-1} $molecule^{-1}$ cm^3	$(1.79 \pm 0.11) \times 10^{-9}$	$(1.35 \pm 0.17) \times 10^{-9}$
C_{IO} intercept / count s^{-1} mW^{-1}	-0.02 ± 0.17	0.20 ± 0.20
C_{IO} / count s^{-1} mW^{-1} $pptv^{-1}$	$(4.46 \pm 0.27) \times 10^{-2}$	$(3.22 \pm 0.40) \times 10^{-2}$
C_{IO} intercept / count s^{-1} mW^{-1}	-0.02 ± 0.17	0.20 ± 0.20

The 15 minute averages have been used in this work. The raw online and offline IO signal was normalised to laser power averaged over the online and offline periods of the 45 minute averaging period, respectively, since fast variations in laser power were found to be spurious, as described in Chapter 3. 65 files which exhibited large 'spikes' in the IO data, caused by scattering of laser light by particles or water droplets in the detection cell, were excluded from the analysis, leaving 4541 data files, totalling 75.7 hours of online data.

As described in Chapter 3, the IO measurements exhibit a negative bias at mixing ratios of IO below the instrumental detection limit. Extensive laboratory work following the cruise using zero air or N_2, as described in section 3.5 in Chapter 3, concluded that the value of the negative bias was 0.7 pptv, i.e. measurements in air containing no IO would produce a value of −0.7 pptv. IO mixing ratios were therefore calculated by dividing the normalised IO signal by C_{IO}, and adding 0.7 pptv. The laboratory-based 'zero' measurements were used to assess the precision of the measurements, which was found to be 0.75 pptv at one standard deviation. The total uncertainty in the measurements was calculated as the sum in quadrature of the calibration uncertainty (12.3 %) and the precision (0.75 pptv). During the cruise the instrument's limit of detection for 15 minutes of online data average ranged from 0.35 to 1.25 pptv, with a mean value of 0.50 pptv. Data below −1 × LOD were excluded from the analysis but have been included in some plots for completeness.

5.6 Overview of IO measurements by LIF

Table 5.2 gives a summary of IO measurements made by the Leeds IO LIF instrument during cruise SO218. The 16th and 17th of November were used for setting up and testing the instrument onboard, and the instrument was operational for the remaining 12 days (18th to the 29th of November). IO remained close to the limit of detection throughout the cruise. A time series of the 15 minute averaged IO data for the whole cruise is shown in Figure 5.12, along with the instrumental limit of detection (red line) and measurement uncertainty (grey shaded area). Negative values have been included to show the spread of the data. The instrument was calibrated on the morning of 27th of November, so there are no ambient IO measurements for that period. Maintenance to the rotary pump was required on 24th November, resulting in a gap in the data. Time series for each day of IO measurements are given in the Supplementary Information.

A map of the cruise track, coloured by IO mixing ratios, is shown in Figure 5.13. During the 19th, 20th and 21st November, IO mixing ratios were low, often below the limit of detection. IO mixing ratios increased sharply overnight on 21st to 22nd November but remained close to the limit of detection. The maximum mixing ratio of 2.44 ± 0.81 pptv was measured at 18:00 (local time) on 26th November when the ship was crossing the Sulu Sea. The observed IO mixing ratios are slightly lower than those measured by MAX-DOAS during the TransBrom cruise from Japan, through the Western Pacific, to Australia, where IO mixing ratios ranged between 1.0 and 2.2 pptv, with a mean value of 1.3 ± 0.9 pptv (Großmann *et al.*, 2013). The SHIVA measurements are within the range of IO measurements reported for other open ocean regions (< 0.2–3.5 pptv) (Allan *et al.*, 2000, Read *et al.*, 2008, Commane, 2009, Mahajan *et al.*, 2010, Volkamer *et al.*, 2010, Mahajan *et al.*, 2012, Dix *et al.*, 2013, Gómez Martín *et al.*, 2013). The IO data were divided into 2 hour time bins according to the local time of day, and a mean IO mixing ratio was calculated for each time bin to form a mean diurnal profile, as shown in Figure 5.14.

Table 5.2. Mean and maximum IO mixing ratios (parts per trillion by volume) during cruise SO218. Uncertainties were calculated as the sum in quadrature of the calibration uncertainty (12.3 %) and the measurement precision (0.75 pptv), as described in Chapter 3.

	Mean mixing ratio / pptv	Maximum mixing ratio / pptv
Daytime	0.80 ± 0.76	2.15 ± 0.80
Nighttime	0.79 ± 0.76	2.44 ± 0.81
All times	0.79 ± 0.76	2.44 ± 0.81

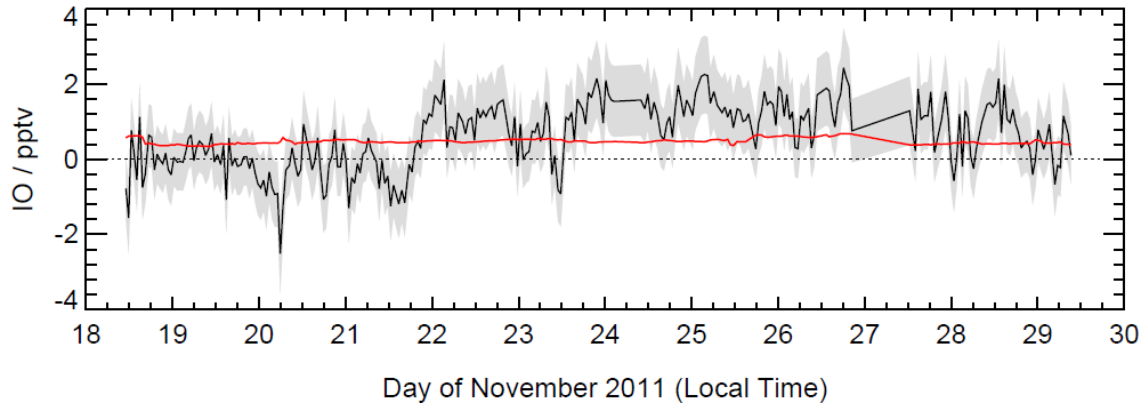

Figure 5.12. Time series of IO during cruise SO218 (black line), and instrumental limit of detection (red line). Grey shading indicates uncertainty on measurements, which is the sum in quadrature of the uncertainty in the field calibration (12.3 %) and the 1σ instrumental precision determined by zero measurements in the laboratory (± 0.75 pptv). Negative data points have been included for completeness. Zero pptv is marked by dotted black line. Data points below the limit of detection cannot be relied upon as a measurement of IO, but are included here to show the IO profile along the cruise. Data were averaged over 15 minutes of online measurements, giving a total averaging time of 45 minutes for each point.

The lack of a clear diurnal profile, and the presence of IO at night, is at odds with the current understanding of iodine chemistry in the open ocean marine boundary layer (*e.g.* Carpenter *et al.*, 2013), which predicts a 'top hat' distribution for IO, with a broad daytime peak and negligible concentrations at night. LP-DOAS measurements of IO off the coast of Tenerife, representative of the open Atlantic Ocean, showed a strong diurnal profile which correlated strongly with solar actinic flux (Allan *et al.*, 2000). Eight months of LP-DOAS measurements at Cape Verde reveal a distinct diurnal 'top hat' profile of IO, with a broad peak around midday and mixing ratios below the detection limit at night (Read *et al.*, 2008, Mahajan *et al.*, 2010).

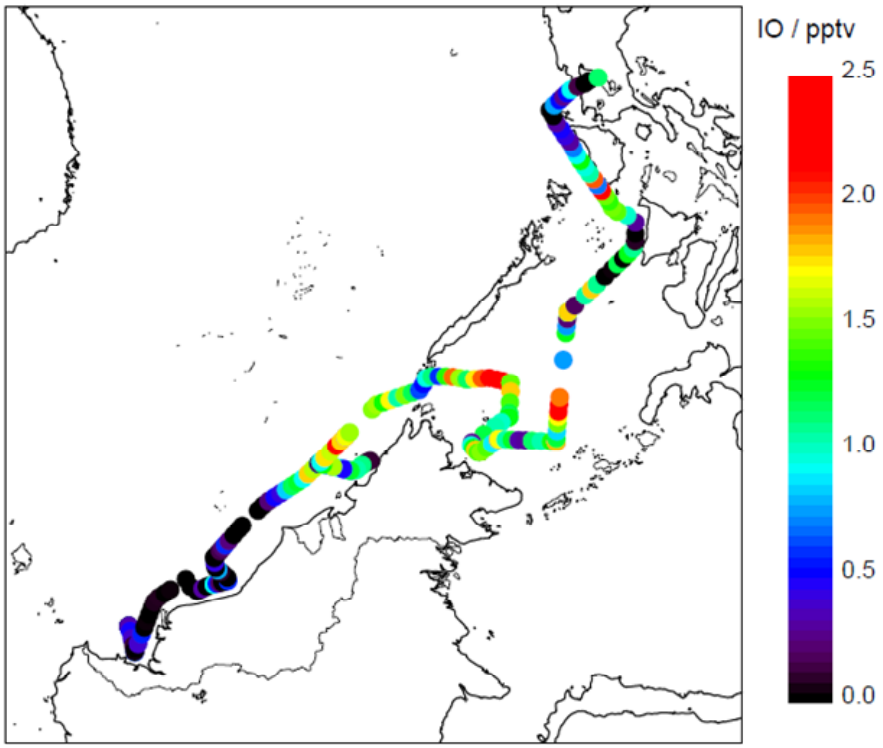

Figure 5.13. Map of cruise track during SO218, coloured by IO mixing ratio, with low mixing ratios in black to blue colours, and high mixing ratios in yellow to red colours.

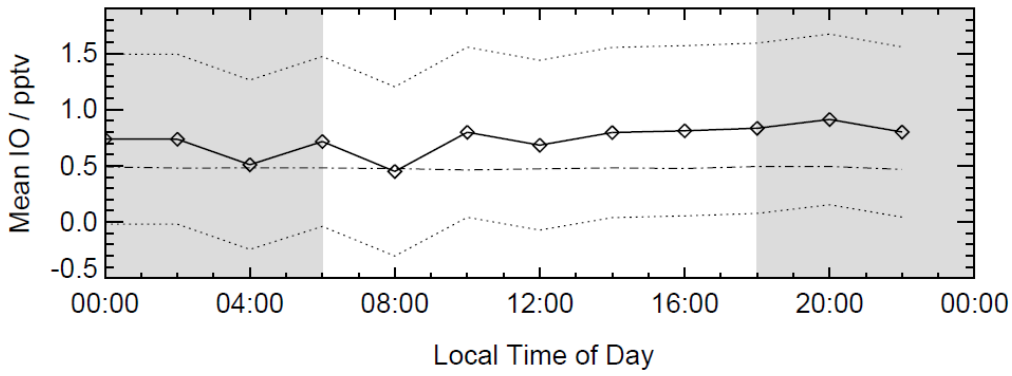

Figure 5.14. Mean diurnal profile of IO during cruise SO218. Dotted lines represent the uncertainty in the measurements. The limit of detection (~0.5 pptv) is shown by the dot-dash line. Night is indicated by the shaded regions.

In contrast, measurements at Cape Grim, Tasmania, showed no daytime diurnal profile, with IO mixing ratios being more dependent on air mass origin than on solar flux (Allan *et al.*, 2000). Up to 1.7 pptv of IO was detected at night by the Leeds LIF instrument during the RHaMBLe cruise north of Tenerife, in a shipping region with relatively high NO_x (Commane, 2009). Nighttime production of IO was attributed to the reaction of

NO_3 with I_2. MAX-DOAS measurements of IO in the Western Pacific showed no diurnal profile on sunny days for solar zenith angles below 84º. A modelling study predicted a morning peak of IO from rapid photolysis of I_2 that had accumulated at night (Großmann *et al.*, 2013). Significant nighttime mixing ratios of IO are more commonly observed in coastal areas, where daytime mixing ratios are high, than in open ocean environments (*e.g.* Saiz-Lopez *et al.*, 2006, Read *et al.*, 2008, Commane *et al.*, 2011). Possible sources of nighttime IO during SHIVA are discussed in section 5.12.2.

It is worth noting that the averaged values shown in Figure 5.14 mask the day-to-day variability present in the IO mixing ratios measured during the cruise. As an example Figure 5.15 shows a time series of IO data from 28th November, exhibiting higher mixing ratios during the day than during the night, as expected from known iodine chemistry. In contrast, Figure 5.16 shows IO data from 23rd November, when IO mixing ratios were below the limit of detection during the middle of the day, and above the limit of detection after sunset. It should also be remembered that the values measured throughout the cruise were close to the limit of detection, so that a strong diurnal profile may not be expected.

5.7 Comparison of IO measurements

5.7.1 Ship-based measurements

IO was measured by three instruments onboard the RV *Sonne*: the Leeds IO LIF instrument, the Heidelberg CE-DOAS instrument, and the Bremen MAX-DOAS instrument. The CE-DOAS instrument was unable to detect IO above the limit of detection, so the data will not be considered further.

The LIF instrument was positioned on the starboard side of the front deck, with the inlet approximately 15 m above sea level, and the MAX-DOAS instrument was positioned on the starboard side of the monkey deck above the bridge, approximately 30 m above sea level (see Figure 5.6). The LIF instrument provides point measurements, while the MAX-DOAS instrument provides spatially averaged measurements along several lines of sight at varying angles between the zenith and the horizon, giving information about

the vertical profile of gas phase absorbers. Slant column densities (SCD) are converted to vertical column densities (VCD) by simulating the air mass factor *A*, which is the ratio between concentrations *c* integrated along the vertical (*V*) and slant (*S*) orientations, respectively. The retrieval of mixing ratios from the vertical column densities relies upon estimated vertical profiles of the species of interest. The mixing ratio of IO in the boundary layer is retrieved from the lowest elevation angle (2º), which corresponds to a 200 m deep layer above the sea surface. The retrieved mixing ratio is averaged throughout this layer. The heights of the two instruments above sea level (~ 15 m for LIF, and ~ 30 m for MAX-DOAS), and the fact that the IO mixing ratio retrieved from the DOAS data is an average value for a 200 m deep layer, are important points to consider. A modelling study of halogen species over the tropical open by Mahajan *et al*. (2010) predicted that IO has a strong vertical gradient immediately above the sea surface, with mixing ratios decreasing by a factor of 2 between 0 and 200 m. Großmann *et al*. (2013) also predict a vertical gradient for IO, with the vertical extent of IO being dependent on the flux of I_2 from the ocean. This being the case, it is expected that the LIF measurements, being point measurements closer to the sea surface, will be higher than the MAX-DOAS measurements, which are elevated above the surface and are averaged throughout the lowest 200 m of the boundary layer.

The daytime data from both instruments are shown as a time series in Figure 5.17. The MAX-DOAS instrument relies on scattered sunlight, and therefore does not provide nighttime measurements. Negative data points, including those below $-1 \times$ LOD, have been shown for the LIF instrument, but were not available for the MAX-DOAS instrument. There is reasonable agreement between the data, with the highest daytime mixing ratio measured by each instrument occurring on the same day of the cruise, and generally higher mixing ratios measured during the second half of the cruise. The maximum daytime IO mixing ratios measured by the LIF and MAX-DOAS instruments were 2.3 and 2.4 pptv, respectively. These values were both measured on the 28th November, at 13:00 (LIF) and 10:00 (MAX-DOAS) local time. The mean daytime mixing ratios measured by the LIF and MAX DOAS instruments, excluding any negative values, were 0.8 pptv and 0.74 pptv, respectively. Note that inclusion of data below the limit of detection in the calculated mean for MAX-DOAS would result in a lower mean mixing ratio.

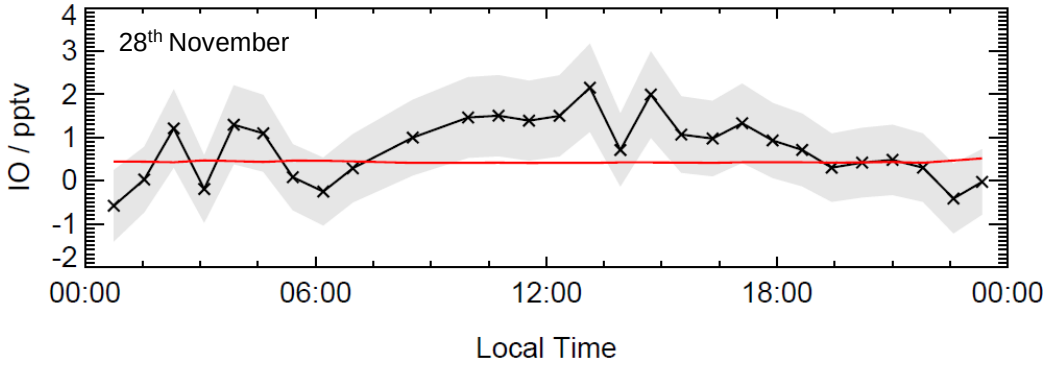

Figure 5.15. Time series of IO mixing ratios (black line and crosses) measured on 28th November, showing higher values during the day than at night. The shaded area represents the uncertainty in the measurements. The red line indicates the limit of detection.

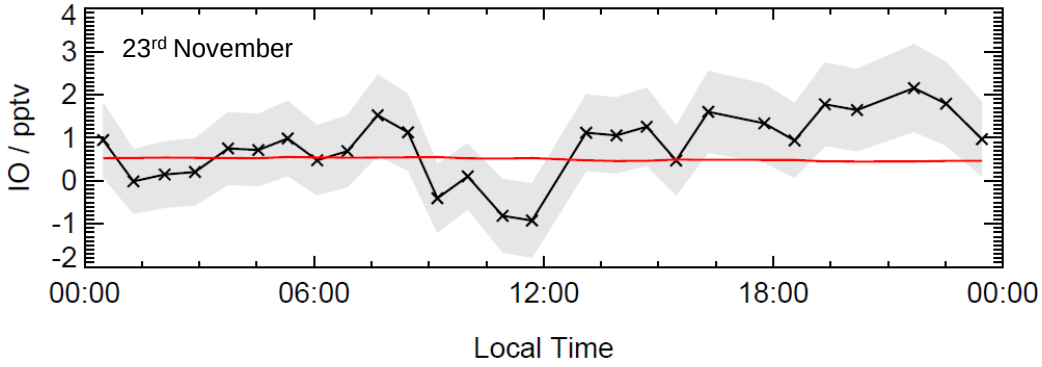

Figure 5.16. Time series of IO mixing ratios (black line and crosses) measured on 23rd November, showing slightly higher values after sunset than during the day. The shaded area represents the uncertainty in the measurements. The red line indicates the limit of detection.

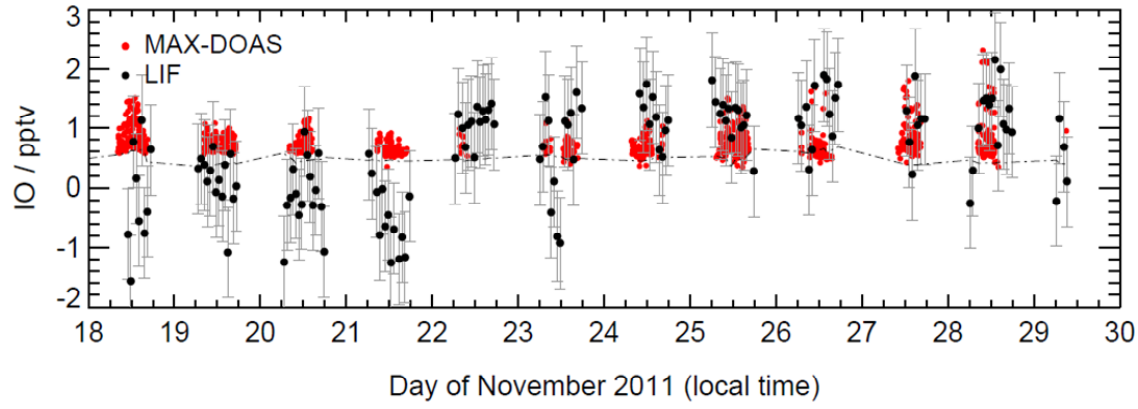

Figure 5.17. Time series of daytime IO mixing ratios measured by the University of Leeds LIF instrument (black data points, grey error bars) and the University of Bremen MAX-DOAS instrument (red points). All daytime LIF data, including negative data points below –1 × LOD, are shown. Error bars give uncertainty on LIF measurements (see section 3.4.3 in Chapter 3 for details). The LIF instrument's LOD is shown by the dot-dash line. The MAX-DOAS LOD was between 0.3 and 0.7 pptv.

The daytime profile of the MAX-DOAS measurements is flat, with very little variation in mixing ratio throughout the day, similar to the profile of the LIF measurements (see Figure 5.14). Within the uncertainty of the LIF measurements, the two data sets are very similar. However, generally higher mixing ratios were measured by the LIF instrument, suggesting that IO mixing ratios decrease with height above the sea surface, in agreement with Mahajan *et al.* (2010).

5.7.2 Satellite-based measurements

Remote sensing of gas species from satellites using the DOAS technique was described in Chapter 3. Schönhardt *et al.* (2008) reported global observations of IO from the SCIAMACHY satellite, showing enhanced IO columns above Antarctica and the Eastern Pacific (up to 7×10^{12} molecule cm^{-2}). Columns over the South China Sea and the Sulu Sea, averaged over September–November 2005 were low, between 0 and 3×10^{12} molecule cm^{-2}, which is equal to or less than the detection limit of the instrument (3−7 molecule cm^{-2}). As discussed in Chapter 3, satellite measurements over oceans are subject to large uncertainty, and the retrieved slant columns are very sensitive to the fit settings, so that the measurements over the South China Sea and Sulu Sea should be treated with caution (Schönhardt *et al.*, 2008). Assuming a maximum IO slant column of 3×10^{12} molecule cm^{-2}, an air mass factor of 1, and a boundary layer height of 1 km, following the work of Gómez Martín *et al.* (2013), the slant column can be converted to an average mixing ratio of approximately 1.4 pptv. Since IO mixing ratios decrease with height above the sea surface, according to the work of Mahajan *et al.* (2010) and Großmann *et al.* (2013), the mixing ratio derived from the satellite measurements will be higher than 1.4 pptv at the surface, which leads to a discrepancy between the satellite and *in situ* measurements. However, satellite measurements may also be sensitive to IO in the free troposphere (Dix *et al.*, 2013) which would reduce the mixing ratio in the boundary layer. Taking this into account, and given the large uncertainty associated with satellite measurements over the ocean, there is no obvious disagreement between the satellite and *in situ* measurements of IO made during SHIVA.

5.8 Overview of I_2 and AIC measurements

A sampling plan for I_2 and AIC measurements was drawn up before the cruise to ensure that measurements were made on each day of the cruise, where possible, and at different times of day. The first two full days of the cruise were dedicated to setting up the IO LIF instrument, so the first I_2 and AIC samples were taken during the first diurnal station, near Kuching, on 18th November. The basic sampling plan was to take four 30 minute samples on each day: shortly after dawn at around 07:00, around solar noon at around 13:00, shortly after sunset at around 19:00, and around midnight. In addition, extra samples were taken during the two 24 hour diurnal stations at 09:00, 11:00, 15:00 and 22:00. In total, 47 I_2 samples and 47 AIC samples were taken.

Table 5.3 gives an overview of I_2 and AIC measurements during the cruise. The maximum I_2 mixing ratio (12.74 pptv) was measured at night, and the maximum AIC mixing ratio (7.56 pptv) was measured during the day. A time series of I_2 is given in Figure 5.18, and a cruise map coloured by I_2 mixing ratio is shown in Figure 5.19. I_2 remained well above the detection limit of 0.17 pptv for most of the cruise, with a minimum mixing ratio of 0.168 pptv measured on 24th November. The maximum I_2 mixing ratio of 12.7 pptv was measured at around 22:00 on 18th November, during the diurnal station near Kuching. I_2 was generally elevated during the first half of the cruise, between Kuching and Kota Kinabalu, compared to the second half of the cruise from Kota Kinabalu through the Sulu Sea, though the mixing ratio was elevated close to Manila on the 28th November. Equivalent plots for AIC are shown in Figure 5.20 and Figure 5.21. AIC remained above the limit of detection of 0.17 pptv throughout the cruise, with a minimum value of 0.49 pptv measured on 23rd November. The highest AIC mixing ratio was measured at around 07:00 on the 19th November, during the diurnal station near Kuching, 9 hours after the peak I_2 mixing ratio was measured. AIC had a flatter profile throughout the cruise compared to the I_2 profile, with a less pronounced decrease in mixing ratio between Kuching and Manila.

Table 5.3. Mean and maximum I_2 and AIC mixing ratios (pptv) during cruise SO218. Uncertainties were calculated as 2σ (2 standard deviations) for single points (see section 5.4.1 for details), or propagated errors for mean values.

		Mean mixing ratio / pptv	Maximum mixing ratio / pptv
Daytime	I_2	1.24 ± 0.01	5.44 ± 0.10
	AIC	2.71 ± 0.02	7.56 ± 0.06
Nighttime	I_2	3.72 ± 0.03	12.74 ± 0.03
	AIC	2.79 ± 0.04	6.54 ± 0.13
All times	I_2	1.98 ± 0.01	12.74 ± 0.03
	AIC	2.74 ± 0.02	7.56 ± 0.06

The I_2 mixing ratios measured during the cruise are much lower than measurements made in coastal regions with dense macroalgae growth, as expected (*e.g.* Saiz Lopez and Plane 2004). Finley and Saltzman (2008) reported I_2 mixing ratios up to 1.5 pptv measured by APCI/MS/MS in oceanic air on the Californian coast. Harris *et al.* (2011) reported denuder-diffusion I_2 measurements from a cruise between Singapore to Wellington, New Zealand, with typical values varying between 10 and 50 pptv. The SHIVA I_2 measurements fall between these two examples of open ocean measurements, being generally higher than the California measurements and lower than the Singapore to New Zealand measurements. There are too few measurements of I_2 over the open ocean to enable further comparison, and no measurements of HOI and ICl over the ocean have previously been reported.

Diurnal profiles of I_2 and AIC have been calculated as described for IO, and are shown in Figure 5.22 and Figure 5.23. I_2 exhibits a clear diurnal profile, with higher mixing ratios at night compared to during the day, due to the absence of loss by photolysis. The profile of AIC is less well defined, though it appears that the mean mixing ratio decreases during daylight hours and recovers at night. The 23:00–01:00 and 01:00–03:00 time bins each contain only one I_2 measurement and one AIC measurement (on 21st November and 23rd November, respectively) and should thus be treated with caution. No samples were taken between 03:00 and 05:00.

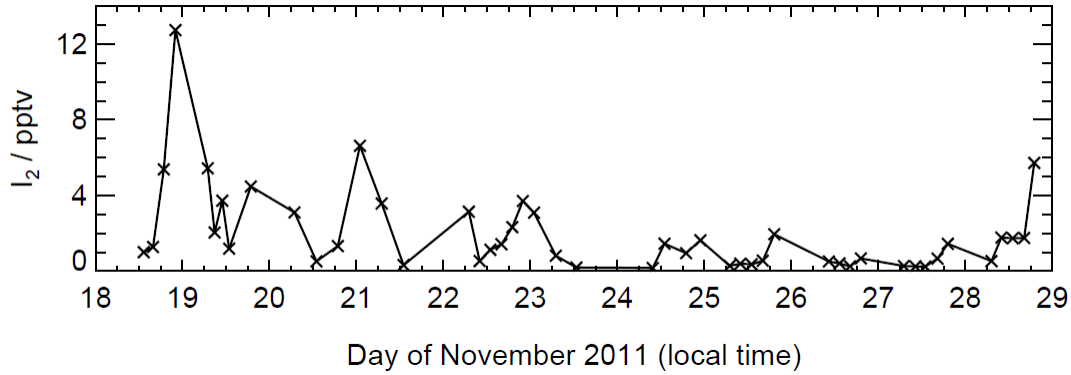

Figure 5.18. Time series of I_2 measured during cruise SO218. Uncertainties in the I_2 measurements, calculated as the standard deviation of 2 analyses from each air sample, ranged from 0.16 % to 17.9 %, with a mean value of 5.8 %.

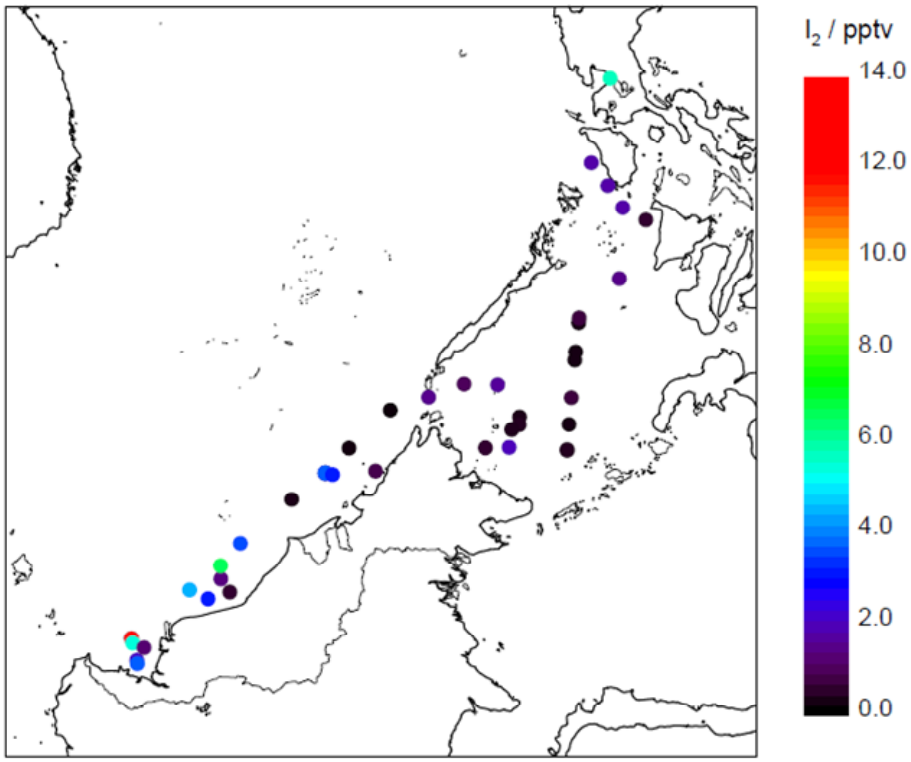

Figure 5.19. Map of cruise track during SO218, coloured by I_2 mixing ratio, with low mixing ratios in black to blue colours, and high mixing ratios in yellow to red colours.

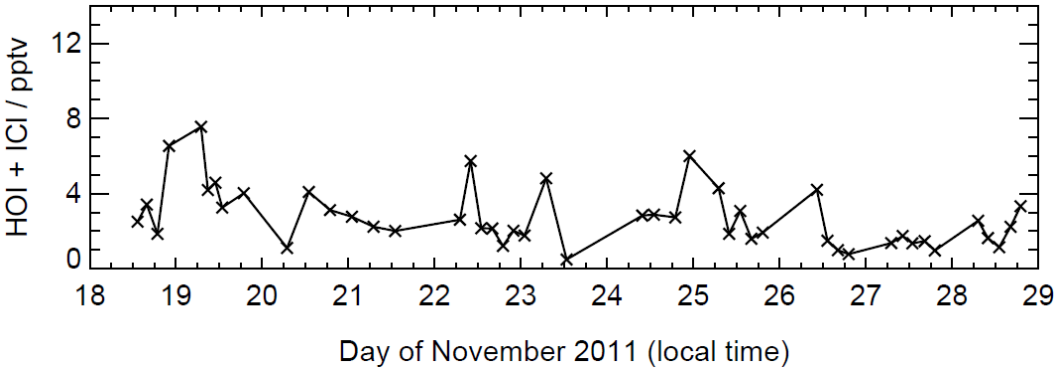

Figure 5.20. Times series of AIC measured during cruise SO218. Uncertainty in the measurements, calculated as the standard deviation of 2 analyses from each air sample, ranged from 0.07 % to 21.5 % with a mean value of 4.7 %.

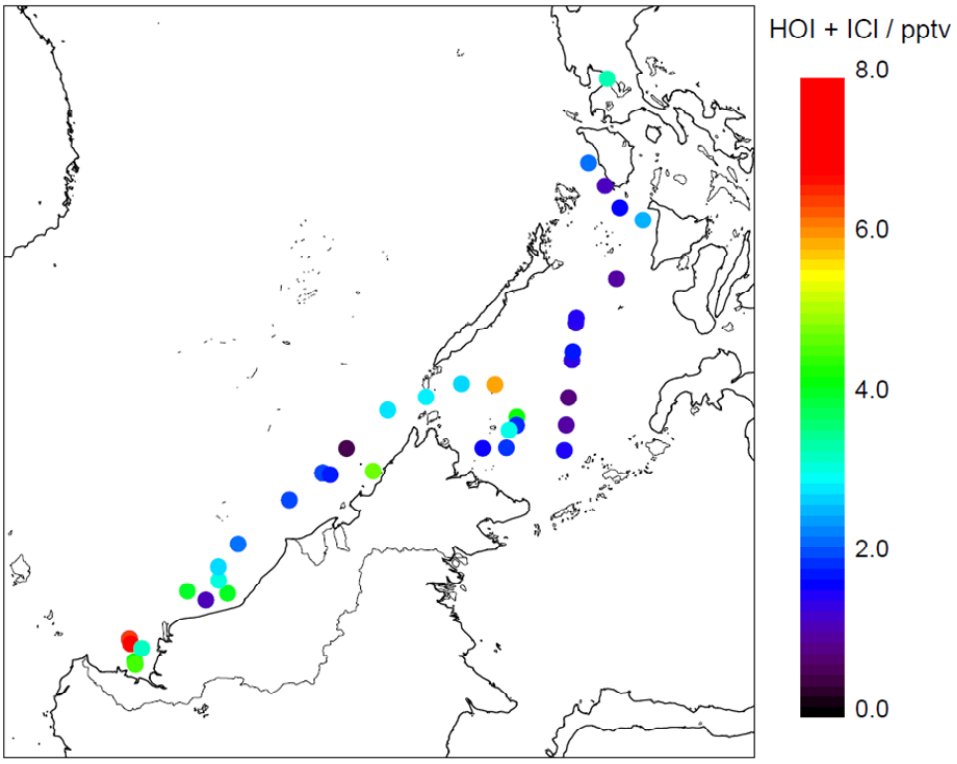

Figure 5.21. Map of cruise track during SO218, coloured by AIC mixing ratio, with low mixing ratios in black to blue colours, and high mixing ratios in yellow to red colours.

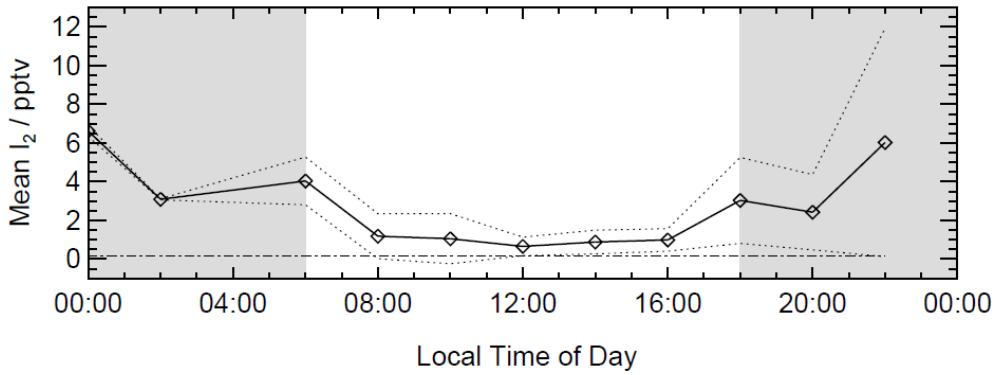

Figure 5.22. Mean diurnal profile of I_2 measured during cruise SO218. Dotted lines represent the uncertainty in the measurements, which was calculated as the standard deviation of the averaged data points, or the uncertainty in the data point where a time bin contains only one data point (23:00–01:00 and 01:00–03:00). The limit of detection (0.17 pptv) is shown by the dot-dash line. Night is indicated by the shaded regions.

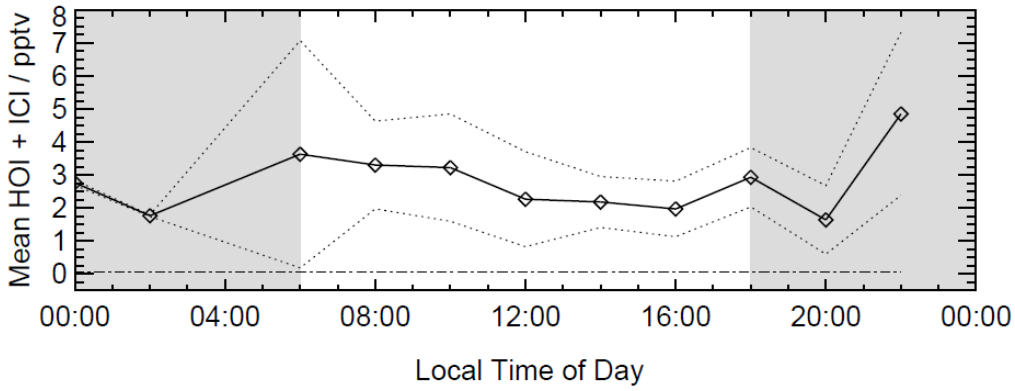

Figure 5.23. Mean diurnal profile of AIC measured during cruise SO218. Dotted lines represent the uncertainty in the measurements, which was calculated as the standard deviation of the averaged data points, or the uncertainty in the data point where a time bin contains only one data point (23:00–01:00 and 01:00–03:00). The limit of detection (0.05 pptv) is shown by the dot-dash line. Night is indicated by the shaded regions.

According to a recent laboratory and modelling study the reaction of O_3 with aqueous iodide at the sea surface leads to emission of HOI from the sea surface at a rate ten times that of the emission of I_2 (Carpenter *et al.*, 2013). ICl was found to contribute less than 1 % to the total iodine flux. The rate of sea-to-air transfer of the evolved species was found to be strongly dependent on equilibration between the sea surface and the layer of the atmosphere immediately above the surface. The flux of HOI is predicted to be suppressed during the daytime due to the build up of HOI from gas-phase reaction between IO and HO_2 (reaction (R1.51)). In contrast, photolysis of I_2 promotes higher I_2

fluxes during the day than at night. The factors controlling I_2, HOI and ICl, and their influence on the measured IO mixing ratios, are discussed further in section 5.9.3.1.

5.9 Controlling factors on the IO mixing ratio

The sources of IO have been investigated by looking for correlations with potential sources of reactive iodine, and with physical and biological parameters measured during the cruise. Correlation between measurements does not imply causality but gives information about the sources of reactive iodine during the cruise, and can improve understanding of iodine release mechanisms. In light of the reasonable agreement between the LIF, MAX-DOAS, and satellite-based DOAS IO data, the proximity of the LIF instrument to the ocean surface, and the high spatial resolution provided by the LIF measurements, the analysis presented here will focus on the LIF data only. The data were paired with various measurements by matching data points by time. Data points without a corresponding time point in either data set were therefore excluded. No negative IO data points were included. Pearson correlation coefficients, *r*, have been calculated for each plot using IDL plotting software, and the significance of the correlations has been judged by referring to a table of critical values of *r*, which gives the probability *p* that the calculated correlation coefficient could be achieved by chance between two random sets of variables. Values of *p* below 0.01 indicate reliable correlation coefficients.

5.9.1 Physical parameters

Previous studies of IO in the marine boundary layer have investigated controls on IO mixing ratio by looking for correlations between IO and oceanic and atmospheric physical parameters (*e.g.* Mahajan *et al.*, 2012, Gómez Martín *et al.*, 2013). The role of sea surface temperature, salinity, depth, air temperature and wind speed in release of reactive iodine from the oceans has been investigated by plotting IO against each variable. The results are shown in Figure 5.24. No strong correlation, positive or negative, is evident between IO and the parameters measured. These results are in contrast to previous studies, in which IO was found to be positively correlated with sea surface temperature (r = 0.71–0.85) and salinity (r = 0.0–0.7), suggesting enhanced sea-

to-air emission or enhanced precursor production with increasing sea surface temperature, and an abiotic emission rate controlled by the availability of aqueous iodide (Mahajan *et al.*, 2012, Gómez Martín *et al.*, 2013, Großmann *et al.*, 2013). It should be noted, however, that the ranges of values of sea surface temperature, air temperature, and salinity are small compared to those in previous studies. For example, Gómez Martín *et al.* (2013) report sea surface temperatures between 18 and 28º C, air temperatures between 20 and 27º C, and salinity between 33.0 and 35.5 PSU (practical salinity units) measured in the Galápagos Islands in the tropical Eastern Pacific. These differences are attributed to the fact that the SHIVA cruise spanned just 2 weeks, while the measurements reported by Gómez Martín *et al.* were taken over a period of 28 months. The SHIVA cruise also took place within a relatively small latitude range (1.4–14.6º N) compared to the TransBrom (42º N to 19º S) and HaloCAST-P (47.6º N to 53.2º S) cruises, during which IO was found to be positively correlated to sea surface temperature and salinity (Mahajan *et al.*, 2012, Großmann *et al.*, 2013). Given the small range of observations of physical parameters made during SHIVA, it is not surprising that no strong correlations can be found.

5.9.2 Biological parameters

Production of molecular iodine and iodine-containing halocarbons by macroalgae in coastal regions is well-documented (Carpenter *et al.*, 1999, Carpenter *et al.*, 2000), but since no regions with macroalgae populations were encountered during the cruise it is more likely that any biological sources of iodine were phytoplankton. There is evidence to suggest that there is a biological route to the formation of precursors of reactive iodine in the remote marine boundary layer (*e.g.* Bronwell *et al.*, 2010), but the role of phytoplankton in production of IO precursors is unclear, with several studies reporting evidence to suggest that sea-to-air emission of iodine may be inhibited by biological activity (Mahajan *et al.*, 2012, Gómez Martín *et al.*, 2013).

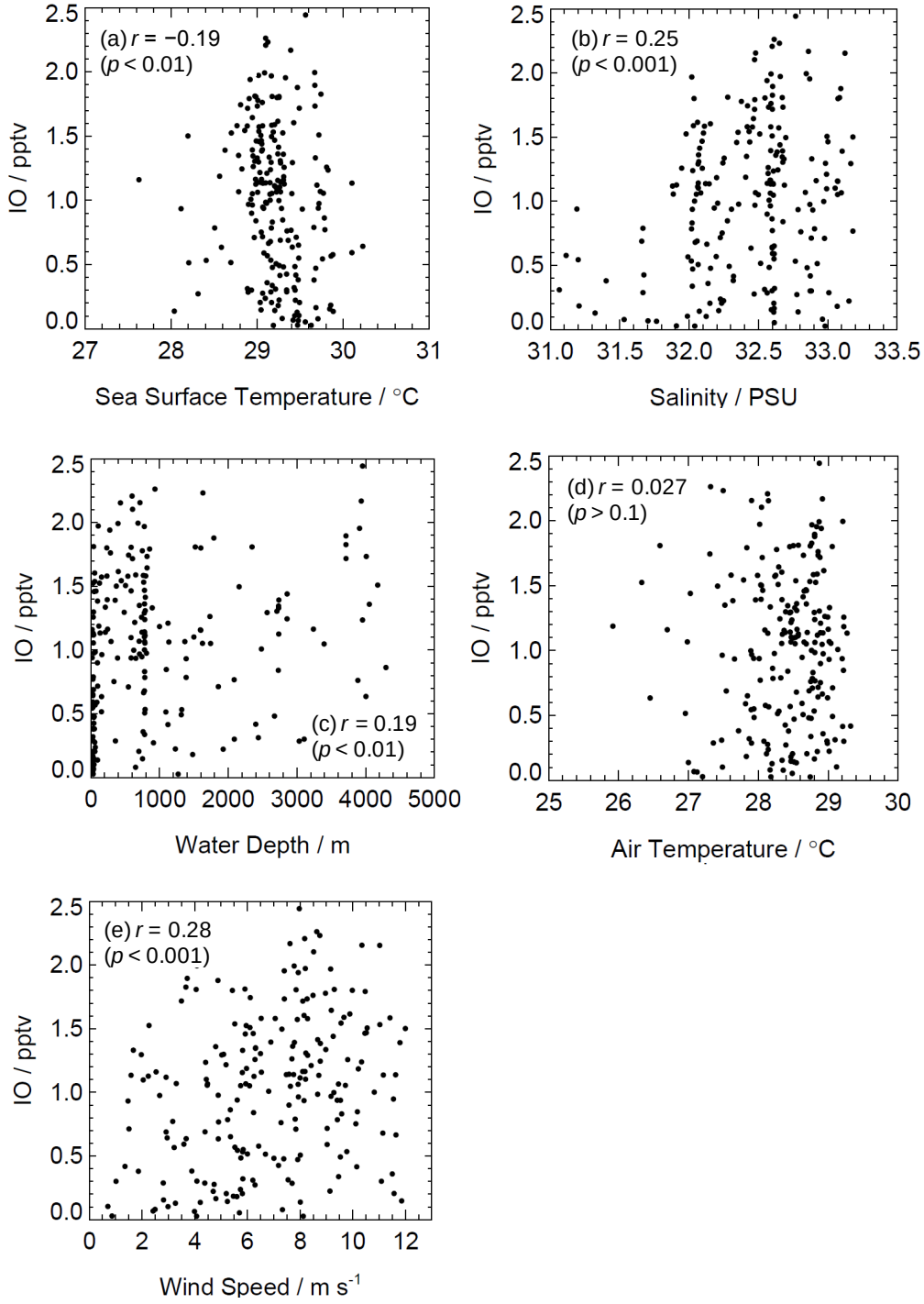

Figure 5.24. IO *versus*: a) sea surface temperature; b) salinity; c) water depth; d) air temperature; e) wind speed. Pearson correlation coefficients, *r*, and significance levels, *p*, are given in the plots. No strong correlation is evident between IO and the parameters measured.

The population density and biological activity of oceanic phytoplankton and cyanobacteria can be assessed by measuring the concentration of photosynthetic pigments, specifically chlorophyll-*a* (Chl-*a*) in seawater samples. During the cruise,

Chl-*a* was measured in underway water samples by filtration of water samples onto glass microfibre filters followed by separation of the pigments by high performance liquid chromatography and detection by fluorescence spectroscopy. Only the surface (underway) and shallow (< 5 m) CTD samples have been used in this work, giving a total of 76 measurements from the 16th to 29th November. These data are shown as a time series in Figure 5.25 and as a coloured cruise track in Figure 5.26. The highest Chl-*a* concentration in the surface and shallow samples was measured on 19th November, near Kuching, with elevated concentrations in the Sulu Sea on 24th November, and approaching Manila on 28th November. The chlorophyll data appear to have a similar profile along the cruise track as I_2 and AIC, but no significant correlation exists between Chl-*a* and the measurements of I_2 and AIC (r = 0.05, p > 0.1, and r = 0.17, p > 0.1, respectively).

If there was a biological source of IO precursors during the cruise, a positive correlation would be expected between IO and Chl-*a*. However, no significant correlation was found between IO and Chl-*a* (r = −0.17, p > 0.1), as shown in Figure 5.27. Gómez Martín *et al*. (2013) and Mahajan *et al*. (2012) have reported negative correlations between IO and Chl-*a* during the CHARLEX measurement campaign in the Galápagos Islands and HaloCAST-P cruise in the eastern Pacific marine boundary layer. Chl-*a* data was from the Aqua MODIS (Moderate Resolution Imaging Spectroradiometer) instrument, which provides daily global ocean surface concentrations with a 9 km horizontal resolution. Daily averaged ship-based measurements of IO were negatively correlated with Chl-*a* (r = −0.7). No correlation was found between ground-based IO measurements and Chl-*a* on a short (5–60 day) timescale, but IO was negatively correlated (r = −0.35) with Chl-*a* on a monthly or seasonal timescale. The authors note that this negative correlation may be caused by the negative correlation of Chl-*a* with sea surface temperature, to which IO is positively correlated. Since the correlation between IO and chlorophyll-*a* is weak, it is not certain that there is biological inhibition of iodine production or emission, as might be the case in previous studies. It is likely, however, that there was not a strong biogenic source of reactive iodine (and therefore IO) during the cruise.

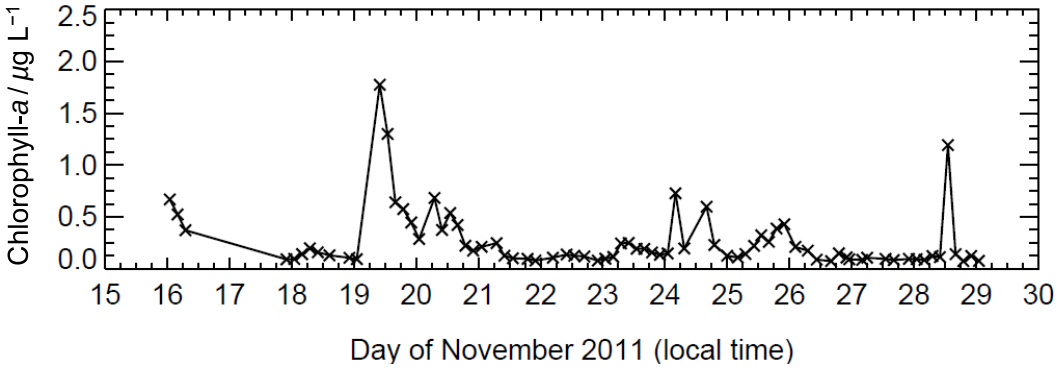

Figure 5.25. Time series of chlorophyll-*a* during cruise SO218.

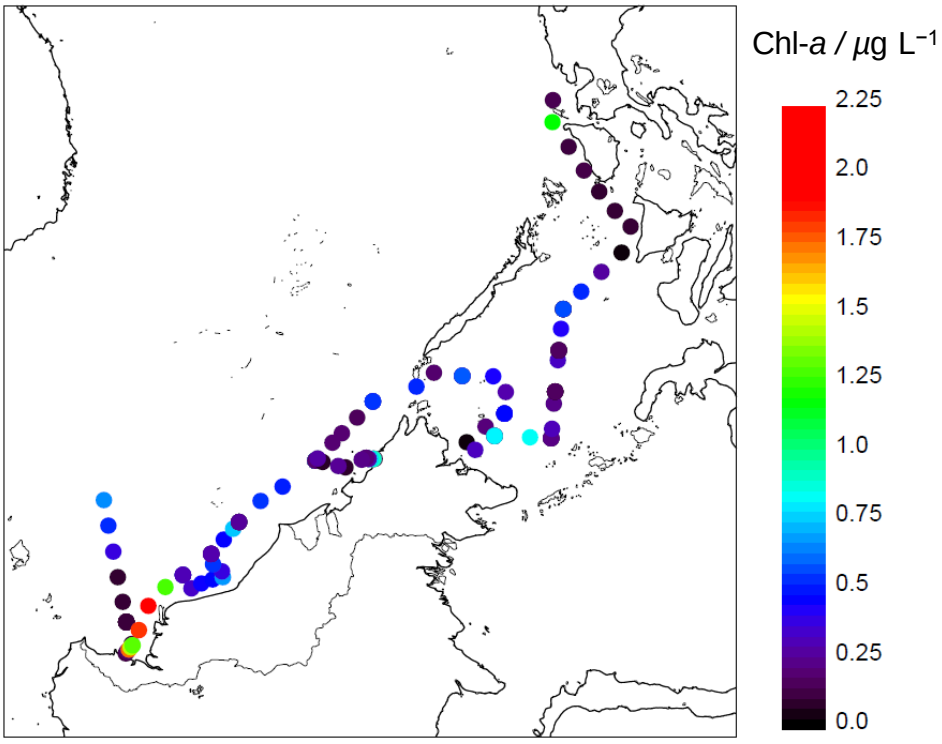

Figure 5.26. Map of cruise track coloured by chlorophyll-*a* concentration, with low mixing ratios in black to blue colours, and high mixing ratios in yellow to red colours.

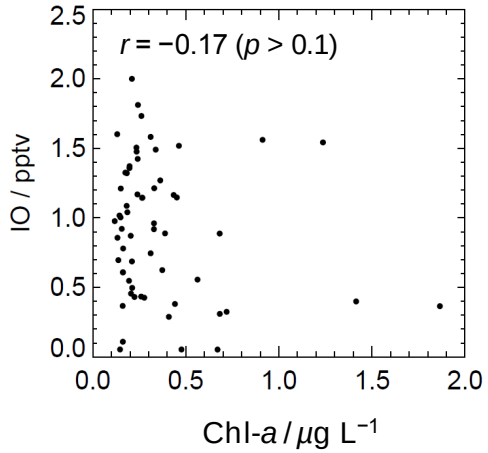

Figure 5.27. IO *versus* chlorophyll-*a*. Pearson correlation coefficient $r = -0.17$ ($p > 0.1$).

5.9.3 Precursors of reactive iodine

Several I and IO precursors were measured during the cruise, as described in section 5.4, in both air and sea water. I_2 and the sum of HOI + ICl (AIC) were measured by diffusion denuder sampling followed by offline GC/MS analysis. Of the halocarbons, CH_3I alone was measured in air, by canister sampling followed by offline GC/MS analysis, and by μDirac. CH_3I, CH_2I_2 and CH_2ICl were all measured in seawater by GC/MS. The air-sea flux of CH_3I has also been calculated.

5.9.3.1 I_2, HOI and ICl

Figure 5.28 shows IO plotted against I_2 and AIC, measured by denuder diffusion sampling and GC/MS analysis. Surprisingly, given that I_2, HOI and ICl represent sources of reactive iodine, there is significant negative correlation between IO and both I_2 and AIC. It is worth considering at this stage the production mechanisms and relative abundances of gas-phase I_2, HOI and ICl. As well as being emitted by macroalgae, I_2 is released from the ocean by the heterogeneous reaction of O_3 with aqueous iodide (*e.g.* Sakamoto *et al.*, 2009, Carpenter *et al.*, 2013):

$$H^+ + I^- + O_3 \rightarrow\rightarrow HOI + O_2 \quad \text{(R5.1)}$$

$$H^+ + HOI + I^- \rightleftharpoons I_2 + H_2O \quad \text{(R5.2)}$$

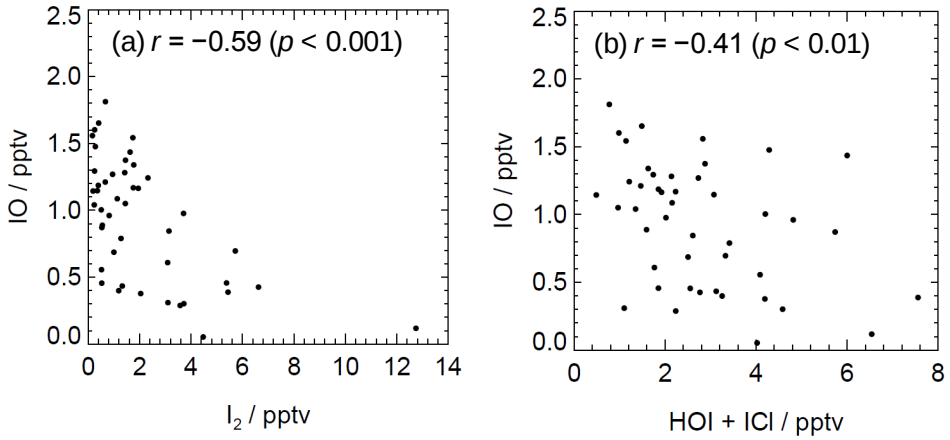

Figure 5.28. IO *versus*: a) I_2; b) AIC. Pearson correlation coefficients are given in the plots.

The reaction of ICl with I^- in sea water can also produce I_2 (Margerum *et al.*, 1986):

$$ICl + I^- \rightleftharpoons I_2Cl^- \quad \text{(R5.3)}$$

$$I_2Cl^- \rightleftharpoons I_2 + Cl^- \quad \text{(R5.4)}$$

$$I_2 + I^- \rightleftharpoons I_3^- \quad \text{(R5.5)}$$

The distributions of the three products I_2Cl^-, I_2 and I_3^- are determined by the availability of I^- and Cl^-. These inorganic release mechanisms are likely to be responsible for the I_2 abundances measured during SHIVA, since no beds of macroalgae were encountered during the cruise. Previous studies of IO in the open ocean boundary layer have concluded that release of I_2 from the ocean surface could account for a missing source of I atoms (Mahajan *et al.*, 2010). Vogt *et al*. (1996) proposed a mechanism for the release of halogens from sea-salt aerosol. HOBr is scavenged by sea-salt aerosol and reacts with Cl^- to release Br_2 to the gas phase as follows:

$$HOBr + Cl^- + H^+ \rightleftharpoons BrCl + H_2O \quad \text{(R5.6)}$$

$$BrCl + Br^- \rightleftharpoons Br_2Cl^- \quad \text{(R5.7)}$$

$$Br_2Cl^- \rightleftharpoons Br_2 + Cl^- \quad \text{(R5.8)}$$

$$Br_2 + h\nu \rightarrow 2Br \quad \text{(R5.9)}$$

$$2(Br + O_3) \rightarrow 2(BrO + O_2) \quad \text{(R5.10)}$$

$$2(BrO + HO_2) \rightarrow 2(HOBr + O_2) \quad \text{(R5.11)}$$

$$\text{Net: } 2\,HO_2 + H^+ + 2O_3 + Br^- + h\nu \rightarrow HOBr + 4\,O_2 + H_2O \quad \text{(R5.12)}$$

Cl atoms are also released to the gas phase following photolysis of BrCl produced in reaction (R5.6):

$$BrCl\ (aq) \rightarrow BrCl\ (g) \quad (R5.13)$$

$$BrCl + h\nu \rightarrow Br + Cl \quad (R5.14)$$

The main fate of the Cl atoms is reaction with ozone and production of HOCl, in reactions analogous to reactions (R5.10) and (R5.11). HOBr and HOCl are the most abundant daytime reactive Br and Cl species, and can both be scavenged by sea salt aerosol to continue the autocatalytic halogen release (Vogt *et al.*, 1996, Vogt *et al.*, 1999). Further modelling work incorporated iodine chemistry into the above scheme, including reactions of HOI in sea-salt aerosol (Vogt *et al.*, 1999):

$$HOI + Cl^- + H^+ \rightleftharpoons ICl + H_2O \quad (R5.15)$$

$$HOI + Br^- + H^+ \rightleftharpoons IBr + H_2O \quad (R5.16)$$

$$HOI + I^- + H^+ \rightleftharpoons I_2 + H_2O \quad (R5.17)$$

These reactions are also known to occur in sea water (Margerum *et al.*, 1986, Wang *et al.*, 1989). ICl is unstable in aqueous solution, reacting readily with Cl^- and I^-, and being rapidly hydrolysed to form HOI and Cl^- (Margerum *et al.*, 1986, Wang *et al.*, 1989). Aqueous I^- also reacts with HOCl and HOBr, in reactions analogous to reaction (R5.6) (McFiggans *et al.*, 2000):

$$HOCl + I^- + H^+ \rightleftharpoons ICl + H_2O \quad (R5.18)$$

$$HOBr + I^- + H^+ \rightleftharpoons IBr + H_2O \quad (R5.19)$$

ICl, IBr and I_2 are released from the aerosol or bulk water phase into the gas phase, so that uptake of HOI and other iodine reservoirs ($IONO_2$, INO_2 and HI) into the aerosol phase represents recycling rather than loss of reactive iodine. However, it should be noted that emission of ICl into the gas phase accounted for only a small fraction (1 %) of total iodine flux from sea water in recent laboratory investigations (Carpenter *et al.*, 2013).

Gas-phase ICl, IBr and I_2 are photolysed to release halogen atoms, meaning that iodine chemistry in reaction (R5.15) and (R5.16) accelerates the release of Br and Cl from aerosols (Vogt *et al.*, 1999). The modelling study also predicted that, during the day,

HOI is ~ 1000 times more abundant than ICl, and that their concentrations are comparable at night when there is no production of HOI through IO + HO_2 (reaction (R1.51)), and aerosol scavenging of HOI becomes important. These results are in agreement with previous modelling studies (Davis *et al.*, 1996). ICl is also produced in the gas-phase reaction between IO and ClO, though this mechanism is less important in the marine boundary layer than in the polar stratosphere, where activation on cloud ice crystals leads to much higher ClO abundances (de Zafra *et al.*, 1987, Solomon *et al.*, 1987, Hanson and Ravishankara, 1991, Hanson and Ravishankara, 1993, Waters *et al.*, 1993).

HOI is produced in the gas-phase reaction between IO and HO_2:

$$IO + HO_2 \rightarrow HOI + O_2 \quad \text{(R1.51)}$$

$$HOI + h\nu \rightarrow OH + I \quad \text{(R1.52)}$$

HOI is also produced in the heterogeneous reaction (R5.1) between O_3 and aqueous iodide, and has recently been shown to be released directly from the aqueous to the gas phase (Carpenter *et al.*, 2013). Carpenter *et al.* found that HOI was the major gaseous iodine species evolved from the reaction of O_3 with iodide at the surface of sea water, supporting previous modelling work that predicted HOI to be the most abundant inorganic iodine species in the marine boundary layer. The authors also found that the sea-to-air flux of HOI is suppressed during the daytime because of the build-up of HOI through gas-phase iodine and HO_x chemistry, in contrast to the relativey flat diurnal profile predicted by Vogt *et al.* (1999). HOI is also produced by some species of marine diatom, though polar species are stronger producers than temperate species (Hill and Manley, 2009). The above results suggests that the daytime AIC measurement is dominated by HOI, since very little ICl is released from the aqueous phase.

Assuming that the rate of recycling of iodine from sea-salt aerosol is fast (McFiggans *et al.*, 2000), and ignoring contributions to reactive iodine from organic sources, it is not clear whether a positive or negative correlation between IO and the inorganic species measured is expected, if at all. For example, increasing IO increases the rate of production of HOI in reaction (R1.51), thereby increasing uptake of HOI into the aerosol phase, assuming that the aerosol is not saturated with HOI. Iodine in aerosol

promotes release of I_2, ICl and IBr into the gas phase through reactions (R5.15) to (R5.17), and the photolysis of these products then leads to production of IO.

Vogt *et al*. (1999) predict a diurnal profile for ICl with maximum values at night and minimum values during the day. This is opposite to the expected diurnal profile of IO, which is expected to show maximum values during the day and low values at night. This behaviour could account for the negative correlation between IO and ICl, though the diurnal profile of IO measured during the cruise did not show the expected 'top hat' distribution, with similar mixing ratios measured during day and night and IO remaining close to or below the limit of detection (see Figure 5.14, Figure 5.15, and Figure 5.16). A modelling study by McFiggans *et al*. (2000), including recycling of iodine through sea-salt aerosol, predicted that mixing ratios of I_x (= I_2, ICl, IBr) would be highest at night, and lowest during the day due to photolysis, with IO showing the opposite diurnal profile.

Carpenter *et al*. (2013) consider the sea-to-air fluxes of I_2 and HOI following reaction of O_3 with iodide at the sea surface. The diurnal flux profiles are determined by the equilibration of each species between the surface and the atmosphere. The authors predict a 'top hat' diurnal profile for the flux of I_2, with higher fluxes during the day than at night, when the absence of photolysis means that I_2 concentrations above the surface can build up, preventing further emission to the gas phase. The flux of HOI is predicted to have the opposite profile, peaking at night and at a minimum during the day, when iodine and HO_x chemistry leads to a build up of gas-phase HOI. A mechanism combining the contribution of iodine-containing halocarbons, HOI and I_2, and constrained by equilibration with atmospheric I_2 and HOI, was able to reproduce measurements of IO made at Cape Verde. These results help to explain the negative correlation observed between IO and I_2, and IO and AIC during cruise SO218, though it is worth noting that IO did not show a distinct diurnal profile, with nighttime mixing ratios similar to those measured during the day, and remained close to or below the limit of detection throughout the cruise.

5.9.3.2 Iodocarbons

Figure 5.29 shows IO plotted against CH_3I measured in air by (a) canister sampling (IFM-GEOMAR and RSMAS) and (b) μDirac (university of Cambridge). The two CH_3I data sets are similar, with the majority of the data points lying between 0.2 and 0.5 pptv, but several high values (1–4 pptv) were measured by the μDirac. This discrepancy is attributed to the higher temporal resolution of the μDirac (1 sample every 45 minutes) compared to the canister sampling (1 sample every 1 or 3 hours). IO is better correlated with CH_3I measured in the canister samples ($r = 0.26$, $p < 0.001$) than CH_3I measured by μDirac ($r = 0.02$, $p > 0.1$). For this reason, the canister data have been used in the IO steady state analysis (see section 5.11). It is not surprising that there is no strong correlation between IO and CH_3I. The photolytic lifetime of CH_3I is 5 to 6 days, so that emissions of CH_3I into the marine boundary layer in the immediate vicinity of the ship would not contribute significantly to the *in situ* measurements of IO. No significant correlation was found between IO and the flux of CH_3I ($r = -0.09$, $p > 0.1$), which was calculated from the sea-to-air concentration difference and a gas exchange velocity as described in section 5.4.2.

Ship-based measurements of IO, CH_3I, chlorophyll-*a* and various oceanic physical parameters in the Eastern Pacific (Mahajan *et al.*, 2012) revealed that IO was positively correlated with CH_3I in air and water ($r = 0.6$), with CH_3I flux ($r = 0.6$), with salinity ($r = 0.6$), and with sea surface temperature ($r = 0.85$), but was negatively correlated with chlorophyll-*a* ($r = -0.7$), suggesting that abiotic production, controlled by the availability of iodide in sea water, dominated reactive iodine. CH_3I was not the dominant source of IO, accounting for ~ 20 % of the IO_x (IO + I) measured during the study, and the authors suggest that the correlation observed was the result of common sources for CH_3I and IO_x. Ground-based measurements in the Galápagos, together with the one dimensional Tropospheric Halogen chemistry Model (THAMO), also found that CH_3I was not a significant source of observed IO_x, contributing around 30 % (Gómez Martín *et al.*, 2013). Figure 5.30 shows IO plotted against oceanic CH_2I_2 (a), CH_3I (b) and CH_2ICl (c) measured in shallow and underway water samples during the cruise. No significant correlation is observed with CH_2I_2, but significant negative correlation is observed with CH_3I ($r = -0.42$, $p < 0.001$) and CH_2ICl ($r = -0.50$, $p < 0.001$).

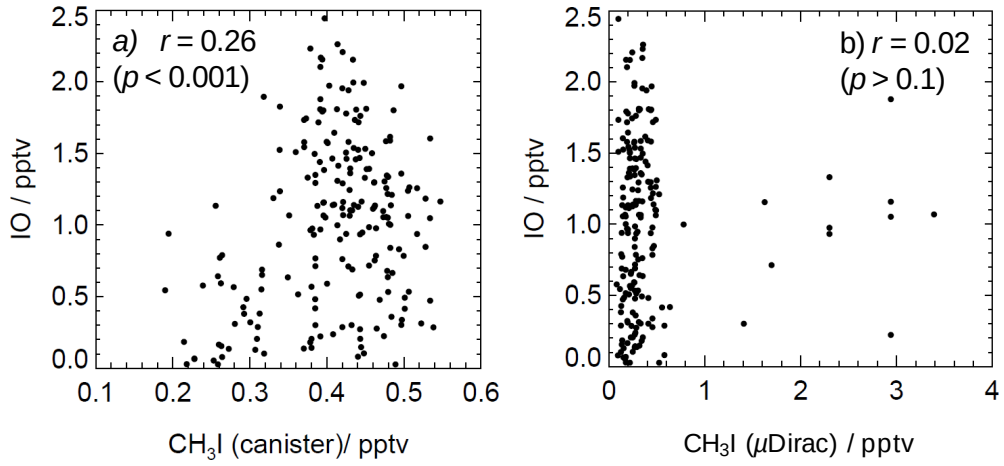

Figure 5.29. IO *versus* CH_3I (air) measured by: a) canister air sample followed by offline GC/MS analysis; b) μDirac onboard. Pearson correlation coefficients, *r*, and significance levels, *p*, are given in each plot, showing weak correlation between IO and the canister measurements.

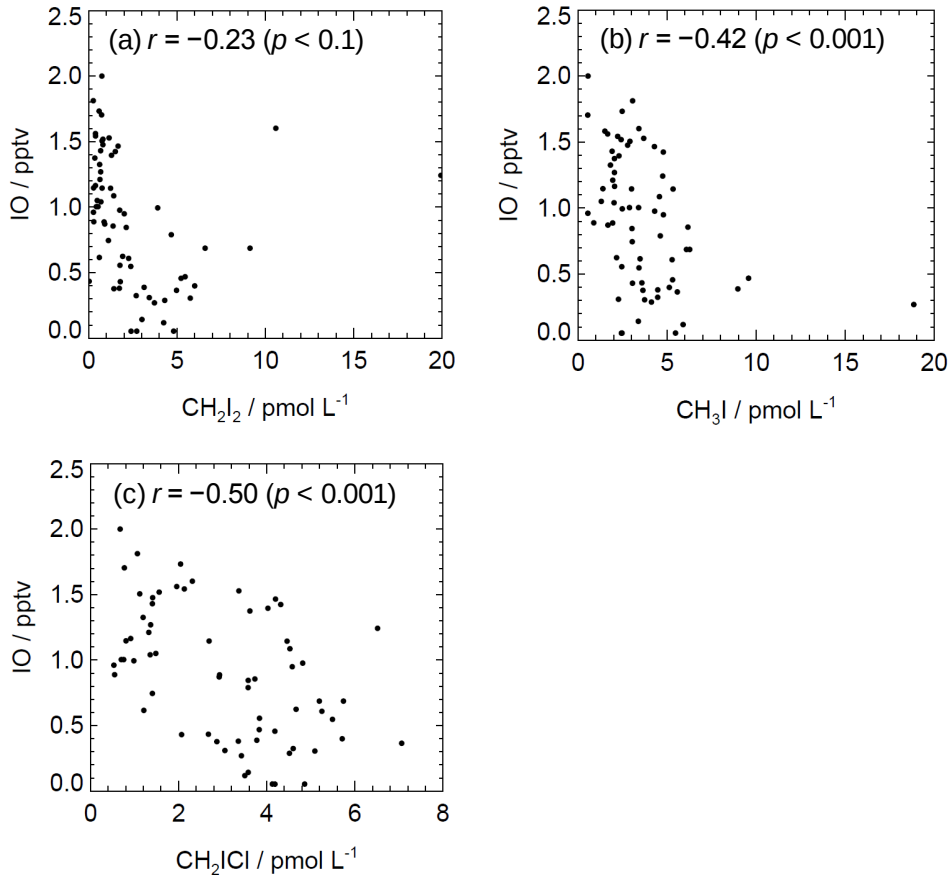

Figure 5.30. IO *versus*: a) CH_2I_2; b) CH_3I; c) CH_2ICl. Pearson correlation coefficients, *r*, and significance levels, *p*, are given in the plots. Significant correlation is evident between IO and CH_3I and CH_2ICl.

CH_3I, CH_2ICl and CH_2I_2 are produced by phytoplankton (Scarratt and Moore, 1999, Yamamoto *et al.*, 2001, Bronwell *et al.*, 2010), but CH_3I and CH_2ICl are also thought to have a photochemical source *via* reactions of iodide and chloride with CH_3 and CH_2I produced by photolysis of CH_3I and CH_2I_2 (Moore and Zafiriou, 1994, Richter and Wallace, 2004, Archer *et al.*, 2007). Several studies have highlighted the importance of the contribution from dihalomethanes to reactive iodine in the marine boundary layer (Klick and Abrahamsson, 1992, Archer *et al.*, 2007, Jones *et al.*, 2010). When considered in conjunction with the weak negative correlation between IO and surface water chlorophyll-*a* concentration, the SHIVA halocarbon data suggest that biological activity may inhibit release of active iodine compounds from the sea, as suggested by Gómez Martín *et al*. (2013).

5.10 Iodine-mediated ozone destruction

The role of iodine in tropospheric ozone destruction was confirmed by measurements and modelling of ozone and halogens in the marine boundary layer (Read *et al.*, 2008). Read *et al*. reported annually averaged ozone loss of 3.3 ± 2.6 ppbv per day between 09:00 and 17:00 UTC (08:00 and 16:00 local time) each day, which could be replicated by a box model only if halogens were included in the chemistry scheme. The combined reactions of IO and BrO were found to contribute 2.07 ppbv per day to the observed ozone destruction, with IO alone contributing 1.24 ppbv per day, and BrO contributing 0.35 ppbv per day. Observations of IO and BrO showed that both radicals displayed diurnal cycles dependent on solar radiation, with maxima during the day and mixing ratios below the instrumental limits of detection at night. Further measurements at this site have confirmed these results (Mahajan *et al.*, 2010).

The range of IO mixing ratios measured during the SHIVA campaign is typical of the open ocean environment, and is similar to the levels measured at Cape Verde in the above work. However, the presence of IO at night, at mixing ratios similar to those measured during the day, was a feature not seen during the Cape Verde measurements. Nevertheless it is of use to assess the contribution made by IO to ozone destruction through a simple correlation plot. Continuous ozone measurements were made during the cruise by DLR using a Thermo Electron 49C ozone monitor on the scientific bridge

of the ship. Daily tropospheric ozone destruction (ΔO_3) has been assessed by calculating a 30 minute average of O_3 around sunrise (06:00 local time, 22:00 UTC) and sunset (18:00 local time, 10:00 UTC) for each day that measurements were available. The sunset mean was subtracted from the sunrise mean to give a daily indication of ozone destruction. No ozone destruction was observed on 5 out of the 15 days for which data were available for the calculations. The mean of ΔO_3 over the 15 days cruise was −0.90 ppbv, which corresponds to a mean *increase* in O_3 between 06:00 and 18:00 rather than a decrease. The mean of ΔO_3 for the days on which ozone destruction was seen is 2.7 ppbv. The maximum daily ozone destruction was 4.7 ppbv on 27th November, the data for which are shown in Figure 5.31. Unfortunately for this analysis, the IO LIF instrument was calibrated during the morning of 27th November, so IO data are available from 12:00 to 00:00 only. The 15 minute averaged IO mixing ratios ranged from 0.0 to 1.9 pptv between these times, with no correlation between IO and ozone being evident. To investigate the role of IO in ozone destruction, daily mean IO mixing ratios have been plotted against ΔO_3. No correlation is evident between IO and ΔO_3 (r = 0.04), indicating that iodine did not play a significant role in controlling ozone mixing ratios during the cruise. Calculation of ΔO_3 was possible on just 11 days, and measurements were taken from a moving platform rather than a ground-based site, so that meaningful comparison to the work of Read *et al*., whose measurements, spanning 8 months, were from a ground-based site with well-characterised air mass origins, is difficult.

To investigate the possibility of ozone destruction on shorter timescales, 1 minute averages of the IO data (total averaging time 3 minutes) have been calculated and compared to 5 minute averages of the O_3 data. Data from the 21st and 22nd November shows some signs that IO may be involved in ozone destruction, as shown in Figure 5.32. The IO data, though more scattered on the 3 minute timescale, show a peak around 00:00 on the 22nd November, coincident with a minimum in ozone mixing ratios, and a minimum around 06:00 on 22nd November, coincident with a maximum in ozone. Despite the apparent link between IO and O_3 during 21st and 22nd November, only weak correlation was found between the data shown in Figure 5.32, with $r = -0.34$ ($p < 0.001$). Iodine therefore played only a limited role in ozone destruction during the cruise.

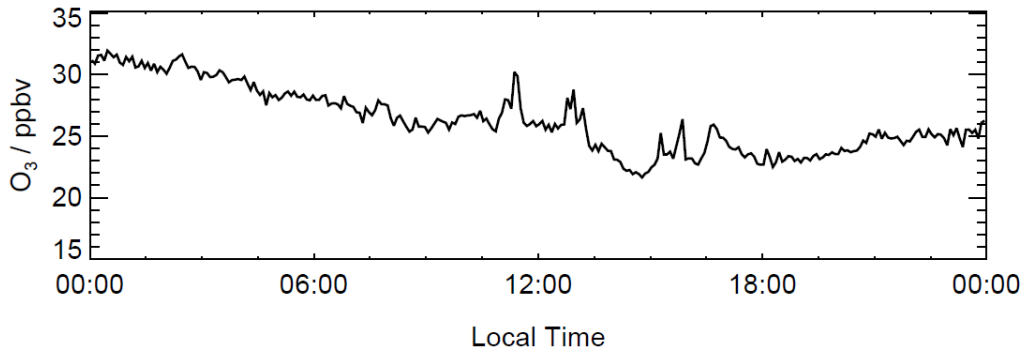

Figure 5.31. Time series of 5 minute averaged O_3 measured on 27th November by Thermo Electron O3 TE49C analyser on the scientific bridge of RV *Sonne*.

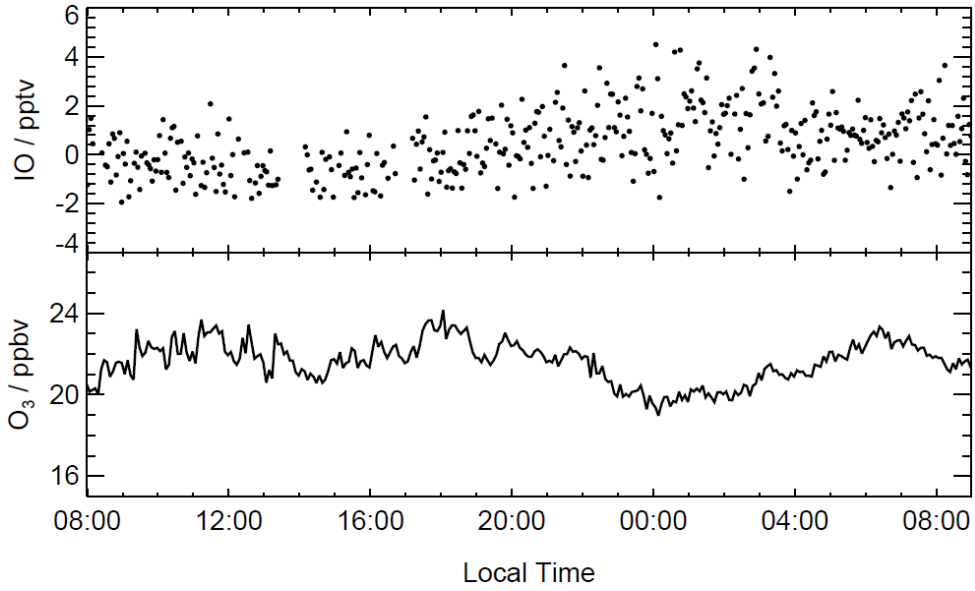

Figure 5.32. Time series of IO data averaged to 1 minute of online data (3 minutes total averaging time), and 5 minute averaged O_3 data, on 21st and 22nd November.

5.11 Steady state analysis of IO

The tropospheric lifetime of IO, dominated by photolysis (Vogt *et al.*, 1999), is sufficiently short that IO can be considered to be in steady state, with its rate of production and rate of loss being equal to one another. The gas-phase processes controlling IO during cruise SO218 have been examined by calculating a steady-state concentration, $[IO]_{SS}$ for each 45 minute IO data point for which the requisite data are available. Negative IO data points were excluded. Measurements of atmospheric CH_2I_2 and CH_2ICl, which are known to contribute to IO production (*e.g.* Mahajan *et al.*, 2010, Großmann *et al.*, 2013), were not available for the SHIVA cruise, so these species have

not been considered in the analysis. Estimates of their concentrations based on previous measurements in the marine boundary layer, or calculations of their expected atmospheric concentrations from their oceanic concentrations, will enable their inclusion in more detailed modelling studies in future work. For simplicity, heterogeneous processes have also been omitted, and will be considered in future work. This work does not therefore represent a comprehensive analysis of IO chemistry, but rather a first look at important production and loss processes based on the measurements available. The production and loss processes controlling IO considered in this work are given in Table 5.4. Production of IO is given by:

$$P_{IO} = k_{P1}[I][O_3] \tag{5.1}$$

and loss of IO is given by:

$$L_{IO} = j_{IO}[IO] + [IO]\left(k_{L4}[NO_2] + k_{L3}[NO] + k_{L2}[HO_2]\right) + k_{L1}[IO]^2 \tag{5.2}$$

where j_{IO} is the IO photolysis frequency, and k_i are the rate constants for the production and loss processes given in Table 5.4. Since IO is in steady state during the day, the sum of P_{IO} and L_{IO} is equal to zero, resulting in the following expression:

$$k_{L1}[IO]_{SS}^2 + [IO]_{SS}\left(k_{L4}[NO_2] + k_{L3}[NO] + k_{L2}[HO_2] + j_{IO}\right) - k_{P1}[I][O_3] = 0 \tag{5.3}$$

Equation (5.3) is evaluated using

$$x = \frac{-b + \sqrt{b^2 - 4ac}}{2a} \tag{5.4}$$

where:

$$x = [IO]_{SS} \tag{5.4a}$$

$$a = k_{L1} = k_{IO+IO} \tag{5.4b}$$

$$b = k_{L4}[NO_2] + k_{L3}[NO] + k_{L2}[HO_2] + j_{IO} \tag{5.4c}$$

$$c = -k_{P1}[I][O_3] \tag{5.4d}$$

Table 5.4. Processes controlling production and loss of IO used in the steady state analysis

	Reaction	Rate Parameter (k or j) / molecule^{-1} cm^3 s^{-1} or s^{-1}	Notes
	Production		
(P1)	$I + O_3 \rightarrow IO + O_2$	$2.3 \times 10^{-11} e^{(-870/T)}$	1
	Loss		
(L1)	$IO + IO \rightarrow$ products	$1.5 \times 10^{-11} e^{(500/T)}$	1
(L2)	$IO + HO_2 \rightarrow HOI + O_2$	$1.4 \times 10^{-11} e^{(540/T)}$	2
(L3)	$IO + NO \rightarrow I + NO_2$	$7.15 \times 10^{-12} e^{(300/T)}$	2
(L4)	$IO + NO_2 + M \rightarrow IONO_2 + M$	$k_0 = 7.5 \times 10^{-31} \times (300/T)^{3.5}$ $k_\infty = 7.6 \times 10^{-12} \times (300/T)^{1.5}$	1,3
(L5)	$IO + h\nu \rightarrow I + O$	0.08	4

Notes
1. Sander *et al.* (2011)
2. Atkinson *et al.* (2007)
3. $k = (k_0[M] / (1 + k_0[M] / k_\infty)) \times 0.6^n$; $n = (1 + (\log_{10} (k_0 [M] / k_\infty))^2)^{-1}$ (Sander *et al.*, 2011)
4. Photolysis frequencies calculated using TUV(Madronich and Flocke, 1998) within DSMACC (Emmerson and Evans, 2009, Stone *et al.*, 2010). Value given is the mean of the data points used in the calculation.

It is therefore necessary to calculate a steady state concentration of I atoms, $[I]_{SS}$, according to the processes given in Table 5.5. Production of I atoms is given by:

$$P_I = j_{IO}[IO] + j_{I_2}[I_2] + j_{HOI}[HOI] + j_{ICl}[ICl] + j_{CH_3I}[CH_3I] + 2k_{P2}[IO]^2 + k_{P3}[IO]^2 + k_{P4}[I_2][OH] + k_{P5}[IO][NO] \quad (5.5)$$

and loss of I atoms is given by:

$$L_I = [I]\left(k_{L6}[O_3] + k_{L7}[HO_2] + k_{L8}[NO] + k_{L9}[NO_2]\right) + k_{L10}[I]^2 \quad (5.6)$$

Equating the sum of equation (5.5) and equation (5.6) to zero yields a steady state expression, which is evaluated in the same way as equation (5.3), with:

$$x = [\mathrm{I}]_{SS} \tag{5.4e}$$

$$a = k_{L10} = k_{I+I} \tag{5.4f}$$

$$b = [\mathrm{I}]\left(k_{L6}[\mathrm{O_3}] + k_{L7}[\mathrm{HO_2}] + k_{L8}[\mathrm{NO}] + k_{L9}[\mathrm{NO_2}]\right) \tag{5.4g}$$

$$c = j_{IO}[\mathrm{IO}] + j_{I_2}[\mathrm{I_2}] + j_{HOI}[\mathrm{HOI}] + j_{ICl}[\mathrm{ICl}] + j_{CH_3I}[\mathrm{CH_3I}] + k_{P2}[\mathrm{IO}]^2 + k_{P3}[\mathrm{IO}]^2 + k_{P4}[\mathrm{I_2}][\mathrm{OH}] + k_{P5}[\mathrm{IO}][\mathrm{NO}] \tag{5.4h}$$

Photolysis frequencies were calculated using the Tropospheric Ultraviolet and Visible (TUV) radiation model version 5.0 (Madronich and Flocke, 1998, Madronich, 2013), constrained by the latitude, longitude and time data recorded during the cruise. To enable TUV to run for each latitude-longitude point in the SO218 data, the model was executed within the Dynamically Simple Model for Atmospheric Chemical Complexity (DSMACC) (Emmerson and Evans, 2009, Stone *et al.*, 2010), using input files containing the latitude, longitude, temperature, pressure and water vapour data. DSMACC outputs concentrations and rates of reactions for each time point given in the input file, and therefore enables calculation of diurnally-varying photolysis rates, for clear-sky conditions, of the iodine source species for each latitude-longitude point in the ship's data. TUV calculates photolysis rates for atmospheric species, but does not include iodine species in its standard form. The species of interest to this work (IO, I_2, HOI, ICl, CH_3I) were added to the user-controlled input files, and to the input files of DSMACC. Absorption cross section data were obtained for each species, and inputted either as a mathematical expression or as a data file containing wavelength and absorption data. An ozone column of 300 Dobson units was assumed. The surface reflectivity was set at 0.1, appropriate to the sea surface. An approximate cloudy sky factor of 0.7 was applied to the photolysis rates generated by TUV, based on precipitation data from the cruise and estimates of cloud coverage provided by Steffen Fuhlbrügge. In future work, wavelength-resolved total incoming radiation measurements from the cruise will be used to provide a more accurate correction of the clear-sky photolysis rates. The steady-state calculation was possible only for times when all the requisite data were available, determined by the frequency of the I_2 and AIC sampling. A steady state concentration was therefore calculated for 31 time points.

Table 5.5. Processes controlling production and loss of I atoms used in the steady state analysis.

	Reaction	Rate Parameter (k or j) / molecule^{-1} cm^3 s^{-1} or s^{-1}	Notes
	Production		
(P2)	$IO + IO \rightarrow 2\ I + O_2$	$0.11 \times 5.4 \times 10^{-11} e^{(180/T)}$	1
(P3)	$IO + IO \rightarrow I + OIO$	$0.76 \times 5.4 \times 10^{-11} e^{(180/T)}$	1
(P4)	$I_2 + OH \rightarrow HOI + I$	2.1×10^{-10}	2
(P5)	$IO + NO \rightarrow I + NO_2$	$7.15 \times 10^{-12} e^{(300/T)}$	3
(P6)	$IO + h\nu \rightarrow I + O$	0.08	4,5
(P7)	$CH_3I + h\nu \rightarrow CH_3 + I$	2.38×10^{-7}	4,5,6
(P8)	$I_2 + h\nu \rightarrow 2\ I$	0.07	4,5
(P9)	$HOI + h\nu \rightarrow OH + I$	0.003	4,5
(P10)	$ICl + h\nu \rightarrow I + Cl$	0.010	4,5
	Loss		
(L6)	$I + O_3 \rightarrow IO + O_2$	$2.3 \times 10^{-11} e^{(-870/T)}$	7
(L7)	$I + HO_2 \rightarrow HI + O_2$	$1.5 \times 10^{-11} e^{(-1090/T)}$	8
(L8)	$I + NO + M \rightarrow INO + M$	$k_0 = 1.8 \times 10^{-32} \times (300/T)$ $k_\infty = 1.7 \times 10^{-11}$	7,9
(L9)	$I + NO_2 + M \rightarrow INO_2 + M$	$k_0 = 3.0 \times 10^{-31} \times (300/T)$ $k_\infty = 6.6 \times 10^{-11}$	7,9
(L10)	$I + I \rightarrow I_2$	$1.0 \times 10^{-32} \times [N_2] + 1.9 \times 10^{-32} \times [O_2]$	10

Notes

1. Atkinson *et al.* (2004); branching ratios Bloss *et al.* (2001)
2. Gilles *et al.* (1999)
3. Atkinson *et al.* (2007)
4. Photolysis frequencies calculated using TUV (Madronich and Flocke, 1998) within DSMACC (Emmerson and Evans, 2009, Stone *et al.*, 2010). Values given are means of the data points used in the calculation.
5. Absorption cross section data from Sander *et al.* (2006), Sander *et al.* (2011)
6. Absorption cross section data from Sander *et al.* (2002)
7. Sander *et al.* (2011)
8. Atkinson *et al.* (2007)
9. $k = (k_0[M] / (1 + k_0[M] / k_\infty)) \times 0.6^n$; $n = (1 + (\log_{10} (k_0 [M] / k_\infty))^2)^{-1}$ (Sander *et al.*, 2011)
10. Jenkin *et al.* (1990)

Measurements of OH and HO_2 were not made during the cruise, and attempted measurements of NO were unsuccessful. OH and HO_2 diurnal profiles were estimated according to measurements in Cape Verde, representative of the tropical open ocean, by Whalley *et al.* (2010) and Vaughan *et al.* (2012, and references therein), with peak noon concentrations of 5.5×10^6 molecule cm^{-3} OH and 2.75×10^8 molecule cm^{-3} HO_2. NO mixing ratios were estimated to be equal to 25 % of NO_2 mixing ratios, according to previous measurements in the open ocean marine boundary layer (Lee *et al.*, 2009, Carpenter *et al.*, 2010), giving a mean NO concentration of 2.0×10^9 molecule cm^{-3} (82.8 pptv) over the points calculated.

The fraction of HOI and ICl in the combined measurement is unknown, so the calculation was performed with 100 % HOI, 100 % ICl, and 50 % of each species. ICl has a higher photolysis rate than HOI, and so using 100 % ICl gives a steady state I atom concentration of 5.00×10^6 molecule cm^{-3}, compared to 4.54×10^6 molecule cm^{-3} for 100 % HOI. As a result, $[IO]_{SS}$ was 1.1 times higher when using 100 % ICl. It is reasonable to assume that HOI makes a larger contribution to the measurement, since it is thought to be the most abundant inorganic iodine species in the atmosphere (Davis *et al.*, 1996, Carpenter *et al.*, 2013). The remainder of the steady state analysis was therefore conducted assuming 100 % HOI. Considerable uncertainty is associated with applying values for OH, HO_2 and NO from measurements in other areas to the current work. The sensitivity of the calculated IO concentration to each of these estimated parameters will be considered in future work.

The results of the calculations are shown as a time series of measured and calculated IO mixing ratios in Figure 5.33. There is good agreement between the calculated and measured values, with a mean calculated to measured ratio of 1.08 (measured/calculated = 1.16). The diurnal profile of the calculated $[IO]_{SS}$ is shown in Figure 5.34, along with the diurnal profile of the measured [IO] used in the calculations. It should be noted that the measured profile shown in Figure 5.34 differs from that shown in Figure 5.14, since only values of [IO] greater than or equal to zero were included in the steady state calculation. The calculated profile shows a maximum during daylight hours, which is similar to the measured profile, but also shows slightly lower IO mixing ratios at night, a feature which is not seen in the measurements.

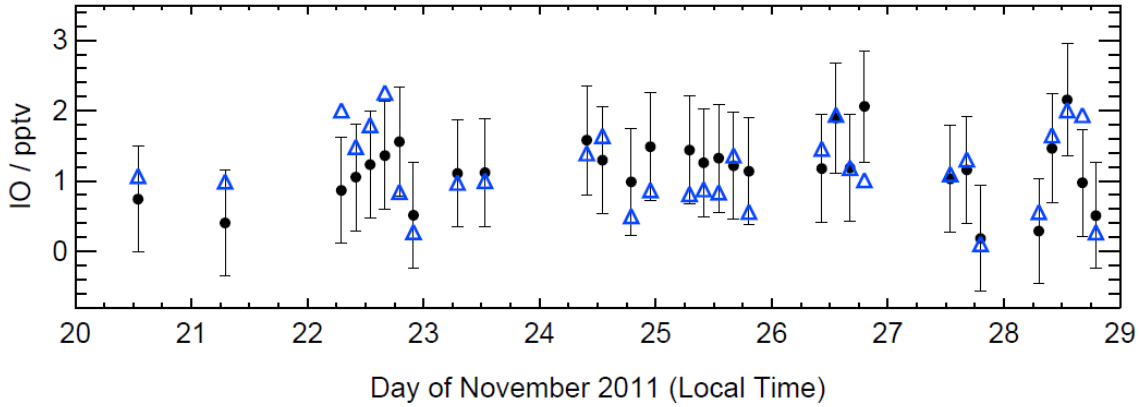

Figure 5.33. Time series of measured IO (black points) and calculated $[IO]_{SS}$ (blue triangles). Error bars give the uncertainty in the IO measurements.

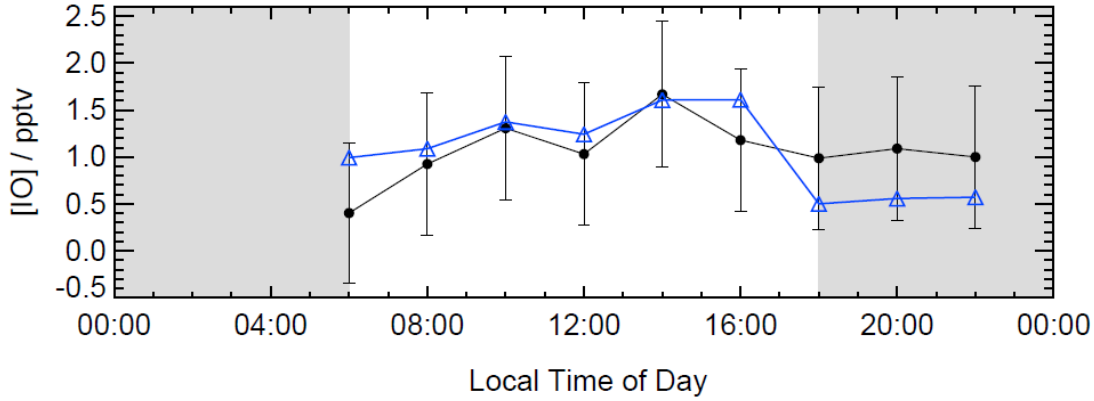

Figure 5.34. Diurnal profile of calculated $[IO]_{SS}$ (blue triangles) and measured [IO] (black data points, with error bars giving uncertainty in measurements).

The steady state calculation does not contain the key reactions which are potential routes to formation of nighttime IO, such as $I_2 + NO_3$ and the heterogeneous reactions of O_3 on the sea surface. Rather, calculated nighttime IO is produced from the gas-phase reaction of $I + O_3$, following production of I atoms from $IO + NO$. This feature is a result of using measured [IO] to calculate steady-state concentrations of [I]. Specific routes to production of I atoms are discussed in more detail below.

The individual contributions of the production and loss processes given in Table 5.4 and Table 5.5 to the steady state concentration of I and IO have been investigated. In this analysis, the sole production mechanism for IO was assumed to be the $I + O_3$ reaction. Figure 5.35 shows the relative contributions of reactions (L1) to (L5) to IO loss in the calculation.

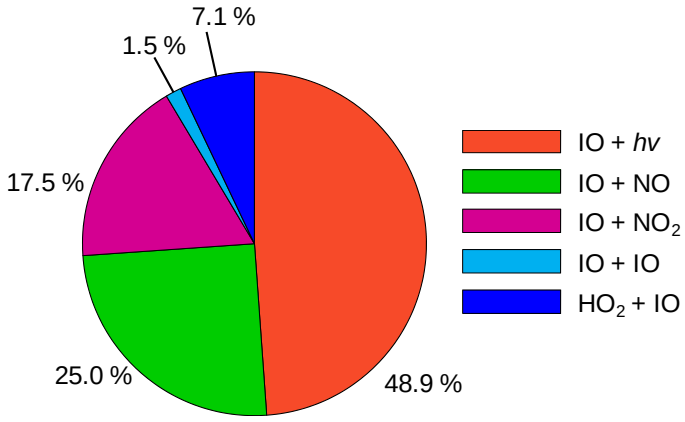

Figure 5.35. Mean contributions to the rate of loss of IO from reactions (L1) to (L5).

IO loss is dominated by photolysis (48.9 %), and IO + NO (25.0 %), but both of these processes are part of null cycles with respect to production and loss, since they are both important routes to formation of I atoms (see Figure 5.36). The remaining loss processes are IO + NO_2 (17.5 %), HO_2 + IO (7.1 %), and IO + IO (1.5 %). The reaction between IO and NO_2 appears to be an important loss process for IO in the steady state calculation. This is in agreement with measurements and a modelling study by Furneaux *et al.* (2010), who found that NO_2 suppressed IO by formation of $IONO_2$ (reaction (L4)). The reaction between I and NO_2 (reaction (L9)) forms the reservoir species INO_2, which represents a further loss of IO overall. Saiz-Lopez and Plane (2004) reported measurements of I_2, IO, OIO and NO_3 at Mace Head, and surmised that the main nighttime sink for IO was likely to be IO + NO_2. Mahajan *et al.* (2009) have reported efficient daytime recycling of iodine from $IONO_2$ through reaction with I. In addition, photolysis of $IONO_2$ yields I + NO_3, and therefore IO through reaction of I with O_3. The question of whether NO_2 represents a source or a sink of IO cannot be answered by the current work, and will be investigated in a more detailed modelling study in the future.

Loss of I atoms is dominated by reaction with O_3 (95.2 %), forming the steady state cycle:

$$I + O_3 \rightarrow IO + O_2 \quad \text{(R1.47)}$$

$$IO + h\nu \rightarrow I + O \quad \text{(R1.48)}$$

$$O + O_2 \rightarrow O_3 \quad \text{(R1.4)}$$

Small contributions to loss of I atoms are made by I + NO_2 (4.7 %), I + HO_2 (0.0061 %), I + NO (0.086 %) and I + I (0.00021 %). Production of I atoms, as shown in Figure 5.36 and Figure 5.37, is dominated by photolysis of IO (45.4 %), which represents a null cycle in terms of processes controlling $[IO]_{SS}$, followed by photolysis of I_2 (26.4 %), and the reaction of IO with NO (23.3 %). Photolysis of HOI contributes 3.7 %. The self-reaction of IO, which is more important when $[IO]_{SS}$ is higher, contributes 1.0 % on average. The contribution from photolysis of CH_3I is negligible, as expected given its long photolytic lifetime. This result is in agreement with the work of Gómez Martín *et al.* (2013) and Mahajan *et al.* (2012). The sum of the contributions from the reactions $CH_3I + h\nu$ and I_2 + OH was 0.2 %.

Figure 5.37 shows a time series of the rate of production of I atoms for each data point in the steady state calculation, as a histogram of the contributions from reactions (P2) to (P9). A clear diurnal cycle is evident in the production of I atoms, determined by photolysis of IO and I_2. Before sunrise and after sunset, the IO self-reaction and the reaction of IO with NO make equal contributions to production of I atoms, with a small contribution from I_2 + OH when OH is present. As mentioned above, these features are the result of using measured [IO] to calculate $[I]_{SS}$, and the calculation does not include production of IO from known nighttime sources such as the reaction of NO_3 with I_2 (Saiz-Lopez and Plane, 2004), and the heterogeneous reaction of O_3 with aqueous iodide at the sea surface (Sakamoto *et al.*, 2009).

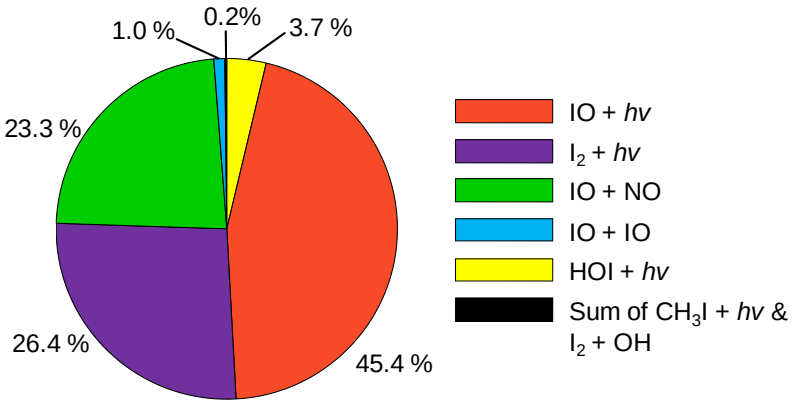

Figure 5.36. Mean contributions to the rate of production of I atoms from reactions (P2) to (P9).

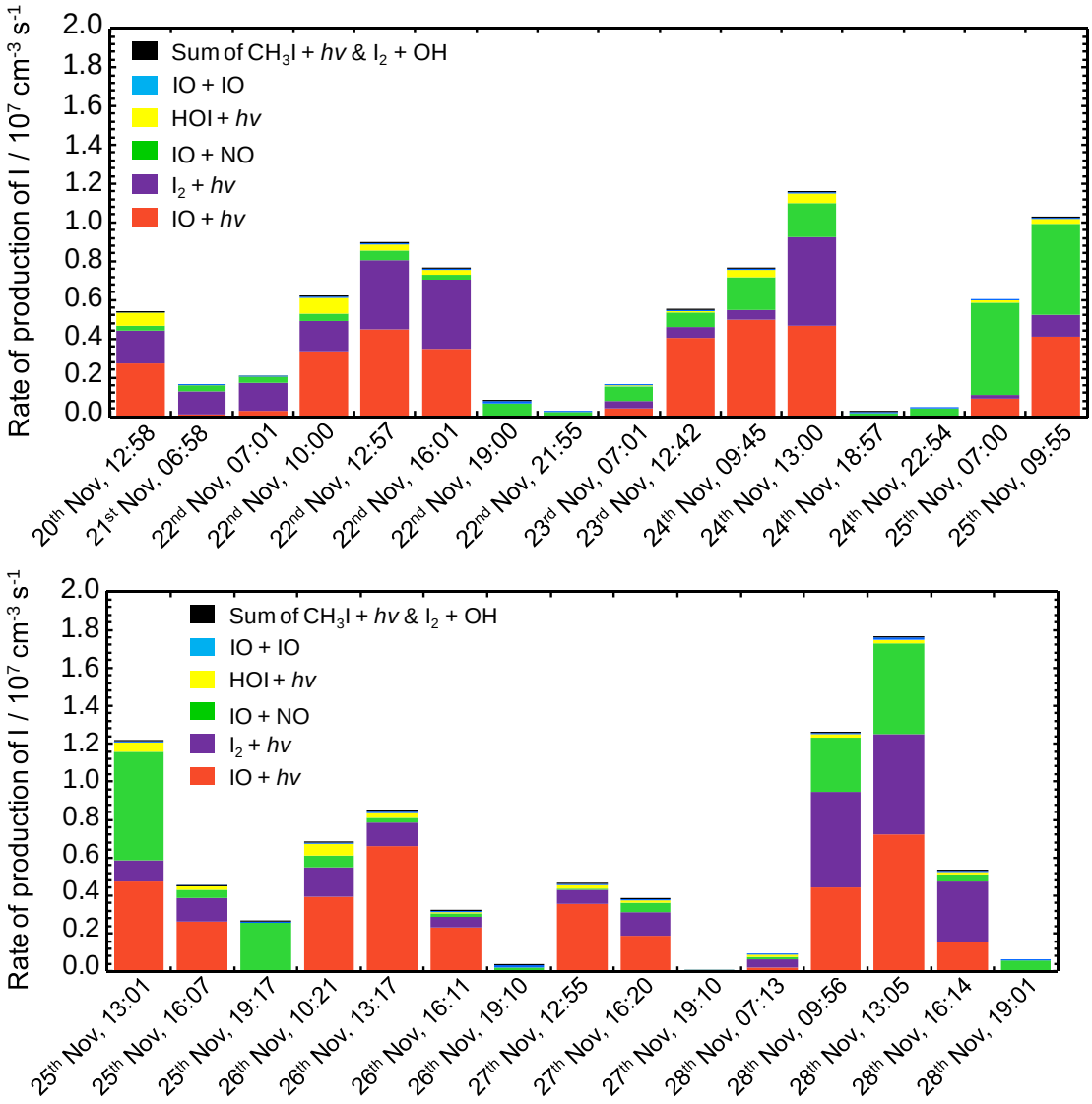

Figure 5.37. Time series of the rate of production of I atoms in the steady state calculations, coloured by the individual contributions from reactions (P2) to (P9). *x*-axis values are day of November 2011 and local time, where local time = UTC + 8h. Columns are centred over a time and date and are not evenly spaced (see Figure 5.33). Local sunrise and sunset were at 06:00 and 18:00, respectively.

This analysis is missing potential sources and sinks of IO, such as the heterogeneous reaction of O_3 with I^- at the sea surface, reaction of NO_3 with I_2, and photolysis of short-lived iodocarbons such as CH_2I_2 and CH_2ICl. It does not therefore represent a comprehensive analysis of IO production and loss during the cruise, but gives an indication of the important processes. A more detailed modelling study will be performed in future work, to fully analyse the processes controlling IO, and to investigate the mechanism of production of IO at night.

5.12 Nighttime IO observations by LIF

The highest IO mixing ratio (2.44 pptv) was measured by the LIF instrument shortly after sunset on 26th November. The ship was crossing the Sulu Sea and during the day elevated levels of IO had been measured by both the LIF instrument and the MAX-DOAS instrument. The mean nighttime IO mixing ratio was 0.79 pptv, which is very close to the daytime mean of 0.80 pptv. The comparable daytime and nighttime mixing ratios are surprising, since known chemistry leading to detectable levels of IO at night in coastal environments relies upon high mixing ratios of I_2 (Saiz-Lopez *et al.*, 2006, Furneaux *et al.*, 2010). Potential interferences in the IO measurements, and possible nighttime sources, are considered here.

5.12.1 Potential interferences

Very high mixing ratios of NO_2 are known to cause an interference in the LIF instrument (see section 3.7 in Chapter 3). Measurements of IO using the Leeds LIF instrument during the RHaMBLe cruise in the north-eastern Atlantic ocean were subject to occasional interference from NO_2 from the ship's exhaust, depending on wind direction and the position of the LIF inlet relative to the stack (Commane, 2009). During periods when the ship's exhaust was being sampled by the LIF instrument, NO_2 mixing ratios were on the order of 200 to 500 ppbv. Although measurements of NO and NO_2 were made using a commercial NO_x analyser during the SHIVA cruise, with the sample attached to the outside of the LIF inlet, the data have been rejected because the temperature difference between the ambient air and the air-conditioned container, where the NO_x analyser was located, caused water to condense in the sampling line and disrupt

the measurements. However, the measurements of NO_2 made by the CE-DOAS instrument located close to the stack on the monkey deck of the ship are considered to be representative of the conditions experienced on the front deck where the LIF instrument was located.

For most of the SHIVA cruise, the NO_2 mixing ratio was between 100 and 400 pptv (see Figure 5.5). The maximum NO_2 mixing ratio measured by the CE-DOAS instrument was 21.5 ppbv. For comparison, measurements of tens of ppbv of NO_2 made during the RHaMBLe cruise onboard the RRS *Discovery* were attributed to influence from the ship's stack (Lee *et al.*, 2010), though much higher values (300–500 ppbv) were recorded during the cruise (Commane, 2009). The area sampled during the SHIVA cruise was therefore not always representative of a pristine marine environment, being occasionally influenced by shipping, oil and gas platforms, and perhaps the ship's exhaust. The NO_2 interference has a magnitude of 0.004 pptv per ppbv of NO_2 (Commane, 2009), resulting in a maximum interference of −0.086 pptv for 21.5 ppbv NO_2 in the SHIVA IO measurements, which is within the 1σ precision of the measurements. Negative interference caused by NO_2 can therefore be ruled out. Positive interference could be caused by very high mixing ratios and significant variability of NO_2 between the online and offline IO measurement periods (Commane, 2009). A time series of nighttime IO and nighttime NO_2 is shown in Figure 5.38. Although there are high values of NO_2 during some nights when IO was detected above the LOD, it is clear that NO_2 did not cause an interference in the IO measurements. A correlation coefficient of $r = -0.29$ ($p < 0.02$) was found between nighttime IO and NO_2, most likely caused by reaction of IO with NO_2, forming the reservoir species $IONO_2$, as discussed in section 5.11.

A further possibility is that the optics inside the detection assembly, and the inside of the fluorescence region, became coated with inorganic iodine species over the course of the cruise. However Figure 5.38 indicates that the nighttime mixing ratios of IO decreased towards the end of the cruise, which would not be the case if the detection cell was contaminated with inorganic iodine.

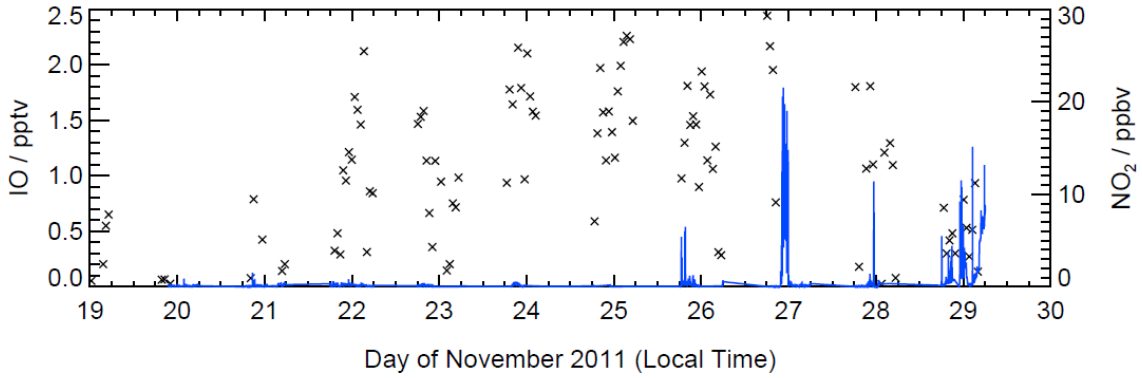

Figure 5.38. Time series of nighttime IO (black crosses) and NO_2 (blue line) measurements during the SHIVA cruise. NO_2 was usually between 100 and 400 pptv during the cruise (see Figure 5.5).

5.12.2 Nighttime sources of IO

The reaction between I_2 and NO_3 has been cited by several authors (Chambers *et al.*, 1992, Saiz-Lopez and Plane, 2004, Kaltsoyannis and Plane, 2008) as the source of nighttime IO:

$$I_2 + NO_3 \rightarrow I + IONO_2 \qquad \text{(R1.75)}$$

$$I + NO_3 \rightarrow IO + NO_2 \qquad \text{(R1.76)}$$

NO_3 was not measured during the SHIVA cruise, and calculation of NO_3 concentrations based on measurements of other species is beyond the scope of this work. However, the observed nighttime mixing ratios of NO_2, ranging from below the detection limit to 21.5 ppbv, with a mean value of 0.7 ppbv, suggest that NO_3 could be present at night. For example, Allan *et al.* reported measurements of NO_2 (~ 1 ppbv) and NO_3 (10–15 ppbv) at Mace Head in semi-polluted air masses arriving from the continent (Allan *et al.*, 2000). Saiz-Lopez and Plane accounted for nighttime measurements of ~ 2 pptv of IO with 10 pptv of NO_3 and a peak I_2 mixing ratio of 40 pptv (Saiz-Lopez *et al.*, 2006). 40−80 pptv NO_3+N_2O_5 was measured at Roscoff, where NO_2 mixing ratios were typically between 1 and 5 ppbv, and O_3 mixing ratios were around 20−30 ppbv, similar to the levels seen during the SHIVA campaign (see Figure 5.4) (Furneaux *et al.*, 2010). However, a photochemical box model constrained to those measurements of NO_3 and O_3 required up to 320 pptv of I_2 to account for the observed nighttime mixing ratios of IO. Such high mixing ratios of I_2 are found only in coastal locations, as demonstrated by the relatively low mixing ratios of I_2 measured during the SHIVA cruise (see Figure

5.18). In addition, IO was found to be negatively correlated with I_2 at night ($r = -0.70$, $p < 0.01$), suggesting that the reaction between NO_3 and I_2 is not responsible for the observed IO mixing ratios.

IO was recently detected in the free troposphere in air masses decoupled from the ocean surface (Dix *et al.*, 2013), indicating a longer effective IO lifetime than current understanding predicts. Short-lived halocarbons such as CH_2I_2, and I_2, emitted at the ocean surface, react within the marine boundary layer, and the short lifetime of IO means that it is unlikely to be transported from the surface to the free troposphere. Rather, the measurements could be explained by photolysis of longer-lived species such as CH_3I, or heterogeneous recycling of iodine from aerosols back to the gas phase through reactions of ozone with iodide (reactions (R1.79) to (R1.83)). These reactions are known to occur in the dark (Sakamoto *et al.*, 2009) and could also explain the unexpected detection of IO at night during the SHIVA project. Although the reaction produces more than 100 times more I_2 than IO, the enhancement of iodine in marine aerosol compared to sea water (*e.g.* Baker, 2004) could make the reaction on aerosols a more important source of IO.

Due to the precision of the IO data (± 0.75 pptv), and the low mixing ratios (0−2.44 pptv), no firm conclusions can be drawn about the nighttime measurements without detailed chemical modelling. However, the negative correlation between IO and I_2 points towards a heterogeneous production mechanism, such as the reaction of O_3 with I^- at the sea surface, rather than the gas-phase reaction between NO_3 and I_2.

5.13 Conclusions

Measurements of IO made during the SHIVA cruise reveal that IO is present at low mixing ratios throughout this area of the remote marine boundary layer, in good agreement with previous measurements of IO made in this region (Großmann *et al.*, 2013). IO was measured by LIF and by MAX-DOAS during the cruise. The two data sets compare favourably, with the mean LIF measurement being 0.80 pptv, and the mean MAX-DOAS measurement being 0.74 pptv. The maximum mixing ratios measured by the two instruments were measured on the same day (28th November),

when the ship was crossing the Sulu Sea. Similar average daytime profiles of IO were measured by both instruments, with very little variation in IO throughout the day. Generally higher mixing ratios were measured by the LIF instrument, which is expected from the predicted vertical gradient of IO above the sea surface (Mahajan *et al.*, 2010, Großmann *et al.*, 2013). Measurements of IO from the SCIAMACHY instrument onboard the Envisat satellite show maximum IO columns of 3×10^{12} molecule cm^{-2}, corresponding to a mixing ratio of 1.4 pptv, assuming an air mass factor of 1 and a boundary layer height of 1 km. Given the large uncertainty in the satellite measurements (Schönhardt *et al.*, 2008), and the potential influence of IO in the free troposphere on the observed IO column (Dix *et al.*, 2013), there is no clear discrepancy between the satellite measurements and the *in situ* LIF measurements made during the cruise.

The maximum IO mixing ratio measured by LIF was 2.4 pptv. Similar mixing ratios were observed during the day and night, a result at odds with current understanding of marine boundary layer iodine chemistry, though there was considerable variability in the diurnal profile between different days of the cruise (see Figure 5.15 and Figure 5.16). Mixing ratios of I_2 and the sum of HOI + ICl (AIC) were measured throughout the cruise by the diffusion-denuder method. The mean I_2 mixing ratio was 1.98 pptv and the mean AIC mixing ratio was 2.74 pptv. Daytime I_2 mixing ratios were lower than at night due to photolysis. No clear diurnal profile was found for AIC.

IO was not found to correlate with sea surface temperature, salinity, air temperature, or wind speed, in contrast to previous studies, where IO was found to be positively correlated with both sea surface temperature and salinity (Mahajan *et al.*, 2012, Gómez Martín *et al.*, 2013, Großmann *et al.*, 2013). The lack of correlation during SHIVA is attributed to the fact that the cruise was relatively short and spanned a small latitudinal range, so that sea surface temperature and salinity varied very little during the cruise. No significant correlation was found between IO and chlorophyll-*a*, suggesting that biological processes were not important for production of IO during SHIVA. This result is in agreement with those of Großmann *et al*. (2013), Gómez Martín *et al*. (2013), and Mahajan *et al*. (2012), who found that IO was negatively correlated with chlorophyll-*a*, and concluded that biological activity was not important for iodine production, and may even be an inhibiting factor.

A weak positive correlation was found between IO and atmospheric CH_3I (r = 0.26), in agreement with Großmann *et al*. (2013) and Gómez Martín *et al*. (2013) who found that due to its long photolytic lifetime in the marine boundary layer, CH_3I is not a major precursor of reactive iodine. Moderate negative correlation was found between IO and oceanic CH_3I (r = −0.42), and between IO and oceanic CH_2ICl (r = −0.50). These results point towards biological activity or products inhibiting the release of reactive iodine from the oceans, as suggested by Gómez Martín *et al*. (2013). Moderate negative correlation was found between IO and atmospheric I_2 (r = −0.59), and between IO and AIC (r = −0.41). These results are surprising, and as yet unexplained, since both I_2 and HOI are known photolytic precursors of iodine atoms, which react with ozone to produce IO. The lack of correlation between IO and O_3 on a 24 hour timescale or on a 5 minute timescale indicates that IO had a limited role in ozone destruction during the cruise.

Calculations of steady state concentrations of IO are in good agreement with the measurements, though large uncertainty is associated with the calculated $[IO]_{SS}$, since the calculation does not include heterogeneous sources of IO such as the $O_3 + I^-$ reaction at the sea surface, and many of the species in the calculation (OH, HO_2, NO, photolysis rates) were estimated from field measurements in other open ocean regions. Previous modelling studies of IO have relied upon fluxes of I_2 from the ocean surface to reproduce observations (Furneaux *et al.*, 2010, Großmann *et al.*, 2013). The measurements of I_2 and AIC made during the SHIVA cruise were therefore a useful tool in predicting the daytime IO concentrations. IO production was dominated by photolysis of I_2, with a significant contribution from photolysis of HOI. The photolysis of CH_3I made a negligible contribution. IO loss was dominated by photolysis, with a significant contribution from the reaction of IO + HO_2. The reaction between IO and NO_2, forming the reservoir species $IONO_2$, appears to be an important loss process for IO.

Chapter 6. Development of a Laser-Induced Phosphorescence instrument for field measurements of glyoxal

This chapter describes the development and initial testing of a laser-induced phosphorescence instrument for measurements of glyoxal that will be deployed in the ORC^3 project fieldwork in 2014 (see Chapter 1 for details).

6.1 Current measurement techniques

Glyoxal is a tracer for fast photochemical oxidation of biogenic and anthropogenic VOCs. Measurements with high spatial and temporal resolution are therefore required to investigate its production and loss. Gas-phase glyoxal has been detected by long-path DOAS (Volkamer *et al.*, 2005), by satellite-based DOAS (Wittrock *et al.*, 2006), by MAX-DOAS (*e.g.* Sinreich *et al.*, 2010) and by laser-induced phosphorescence (LIP) (*e.g.* Huisman *et al.*, 2011). Glyoxal has also been measured by derivatisation with 2,4-dinitrophenylhydrazine and detection by liquid chromatography coupled with mass spectrometry (*e.g.* François *et al.*, 2005), and by derivatisation with o-(2,3,4,5,6-pentafluorobenzyl)-hydroxylamine (PFBHA) and detection by gas chromatography coupled with mass spectrometry (*e.g.* Spaulding *et al.*, 2002). DOAS and LIP techniques have good sensitivity and temporal resolution, with MAX-DOAS offering remote sensing and LIP offering point measurements.

The Madison laser-induced phosphorescence instrument (MAD-LIP, 3σ LOD = 18 pptv in 1 minute) (Huisman *et al.*, 2008) was first deployed during the 2007 BEARPEX measurement campaign in California. The MAD-LIP instrument has since been redeveloped to use the Laser-Induced Phosphorescence of (methyl)GLyOxal Spectrometry method (LIPGLOS, 3σ LOD = < 4 pptv in 5 minutes) (Henry *et al.*, 2012). The LIPGLOS instrument makes use of the time-dependent decay of

phosphorescence from glyoxal and methyl glyoxal to quantify their concentrations, rather than integrating the phosphorescence signal over the duration of the decay, which is the approach taken in LIF and LIP measurements. A continuous-mode laser can be used, which makes the instrument lighter, more compact, and less expensive than the MAD-LIP instrument.

Glyoxal is detected by LIP at a wavelength close to that used for detection of IO in the Leeds IO LIF instrument (λ ~ 440 nm). The similarity of the techniques, and the suitability of the current laser system for probing glyoxal phosphorescence, should make the development of a glyoxal instrument from the current IO instrument possible. The ability to measure both IO and glyoxal using the same instrument, with limited reconfiguration and therefore a short change-over time, is also an attractive prospect, given the importance of each species in the marine boundary layer. The Leeds glyoxal laser-induced phosphorescence instrument is based around the IO LIF instrument described in Chapter 3, and follows the design of the Madison glyoxal LIP instrument (MAD-LIP) described by Huisman *et al*. (2009).

6.2 Glyoxal detection by Laser-Induced Phosphorescence

6.2.1 Phosphorescence scheme

The vibrationless electronic transition from the ground state, ^1A_g (S_0), to the ^1A_u (S_1) excited state of glyoxal occurs around λ = 455 nm (21977 cm^{-1}) (Brand, 1954). Figure 6.1 shows a high-resolution absorption spectrum of glyoxal in the region of this transition, recorded by Volkamer *et al*. (2005). The spectrum consists of numerous rovibrational bands, some of which have been labelled with the vibrational mode excited in the transition according to the values given by Beyer *et al*. (1974). The strong absorption feature at λ = 440 nm is due to the $v_8' = 1 \leftarrow v_0'' = 0$ or 8_0^1 transition (Brand, 1954). The v_8 vibrational mode is C–H wagging, with a vibrational frequency of 1048 cm^{-1} in the ground state, and 735 cm^{-1} in the excited state (Brand, 1954, Holzer and Ramsay, 1970).

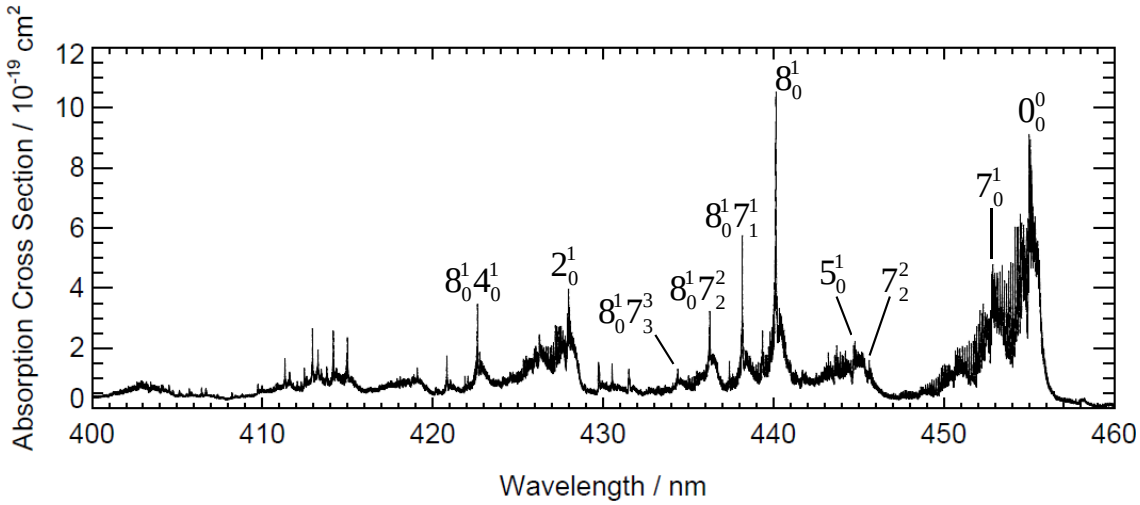

Figure 6.1. Absorption spectrum of glyoxal around the $^1A_u \leftarrow {}^1A_g$ transition, measured by Volkamer *et al.* (2005). Selected rovibronic bands have been labelled according to the values given by Beyer *et al.* (1974).

The 8_0^1 transition is ideal for excitation in laser-induced phosphorescence spectroscopy, since the absorption spectrum around $\lambda = 440$ nm is sufficiently structured to enable tuning of the laser wavelength to an 'online' and an 'offline' position, as for IO laser-induced fluorescence spectroscopy, and the transition is strong in absorption (Brand, 1954, Volkamer *et al.*, 2005, Huisman *et al.*, 2008). The excited singlet state undergoes collision-induced intersystem crossing to the ^3A_u (T_1) state with near-unity yield at pressures exceeding 1 Torr (Anderson *et al.*, 1973) (see Figure 6.2). Phosphorescence from the triplet state is long-lived, with a lifetime of $\sim 10\,\mu$s in 100 Torr of air (Huisman *et al.*, 2008) determined by quenching by O_2 ($k = 0.003\,\mu s^{-1}$ Torr^{-1}, collision-free lifetime = 3.29 ms) (Yardley, 1972). This lifetime is long enough to delay photon counting until the laser pulse and short-lived fluorescence inside the cell have decayed completely, thereby minimising the background signal. The strongest phosphorescence from the triplet state occurs from the $v_0'' = 0 \leftarrow v_0' = 0$ transition at $\lambda = 520.8$ nm (19196 cm^{-1}) (Holzer and Ramsay, 1970). The collection optics are therefore optimised to transmit this wavelength. The excitation and phosphorescence scheme is shown in Figure 6.2.

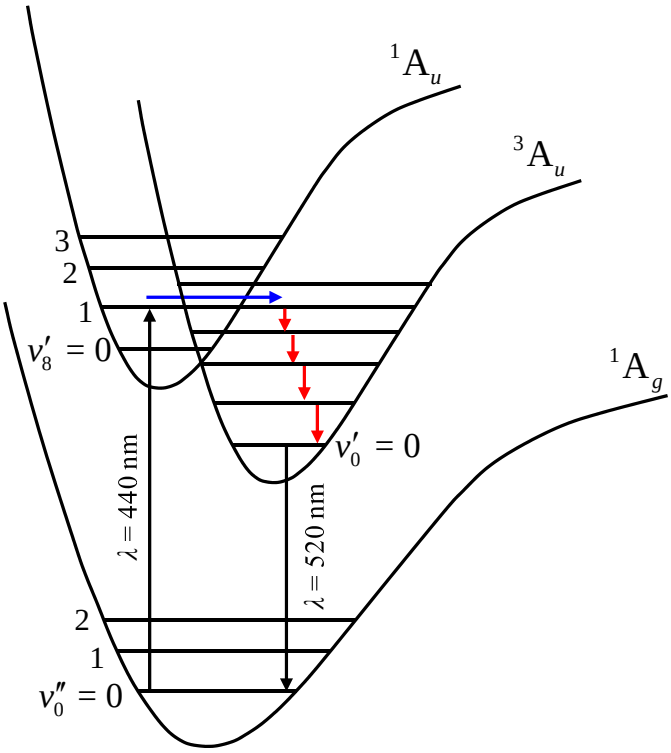

Figure 6.2. Schematic of electronic processes in detection of glyoxal by laser-induced phosphorescence, showing excitation from ^1A_g (S_0) to ^1A_u (S_1) at λ = 440 nm, intersystem crossing between ^1A_u (S_1) and ^3A_u (T_1) (blue arrow), vibrational (non-radiative) relaxation (red arrows), and phosphorescence from ^3A_u (T_1) to ^1A_g (S_0) at λ = 520 nm. Figure adapted from Salter *et al*. (2013a).

6.2.2 Laser system and optics

The laser system is as described in Chapter 3 for detection of IO by laser-induced fluorescence, with the exception that the Ti:Sapphire laser is tuned to λ = 880 nm and frequency-doubled to give 30–50 mW of light at $\lambda \sim 440$ nm. Laser light is delivered to the phosphorescence cell as an open beam rather than *via* optical fibres. This configuration has been found to significantly reduce background signal caused by laser scattered light, since it is difficult to collimate light exiting from a fibre. The arrangement of the laser, delivery optics, and phosphorescence cell used during laboratory testing is shown in Figure 6.3. The laser, optics and phosphorescence cell are fixed to a single breadboard to facilitate alignment, and the pump is located on the floor beneath the workbench. On exiting the casing the laser beam width is approximately 2 mm.

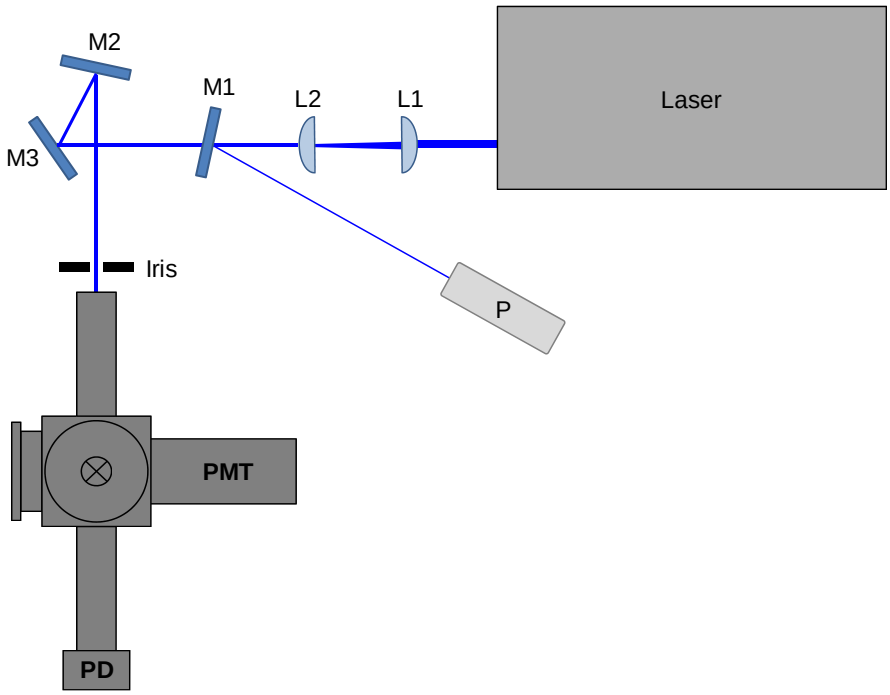

Figure 6.3. Arrangement of laser, optics and phosphorescence cell for laboratory glyoxal experiments, showing: Focussing and collimating lenses (L1, L2); beamsplitter (M1); wavemeter probe (P); alignment turning mirrors (M2, M3); iris; photomultiplier tube (PMT); and photodiode (PD). View of detection cell is from above, showing the inlet. The connection to the pump is on underside of the cell, and the pump is located beneath the workbench.

To minimise laser scattered light in the background signal, the laser beam is focussed and collimated by the two lenses L1 (25 mm diameter, 50 mm focal length, uncoated) and L2 (25 mm diameter, 25 mm focal length, uncoated) to give a beam width of approximately 1 mm. An iris immediately before the baffled input arm further minimises stray light inside the cell. The laser wavelength is monitored by reflecting a small fraction of the beam onto the probe of a wavemeter (Coherent WaveMaster; resolution: ± 0.001 nm; accuracy: ± 0.005 nm) using an uncoated glass flat. Laser light is directed into a 210 mm long baffled input arm by two turning mirrors M2 and M3 (both 1 inch diameter with broadband dielectric coating; reflectivity > 99 % at $\lambda = 400{-}750$ nm). The laser beam is aligned through the centre of the input and output arms, and the alignment is optimised by minimising the background signal recorded by the photon counting card. The laser power is measured by a photodiode (UDT Instruments UDT-555UV) positioned at the end of a 210 mm long baffled output arm.

6.2.3 Inlet and phosphorescence cell

Ambient air is drawn through a ⅛ inch internal diameter stainless steel Swagelok union mounted in a flat circular plate on top of the phosphorescence cell. The fitting facilitates connection to Teflon sampling lines in the laboratory and in the field, enabling the instrument to be positioned some distance from the sampling location, and helping to eliminate solar scattered light from the background signal (see section 6.2.4). Unlike the HO_x and IO instruments, the inlet opens directly into the phosphorescence cell. This approach is not viable in HO_x measurements, where gas expansion to a much lower pressure through a small pinhole is required to extend the OH fluorescence lifetime beyond the laser pulse, or in IO measurements, where sampling through a Teflon tube causes significant radical wall losses.

The phosphorescence cell is a 110 mm long, black anodised aluminium cylinder with an internal diameter of 50 mm, giving a total distance of 65 mm between the top of the inlet and the laser excited phosphorescence region. A dry scroll vacuum pump (Agilent Technologies, IDP-3) provides a constant pumping speed of 60 L min^{-1}, reduced to 5 L min^{-1} by a butterfly valve downstream of the phosphorescence cell. When used in the laboratory, the cell is connected to the pump with approximately 2 m of NW16 flexible steel bellows. The use of a small, dry scroll pump is a significant advantage over the large oil rotary pumps required for HO_x and IO measurements, in terms of power consumption (~ 200 W when running, compared to 5 kW for FAGE pumps) and space requirements, maintenance, weight, and noise levels. The input and output arms, photodetector, and retroreflector are mounted in black anodised aluminium cylinders, which are sealed to the phosphorescence cell by round, uncoated Suprasil windows between two o-rings.

6.2.4 Photon collection and timing

Photons are detected by a photomultiplier tube (PMT) (Sens-Tech P25PC photodetector module, 15 % quantum efficiency at λ = 520 nm) positioned perpendicular to the laser beam and the gas flow. Light from the phosphorescence region passes through a Suprasil window and an interference filter centred at λ = 520 nm (Semrock, FF02-520/28, > 93 % average transmission, 28 nm minimum bandwidth) which removes laser

scattered light. The light is focussed by two lenses located in the PMT arm (2 inch diameter, 52 mm focal length, anti-reflection coated at $\lambda = 521$ nm) onto the photocathode. A retroreflector (CVI Optics fused silica plano-concave spherical mirror, broadband coated, radius of curvature = 50.8 mm) positioned opposite the detector maximises the collection of light from the phosphorescence region. The signal from the PMT is sent to a photon counting card (Becker & Hickl, PMS 400, for details see Chapter 2, section 1.4.5) in the data acquisition computer.

The laser is triggered by a pulse from a delay generator (Berkeley Nucleonics Corporation, Model 555 Delay-Pulse Generator) which also controls the signal acquisition timing. The photomultiplier tube remains switched on during the entire measurement cycle, and data acquisition timing is achieved by triggering the photon counting card with the delay generator. The optimum photon counting timing was determined by monitoring the signal from the photon counting card using the Becker & Hickl operating software. The delay between the laser pulse and the start of photon counting, and the width of the photon counting gate, were adjusted to minimise the number of counts from laser scattered light and short-lived fluorescence from the cell anodising dye (see Chapter 3, section 1.3.3), and to maximise the number of counts from glyoxal phosphorescence.

Figure 6.4 shows the optimum timing of the laser pulse, glyoxal phosphorescence and photon counting for a cell pressure of 100 Torr. Glyoxal phosphorescence peaks shortly after the laser pulse, and lasts for approximately 30 μs depending on the pressure in the detection cell (collision-free lifetime = 3.29 ms). Solar scattered light is eliminated by sampling *via* Teflon tubing inside stainless steel flexible bellows vacuum hose. Photons are therefore collected in a single gate which begins 2.5 μs after the start of the laser pulse (to minimise laser scattered light and short-lived fluorescence) and lasts for 35 μs. The signal is integrated over 5000 sweeps, or 1 second at the 5 kHz laser pulse repetition rate. The maximum specified dark count rate for the PMT is 200 s^{-1}, which gives a maximum dark count rate of 35 s^{-1} when integrated over 35 μs at the laser repetition rate of 5000 Hz. The background signal measured in the laboratory is significantly lower than this (*e.g.* 2.2 count s^{-1} mW^{-1} when sampling N_2 during the calibration. See section 6.3.4), and is dominated by laser scattered light.

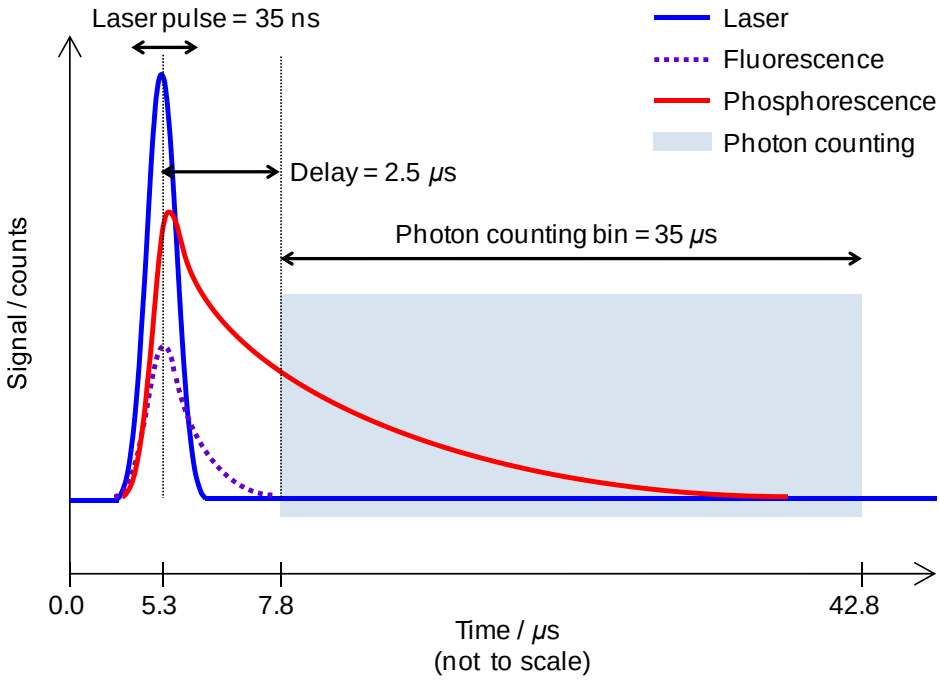

Figure 6.4. Timing scheme for signal acquisition in laser-induced phosphorescence of glyoxal, with the start of the cycle (time = 0.0 μs) defined by the laser trigger. The blue line represents the Ti:Sapphire laser pulse at λ = 440 nm, the dashed purple line represents fluorescence from the cell anodising dye (see Chapter 3), the red line represents glyoxal phosphorescence, and the shaded blue area represents photon counting. The 1/*e* lifetime of the short-lived fluorescence is approximately 2 μs.

6.3 Instrument development

6.3.1 Method of preparation of glyoxal

Glyoxal was prepared by James Lockhart in the Dainton Laboratory at the University of Leeds using the method described by Volkamer *et al*. (2005). Equal masses of glyoxal trimer dihydrate (Fluka, ≥ 95 %) and phosphorous pentoxide (P_2O_5, Sigma-Aldrich, ≥ 98.5 %) were heated under vacuum to ~ 160 ºC. A flow of nitrogen (BOC, oxygen-free) was passed over the heated sample into a collection chamber, where solid glyoxal was collected at ~ −70 ºC. Pure gas-phase glyoxal (sublimed from the crystals at room temperature) was stored in a darkened Pyrex bulb and diluted with nitrogen (BOC, oxygen-free nitrogen) to the required concentration before use. During laboratory testing, the glyoxal was diluted further with synthetic air (BOC, compressed air, BTCA 178) by mixing flows with two mass flow controllers.

6.3.2 Recording of laser-induced phosphorescence spectra

The ideal online and offline laser wavelengths have been investigated by recording a laser-induced phosphorescence spectrum over the wavelength range of interest. The laser wavelength is controlled by a stepper motor which changes the angle of incidence of the diffraction grating in the Ti:Sapphire cavity. Custom-built control and data acquisition software controls the stepper motor, and the wavelength is monitored using the wavemeter. Each wavelength change takes approximately 100 μs to execute, after which time signal from the detector is integrated over 1 second before the next wavelength change. The minimum step size that can be set by the operator is approximately 0.25 pm (0.013 cm^{-1} at λ = 440 nm), which is below the 1 pm resolution of the wavemeter. The laser wavelength is recorded at every data point and the effective step size can be found by dividing by the number of data points between each wavelength change recorded by the wavemeter. The number of data points between each 1 pm change should be the same for a given step size, but it was found to change during a single wavelength scan so that the step size was not constant. It is not clear whether this is caused by the stepper motor not moving the grating for several points, or whether the step size becomes smaller or larger than intended due to backlash or slipping in the motor system. The laser wavelength is always approached from the short wavelength side so that any backlash should be accounted for. The laser linewidth and the minimum step size of the stepper motor determine the resolution and appearance of the resulting spectrum. The ideal online and offline wavelengths give a maximum online signal and a minimum offline signal with the minimum wavelength change, since the duty cycle of a measurement is partly determined by the time taken to move between the online and offline wavelengths.

Figure 6.5 shows a high-resolution absorption spectrum of glyoxal (Volkamer *et al.*, 2005) (hereafter referred to as the reference spectrum) overlayed on a laser-induced phosphorescence spectrum recorded in the laboratory, showing coincident peaks and troughs. The wavelength step size was set to 0.25 pm per point and the actual step size ranged between 0.1 pm and 10 pm.

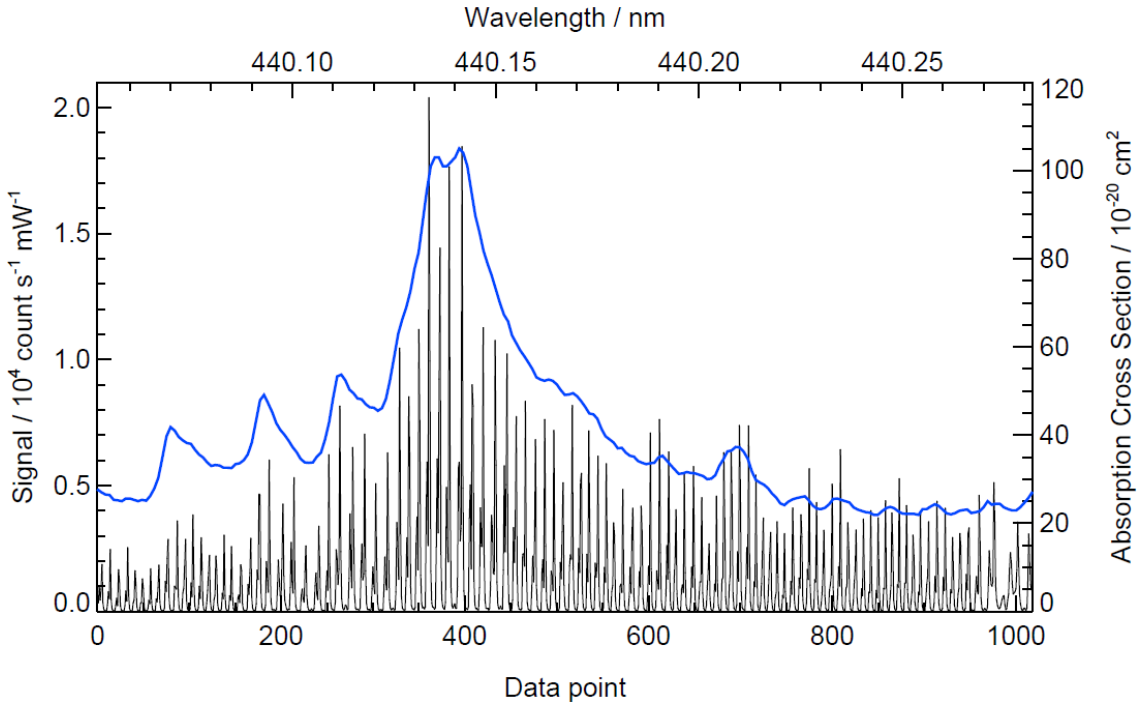

Figure 6.5. High-resolution absorption spectrum of glyoxal (blue line, top and right hand axis) (Volkamer *et al.*, 2005) and laser-induced phosphorescence spectrum (black line, bottom and left hand axis) recorded in 1.7 ppbv of glyoxal in 120 Torr of air ([Gly] in detection cell = 6.7×10^9 molecule cm^{-3}). The maximum phosphorescence signal was obtained with a laser wavelength of λ = 440.131 nm. The laser wavelength step size was set to 0.25 pm per data point.

Since the stepper motor does not give regular wavelength step sizes, the measured laser-induced phosphorescence spectrum was adjusted to match the peaks in the reference spectrum, though the low and high wavelength limits are given by the wavemeter. The maximum phosphorescence signal was obtained at an excitation wavelength of λ = 440.131 nm, which corresponds to the $^1A_u\left(v_8' = 1\right) \leftarrow {}^1A_g\left(v_0'' = 0\right)$ transition (8_0^1 in Figure 6.1) (King, 1957, Beyer *et al.*, 1974). The strong signal from this narrow transition makes λ = 440.131 nm an ideal online wavelength, with an offline wavelength easily accessible to the low wavelength side where the baseline counts of the measured spectrum are small.

6.3.2.1 Rotational analysis of glyoxal

The spectrum shown in Figure 6.5 has the appearance of a congested rotationally-resolved spectrum, and is reasonably well matched to the high resolution absorption spectrum measured by Volkamer *et al.* (2005). The adjacent peak separation varies

between 0.0020 nm (0.103 cm^{-1}) and 0.0028 nm (0.145 cm^{-1}). The laser linewidth is ~ 0.045 cm^{-1} at λ = 440 nm (estimated from the linewidth at λ = 308 nm given in the laser specifications), so it is possible that the narrow peaks in the measured spectrum are resolved rotational lines within the $^1A_u\left(v_8'=1\right) \leftarrow {}^1A_g\left(v_0''=0\right)$ transition. In the ground and first electronically excited states, glyoxal exists in the planar *trans* configuration with C_{2h} symmetry (Dykstra and Schaefer, 1975). Glyoxal is a near-prolate asymmetric top, with moments of inertia $I_C > I_B \gg I_A$, but can be approximated as a prolate symmetric top, with moments of inertia $I_C \approx I_B \gg I_A$. The inertial *A* axis is located approximately along a line joining the two O atoms, *B* is located approximately along a line joining the two H atoms, and *C* is perpendicular to the molecular plane (Pörtner *et al.*, 2002). Neglecting centrifugal distortion, the rotational terms values (energy levels, F / cm^{-1}), of a prolate symmetric top are given by:

$$F(J,K) = BJ(J+1) + (A-B)K^2 \;;\; J = 0,1,2\ldots,\; K = 0,1\ldots J \tag{6.1}$$

where *J* and *K* are the quantum numbers associated with the total angular momentum and its component along the inertial *A* axis, respectively. *A*, *B*, and *C* are rotational constants that depend on the vibrational and electronic state of the molecule, and are given by:

$$A = \frac{h}{8\pi^2 c I_A};\; B = \frac{h}{8\pi^2 c I_B};\; C = \frac{h}{8\pi^2 c I_C} \tag{6.2}$$

For a symmetric top all rotational levels with $K > 0$ are doubly degenerate. The classical explanation for this effect is that rotation about the inertial *A* axis can occur in a clockwise or anticlockwise direction, which results in the same angular momentum for a symmetric top with $I_B = I_C$. For a slightly asymmetric top the rotational terms values are similar but all levels with $K > 0$ are split into two components, the splitting being greatest for low values of *K*. The rotational term values of an asymmetric top can be approximated by:

$$F(J,K) = \bar{B}J(J+1) + (A-\bar{B})K^2 \tag{6.3}$$

where $\bar{B}$ is a rotational constant given by:

$$\bar{B} = \frac{1}{2}(B + C) \tag{6.4}$$

For $K = 1$, the K doubling is given by (Pebay Peyroula and Jost, 1987):

$$\Delta E(K = 1) = \frac{B - C}{2} J(J + 1) \tag{6.5}$$

The $^1A_g(v_8' = 1) \leftarrow {}^1A_u(v_0'' = 0)$ transition is a perpendicular A + B type band, in which the transition dipole moment change has components parallel to the inertial A and B axes, respectively, and perpendicular to the principal axis of rotation (the C inertial axis) (Pebay Peyroula and Jost, 1987). The selection rules for rotational transitions are therefore $\Delta J = 0, \pm 1$ and $\Delta K = 0, \pm 1$ (Pebay Peyroula and Jost, 1987), so that the rotational spectrum is expected to consist of $K' \leftarrow K''$ sub-bands consisting of P, Q, and R branches due to the accompanying change in J, further complicated by the K splitting (King, 1957).

Numerous studies have focussed on the $v_0' = 0 \leftarrow v_0'' = 0$ transition at λ = 455 nm (King, 1957, Paldus and Ramsay, 1967, Cole *et al.*, 1976, Spangler *et al.*, 1983, Pörtner *et al.*, 2002), but only one rotationally-resolved study of the $v_8' = 1 \leftarrow v_0'' = 0$ transition exists in the literature. Pebay Peyroula and Jost (1987) studied several rovibrational bands of the $^1A_g \leftarrow {}^1A_u$ transition in a supersonic jet expansion. Rotational constants for the ground and excited states of glyoxal from Pebay Peyroula and Jost (1987) are given in Table 6.1. Using equation (6.3), equation (6.5), and the values in Table 6.1, a simplified calculation of the spacing between rotational lines in the R branch of the $K' = 1 \leftarrow K'' = 0$ sub-band is possible. When K doubling is taken into account the spacing is calculated to range between 0.01 cm^{-1} and 0.36 cm^{-1}. Neglecting K doubling the spacing is calculated to range between 0.11 cm^{-1} to 0.30 cm^{-1}. These values are in reasonable agreement with the adjacent peak separation in the measured spectrum in Figure 6.5, and with the jet-cooled rotational spectrum given by Pebay Peyroula and Jost (1987).

Table 6.1. Rotational constants for the prolate symmetric top approximation of glyoxal (Pebay Peyroula and Jost, 1987)

	A	B	C	$\bar{B}$
$S_1\ (^1A_u)\ \left(v_8' = 1\right)$	1.946203	0.154676	0.143550	0.149113
$S_0\ (^1A_g)\ \left(v_0'' = 0\right)$	1.844003	0.160044	0.147329	0.153687

At room temperature the rotational spectrum is expected to be too congested to distinguish individual rotational lines (Pebay Peyroula and Jost, 1987) but it is likely that there is a degree of cooling of the gas sampled by the LIP inlet as it expands from ~ 760 Torr to ~ 100 Torr through the ⅛ inch diameter inlet. Many of the peaks in Figure 6.5 and subsequent spectra (see Figure 6.6 to Figure 6.9) are doublets, suggesting that the spectra consist of overlapping sub-bands. Birss *et al*. (1970) note that the Q branches $(\Delta J = 0)$ of the $K' = 1 \leftarrow K'' = 0$ and $K' = 0 \leftarrow K'' = 1$ sub-bands in the $v_0' = 0 \leftarrow v_0'' = 0$ transition become coincident at high values of *J*, with the intensities of the two Q branches being in the ratio 3:1. The authors calculate that the separations between corresponding lines in the two Q branches decrease from 0.370 cm^{-1} for *J* = 35 to 0.116 cm^{-1} for *J* = 45. The well-resolved doublet peak ratio in the spectrum in Figure 6.5 is 3:1, in agreement with Birss *et al*.

In summary, the measured spectrum is in good agreement with rotational analyses of the $v_8' = 1 \leftarrow v_0'' = 0$ and $v_0' = 0 \leftarrow v_0'' = 0$ transitions given in the literature. Simulation of a rotational spectrum of the $v_8' = 1 \leftarrow v_0'' = 0$ transition with the PGOPHER simulation program (C. M. Western, 2013 University of Bristol) will aid interpretation of the measured spectrum (see section 6.4.8). In addition, following the work of Creasey *et al.* (1997), the LIP inlet can be moved closer to the excitation axis and phosphorescence region, so that the effects of cooling can be maximised. This will reduce the complexity of the rotational spectrum and, along with the simulated spectrum, will enable assignment of the rotational lines.

6.3.2.2 Instrumental effects

It was postulated that the high peak signal and low baseline could be caused by an instrumental artefact such as repeated saturation and recovery of the photon counting card, caused by the strong phosphorescence signal. To test this, the signal from the PMT was mimicked by a regular 1.5 V pulse from a second delay-pulse generator, and sent to the photon counting card. The pulse rate was varied from 100 s^{-1} to 10000 s^{-1} and the signal was monitored using the Becker & Hickl software. The effect could not be reproduced by this false signal method, and so the possibility of saturation of the photon counting card was ruled out.

6.3.2.3 Reproducibility of phosphorescence spectra

During the laboratory experiments, it was not always possible to reproduce the results shown in Figure 6.5. Repeated spectra recorded under the same sampling conditions gave different results. Several examples of this and possible causes are now discussed. Figure 6.6 shows three consecutive spectra, between λ = 440.100 nm and λ = 440.200 nm, showing the changing appearance of the spectrum with repeated scans under identical conditions. Doublet peaks, attributed to overlapping branches of *K* sub-bands (see section 6.3.2.1) are visible in spectra 1 and 3, but not in spectrum 2. The programmed wavelength step size was 0.25 pm per point (as for the spectrum in Figure 6.5), but ranged between effective step sizes of 0.08 pm and 99 pm. The maximum signal in each spectrum was measured at λ = 440.131 nm (1), λ = 440.132 nm (2), and λ = 440.132 nm (3), which demonstrates the reproducibility of the overall shape of the spectrum, but highlights the difficulty in finding the exact online wavelength with the laser stepper motor. Repeated spectra which showed similar structure to that shown in Figure 6.5 were found to have maximum phosphorescence signal at wavelengths between λ = 440.129 nm and λ = 440.133 nm.

There is no clear pattern between the effective laser wavelength step size and the appearance of the spectrum, but it is likely that the inconsistency in the appearance of the spectrum was caused by problems with the laser wavelength stepping. The spectral linewidths measured in Figure 6.5 were on the order of 0.4 pm, which is not

significantly wider than the minimum reliable wavelength step size of 0.25 pm. Each laser wavelength scan could begin at a slightly different wavelength, enabled by the resolution of the wavemeter and the backlash in the stepper motor system. This could result in successive scans finding or missing the peaks of the spectral lines, as appears to be the case in Figure 6.6. This not only makes reliably finding the online position impossible, but has a significant effect on the signal measured from the glyoxal phosphorescence.

Figure 6.7 shows two phosphorescence spectra between λ = 440.052 nm and λ = 440.200 nm with a wavelength step size of 0.5 pm per data point. The larger step size gives lower resolution spectra than those shown in Figure 6.5 and Figure 6.6, the general shapes of which are in reasonable agreement with the reference spectrum shown in Figure 6.5 (Volkamer *et al.*, 2005), but the structure of each spectrum is clearly different, with the upper spectrum appearing to have lower resolution than the lower. The maximum phosphorescence signals were measured at λ = 440.130 nm and λ = 440.133 nm.

Figure 6.8 shows three examples of spectra recorded under identical sampling conditions. The phosphorescence signal increases from the first spectrum to the third. This is attributed to the build up of glyoxal inside the gas delivery lines and on the walls of the cell. The maximum phosphorescence signal was measured at slightly different wavelengths in each scan (λ = 444.133 nm, λ = 440.139 nm, and λ = 440.130 nm). The resolution of each spectrum appears to decrease from the first to the third, and the peak heights to the long wavelength side of the maximum peak are different in each spectrum. All three spectra contain doublet peaks, though not at the same wavelength. These effects are all attributed to backlash in the laser stepping system.

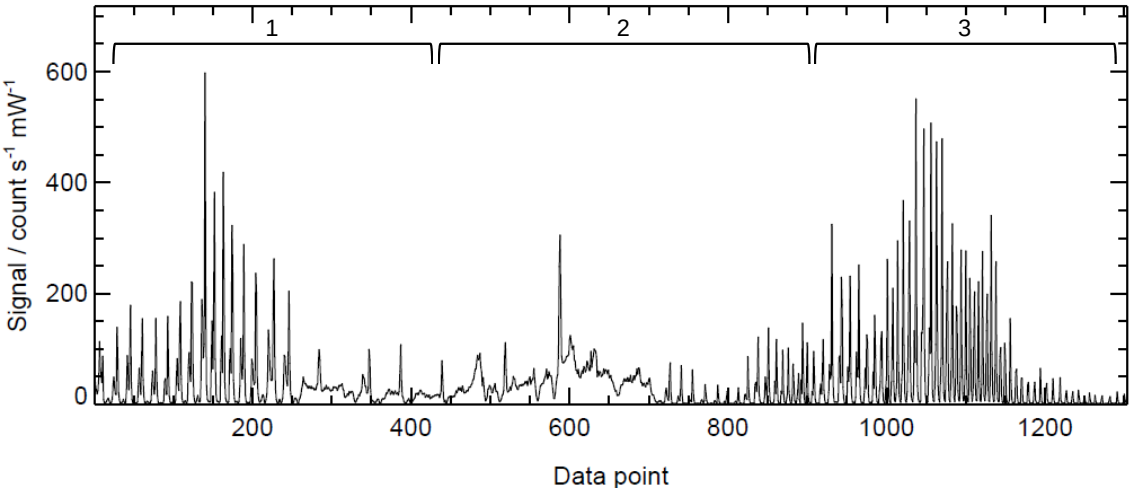

Figure 6.6. Three consecutive scans of laser wavelength, between λ = 440.100 nm and λ = 440.200 nm with a programmed wavelength step size of 0.25 pm per data point, showing apparent change in resolution of wavelength stepping between different scans. The maximum phosphorescence signal was measured at λ = 440.131 nm (scan 1), λ = 440.132 nm (scan 2), and λ = 440.132 nm (scan 3).

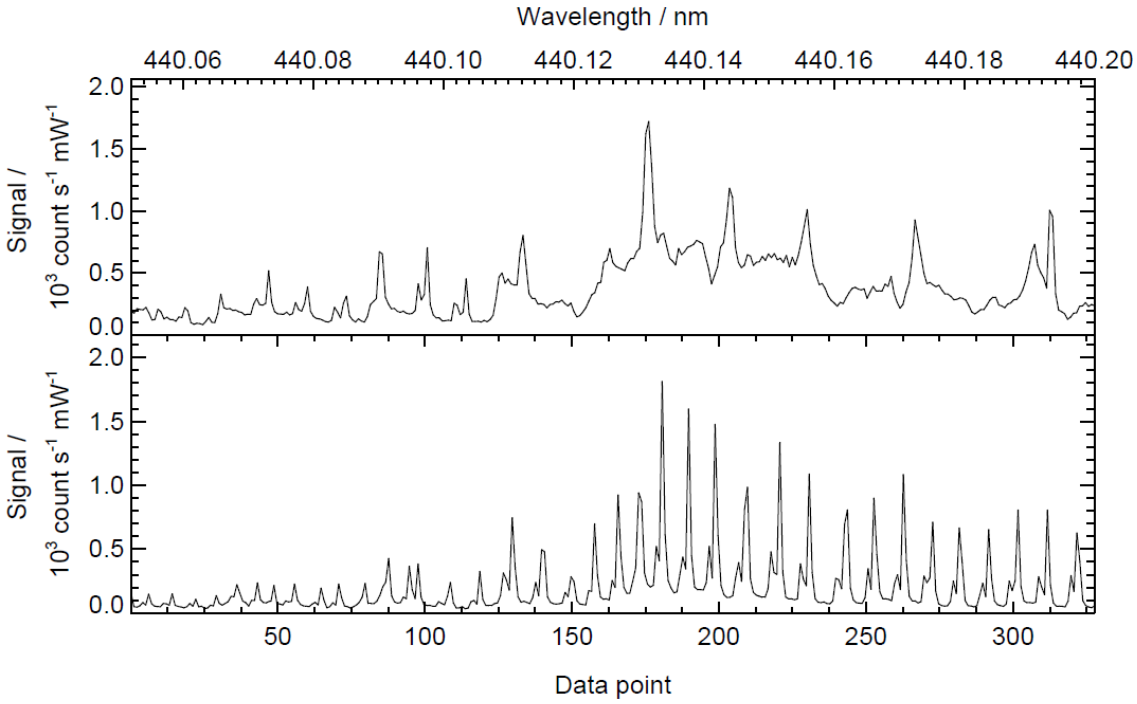

Figure 6.7. Comparison of two wavelength scans under the same conditions (1.7 ppbv glyoxal in 100 Torr of air), between λ = 440.052 nm and λ = 440.200 nm with a wavelength step size of 0.5 pm per data point. The wavelength scale is approximate, and the changing wavelength step size throughout both scans gives a mismatch of peak positions. The maximum phosphorescence signals were measured at λ = 440.130 nm and λ = 440.133 nm, respectively.

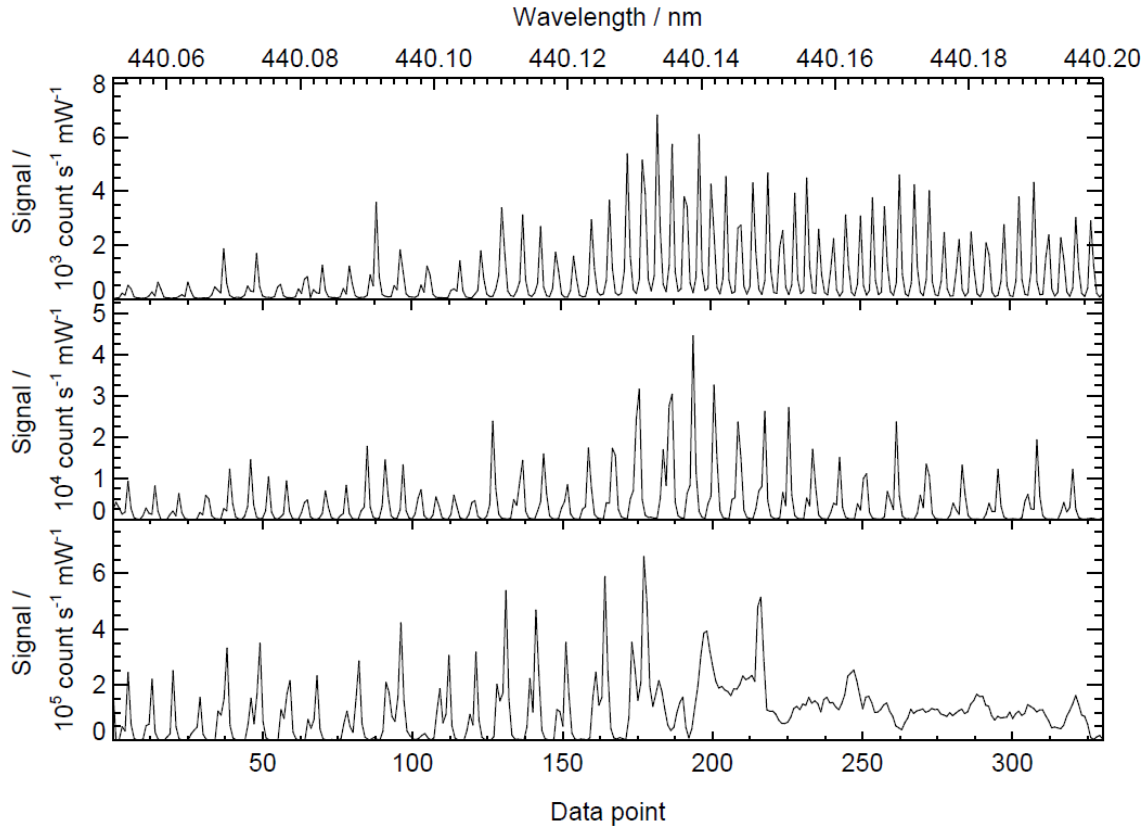

Figure 6.8. Comparison of three laser wavelength scans under the same conditions (1.7 ppbv glyoxal in 100 Torr air), between λ = 440.051 nm and λ = 440.200 nm with a wavelength step size of 0.5 pm per data point. The *y* axis scales are different in each panel due to increasing glyoxal concentration in the detection cell (top = lowest [Gly], bottom = highest [Gly]).

The problems encountered with the laser wavelength scanning system mean that it is not possible to reliably locate an online and offline wavelength without a reference cell to monitor the glyoxal signal as the laser wavelength is scanned, analogous to the HO_x reference cell for the FAGE technique (see Chapter 2). Improvements to the instrument, including construction of a reference cell, are discussed in section 6.4. For the rest of laboratory experiments described here the wavelength was set at $\lambda \sim 440.131$ nm to maximise the glyoxal signal. However, even when the laser wavelength was supposedly fixed, variations in signal similar in appearance but smaller in magnitude to those seen during the wavelength scans were evident. This feature is discussed more in section 6.3.4.

Following sampling of high mixing ratios of glyoxal (1–2 ppbv), a phosphorescence spectrum could be obtained even when sampling laboratory air, synthetic air, or nitrogen. Figure 6.9 shows the signal obtained when sampling nitrogen during three

repeated scans of the laser wavelength between λ = 440.125 nm and λ = 440.170 nm, with the phosphorescence spectrum, including doublet peaks, evident during each scan. The signal intensity decreased over the three spectra as glyoxal was removed from the cell and gas delivery lines, and evidence of laser wavelength stepping instability is obvious in the final scan. Glyoxal deposits on the walls of the cell and on the cell optics. In future laboratory or field work, the cell will need to be heated to ensure that glyoxal does not deposit to surfaces inside the cell, following the method of Huisman *et al*. (2009).

6.3.2.4 Phosphorescence temporal decays

To confirm the presence of glyoxal in the cell, the decay of the glyoxal phosphorescence was measured for 1.7 ppbv of glyoxal in 100 Torr of nitrogen (BOC, oxygen-free nitrogen) and in 100 Torr of synthetic air (BOC compressed air, BTCA 178). The laser wavelength was tuned to 440.129 nm, though fluctuations in signal intensity were evident during the experiments. Data were recorded on the Becker & Hickl PMS 400 photon counting card and the associated software. Photon counting started 2.5 μs after the beginning of the laser pulse. Phosphorescence decays were recorded over 150 data points, with each data point integrated over 1.25 μs to give a total photon counting time of 187.5 μs so that counting finished shortly before the next laser pulse. This was sufficiently long to monitor the total decay in air, but not long enough to monitor the total decay in nitrogen. As expected, the absence of a triplet quencher when measuring in nitrogen extended the phosphorescence lifetime, as shown in Figure 6.10.

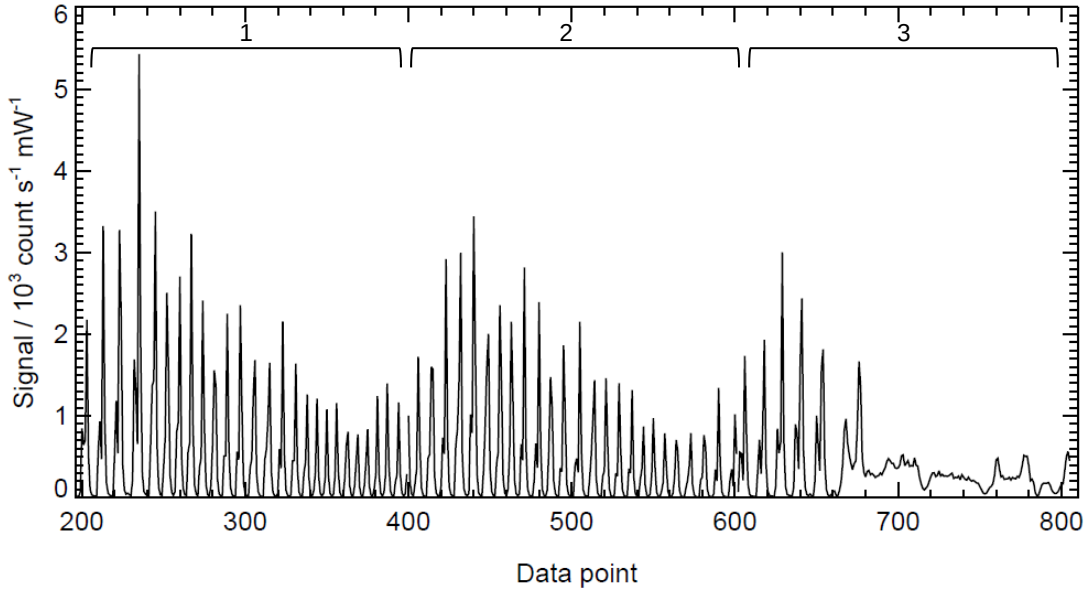

Figure 6.9. Three repeated scans of the laser between λ = 440.125 nm and λ = 440.170 nm, whilst the inlet was sampling N_2. Glyoxal from previous experiments remained in the cell, producing a phosphorescence spectrum.

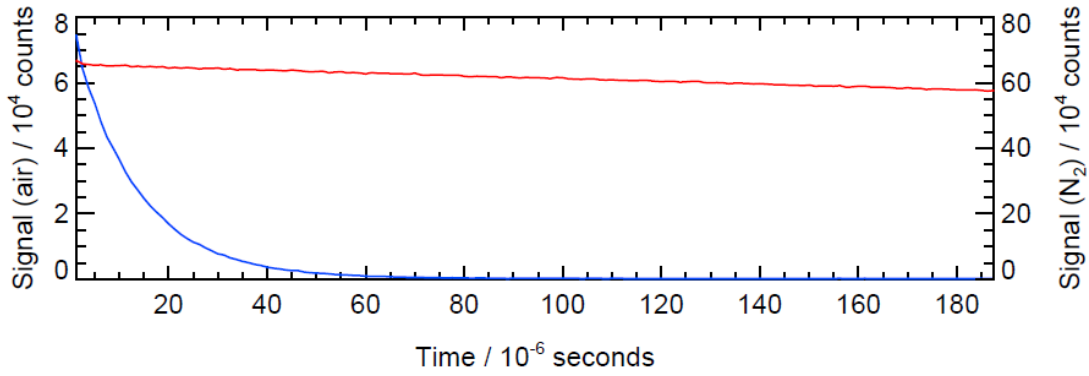

Figure 6.10. Glyoxal phosphorescence signal measured in 1.7 ppbv of glyoxal in 100 Torr of air (blue line, left hand axis) and 100 Torr of nitrogen (red line, right hand axis), showing extended phosphorescence lifetime in nitrogen due to absence of a triplet quencher. The beginning of the phosphorescence is missing from both decay profiles, since photon counting begins 2.5 μs after the start of the laser pulse.

The glyoxal phosphorescence lifetime in air, τ , was determined by fitting the following exponential function to the data using least-squares regression in OriginPro 9:

$$S_t = S_0 \exp(-kt) \tag{6.6}$$

$$k = k_{\text{rad}} + k_{\text{q,O}_2}[\text{O}_2] + k_{\text{q,Gly}}[\text{Gly}] \tag{6.7}$$

where S_0 is the initial signal, S_t is the signal at time t, k is the overall decay constant (equal to $1/\tau$), k_{rad} is the first order radiative decay constant (= 304.0 ± 9.2 s^{-1}), $k_{q,O2}$ is the second order rate constant for quenching of the triplet state by collision with O_2 (= 0.0030 ± 0.0001 μs^{-1} $Torr^{-1}$), $k_{q,Gly}$ is the second order rate constant for quenching of the triplet state by collision with ground-state glyoxal (= 0.0116 ± 0.0010 μs^{-1} $Torr^{-1}$), and [O_2] and [Gly] are the pressures of O_2 (0.2 Torr at 100 Torr total pressure) and glyoxal (1.7×10^{-7} Torr at 1.7 ppbv of glyoxal in 100 Torr total pressure) in the detection cell (all rate constants from Yardley, 1972). At the mixing ratios of glyoxal used in these experiments, the contribution from $k_{q,Gly}$ is negligible (0.00065 %). An example of an exponential fit to the data is given in Figure 6.11.

The average phosphorescence lifetime from 4 decay profiles was 12.7 ± 0.05 μs in 100 Torr of air, in excellent agreement with the results of Henry *et al*. (2012). The rate constant for quenching by O_2 was calculated to be 0.0039 ± 0.0003 μs^{-1} $Torr^{-1}$, which exceeds the literature value by more than the combined errors of the two values. The phosphorescence lifetime in nitrogen was found to be 1.35 ms, giving a radiative decay rate constant of 742.5 ± 4.1 s^{-1}. This is significantly higher than the first order radiative decay constant (304.0 ± 9.2 s^{-1}) given by Yardley (1972). The difference is attributed to impurities, most likely O_2, in the nitrogen cylinder. 0.15 Torr of O_2 (0.15 % in 100 Torr of N_2) is sufficient to decrease the phosphorescence lifetime to the value measured here. In addition, glyoxal is known to be readily lost to solid surfaces at moderate relative humidities (RH > 30 %) (Kroll *et al.*, 2005), so it is possible that triplet glyoxal diffuses away from the detection region sufficiently rapidly to reduce the observed signal. Given the impurities that could be present in the air and nitrogen cylinders, and the excellent agreement with Henry *et al.* (2012), these discrepancies are not considered to be problematic. However, the effects of relative humidity on the sensitivity of the instrument will be investigated in future work.

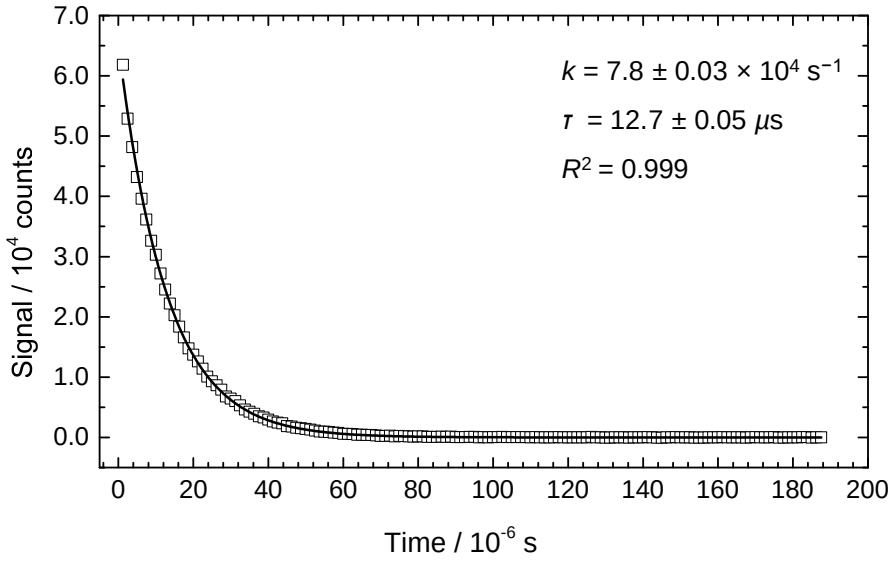

Figure 6.11. Glyoxal phosphorescence signal recorded in 1.7 ppbv of glyoxal in 100 Torr of synthetic air (squares) with an exponential fit to the data (black line, $R^2 > 0.999$). Decay constant $k = 7.8 \pm 0.03 \times 10^4$ s^{-1}, giving a phosphorescence lifetime $\tau = 12.7 \pm 0.05$ μs.

It was noticed that one of the decays recorded in air (not shown) was best described by a biexponential function, indicating that two decay pathways were active in the cell. The second decay is considerably faster than the glyoxal decay, with a lifetime of ~ 0.5 μs. It is likely to be fluorescence of the anodising dye inside the cell, which has been reported previously (Commane, 2009). The interference will be present at online and offline wavelengths, and therefore does not present a problem to the measurements at the moment, but moving the photon counting gate out by 0.5 μs to give a total delay of 3 μs would avoid counting the dye phosphorescence as part of the glyoxal signal.

6.3.3 Sensitivity to pressure

The sensitivity of the instrument is a function of pressure, and the optimal cell pressure is a balance between maximising the number of glyoxal molecules excited, and minimising quenching by O_2 molecules in ambient air. The detection cell pressure is controlled by a butterfly valve between the cell and the pumping line. With the valve fully open, a minimum cell pressure of ~ 30 Torr can be achieved, and closing the valve sets the cell pressure to atmospheric pressure (~ 760 Torr). The effect of cell pressure on the phosphorescence signal was investigated by setting the laser wavelength to $\lambda = 440.129$ nm to achieve maximum phosphorescence signal (see Figure 6.5), and

introducing 1.7 ppbv of glyoxal in synthetic air (BOC, compressed air, BTCA 178) into the cell. The photon counting gate was extended from 35 μs to 100 μs to account for the expected extended phosphorescence lifetime at lower pressures. The cell pressure was controlled using the butterfly valve.

Figure 6.12 shows an example of an experiment in which the detection cell pressure was changed between ~ 30 and ~ 760 Torr. At the end of the experiment the valve was opened and closed several times in quick succession, and the glyoxal signal increased rapidly with each pressure decrease. It is assumed that the high signal recorded during these rapid pressure changes is the result of glyoxal depositing on the walls of the sampling line and phosphorescence cell while the valve is closed, and then being removed by the sudden decrease in pressure and increase in flow rate. Whilst these experiments demonstrate that glyoxal readily deposits to the cell walls, the effect should not present a problem for normal experiments or field measurements when the cell will be heated following the method of Huisman *et al.* (2009) (see section 6.4.2). Figure 6.13 shows the effect of cell pressure on glyoxal signal for the data in Figure 6.12. The very high signal from the end of the experiment has been excluded from the plot to highlight the main trend. The maximum phosphorescence signal was measured at ~ 80 Torr. The cell will therefore be maintained at this pressure for future measurements.

6.3.4 Sensitivity and limit of detection

Since it was not possible to position the laser wavelength at a stable ‘online’ position (see section 6.3.2.3), the laser wavelength was set to 440.130 nm, and the instrument was calibrated by monitoring the peak and baseline (or ‘online’ and ‘offline’) signals at several different concentrations of glyoxal. This is similar to the ‘on-off resonance’ method used by the Jülich HO_x group, in which the laser is repeatedly scanned over an OH rotational line (*e.g.* Holland *et al.*, 1998), and may well be the approach taken for glyoxal data analysis in the future. The laser wavelength was not scanned during the calibration, but, as mentioned in section 6.3.2.3, even when the stepper motor was not active the wavelength was seen to vary by up to 5 pm, resulting in the wavelength stepping on and off a rotational line during the calibration.

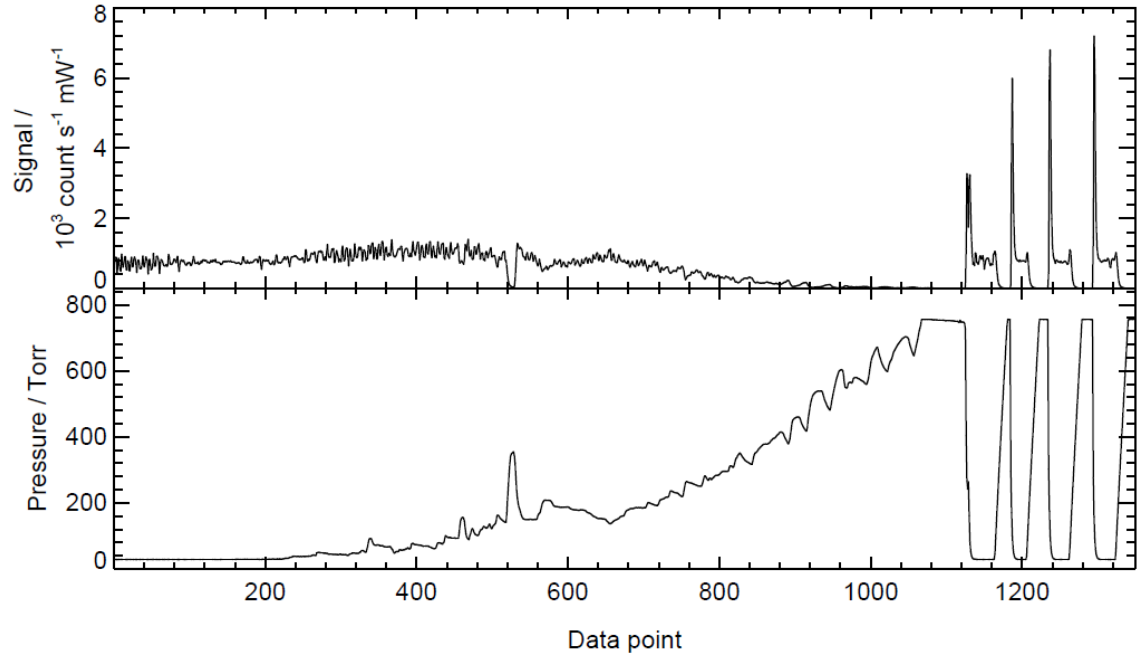

Figure 6.12. Example of pressure experiments, showing phosphorescence signal (top panel) and detection cell pressure (lower panel). The fast pressure changes at the end of the experiment (data point 11000 onwards) show spikes in the glyoxal signal that are significantly higher than the signal recorded at those pressures earlier in the experiment, suggesting that glyoxal may be removed from the cell walls with rapid decreases in pressure.

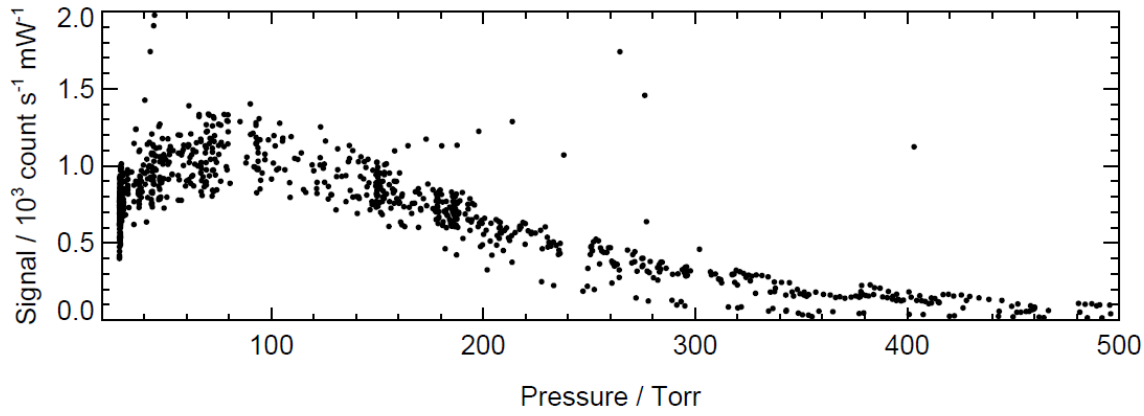

Figure 6.13. Detection cell pressure versus glyoxal phosphorescence signal, showing maximum signal at 80 Torr.

An example of the glyoxal data during the calibration is shown in Figure 6.14. There is no obvious pattern between the signal and the laser wavelength, since the wavemeter has a resolution of 1 pm and therefore does not record small wavelength changes, and the wavelength can be seen to increase and decrease during the calibration.

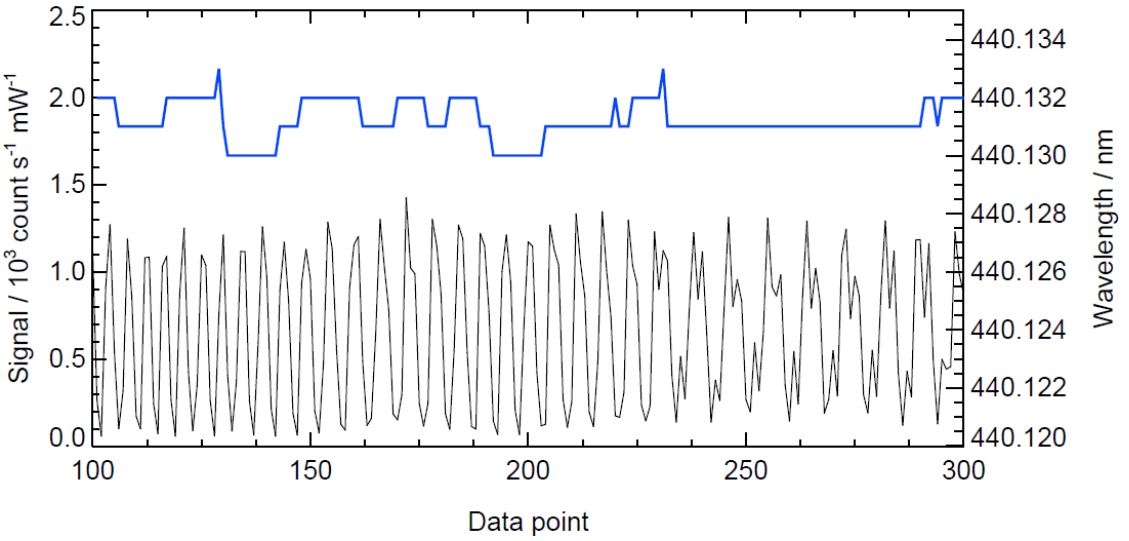

Figure 6.14. Section of data from glyoxal calibration at [Gly] = 6.7 × 10^{10} molecule cm^{-3} and a detection cell pressure of 120 Torr, showing rapidly varying signal (left hand axis, black line) caused by fluctuations in laser wavelength (right hand axis, blue line). The wavemeter has a resolution of 1 pm, meaning that small wavelength steps between those shown were not detected.

It is unlikely that the changes in recorded wavelength were caused by the wavemeter, since it has been shown to give a stable reading when measuring the wavelength of a He:Ne laser. Assuming that the spectral lines are on the order of 0.4 pm as shown in Figure 6.5, the peaks shown in Figure 6.14 could be produced with wavelength step sizes of 0.2 pm or less, which is quite possible with instabilities in the stepper motor system.

Data were normalised to laser power, and the means of the 'online' (peak) and 'offline' (trough) data points, S_{On} and S_{Off}, were calculated for each glyoxal concentration. The mean offline signal was subtracted from the mean online signal to give $Sig_{Gly} = S_{On} - S_{Off}$. A range of glyoxal concentrations between 0.0 and 13.4 × 10^{10} molecule cm^{-3} were produced by diluting glyoxal from the bulb with synthetic air using mass flow controllers. The uncertainty in the concentration of glyoxal in the bulb (approximately 20 %) outweighs the uncertainty in the flows through the mass flow controllers, and contributes significantly to the accuracy of the calibration. However, this first calibration serves to indicate a likely lower limit to the instrument's sensitivity. The uncertainty in the glyoxal signal is taken to be the combined precision (standard deviations) of S_{On} and S_{Off}.

The results of the calibration are shown in Figure 6.15. The data are best described by a second order polynomial. The instrument was calibrated at concentrations much higher than ambient conditions (see Table 1.5), which may be a contributing factor, since glyoxal is known to deposit to surfaces such as gas delivery lines and the inside of the phosphorescence cell (Huisman *et al.*, 2008). The background or offline signal, S_{Off}, was seen to increase with increasing glyoxal concentration, as shown in Figure 6.16. The phosphorescence spectra shown in Figure 6.5 and Figure 6.7 have a non-zero baseline around λ = 440.130 nm, though the ratio of the baseline signal to the peak signal is large (100:1 at λ = 440.130 nm). Increasing the glyoxal concentration will increase the signal at the baseline, and may therefore decrease the difference in signal at the online and offline positions. In addition, deposition of glyoxal to the inside of the phosphorescence cell will increase with increasing concentration, and further increase the background signal. It is possible that with a heated cell, and at atmospherically relevant concentrations, the calibration plot will be linear. This is an issue that needs to be addressed in future work. For the purposes of calculating a limit of detection, a straight line was fit to the data shown in Figure 6.15, giving the instrument's sensitivity to glyoxal, C_{Gly}, as $1.01 \pm 0.12 \times 10^{-8}$ count s^{-1} mW^{-1} $molecule^{-1}$ cm^3 (36.6 ± 2.3 count s^{-1} mW^{-1} $ppbv^{-1}$).

The limit of detection for the data analysis method described above is given by:

$$\left[\mathrm{Gly}\right]_{\mathrm{min}} = \frac{T}{C_{\mathrm{Gly}} \times P} \sigma_{\mathrm{Off}} \sqrt{\frac{1}{m} + \frac{1}{n}} \qquad (6.8)$$

where $\left[\mathrm{Gly}\right]_{\mathrm{min}}$ is the minimum detectable glyoxal concentration, (the limit of detection), T is the t-distribution statistic for the chosen confidence interval ($T \sim 2$ for $p < 0.05$), C_{Gly} is the instrument sensitivity determined in a calibration, P is the mean online laser power over a given period, σ_{Off} is the standard deviation of the un-normalised background (offline) signal, and m and n are the number of 1 s online and offline points, respectively. Since the photon counting signal can be described by a Poisson distribution, σ_{Off} is defined as:

$$\sigma_{\mathrm{Off}} = \sqrt{\left(S_{\mathrm{lb}} + S_{\mathrm{dc}}\right)_{\mathrm{mean}}} \tag{6.9}$$

where S_{lb} is the signal due to laser scatter (typically 2–3 counts mW^{-1}) and S_{dc} is the signal due to dark counts (typically zero). For 60 online points, with an average laser power of 15 mW, and assuming a value for σ_{Off} of 10.2 count s^{-1} (taken from the calibration at 1.33×10^{10} molecule cm^{-3} glyoxal), the limit of detection was calculated to be 2.5×10^{7} molecule cm^{-3}, or 6.8 pptv. This is a promising start to the instrument development, and probably represents an upper limit on the detection limit, since the standard deviation of the background signal was seen to increase with increasing glyoxal concentration during the calibration, as shown in Figure 6.17.

6.4 Improvements and future work

6.4.1 Laser wavelength control

The Ti:Sapphire wavelength control stepper motor has recently been replaced with a rotation stage, and the Ti:Sapphire laser assembly has been rebuilt into a pressure-sealed aluminium casing. It is hoped that the replacement of the stepper motor will eliminate the fluctuations in laser wavelength observed when the motor should have been stationary. Wavelength scans performed with the rotation stage will be a useful comparison to those presented in section 6.3.2, and any effects of the laser wavelength stepping on the appearance of the spectra should be eliminated. If the small changes in laser wavelength when the grating is stationary are eliminated, the ideal online and offline wavelengths can be found. If the fluctuations are not eliminated, the data acquisition will be as described in section 6.3.4.

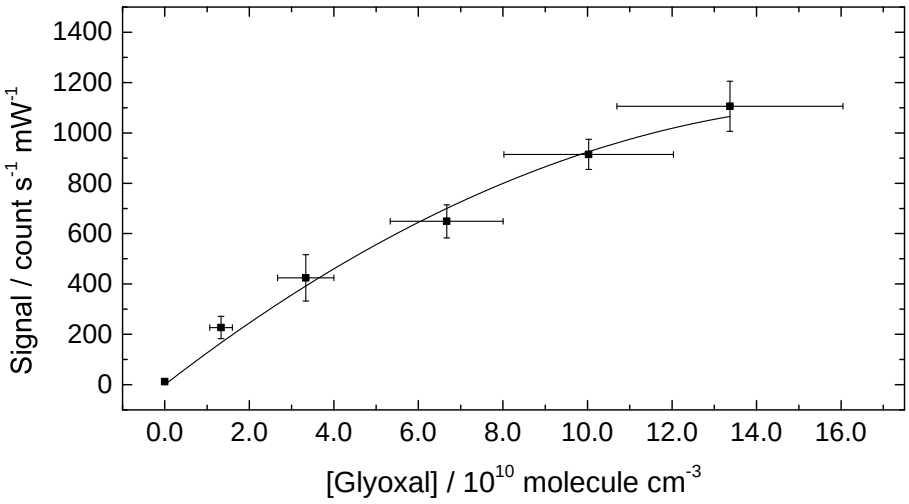

Figure 6.15. Results from a calibration of the glyoxal instrument at a detection cell pressure of 120 Torr. Data points represent average 'online−offline' for 3–8 minutes of data (time varies for each point), as described on page 290. *x* and *y* error bars represent the estimated uncertainty in the concentration of glyoxal, and the combined precision (standard deviations) of the online and offline points, respectively. The data are best described by a second order polynomial: $y = -3.77\times10^{-20}x^2 + 1.30\times10^{-8}x$.

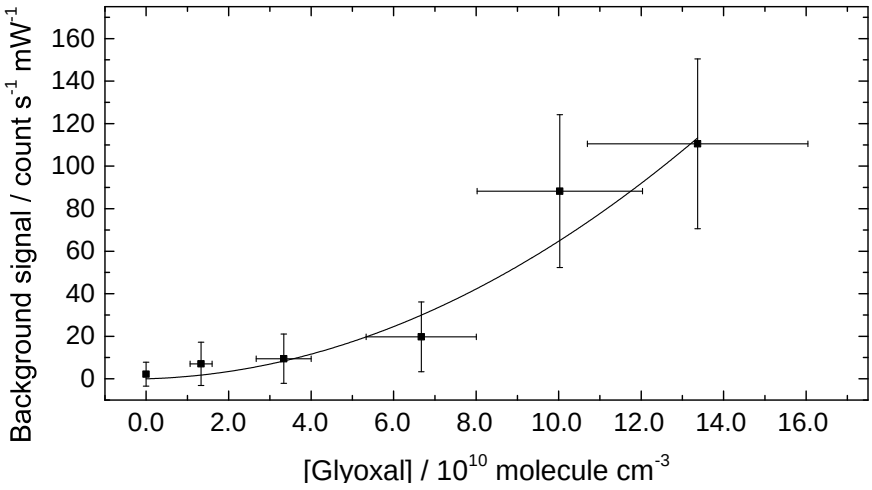

Figure 6.16. Normalised background (offline) signal versus glyoxal concentration during the calibration, showing a fast increase in background signal at high concentrations. A polynomial fit to the data gives $y = 5.95\times10^{-21}x^2 + 5.23\times10^{-11}x$.

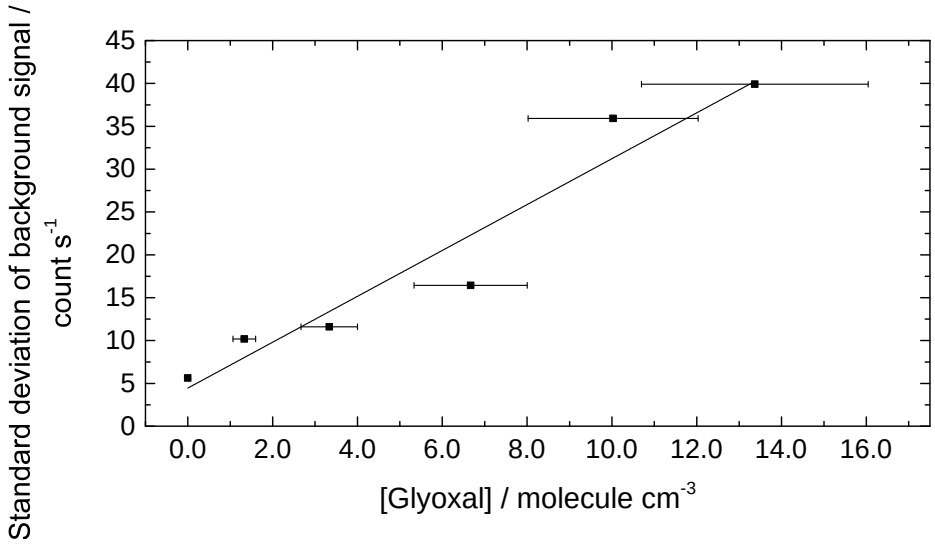

Figure 6.17. Standard deviation of un-normalised background signal versus glyoxal concentration during the calibration, showing increasing standard deviation with increasing concentration.

6.4.2 Heating the phosphorescence cell

As shown in Figure 6.9 and Figure 6.12, glyoxal deposits to the walls and optics inside the phosphorescence cell, so that sampling high concentrations causes an interference in later measurements. The detection cell assembly will be enclosed in a black plastic or metal box, and a heating tape will be installed around the outside of the cell to ensure that the cell walls and optics are maintained at a suitable temperature. Huisman *et al.* (2008) and Henry *et al.* (2012) report that heating the cell to ~ 35º C is sufficient to avoid deposition of glyoxal. Heating will be controlled by thermocouples inside and outside the phosphorescence cell, and temperature control units.

6.4.3 Reference cell

To aid the finding of the online and offline wavelengths, a reference cell will be developed. The design will be similar to the reference cell used in HO_x measurements (see Chapter 2), with glyoxal generated inside the cell from the reaction between OH and acetylene, and a small amount of laser light directed through the cell. A mercury pen-ray lamp will generate OH by photolysis of water vapour in a humidified flow of air. Dilute acetylene in air will be introduced as a second flow. A photodiode will

monitor laser power in the cell, and the phosphorescence signal will be recorded by a PMT and photon counting card. If the rotation stage gives better control over laser wavelength and eliminates the modulation in signal seen at fixed wavelengths, the reference cell should enable positioning of the laser wavelength at the ideal online position of λ = 440.131 nm, and at an offline wavelength to the short wavelength side of this value. This should decrease the scatter in the online and offline measurements, and therefore improve the sensitivity of the instrument.

Deposition of glyoxal to the walls of the reference cell will be monitored periodically by flushing the reference cell with synthetic air and monitoring the signal for signs of glyoxal. The cell may need to be heated to ensure that glyoxal does not deposit to the walls of the cell. An alternative source of glyoxal may be preferable to acetylene should the cell need to be heated, due to the risk of explosion.

6.4.4 Timing

As noted in section 6.3.2.4 the presence of a fast fluorescence signal has been detected along with glyoxal phosphorescence. Extending the beginning of the photon counting to 3 μs after the start of the laser pulse will exclude this fast element, at the expense of some glyoxal phosphorescence signal. However, integrating over the remaining phosphorescence decay should ensure that the measurement remains sensitive. If delaying the onset of photon counting significantly reduces the sensitivity, the timing will be reset to begin 2.5 μs after the start of the laser pulse. The interfering signal has been attributed to fluorescence of the anodising dye inside the cell (Commane, 2009) and the magnitude of the interference is expected to be similar at the online and offline wavelengths.

6.4.5 Calibration

The instrument will be calibrated at atmospherically relevant concentrations of glyoxal, to investigate whether the non-linear dependence of signal on glyoxal exists at lower concentrations, and to minimise the uncertainty in the calibration at concentrations expected in the field. Glyoxal will be produced with a known yield by reaction of OH, generated in the HO_x calibration wand described in Chapter 2, with acetylene. This

method will produce glyoxal at atmospherically relevant concentrations (10^7 molecule cm^{-3}, or pptv levels).

6.4.6 Testing for interference

NO_2 has the potential to cause an interference in glyoxal measurements due to absorption in the region of λ = 440 nm (Sander *et al.*, 2002) and fluorescence around λ = 520 nm (Commane, 2009). The interference is expected to be negligible, as for the IO LIF instrument (see chapter 3), but the magnitude will be dependent on the difference in absorption cross section of NO_2 at the online and offline wavelengths for glyoxal. The effect of adding NO_2 to the phosphorescence cell will therefore be investigated, and the results will be taken into account when choosing an online and an offline wavelength.

Glyoxal is known to deposit readily onto to solid surfaces at moderate relative humidities (RH > 30 %) (Kroll *et al.*, 2005). This has the potential to affect the sensitivity of the instrument to glyoxal by encouraging deposition of excited glyoxal to the walls of the detection cell, effectively quenching phosphorescence. The effects of relative humidity on sensitivity will be investigated by calibrating the instrument at a range of water vapour concentrations, as for the FAGE instrument described in Chapter 2.

6.4.7 ORC^3 Fieldwork

The instrument will be deployed during fieldwork at the Cape Verde Atmospheric Observatory as part of the ORC^3 project (see Chapter 1). Good temporal resolution and sensitivity are required for measurements of glyoxal in the remote ocean boundary layer. The calibration reported in section 6.3.4 indicates that the instrument is already very sensitive to glyoxal, with a limit of detection of 2.5×10^7 molecule cm^{-3} or 6.8 pptv based on a linear fit to the calibration data. Calibration of the instrument at atmospherically relevant glyoxal concentrations will give a better indication of the instrument sensitivity and will instruct any work necessary to improve sensitivity. During the fieldwork the instrument will be located in the main measurement container laboratory at the observatory site. Sampling will be through a shared glass inlet. It is

possible that glyoxal will be lost on the walls of the inlet, so a short glass inlet will be constructed and tested in the laboratory prior to the fieldwork to characterise any loss processes. The instrument needs to be portable and robust for fieldwork applications, and will therefore be housed in a double 19 inch aircraft rack, in a similar configuration to the IO LIF instrument (see Chapter 3). The Nd:YAG laser, Ti:Sapphire laser, and optics will be mounted on an optical breadboard on the top of the rack. The detection cell assembly and associated optics will be mounted alongside the laser to enable reliable alignment of the laser light into the cell. Both lasers and the optics will be covered with an aluminium casing to ensure that no dirt contaminates the optics, and to enclose the laser beam.

6.4.8 Simulation of glyoxal rotational spectrum

To aid interpretation of the glyoxal spectra measured in this work, a rotational spectrum will be simulated using the PGOPHER simulation program (C. M. Western, University of Bristol). PGOPHER is capable of simulating microwave, infra-red and electronic absorption and emission spectra for linear, symmetric, and asymmetric rotors, based on known rotational constants. Alternatively, rotational constants can be determined by fitting the simulated spectrum to measured line positions or line intensities. It is therefore ideal for interpretation of the spectra measured in this work. Good agreement between the spectrum simulated using the rotational constants given by Pebay Peyroula and Jost (1987) and the spectra measured in this work will confirm that rotational lines have been resolved in the measured spectra, as suggested by the close agreement with the literature (see section 6.3.2.1).

6.5 Conclusions

A sensitive and selective instrument for field measurements of glyoxal at pptv levels, employing laser-induced phosphorescence, has been developed. The first calibration of the instrument revealed that the relationship between glyoxal concentration and signal is non-linear at very high concentrations, probably due to deposition of glyoxal inside the cell, or to structure in the baseline of the phosphorescence spectrum around λ = 440.130 nm. This problem will be addressed by heating the phosphorescence cell to

eliminate deposition of glyoxal, and by calibrating at atmospherically relevant glyoxal concentrations. The instrument's 1 minute limit of detection is 2.5×10^7 molecule cm^{-3}, or 6.8 pptv. Improvements to the instrument, outlined in section 6.4, will be made prior to deployment during the ORC^3 fieldwork in Cape Verde.

Chapter 7. Summary and future work

Chapter 1 of this thesis introduced three important societal concerns which are being addressed through the study of atmospheric science: climate change, air quality, and stratospheric ozone depletion. Field measurements and modelling are vital to the improvement of our understanding of these aspects of the atmosphere, and our ability to predict the effects of anthropogenic emissions on local, regional and global scales. This project has investigated two areas of tropospheric chemistry about which relatively little is known. The first is nighttime oxidation and radical chemistry, which has impacts on air quality in urban regions and on the oxidising capacity of the atmosphere. The second is the chemistry of reactive halogen species in the marine boundary layer, which has impacts on tropospheric ozone destruction, new particle formation, and the ratios NO/NO_2 and OH/HO_2. The measurements made during this project have been compared to model results, and have enabled analysis of the processes controlling the concentrations of the radical species OH, HO_2, and IO. In addition to the field measurements and analysis in this project, a glyoxal laser-induced phosphorescence instrument has been developed in preparation for a field measurement campaign in 2014.

7.1 Summary of results

The RONOCO project was the first dedicated study of nighttime oxidation chemistry to involve simultaneous measurements of OH, HO_2, RO_2, N_2O_5, and NO_3. Concentrations of OH and HO_2 were made using the University of Leeds aircraft FAGE instrument onboard the FAAM BAe-146 research aircraft during a series of nighttime and daytime flights over the UK. Concentrations of OH did not exceed the instrument's limit of detection during the nighttime flights, placing upper limits of 1.8×10^6 molecule cm^{-3} and 6.4×10^5 molecule cm^{-3} on the ambient OH concentrations during the summer and winter flights, respectively. HO_2 was consistently detected at night, reaching a maximum mixing ratio of 13.6 pptv during a particularly polluted summer nighttime flight. This value was higher than HO_2 measurements made during daytime flights

during September and January, indicating that radical chemistry can remain active throughout the night under the right conditions. The routes to production of HO_2 radical production at night have been investigated using supporting measurements made during the flights. During summer, NO_3 dominated alkene reactivity at night, and therefore instantaneous production of HO_2. In winter the concentrations of NO_3 were much reduced, and O_3 dominated alkene reactivity and production of HO_2. Strong positive correlation between HO_2 and NO_3 during several flights has been attributed to the production of HO_2 in reactions of NO_3 with alkenes, confirming the importance of this channel for HO_x radical production, in agreement with the results of a modelling study by Stone *et al*. (2013). The combined rate of reaction of O_3 and NO_3 with alkenes was higher on average during the summer nighttime flights than during the winter daytime flights, indicating that the summer nighttime troposphere can be equally important as the winter daytime troposphere for the oxidation and removal of VOCs. Nocturnal oxidation is a little-studied area of atmospheric chemistry, and the measurements of OH and HO_2 made during the RONOCO project have contributed to a relatively sparse observational database, and have been compared to the results of a box modelling study, which in turn will improve the treatment of nocturnal oxidation chemistry in regional and global models.

Ship-based measurements of IO, I_2, and the sum of HOI + ICl during the SHIVA project have added to the relatively sparse open-ocean observational database of these compounds, and have enabled a simple analysis of the processes controlling the concentration of IO in the marine boundary layer. Significant improvements to the LIF instrument, including reduction of the the instrument's limit of detection and installation in a shipping container at the front of the ship, enabled successful measurements of low levels of IO free from interference from the ship's stack. While the overall focus of the SHIVA project was the contribution of biogenic halogenated VSLS to stratospheric ozone depletion, the measurements of reactive iodine species made during the cruise provide insight into several aspects of marine boundary layer iodine chemistry. IO was found to be present at low levels, with a mean mixing ratio of 0.8 pptv, throughout this region of the marine boundary layer. No correlation was found between IO and oceanic concentrations of chlorophyll-*a*, supporting the hypothesis that the main precursors of iodine in open ocean regions are not biogenic in origin. A negative correlation between

IO and oceanic concentrations of CH_3I and CH_2ICl suggests that there is a biological mechanism for inhibition of iodine release. Iodine chemistry was not found to play a significant role in ozone depletion in the marine boundary layer during the cruise, in contrast with previous studies, suggesting that more observations and modelling are required to fully understand this mechanism. Several modelling studies of marine boundary layer iodine chemistry have required a substantial sea-to-air flux of I_2 to account for a missing source of IO, and a recent laboratory and modelling study has shown that HOI is an important source of I atoms in the marine boundary layer. The steady-state analysis presented in Chapter 5 of this work showed that IO production during the SHIVA cruise was dominated by photolysis of I_2, with a significant contribution from photolysis of HOI. This result supports the previous measurement and modelling studies. The measurements of I_2 and the sum of HOI + ICl provide an excellent opportunity for further investigation of open ocean reactive iodine chemistry. The contribution of the IO measurements to the observational database will aid improvement of model predictions of the impacts of IO on HO_x in the tropical marine boundary layer, and the resulting impacts on the oxidation capacity of this globally important region.

Finally, a glyoxal laser-induced phosphorescence instrument has been built, tested and calibrated. The instrument is capable of measuring low ambient concentrations of glyoxal, with a 1 minute limit of detection of 2.5×10^7 molecule cm^{-3} (6.8 pptv). Following further development the instrument will be deployed during the Oceanic Reactive Carbon: Climate Impacts project (ORC^3) in 2014.

7.2 Future work

Decomposition of Criegee intermediates has been identified as a likely cause of interference in FAGE measurements of OH in forested regions (Mao *et al.*, 2012). The interference is instrument-specific, and the aircraft FAGE instrument will be tested for this interference prior to future measurement campaigns. The introduction of an OH scavenger prior to the FAGE inlet will provide a useful measure of this interference during field measurements. The FAGE laser system has recently been rebuilt into a sealed aluminium casing, with the diffraction grating stepper motor being replaced by a

motorised rotation stage. These improvements will enable faster scanning between the online and offline wavelengths, and will improve the stability of the laser wavelength during ascents and descents in future airborne field campaigns.

The uncertainty in the calibration of the IO LIF instrument, and therefore in IO measurements, could be reduced by development of an IO reference cell, which would enable more accurate and reproducible location of the online wavelength. The negative bias exhibited in measurements of IO during the SHIVA fieldwork, and in laboratory testing, should be monitored before, during, and after future measurement campaigns in order that appropriate adjustments can be made to field data. To this end, background measurements in synthetic air or nitrogen should be made during field campaigns. During development of a laser-induced phosphorescence instrument for field measurements of glyoxal, which was based on the design of the IO LIF instrument, it was found that an open beam delivery of the laser light significantly reduced the background signal in the cell caused by laser scatter. Delivery of the laser light *via* optical fibres is convenient in HO_x measurements where signal acquisition is delayed until after the laser pulse and scatter have died away, but is less than ideal for measurements that do not employ time gated photon counting because it is difficult to collimate the laser beam after it leaves the fibre. Development of the IO instrument to enable a free laser beam would undoubtedly reduce the background signal in the cell, and would therefore improve the limit of detection.

The analysis of production of HO_2 during the RONOCO project has highlighted the need for more reliable RO_2 measurements. Without a measurement of RO_2 radicals it is not possible to use the measurements alone to determine the rate of production of HO_2, or the HO_2 yield from NO_3 and O_3 reactions. The presence of unmeasured unsaturated VOCs during the RONOCO campaign, suggested by the box modelling study (Stone *et al.*, 2013) and confirmed by 2 dimensional GC analysis, has implications for the conclusions drawn from the analysis based on the observations, and has significant impacts on the success of the model in predicting radical species concentrations. Future studies of tropospheric oxidation chemistry should strive to measure a wider range of VOCs in order that sources and sinks of radical species can be more fully accounted for.

The location of the LIF instrument at the front of the ship during the SHIVA cruise appears to have been successful in ensuring that air free from contamination by the ship's stack was sampled by the instrument, since there is no evidence for interference caused by NO_2 in the IO measurements. However, measurements of NO and NO_2 from the container in which the LIF instrument was housed were unsuccessful due to the air conditioning in the container causing condensation of ambient water vapour inside the NO_x analyser. Heating of the analyser and sampling line would prevent this occurring in future studies, enabling reliable NO_x measurements, and confirmation of the absence or presence of interference from the ship's stack. Measurements of IO made during the SHIVA project have been reproduced reasonably well by steady state calculations, but large uncertainty is associated with the calculated $[IO]_{SS}$, since a number of the input parameters were estimated from field measurements in other open ocean regions, and heterogeneous processes were not included in the calculations. A more detailed modelling study, including heterogeneous processes at the sea surface and on aerosols, will be conducted to investigate the main sources and sinks of reactive iodine in the South China Sea. Wavelength-resolved total incoming radiation measurements from the cruise will provide a more accurate correction of the clear-sky photolysis rates than the approximation used in the present work. Future studies of open-ocean sources and sinks of reactive iodine should include measurements of I_2 and HOI, since these species are believed to be important precursors in the marine boundary layer. Measurements of the short-lived iodocarbons CH_2I_2, CH_2ICl and CH_2IBr are also important when considering sources of reactive iodine, and should be included in future studies.

Following the initial development and testing of the glyoxal LIP instrument, numerous improvements and areas for further development have been suggested. These include testing of a new grating rotation stage, heating of the phosphorescence cell to prevent deposition of glyoxal to the inside of the cell, development of a reference cell to enable precise tuning of the laser to the online and offline wavelengths, calibration of the instrument at atmospherically relevant concentrations of glyoxal, and preparation of the instrument for fieldwork. In addition, simulation of a glyoxal rotational spectrum will aid interpretation of the phosphorescence spectra recorded with the instrument. These developments are described in more detail in section 6.4 of Chapter 6. The *in situ* glyoxal measurements provided by the instrument during the ORC^3 fieldwork will make

a valuable contribution to the currently sparse observational database, and will be an important input into the global chemistry-climate modelling studies that are a major part of the ORC^3 project, thereby improving our understanding of the role of oceanic carbon in tropospheric gas- and aerosol-phase chemistry, and its impacts on climate change.

Bibliography

Abbatt, J. P. D., Lee, A. K. Y. and Thornton, J. A., *Quantifying trace gas uptake to tropospheric aerosol: recent advances and remaining challenges*, Chemical Society Reviews, 41 (19), 6555-6581, 2012

Alicke, B., Hebestreit, K., Stutz, J. and Platt, U., *Iodine oxide in the marine boundary layer*, Nature, 397 (6720), 572-573, 1999

Allan, B. J., McFiggans, G., Plane, J. M. C. and Coe, H., *Observations of iodine monoxide in the remote marine boundary layer*, Journal of Geophysical Research: Atmospheres, 105 (D11), 14363-14369, 2000

Allan, B. J., McFiggans, G., Plane, J. M. C., Coe, H. and McFadyen, G. G., *The nitrate radical in the remote marine boundary layer*, Journal of Geophysical Research: Atmospheres, 105 (D19), 24191-24204, 2000

Allan, B. J. and Plane, J. M. C., *A Study of the Recombination of IO with NO_2 and the Stability of INO_3: Implications for the Atmospheric Chemistry of Iodine*, Journal of Physical Chemistry A, 106 (37), 8634-8641, 2002

Anderson, L. G., Parmenter, C. S. and Poland, H. M., *Collision induced intersystem crossing. The photophysics of glyoxal vapor excited at 4358 Å*, Chemical Physics, 1 (5), 401-417, 1973

Anttila, T., Langmann, B., Varghese, S. and O'Dowd, C., *Contribution of Isoprene Oxidation Products to Marine Aerosol over the North-East Atlantic*, Advances in Meteorology, 2010 (482603), 1-10, 2010

Apel, E., Hornbrook, R. S., Emmons, L. K., Campos, T. L., Volkamer, R. M., Pierce, R. B., Hills, A. J., Fried, A., Richter, D., Walega, J., Weibring, P., Dix, B. and Baidar, S., *Observations and modeling of formaldehyde during TORERO*, American Geophysical Union Fall Meeting, San Francisco, 2012

Archer, S. D., Goldson, L. E., Liddicoat, M. I., Cummings, D. G. and Nightingale, P. D., *Marked seasonality in the concentrations and sea-to-air flux of volatile iodocarbon compounds in the western English Channel*, Journal of Geophysical Research: Oceans, 112 (C8), C08009-C08024, 2007

Arnold, S., Carpenter, L. and Lewis, A. C., *Oceanic Reactive Carbon: Chemistry-Climate impacts (ORC^3)*, Grant Application Case for Support, 2013

Arnold, S. R., Spracklen, D. V., Williams, J., Yassaa, N., Sciare, J., Bonsang, B., Gros, V., Peeken, I., Lewis, A. C., Alvain, S. and Moulin, C., *Evaluation of the global oceanic isoprene source and its impacts on marine organic carbon aerosol*, Atmospheric Chemistry and Physics, 9 (4), 1253-1262, 2009

Arnold, S. R., Spracklen, D. V., Gebhardt, S., Custer, T. G., Williams, J., Peeken, I. and Alvain, S., *Relationships between atmospheric organic compounds and air-mass exposure to marine biology*, Environmental Chemistry, 7 (3), 232-241, 2010

Aschmann, J., Sinnhuber, B.-M., Atlas, E. L. and Schauffler, S. M., *Modeling the transport of very short-lived substances into the tropical upper troposphere and lower stratosphere*, Atmospheric Chemistry and Physics, 9 (23), 9237-9247, 2009

Ashfold, M. J., Harris, N. R. P., Atlas, E. L., Manning, A. J. and Pyle, J. A., *Transport of short-lived species into the Tropical Tropopause Layer*, Atmospheric Chemistry and Physics, 12 (14), 441-478, 2012

Atkinson, R., *Atmospheric Reactions of Alkoxy and β-Hydroxyalkoxy Radicals*, International Journal of Chemical Kinetics, 29 (2), 99-111, 1997

Atkinson, R., *Gas-phase tropospheric chemistry of volatile organic compounds: 1. alkanes and alkenes*, Journal of Physical and Chemical Reference Data, 26 (2), 215-290, 1997

Atkinson, R. and Arey, J., *Gas-phase tropospheric chemistry of biogenic volatile organic compounds: a review*, Atmospheric Environment, 37 (S2), 197-219, 2003

Atkinson, R. and Arey, J., *Atmospheric degradation of volatile organic compounds*, Chemical Reviews, 103 (12), 4605-4638, 2003

Atkinson, R., Baulch, D. L., Cox, R. A., Crowley, J. N., Hampson, R. F., Hynes, R. G., Jenkin, M. E., Rossi, M. J. and Troe, J., *Evaluated kinetic and photochemical data for atmospheric chemistry: Volume I - gas phase reactions of O_x, HO_x, NO_x and SO_x species*, Atmospheric Chemistry and Physics, 4 (6), 1461-1738, 2004

Atkinson, R., Baulch, D. L., Cox, R. A., Crowley, J. N., Hampson, R. F., Hynes, R. G., Jenkin, M. E., Rossi, M. J. and Troe, J., *Evaluated kinetic and photochemical*

data for atmospheric chemistry: Volume III - gas phase reactions of inorganic halogens, Atmospheric Chemistry and Physics, 7 (4), 981-1191, 2007

Baardsen, E. L. and Terhune, R. W., *Detection of OH in the atmosphere using a dye laser*, Applied Physics Letters, 21 (5), 209-211, 1972

Bailey, A. E., Heard, D. E., Paul, P. H. and Pilling, M. J., *Collisional quenching of OH ($A\ ^2\Sigma^+$ v'=0) by N_2, O_2 and CO_2 between 204 and 294 K. Implications for atmospheric measurements of OH by laser-induced fluorescence*, Journal of the Chemical Society, Faraday Transactions, 93 (16), 2915-2920, 1997

Bailey, A. E., Heard, D. E., Henderson, D. A. and Paul, P. H., *Collisional quenching of OH ($A\ ^2\Sigma^+$ v'=0) by H_2O between 211 and 294 K and the development of a unified model for quenching*, Chemical Physics Letters, 302 (1-2), 132-138, 1999

Baker, A., Tunnicliffe, C. and Jickells, T. D., *Iodine speciation and deposition fluxes from the marine atmosphere*, Journal of Geophysical Research: Atmospheres, 106 (D22), 28743-28749, 2001

Baker, A. R., *Inorganic iodine speciation in tropical Atlantic aerosol*, Geophysical Research Letters, 31 (23), L23S02-L23S06, 2004

Baldasano, J. M., Valera, E. and Jiménez, P., *Air quality data from large cities*, Science of the Total Environment, 307 (1-3), 141-165, 2003

Ball, S. M. and Jones, R. L., *Broad-band cavity ring-down spectroscopy*, Chemical Reviews, 103 (12), 2003

Bandow, H. and Washida, N., *Ring-cleavage Reactions of Aromatic Hydrocarbons Studied by FT-IR Spectroscopy. III. Photooxidation of 1,2,3-, 1,2,4-, and 1,3,5-Trimethylbenzenes in the NO_x-Air System*, Bulletin of the Chemical Society of Japan, 58 (9), 2549-2555, 1985

Barrie, L. A., Bottenheim, J. W., Schnell, R. C., Crutzen, P. J. and Rasmussen, R. A., *Ozone destruction and photochemical reactions at polar sunrise in the lower Arctic atmosphere*, Nature, 334 (14), 138-141, 1988

Barrie, L. A., den Hartog, G., Bottenheim, J. W. and Landsberger, S., *Anthropogenic aerosols and gases in the lower troposphere at Alert, Canada, in April 1986*, Journal of Atmospheric Chemistry, 9 (1), 101-127, 1989

Beale, R., Liss, P. S. and Nightingale, P. D., *First oceanic measurements of ethanol and propanol*, Geophysical Research Letters, 37 (24), L24607-L24612, 2010

Becker, K. H., Bechara, J. and Brockmann, K. J., *Studies on the formation of H_2O_2 in the ozonolysis of alkenes*, Atmospheric Environment, 27A (1), 57-61, 1993

Bedjanian, Y., Romanias, M. N. and El Zein, A., *Uptake of HO_2 radicals on Arizona Test Dust*, Atmospheric Chemistry and Physics, 13 (13), 6461-6471, 2013

Bekki, S. and Bodeker, G. E., *Future Ozone and Its Impact on Surface UV*, Chapter 3 in Scientific Assessment of Ozone Depletion: 2010, Global Ozone Research and Monitoring Project, Report No. 52, World Meteorological Organisation, Geneva, Switzerland, 2010

Bekooy, J. P., Leo Meerts, W. and Dymanus, A., *High-resolution laser-rf spectroscopy on the $A^2\Pi_{3/2}$-$X^2\Pi_{3/2}$ system of lodine oxide (IO)*, Journal of Molecular Spectroscopy, 102 (2), 320-343, 1983

Bell, N., Hsu, L., Jacob, D. J., Schultz, M. G., Blake, D. R., Butler, J. H., King, D. B., Lobert, J. M. and Maier-Reimer, E., *Methyl iodide: Atmospheric budget and use as a tracer of marine convection in global models*, Journal of Geophysical Research: Atmospheres, 107 (D17), ACH 8-1–ACH 8-12, 2002

Berndt, T. and Böge, O., *Kinetics of Oxirane Formation in the Reaction of Nitrate Radicals with Tetramethylethylene*, Berichte der Bunsengesellschaft für physikalische Chemie, 98 (6), 869-871, 1994

Bernstein, L., Bosch, P., Canziani, O., Chen, Z., Christ, R., Davidson, O., Hare, W., Huq, S., Karoly, D., Kattsov, V., Kundzewicz, Z., Liu, J., Lohmann, U., Manning, M., Matsuno, T., Menne, B., Metz, B., Mirza, M., Nicholls, N., Nurse, L., Pachauri, R., Palutikof, J., Parry, M., Qin, D., Ravindranath, N., Reisinger, A., Ren, J., Riahi, K., Rosenzweig, C., Rusticucci, M., Schneider, S., Sokona, Y., Solomon, S., Stott, P., Stouffer, R., Sugiyama, T., Swart, R., Tirpak, D., Vogel, C. and Yohe, G., *Climate Change 2007: Synthesis Report*, Contribution of Working Groups I, II and III to the Fourth Assessment Report of the Intergovernmental Panel on Climate Change, R. K. Pachauri and A. Reisinger, (eds.), IPCC, Geneva, Switzerland, 2007

Berresheim, H., Elste, T., Plass-Dülmer, C., Eisele, F. L. and Tanner, D. J., *Chemical ionization mass spectrometer for long-term measurements of atmospheric OH and H_2SO_4*, International Journal of Mass Spectrometry, 202 (1-3), 91-109, 2000

Betterton, E. A. and Hoffman, M. R., *Henry's Law Constants of Some Environmentally Important Aldehydes*, Environmental Science & Technology, 22 (12), 1415-1418, 1988

Bevington, P. R. and Robinson, D. K., *Data Reduction and Error Analysis for the Physical Sciences*, McGraw-Hill, New York, 2003

Bey, I., Aumont, B. and Toupance, G., *A modeling study of the nighttime radical chemistry in the lower continental troposphere 2. Origin and evolution of HO_x*, Journal of Geophysical Research: Atmospheres, 106 (D9), 9991-10001, 2001

Beyer, R. A., Zittel, P. F. and Lineberger, W. C., *Relaxation in the ^1A_u state of glyoxal. 1. Collision-free lifetimes of single vibrational levels*, Journal of Chemical Physics, 62 (10), 4016-4024, 1974

Birss, F. W., Brown, J. M., Cole, A. R. H., Lofthus, A., Krishnamachari, S. L. N. G., Osborne, G. A., Paldus, J., Ramsay, D. A. and Watmann, L., *The 4550 Å band system of glyoxal. II. Vibration - rotational analyses for 12 bands of $C_2H_2O_2$*, Canadian Journal of Physics, 48 (10), 1230-1241, 1970

Bloss, C., Wagner, V., Bonzanini, A., Jenkin, M. E., Wirtz, K., Martin-Reviejo, M. and Pilling, M. J., *Evaluation of detailed aromatic mechanisms (MCMv3 and MCMv3.1) against environmental chamber data*, Atmospheric Chemistry and Physics, 5 (3), 623-639, 2005

Bloss, W. J., Rowley, D. M., Cox, R. A. and Jones, R. L., *Kinetics and Products of the IO Self-Reaction*, Journal of Physical Chemistry A, 105 (33), 7840-7854, 2001

Bloss, W. J., Evans, M. J., Lee, J. D., Sommariva, R., Heard, D. E. and Pilling, M. J., *The oxidative capacity of the troposphere: Coupling of field measurements of OH and a global chemistry transport model*, Faraday Discussions, 130 (1), 425-436, 2005

Bloss, W. J., Lee, J. D., Johnson, G. P., Sommariva, R., Heard, D. E., Saiz-Lopez, A., Plane, J. M. C., McFiggans, G., Coe, H., Flynn, M., Williams, P., Rickard, A. R. and Fleming, Z. L., *Impact of halogen monoxide chemistry upon boundary layer OH and HO_2 concentrations at a coastal site*, Geophysical Research Letters, 32 (6), L06814-L06818, 2005

Bloss, W. J., Lee, J. D., Heard, D. E., Salmon, R. A., Bauguitte, S. J. B., Roscoe, H. K. and Jones, A. E., *Observations of OH and HO_2 radicals in coastal Antarctica*, Atmospheric Chemistry and Physics, 7 (16), 4171-4185, 2007

Bloss, W. J., Camredon, M., Lee, J. D., Heard, D. E., Plane, J. M. C., Saiz-Lopez, A., Bauguitte, S. J. B., Salmon, R. A. and Jones, A. E., *Coupling of HO_x, NO_x and halogen chemistry in the antarctic boundary layer*, Atmospheric Chemistry and Physics, 10 (21), 10187-10209, 2010

Bonsang, B., Gros, V., Peeken, I., Yassaa, N., Bluhm, K., Zoellner, E., Sarda-Esteve, R. and Williams, J., *Isoprene emission from phytoplankton monocultures: the relationship with chlorophyll-a, cell volume and carbon content*, Environmental Chemistry, 7 (6), 554-563, 2010

Borrego, C., Gomes, P., Barros, N. and Miranda, A. I., *Importance of handling organic atmospheric pollutants for assessing air quality*, Journal of Chromatography A, 889 (1–2), 271-279, 2000

Bottenheim, J. W. and Gallant, A. G., *Measurements of NO_y species and O_3 at 82 N^o latitude*, Geophysical Research Letters, 13 (2), 113-116, 1986

Brand, J. C. D., *Vibration analysis of the low-frequency absorption system of glyoxal as a ^1A_g - ^1A_u transition*, Transactions of the Faraday Society, 50 (1), 431-444, 1954

Brandenburger, U., Brauers, T., Dorn, H. P., Hausmann, M. and Ehhalt, D. H., *In-situ measurements of tropospheric hydroxyl radicals by folded long-path laser absorption during the field campaign POPCORN*, Journal of Atmospheric Chemistry, 31 (1-2), 181-204, 1998

Brauers, T., Hausmann, M., Bister, A., Kraus, A. and Dorn, H. P., *OH radicals in the boundary layer of the Atlantic Ocean 1. Measurements by long-path laser absorption spectroscopy*, Journal of Geophysical Research: Atmospheres, 106 (D7), 7399-7414, 2001

Brioude, J., Portmann, R. W., Daniel, J. S., Cooper, O. R., Frost, G. J., Rosenlof, K. H., Granier, C., Ravishankara, A. R., Montzka, S. A. and Stohl, A., *Variations in ozone depletion potentials of very short-lived substances with season and emission region*, Geophysical Research Letters, 37 (19), L19804-L19808, 2010

Broadgate, W. J., Malin, G., Küpper, F. C., Thompson, A. and Liss, P. S., *Isoprene and other non-methane hydrocarbons from seaweeds: a source of reactive hydrocarbons to the atmosphere*, Marine Chemistry, 88 (1-2), 61-73, 2004

Bronwell, D. K., Moore, R. M. and Cullen, J. J., *Production of methyl halides by Prochlorococcus and Synechococcus*, Global Biogeochemical Cycles, 24 (2), GB2002-GB2009, 2010

Brown, S. S., *Absorption Spectroscopy in High-Finesse Cavities for Atmospheric Studies*, Chemical Reviews, 103 (12), 5219-5238, 2003

Brown, S. S., Dibb, J. E., Stark, H., Aldener, M., Vozella, M., Whitlow, S., Williams, E. J., Lerner, B. M., Jakoubek, R., Middlebrook, A. M., DeGouw, J. A., Warneke, C., Goldan, P. D., Kuster, W. C., Angevine, W. M., Sueper, D. T., Quinn, P. K., Bates, T. S., Meagher, J. F., Fehsenfeld, F. C. and Ravishankara, A. R., *Nighttime removal of NO_x in the summer marine boundary layer*, Geophysical Research Letters, 31 (7), L07108-L07113, 2004

Brown, S. S., Dubé, W. P., Peischl, J., Ryerson, T., Atlas, E., Warneke, C., de Gouw, J. A., te Lintel Hekkert, S., Brock, C. A., Flocke, F., Trainer, M., Parrish, D. D., Feshenfeld, F. C. and Ravishankara, A., *Budgets for nocturnal VOC oxidation by nitrate radicals aloft during the 2006 Texas Air Quality Study*, Journal of Geophysical Research: Atmospheres, 116 (D24), D24305-D24320, 2011

Brown, S. S. and Stutz, J., *Nighttime radical observations and chemistry*, Chemical Society Reviews, 41 (19), 6405-6447, 2012

Burkholder, J. B., Curtius, J., Ravishankara, A. R. and Lovejoy, E. R., *Laboratory studies of the homogeneous nucelation of iodine oxides*, Atmospheric Chemistry and Physics, 4 (1), 19-34, 2004

Butler, J. H., King, D. B., Lobert, J. M., Montzka, S. A., Yvon-Lewis, S. A., Hall, B. D., Warwick, N. J., Mondeel, D. J., Aydin, M. and Elkins, J. W., *Oceanic distributions of emissions and short-lived halocarbons*, Global Biogeochemical Cycles, 21 (1), GB1023-GB1034, 2007

Bytnerowicz, A. and Fenn, M. E., *Nitrogen deposition in California forests: A review*, Environmental Pollution, 92 (2), 127-146, 1996

Caldwell, M. M., Björn, L. O., Bornman, J. F., Flint, S. D., Kulandaivelu, G., Teramura, A. H. and Tevini, M., *Effects of increased solar ultraviolet radiation on terrestrial ecosystems*, Journal of Photochemistry and Photobiology B: Biology, 46 (1-3), 40-52, 1998

Calvert, J. G., Su, F., Bottenheim, J. and Strausz, O. P., *Mechanism of the homogeneous oxidation of sulfur dioxide in the troposphere*, Atmospheric Environment, 12 (1-3), 197-226, 1978

Campbell-Lendrum, D. and Corvalán, C., *Climate Change and Developing-Country Cities: Implications for Environmental Health and Equity*, Journal of Urban Health: Bulletin of the New York Academy of Medicine, 84 (1), 109-117, 2007

Campos, M. L. A. M., Farrenkopf, A. M., Jickells, T. D. and Luther, G. W., *A comparison of dissolved iodine cycling at the Bermuda Atlantic Time-series Station and Hawaii Ocean Time-series Station*, Deep-Sea Research II, 43 (2-3), 455-466, 1996

Cantrell, C. A., Stedman, D. H. and Wendel, G. J., *Measurement of atmospheric peroxy radicals by chemical amplification*, Analytical Chemistry, 56 (8), 1496-1502, 1984

Cantrell, C. A., Zimmer, A. and Tyndall, G. S., *Absorption cross sections for water vapor from 183 to 193 nm*, Geophysical Research Letters, 24 (17), 2195-2198, 1997

Carlton, A. G., Wiedinmyer, C. and Kroll, J. H., *A review of Secondary Organic Aerosol (SOA) formation from isoprene*, Atmospheric Chemistry and Physics, 9 (14), 4987-5005, 2009

Carpenter, L. J., Sturges, W. T., Penkett, S. A., Liss, P. S., Alicke, B., Hebestreit, K. and Platt, U., *Short-lived alkyl iodides and bromides at Mace Head, Ireland: Links to biogenic sources and halogen oxide production*, Journal of Geophysical Research: Atmospheres, 104 (D1), 1679-1689, 1999

Carpenter, L. J., Malin, G., Liss, P. S. and Küpper, F. C., *Novel biogenic iodine-containing trihalomethanes and other short-lived halocarbons in the coastal East Atlantic*, Global Biogeochemical Cycles, 14 (4), 1191-1204, 2000

Carpenter, L. J., Hebestreit, K., Platt, U. and Liss, P. S., *Coastal zone production of IO precursors: a 2-dimensional study*, Atmospheric Chemistry and Physics, 1 (1), 9-18, 2001

Carpenter, L. J., *Iodine in the marine boundary layer*, Chemical Reviews, 103 (12), 4953-4962, 2003

Carpenter, L. J., Read, K. A., Lee, J. D., Moller, S., Lewis, A. C., Hopkins, J., Purvis, R., Fleming, Z. L., Leigh, R. J., Monks, P. S., Arunasalam, K., Manning, A.,

Vaughan, S., Heard, D. E., Plane, J. M. C., Mahajan, A., Oetjen, H., Herrmann, H., Muller, K., Tegen, I., Wiedensohler, A., Achterberg, E., Patey, M., Wallace, D., Mendes, L., Lopez, H. and Faria, B. V. E., *Seasonal characteristics of tropical marine boundary layer air measured at the Cape Verde Atmospheric Observatory*, Journal of Atmospheric Chemistry, 67 (2-3), 67-87, 2010

Carpenter, L. J., MacDonald, S. M., Shaw, M. D., Kumar, R., Saunders, R. W., Parthipan, R., Wilson, J. and Plane, J. M. C., *Atmospheric iodine levels influenced by sea surface emissions of inorganic iodine*, Nature Geoscience, 6 (2), 108-111, 2013

Chambers, R. M., Heard, A. C. and Wayne, R. P., *Inorganic Gas-Phase Reactions of the Nitrate Radical: $I_2 + NO_3$ and $I + NO_3$*, Journal of Physical Chemistry, 96 (8), 3321-3331, 1992

Chameides, W. and Walker, J. C. G., *A Photochemical Theory of Tropospheric Ozone*, Journal of Geophysical Research, 78 (36), 8751-8760, 1973

Chameides, W. L. and Davis, D. D., *Iodine: Its Possible Role in Tropospheric Photochemistry*, Journal of Geophysical Research: Oceans, 85 (C12), 7383-7398, 1980

Chang, W. N., Heikes, B. G. and Lee, M. H., *Ozone deposition to the sea surface: chemical enhancement and wind speed dependence*, Atmospheric Environment, 38 (7), 1053-1059, 2004

Charlson, R. J., Lovelock, J. E., Andreae, M. O. and Warren, S. G., *Oceanic phytoplankton, atmospheric sulphur, cloud albedo and climate*, Nature, 326 (6114), 655-661, 1987

Chatfield, R. B. and Crutzen, P. J., *Are There Interactions of Iodine and Sulfur Species in Marine Air Photochemistry?*, Journal of Geophysical Research: Atmospheres, 95 (D13), 22319-22341, 1990

Chen, G., Davis, D., Crawford, J., Hutterli, L. M., Huey, L. G., Slusher, D., Mauldin, L., Eisele, F., Tanner, D., Dibb, J., Buhr, M., McConnell, J., Lefer, B., Shetter, R., Blake, D., Song, C. H., Lombardi, K. and Arnoldy, J., *A reassessment of HO_x South Pole chemistry based on observations recorded during ISCAT 2000*, Atmospheric Environment, 38 (32), 5451-5461, 2004

Chen, G., Huey, L. G., Crawford, J. H., Olson, J. R., Hutterli, M. A., Sjostedt, S., Tanner, D., Dibb, J., Lefer, B., Blake, N., Davis, D. and Stohl, A., *An assessment of the polar HO_x photochemical budget based on 2003 Summit Greenland field observations*, Atmospheric Environment, 41 (36), 7806-7820, 2007

Chipperfield, M. P., *New version of the TOMCAT/SLIMCAT off-line chemical transport model: Intercomparison of stratospheric tracer experiments*, Quarterly Journal of the Royal Meteorological Society, 132 (617), 1179-1203, 2006

Chuck, A. L., Turner, S. M. and Liss, P. S., *Oceanic distributions and air-sea fluxes of biogenic halocarbons in the open ocean*, Journal of Geophysical Research: Oceans, 110 (C10), C10022-C10034, 2005

Cole, A. R. H., Cross, K. J. and Ramsay, D. A., *Rotational Structure of the (0-0) Visible Band of Glyoxal-d_1. A Reanalysis*, Journal of Physical Chemistry, 80 (11), 1221-1223, 1976

Coleman, E. H., Gaydon, A. G. and Vaidya, W. M., *Spectrum of Iodine Oxide (IO) in Flames*, Nature, 162 (4107), 108-109, 1948

Commane, R., *Understanding Radical Chemistry Throughout the Troposphere using Laser-Induced Fluorescence Spectroscopy*, PhD Thesis, University of Leeds, 2009

Commane, R., Floquet, C. F. A., Ingham, T., Stone, D., Evans, M. J. and Heard, D. E., *Observations of OH and HO_2 radicals over West Africa*, Atmospheric Chemistry and Physics, 10 (18), 8783-8801, 2010

Commane, R., Seitz, K., Bale, C. S. E., Bloss, W. J., Buxmann, J., Ingham, T., Platt, U., Pöhler, D. and Heard, D. E., *Iodine monoxide at a clean marine coastal site: observations of high frequency variations and inhomogeneous distributions*, Atmospheric Chemistry and Physics, 11 (13), 6721-6733, 2011

Connelly, B. M., De Haan, D. O. and Tolbert, M. A., *Heterogeneous Glyoxal Oxidation: A Potential Source of Secondary Organic Aerosol*, Journal of Physical Chemistry A, 116 (24), 6180-6187, 2012

Corrigan, A. L., Hanley, S. W. and De Haan, D. O., *Uptake of Glyoxal by Organic and Inorganic Aerosol*, Environmental Science & Technology, 42 (12), 4428-4433, 2008

Cox, R. A. and Coker, G. B., *Absorption Cross Section and Kinetics of IO in the Photolysis of CH_3I in the Presence of Ozone*, Journal of Physical Chemistry, 87 (23), 4478-4484, 1983

Creasey, D. J., Halford-Maw, P. A., Heard, D. E., Pilling, M. J. and Whitaker, B. J., *Implementation and initial deployment of a field instrument for measurement of OH and HO_2 in the troposphere by laser-induced fluorescence*, Journal of the Chemical Society, Faraday Transactions, 93 (16), 2907-2913, 1997

Creasey, D. J., Heard, D. E., Pilling, M. J., Whitaker, B. J., Berzins, M. and Fairlie, R., *Visualisation of a supersonic free-jet expansion using laser-induced fluorescence spectroscopy: Application to the measurement of rate constants at ultralow temperatures*, Applied Physics B: Lasers and Optics, 65 (3), 375-391, 1997

Creasey, D. J., Heard, D. E. and Lee, J. D., *Eastern Atlantic Spring Experiment 1997 (EASE97) 1. Measurements of OH and HO_2 concentrations at Mace Head, Ireland*, Journal of Geophysical Research: Atmospheres, 107 (D10), ACH 3-1–ACH 3-15, 2002

Crosley, D. R., *The Measurement of OH and HO_2 in the Atmosphere*, Journal of the Atmospheric Sciences, 52 (19), 3299-3314, 1995

Crutzen, P., *A Discussion of the Chemistry of Some Minor Constituents in the Stratosphere and Troposphere*, Pure and Applied Geophysics, 106-108 (1), 1385-1399, 1973

Crutzen, P. J., *Photochemical reactions initiated by and influencing ozone in unpolluted tropospheric air*, Tellus, 26A (1-2), 47-57, 1974

Cunliffe, M., Engel, A., Frka, S., Gašparović, B., Guitart, C., Murrell, J. C., Salter, M., Stolle, C., Upstill-Goddard, R. and Wurl, O., *Sea surface microlayers: A unified physicochemical and biological perspective of the air–ocean interface*, Progress in Oceanography, 109 (1), 104-116, 2013

Davis, D. D., Rodgers, M. O., Fischer, S. D. and Asai, K., *An Experimental Assessment of the O_3/H_2O Interference Problem in the Detection of Natural Levels of OH via Laser Induced Fluorescence*, Geophysical Research Letters, 8 (1), 69-72, 1981

Davis, D. D., Crawford, J., Liu, S. C., McKeen, S. A., Bandy, A., Thornton, D., Rowland, F. and Blake, D. R., *Potential impact of iodine on tropospheric levels*

of ozone and other critical oxidants, Journal of Geophysical Research: Atmospheres, 101 (D1), 2135-2147, 1996

de Gouw, J. A., Middlebrook, A. M., Warneke, C., Goldan, P. D., Kuster, W. C., Roberts, J. M., Fehsenfeld, F., Worsnop, D. R., Canagaratna, M. R., Pszenny, A. A. P., Keene, W. C., Marchewka, M., Bertman, S. B. and Bates, T. S., *Budget of organic carbon in a polluted atmosphere: Results from the New England Air Quality Study in 2002*, Journal of Geophysical Research: Atmospheres, 110 (D16), D16305-D16327, 2005

de Zafra, R. L., Jaramillo, M., Parrish, A., Solomon, P., Connor, B. and Barrett, J., *High concentrations of chlorine monoxide at low altitudes in the Antarctic spring stratosphere: diurnal variation*, Nature, 328 (6129), 408-411, 1987

Dechapanya, W., Russell, M. and Allen, D. T., *Estimates of Anthropogenic Secondary Organic Aerosol Formation in Houston, Texas*, Aerosol Science and Technology, 38 (S1), 156-166, 2004

Derwent, R. G., Jenkin, M. E., Saunders, S. M., Pilling, M. J. and Passant, N. R., *Multi-day ozone formation for alkenes and carbonyls investigated with a master chemical mechanism under European conditions*, Atmospheric Environment, 39 (4), 627-635, 2005

Dessens, O., Zeng, G., Warwick, N. and Pyle, J. A., *Short-lived bromine compounds in the lower stratosphere; impact of climate change on ozone*, Atmospheric Science Letters, 10 (3), 201-206, 2009

Diffenbaugh, N. S. and Field, C. B., *Changes in Ecologically Critical Terrestrial Climate Conditions*, Science, 341 (6145), 486-492, 2013

Dillon, T. J., Tucceri, M. E., Sander, R. and Crowley, J. N., *LIF studies of iodine oxide chemistry. Part 3. Reactions IO + NO_3 → OIO + NO_2, I + NO_3 → IO + NO_2, and CH_2I + O_2 → (products): implications for the chemistry of the marine atmosphere at night*, Physical Chemistry Chemical Physics, 10 (11), 1540-1554, 2008

Dix, B., Baidar, S., Schönhardt, A. and Volkamer, R., *IO and Glyoxal measured in the FT during the TORERO campaign - Implications for Satellite Retrievals*, American Geophysical Union Fall Meeting, San Francisco, 2012

Dix, B., Baidar, S., Bresch, J. F., Hall, S. R., Schmidt, S., Wang, S. and Volkamer, R., *Detection of iodine monoxide in the tropical free troposphere*, Proceedings of the National Academy of Sciences, 110 (6), 2035-2040, 2013

Donahue, N. M., Kroll, J. H., Anderson, J. G. and Demerjian, K. L., *Direct observation of OH production from the ozonolysis of olefins*, Geophysical Research Letters, 25 (1), 59-62, 1998

Dorf, M., Butler, J. H., Butz, A., Camy-Peyret, C., Chipperfield, M. P., Kritten, L., Montzka, S. A., Simmes, B., Weidner, F. and Pfeilsticker, K., *Long-term observations of stratospheric bromine reveal slow down in growth*, Geophysical Research Letters, 33 (24), L24803-L24807, 2006

Dorn, H. P., Brandenburger, U., Brauers, T., Hausmann, M. and Ehhalt, D. H., *In-situ detection of tropospheric OH radicals by folded long-path laser absorption. Results from the POPCORN field campaign in August 1994*, Geophysical Research Letters, 23 (18), 2537-2540, 1996

Douglass, A. and Fioletov, V., *Stratospheric Ozone and Surface Ultraviolet Radiation*, Chapter 2 in Scientific Assessment of Ozone Depletion: 2010, Global Ozone Research and Monitoring Project, Report No. 52, World Meteorological Organization, Geneva, Switzerland, 2010

Draxler, R. R. and Hess, G. D., *Description of the HYSPLIT_4 modeling system*, NOAA Technical Memorandum, ERL ARL-224, NOAA Air Resources Laboratory, Silver Spring, Maryland, 1997

Draxler, R. R. and Hess, G. D., *An overview of the HYSPLIT_4 modeling system of trajectories, dispersion, and deposition*, Australian Meteorological Magazine, 47 (4), 295-308, 1998

Draxler, R. R., *HYSPLIT4 user's guide*, NOAA Technical Memorandum, ERL ARL-230, NOAA Air Resources Laboratory, Silver Spring, Maryland, 1999

Draxler, R. R. and Rolph, G. D., HYSPLIT (HYbrid Single-Particle Lagrangian Integrated Trajectory) Model, *via* NOAA ARL READY Website (http://ready.arl.noaa.gov/HYSPLIT.php), NOAA Air Resources Laboratory, Silver Spring, Maryland, 2013

Dusanter, S., Vimal, D., Stevens, P. S., Volkamer, R. and Molina, L. T., *Measurements of OH and HO_2 concentrations during the MCMA-2006 field campaign - Part*

1: Deployment of the Indiana University laser-induced fluorescence instrument, Atmospheric Chemistry and Physics, 9 (5), 1665-1685, 2009

Dusanter, S., Vimal, D., Stevens, P. S., Volkamer, R., Molina, L. T., Baker, A., Meinardi, S., Blake, D., Sheehy, P., Merten, A., Zhang, R., Zheng, J., Fortner, E. C., Junkermann, W., Dubey, M., Rahn, T., Eichinger, B., Lewandowski, P., Prueger, J. and Holder, H., *Measurements of OH and HO_2 concentrations during the MCMA-2006 field campaign - Part 2: Model comparison and radical budget*, Atmospheric Chemistry and Physics, 9 (18), 6655-6675, 2009

Dykstra, C. E. and Schaefer, F., *Electronic Structure of Dicarbonyls. The Ground State of Glyoxal*, Journal of the American Chemical Society, 97 (25), 7210-7215, 1975

Edwards, G. D., Cantrell, C., Stephens, S., Hill, B., Goyea, O., Shetter, R., Mauldin, R. L., Kosciuch, E., Tanner, D. and Eisele, F., *Chemical Ionization Mass Spectrometer Instrument for the Measurement of Tropospheric HO_2 and RO_2*, Analytical Chemistry, 75 (20), 5317-5327, 2003

Edwards, P., Evans, M. J., Commane, R., Ingham, T., Stone, D., Mahajan, A. S., Oetjen, H., Dorsey, J. R., Hopkins, J. R., Lee, J. D., Moller, S. J., Leigh, R., Plane, J. M. C., Carpenter, L. J. and Heard, D. E., *Hydrogen oxide photochemistry in the northern Canadian spring time boundary layer*, Journal of Geophysical Research: Atmospheres, 116 (D22), D22306-D22327, 2011

Edwards, P. M., *Tropospheric Oxidation from the Tropics to the Poles*, PhD Thesis, University of Leeds, 2011

Edwards, P. M., Evans, M. J., Furneaux, K. L., Hopkins, J., Ingham, T., Jones, C., Lee, J. D., Lewis, A. C., Moller, S. J., Stone, D., Whalley, L. K. and Heard, D. E., *OH reactivity in a South East Asian Tropical rainforest during the Oxidant and Particle Photochemical Processes (OP3) project*, Atmospheric Chemistry and Physics Discussions, 13 (2), 5233-5278, 2013

Ehhalt, D. H., *Photooxidation of trace gases in the troposphere*, Physical Chemistry Chemical Physics, 1 (24), 5401-5408, 1999

Eisele, F. L. and Tanner, D. J., *Ion-Assisted Tropospheric OH Measurements*, Journal of Geophysical Research: Atmospheres, 96 (D5), 9295-9308, 1991

Eisele, F. L., Mauldin, R. L., Tanner, D. J., Fox, J. R., Mouch, T. and Scully, T., *An inlet/sampling duct for airborne OH and sulfuric acid measurements*, Journal of Geophysical Research: Atmospheres, 102 (D23), 27993-28001, 1997

Emmerson, K. M., Carslaw, N. and Pilling, M. J., *Urban Atmospheric Chemistry During the PUMA Campaign 2: Radical Budgets for OH, HO_2 and RO_2*, Journal of Atmospheric Chemistry, 52 (2), 165-183, 2005

Emmerson, K. M., Carslaw, N., Carslaw, D. C., Lee, J. D., McFiggans, G., Bloss, W. J., Gravestock, T., Heard, D. E., Hopkins, J., Ingham, T., Pilling, M. J., Smith, S. C., Jacob, M. and Monks, P. S., *Free radical modelling studies during the UK TORCH Campaign in Summer 2003*, Atmospheric Chemistry and Physics, 7 (1), 167–181, 2007

Emmerson, K. M. and Carslaw, N., *Night-time radical chemistry during the TORCH campaign*, Atmospheric Environment, 43 (20), 3220-3226, 2009

Emmerson, K. M. and Evans, M. J., *Comparison of tropospheric gas-phase chemistry schemes for use within global models*, Atmospheric Chemistry and Physics, 9 (5), 1831-1845, 2009

Ervens, B. and Volkamer, R., *Glyoxal processing by aerosol multiphase chemistry: towards a kinetic modeling framework of secondary organic aerosol formation in aqueous particles*, Atmospheric Chemistry and Physics, 10 (17), 8219-8244, 2010

Facchini, M. C., Rinaldi, M., Decesari, S., Carbone, C., Finessi, E., Mircea, M., Fuzzi, S., Ceburnis, D., Flanagan, R., Nilsson, E. D., de Leeuw, G., Martino, M., Woeltjen, J. and O'Dowd, C. D., *Primary submicron marine aerosol dominated by insoluble organic colloids and aggregates*, Geophysical Research Letters, 35 (17), L17814-L17819, 2008

Faloona, I. C., Tan, D., Lesher, R. L., Hazen, N. L., Frame, C. L., Simpas, J. B., Harder, H., Martinez, M., di Carlo, P., Ren, X. and Brune, W. H., *A Laser-Induced Fluorescence Instrument for Detecting Troposhperic OH and HO_2: Characteristics and Calibration*, Journal of Atmospheric Chemistry, 47 (2), 139-167, 2004

Farman, J. C., Gardiner, B. G. and Shanklin, J. D., *Large losses of total ozone in Antarctica reveal seasonal ClO_x/NO_x interaction*, Nature, 315 (6016), 207-210, 1985

Feierabend, K. J., Zhu, L., Talukdar, R. and Burkholder, J. B., *Rate Coefficients for the OH + HC(O)C(O)H (Glyoxal) Reaction between 210 and 390 K*, Journal of Physical Chemistry A, 112 (1), 73-82, 2007

Fick, J., Pommer, L., Nilsson, C. and Andersson, B., *Effect of OH radicals, relative humidity, and time on the composition of the products formed in the ozonolysis of α-pinene*, Atmospheric Environment, 37 (29), 4087-4096, 2003

Fiedler, S. E., Hese, A. and Ruth, A. A., *Incoherent broad-band cavity-enhanced absorption spectroscopy*, Chemical Physics Letters, 371 (3-4), 284-294, 2003

Finley, B. D. and Saltzmann, E. S., *Observations of Cl_2, Br_2, and I_2 in coastal marine air*, Journal of Geophysical Research: Atmospheres, 113 (D21), D21301-D21314, 2008

Fleming, Z. L., Monks, P. S., Rickard, A. R., Heard, D. E., Bloss, W. J., Seakins, P. W., Still, T. J., Sommariva, R., Pilling, M. J., Morgan, R., Green, T. J., Brough, N., Mills, G. P., Penkett, S. A., Lewis, A. C., Lee, J. D., Saiz-Lopez, A. and Plane, J. M. C., *Peroxy radical chemistry and the control of ozone photochemistry at Mace Head, Ireland during the summer of 2002*, Atmospheric Chemistry and Physics, 6 (8), 2193-2214, 2006

Floquet, C. F. A., *Airborne Measurements of Hydroxyl Radicals by Fluorescence Assay by Gas Expansion*, PhD Thesis, University of Leeds, 2006

Forster, P., Ramaswamy, V., Artaxo, P., Bernsten, T., Betts, R., Fahey, D. W., Haywood, J., Lean, J., Lowe, D. C., Myhre, G., Nganga, J., Prinn, R., Raga, G., Schulz, M. and Van Dorland, R., *Changes in Atmospheric Constituents and in Radiative Forcing*, Chapter 2 in Climate Change 2007: The Physical Science Basis. Contribution of Working Group I to the Fourth Assessment Report of the Intergovernmental Panel on Climate Change, S. Solomon, D. Qin, M. Manning, Z. Chen, M. Marquis, K. B. Averyt, M. Tignor and H. L. Miller, (eds.), Cambridge University Press, Cambridge and New York, 2007

François, S., Perraud, V., Pflieger, M., Monod, A. and Wortham, H., *Comparative study of glass tube and mist chamber sampling techniques for the analysis of gasesous carbonyl compounds*, Atmospheric Environment, 39 (35), 6642-6653, 2005

Frieß, U., Sihler, H., Sander, R., Pöhler, D., Yilmaz, S. and Platt, B., *The vertical distribution of BrO and aerosols in the Arctic: Measurements by active and*

passive differential optical absorption spectroscopy, Journal of Geophysical Research: Atmospheres, 116 (D14), D00R04-D00R19, 2011

Fu, T.-M., Jacob, D. J., Wittrock, F., Burrows, J. P., Vrekoussis, M. and Henze, D. K., *Global budgets of atmospheric glyoxal and methylglyoxal, and implications for formation of secondary organic aerosols*, Journal of Geophysical Research: Atmospheres, 113 (D15), D15303-D15320, 2008

Fuchs, H., Bohn, B., Hofzumahaus, A., Holland, F., Lu, K. D., Nehr, S., Rohrer, F. and Wahner, A., *Detection of HO_2 by laser-induced fluorescence: Calibration and intereferences from RO_2 radicals*, Atmospheric Measurement Techniques, 4 (6), 1255-1302, 2011

Fuchs, H., Dorn, H.-P., Bachner, M., Bohn, B., Brauers, T., Gomm, S., Hofzumahaus, A., Holland, F., Nehr, S., Rohrer, F., Tillmann, R. and Wahner, A., *Comparison of OH concentration measurements by DOAS and LIF during SAPHIR chamber experiments at high OH reactivity and low NO concentration*, Atmospheric Measurement Techniques, 5 (7), 1611-1626, 2012

Fueglistaler, S., Bonazzola, M., Haynes, P. H. and Peter, T., *Stratospheric water vapor predicted from the Lagrangian temperature history of air entering the stratosphere in the tropics*, Journal of Geophysical Research: Atmospheres, 110 (D8), D08107-D08117, 2005

Fueglistaler, S., Dessler, A. E., Dunkerton, T. J., Folkins, I., Fu, Q. and Mote, P. W., *Tropical tropopause layer*, Review of Geophysics, 47 (1), RG1004-RG1035, 2009

Furneaux, K., Whalley, L. K., Heard, D. E., Atkinson, H. M., Bloss, W. J., Flynn, M. J., Gallagher, M. W., Ingham, T., Kramer, L., Lee, J. D., Leigh, R., McFiggans, G. B., Mahajan, A. S., Monks, P. S., Oetjen, H., Plane, J. M. C. and Whitehead, J. D., *Measurements of iodine monoxide at a semi polluted coastal location*, Atmospheric Chemistry and Physics, 10 (8), 3645-3663, 2010

Furneaux, K. L., *Field Studies of the Chemistry of Free-Radicals in the Troposphere using Laser Induced Fluorescence Spectroscopy*, PhD thesis, 2009

Gálvez, O., Gómez Martín, J. C., Gómez, P. C., Saiz-Lopez, A. and Pacios, L. F., *A theoretical study on the formation of iodine oxide aggregates and monohydrates*, Physical Chemistry Chemical Physics, Advance Article, DOI: 10.1039/c3cp51219c, 2013

Gantt, B., Meshkidze, N. and Kamykowski, D., *A new physically-based quantification of marine isoprene and primary organic aerosol emissions*, Atmospheric Chemistry and Physics, 9 (14), 4915-4927, 2009

Garland, J. A., Elzerman, A. W. and Penkett, S. A., *The mechanism for dry deposition of ozone to seawater surfaces*, Journal of Geophysical Research: Oceans, 85 (C12), 7488-7492, 1980

Garland, J. A. and Curtis, H., *Emission of Iodine From the Sea Surface in the Presence of Ozone*, Journal of Geophysical Research: Oceans, 86 (C4), 3183-3186, 1981

George, I. J., Matthews, P. S. J., Whalley, L. K., Brooks, B., Goddard, A., Baeza-Romero, M. T. and Heard, D. E., *Measurements of uptake coefficients for heterogeneous loss of HO_2 onto submicron inorganic salt aerosols*, Physical Chemistry Chemical Physics, 15 (31), 12829-12845, 2013

German, K. R., *Direct measurement of the radiative lifetimes of the $A\,^2\Sigma^+$ ($v' = 0$) states of OH and OD*, Journal of Chemical Physics, 62 (7), 2584-2588, 1975

Geyer, A., Bächmann, K., Hofzumahaus, A., Holland, F., Konrad, S., Klüpfel, T., Pätz, H.-W., Perner, D., Mihelcic, D., Schäfer, H.-J., Volz-Thomas, A. and Platt, U., *Nighttime formation of peroxy and hydroxyl radicals during the BERLIOZ campaign: Observations and modeling studies*, Journal of Geophysical Research: Atmospheres, 108 (D4), 8249-8263, 2003

Geyer, A. and Stutz, J., *The vertical structure of OH-HO_2-RO_2 chemistry in the nocturnal boundary layer: A one-dimensional model study*, Journal of Geophysical Research: Atmospheres, 109 (D16), D16301-D16316, 2004

Gherman, T. and Romanini, D., *Mode-locked cavity-enhanced absorption spectroscopy*, Optics Express, 10 (19), 1033-1042, 2002

Gilles, M. K., Turnipseed, A. A., Talukdar, R. K., Rudich, Y., Villalta, P. W., Huey, L. G., Burkholder, J. B. and Ravishankara, A. R., *Reactions of $O(^3P)$ with Alkyl Iodides: Rate Coefficients and Reaction Products*, Journal of Physical Chemistry, 100 (33), 14005-14015, 1996

Gilles, M. K., Burkholder, J. B. and Ravishankara, A. R., *Rate coefficients for the reaction of OH with Cl_2, Br_2, and I_2 from 235 to 354 K*, International Journal of Chemical Kinetics, 31 (6), 417-424, 1999

Glowacki, D. R., Goddard, A., Hemavibool, K., Malkin, T. L., Commane, R., Anderson, F., Bloss, W. J., Heard, D. E., Ingham, T., Pilling, M. J. and

Seakins, P. W., *Design of and initial results from a Highly Instrumented Reactor for Atmospheric Chemistry (HIRAC)*, Atmospheric Chemistry and Physics, 7 (20), 5371–5390, 2007

Gómez Martín, J. C., Spietz, P. and Burrows, J. P., *Kinetic and Mechanistic Studies of the I_2/O_3 Photochemistry*, Journal of Physical Chemistry A, 111 (2), 306-320, 2007

Gómez Martín, J. C., Gálvez, O., Baeza-Romero, M. T., Ingham, T., Plane, J. M. C. and Blitz, M., *On the mechanism of iodine oxide particle formation*, Physical Chemistry Chemical Physics, Advance Article, DOI: 10.1039/c3cp51217g, 2013

Gómez Martín, J. C., Mahajan, A. S., Hay, T. D., Prados-Román, C., Ordoñez, C., MacDonald, S. M., Plane, J. M. C., Sorribas, M., Gil, M., Paredes Mora, J. F., Agama Reyes, M. V., Oram, D. E., Leedham, E. and Saiz-Lopez, A., *Iodine chemistry in the eastern Pacific marine boundary layer*, Journal of Geophysical Research: Atmospheres, 118 (2), 887-904, 2013

Gravestock, T., Blitz, M. A. and Heard, D. E., *A laser induced fluorescence study relating to physical properties of the iodine monoxide radical*, Physical Chemistry Chemical Physics, 12 (4), 823-834, 2010

Green, T. J., Reeves, C. E., Brough, N., Edwards, G. D., Monks, P. S. and Penkett, S. A., *Airborne measurements of peroxy radicals using the PERCA technique*, Journal of Environmental Monitoring, 5 (1), 75-83, 2003

Green, T. J., Reeves, C. E., Fleming, Z. L., Brough, N., Rickard, A. R., Bandy, B., Monks, P. S. and Penkett, S. A., *An improved dual channel PERCA instrument for atmospheric measurements of peroxy radicals*, Journal of Environmental Monitoring, 8 (5), 530-536, 2006

Greenblatt, G. D. and Ravishankara, A. R., *Laboratory studies on the stratospheric NO_x production rate*, Journal of Geophysical Research: Atmospheres, 95 (D4), 3539-3547, 1990

Grilli, R., Méjean, G., Kassi, S., Ventrillard, I., Abd-Alrahman, C. and Romanini, D., *Frequency Comb Based Spectrometer for in Situ and Real Time Measurements of IO, BrO, NO_2, and H_2CO at pptv and ppqv Levels*, Environmental Science & Technology, 46 (19), 10704-10710, 2012

Grilli, R., Legrand, M., Kukui, A., Méjean, G., Preunkert, S. and Romanini, D., *First investigations of IO, BrO, and NO_2 summer atmospheric levels at a coastal East Antarctic site using mode-locked cavity enhanced absorption spectroscopy*, Geophysical Research Letters, 40 (4), 791-796, 2013

Grosjean, D., *Gas-Phase Reaction of Ozone with 2-Methyl-2-butene: Dicarbonyl Formation from Criegee Biradicals*, Environmental Science & Technology, 24 (9), 1428-1432, 1990

Grosjean, D., Grosjean, E. and Moreira, L. F. R., *Speciated Ambient Carbonyls in Rio de Janeiro, Brazil*, Environmental Science & Technology, 36 (7), 1389-1395, 2002

Grosjean, E. and Grosjean, D., *The Reaction of Unsaturated Aliphatic Oxygenates with Ozone*, Journal of Atmospheric Chemistry, 32 (2), 205-232, 1999

Großmann, K., Frieß, U., Peters, E., Wittrock, F., Lampel, J., Yilmaz, S., Tschritter, J., Sommariva, R., von Glasow, R., Quack, B., Krüger, K., Pfeilsticker, K. and Platt, U., *Iodine monoxide in the Western Pacific marine boundary layer*, Atmospheric Chemistry and Physics, 13 (6), 3363-3378, 2013

Haggerstone, A. L., Carpenter, L. J., Carslaw, N. and McFiggans, G., *Improved model predictions of HO_2 with gas to partical mass transfer rates calculated using aerosol number size distibutions*, Journal of Geophysical Research: Atmospheres, 110 (D4), D04303-D04311, 2005

Hanabusa, M., Wang, C. C., Japar, S., Killinger, D. K. and Fisher, K., *Pulsewidth dependence of ozone interference in the laser fluorescence measurement of OH in the atmosphere*, Journal of Chemical Physics, 66 (5), 2118-2121, 1977

Hanke, M., Uecker, J., Reiner, T. and Arnold, F., *Atmospheric peroxy radicals: ROXMAS, a new mass-spectrometric methodology for speciated measurements of HO_2 and ΣRO_2 and first results*, International Journal of Mass Spectrometry, 231 (2-3), 91-99, 2002

Hanson, D. R. and Ravishankara, A. R., *The Reaction Probabilities of $ClONO_2$ and N_2O_5 on Polar Stratospheric Cloud Materials*, Journal of Geophysical Research: Atmospheres, 96 (D3), 5081-5090, 1991

Hanson, D. R. and Ravishankara, A. R., *Reaction of $ClONO_2$ with HCl on NAT, NAD, and Frozen Sulfuric Acid and Hydrolysis of N_2O_5 and $ClONO_2$ on Frozen*

Sulfuric Acid, Journal of Geophysical Research: Atmospheres, 98 (D12), 22931-22936, 1993

Happell, J. D. and Wallace, D. W. R., *Methyl iodide in the Greenland/Norwegian Seas and the tropical Atlantic Ocean: Evidence for photochemical production*, Geophysical Research Letters, 23 (16), 2105-2108, 1996

Hard, T. M., O'Brien, R. J., Chan, C. Y. and Mehrabzadeh, A. A., *Tropospheric Free Radical Determination by FAGE*, Environmental Science & Technology, 18 (10), 768-777, 1984

Harris, D. C., *Quantitative Chemical Analysis*, W. H. Freeman and Company, New York, 2003

Harris, N. R. P., Johnston, P. V., Kreher, K., Harvey, M., Hay, T. D., Robinson, A. D., Ashfold, M. J., Archibald, A., Pyle, J. A., Huang, R.-J. and Hoffmann, T., *Halogen species in the marine boundary layer between Singapore and Wellington, New Zealand*, AGU Fall Meeting, San Francisco, 2011

Harrison, R. M., Yin, J., Tilling, R. M., Cai, X., Seakins, P. W., Hopkins, J. R., Lansley, D. L., Lewis, A. C., Hunter, M. C., Heard, D. E., Carpenter, L. J., Creasey, D. J., Lee, J. D., Pilling, M. J., Carslaw, N., Emmerson, K. M., Redington, A., Derwent, R. G., Ryall, D., Mills, G. and Penkett, S. A., *Measurement and modelling of air pollution and atmospheric chemistry in the U.K. West Midlands conurbation: Overview of the PUMA Consortium project*, Science of the Total Environment, 360 (1-3), 5-25, 2006

Harwood, M. H., Burkholder, J. B., Hunter, M., Fox, R. W. and Ravishankara, A. R., *Absorption cross sections and self-reaction kinetics of the IO radical*, Journal of Physical Chemistry A, 101 (5), 853-863, 1997

Hastings, W. P., Koehler, C. A., Bailey, E. L. and De Haan, D. O., *Secondary Organic Aerosol Formation by Glyoxal Hydration and Oligomer Formation: Humidity Effects and Equilibrium Shifts during Analysis*, Environmental Science & Technology, 39 (22), 8728-8735, 2005

Hausmann, M., Brandenburger, U., Brauers, T. and Dorn, H. P., *Detection of tropospheric OH radicals by long-path differential-optical-absorption spectroscopy: Experimental setup, accuracy, and precision*, Journal of Geophysical Research: Atmospheres, 102 (D13), 16011-16022, 1997

Hayase, S., Yabushita, A., Kawasaki, M., Enami, S., Hoffmann, M. and Colussi, A. J., *Heterogeneous Reaction of Gaseous Ozone with Aqueous Iodide in the Presence of Aqueous Organic Species*, Journal of Physical Chemistry A, 114 (19), 6016-6021, 2010

Hayase, S., Yabushita, A. and Kawasaki, M., *Iodine Emission in the Prescence of Humic Substances at the Water's Surface*, Journal of Physical Chemistry A, 116 (24), 5779-5783, 2012

Heald, C. L., Jacob, D. J., Park, R. J., Russell, L. M., Huebert, B. J., Seinfeld, J. H., Liao, H. and Weber, R. J., *A large organic aerosol source in the free troposphere missing from current models*, Geophysical Research Letters, 32 (18), L18809-L18813, 2005

Heard, D. E. and Pilling, M. J., *Measurement of OH and HO_2 in the Troposphere*, Chemical Reviews, 103 (12), 5163-5198, 2003

Heard, D. E., Carpenter, L. J., Creasey, D. J., Hopkins, J. R., Lee, J. D., Lewis, A. C., Pilling, M. J., Seakins, P. W., Carslaw, N. and Emmerson, K. M., *High levels of the hydroxyl radical in the winter urban troposphere*, Geophysical Research Letters, 31 (18), L18112-L18117, 2004

Heard, D. E., *Atmospheric field measurements of the hydroxyl radical using laser-induced fluorescence spectroscopy*, Annual Review of Physical Chemistry, 57 (1), 191–216, 2006

Heikes, B. G., Chang, W. N., Pilson, M. E. Q., Swift, E., Singh, H. B., Guenther, A., Jacob, D. J., Field, B. D., Fall, R., Riemer, D. and Brand, L., *Atmospheric methanol budget and ocean implication*, Global Biogeochemical Cycles, 16 (4), 80-1–80-13, 2002

Hendrick, F., Johnston, P. V., De Mazière, M., Fayt, C., Hermans, C., Kreher, K., Theys, N., Thomas, A. and van Roozendael, M., *One-decade trend analysis of stratospheric BrO over Harestua (60ºN) and Lauder (45ºS) reveals a decline*, Geophysical Research Letters, 35 (14), L14801-L14805, 2008

Henry, S. B., Kammrath, A. and Keutsch, F. N., *Quantification of gas-phase glyoxal and methylglyoxal via the Laser-Induced Phosphorescence of (methyl)GLyOxal Spectrometry (LIPGLOS) Method*, Atmospheric Measurement Techniques, 5 (1), 181-192, 2012

Hill, V. L. and Manley, S. L., *Release of reactive bromine and iodine from diatoms and its possible role in halogen transfer in polar and tropical oceans*, Limnology and Oceanography, 54 (3), 812-822, 2009

Hoffmann, T., O'Dowd, C. D. and Seinfeld, J. H., *Iodine oxide homogeneous nucleation: An explanation for coastal new particle production*, Geophysical Research Letters, 28 (10), 1949-1952, 2001

Hofzumahaus, A., Aschmutat, U., Hessling, M., Holland, F. and Ehhalt, D. H., *The measurement of tropospheric OH radicals by laser-induced fluorescence spectroscopy during the POPCORN field campaign*, Geophysical Research Letters, 23 (18), 2541-2544, 1996

Holland, F., Hessling, M. and Hofzumahaus, A., *In Situ Measurement of Tropospheric OH Radicals by Laser-Induced Fluorescence - A Description of the KFA Instrument*, Journal of the Atmospheric Sciences, 52 (19), 3393-3401, 1995

Holland, F., Aschumutat, U., Heßling, F., Hofzumahaus, A. and Ehhalt, D. H., *Highly Time Resolved Measurements of OH during POPCORN Using Laser-Induced Fluorescence Spectroscopy*, Journal of Atmospheric Chemistry, 31 (1-2), 205-225, 1998

Holland, F., Hofzumahaus, A., Schafer, R., Kraus, A. and Patz, H. W., *Measurements of OH and HO_2 radical concentrations and photolysis frequencies during BERLIOZ*, Journal of Geophysical Research: Atmospheres, 108 (D4), PHO 2-1–PHO 2-23, 2003

Holzer, W. and Ramsay, D. A., *Laser-induced emission from glyoxal*, Canadian Journal of Physics, 48 (15), 1759-1765, 1970

Hönninger, G. and Platt, U., *Observations of BrO and its vertical distribution during surface ozone depletion at Alert*, Atmospheric Environment, 36 (15-16), 2481-2489, 2002

Hönninger, G., von Friedeburg, C. and Platt, U., *Multi axis differential optical absorption spectroscopy (MAX-DOAS)*, Atmospheric Chemistry and Physics, 4 (1), 231-254, 2004

Hornbrook, R. S., Crawford, J. H., Edwards, G. D., Goyea, O., Mauldin III, R. L., Olson, J. S. and Cantrell, C. A., *Measurements of tropospheric HO_2 and RO_2 by oxygen dilution modulation and chemical ionization mass spectrometry*, Atmospheric Measurement Techniques, 4 (4), 735-756, 2011

Horowitz, L. W., Walters, S., Mauzerall, D., Emmons, L. K., Rasch, P. J., Granier, C., Tie, X., Lamarque, J.-F., Schultz, M. G., Tyndall, G. S., Orlando, J. J. and Brasseur, G., *A global simulation of tropospheric ozone and related tracers: Description and evaluation of MOZART, version 2*, Journal of Geophysical Research: Atmospheres, 108 (D24), ACH 16-1–ACH 16-29, 2003

Hosking, J. S., Russo, M. R., Braesicke, P. and Pyle, J. A., *Modelling deep convection and its impacts on the tropical tropopause layer*, Atmospheric Chemistry and Physics, 10 (22), 11175-11188, 2010

Hossaini, R., Chipperfield, M. P., Dhomse, S., Ordoñez, C., Saiz-Lopez, A., Abraham, N. L., Archibald, A., Braesicke, P., Telford, P., Warwick, N., Yang, X. and Pyle, J. A., *Modelling future changes to the stratospheric source gas injection of biogenic bromocarbons*, Geophysical Research Letters, 39 (20), L20813-L20817, 2012

Huang, R.-J. and Hoffmann, T., *Development of a Coupled Diffusion Denuder System Combined with Gas Chromatography/Mass Spectrometry for the Separation and Quantification of Molecular Iodine and the Activated Iodine Compounds Iodine Monochloride and Hypoiodous Acid in the Marine Atmosphere*, Analytical Chemistry, 81 (5), 1777-1783, 2009

Huang, R.-J., Hou, X. and Hoffmann, T., *Extensive Evaluation of a Diffusion Denuder Technique for the Quantification of Atmospheric Stable and Radioactive Molecular Iodine*, Environmental Science & Technology, 44 (13), 5061-5066, 2010a

Huang, R.-J., Seitz, K., Buxmann, J., Pöhler, D., Hornsby, K. E., Carpenter, L. J., Platt, U. and Hoffmann, T., *In situ measurements of molecular iodine in the marine boundary layer: the link to macroalgae and the implications for O_3, IO, OIO and NO_x*, Atmospheric Chemistry and Physics, 10 (10), 4823-4833, 2010b

Huisman, A. J., Hottle, J. R., Coens, K. L., DiGangi, J. P., Galloway, M. M., Kammrath, A. and Keutsch, F. N., *Laser-Induced Phosphorescence for the in Situ Detection of Glyoxal at Part per Trillion Mixing Ratios*, Analytical Chemistry, 80 (15), 5884-5891, 2008

Huisman, A. J., Hottle, J. R., Galloway, M. M., DiGangi, J. P., Coens, K. L., Choi, W., Faloona, I. C., Gilman, J. B., Kuster, W. C., de Gouw, J., Bouvier-Brown, N. C., Goldstein, A. H., LaFranchi, B. W., Cohen, R. C., Wolfe, G. M., Thornton,

J. A., Docherty, K. S., Farmer, D. K., Cubison, M. J., Jimenez, J. L., Mao, J., Brune, W. H. and Keutsch, F. N., *Photochemical modeling of glyoxal at a rural site: observations and analysis from BEARPEX 2007*, Atmospheric Chemistry and Physics, 11 (17), 8883-8897, 2011

Itoh, N., Tsujita, M., Ando, T., Hisatomi, G. and Higashi, T., *Formation and emission of monohalomethanes from marine algae*, Phytochemistry, 45 (1), 67-73, 1997

Jacob, D. J., *Heterogeneous chemistry and tropospheric ozone*, Atmospheric Environment, 34 (12-14), 2131-2159, 2000

Jacob, D. J. and Winner, D. A., *Effect of climate change on air quality*, Atmospheric Environment, 43 (1), 51-63, 2009

Jammoul, A., Dumas, S., D'Anna, B. and George, C., *Photoinduced oxidation of sea salt halides by aromatic ketones: a source of halogenated radicals*, Atmospheric Chemistry and Physics, 9 (13), 4229-4237, 2009

Jenkin, M. E., Cox, R. A. and Candeland, D. E., *Photochemical Aspects of Tropospheric Iodine Behaviour*, Journal of Atmospheric Chemistry, 2 (4), 359-375, 1985

Jenkin, M. E., Cox, R. A., Mellouki, A., Le Bras, G. and Poulet, G., *Kinetics of the reaction of iodine atoms with hydroperoxy radicals*, Journal of Physical Chemistry, 94 (7), 2927-2934, 1990

Jenkin, M. E., Saunders, S. M. and Pilling, M. J., *The tropospheric degradation of volatile organic compounds: A protocol for mechanism development*, Atmospheric Environment, 31 (1), 81-104, 1997

Jenkin, M. E., Saunders, S. M., Wagner, V. and Pilling, M. J., *Protocol for the development of the Master Chemical Mechanism, MCM v3 (Part B): tropospheric degradation of aromatic volatile organic compounds*, Atmospheric Chemistry and Physics, 3 (1), 181-193, 2003

Johnson, D. and Marston, G., *The gas-phase ozonolysis of unsaturated volatile organic compounds in the troposphere*, Chemical Society Reviews, 37 (4), 699–716, 2008

Johnston, H. S., Floyd Davis, H. and Lee, Y. T., *NO_3 Photolysis Product Channels: Quantum Yields from Observed Energy Thresholds*, Journal of Physical Chemistry, 100 (12), 4713-4723, 1996

Jones, C. E., Hornsby, K. E., Dunk, R. M., Leigh, R. J. and Carpenter, L. J., *Coastal measurements of short-lived reactive iodocarbons and bromocarbons at Roscoff, Brittany during the RHaMBLe campaign*, Atmospheric Chemistry and Physics, 9 (22), 8757-8769, 2009

Jones, C. E., Hornsby, K. E., Sommariva, R., Dunk, R., von Glasow, R., McFiggans, G. B. and Carpenter, L. J., *Quantifying the contribution of marine organic gases to atmospheric iodine*, Geophysical Research Letters, 37 (18), L18804-L18810, 2010

Kalnay, E., Kanamitsu, M., Kistler, R., Collins, W., Deaven, D., Gandin, L., Iredell, M., Saha, S., White, G., Woollen, J., Zhu, Y., Chelliah, M., Ebisuzaki, W., Higgins, W., Janowiak, J., Mo, K. C., Ropelewski, C., Wang, J., Leetmaa, A., Reynolds, R., Jenne, R. and Joseph, D., *The NCEP/NCAR 40-Year Reanalysis Project*, Bulletin of the American Meteorological Society, 77 (3), 437-471, 1996

Kaltsoyannis, N. and Plane, J. M. C., *Quantum chemical calculations on a selection of iodine-containing species (IO, OIO, INO_3, $(IO)_2$, I_2O_3, I_2O_4 and I_2O_5) of importance in the atmosphere*, Physical Chemistry Chemical Physics, 10 (13), 1723-1733, 2008

Kanakidou, M., Seinfeld, J. H., Pandis, S. N., Barnes, I., Dentener, F. J., Facchini, M. C., Van Dingenen, R., Ervens, B., Nenes, A., Nielsen, C. J., Swietlicki, E., Putaud, J. P., Balkanski, Y., Fuzzi, S., Horth, J., Moortgat, G. K., Winterhalter, R., Myhre, C. E. L., Tsigaridis, K., Vignati, E., Stephanou, E. G. and Wilson, J., *Organic aerosol and global climate modelling: a review*, Atmospheric Chemistry and Physics, 5 (4), 1053-1123, 2005

Kanaya, Y., Sadanaga, Y., Matsumoto, J., Sharma, U. K., Hirokawa, J., Kajii, Y. and Akimoto, H., *Nighttime observation of the HO_2 radical by an LIF instrument at Oki Island, Japan, and its possible origins*, Geophysical Research Letters, 26 (14), 2179-2182, 1999

Kanaya, Y., Sadanaga, Y., Hirokawa, J., Kajii, Y. and Akimoto, H., *Development of a Ground-Based LIF Instrument for Measuring HO_x Radicals: Instrumentation and calibrations*, Journal of Atmospheric Chemistry, 38 (1), 73-110, 2001

Kanaya, Y., Cao, R., Kato, S., Miyakawa, Y., Kajii, Y., Tanimoto, H., Yokouchi, Y., Mochida, M., Kawamura, K. and Akimoto, H., *Chemistry of OH and HO_2 radicals observed at Rishiri Island, Japan, in September 2003: Missing*

daytime sink of HO_2 and positive nighttime correlations with monoterpenes., Journal of Geophysical Research: Atmospheres, 112 (D11), D11308-D11425, 2007

Kane, R. P., *Ozone depletion, related UVB changes and increased skin cancer incidence*, International Journal of Climatology, 18 (4), 457-472, 1998

Kieber, D. J. and Mopper, K., *Photochemical formation of glyoxylic and pyruvic acids in seawater*, Marine Chemistry, 21 (2), 135-149, 1987

King, G. W., *Excited States of Glyoxal*, Journal of the Chemical Society, 1957 (1), 5054-5063, 1957

Klick, S. and Abrahamsson, K., *Biogenic Volatile Iodated Hydrocarbons in the Ocean*, Journal of Geophysical Research: Oceans, 97 (C8), 12683-12687, 1992

Kloster, S., Six, K. D., Feichter, J., Maier-Reimer, E., Roeckner, E., Wetzel, P., Stier, P. and Esch, M., *Response of dimethylsulfide (DMS) in the ocean and atmosphere to global warming*, Journal of Geophysical Research: Biogeosciences, 112 (G3), G03005-G03018, 2007

Klotz, B., Graedler, F., Sørensen, S., Barnes, I. and Becker, K.-H., *A kinetic study of the atmospheric photolysis of α-dicarbonyls*, International Journal of Chemical Kinetics, 33 (1), 9-20, 2001

Ko, M. K. W. and Poulet, G., *Very Short-Lived Halogen and Sulfur Substances*, Chapter 2 in Scientific Assessment of Ozone Depletion: 2002, Global Ozone Research and Monitoring Project Report No. 47, World Meteorological Association, Geneva, Switzerland, 2003

Kreher, K., Johnston, P. V. and Wood, S. W., *Ground-based measurements of tropospheric and stratospheric BrO at Arrival Heights, Antarctica*, Geophysical Research Letters, 24 (23), 3021-3024, 1997

Kroll, J. H., Clarke, J. S., Donahue, N. M., Anderson, J. G. and Demerjian, K. L., *Mechanism of HO_x Formation in the Gas-Phase Ozone-Alkene reaction. 1. Direct, Pressure-Dependent Measurements of Prompt OH Yields*, Journal of Physical Chemistry A, 105 (9), 1554-1560, 2001

Kroll, J. H., Sahay, S. R., Anderson, J. G., Demerjian, K. L. and Donahue, N. M., *Mechanism of HO_x Formation in the Gas-Phase Ozone-Alkene Reaction. 2. Prompt versus Thermal Dissociation of Carbonyl Oxides to Form OH*, Journal of Physical Chemistry A, 105 (18), 4446-4457 2001

Kroll, J. H., Donahue, N. M., Cee, V. J., Demerjian, K. L. and Anderson, J. G., *Gas-Phase Ozonolysis of Alkenes: Formation of OH from Anti Carbonyl Cxides*, Journal of the American Chemical Society, 124 (29), 8518-8519, 2002

Kroll, J. H., Ng, N. L., Murphy, S. M., Varutbangkul, V., Flagan, R. C. and Seinfeld, J. H., *Chamber studies of secondary organic aerosol growth by reactive uptake of simple carbonyl compounds*, Journal of Geophysical Research: Atmospheres, 110 (D23), D23207-D23217, 2005

Kukui, A., Ancellet, G. and Le Bras, G., *Chemical ionisation mass spectrometer for measurements of OH and Peroxy radical concentrations in moderately polluted atmospheres*, Journal of Atmospheric Chemistry, 61 (2), 133-154, 2008

Küpper, F. C., Carpenter, L. J., McFiggans, G. B., Palmer, C. J., Waite, T. J., Boneberg, E.-M., Woitsch, S., Weiller, M., Abela, R., Grolimund, D., Potin, P., Butler, A., Luther, G. W., Kroneck, P. M. H., Meyer-Klaucke, W. and Feiters, M. C., *Iodide accumulation provides kelp with an inorganic antioxidant impacting atmospheric chemistry*, Proceedings of the National Academy of Sciences, 105 (19), 6954-6958, 2008

Laaksonen, A., Kulmala, M., O'Dowd, C. D., Joutsensaari, J., Vaattovaara, P., Mikkonen, S., Lehtinen, K. E. J., Sogacheva, L., Dal Maso, M., Aalto, P., Petäjä, T., Sogachev, A., Yoon, Y. J., Lihavainen, H., Nilsson, D., Facchini, M. C., Cavalli, F., Fuzzi, S., Hoffmann, T., Arnold, F., Hanke, M., Sellegri, K., Umann, B., Junkermann, W., Coe, H., Allan, J. D., Alfarra, M. R., Worsnop, D. R., Riekkola, M.-L., Hyötyläinen, T. and Viisanen, Y., *The role of VOC oxidation products in continental new particle formation*, Atmospheric Chemistry and Physics, 8 (10), 2657-2665, 2008

Langmann, B., Scannell, C. and O'Dowd, C., *New Directions: Organic matter contribution to marine aerosols and cloud condensation nuclei*, Atmospheric Environment, 42 (33), 7821-7822, 2008

Lanzendorf, E. J., Hanisco, T. F., Donahue, N. M. and Wennberg, P. O., *Comment on: "The measurement of tropospheric OH radicals by laser-induced fluorescence spectroscopy during the POPCORN field campaign" by Hofzumahaus et al. and "Intercomparison of tropospheric OH radical measurements by multiple folded long-path laser absorption and laser induced fluorescence" by Brauers et al.*, Geophysical Research Letters, 24 (23), 3037-3038, 1997

Lapina, K., Heald, C. L., Spracklen, D. V., Arnold, S. R., Allan, J. D., Coe, H., McFiggans, G., Zorn, S. R., Drewnick, F., Bates, T. S., Hawkins, L. N., Russell, L. M., Smirnov, A., O'Dowd, C. D. and Hind, A. J., *Investigating organic aerosol loading in the remote marine environment*, Atmospheric Chemistry and Physics, 11 (17), 8847-8860, 2011

Law, K. S. and Sturges, W. T., *Halogenated Very Short-Lived Substances*, Chapter 2 in Scientific Assessment of Ozone Depletion: 2006, Global Ozone Research and Monitoring Project, Report No. 50, World Meteorological Organization, Geneva, Switzerland, 2007

Lee, J. D., Lewis, A. C., Monks, P. S., Jacob, M., Hamilton, J. F., Hopkins, J. R., Watson, N. M., Saxton, J. E., Ennis, C., Carpenter, L. J., Carslaw, N., Fleming, Z. L., Bandy, A., Oram, D. E., Penkett, S. A., Slemr, J., Norton, E. G., Rickard, A. R., Whalley, L. K., Heard, D. E., Bloss, W. J., Gravestock, T., Smith, S. C., Stanton, J., Pilling, M. J. and Jenkin, M. E., *Ozone photochemistry and elevated isoprene during the UK heatwave of August 2003*, Atmospheric Environment, 40 (39), 7598– 7613, 2006

Lee, J. D., Moller, S. J., Read, K. A., Lewis, A. C., Mendes, L. and Carpenter, L. J., *Year-round measurements of nitrogen oxides and ozone in the tropical North Atlantic marine boundary layer*, Journal of Geophysical Research: Atmospheres, 114 (D21), D21302-D21316, 2009

Lee, J. D., McFiggans, G. B., Allan, J. D., Baker, A. R., Ball, S. M., Benton, A. K., Carpenter, L. J., Commane, R., Finley, B. D., Evans, M., Fuentes, E., Furneaux, K., Goddard, A., Good, N., Hamilton, J. F., Heard, D. E., Herrmann, H., Hollingsworth, A., Hopkins, J. R., Ingham, T., Irwin, M., Jones, C. E., Jones, R. L., Keene, W. C., Lawler, M. J., Lehmann, S., Lewis, A. C., Long, M. S., Mahajan, A. S., Methven, J., Moller, S. J., Müller, T., Niedermeier, N., O'Doherty, S. J., Oetjen, H., Plane, J. M. C., Pszenny, A. A. P., Read, K. A., Saiz-Lopez, A., Saltzman, E. S., Sander, R., von Glasow, R., Whalley, L. K., Wiedensohler, A. and Young, D., *Reactive Halogens in the Marine Boundary Layer (RHaMBLe): the tropical North Atlantic experiments*, Atmospheric Chemistry and Physics, 10 (3), 1031-1055, 2010

Leedham, E., Hughes, C., Keng, F. S. L., Phang, S.-M., Malin, G. and Sturges, W. T., *Emission of atmospherically significant halocarbons by naturally occurring and farmed tropical macroalgae*, Biogeosciences, 10 (6), 3615-3633, 2013

Levine, J. G., Braesicke, P., Harris, N. R. P., Savage, N. H. and Pyle, J. A., *Pathways and timescales for troposphere-to-stratosphere transport via the tropical tropopause layer and their relevance for very short lived substances*, Journal of Geophysical Research: Atmospheres, 112 (D4), D04308-D04333, 2007

Levy, H., *Normal Atmosphere: Large Radical and Formaldehyde Concentrations Predicted*, Science, 173 (3992), 141-143, 1971

Levy, H., *Photochemistry of the lower troposphere*, Planetary and Space Science, 20 (6), 919-935, 1972

Lewis, A. C., Seakins, P. W., Heard, D. E., McQuaid, J. B., Bartle, K. D. and Pilling, M. J., *In situ, gas chromatographic measurements of non-methane hydrocarbons and dimethyl sulfide at a remote coastal location (Mace Head, Eire) July-August 1996*, Journal of the Chemical Society, Faraday Transactions, 93 (16), 2921-2927, 1997

Lewis, E. R. and Schwartz, S. E., *Sea Salt Aerosol Production: Mechanisms, Methods, Measurements and Models - A Critical Review*, Geophysical Monograph Series, American Geophysical Union, Washington, DC, USA, 2004

Liakakou, E., Vrekoussis, M., Bonsang, B., Donousis, C., Kanakidou, M. and Mihalopoulos, N., *Isoprene above the Eastern Mediterranean: Seasonal variation and contribution to the oxidation capacity of the atmosphere*, Atmospheric Environment, 41 (5), 1002-1010, 2007

Liggio, J., Li, S.-M. and McLaren, R., *Reactive uptake of glyoxal by particulate matter*, Journal of Geophysical Research: Atmospheres, 110 (D10), D10304-D10317, 2005

Lim, Y. B., Tan, Y., Perri, M. J., Seitzinger, S. P. and Turpin, B. J., *Aqueous chemistry and its role in secondary organic aerosol (SOA) formation*, Atmospheric Chemistry and Physics, 10 (21), 10521-10539, 2010

Lin, Y., Donner, L. J., Petch, J., Bechtold, P., Boyle, J., Klein, S. A., Komori, T., Wapler, K., Willett, M., Xie, X., Zhao, M., Xie, S., McFarlane, S. A. and Schumacher, C., *TWP-ICE global atmospheric model intercomparison:*

Convection responsiveness and resolution impact, Journal of Geophysical Research: Atmospheres, 117 (D9), D09111-D09116, 2012

Liu, X., Jeffries, H. E. and Sexton, K. G., *Hydroxyl radical and ozone initiated photochemical reactions of 1,3-butadiene*, Atmospheric Environment, 33 (18), 3005-3022, 1999

Lohmann, U. and Feichter, J., *Global indirect aerosol effects: a review*, Atmospheric Chemistry and Physics, 5 (3), 715-737, 2005

Luo, G. and Yu, F., *A numerical evaluation of global oceanic emissions of α-pinene and isoprene*, Atmospheric Chemistry and Physics, 10 (5), 2007-2015, 2010

MacDonald, S. M., Oetjen, H., Mahajan, A. S., Whalley, L. K., Edwards, P. M., Heard, D. E., Jones, C. E. and Plane, J. M. C., *DOAS measurements of formaldehyde and glyoxal above a south-east Asian tropical rainforest*, Atmospheric Chemistry and Physics, 12 (13), 5949-5962, 2012

Macintyre, H. L. and Evans, M. J., *Parameterisation and impact of aerosol uptake of HO_2 on a global tropospheric model*, Atmospheric Chemistry and Physics, 11 (21), 10965-10974, 2011

Madronich, S. and Flocke, S., *The role of solar radiation in atmospheric chemistry*, in Handbook of Environmental Chemistry, P. Boule (ed.), Springer-Verlag, Heidelberg. 1998

Madronich, S., McKenzie, R. L., Björn, L. O. and Caldwell, M. M., *Changes in biologically active ultraviolet radiation reaching the Earth's surface*, Journal of Photochemistry and Photobiology B: Biology, 46 (1-3), 5-19, 1998

Madronich, S., Tropospheric Ultraviolet and Visible (TUV) Radiation Model, *via* http://cprm.acd.ucar.edu/Models/TUV/, Chemical Processing and Regional Modeling, Atmospheric Chemistry Division, National Center for Atmospheric Research, Boulder, 2013

Magneron, I., Thévenet, R., Mellouki, A. and Le Bras, G., *A Study of the Photolysis and OH-initiated Oxidation of Acrolein and trans-Crotonaldehyde*, Journal of Physical Chemistry A, 106 (11), 2526-2537, 2002

Mahajan, A. S., Oetjen, H., Saiz-Lopez, A., Lee, J. D., McFiggans, G. B. and Plane, J. M. C., *Reactive iodine species in a semi-polluted environment*, Geophysical Research Letters, 36 (16), L16803-L16809, 2009

Mahajan, A. S., Plane, J. M. C., Oetjen, H., Mendes, L., Saunders, R. W., Saiz-Lopez, A., Jones, C. E., Carpenter, L. J. and McFiggans, G., *Measurement and modelling of reactive halogen species over the tropical Atlantic Ocean*, Atmospheric Chemistry and Physics, 10 (10), 4611-4624, 2010

Mahajan, A. S., Whalley, L. K., Kozlova, E., Oetjen, H., Mendez, L., Furneaux, K. L., Goddard, A., Heard, D. E., Plane, J. M. C. and Saiz-Lopez, A., *DOAS observations of formaldehyde and its impact on the HO_x balance in the tropical Atlantic marine boundary layer*, Journal of Atmospheric Chemistry, 66 (3), 167-178, 2010

Mahajan, A. S., Sorribas, M., Gómez Martín, J. C., MacDonald, S. M., Gil, M., Plane, J. M. C. and Saiz-Lopez, A., *Concurrent observations of atomic iodine, molecular iodine and ultrafine particles in a coastal environment*, Atmospheric Chemistry and Physics, 11 (6), 2545-2555, 2011

Mahajan, A. S., Gómez Martín, J. C., Hay, T. D., Royer, S.-J., Yvon-Lewis, S., Liu, Y., Hu, L., Prados-Román, C., Ordoñez, C., Plane, J. M. C. and Saiz-Lopez, A., *Latitudinal distribution of reactive iodine in the Eastern Pacific and its link to open ocean sources*, Atmospheric Chemistry and Physics, 12 (23), 11609-11617, 2012

Mäkelä, J. M., Hoffmann, T., Holzke, C., Väkevä, M., Suni, T., Mattila, T., Aalto, P. P., Tapper, U., Kauppinen, E. I. and O'Dowd, C. D., *Biogenic iodine emissions and identification of end-products in coastal ultrafine particles during nucleation bursts*, Journal of Geophysical Research: Atmospheres, 107 (D19), PAR 14-1–PAR 14-14, 2002

Manley, S. L. and de la Cuesta, J. L., *Methyl iodide production from marine phytoplankton cultures*, Limnology and Oceanography, 42 (1), 142-147, 1997

Mao, J., Ren, X., Brune, W. H., Olson, J. R., Crawford, J. H., Fried, A., Huey, L. G., Cohen, R. C., Heikes, B., Singh, H. B., Blake, D. R., Sachse, G. W., Diskin, G. S., Hall, S. R. and Shetter, R. E., *Airborne measurement of OH reactivity during INTEX-B*, Atmospheric Chemistry and Physics, 9 (1), 163-173, 2009

Mao, J., Jacob, D. J., Evans, M. J., Olson, J. R., Ren, X., Brune, W. H., Clair, J. M. S., Crounse, J. D., Spencer, K. M., Beaver, M. R., Wennberg, P. O., Cubison, M. J., Jimenez, J. L., Fried, A., Weibring, P., Walega, J. G., Hall, S. R., Weinheimer, A. J., Cohen, R. C., Chen, G., Crawford, J. H., McNaughton, C.,

Clarke, A. D., Jaeglé, L., Fisher, J. A., Yantosca, R. M., Le Sager, P. and Carouge, C., *Chemistry of hydrogen oxide radicals (HO_x) in the Arctic troposphere in spring*, Atmospheric Chemistry and Physics, 10 (13), 5823-5838, 2010

Mao, J., Ren, X., Zhang, L., Van Duin, D. M., Cohen, R. C., Park, J.-H., Goldstein, A. H., Paulot, F., Beaver, M. R., Crounse, J. D., Wennberg, P. O., DiGangi, J. P., Henry, S. B., Keutsch, F. N., Park, C., Schade, G. W., Wolfe, G. M., Thornton, J. A. and Brune, W. H., *Insights into hydroxyl measurements and atmospheric oxidation in a California forest*, Atmospheric Chemistry and Physics, 12 (17), 8009-8020, 2012

Mao, J., Fan, S., Jacob, D. J. and Travis, K. R., *Radical loss in the atmosphere from Cu-Fe redox coupling in aerosols*, Atmospheric Chemistry and Physics, 13 (2), 509-519, 2013

Margerum, D. W., Dickson, P. N., Nagy, J. C., Kumar, K., Bowers, C. P. and Fogelman, K. D., *Kinetics of the Iodine Monochloride Reaction with Iodide Measured by the Pulsed-Accelerated-Flow Method*, Inorganic Chemistry, 25 (27), 4900-4904, 1986

Martin, R. V., Jacob, D. J., Yantosca, R. M., Chin, M. and Ginoux, P., *Global and regional decreases in tropospheric oxidants from photochemical effects of aerosols*, Journal of Geophysical Research: Atmospheres, 108 (D3), ACH 6-1 - ACH 6-9, 2003

Martinez, M., Harder, H., Ren, X., Lesher, R. L. and Brune, W. H., *Measuring atmospheric naphthalene with laser-induced fluorescence*, Atmospheric Chemistry and Physics, 4 (2), 563-569, 2004

Martinez, M., Harder, H., Kubistin, D., Rudolf, M., Bozem, H., Eerdekens, G., Fischer, H., Gurk, C., Klupfel, T., Konigstedt, R., Parchatka, U., Schiller, C. L., Stickler, A., Williams, J. and Lelieveld, J., *Hydroxyl radicals in the tropical troposphere over the Suriname rainforest: airborne measurements*, Atmospheric Chemistry and Physics, 10 (4), 3759-3773, 2008

Martinez, M., Harder, H., Kubistin, D., Rudolf, M., Bozem, H., Eerdekens, G., Fischer, H., Klüpfel, T., Gurk, C., Königstedt, R., Parchatka, U., Schiller, C. L., Stickler, A., Williams, J. and Lelieveld, J., *Hydroxyl radicals in the tropical*

troposphere over the Suriname rainforest: airborne measurements, Atmospheric Chemistry and Physics, 10 (8), 3759-3773, 2010

Martinez, R. I. and Herron, J. T., *Stopped-Flow Studies of the Mechanisms of Ozone-Alkene Reactions in the Gas Phase: trans-2-Butene*, Journal of Physical Chemistry, 92 (16), 4644-4648 1988

Martino, M., Liss, P. S. and Plane, J. M. C., *The Photolysis of Dihalomethanes in Surface Seawater*, Environmental Science & Technology, 39 (18), 7097-7101, 2005

Mather, J. H., Stevens, P. S. and Brune, W. H., *OH and HO_2 measurements using laser-induced fluorescence*, Journal of Geophysical Research: Atmospheres, 102 (D5), 6427-6436, 1997

McFiggans, G., Plane, J. M. C., Allan, B. J., Carpenter, L. J., Coe, H. and O'Dowd, C., *A modeling study of iodine chemistry in the marine boundary layer*, Journal of Geophysical Research: Atmospheres, 105 (D11), 14371-14385, 2000

McFiggans, G. B., Bale, C. S. E., Ball, S. M., Beames, J. M., Bloss, W. J., Carpenter, L. J., Dorsey, J., Dunk, R., Flynn, M. J., Furneaux, K., Gallagher, M. W., Heard, D. E., Hollingsworth, A., Hornsby, K. E., Ingham, T., Jones, C. E., Jones, R. L., Kramer, L., Langridge, J. M., Leblanc, C., LeCrane, J.-P., Lee, J. D., Leigh, R. J., Longley, I., Mahajan, A. S., Monks, P. S., Oetjen, H., Orr-Ewing, A. J., Plane, J. M. C., Potin, P., Shillings, A. J. L., Thomas, F., von Glasow, R., Wada, R., Whalley, L. K. and Whitehead, J. D., *Iodine-mediated coastal particle formation: an overview of the Reactive Halogens in the Marine Boundary Layer (RHaMBLe) Roscoff coastal study*, Atmospheric Chemistry and Physics, 10 (6), 2975-2999, 2010

Mead, M. I., Khan, M. A. H., White, I. R., Nickless, G. and Shallcross, D. E., *Methyl halide emission estimates from domestic biomass burning in Africa* Atmospheric Environment, 42 (21), 5241-5250, 2008

Meinen, J., Thieser, J., Platt, U. and Leisner, T., *Technical Note: Using a high finesse optical resonator to provide a long light path for differential optical absorption spectroscopy: CE-DOAS*, Atmospheric Chemistry and Physics, 10 (8), 3901-3914, 2010

Meskhidze, N. and Nenes, A., *Phytoplankton and Cloudiness in the Southern Ocean*, Science, 314 (5804), 1419-1423, 2006

Mihelcic, D., Musgen, P. and Ehhalt, D. H., *An Improved Method of Measuring Tropospheric NO_2 and RO_2 by Matrix Isolation and Electron Spin Resonance*, Journal of Atmospheric Chemistry, 3 (3), 341-361, 1985

Mihelcic, D., Volz-Thomas, A., Patz, H. W. and Kley, D., *Numerical Analysis of ESR Spectra from Atmospheric Samples*, Journal of Atmospheric Chemistry, 11 (3), 271-297, 1990

Mihelcic, D., Klemp, D., Müsgen, P., Pätz, H. W. and Volz-Thomas, A., *Simultaneous Measurements of Peroxy and Nitrate Radicals at Schauinsland*, Journal of Atmospheric Chemistry, 16 (4), 313-335, 1993

Mihelcic, D., Holland, F., Hofzumahaus, A., Hoppe, L., Konrad, S., Musgen, P., Patz, H. W., Schafer, H. J., Schmitz, T., Volz-Thomas, A., Bachmann, K., Schlomski, S., Platt, U., Geyer, A., Alicke, B. and Moortgat, G. K., *Peroxy radicals during BERLIOZ at Pabstthum: Measurements, radical budgets and ozone production*, Journal of Geophysical Research: Atmospheres, 108 (D4), PHO 9-1 - PHO 9-9, 2003

Miyake, Y. and Tsunogai, S., *Evporation of Iodine from the Ocean*, Journal of Geophysical Research, 68 (13), 3989-3993, 1963

Miyazaki, K., Parker, A. E., Fittschen, C., Monks, P. S. and Kajii, Y., *A new technique for the selective measurement of atmospheric peroxy radical concentrations of HO_2 and RO_2 using denuding method*, Atmospheric Measurement Techniques, 3 (6), 3291-3307, 2010

Molina, L. T., Kolb, C. E., de Foy, B., Lamb, B. K., Brune, W. H., Jimenez, J. L., Ramos-Villegas, R., Sarmiento, J., Paramo-Figueroa, V. H., Cardenas, B., Gutierrez-Avedoy, V. and Molina, M. J., *Air quality in North America's most populous city - overview of the MCMA-2003 campaign*, Atmospheric Chemistry and Physics, 7 (10), 2447-2473, 2007

Molina, M. J. and Rowland, F. S., *Stratospheric sink for chlorofluoromethanes: chlorine atom catalysed destruction of ozone*, Nature, 249 (5460), 810-812, 1974

Montzka, S. A. and Reimann, S., *Ozone-Depleting Substances (ODSs) and Related Chemicals*, Chapter 1 in Scientific Assessment of Ozone Depletion: 2010, Global Ozone Research and Monitoring Project, Report No. 52, World Meteorological Organization, Geneva, Switzerland, 2010

Moore, R. M. and Tokarczyk, R., *Volatile biogenic halocarbons in the Northwest Atlantic*, Global Biogeochemical Cycles, 7 (1), 195-210, 1993

Moore, R. M. and Zafiriou, O. C., *Photochemical production of methyl iodide in seawater*, Journal of Geophysical Research: Atmospheres, 99 (D8), 16415-16420, 1994

Moore, R. M., Webb, M., Tokarczyk, R. and Wever, R., *Bromoperoxidase and iodoperoxidase enzymes and production of halogenated methanes in marine diatom cultures*, Journal of Geophysical Research: Oceans, 101 (C9), 20899-20908, 1996

Moortgat, G., *Important photochemical processes in the atmosphere*, Pure and Applied Chemistry, 73 (3), 487-490, 2001

Müller, K., van Pinxteren, D., Plewka, A., Svrcina, B., Kramberger, H., Hofmann, D., Bächmann, K. and Herrmann, H., *Aerosol characterisation at the FEBUKO upwind station Goldlauter (II): Detailed organic chemical characterisation*, Atmospheric Environment, 39 (23-24), 4219-4231, 2005

Nakano, Y., Enami, S., Nakamichi, S., Aloisio, S., Hashimoto, S. and Kawasaki, M., *Temperature and pressure dependence study of the reaction of IO radicals with dimethyl sulfide by cavity ring-down laser spectroscopy*, Journal of Physical Chemistry A, 107 (33), 6381-6387, 2003

Neeb, P., Sauer, F., Horie, O. and Moortgat, G. K., *Formation of hydroxymethyl hydroperoxide and formic acid in alkene ozonolysis in the presence of water vapour*, Atmospheric Environment, 31 (10), 1417-1423, 1997

Neuroth, R., Dorn, H. P. and Platt, U., *High Resolution Spectral Features of a Series of Aromatic Hydrocarbons and BrO: Potential Interferences in Atmospheric OH-Measurements*, Journal of Atmospheric Chemistry, 12 (3), 287-298, 1991

Newman, S. M., Howie, W. H., Lane, I. C., Upson, M. R. and Orr-Ewing, A. J., *Predissociation of the A $^2\Pi_{3/2}$ state of IO studied by cavity ring-down spectroscopy*, Journal of the Chemical Society, Faraday Transactions, 94 (18), 2681-2688, 1998

Nightingale, P. D., Malin, G., Law, C. S., Watson, A. J., Liss, P. S., Liddicoat, M. I., Boutin, J. and Upstill-Goddard, R., *In situ evaluation of air-sea gas exchange parameterizations using novel conservative and volatile tracers*, Global Biogeochemical Cycles, 14 (1), 373-387, 2000

Nishida, S., Takahashi, K., Matsumi, Y., Taniguchi, N. and Hayashida, S., *Formation of $O(^3P)$ Atoms in the Photolysis of N_2O at 193 nm and $O(^3P) + N_2O$ Product Channel in the Reaction of $O(^1D) + N_2O$*, Journal of Physical Chemistry A, 108 (13), 2451-2456, 2004

Nizkorodov, S. A., Sander, S. P. and Brown, L. R., *Temperature and Pressure Dependence of High-Resolution Air-Broadened Absorption Cross Sections of NO_2 (415−525 nm)*, Journal of Physical Chemistry A, 108 (22), 4864-4872, 2004

NOAA, El Niño and La Niña Years and Intensities, based on Oceanic Niño Index (ONI), *via* http://www.elnino.noaa.gov/lanina.html, National Oceanographic and Atmospheric Administration, Boulder, 2013

Novelli, A., *Assessment of the role of stabilized Criegee intermediates in OH radical measurements by LIF*, Atmospheric Chemical Mechanisms, Davis, California, 2012

Nunes, F. M. N., Veloso, M. C. C., Pereira, P. A. d. P. and Andrade, J. B., *Gas-phase ozonolysis of the monoterpenoids (S)-(+)-carvone, (R)-(-)-carvone, (-)-carveol, geranoil and citral*, Atmospheric Environment, 39 (40), 7715-7730, 2005

O'Dowd, C., Facchini, M. C., Cavalli, F., Ceburnis, D., Mircea, M., Desesari, S., Fuzzi, S., Yoon, Y. J. and Putaud, J. P., *Biogenically driven organic contribution to marine aerosol*, Nature, 431 (7009), 676-680, 2004

O'Dowd, C. and De Leeuw, G., *Marine aerosol production: a review of the current knowledge*, Philosophical Transactions of the Royal Society A, 365 (1856), 1753-1774, 2007

O'Dowd, C. D., Jimenez, J. L., Bahreini, R., Flagan, R. C., Seinfeld, J. H., Hameri, K., Pirjola, L., Kulmala, M., Jennings, S. G. and Hoffman, T., *Marine aerosol formation from biogenic emissions*, Nature, 417 (6889), 632-636, 2002

O'Dowd, C. D., Facchini, M. C., Cavalli, F., Ceburnis, D., Mircea, M., Decesari, S., Fuzzi, S., Yoon, Y. J. and Putaud, J. P., *Biogenically driven organic contribution to marine aerosol*, Nature, 431 (7009), 676-680, 2004

O'Neill, E. and Hinrichs, R. Z., *Production of molecular iodine from the heterogeneous reaction of nitrogen dioxide with solid potassium iodide*, Journal of Geophysical Research: Atmospheres, 116 (D1), D01301-D01309, 2011

Oltmans, S. J., *Surface Ozone Measurements in Clean Air*, Journal of Geophysical Research: Oceans, 86 (C2), 1174-1180, 1981

Oltmans, S. J. and Komhyr, W. D., *Surface Ozone Distributions and Variations From 1973-1984: Measurements at the NOAA Geophysical Monitoring for Climatic Change Baseline Observations*, Journal of Geophysical Research: Atmospheres, 91 (D4), 5229-5236, 1986

Orlando, J. J., Tyndall, G. S. and Wallington, T. J., *The atmospheric chemistry of alkoxy radicals*, Chemical Reviews, 103 (12), 4657-4689, 2003

Paldus, J. and Ramsay, D. A., *The 4550 Å band system of glyoxal. 1. Rotational analyses of the (0-0) bands for $C_2H_2O_2$, C_2HDO_2, and $C_2D_2O_2$*, Canadian Journal of Physics, 45 (3), 1389-1412, 1967

Palmer, C. J. and Reason, C. J., *Relationships of surface bromoform concentrations with mixed layer depth and salinity in the tropical oceans*, Global Biogeochemical Cycles, 23 (2), GB2014-GB2024, 2009

Palmer, P. I., Jacob, D. J., Chance, K., Martin, R. V., Spurr, R. J. D., Kurosu, T. P., Bey, I., Yantosca, R., Fiore, A. and Li, Q. B., *Air mass factor formulation for spectroscopic measurements from satellites: Application to formaldehyde retrievals from the Global Ozone Monitoring Experiment*, Journal of Geophysical Research: Atmospheres, 106 (D13), 14539-14550, 2001

Palmer, P. I. and Shaw, S. L., *Quantifying global marine isoprene fluxes using MODIS chlorophyll observations*, Geophysical Research Letters, 32 (9), L09805-L09810, 2005

Paulson, S. E. and Orlando, J. J., *The reactions of ozone with alkenes: An important source of HO_x in the boundary layer*, Geophysical Research Letters, 23 (25), 3727-3730, 1996

Pebay Peyroula, E. and Jost, R., *$S_1 \leftarrow S_0$ laser excitation spectra of glyoxal in a supersonic jet: High-resolution rotational analysis*, Journal of Molecular Spectroscopy, 121 (1), 167-176, 1987

Peters, C., Pechtl, S., Stutz, J., Hebestreit, K., Hönninger, G., Heumann, K. G., Schwarz, A., Winterlik, J. and Platt, U., *Reactive and organic halogen species in three different European coastal environments*, Atmospheric Chemistry and Physics, 5 (12), 3357-3375, 2005

Pisso, I., Haynes, P. H. and Law, K. S., *Emission location dependent ozone depletion potentials for very short-lived halogenated species*, Atmospheric Chemistry and Physics, 10 (24), 12025-12036, 2010

Plane, J. M. C. and Nien, C.-F., *Differential optical absorption spectrometer for measuring atmospheric trace gases*, Review of Scientific Instruments, 63 (3), 1867-1876, 1992

Plane, J. M. C. and Saiz-Lopez, A., *UV-Visible Differential Optical Absorption Spectroscopy (DOAS)*, in Analytical Techniques for Atmospheric Measurement, D. E. Heard (ed.), Blackwell, Oxford. 2006

Platt, U., *Modern methods of the measurement of atmospheric trace gases, Invited Lecture*, Physical Chemistry Chemical Physics, 1 (24), 5409-5415, 1999

Platt, U., Meinen, J., Pöhler, D. and Leisner, T., *Broadband Cavity Enhanced Differential Optical Absorption Spectroscopy (CE-DOAS) - applicability and corrections*, Atmospheric Measurement Techniques, 2 (2), 713-723, 2009

Pöhler, D., Horbanski, M., Schmitt, S., Anthofer, M., Tschritter, J. and Platt, U., *Observations of IO hot-spots at coastal sites with the combination of a mobile CE- and LP- DOAS*, European Geophysical Union General Assembly, Vienna, 2012

Pörtner, N., Toennies, J. P. and Vilesov, A. F., *The observation of large changes in the rotational constants of glyoxal in superfluid helium droplets upon electronic excitation*, Journal of Chemical Physics, 117 (13), 6054-6060, 2002

Possanzini, M., Tagliacozzo, G. and Cecinato, A., *Ambient Levels and Sources of Lower Carbonyls at Montolibretti, Rome (Italy)*, Water Air and Soil Pollution, 183 (1-4), 447-454, 2007

Pyle, J. A., Warwick, N., Yang, X., Young, P. J. and Zeng, G., *Climate/chemistry feedbacks and biogenic emissions*, Philosophical Transactions of the Royal Society A, 365 (1856), 1727-1740, 2007

Quack, B. and Wallace, D. W. R., *Air-sea flux of bromoform: Controls, rates, and implications*, Global Biogeochemical Cycles, 17 (1), 1023-1050, 2003

Quack, B., Atlas, E., Petrick, G., Stroud, V., Schauffler, S. and Wallace, D. W. R., *Oceanic bromoform sources for the tropical atmosphere*, Geophysical Research Letters, 31 (23), L23S05-L23S09, 2004

Quack, B., Atlas, E. L., Petrick, G. and Wallace, D. W. R., *Bromoform and dibromomethane above the Mauritanian upwelling: Atmospheric distributions and oceanic emissions*, Journal of Geophysical Research: Atmospheres, 112 (D9), D09312-D09321, 2007

Raventós-Duran, M. T., Percival, C. J., McGillen, M. R., Hamer, P. D. and Shallcross, D. E., *Kinetics and branching ratio studies of the reaction of $C_2H_5O_2$ + HO_2 using chemical ionisation mass spectrometry*, Physical Chemistry Chemical Physics, 9 (31), 4338-4348, 2007

Read, K. A., Mahajan, A. S., Carpenter, L. J., Evans, M. J., Faria, B. V. E., Heard, D. E., Hopkins, J. R., Lee, J. D., Moller, S. J., Lewis, A. C., Mendes, L., McQuaid, J. B., Oetjen, H., Saiz-Lopez, A., Pilling, M. J. and Plane, J. M. C., *Extensive halogen-mediated ozone destruction over the tropical Atlantic Ocean*, Nature, 453 (7199), 1232-1235, 2008

Read, K. A., Carpenter, L. J., Arnold, S. R., Beale, R., Nightingale, P. D., Hopkins, J. R., Lewis, A. C., Lee, J. D., Mendes, L. and Pickering, S. J., *Multiannual Observations of Acetone, Methanol, and Acetaldehyde in Remote Tropical Atlantic Air: Implications for Atmospheric OVOC Budgets and Oxidative Capacity*, Environmental Science & Technology, 46 (20), 11028-11039, 2012

Reader, J. and Corliss, C. H., *Line Spectra of the Elements*, in CRC Handbook of Chemistry and Physics (Internet Version), 94th Edition, W. M. Haynes, T. J. Bruno and D. R. Lide (eds.), CRC Press/Taylor and Francis, Boca Raton, Florida, 2013-2014

Reeser, D. I., George, C. and Donaldson, D. J., *Photooxidation of Halides by Chlorophyll at the Air-Salt Water Interface*, Journal of Physical Chemistry A, 113 (30), 8591-8595, 2009

Reeser, D. I. and Donaldson, D. J., *Influence of water surface properties on the heterogeneous reaction between $O_{3(g)}$ and $I_{(aq)}^-$*, Atmospheric Environment, 45 (34), 6116-6120, 2011

Ren, X., Harder, H., Martinez, M., Lesher, R., Oliger, A., Shirley, T., Adams, J., Simpas, J. B. and Brune, W. H., *HO_x concentrations and OH reactivity observations in New York City during PMTACS-NY2001*, Atmospheric Environment, 37 (26), 3627-3637, 2003a

Ren, X., Harder, H., Martinez, M., Lesher, R., Oliger, A., Simpas, J. B., Brune, W. H., Schwab, J. J., Demerjian, K. L., He, Y., Zhou, X. and Gao, H., *OH and HO_2 chemistry in the urban atmosphere of New York City*, Atmospheric Environment, 37 (26), 3639-3651, 2003b

Ren, X., Harder, H., Martinez, M., Faloona, I., Tan, D., Lesher, R., Di Carlo, P., Simpas, J. B. and Brune, W. H., *Interference Testing for Atmospheric HO_x Measurements by Laser-Induced Fluorescence*, Journal of Atmospheric Chemistry, 47 (2), 169-190, 2004

Ren, X., Brune, W. H., Mao, J., Mitchell, M. J., Lesher, R., Simpas, J. B., Metcalf, A. R., Schwab, J. J., Cai, C., Li, Y., Demerjian, K. L., Felton, H. D., Boynton, G., Adams, A., Perry, J., He, Y., Zhou, X. and Hou, J., *Behavior of OH and HO_2 in the winter atmosphere in New York City*, Atmospheric Environment, 40 (S2), 252-263, 2006

Ren, X., Brune, W. H., Oliger, A., Metcalf, A. R., Simpas, J. B., Shirley, T., Schwab, J. J., Bai, C., Roychowdhury, U., Li, Y., Cai, C., Demerjian, K. L., He, Y., Zhou, X., Gao, H. and Hou, J., *OH, HO_2, and OH reactivity during the PMTACS-NY Whiteface Mountain 2002 campaign: Observations and model comparison*, Journal of Geophysical Research: Atmospheres, 111 (D10), D10S03-D10S15, 2006

Ren, X., Olson, J. R., Crawford, J. H., Brune, W. H., Mao, J., Long, R. B., Chen, Z., Chen, G., Avery, M. A., Sachse, G. W., Barrick, J. D., Diskin, G. S., Huey, L. G., Fried, A., Cohen, R. C., Heikes, B., Wennberg, P. O., Singh, H. B., Blake, D. R. and Shetter, R. E., *HO_x chemistry during INTEX-A 2004: Observation, model calculation, and comparison with previous studies*, Journal of Geophysical Research: Atmospheres, 113 (D5), D05310-D05323, 2008

Ren, X., Mao, J., Brune, W. H., Cantrell, C. A., Mauldin III, R. L., Hornbrook, R. S., Kosciuch, E., Olson, J. R., Crawford, J. H., Chen, G. and Singh, H. B., *Airborne intercomparison of HO_x measurements using laser-induced fluorescence and chemical ionization mass spectrometry during ARCTAS*, Atmospheric Measurement Techniques, 5 (8), 2025-2037, 2012

Richter, U. and Wallace, D. W. R., *Production of methyl iodide in the tropical Atlantic Ocean*, Geophysical Research Letters, 31 (23), L23S03-L23S07, 2004

Rinaldi, M., Decesari, S., Finessi, E., Giulianelli, L., Carbone, C., Fuzzi, S., O'Dowd, C. D., Ceburnis, D. and Facchini, M. C., *Primary and Secondary Organic Marine Aerosol and Oceanic Biological Activity: Recent Results and New Perspectives for Future Studies*, Advances in Meteorology, 2010 (310682), 1-10, 2010

Roelofs, G. J., *A GCM study of organic matter in marine aerosol and its potential contribution to cloud drop activation*, Atmospheric Chemistry and Physics, 8 (3), 709-719, 2008

Rohrer, F. and Berresheim, H., *Strong correlation between levels of tropospheric hydroxyl radicals and solar ultraviolet radiation*, Nature, 442 (7099), 184-187, 2006

Rolph, G. D., Real-time Environmental Applications and Display sYstem (READY) Website, *via* http://ready.arl.noaa.gov, NOAA, Silver Spring, Maryland, 2013

Sadanaga, Y., Yoshino, A., Shungo, K. and Yoshizumi, K., *Measurements of OH Reactivity and Photochemical Ozone Production in the Urban Atmosphere*, Environmental Science & Technology, 39 (22), 8847-8852, 2005

Saiz-Lopez, A. and Plane, J. M. C., *Novel iodine chemistry in the marine boundary layer*, Geophysical Research Letters, 31 (5), L04112-L04116, 2004

Saiz-Lopez, A., Plane, J. M. C., McFiggans, G., Williams, P. I., Ball, S. M., Bitter, M., Jones, R. L., Hongwei, C. and Hoffmann, T., *Modelling molecular iodine emissions in a coastal marine environment: the link to new particle formation*, Atmospheric Chemistry and Physics, 6 (4), 883-895, 2006

Saiz-Lopez, A., Shillito, J. A., Coe, H. and Plane, J. M. C., *Measurements and modelling of I_2, IO, OIO, BrO and NO_3 in the mid-latitude marine boundary layer*, Atmospheric Chemistry and Physics, 6 (6), 1513-1528, 2006

Saiz-Lopez, A., Chance, K., Liu, X., Kurosu, T. P. and Sander, S. P., *First observations of iodine oxide from space*, Geophysical Research Letters, 34 (12), L12812-L12817, 2007

Saiz-Lopez, A., Lamarque, J.-F., Kinnison, D. E., Tilmes, S., Ordoñez, C., Orlando, J. J., Conley, A. J., Plane, J. M. C., Mahajan, A. S., Sousa Santos, G., Atlas, E. L., Blake, D. R., Sander, R., Schauffler, S., Thompson, A. M. and Brasseur, G., *Estimating the climate significance of halogen-driven ozone loss in the tropical marine troposphere*, Atmospheric Chemistry and Physics, 12 (9), 3939-3949, 2012

Saiz-Lopez, A., Plane, J. M. C., Baker, A. R., Carpenter, L. J., von Glasow, R., Gómez Martín, J. C., McFiggans, G. B. and Saunders, R. W., *Atmospheric Chemistry of Iodine*, Chemical Reviews, 112 (3), 1773-1804, 2012

Sakamoto, Y., Yabushita, A., Kawasaki, M. and Enami, S., *Direct Emission of I_2 Molecule and IO Radical from the Heterogeneous Reactions of Gaseous Ozone with Aqueous Potassium Iodide Solution*, Journal of Physical Chemistry A, 113 (27), 7707-7713, 2009

Salisbury, G., Rickard, A. R., Monks, P. S., Allan, B. J., Bauguitte, S. J. B., Penkett, S. A., Carslaw, N., Lewis, A. C., Creasey, D. J., Heard, D. E., Jacobs, P. J. and Lee, J. D., *Production of peroxy radicals at night via reactions of ozone and the nitrate radical in the marine boundary layer*, Journal of Geophysical Research: Atmospheres, 106 (D12), 12669-12687, 2001

Salter, R. J., Blitz, M. A., Heard, D. E., Kovács, T., Pilling, M. J., Rickard, A. R. and Seakins, P. W., *Quantum yields for the photolysis of glyoxal below 350 nm and parameterisations for its photolysis rate in the troposphere*, Physical Chemistry Chemical Physics, 15 (14), 4984-4994, 2013a

Salter, R. J., Blitz, M. A., Heard, D. E., Pilling, M. J. and Seakins, P. W., *Pressure and temperature dependent photolysis of glyoxal in the 355-414 nm region: evidence for dissociation from multiple states*, Physical Chemistry Chemical Physics, 15 (17), 6516-6526, 2013b

Sander, S. P., Friedl, R. R., Golden, D. M., Kurylo, M. J., Huie, R. E., Orkin, V. L., Moortgat, G. K., Ravishankara, A. R., Kolb, C. E., Molina, M. J. and Finlayson-Pitts, B., J., *Chemical Kinetics and Photochemical Data for Use in Atmospheric Studies. Evaluation Number 14*, JPL Publication 02-25, Jet Propulsion Laboratory, Pasadena, 2002

Sander, S. P., Friedl, R. R., Golden, D. M., Kurylo, M. J., Moortgat, G. K., Keller-Rudek, H., Wine, P. H., Ravishankara, A. R., Kolb, C. E., Molina, M. J., Finlayson-Pitts, B., J., Huie, R. E. and Orkin, V. L., *Chemical Kinetics and Photochemical Data for Use in Atmospheric Studies. Evaluation Number 15*, JPL Publication 06-02, Jet Propulsion Laboratory, Pasadena, 2006

Sander, S. P., Abbatt, J., Barker, J. R., Burkholder, J. B., Friedl, R. R., Golden, D. M., Huie, R. E., Kolb, C. E., Kurylo, M. J., Moortgat, G. K., Orkin, V. L. and Wine, P. H., *Chemical Kinetics and Photochemical Data for Use in*

Atmospheric Studies. Evaluation Number 17, JPL Publication 10-6, Jet Propolusion Laboratory, Pasadena, 2011

Saunders, S. M., Jenkin, M. E., Derwent, R. G. and Pilling, M. J., *Protocol for the development of the Master Chemical Mechanism, MCM v3 (Part A): tropospheric degradation of non-aromatic volatile organic compounds*, Atmospheric Chemistry and Physics, 3 (1), 161-180, 2003

Scarratt, M. G. and Moore, R. M., *Production of chlorinated hydrocarbons and methyl iodide by the red microalga Porphyridium purpureum*, Limnology and Oceanography, 44 (3), 703-707, 1999

Schall, C., Heumann, K. G. and Kirst, G. O., *Biogenic volatile organoiodine and organobromine hydrocarbons in the Atlantic Ocean from 42ºN to 72ºS*, Fresenius' Journal of Analytical Chemistry, 359 (3), 298-305, 1997

Schauffler, S. M., Atlas, E. L., Blake, D. R., Flocke, F., Lueb, R. A., Lee-Taylor, J. M., Stroud, V. and Travnicek, W., *Distributions of brominated organic compounds in the troposphere and lower stratosphere*, Journal of Geophysical Research: Atmospheres, 104 (D17), 21513-21535, 1999

Schlosser, E., Bohn, B., Brauers, T., Dorn, H.-P., Fuchs, H., Häseler, R., Hofzumahaus, A., Holland, F., Rohrer, F., Rupp, L. O., Siese, M., Tillmann, R. and Wahner, A., *Intercomparison of Two Hydroxyl Radical Measurement Techniques at the Atmosphere Simulation Chamber SAPHIR*, Journal of Atmospheric Chemistry, 56 (2), 187-205, 2007

Schlosser, E., Brauers, T., Dorn, H. P., Fuchs, H., Häseler, R., Hofzumahaus, A., Holland, F., Wahner, A., Kanaya, Y., Kajii, Y., Miyamoto, K., Nishida, S., Watanabe, K., Yoshino, A., Kubistin, D., Martinez, M., Rudolf, M., Harder, H., Berresheim, H., Elste, T., Plass-Dülmer, C., Stange, G. and Schurath, U., *Technical Note: Formal blind intercomparison of OH measurements: results from the international campaign HOxComp*, Atmospheric Chemistry and Physics, 9 (20), 7923-7948, 2009

Schmitter, A., Oschlies, A., Damon Matthews, H. and Galbraith, E. D., *Future changes in climate, ocean circulation, ecosystems, and biogeochemical cycling simulated for a business-as-usual CO_2 emission scenario until year 4000 AD*, Global Biogeochemical Cycles, 22 (1), GB1013-GB1034, 2008

Schönhardt, A., Richter, A., Wittrock, F., Kirk, H., Oetjen, H., Roscoe, H. K. and Burrows, J. P., *Observations of iodine monoxide columns from satellite*, Atmospheric Chemistry and Physics, 8 (3), 637-653, 2008

Schönhardt, A., Begoin, M., Richter, A., Wittrock, F., Kaleschke, L., Gómez Martín, J. C. and Burrows, J. P., *Simultaneous satellite observations of IO and BrO over Antarctica*, Atmospheric Chemistry and Physics, 12 (14), 6565-6580, 2012

Schönhardt, A., Richter, A. and Burrows, J. P., *IO columns and the relation to chlorophyll-a as observed from satellite*, European Geophysical Union General Assembly 2012, Vienna, 2012

Seitz, K., Buxmann, J., Pöhler, D., Sommer, T., Tschritter, J., Neary, T., O'Dowd, C. D. and Platt, U., *The spatial distribution of the reactive iodine species IO from simultaneous active and passive DOAS observations*, Atmospheric Chemistry and Physics, 10 (5), 2117-2128, 2010

Shaw, S. L., Chisholm, S. W. and Prinn, R. G., *Isoprene production by Prochlorococcus, a marine cyanobacterium, and other phytoplankton*, Marine Chemistry, 80 (4), 227-245, 2003

Shaw, S. L., Gantt, B. and Meskhidze, N., *Production and Emissions of Marine Isoprene and Monoterpenes: A Review*, Advances in Meteorology, 2010 (408696), 1-24, 2010

Sheehy, P. M., Volkamer, R., Molina, L. T. and Molina, M. J., *Oxidative capacity of the Mexico City atmosphere - Part 2: A RO_x radical cycling perspective*, Atmospheric Chemistry and Physics, 10 (14), 6993-7008, 2010

Shilling, J. E., Zaveri, R. A., Fast, J. D., Kleinman, L., Alexander, M. L., Canagaratna, M. R., Fortner, E., Hubbe, J. M., Jayne, J. T., Sedlacek, A., Setyan, A., Springston, S., Worsnop, D. R. and Zhang, Q., *Enhanced SOA formation from mimxed anthropogenic and biogenic emissions during the CARES campaign*, Atmospheric Chemistry and Physics, 13 (4), 2091-2113, 2013

Shirley, T. R., Brune, W. H., Ren, X., Mao, J., Lesher, R., Cardenas, B., Volkamer, R., Molina, L. T., Molina, M. J., Lamb, B., Velasco, E., Jobson, T. and Alexander, M., *Atmospheric oxidation in the Mexico City Metropolitan Area (MCMA) during April 2003*, Atmospheric Chemistry and Physics, 6 (9), 2753-2765, 2006

Sillman, S., *Tropospheric ozone: The debate over control strategies*, Annual Review of Energy and the Environment, 18 (1), 31-56, 1993

Singh, H. B., Gregory, G. L., Anderson, B., Browell, E., Sachse, G. W., Davis, D. D., Crawford, J., Bradshaw, J. D., Talbot, R., Blake, D. R., Thornton, D., Newell, R. and Merrill, J., *Low ozone in the marine boundary layer of the tropical Pacific Ocean: Photochemical loss, chlorine atoms, and entrainment*, Journal of Geophysical Research: Atmospheres, 101 (D1), 1907-1917, 1996

Singh, H. B., Tabazadeh, A., Evans, M. J., Field, B. D., Jacob, D. J., Sachse, G., Crawford, J. H., Shetter, R. and Brune, W. H., *Oxygenated volatile organic chemicals in the oceans: Inferences and implications based on atmospheric observations and air-sea exchange models*, Geophysical Research Letters, 30 (16), 1862-1867, 2003

Sinha, V., Williams, J., Meyerhöfer, M., Riebesell, U., Paulino, A. I. and Larsen, A., *Air-sea fluxes of methanol, acetone, acetaldehyde, isoprene and DMS from a Norwegian fjord following a phytoplankton bloom in a mesocosm experiment*, Atmospheric Chemistry and Physics, 7 (3), 739-755, 2007

Sinreich, R., Volkamer, R., Filsinger, F., Frieß, U., Kern, C., Platt, U., Sebastián, O. and Wagner, T., *MAX-DOAS detection of glyoxal during ICARTT 2004*, Atmospheric Chemistry and Physics, 7 (5), 1293-1303, 2007

Sinreich, R., Coburn, S. C., Dix, B. and Volkamer, R., *Ship-based detection of glyoxal over the remote tropical Pacific Ocean*, Atmospheric Chemistry and Physics, 10 (23), 11359-11371, 2010

Sjostedt, S. J., Huey, L. G., Tanner, D. J., Peischl, J., Chen, G., Dibb, J. E., Lefer, B., Hutterli, M. A., Beyersdorf, A. J., Blake, N. J., Blake, D. R., Sueper, D., Ryerson, T., Burkhart, J. and Stohl, A., *Observations of hydroxyl and the sum of peroxy radicals at Summit, Greenland during summer 2003*, Atmospheric Environment, 41 (24), 5122-5137, 2007

Skoog, D. A., West, D. M. and Holler, F. J., *Fundamentals of Analytical Chemistry*, Harcourt Brace and Company, Orlando, 1996

Smith, D. F., Kleindienst, T. E. and McIver, C. D., *Primary Product Distributions from the Reaction of OH with m-, p-Xylene, 1,2,4- and 1,3,5-Trimethylbenzene*, Journal of Atmospheric Chemistry, 34 (3), 339-364, 1999

Smith, G. P. and Crosley, D. R., *A Photochemical Model of Ozone Interference Effects in Laser Detection of Tropospheric OH*, Journal of Geophysical Research: Atmospheres, 95 (D10), 16427-16442, 1990

Smith, S. C., Lee, J. D., Bloss, W. J., Johnson, G. P. and Heard, D. E., *Concentrations of OH and HO_2 during NAMBLEX: measurements and steady state analysis*, Atmospheric Chemistry and Physics, 6 (5), 1435–1453, 2006

Smith, S. C., *Atmospheric Measurements of OH and HO_2 using the FAGE technique: Instrument development and data analysis*, PhD Thesis, University of Leeds, 2007

Smythe-Wright, D., Peckett, C., Boswell, S. and Harrison, R., *Controls on the production of organohalogens by phytoplankton: Effect of nitrate concentraton and grazing*, Journal of Geophysical Research: Biogeosciences, 115 (G3), G03020-G03031, 2010

Solomon, S., Garcia, R. R., Sherwood Roland, F. and Wuebbles, D. J., *On the depletion of Antarctic ozone*, Nature, 321 (6072), 755-758, 1986

Solomon, S., Connor, B., de Zafra, R. L., Parrish, A., Barrett, J. and Jaramillo, M., *High concentrations of chlorine monoxide at low altitudes in the Antarctic spring stratosphere: secular variation*, Nature, 328 (6129), 411-413, 1987

Solomon, S., Garcia, R. R. and Ravishankara, A. R., *On the Role of Iodine in Ozone Depletion*, Journal of Geophysical Research: Atmospheres, 99 (D10), 20491-20499, 1994

Solomon, S. D., Qin, D., Manning, M., Alley, R. B., Berntsen, T., Bindoff, N. L., Chen, Z., Chidthaisong, A., Gregory, J. M., Hegerl, G. C., Heimann, M., Hewitson, B., Hoskins, B. J., Joos, F., Jouzel, J., Kattsov, V., Lohmann, U., Matsuno, T., Molina, M., Nicholls, N., Overpeck, J., Raga, G., Ramaswamy, V., Ren, J., Rusticucci, M., Somerville, R., Stocker, T. F., Whetton, P., Wood, R. A. and Wratt, D., *Technical Summary*, Climate Change 2007: The Physical Science Basis. Contribution of Working Group I to the Fourth Assessment Report of the Intergovernmental Panel on Climate Change, S. D. Solomon, M. Qin, M. Manning, Z. Chen, M. Marquis, K. B. Averyt, M. Tignor and H. L. Miller, (eds.), Cambridge University Press, Cambridge and New York, 2007

Sommariva, R., Haggerstone, A. L., Carpenter, L. J., Creasey, D. J., Carslaw, N., Heard, D. E., Lee, J. D., Lewis, A. C., Pilling, M. J. and Zador, J., *OH and HO_2*

chemistry in clean marine air during SOAPEX-2, Atmospheric Chemistry and Physics, 4 (3), 839-856, 2004

Sommariva, R., Bloss, W. J., Brough, N., Carslaw, N., Flynn, M., Haggerstone, A.-L., Heard, D. E., Hopkins, J. R., Lee, J. D., Lewis, A. C., McFiggans, G., Monks, P. S., Penkett, S. A., Pilling, M. J., Plane, J. M. C., Read, K. A., Saiz-Lopez, A., Rickard, A. R. and Williams, P. I., *OH and HO_2 chemistry during NAMBLEX: roles of oxygenates, halogen oxides and heterogeneous uptake*, Atmospheric Chemistry and Physics, 6 (4), 1135-1153, 2006

Sommariva, R., Pilling, M. J., Bloss, W. J., Heard, D. E., Lee, J. D., Fleming, Z. L., Monks, P. S., Plane, J. M. C., Saiz-Lopez, A., Ball, S. M., Bitter, M., Jones, R. L., Brough, N., Penkett, S. A., Hopkins, J. R., Lewis, A. C. and Read, K. A., *Night-time radical chemistry during the NAMBLEX campaign*, Atmospheric Chemistry and Physics, 7 (3), 587-598, 2007

Sommariva, R. and von Glasow, R., *Multiphase Halogen Chemistry in the Tropical Atlantic Ocean*, Environmental Science & Technology, 46 (18), 10429-10437, 2012

Spangler, L. H., Matsumoto, Y. and Pratt, D. W., *Direct Excitation of Triplet States in Supersonic Jets. Rotationally Resolved $^3A_u \leftarrow {}^1A_g$ Laser-Induced Phosphorescence Spectrum of Glyoxal*, Journal of Physical Chemistry, 87 (24), 4781-4783, 1983

Spaulding, R. S., Talbot, R. W. and Charles, M. J., *Optimization of a Mist Chamber (Cofer Scrubber) for Sampling Water-Soluble Organics in Air*, Environmental Science & Technology, 36 (8), 1798-1808, 2002

Spracklen, D. V., Pringle, K. J., Carslaw, K. S., Chipperfield, M. P. and Mann, G. W., *A global off-line model of size-resolved aerosol microphysics: I. Model development and prediction of aerosol properties*, Atmospheric Chemistry and Physics, 5 (8), 2227-2252, 2005

Spracklen, D. V., Arnold, S. R., Sciare, J., Carslaw, K. S. and Pio, C., *Globally significant oceanic source of organic carbon*, Geophysical Research Letters, 35 (12), L12811-L12816, 2008

Stevens, P. S., Mather, J. H. and Brune, W. H., *Measurement of Tropospheric OH and HO_2 by laser-induced fluorescence at low pressure*, Journal of Geophysical Research: Atmospheres, 99 (D2), 3543-3557, 1994

Stevens, P. S., Mather, J. H., Brune, W. H., Eisele, F., Tanner, D., Jefferson, A., Cantrell, C., Shetter, R., Sewall, S., Fried, A., Henry, B., Williams, E., Baumann, K., Goldan, P. and Kuster, W., *HO_2/OH and RO_2/HO_2 ratios during the Tropospheric OH Photochemistry Experiment: Measurement and theory*, Journal of Geophysical Research: Atmospheres, 102 (D5), 6379-6391, 1997

Stevenson, D. S., Young, P. J., Naik, V., Lamarque, J. F., Shindell, D. T., Voulgarakis, A., Skeie, R. B., Dalsoren, S. B., Myhre, G., Bernsten, T. K., Folberth, G. A., Rumbold, S. T., Collins, W. J., MacKenzie, I. A., Doherty, R. M., Zeng, G., van Noije, T. P. C., Strunk, A., Bergmann, D., Cameron-Smith, P., Plummer, D. A., Strode, S. A., Horowitz, L., Lee, Y. H., Szopa, S., Sudo, K., Nagashima, T., Josse, B., Cionni, I., Righi, M., Eyring, V., Conley, A., Bowman, K. W., Wild, O. and Archibald, A., *Tropospheric ozone changes, radiative forcing and attribution to emissions in the Atmospheric Chemistry and Climate Model Intercomparison Project (ACCMIP)*, Atmospheric Chemistry and Physics, 13 (6), 3063-3085, 2013

Stimpfle, R. M. and Anderson, J. G., *In-situ detection of OH in the lower stratosphere with a balloon borne high repetition rate laser system*, Geophysical Research Letters, 15 (13), 1503-1506, 1988

Stohl, A., Forster, C., Frank, A., Seibert, P. and Wotawa, G., *Technical note: The Lagrangian particle dispersion model FLEXPART version 6.2*, Atmospheric Chemistry and Physics, 5 (9), 2461-2474, 2005

Stone, D., Evans, M. J., Commane, R., Ingham, T., Floquet, C. F. A., McQuaid, J. B., Brookes, D. M., Monks, P. S., Purvis, R., Hamilton, J. F., Hopkins, J., Lee, J., Lewis, A. C., Stewart, D., Murphy, J. G., Mills, G., Oram, D., Reeves, C. E. and Heard, D. E., *HO_x observations over West Africa during AMMA: impact of isoprene and NO_x*, Atmospheric Chemistry and Physics, 10 (19), 9415-9429, 2010

Stone, D., Evans, M. J., Edwards, P. M., Commane, R., Ingham, T., Rickard, A. R., Brookes, D. M., Hopkins, J., Leigh, R. J., Lewis, A. C., Monks, P. S., Oram, D., Reeves, C. E., Stewart, D. and Heard, D. E., *Isoprene oxidation mechanisms: measurements and modelling of OH and HO_2 over a South-East Asian tropical rainforest during the OP3 field campaign*, Atmospheric Chemistry and Physics, 11 (14), 6749-6771, 2011

Stone, D., Whalley, L. K. and Heard, D. E., *Tropospheric OH and HO_2 radicals: field measurements and model comparisons*, Chemical Society Reviews, 41 (19), 6348-6404, 2012

Stone, D., Evans, M. J., Walker, H. M., Ingham, T., Vaughan, S., Ouyang, B., Kennedy, O. J., McLeod, M. W., Jones, R. L., Hopkins, J., Punjabi, S., Lidster, R., Hamilton, J. F., Lee, J. D., Lewis, A. C., Carpenter, L. J., Forster, G., Oram, D., Reeves, C. E., Baugitte, S., Morgan, W., Coe, H., Aruffo, E., Dari-Salisburgo, C., Giammaria, F., Di Carlo, P. and Heard, D. E., *Radical chemistry at night: comparisons between observed and modelled HO_x, NO_3 and N_2O_5 during the RONOCO project*, Atmospheric Chemistry and Physics Discussions, 13 (4), 9519-9566, 2013

Streets, D. G., Fu, J. S., Jang, C. J., Hao, J., He, K., Tang, X., Zhang, Y., Wang, Z., Li, Z., Zhang, Q., Wang, L., Wang, B. and Yu, C., *Air quality during the 2008 Beijing Olympic Games*, Atmospheric Environment, 41 (3), 480-492, 2007

Stull, R. B., *An Introduction to Boundary Layer Meteorology*, Kluwer Academic Publishers, Dordrecht, 1988

Su, F., Calvert, J. G. and Shaw, J. H., *A FT IR spectroscopic study of the ozone-ethene reaction mechanism in oxygen-rich mixtures*, Journal of Physical Chemistry, 84 (3), 239-246, 1980

Taatjes, C. A., Meloni, G., Selby, T. M., Trevitt, A. J., Osborn, D. L., Percival, C. J. and Shallcross, D. E., *Direct Observation of the Gas-Phase Criegee Intermediate (CH_2OO)*, Journal of the American Chemical Society, 130 (36), 11883-11885, 2008

Taketani, F., Kanaya, Y. and Akimoto, H., *Kinetics of heterogeneous reactions of HO_2 radical at ambient concentration levels with $(NH_4)_2SO_4$ and NaCl aerosol particles*, Journal of Physical Chemistry A, 112 (11), 2370-2377, 2008

Talukdar, R., Zhu, L., Feierabend, K. J. and Burkholder, J. B., *Rate coefficients for the reaction of methylglyoxal (CH_3COCHO) with OH and NO_3 and glyoxal $(HCO)_2$ with NO_3*, Atmospheric Chemistry and Physics, 11 (21), 10837-10851, 2011

Tan, D., Faloona, I., Simpas, J. B., Brune, W., Olson, J., Crawford, J., Avery, M., Sachse, G., Vay, S., Sandholm, S., Guan, H. W., Vaughn, T., Mastromarino, J., Heikes, B., Snow, J., Podolske, J. and Singh, H., *OH and HO_2 in the tropical*

Pacific: Results from PEM-Tropics B, Journal of Geophysical Research: Atmospheres, 106 (D23), 32667-32681, 2001

Tegtmeier, S., Krüger, K., Quack, B., Atlas, E. L., Pisso, I., Stohl, A. and Yang, X., *Emission and transport of bromocarbons: from the West Pacific ocean into the stratosphere*, Atmospheric Chemistry and Physics, 12 (22), 10633-10648, 2012

Thalman, R. and Volkamer, R., *Inherent calibration of a blue LED-CE-DOAS instrument to measure iodine oxide, glyoxal, methyl glyoxal, nitrogen dioxide, water vapour and aerosol extinction in open cavity mode*, Atmospheric Measurement Techniques, 3 (6), 1797-1814, 2010

Thornton, J. and Abbatt, J. P. D., *Measurements of HO_2 uptake to aqueous aerosol: Mass accommodation coefficients and net reactive loss*, Journal of Geophysical Research: Atmospheres, 110 (D8), D08309-D08321, 2005

Thornton, J. A., Jaeglé, L. and McNeill, V. F., *Assessing known pathways for HO_2 loss in aqueous atmospheric aerosols: Regional and global impacts on tropospheric oxidants*, Journal of Geophysical Research: Atmospheres, 113 (D5), D05303-D05318, 2008

Vaattovaara, P., Huttunen, P. E., Yoon, Y. J., Joutsensaari, J., Lehtinen, K. E. J., O'Dowd, C. D. and Laaksonen, A., *The composition of nucleation and Aitken modes particles during coastal nucleation events: evidence for marine secondary organic contribution*, Atmospheric Chemistry and Physics, 6 (12), 4601-4616, 2006

van Pinxteren, M. and Herrmann, H., *Glyoxal and methylglyoxal in Atlantic seawater and marine aerosol particles: method development and first application during Polarstern cruise ANT XXVII/4*, Atmospheric Chemistry and Physics Discussions, 13 (6), 15301-15331, 2013

Varner, R. K., Zhou, Y., Russo, R. S., Wingenter, O. W., Atlas, E. L., Stroud, C., Mao, H., Talbot, R. and Sive, B. C., *Controls on atmospheric chloroiodomethane (CH_2ClI) in marine environments*, Journal of Geophysical Research: Atmospheres, 113 (D10), D10303-D10316, 2008

Vaughan, S., Ingham, T., Whalley, L. K., Stone, D., Evans, M. J., Read, K. A., Lee, J. D., Moller, S. J., Carpenter, L. J., Lewis, A. C., Fleming, Z. L. and Heard, D. E., *Seasonal observations of OH and HO_2 in the remote tropical marine boundary layer*, Atmospheric Chemistry and Physics, 12 (4), 2149-2172, 2012

Vogt, R., Crutzen, P. J. and Sander, R., *A mechanism for halogen release from sea-salt aerosol in the remote marine boundary layer*, Nature, 383 (6599), 327-330, 1996

Vogt, R., Sander, R., von Glasow, R. and Crutzen, P. J., *Iodine Chemistry and its Role in Halogen Activation and Ozone Loss in the Marine Boundary Layer: A Model Study*, Journal of Atmospheric Chemistry, 32 (3), 375-395, 1999

Volkamer, R., Platt, U. and Wirtz, K., *Primary and Secondary Glyoxal Formation from Aromatics: Experimental Evidence for the Bicycloalkyl-Radical Pathway from Benzene, Toluene, and p-Xylene*, Journal of Physical Chemistry A, 105 (33), 7865-7874, 2001

Volkamer, R., Molina, L. T., Molina, M. J., Shirley, T. and Brune, W. H., *DOAS measurement of glyoxal as an indicator for fast VOC chemistry in urban air*, Geophysical Research Letters, 32 (8), L08806-L08810, 2005

Volkamer, R., Spietz, P., Burrows, J. and Platt, U., *High-resolution absorption cross-section of glyoxal in the UV-vis and IR spectral ranges*, Journal of Photochemistry and Photobiology A: Chemistry, 172 (1), 35-46, 2005

Volkamer, R., Jimenez, J. L., San Martini, F., Dzepina, K., Zhang, Q., Salcedo, D., Molina, L. T., Worsnop, D. R. and Molina, M. J., *Secondary organic aerosol formation from anthropogenic air pollution: Rapid and higher than expected*, Geophysical Research Letters, 33 (17), L17811-L17815, 2006

Volkamer, R., San Martini, F., Molina, L. T., Salcedo, D., Jimenez, J. L. and Molina, M. J., *A missing sink for gas-phase glyoxal in Mexico City: Formation of secondary organic aerosol*, Geophysical Research Letters, 34 (19), L19807-L19812, 2007

Volkamer, R., Coburn, S. C., Dix, B. K. and Sinreich, R., *The Eastern Pacific Ocean is a source for short lived atmospheric gases: Glyoxal and Iodine Oxide*, Newsletter of the Climate Variability and Predictability Programme (CLIVAR): Exchanges, 53, 2010

Volkamer, R., Sheehy, P., Molina, L. T. and Molina, M. J., *Oxidative capacity of the Mexico City atmosphere - Part 1: A radical source perspective*, Atmospheric Chemistry and Physics, 10 (14), 6969-6991, 2010

Volkamer, R. and Apel, E., *Observation and modeling of short-lived oxygenated hydrocarbons in the tropical free troposphere*, European Geophysical Union General Assembly, Vienna, 2013

von Glasow, R., Sander, R., Bott, A. and Crutzen, P. J., *Modeling halogen chemistry in the marine boundary layer 1. Cloud-free MBL*, Journal of Geophysical Research: Atmospheres, 107 (D17), 4341-4357, 2002

Vranckx, S., Peeters, J. and Carl, S. A., *Absolute rate constant and $O(^3P)$ yield for the $O(^1D)+N_2O$ reaction in the temperature range 227 K to 719 K*, Atmospheric Chemistry and Physics, 8 (20), 6261-6272, 2008

Wada, R., Beames, J. M. and Orr-Ewing, A. J., *Measurement of IO radical concentrations in the marine boundary layer using a cavity ring-down spectrometer*, Journal of Atmospheric Chemistry, 58 (1), 69-87, 2007

Wagner, N. L., Dubé, W. P., Washenfelder, R. A., Young, C. J., Pollack, I. B., Ryerson, T. B. and Brown, S. S., *Diode laser-based cavity ring-down instrument for NO_3, N_2O_5, NO, NO_2 and O_3 from aircraft*, Atmospheric Measurement Techniques, 4 (6), 1227-1240, 2011

Wang, C. C. and Davis Jr, L. I., *Measurement of Hydroxyl Concentrations in Air Using a Tunable UV Laser Beam*, Physics Review Letters, 32 (7), 349-352, 1974

Wang, C. C., Davis Jr., L. I., Wu, C. H., Japar, S., Niki, H. and Weinstock, B., *Hydroxyl radical concentrations measured in ambient air*, Science, 189 (4205), 797, 1975

Wang, C. C., Davis, L. I., Jr., Wu, C. H. and Japar, S., *Laser-induced dissociation of ozone and resonance fluorscence of OH in ambient air*, Applied Physics Letters, 28 (1), 14-16, 1975

Wang, Y. L., Nagy, J. C. and Margerum, D. W., *Kinetics of Hydrolysis of Iodine Monochloride Measured by the Pulsed-Accelerated-Flow Method*, Journal of the American Chemical Society, 111 (20), 7838-7844, 1989

Warneck, P., *Multi-Phase Chemistry of C_2 and C_3 Organic Compounds in the Marine Atmosphere*, Journal of Atmospheric Chemistry, 51 (2), 119-159, 2005

Washenfelder, R. A., Langford, A. O., Fuchs, H. and Brown, S. S., *Measurement of glyoxal using an incoherent broadband cavity enhanced absorption spectrometer*, Atmospheric Chemistry and Physics, 8 (24), 7779-7793, 2008

Waters, J. W., Froidevaux, L., Read, W. G., Manney, G. L., Elson, L. S., Flower, D. A., Jarnot, R. F. and Harwood, R. S., *Stratospheric ClO and ozone from the Microwave Limb Sounder on the Upper Atmosphere Research Satellite*, Nature, 362 (6421), 597-602, 1993

Wayne, R. P., *Chemistry of Atmospheres*, Oxford University Press, New York, 2000

Weinstock, B., *Carbon monoxide: Residence Time in the Atmosphere*, Science, 168 (3902), 224-225, 1969

Weinstock, B. and Niki, H., *Carbon Monoxide Balance in Nature*, Science, 176 (4032), 290-292, 1972

Welz, O., Savee, J. D., Osborn, D. L., Vasu, S. S., Percival, C. J., Shallcross, D. E. and Taatjes, C. A., *Direct Kinetic Measurements of Criegee Intermediate (CH_2OO) Formed by Reaction of CH_2I with O_2*, Science, 335 (6065), 204-207, 2012

Wessel, S., Aoki, S., Winkler, P., Weller, R., Herber, A., Gernandt, H. and Schrems, O., *Tropospheric ozone depletion in polar regions. A comparison of observations in the Arctic and Antarctic*, Tellus, 50B (1), 34-50, 1998

Western, C. M., *PGOHPER, a Program for Simulating Rotational Structure, via* http://pgopher.chm.bris.ac.uk, University of Bristol, 2013

Whalley, L. K., Furneaux, K. L., Gravestock, T. J., Atkinson, H. M., Bale, C. S. E., Ingham, T., Bloss, W. J. and Heard, D. E., *Detection of iodine monoxide radicals in the marine boundary layer using laser induced fluorescence spectroscopy*, Journal of Atmospheric Chemistry, 58 (1), 19-39, 2007

Whalley, L. K., Furneaux, K. L., Goddard, A., Lee, J. D., Mahajan, A., Oetjen, H., Read, K. A., Kaaden, N., Carpenter, L. J., Lewis, A. C., Plane, J. M. C., Saltzman, E. S., Wiedensohler, A. and Heard, D. E., *The chemistry of OH and HO_2 radicals in the boundary layer over the tropical Atlantic Ocean*, Atmospheric Chemistry and Physics, 10 (4), 1555-1576, 2010

Whalley, L. K., Edwards, P. M., Furneaux, K. L., Goddard, A., Ingham, T., Evans, M. J., Stone, D., Hopkins, J. R., Jones, C. E., Karunaharan, A., Lee, J. D., Lewis, A. C., Monks, P. S., Moller, S. J. and Heard, D. E., *Quantifying the magnitude of a missing hydroxyl radical source in a tropical rainforest*, Atmospheric Chemistry and Physics, 11 (14), 7223-7233, 2011

Whalley, L. K., Blitz, M. A., Desservettaz, M., Seakins, P. W. and Heard, D. E., *Reporting the sensitivity of Laser Induced Fluorescence instruments used for*

HO_2 detection to an interference from RO_2 radicals and introducing a novel approach that enables HO_2 and certain RO_2 types to be selectively measured, Atmospheric Measurement Techniques Discussions, 6 (4), 6249-6292, 2013

Wheeler, T. and von Braun, J., *Climate Change Impacts on Global Food Security*, Science, 341 (6145), 508-513, 2013

WHO, *Air Quality Guidelines: Global Update 2005: Particulate matter, ozone, nitrogen dioxide, and sulfur dioxide*, World Health Organization, Copenhagen, Denmark, 2006

WHO and UN-HABITAT, *Hidden Cities: Unmasking and overcoming health inequalities in urban settings*, World Health Organisation and United Nations Human Settlements Program, Geneva, Switzerland, 2010

Winiberg, F., Smith, S. C., Ingham, T., Malkin, T., Heard, D. E. and Seakins, P. W., *Pressure dependent calibration of a FAGE HO_x instrument using HIRAC*, paper in preparation, 2013

Wittrock, F., Richter, A., Oetjen, H., Burrows, J. P., Kanakidou, M., Myriokefalitakis, S., Volkamer, R., Beirle, S., Platt, U. and Wagner, T., *Simultaneous global observations of glyoxal and formaldehyde from space*, Geophysical Research Letters, 33 (16), L16804-L16809, 2006

WMO, *Executive Summary of the Scientific Assessment of Ozone Depletion: 2010, Global Ozone Research and Monitoring Project*, World Meteorological Organisation, Geneva, Switzerland, 2010

Wong, G. T. F. and Cheng, X.-H., *Dissolved organic iodine in marine waters: role in the estuarine geochemistry of iodine*, Journal of Environmental Monitoring, 3 (2), 257-263, 2001

Wong, K. W. and Stutz, J., *Influence of nocturnal vertical stability on daytime chemistry: A one-dimensional model study*, Atmospheric Environment, 44 (31), 3753-3760, 2010

Wurzler, S., Flossmann, A. I., Pruppacher, H. R. and Schwartz, S. E., *The Scavenging of Nitrate by Clouds and Precipitation*, Journal of Atmospheric Chemistry, 20 (3), 259-280, 1995

Yamamoto, H., Yokouchi, Y., Otsuki, A. and Itoh, H., *Depth profiles of volatile halogenated hydrocarbons in seawater in the Bay of Bengal*, Chemosphere, 45 (3), 371-377, 2001

Yardley, J. T., *Collisional Quenching and Photochemistry of trans-Glyoxal (^3A_u) Molecules* Journal of Chemical Physics, 56 (12), 6192-6197, 1972

Yassaa, N., Peeken, I., Zöllner, E., Bluhm, K., Arnold, S., Spracklen, D. and Williams, J., *Evidence for marine production of monoterpenes*, Environmental Chemistry, 5 (6), 2008, 2008

Yokouchi, Y., Osada, K., Wada, M., Hasebe, F., Agama, M., Murakami, R., Mukai, H., Nojiri, Y., Inuzuka, Y., Toom-Sauntry, D. and Fraser, P., *Global distribution and seasonal concentration change of methyl iodide in the atmosphere*, Journal of Geophysical Research: Atmospheres, 113 (D18), D18311-D18320, 2008

Yu, J., Flagan, R. C. and Seinfeld, J. H., *Identification of Products Containing -COOH, -OH, and -C=O in Atmospherix Oxidation of Hydrocarbons*, Environmental Science & Technology, 32 (16), 2357-2370, 1998

Yu, S., Bhave, P. V., Dennis, R. L. and Mathur, R., *Seasonal and Regional Variations of Primary and Secondary Organic Aerosols over the Continental United States: Semi-Empirical Estimates and Model Evaluation*, Environmental Science & Technology, 41 (13), 4690-4697, 2007

Zeng, G., Heard, D. E., Pilling, M. J. And Robertson, S. H., *A master equation study of laser-generated interference in the detection of hydroxyl radicals using laser-induced fluorescence*, Geophysical Research Letters, 25 (24), 4497-4500, 1998

Zhang, R., Suh, I., Zhao, J., Zhang, D., Fortner, E. C., Tie, X., Molina, L. T. and Molina, M. J., *Atmospheric New Particle Formation Enhanced by Organic Acids*, Science, 304 (5676), 1487-1490, 2004

Zhou, X. and Mopper, K., *Apparent Partition Coefficients of 15 Carbonyl Compounds between Air and Seawater and between Air and Freshwater; Implications for Air-Sea Exchange*, Environmental Science & Technology, 24 (12), 1864-1869, 1990

Zhou, X. and Mopper, K., *Photochemical production of low-molecular-weight carbonyl compounds in seawater and surface microlayer and their air-sea exchange*, Marine Chemistry, 56 (3-4), 201-213, 1997

Zingler, J. and Platt, U., *Iodine oxide in the Dead Sea Valley: Evidence for inorganic sources of boundary layer IO*, Journal of Geophysical Research: Atmospheres, 110 (D7), D07307-D07317, 2005

Appendix A

Table A1. Summary of science flights during summer RONOCO campaign at East Midlands Airport, during which FAGE was operational.

Flight	Date	Take-off and landing times (local time)	Aims
B534	16/07/2010	22:00–02:20	Profile descent from 10,000 ft to 1500 ft from The Wash towards Whitby. Missed approach at Newcastle Airport.
B535	17/07/2010	22:15–02:15	Run at 1500 ft south along the Norfolk coast to Dover. Missed approach at Southend Airport. Series of north–south runs at 1500 ft to detect the Humberside plume.
B536	19/07/2010	22:00–02:00	Missed approach at Southend Airport. Anti-clockwise circuit of London. Missed approaches at Northolt, Gatwick and Southend airports. Transect the London plume in the Thames Estuary.
B537	20/07/2010	22:00–02:20	Profile descent from 11,000 ft to 1500 ft down the Norfolk coast. Missed approach at Southend Airport. Series of runs at altitudes between 1500 ft and upper boundary of polluted air to intercept the plume.
B538	22/07/2010	22:00–02:00	Profile descent from 11,000 ft to 1500 ft from Bristol to south of Pembroke. Detect the plume off the Severn Estuary. Look for ship plumes in the English Channel.
B539	24/07/2010	22:00–02:00	Profile descent from 11,000 ft to 1500 ft, south along the Norfolk coast to Dover or until the aircraft passes into clean air. Profile ascent from 1500 ft to 5000 ft over North Sea. North–south runs at 1500 ft off east coast.
B541	28/07/2010	00:00–04:00	Profile descent from 10,000 ft to 1500 ft heading east from Cromer. Run south at 1500 ft to the Thames Estuary. Missed approach at Southend Airport. Run along coast towards Isle of Wight at 1500 ft. Series of north east–south west NE-SW runs in English Channel including profile ascents and descents to 7000 ft. Series of runs parallel to the south-east coast.

Table A2. Summary of science flights during the SeptEx campaign at East Midlands Airport, during which FAGE was operational

Flight	Date	Take-off and landing times (local time)	Aims
B545	31/08/2010	13:45–18:30	Repeat run along south Cornwall and Devon coasts, between points south of Land's End and Torquay, at altitudes of 5000 ft, 2500 ft, 1000 ft and 100 ft.
B546	01/09/2010	10:00–14:00	Biogenics over East Anglia: Follow the East Anglian coast at 1300 ft to a point south of The Wash; continue inland and circuit of East Anglia at 1300 ft; missed approach at Norwich Airport; ascend to 5000 ft and repeat the circuit; descend to 1300 ft and repeat the circuit
B547a	02/09/2010	09:00–13:00	Fly out to Norfolk coast and descend to minimum safe altitude (~350 m, minimum during flight = 100 m); turn south and follow UK coast, west along the English Channel, crossing Cornwall, then head north above the Irish Sea to land at Prestwick Airport.
B547b	02/09/2010	14:30–18:30	Fly west from Prestwick until over the Inner Hebrides, then descend to the minimum safe altitude (between 200 and 350 m; minimum during flight = 100 m) and head north. Follow the coast of Scotland round to the North Sea then head south along the coast until The Wash.
B548	03/09/2010	10:00–14:15	Anti-clockwise circuit of London at 2300 ft, including missed approaches at Southend, Northolt, and Biggin Hill airports. Repeat circuit.
B549	03/09/2010	16:20–20:30	Dusk flight in North Sea and English Channel. Run down east coast at 5000 ft. Profile descent to 100 ft at a point south of Eastbourne. Continue at 100 ft over Channel until a point south of Bournemouth. Return to south of Eastbourne at 1500 ft. Repeat westwards run at 2500 ft. Repeat eastwards run at 1500 ft (after dusk).
B550a	05/09/2010	09:00–13:00	Biogenics and plume evolution. Circuit of Norwich at 1300ft to intersect biogenic plume. Run north at 1000 ft to the Humber Estuary, with a profile descent to 50 ft followed by ascent to 6000 ft to determine altitude for remaining flight. East-west transits over North Sea off Humberside, at 350 m to intersect urban/industrial plume.
B550b	05/09/2010	14:30–18:00	Biogenics and plume evolution. Circuit of Norwich at 1300ft to intersect biogenic plume. Head north up the east coast, including a profile descent to 50 ft followed by ascent to 6000 ft. Fly in a box pattern off the north-east coast at ~ 200 m.
B552	09/09/2010	09:00–11:45	Ship plume flight. Descend to 3000 ft and look for large vessels in North Sea. Descend to 500 ft to mark position of the ship. Return to 3000 ft and transit back and forth to intersect the plume at increasing distance from the ship. Fly over ship again.

Table A3. Summary of science flights during winter RONOCO campaign at East Midlands Airport, during which FAGE was operational.

Flight	Date	Take-off and landing times (local time)	Aims
B564	11/1/2011	18:00–22:15	Nighttime flight along east coast. Profile descent from The Wash to Northumbrian coast, then missed approach at Newcastle airport. Profile descent after missed approach. Castle wall pattern down east coast at 1500 ft.
B565	14/1/2011	17:00–21:44	Nighttime flight over North Sea. Profile descent to north Norfolk coast. Castle wall pattern heading north east towards Cleaver Bank, at 1500 ft, to intersect Humberside plume.
B566	16/1/2011	18:00–22:50	Nighttime flight over North Sea. Profile descent to 1500 ft off Lincolnshire coast. Head north up the coast, then box pattern heading north east off Whitby to detect plume off east coast/Humberside.
B567	18/1/2011	06:00–10:50	Dawn flight up and down east coast. Missed approach at East Midlands airport, then at Humberside airport. Descend to 1500 ft over the Wash then head north up the coast. Missed approach at Edinburgh airport. Profile descent through Edinburgh plume over the Firth of Forth. Return south down coast, parallel to northern leg but offset to the east. Profile through the Humberside plume.
B568	19/1/2011	14:50–19:50	Dusk flight over English Channel. Descend to 500 ft over the Channel, then head east to a point south of Eastbourne. Continue to a point south of Dover, then return west with profiles between 2000 ft and 50 ft. Missed approach at Lydd airport. Repeat east–west runs at 1500 ft.
B569	20/1/2011	14:30–19:20	Dusk flight to Edinburgh. Head to a point just off north east coast, south of Scottish border. Descend to 500 ft. Run north across direction of wind to intersect plume. Box pattern over North Sea, drifting with wind at 1500 ft. Missed approach at Edinburgh airport.
B570	23/1/2011	15:00–19:30	Dusk flight around south coast. Head east along the Channel, with vertical sawtooth patterns between 50 ft to just above the polluted layer. Return west and perform sawtooth patterns. Perform eastward run at 1500 ft, displaced south from the first eastward run. Missed approach at Shoreham airport, Bournemouth airport, and Exeter airport. Final eastward run along Channel at 1500 ft.
B571	24/1/2011	12:50–17:40	Daytime flight near Weybourne, for Met Office AQUM project. Head to a point east of Norfolk over North Sea. Turn west and profile down to 50 ft. Profile up to ~ 500 ft above the polluted layer. Perform easterly and westerly runs with vertical sawtooth profiles between 50 and 500 ft. Head north 30 miles and perform westerly then easterly runs, profiling between 50 and 500 ft. Repeat twice, offset to the south.

Table A4. Details of instruments, species measured, and operators onboard BAe-146 research aircraft during RONOCO and SeptEx flights. FAAM = Facility for Airborne Atmospheric Measurements.

Instrument	Species Measured	Technique	Operator
Core Chemistry CO Aerolaser	CO	Commercial gas analyser: VUV (λ = 150 nm) fast fluorescence	FAAM
Core Chemistry O_3, TECO	O_3	Commercial gas analyser: UV (λ = 254 nm) absorption by ozone; photometric analysis	FAAM
FAAM Fast NO_x and TECO NO_x	NO, NO_2, NO_x ($NO + NO_2$)	Commercial gas analyser: chemiluminescence from $NO + O_3$ reaction	FAAM
PSAP (Particle Soot/Absorption Photometer)	Fine particle soot	Change in optical transmission of a filter caused by particle deposition	FAAM
CPC (Condensation Particle Counter)	Total aerosol number or average aerosol size distribution	Particles enlarged by condensing agent butan-1-ol, and detected by scattering of laser light	FAAM/ University of Manchester
CCN (Cloud Condensation Nuclei Counter)	CCN	Sample flowed through heated column; particles exiting the column are counted and sized	FAAM/ University of Manchester
AMS	Aerosol composition	Time of Flight Aerosol Mass Spectrometry	University of Manchester
CIMS	HNO_3	Fast response Chemical Ionisation Mass Spectrometry	University of Manchester
WAS	Whole air sample including VOCs	Canister air sample followed by laboratory-based GC, including VOCs	University of York
PERCA	Sum of total peroxy radicals [$RO_2 + HO_2$]	Chemical amplification	University of Leicester
BBCEAS	NO_3, N_2O_5	Broadband cavity - enhanced absorption spectroscopy	University of Cambridge
PTR-MS	Oxygenates, VOCs	Mass Spectrometry	University of East Anglia
Peroxide	Total peroxide	Peroxide stripped from sample air by stripping coil and measured by fluorimetry	University of East Anglia
Formaldehyde	Formaldehyde	Hantzsch technique: Liquid-phase reaction of formaldehyde followed by fluorescence detection of resulting adduct	University of East Anglia
PAN-GC	Peroxyacetyl nitrate	Gas chromatography instrument onboard aircraft	University of York
LIF	NO_2	Laser-induced fluorescence	University of L'Aquila, Italy
FAGE	OH, HO_2	Laser-induced fluorescence at low pressure	University of Leeds

Table A5. Mean concentrations and, in parentheses, mixing ratios of alkenes measured during summer flights (hydrocarbon data courtesy of Dr James Lee, Shalini Punjabi and Prof. Ally Lewis, University of York and NCAS).

	Concentration / molecule cm^{-3}, mixing ratio / pptv			
	Dawn	Day	Dusk	Night
ethene	9.3×10^8 (39.0)		1.2×10^9 (52.7)	1.3×10^9 (55.0)
propene	3.0×10^8 (12.0)		2.5×10^8 (10.6)	3.1×10^8 (13.5)
iso-butene	2.4×10^7 (1.0)		4.3×10^7 (1.8)	7.0×10^7 (3.0)
trans-2-butene	1.9×10^7 (0.8)		4.1×10^7 (1.7)	4.2×10^7 (1.8)
cis-2-butene	0.0 (0.0)		0.0 (0.0)	1.2×10^6 (0.05)
1,3-butadiene	2.3×10^7 (1.0)		4.5×10^6 (0.2)	4.2×10^7 (1.8)
1-butene	4.5×10^7 (1.9)		5.9×10^7 (2.5)	9.0×10^7 (3.9)
1-pentene	2.3×10^7 (1.0)		4.8×10^6 (0.2)	2.0×10^7 (0.9)
trans-2-pentene	0.0 (0.0)		0.0 (0.0)	5.8×10^5 (0.03)
isoprene	4.6×10^6 (0.2)		2.1×10^6 (0.09)	1.6×10^7 (0.7)

Table A6. Mean concentrations and, in parentheses, mixing ratios of alkenes measured during SeptEx flights (hydrocarbon data courtesy of Dr James Lee, Shalini Punjabi and Prof. Ally Lewis, University of York and NCAS).

	Concentration / molecule cm^{-3}, mixing ratio / pptv			
	Dawn	Day	Dusk	Night
ethene		1.0×10^9 (42.6)		
propene		1.4×10^8 (5.7)		
iso-butene		2.9×10^7 (1.2)		
trans-2-butene		1.7×10^7 (0.7)		
cis-2-butene		0.0 (0.0)		
1,3-butadiene		8.4×10^6 (0.3)		
1-butene		2.6×10^7 (1.1)		
1-pentene		0.0 (0.0)		
trans-2-pentene		0.0 (0.0)		
isoprene		2.7×10^7 (1.1)		

Table A7. Mean concentrations and, in parentheses, mixing ratios of alkenes measured during winter flights (hydrocarbon data courtesy of Dr James Lee, Shalini Punjabi and Prof. Ally Lewis, University of York and NCAS).

	Concentration / molecule cm^{-3}, mixing ratio / pptv			
	Dawn	Day	Dusk	Night
ethene	2.1×10^9 (80.5)	1.7×10^9 (67.7)	1.3×10^9 (53.0)	2.6×10^9 (104.5)
propene	2.8×10^8 (10.7)	3.0×10^8 (12.1)	3.0×10^8 (12.0)	5.3×10^8 (21.5)
iso-butene	5.0×10^7 (2.0)	5.7×10^7 (2.3)	6.1×10^7 (2.4)	8.3×10^7 (3.4)
trans-2-butene	3.0×10^7 (1.2)	1.6×10^7 (0.7)	1.7×10^7 (0.7)	3.9×10^7 (1.6)
cis-2-butene	0.0 (0.0)	0.0 (0.0)	0.0 (0.0)	0.0 (0.0)
1,3-butadiene	2.6×10^6 (0.1)	9.2×10^6 (0.4)	0.0 (0.0)	1.9×10^7 (0.8)
1-butene	3.8×10^7 (1.5)	3.5×10^7 (1.4)	5.3×10^7 (2.1)	8.3×10^7 (3.4)
1-pentene	0.0 (0.0)	3.1×10^6 (0.1)	1.2×10^7 (0.5)	6.4×10^6 (0.3)
trans-2-pentene	0.0 (0.0)	0.0 (0.0)	9.4×10^5 (0.03)	7.1×10^5 (0.03)
isoprene	0.0 (0.0)	0.0 (0.0)	0.0 (0.0)	0.0 (0.0)

Table A8. Rate constants from the MCM v3.2 (Jenkin *et al*., 1997, Saunders *et al*., 2003) for the reactions of O_3-initiated RO_2 radicals with various species (HO_2, NO, NO_3, and RO_2, respectively). Only those RO_2 radicals which produce HO_2 are shown. $BR_{RO2,prop}$ is the branching ratio for the radical-propagating $RO_2 + RO_2$ channel, which produces the alkoxy (RO) radical. k_2 to k_5 are the rate constants as shown in Figure 4.14 for CH_3O_2. Rate constants are given in units of $molecule^{-1}\ cm^3\ s^{-1}$.

	k_2	k_3	k_4	k_5	$BR_{RO2,prop}$
CH_3O_2	3.8E−13•exp(780/t)	2.3E−12•exp(360/t)	2.3E−12	1.82E−13• exp(416/t)	0.33
$C_2H_5O_2$	4.3E−13•exp(870/t)	2.6E−12•exp(380/t)	2.3E−12	3.10E−13	0.6
$NC_3H_7O_2$	1.5E−13•exp(1300/t)	2.9E−12•exp(350/t)	2.3E−12	6.00E−13	0.6

Table A9. Mean concentrations and, in parentheses, mixing ratios of NO_3 and O_3 during summer, SeptEx and winter flights.

	Mean concentration / molecule cm^{-3}, mixing ratio / pptv for NO_3, ppbv for O_3					
	Summer		SeptEx		Winter	
	O_3 / 10^{11}	NO_3 / 10^8	O_3 / 10^{11}	NO_3 / 10^8	O_3 / 10^{11}	NO_3 / 10^8
Dawn	4.9 (20.8)	0.0 (0.0)			11.1 (43.3)	1.7 (6.6)
Day			9.8 (40.1)	0.0 (0.0)	9.8 (39.6)	0.9 (3.5)
Dusk	10.3 (43.5)	5.2 (21.9)			9.5 (37.7)	1.1 (4.4)
Night	9.6 (40.5)	5.8 (24.5)			9.4 (38.2)	2.0 (8.2)

Table A 10. Rate constants from the MCM v3.2 (Jenkin *et al*., 1997, Saunders *et al*., 2003) for reactions of NO_3 with alkenes, and for subsequent reactions. Where NO_3 + alkene can produce two different RO_2 radicals, the alkenes are labelled (a) and (b) and each channel is treated separately. In these cases, the branching ratios of this initial step are given with k_1. Branching ratios are also given for k_2 (RO_2 + HO_2). Where a channel is not active for a particular alkene, the rate constant has been left blank. Rate constants are given in units of molecule^{-1} cm^3 s^{-1}.

Alkene	k_1 (NO_3 + alkene)	k_2	k_3	k_4	k_5	k_6	k_7
ethene	3.3E−12•exp(−2880/T)	0.387•2.91E−13•exp(1300/T)	2.7E−12•exp(360/T)	2.3E−12	6.0E−13	2.5E−14•exp(−300/T)	7.0E+03
propene (a)	0.35•4.6E−13•exp(−1155/T)	0.52•2.91E−13•exp(1300/T)	2.7E−12•exp(360/T)	2.3E−12	6.0E−13	2.5E−14•exp(−300/T)	7.0E+03
propene (b)	0.65•4.6E−13•exp(−1155/T)	0.52•2.91E−13•exp(1300/T)	2.7E−12•exp(360/T)	2.3E−12	4.0E−14	2.5E−14•exp(−300/T)	7.0E+03
1-butene (a)	0.65•3.2E−13•exp(−950/T)	0.625•2.91E−13•exp(1300/T)	2.7E−12•exp(360/T)	2.3E−12	2.5E−13	2.5E−14•exp(−300/T)	7.0E+03
1-butene (b)	0.32•3.2E−13•exp(−950/T)	0.625•2.91E−13•exp(1300/T)	2.7E−12•exp(360/T)	2.3E−12	2.0E−12	2.5E−14•exp(−300/T)	7.0E+03
iso-butene (a)	0.2•3.4E−13	0.625•2.91E−13•exp(1300/T)	2.7E−12•exp(360/T)	2.3E−12	1.3E−12	2.5E−14•exp(−300/T)	7.0E+03
iso-butene (b)	0.8•3.4E−13	0.625•2.91E−13•exp(1300/T)	2.7E−12•exp(360/T)	2.3E−12	6.7E−15		1.0E+06
trans-2-butene	3.90E−13	0.625•2.91E−13•exp(1300/T)	2.7E−12•exp(360/T)	2.3E−12	2.5E−13	2.5E−14•exp(−300/T)	4.0E+04
cis-2-butene	3.50E−13	0.625•2.91E−13•exp(1300/T)	2.7E−12•exp(360/T)	2.3E−12	2.5E−13	2.5E−14•exp(−300/T)	4.0E+04
1,3-butadiene (a)	0.5•1.03E−13	0.625•2.91E−13•exp(1300/T)	2.7E−12•exp(360/T)	2.3E−12	2.5E−13	2.5E−14•exp(−300/T)	
1,3-butadiene (b)	0.5•.03E−13	0.625•2.91E−13•exp(1300/T)	2.7E−12•exp(360/T)	2.3E−12	2.5E−13	2.5E−14•exp(−300/T)	
trans-2-pentene (a)	0.5•3.70E−13	0.706•2.91E−13•exp(1300/T)	2.7E−12•exp(360/T)	2.3E−12	2.5E−13	2.5E−14•exp(−300/T)	4.0E+04
trans-2-pentene (b)	0.5•3.70E−13	0.706•2.91E−13•exp(1300/T)	2.7E−12•exp(360/T)	2.3E−12	2.5E−13	2.5E−14•exp(−300/T)	4.0E+04
1-pentene (a)	0.65•1.20E−14	0.706•2.91E−13•exp(1300/T)	2.7E−12•exp(360/T)	2.3E−12	2.5E−13	2.5E−14•exp(−300/T)	7.0E+03
1-pentene (b)	0.35•1.20E−14	0.706•2.91E−13•exp(1300/T)	2.7E−12•exp(360/T)	2.3E−12	1.3E−12	2.5E−14•exp(−300/T)	7.0E+03
iso-prene	3.15E−12•exp(−450/T)	0.706•2.91E−13•exp(1300/T)	2.56E−12•exp(360/T)	2.3E−12	1.3E−12	2.5E−14•exp(−300/T)	

Table A11. Rate constants from the MCM v3.2 (Jenkin *et al.*, 1997, Saunders *et al.*, 2003) for the reactions of O_3 with alkenes. Where O_3 + alkene can produce two different RO_2 radicals, the branching ratios have been given with k_1, and each channel has been treated separately. k_{dec}, the rate constant for decomposition of the Criegee radical, is 1.0×10^6 molecule^{-1} cm^3 s^{-1}. Branching ratios are also given for decomposition of the Criegee intermediate *via* channels producing HO_2, HO_2 + RO_2, and RO_2.

Alkene	k_1 (O_3 + alkene) / molecule^{-1} cm^3 s^{-1}	Branching ratio to HO_2 (BR_{HO2})	Branching ratio to HO_2 + RO_2 ($BR_{HO2,RO2}$)	Branching ratio to RO_2 (BR_{RO2})
ethene	9.1E−15•exp(−2580/T)	0.13		
propene (a)	0.5•5.5E−15•exp(−1880/T)	0.36		
propene (b)	0.5•5.5E−15•exp(−1880/T)		0.2	0.36
iso-butene (a)	0.5•2.7E−15•exp(−1630/T)	0.82		
iso-butene (a)	0.5•2.7E−15•exp(−1630/T)			0.82
trans-2-butene (a)	6.64E−15•exp(−1059/T)		0.125	0.57
1,3-butadiene (a)	0.5•1.34E−14•exp(−2283/T)	0.08		
1,3-butadiene (b)	0.5•1.34E−14•exp(−2283/T)	0.76		
1-butene (a)	0.5•3.55E−15•exp(−1745/T)	0.36		
1-butene (b)	0.5•3.55E−15•exp(−1745/T)		0.2	0.36
cis-2-butene	3.22E−15•exp(−968/T)		0.125	0.57
trans-2-pentene (a)	0.5•1.60E−16		0.125	0.57
trans-2-pentene (b)	0.5•1.60E−16		0.125	0.57
1-pentene (a)	0.5•1.0E−17	0.36		
1-pentene (b)	0.5•1.0E−16		0.2	0.36
isoprene (a)	0.2•1.03E−14•exp(−1995/T)		0.255	0.27
isoprene (b)	0.2•1.03E−14•exp(−1995/T)	0.27		
isoprene (c)	0.2•1.03E−14•exp(−1995/T)	0.27		
isoprene (d)	0.2•1.03E−14•exp(−1995/T)		0.255	0.27

Appendix B

Table B1. Oceanic measurements during cruise SO218. Details of instruments, species or parameters measured and operators RV *Sonne* during the SHIVA Western Pacific measurement campaign.

Instrument	Species or parameters measured	Technique	Operator
GC-MS	Halocarbons, oxygenated VOCs, dimethyl sulphide, N_2O, CH_4,	Gas chromatography coupled with mass spectrometry. *In situ* and post-cruise analysis	IFM-GEOMAR[a]
GC-ECD	Halocarbons, iodate (IO_3^-), iodide (I^-)	Gas chromatography coupled with electron capture ionization and detection	IFM-GEOMAR
Filtration and microscopy	Phytoplankton	Size, cell number and species composition measured by filtering seawater and observing samples through microscope	AWI[b]
FRRF	Chlorophyll-*a*	Fast repetition rate fluorometry of chlorophyll-*a*	AWI, UPH[c]
Filtration, HPLC	Phytoplankton pigments	Oceanic pigments collected by filtration of seawater samples and separated by high-performance liquid chromatography	AWI
Bongo net	Zooplankton	Species composition and abundance, and molecular biology. Samples collected with fine mesh net drawn through water	UM[d]
Net and filtration	Microbial community	Species composition and abundance, and molecular biology. Samples collected with fine mesh net and by filtering water samples	UNIMAS[e]
Contros 'HydroC' sensor	PCO_2 (dissolved carbon dioxide)	Diffusion of CO_2 through membrane followed by infrared spectrometry	IFM-GEOMAR
Oxygen optode	PO_2 (dissolved oxygen)	Diffusion of O_2 through membrane followed by fluorescence quenching	IFM-GEOMAR
AutoAnalyzer	Oceanic nutrients	Post-cruise continuous flow analysis of nitrate and phosphate	IFM-GEOMAR
CDOM Filtration	Humic acids	Filtration of seawater samples to collect organic matter. Absorption spectroscopy.	IFM-GEOMAR, AWI
CTD	Salinity, temperature, depth	Conductivity, temperature, depth (CTD) instrument deployed at all depths while ship was stationary	IFM-GEOMAR
Bottle rosette sampler	Water samples, various species	VSLS, OVOC, DMS, nutrients, N_2O, CH_4, O_2	IFM-GEOMAR

Table B1 (continued).

Instrument	Species or parameters measured	Technique	Operator
Thermo-salinograph	Salinity, temperature	Continuous measurements in surface sea water	IFM-GEOMAR
ADCP	Surface currents	Acoustic Doppler Current Profiler. Direction of water flow of upper 200 m	IFM-GEOMAR, UM
Water age tracer	CFCs	Post-cruise gas chromatography analysis of CFCs to determine water age in Sulu Sea	IFM-GEOMAR
RAMSES	Radiation	Upward and downward spectral radiation measurements	AWI

a. Helmholtz Centre for Ocean Research, Kiel, Germany
b. Alfred Wegener Institute for Polar and Marine Research, Bremerhaven, Germany
c. Marine Science Institute, University of the Philippines, Diliman, Quezon City, Philippines
d. University of Malaya, Kuala Lumpur, Malaysia
e. University of Malaya Sarawak, Koto Samarahan, Sarawak, Malaysia

Table B2. Atmospheric measurements during cruise SO218. Details of instruments, species or parameters measured, and operators RV *Sonne* during the SHIVA Western Pacific measurement campaign.

Instrument	Species or parameters measured	Technique	Operator
μ-DIRAC	Halocarbons	Temperature-programmed gas chromatography coupled with electron capture ionization and detection	UCAM[a], IFM-GEOMAR, RSMAS[b]
MAX-DOAS	BrO, IO	Multi-axis differential absorption spectroscopy	UHEI[c], UBREM[d]
Aerosol filtering	Br in aerosol	Aerosol capture on filters	UEA[e], IFM-GEOMAR
PICARRO G1301 Analyser	CH_4, CO_2, H_2O	Wavelength-scanned near IR cavity ring down spectroscopy	DLR[f]
Thermo O3 TE49C	O_3	Commercial analyser using UV absorption spectroscopy	DLR
Aero-Laser AL5001	CO	Commercial analyser using vacuum UV fluorimetry of CO	DLR
Diffusion denuder system	I_2, HOI + ICl	Diffusion denuder tube sampling followed by post-cruise GC analysis	ULEEDS[g], UMAINZ[h]

Table B2 (continued).

Instrument	Species or parameters measured	Technique	Operator
LIF	IO	Laser-induced fluorescence spesctroscopy	ULEEDS
AIMS-1, AIMS-2	BrO, Br, HBr, SO_2, HCl	Chemical ionization mass spectrometry	DLR
Radio sonde	Temperature, pressure, humidity, wind speed	Balloon-borne sondes up to 30 km altitude	IFM-GEOMAR
Ozone sonde	O_3 vertical profiles	Balloon-borne sondes up to 30 km altitude	IFM-GEOMAR
Tracer release	Perfluorocarbon	Release of tracer and detection from DLR Falcon aircraft	DLR
Disdrometer	Precipitation, rain drop size	*In situ* measurements	IFM-GEOMAR
Ship instruments	Position, temperature, pressure, humidity, wind speed and direction, water depth		IFM-GEOMAR

a. University of Cambridge, UK
b. Rosenstiel School of Marine and Atmospheric Science, University of Miami, USA
c. Institute of Environmental Physics, University of Heidelberg, Germany
d. Institute of Environmental Physics, University of Bremen, Germany
e. University of East Anglia, UK
f. German Aerospace Centre, Oberpfaffenhofen, Germany